Cranfield University

School of Engineering

PhD Thesis

Adam Ruggles

Flame Behaviour in an Acoustically Forced Gas Turbine Combustor.

Supervisor Prof B Moss

March 2009

This thesis is submitted in partial fulfilment of the requirements for the Degree of Doctor of Philosophy.

ABSTRACT

A swirl stabilised dump combustor capable of imposing flow perturbations creating combustion instabilities has been designed and commissioned. The capability of supplying different fuel mixtures (methane hydrogen blends) has been incorporated. Additional capability is the facility to preheat the combustion air prior to chamber entry and to be able to introduce dilution air into the chamber. The chamber itself is of fused silica quartz to allow non-intrusive optical diagnostics.

High speed CH* Chemiluminescence has been performed to qualitative characterise the unstable heat release rate of pure methane and methane hydrogen blended flames to allow analysis of the mean deconvoluted flame structure. High speed Stereoscopic Particle Imaging Velocimetry (SPIV) has been used to acquire the flow field throughout the chamber and focusing upon the Annulus entry. These diagnostics have been phase locked to the imposed perturbation.

A selection of conditions is presented with three different perturbation frequencies within the low frequency range. These reveal vastly different reacting and flow field structures. The difference of structures is attributed to behaviour of the IRZ (Internal Recirculation Zone) and CRZ (Corner Recirculation Zone) in altering the flame shape. All conditions exhibited the axisymmetric/bubble vortex breakdown mechanism responsible for stabilisation. Both single cell and double cell structures were observed in the mean flow field vector maps. The mechanism of oscillating heat release rate is attributed to oscillations of flame surface area. Profiles of integrated heat release rate and flame exhibit the same profile shape and behaviour correlating very well. The inclusion of hydrogen had no quantifiable impact upon the mean reacting or flow field structures using the current diagnostics. Investigation into the nature of the turbulence of the shear layers close to the annulus is presented for three perturbation frequencies. This highlighted periodic structures within the turbulence corresponding to the imposed perturbation frequency. It was found that excitation of both shear layers for all turbulent components was not always true and depended upon the perturbation frequency and flow structure close to the annulus. Two oppositely rotating vorticity structures were revealed attached to the outer and inner circumference of the annulus. These structures protruded into the chamber and spread radially. Frequency analysis of these two structures revealed both were oscillating at the perturbation frequency indicating vorticity shedding. The mean vorticity structures are shown to be influenced also by the behaviour of the recirculation zones.

ACKNOWLEDGEMENTS

In the process of completing this work the list of people to thank for their time, knowledge input and general support grew with the years. I must thank in particular my fellow colleagues at Cranfields' former Optical Diagnostic group, Alessio, Dimitry, Edouard, Edouardo, Eudoxious, Thierry, Nick, Maz and Fathia. Their shared experiences and encouragement made me feel I was not alone when the times were tough and were always ready to cheer me up. I would also like to thank colleagues within the Turbulence group, Ben, Marco (Big), Marco (Little) and Sanjay who also offered advice and insight.

I would like to thank Dr James Kelman for supervising me through this study, technical advice and his full support, Professor Douglas Greenhalgh who managed our group, and finally Professor Barrie Moss for supervision and help during my final months.

Special thanks must go to the technical staff at Cranfield who went out of their way to help during the most fraught period of my life, Alan Hutchinson, Brian Scully, Clive Wood, David Whittington and Derek Brown.

I would like to thank my parents whose continued support and encouragement through my education has allowed me the opportunities and experiences I have today. Finally I would like to acknowledge my brother, Ian for his exuberant optimism.

LIST OF CONTENTS

LIST OF FIGURES

LIST OF TABLES

NOTATION

Roman Symbols

Symbol	Description	Unit
a	Cylinder radius	m
$\|a\|$	Normalised spatial velocity gradient acting across a PIV interrogation window	
B_{mn}	Roots of the Bessel Function	
$B_G(x, y)$	Background image collected by camera	
c	Speed of sound in a gas/gas mixture	ms^{-1}
C_P	Specific Heat at constant pressure	$JKg^{-1}K^{-1}$
C_V	Specific Heat at constant volume	$JKg^{-1}K^{-1}$
$C(dx, dy)$	Correlation between the first and second images at horizontal and vertical displacements within an interrogation window.	
d	Arbitrary particle diameter	
d_D	Displacement correlation peak diameter	
d_{eq}	Equivalent diameter of Annulus	mm
d_0	Distance from Object plane to Lens Plane	mm
d_p	Seeding particle diameter	µm
D	Jet Diameter	
D_a	Damköhler number	
D_I	PIV Interrogation window dimension	
D_{ij}	Deconvolution Operator	
D_{TH}	Thermal Diffusivity	m^2s^{-1}
d_t	Particle Image Diameter	
dx	Pixel horizontal displacement of the cross correlation technique used for PIV processing	
dy	Pixel vertical displacement of the cross correlation technique used for PIV processing	
$E_B(x, y)$	Dc level (Dark Current) of camera	
e_{ij}	Rate of strain/deformation tensor	
e_{ds}	Error associated with the Lavision correlation algorithms	pixels
e_{vi}	Error associated with measured velocity component i	ms^{-1}
F	Les Filter	
fi	Most amplified frequency of a shear layer	Hz
f_j	Preferred frequency of a shear layer	Hz
f_{mnq}	Frequency of modes and harmonics of the longitudinal, radial and tangential dimensions of a cylinder.	Hz

Symbol	Description	Unit
f_{puls}	Perturbation frequency applied to a flow	Hz
F_I	Loss of displacement correlation due to in plane motions	
$F_F(x,y)$	FlatField (Optical response) image of camera	
$F(r)$	Field function	
F_0	Loss of displacement correlation due to out of plane motions	
F_n	Final Image Number	
g	Gravitational acceleration	ms^{-2}
h_s	Enthalpy (Sensible)	JKg^{-1}
$I(x,y)$	Desired collected light by camera	
$I_1(x,y)$	Pixel intensity in the first Interrogation window	
$I_{1avg}(x,y)$	Mean intensity in the first Interrogation window	
$I_2(x,y)$	Pixel intensity in the second Interrogation window	
$I_{2avg}(x+dx,y+dy)$	Mean intensity in the second Interrogation window	
k	Strain	
K_a	Karolovitz number	
L	Length of cylinder	m
$Li(x,t)$	The ith damping process with respect to time and space	
l_t	Integral length scale of turbulence	
M	Magnification	
m	Radial mode	
N	Actual seeding density	
N_I	Initial seeding density	
n	Tangential mode	
n_r	Raw Image Number	
p	Pressure	Bar
$P(r)$	Line of sight integrated Field function	
P'	Instantaneous pressure fluctuation	
q	Longitudinal mode	
Q	Correlation strength	
Q'	Instantaneous heat release	
R	Outer Radius of Annulus	mm
Re	Reynolds Number	
R_h	Inner Radius of Annulus/Radius of Bluff Body	mm
R_{Mix}	Gas Constant for a mixture	
R_U	Universal Gas Constant	
$R_I(x,y)$	Raw image recorded by camera	

Symbol	Description	Unit
S	Swirl Number. Dimensionless number yielding the ratio of angular momentum flux and linear momentum.	
St_i	Strouhal number of most amplified frequency of a shear layer	ms^{-1}
St_j	Strouhal number of preferred frequency of a shear layer	ms^{-1}
Str	Strouhal Number. Dimensionless number relating a length scale, velocity and frequency	
s_d	Reaction Zone Displacement Speed	ms^{-1}
s_L	Laminar Flame Speed	ms^{-1}
s_T	Turbulent Flame Speed	ms^{-1}
T	Temperature	^oK
$\overline{u}_x$	Mean Axial Velocity	ms^{-1}
$\overline{u}$	Mean Absolute Velocity	ms^{-1}
u_{rms}	RMS of Absolute Velocity	ms^{-1}
u_i	Velocity Component	
u_θ	Settling velocity of seeding particle	ms^{-1}
V_K	Diffusion velocity of species K	
vx	Radial Velocity Component	ms^{-1}
vy	Axial Velocity Component	ms^{-1}
vz	Tangential Velocity Component	ms^{-1}
| v |	Absolute Velocity	ms^{-1}
Y_K	Species k mass fraction	

Greek Symbols

Symbol	Description	Unit
α	Scheimpflug angle – between lens and image planes	^{o}
ε	Kinetic Energy Dissipation	m^2s^{-3}
ε_b	Displacement correlation peak bias error	
ρ	Fluid Density	Kgm^{-3}
ρ_f	Fluid density	Kgm^{-3}
θ	Angle between object and lens planes	^{o}
θ_0	Momentum Thickness of a shear layer	mm
ρ_p	Density of seeding particle material	Kgm^{-3}
λ	Wavelength of Light	nm
Φ	Equivalence ratio of a premixed combustible mixture	
τ_c	Characteristic time scale of combustion	s
τ_m	Characteristic time scale of turbulent scale	s
τ_{ij}	Stress Tensor	

Symbol	Description	Unit
Θ	Reduced Temperature function (also known as the progress variable)	
$\dot{\omega}$	Reaction Rate	$Molcm^{-3}s^{-1}$
δ_L	Laminar Flame Thickness	mm
δ_T	Turbulent Flame Thickness	mm
$\delta^r(\ )$	Error of variable	
γ	The adiabatic index - ratio of Specific Heats	
Γ_1	Vortex centre scalar	
Γ_2	Vortex boundary scalar	
μ	Fluid Viscosity	$Kgm^{-1}s^{-1}$
Δt	Time separation between successive laser pulses	µs
Δ	Uncertainty of following variable	
ΔX_0	Mean displacement within PIV interrogation cell	
∇U_{ij}	Velocity gradient tensor	
Ω_{ij}	Vorticity/Rotation tensor	

ACRONYMS

Abbreviation	Description
CCD	Charge Coupled Device
CFD	Computational Fluid Dynamics
CMOS	Complimentary Metal Oxide Semiconductor
CRF	Combustion Research Facility
CRZ	Corner Recirculation Zone
DNS	Direct Numerical Simulation
EM	Electro Magnetic
FFT	Fast Fourier Transform
FTF	Flame Transfer Function
FSD	Flame Surface Density
ICCD	Intensified Charge Coupled Device
IRZ	Internal Recirculation Zone
LDA	Laser Doppler Anemometry
LDV	Laser Doppler Velocimetry
LES	Large Eddy Simulation
LPC	Lean Premixed Combustion
NO_x	Oxides of Nitrogen
PAH	Polycyclic Aromatic Hydrocarbons
PDF (or pdf)	Probability Density Function
PIV	Particle Image Velocimetry
PLIF	Planar Laser Induced Fluorescence
ppmv	Particles per million volume of dry air
PTV	Particle Tracking Velocimetry
PVC	Precessing Vortex Core
RANS	Reynolds Averaged Navier Stokes
RSG	Relative Specific Gravity
SE	Standard Error
SCR	Selective Catalytic Reduction
SO_x	Oxides of Sulphur
SPIV	Stereo Particle Image Velocimetry
SNR	Signal to Noise Ratio
STP	Atmospheric Standard Temperature and Pressure
RMS (or rms)	Root Mean Square

INTRODUCTION

The utilisation of combustion as a means of converting the potential energy in hydrocarbons to useful energy to perform work has been the key to the rapid development of the civilisations of man. From simply providing heat energy for warmth to enabling the industrial revolution of Britain in the 18th and 19th centuries, the heat energy released by combustion has allowed man to develop his surroundings and create almost any mechanical device, vehicle or weapon he has desired. Advancements in technology have been possible because of advancements in the knowledge and the application of combustion. It was the rapid industrial drive that encouraged scientists and engineers to learn more about combustion. This knowledge led to increased energy efficiency, a reduction in the size of many devices, optimisation of energy cycles, reduction in harmful by products and improved worker safety. Centuries later, man is still dependent upon combustion and hydrocarbons as energy carriers. Combustion is responsible for the majority of the electrical energy created that powers the modern home and workplace (Nuclear being the other dominant source of electrical power), and is also the primary mechanism that provides energy for man's vehicles. On a planet which has seen an exponential increase in man's numbers and development, the pressure on finite reserves of hydrocarbon sources and concern over the environmental consequences, ever more stringent environmental restrictions are being made regarding the emissions and pollutants of any combustion process. Coupled with the drive for increased efficiency, combustion science has evolved into one of the most complex subjects in order to meet these challenges.

Combustion science is a culmination of many disciplines involving chemistry, fluid mechanics and thermodynamics simultaneously. Most treatments of combustion subdivide the topic into premixed, a homogenously premixed mixture of fuel and oxidant prior to combustion, or diffusion flames, where the fuel and oxidant are introduced at the point of reaction. Both of these categories can be further divided into laminar and turbulent areas whereby turbulence increases the complexity of any combustion description. Most practical devices, including gas turbines, operate in a turbulent regime. The preferred approach of gas turbine engineers to meet more stringent regulations has been to adopt Lean Premixed Combustion (Dry Low NO_x). The term 'lean' refers to a further subdivision of the premixed flame where stoichiometry is used as a divisor. The other subdivisions are 'rich' and 'stoichiometric'.

LPC in gas turbines has been chosen as the preferred strategy to achieve pollutant reduction. This method was chosen because of the identification of a regime where the flame temperature can be reduced to a value that minimises NO_x and the corresponding equivalence ratio is lean promoting complete oxidation of CO and UHC. The reduction of flame temperature has no negative impacts upon power output as the hot gases would have been cooled by dilution air prior to turbine entry. The transition to LPC has incurred a severe drawback, one of combustion instabilities. It has been found that unsteady heat release and unsteady pressure waves can occur and become coupled through one of several

mechanisms, if satisfying the Rayleigh criterion the instability becomes self-sustaining and in some situations self-amplifying. The implications of this are varying performance, flame stability issues, unacceptable pollutant performance and structural damage. Due to the complex coupling of a wide range of simultaneous processes occurring during the instability detailed experiments are required to advance the understanding of the instability phenomenon.

Hydrogen addition to natural gas (methane) for LPC has recently been considered as a viable solution to improving the stability and efficiency of the combustion system. Hydrogen posses a much higher flame speed, a lower flammability limit and higher flame temperature than methane which could provide flame stability and response benefits. Extension of the lean flammability limit and an increased radical population allow for the reduction in equivalence ratio and attainable flame temperature. This allows the reduction of temperature dependent NO_x. The increased number of radicals creates a more strain resistant flame which is then able to complete the oxidation of UHC and CO. The inclusion of hydrogen and reduction of equivalence ratio also results in a reduction of CO_2.

In parallel to experimentation CFD has evolved to a point where it is able to predict the behaviour and occurrence of instabilities in simplified but large scale combustion chambers. LES is the most promising CFD technique for research purposes and is a compromise between RANS and DNS, both of which are limited in their application to the phenomena of instabilities. Although promising, LES of combusting flows is still new and itself suffers from a serious disadvantage of not being able to resolve the flame front on its computational grid. The description of the most important feature of the flow, the reaction zone, is therefore treated by sub grid models. Most simulations of a combustor are accompanied by an experimental data set for validation, refinement of the numerics, and development of a flame speed or reaction rate model. The advantage of LES over experiments is that once correct the results will allow the engineer to view the flow field and any scalar field (provided it was computed) in the 3D environment. These variables may not be possible to measure experimentally. LES can also be used to develop less costly 1D codes that provide an approximate 'correct' solution.

Combustion experimentation has advanced greatly with the application of laser and optical diagnostics replacing physical probes which alter the fluid behaviour they are sampling. Laser/optical methods are typically used in conjunction with a CCD/ICCD camera to allow a non intrusive measurement that is frozen in time with respect to the combusting field. The most common Chemiluminescence, Mie scattering, Rayleigh scattering, Raman scattering, and PLIF can be used to measure heat release rate, visualise the flow, measure the flow field velocity (PIV), the flame temperature, mole fraction, species concentration and reaction zone marking. Careful selection of the appropriate diagnostic applied to a specific combustion arrangement can offer an invaluable insight to the combustion process.

This thesis is part of an IEA gas Turbine project investigating the impact of hydrogen addition to methane for gas turbine LPC. In conjunction with the US DOE and CRF (SNL) an international collaboration has been instigated to develop similar swirl stabilised dump combustors that will investigate different

aspects of combustion. Databases will be generated for the express purpose of LES model validation that will occur simultaneously with other institutes part of the program. The experimental work of this thesis was to adapt the baseline design of the swirl burner and to artificially force the flow making the combustion unstable. The application of high speed CH Chemiluminescence and high speed Stereo PIV was performed to gain an insight into the reacting and flow field structures of various flows and perturbations. A database of conditions was collected and processed for the express purpose of model validation.

Chapters 1 to 4 describe the background to this work. Chapter 1 describes the formation of key pollutants within the combustion chamber. Their impact upon the atmosphere is described and highlighted as a major motivation for this work. Reduction strategies are discussed leading to the selection of LPC as the most desirable option for cleaner combustion. Chapter 2 firstly describes the typical stabilisation mechanism for swirl dump combustors before moving on to give an overview of instability feedback mechanisms necessary that can perpetuate the instability. A review of experimental investigations of swirl stabilised dump combustors is then undertaken with emphasis upon laser diagnostic applications. Observations and results are highlighted along with the difficulty in attaining this data. The inclusion of hydrogen is then analysed with respect to strain, flame speed, stabilisation advantages and pollutant reduction benefits. Chapter 3 offers an overview of the different computational approaches. A more detailed explanation of LES is given, highlighting the potential advances over RANS. Current limitations of the application of LES are covered emphasising the need for high quality experimental validation. Finally results of LES of swirling dump combustors during unstable operation are presented complementing the experimental observations of the previous chapter. Chapter 4 describes the application of non intrusive laser diagnostics to combustion science. In particular the application of techniques that yield information regarding flame structure, heat release rate and the chamber flow field.

A detailed description of the manufactured swirl burner is given in Chapter 5. Overviews of each subassembly are given concentrating on the key features for each assembly. The gas flow control system is also described. The lean limits for various flow rates and imposed instability frequencies are given. The database created by this work is shown. For the conditions presented in this thesis a greater analysis is given commencing with sensory data of pressure and temperature prior to chamber entry.

A comprehensive description of the optical arrangements for the diagnostics used is presented in Chapter 6. The experimental parameters are described and the processing strategy adopted for each diagnostics is given. An account of the difficulties encountered regarding acquisition of flow field data is given to elucidate the experimental choices made to overcome these challenges. A thorough uncertainty analysis is included of the diagnostics used including a treatment of statistical uncertainties.

Chapter 7 presents the mean reacting fields and flow fields phase locked to the induced perturbation for pure methane. Flow field features are identified and their behaviour described. Comparisons are made of the different perturbation frequencies and hydrogen content.

Chapter 8 is dedicated to defining the local turbulence close to the annulus within the shear layers. Phase dependent RMS profiles are presented according to a triple decomposition approach and are analysed with turbulent PDFs, Reynolds stress profiles and turbulent frequency spectra.

Chapter 9 concerns the nature of the vorticity and identified vortices for each condition. An investigation of whether coherent vortex shedding is present is performed. In addition the frequency of vorticity and vortex shedding is addressed.

Finally Chapters 10, 11 and 12 contain the conclusions and recommendations from this work. A comparison of the instabilities observed in this work with those considered in earlier chapters is made. Emphasis is made upon improving the experimental set up regarding the application and practical difficulties that are inherent of investigations in enclosed combustion. Other recommendations are made regarding what is required to obtain a complete understanding of combustion instabilities from an experimental aspect.

1 EMISSIONS AND THE ENVIRONMENT

Gas turbine combustion is a steady flow process in which the hydrocarbon fuel is burned with a large amount of excess air to keep the turbine inlet temperature at an appropriate value. This is essentially a clean process and until recently there was no concern over emissions. This has changed and now the reduction of emissions has become the most important factor of gas turbine design. This is due to increased understanding of pollution and with increasing number of gas turbines used through out the world.

The equations for combustion express conservation of mass in molecular terms following the re-arrangement of molecules during the combustion process.

$$C_xH_y + \left(x + \frac{y}{4}\right)O_2 \rightarrow xCO_2 + \frac{y}{2}H_2O \qquad \text{Eq 1-1}$$

Current gas turbines in use today were designed to operate with a rich equivalence ratio to affect maximum engine performance across the whole power range. While performance was achieved it has led to the formation of pollution in the forms of nitrogen oxides (NO_x), sulphur oxides (SO_x), carbon dioxide (CO_2), carbon monoxide (CO), unburned hydrocarbons (UHC) and smoke (soot). The social, political and environmental concerns over emissions have led to the research and development of combustion technologies that will minimise these emissions over the power range. It will be shown that solutions for a particular pollutant are conflicting with the reduction of other pollutants. This has led to innovative ideas and an increased understanding of emission formation and reduction.

For every kilogram of oxygen in the atmosphere there is 3.29kg of nitrogen also present. This is normally considered to be inert and unchanged at the exhaust of a gas turbine. However, within the combustor small amounts of nitrogen oxides are formed where the temperature is extremely high. The simplified analysis of the combustion reaction assumes complete combustion of the carbon in the fuel to CO_2. In reality the process is never complete and results in CO and UHC also being present at the exhaust. As already mentioned a large amount of excess air is used, implying that a substantial amount of oxygen will also be found at the exhaust. Therefore the contents of the exhaust gas will contain carbon dioxide, oxygen, nitrogen, water and low concentrations of pollutants. Among these the amount of carbon dioxide is important due to its association with atmospheric changes.

The pollutants that will be present in the exhaust gas include nitrogen oxides, carbon monoxide, unburned hydrocarbons, sulphur oxides and soot. Although the amount of these pollutants as a proportion of the total exhaust mass is small, the large exhaust flows produce significant amounts of these pollutants. Specifically with regard to industrial gas turbines which operate for long periods of time the quantity of pollutants will increase dramatically. This will lead to a high concentration of pollutants in the surrounding area. This was first experienced in

Los Angeles, America, where the increased number of nitrogen oxides reacted with the abundant sunlight, combined with the local geography to form brown smog [1]. Gas turbines are increasingly used for electrical power generation where they are operated at a fixed level for long periods of time. In conjunction with cogeneration installations, which operate at full load continuously and are located closer to residential areas, they have become affected by strict emission regulation for environmental and human health reasons.

1.1 Emission Formation

The pollutants and emissions with the largest environmental impact have been exposed to a number of international and national legislations in order to reduce the amounts produced. The dominant emission of any combustion process is CO_2 and is a result of hydrocarbon oxidation. As more knowledge concerning global warming and the impact of atmospheric CO_2 becomes known a growing need to reduce the amount of man made CO_2 atmospheric deposits is needed. Principally the only way to reduce CO_2 emission is to reduce the amount of hydrocarbon combustion through more efficient combustion or combustion of hydrogen which has no carbon. The formation of pollutants within the gas turbine combustor is not straight forward. Their formation occurs at different operating conditions and therefore under different combustor conditions. NO_x is produced at higher power levels compared to CO and UHC which are indicative of lower power levels. The reasons for this will be explained.

1.1.1 Nitrogen Oxides

The formation of nitrogen oxides (nitric oxide, NO, and nitrogen dioxide, NO_2) can be attributed to four chemical production mechanisms within the combustor; Thermal NO, Prompt NO, Nitrous oxide reactions, and finally Fuel NO. As this thesis is based upon methane and hydrogen combustion there is no fuel bounded nitrogen. As a consequence the formation of NO through the associated mechanisms of fuel bound nitrogen will not be pursued further. From these sources the greatest contribution is from Thermal NO, followed by Prompt NO and finally NO from the Nitrous oxide mechanisms. The proportion of nitric oxide of NO_x is far greater than that of nitrogen dioxide due to post flame oxidation.

As its name suggests Thermal NO is produced within local hot spots of the combustor and are created according to the Zeldovich reactions between atmospheric nitrogen and oxygen atoms as shown in Eq 1-2 [2]. The first two reactions are endothermic and require both atomic oxygen and nitrogen which are present in large quantities at temperatures above 1800K. The final reaction requires two radicals, atomic nitrogen and hydroxyl, and is only important at higher temperatures. The creation of Thermal NO once above 1800K increases exponentially. This temperature threshold is due to the large activation energy required to form NO. Thermal NO is also very sensitive to temperature changes once above this threshold. A mean flame temperature of 2200K undergoing a fluctuation of 90K will experience a change in the rate of NO_x formation by a factor of approximately two [3]. The Zeldovich reactions are fast reactions and as such reducing the residence time has a minimal reducing effect. In order to

reduce the creation of Thermal NO_x it is clear that control of the flame temperature must be achieved and kept below 1800K.

$$\begin{aligned} N_2 + O &\leftrightarrow NO + N \\ N + O_2 &\leftrightarrow NO + O \\ N + OH &\leftrightarrow NO + H \end{aligned} \qquad \text{Eq 1-2}$$

Prompt NO is a complex fast reaction mechanism [4] and is formed locally at the reaction zone under rich or ultra lean conditions where there is an abundance of radicals. Under rich conditions (Φ>1) carbon containing radicals (CH, HCN and CN) attack nitrogen molecules [5]. Ultra lean conditions will produce O and OH radicals which will attack the nitrogen. Prompt NO becomes noticeable when low combustion temperatures are experienced and Thermal NO is diminished.

Nitric oxide (NO) may also be created through the nitrous oxide (N_2O) reactions [6]. Nitrous oxide is an intermediate species which is of particular importance in lean methane flames for the creation of NO [7]. At high temperatures N_2O is formed within the flame front via a recombination reaction involving N_2, O and a third body. For lower temperatures (<1350K) the reaction of N_2 and HO_2 produces OH and N_2O. Once formed the possible paths for N_2O are; dissociation via a third body collision - a reversal of its creation just outlined, dissociation by the radicals O and H, and finally conversion to NO.

$$\begin{aligned} N_2O + H &\leftrightarrow N_2 + OH \\ N_2O + O &\leftrightarrow N2 + O \\ N_2O + OH &\leftrightarrow N_2 + HO_2 \\ N_2O + O &\leftrightarrow NO + NO \end{aligned} \qquad \text{Eq 1-3}$$

Here the first reaction is common for rich flames where as the remaining three are more important for lean flames.

Nitrous Oxide itself may be emitted as a pollutant although in quantities smaller than the preceding oxides it still plays an important part in ozone tropospheric chemistry due to its long lifetime. Formation is from the reactions outlined above and also through those below [8].

$$\begin{aligned} NH + NO &\leftrightarrow N_2O + H \\ NCO + NO &\leftrightarrow N_2O + CO \\ N_2 + O + M &\leftrightarrow N_2O + M \end{aligned} \qquad \text{Eq 1-4}$$

The first reaction is important under low temperature conditions. The second and third reactions become important in rich conditions, the third even more so at high temperatures in large O atom concentrations. N_2O can be removed via a reaction with H resulting in N_2 and OH. This reaction is temperature dependent and can be impeded by quenching resulting in N_2O increases.

Nitrogen dioxide, NO_2, is formed predominantly in the gas turbine dilution zones, the turbine and the exhaust sections where there is a large concentration of NO

and excess air. As the second half of NO_x, nitrogen dioxide is always present in small amounts compared to its partner nitric oxide. At the flame front the forming reaction is HO_2 with NO [7].

$$NO + HO_2 \leftrightarrow NO_2 + OH$$
$$NO + O_2 \leftrightarrow NO_2 + O_2 \qquad \text{Eq 1-5}$$

Nitrogen dioxide as mentioned can form in the exhaust where there is a high presence of NO, low temperatures and low hydrocarbon presence with a reaction with molecular oxygen. The presence of fast removal reactions at high temperatures however reduce nitrogen dioxide to a transient species with regards to combustion and explain its small contribution to NO_x.

$$NO_2 + H \leftrightarrow NO + OH$$
$$NO_2 + O \leftrightarrow NO + O_2 \qquad \text{Eq 1-6}$$

The formation of the different nitrogen oxides outlined indicates different reaction mechanisms for their creation. Specifically concentrating upon NO, it is evident that Thermal NO is dependent upon large concentrations of atomic oxygen [2, 9] and that this reaction is temperature sensitive. The highest temperatures within the combustor will occur locally at the reaction zone and within its proximity. Prompt NO_x is formed via carbon and hydrocarbon radical attack of nitrogen. These radicals will be of highest concentration at the reaction zone. The absolute concentration of these radicals is dependent upon the equivalence ratio of the mixture. For lean or rich combustion these will react with nitrogen. Prompt NO is opposite to thermal NO in that the key reaction has a smaller activation energy and is thusly more prominent at lower temperatures. As well as being less sensitive to temperature fluctuations .The formation of NO via the Nitrous Oxide mechanism is dependent upon the quantity of nitrous oxide. This quantity is controlled by reactions with atomic hydrogen and is temperature dependent. The effect of pressure upon NO formation depends upon temperature. At temperatures where thermal NO is dominant increases in pressure produce small increases in NO_x concentration. At lower temperatures where Prompt NO and Nitrous oxide NO are dominant pressure appears to have no impact upon NO_x concentration. The general trend identified from the literature is NO_x proportional to $Pressure^n$. Where n was found to increase with temperature until approximately 0.5 where by NO_x is once again dominated by Thermal NO [3]. The exact dependence of NO_x upon pressure is still unclear and there is a wide range of values for n dependent upon combustion geometry and equivalence ratio [10]. Therefore two interlinked variables can be identified that are responsible and are controllable for NO_x creation, flame temperature and equivalence ratio. Flame temperature is theoretically a maximum at stoichiometric conditions. The creation of NO_x as a whole is exponentially dependent upon flame temperature with significant quantities produced above 1850K [2]. This is due to the dominant contribution of thermal NO to total NO_x. NO_x also displays a linear dependence upon the residence time of the nitrogen within the flame zone. This dependence decreases as leaner equivalence ratios are used [11].

1.1.2 Carbon Monoxide

Carbon Monoxide is a result of incomplete oxidation in the combustor. At the flame front the oxidising radicals such as OH, HCO react faster with hydrocarbon species than CO. CO oxidation therefore occurs after the gases have left the flame zone when hydrocarbon species concentrations have dropped. As a consequence of oxidation occurring post flame, the oxidation rate is reduced due to low post flame temperatures [3]. The oxidation rate can be reduced further if there is insufficient oxygen to form CO_2 such as in rich flames. Other explanations for a reduced oxidation rate include quenching of post flame products due to cold combustor walls, inadequate mixing of fuel and air prior to combustion creating locally excessive rich and lean pockets resulting in incomplete combustion, insufficient burning rates due to deficient residence times or aerodynamic strain (high velocity gradients). In all flames CO will be produced by dissociation of CO_2 and thusly the emission of CO is unavoidable at any stoichiometry. The amount produced can be minimised with equivalence ratios between 0.7-0.9 [12]. This corresponds to a sufficiently high flame temperature and a sufficient quantity of oxidising radicals. The major reaction of CO removal is;

$$CO + OH \rightarrow CO_2 + H \qquad \text{Eq 1-7}$$

Above an equivalence ratio of 1.0 and oxygen levels are insufficient to complete the reaction process transforming the C to CO_2. Below 0.7 the post flame temperature is lower, requiring longer residence times to complete oxidation and an increase of dissociation from CO_2. In both of these cases oxidation is achieved by;

$$CO + H_2O \rightarrow CO_2 + H_2 \qquad \text{Eq 1-8}$$

Maintaining an optimum equivalence ratio to achieve a maximum flame temperature minimises the amount of CO produced by accelerating the conversion of CO to CO_2. The combination of a lean equivalence ratio and high flame temperatures will reduce the propensity for incomplete combustion and therefore CO.

1.1.3 Unburned Hydrocarbons

Unburned Hydrocarbons (UHC) consist of fuel in the form of vapour and products of thermal degradation of the parent fuel to species of lower molecular weight. The occurrence of UHC is testimony to incomplete combustion and is attributed to poor mixing of the fuel and air prior to combustion, poor chemical combustion rates from either an insufficient flame temperature or a rich equivalence ratio, and non uniform combustion within the chamber. The behaviour of UHC is similar to that of CO, although with more complex kinetics.

1.1.4 Sulphur Oxides

The sulphur contained within the hydrocarbon fuel will be entirely oxidised to form sulphur dioxide, SO_2, and sulphur trioxide SO_3. The only viable solutions

are to remove the sulphur content prior to combustion, or the use of a fuel without sulphur content, such as methane (natural gas) or hydrogen.

1.1.5 Soot

Carbon particulates are produced by rich mixtures or locally rich parts of lean flames due to non uniform mixing. The formation of soot consists of four steps; inception, surface growth, oxidation and coagulation, with coagulated particles becoming clusters by agglomeration. Their introduction into the atmosphere is undesired as the soot can contain Polycyclic Aromatic Hydrocarbons (PAHs), which have the potential to cause cancer. Soot particles contain primarily carbon and hydrogen. The soot process is not fully understood and work is being carried out to develop suitable models, from this work trends have been identified. For example premixed flames show a decrease in soot formation with increased temperature. The opposite is observed for diffusion flames [13]. In practical systems the majority of soot is oxidised before leaving the combustor, but the remaining soot plus additional hydrocarbons become a source of air pollution called particulates.

1.1.6 Summary

To surmise the formation of NO_x is dependent upon the equivalence ratio, flame temperature and to a lesser extent pressure within the combustor. The two important variables are linked. The same is true for CO where it has been identified that fuel rich flames and insufficiently hot flames exhibit increased CO emissions. This is due to insufficient oxidation. The trend of UHC follows that of CO for the same reasoning. Figure 1-1 shows the effect of equivalence ratio and flame temperature upon these emissions. As can be seen from the first graph NO_x emissions are a maximum slightly on the lean side of stoichiometry. The emission then falls rapidly by using leaner or richer mixtures. The same graph shows both CO and UHC which exhibit a minimum for lean mixtures, while increasing for rich and ultra lean mixtures. The second graph shows the effect of temperature upon NO_x and CO. NO_x shows an exponential rise when the temperature exceeds 1700K. CO shows a corresponding decrease at this temperature before starting to rise again at 1900K. From these two graphs and the review of emission formation it is clear that to minimise these pollutants a lean equivalence ratio should be used while maintaining the combustion temperature between 1700K to 1900K.

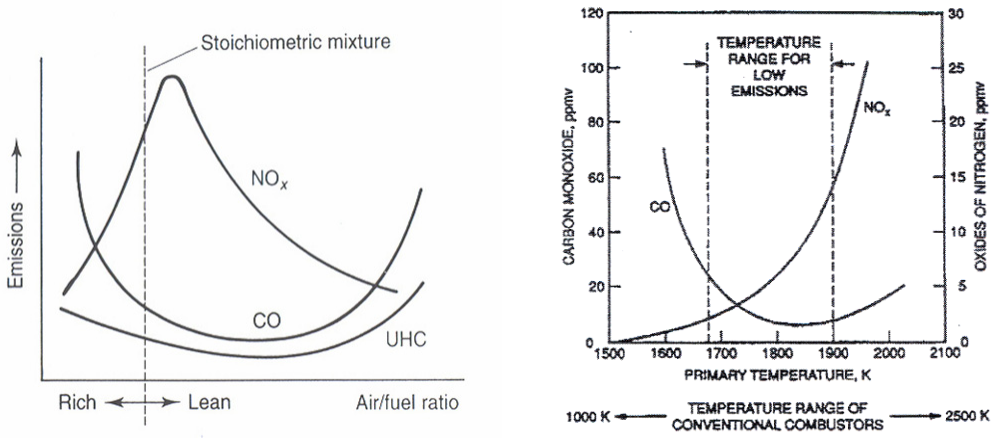

Figure 1-1 Left: Graph showing behaviour of NO_x, UHC and CO emissions against Air fuel ratio [14]. Right: Graph showing NO_x and CO emissions against temperature [12].

1.2 Atmospheric Impact

The activities of man are not without effects upon his surroundings and combustion is no different. The impact of gas turbine combustion, specifically here for power generation, upon the earth's atmosphere is the dominant driving force for gas turbine research. The subject of combustion product interaction within the atmosphere is complex and the magnitude of their effect is under much debate. Key areas of interest are the rise of global temperatures, the destruction of the ozone layer within the stratosphere and the creation of local smog.

Of importance for land based gas turbines is the impact of emissions in the troposphere, particularly within the boundary layer in contact with the surface. As combustion is used in a vast range of industries and commodities the CO_2 created by man is reaching substantial levels and is not without effect. Fossil fuel consumption has led to an increase of atmospheric CO_2 content from 280ppmv in pre-industrial times to 358ppmv in 1994 corresponding to 750G tonnes [15]. The results of increased CO_2 levels are interference with the natural global carbon cycle and green house effect. In parallel to disruption to the green house effect photochemical smog has been well documented in the proximity of urban, industrialised areas where primary pollutants cause the creation of secondary pollutants such as O_3 which in excessive concentrations become detrimental to health.

To account for increased troposphere O_3 levels and photochemical smog it has been shown that O_3 can be formed via the oxidation of CH_4 and CO with the OH radical. Carbon monoxide content can be increased above natural levels by gas turbine combustion emission and by oxidation of UHCs with OH via intermediate species. Once oxidised the products then react with NO to form NO_2 [16, 17].

$$\begin{aligned} CH_4 + OH &\rightarrow CH_3 + H_2O & \qquad CO + OH &\rightarrow CO_2 + H \\ CH_3 + O_2 + M &\rightarrow CH_3O_2 + M & \qquad H + O_2 + M &\rightarrow HO_2 + M \\ CH_3O_2 + NO &\rightarrow CH_3O + NO_2 & \qquad HO_2 + NO &\rightarrow OH + NO_2 \end{aligned} \qquad \text{Eq 1-9}$$

This conversion of NO to NO_2 is done by HO_2 and RO_2 where R is any alkyl. Once converted the NO_2 is photolysed by the sun's radiation, forming NO and O which reacts with O_2 to form O_3.

$$\begin{aligned} NO_2 + hv(\lambda \le 435nm) &\rightarrow NO + O \\ O + O_2 + M &\rightarrow O_3 + M \end{aligned} \qquad \text{Eq 1-10}$$

This series of reactions can be one possible explanation for the increase of overall background O_3 levels. In polluted areas there is an abundance of NO_x and CO, the majority of which is NO and can be converted slowly to NO_2 by reacting with O_2. Once formed the NO_2 will react with sunlight resulting in O. This will react with O_2 to form O_3. This contribution to O_3 concentration will be determined by the sunlight intensity and the NO_2/NO ratio. In addition O_3 may be formed via the reactions with polluting CO and tropospheric chemistry involving naturally occurring CO and CH_4. None of these sources are sinks for the radicals involved which means that they are continuously recycled in these reactions during daylight.

As well as affecting atmospheric changes these pollutants presence leads to the formation of atmospheric acids. The strong acids are sulphuric acid (H_2SO_4), nitric acid (HNO_3), hydrochloric acid (HCI), and methane sulfonic acid (CH_3SO_3H). Although all are detrimental only nitric and sulphuric acid will be considered here. Nitric acid is formed by a reaction between NO_2 and OH.

$$NO_2 + OH \rightarrow HNO_3 \qquad \text{Eq 1-11}$$

The reaction is limited to hours of daylight when the OH radical is produced. During the night a different reaction, NO_2 with O_3 producing NO_3 becomes dominant (normally NO_3 photolysed during daylight). This radical is then converted by hydrogen abstraction from a hydrocarbon or aldehyde. Sulphuric acid can be produced by a number of different mechanisms and either in gaseous or aqueous phase. H_2SO_4 concentrations are dependent on the concentrations of oxidants and therefore are extremely variable. By far the most dominant gaseous mechanism is with the OH radical.

$$\begin{aligned} SO_2 + OH &\rightarrow HOSO \\ HOSO_2 + O_2 &\rightarrow HO_2 + SO_3 \\ SO_3 + H_2O &\rightarrow H_2SO_4 \end{aligned} \qquad \text{Eq 1-12}$$

In the presence of water, in the form of fog, clouds or rain, SO_2 will dissolve and aqueous phase oxidation can occur. Once atmospheric acids are formed they can leave the atmosphere with precipitation creating acid rain.

1.3 Emission Reduction Stratagems

Gas turbines were traditionally operated in the non premixed mode with rich mixtures. As a result of the turbulent flow field and variable mixing the stoichiometric flame fronts resulted in high NO_x emissions of 200 ppmvd.

Emissions control for NO_x was first applied to stationary gas turbines in the 1970's Los Angeles. It was found that using water injection when burning oil could reduce the NO_x emission to 75 ppmv. This figure was adopted as the standard and all new installations have had to meet this figure. Over time this figure has been refined further [18]. Regulations regarding industrial gas turbines are unique to each country and sometimes within a country if the environment is particularly sensitive (southern California).

Three techniques have been developed that will minimise emissions. The first has already been mentioned and that is of water (or steam) injection. The water is injected into the combustion chamber to lower the flame temperature. It was found that a 40% reduction of NO_x was achieved [18]. To achieve this half as much water as fuel was required and to reduce NO_x further water and fuel may be of equal proportions. The implications of this is vast amounts of water are needed considering all the gas turbines in use and the period of operation. Also the water needed must be demineralised so not to cause corrosion of the components. The disadvantages of this method are the cost of the water and its availability in different countries. The environment also poses a problem if the ambient temperature is below freezing for long periods of time. Thus increasing cost with the need for insulation and heating. Finally it was found that although increasing the water fuel ratio decreases NO_x it leads to an increase in both CO and UHC as the flame temperature is lowered further.

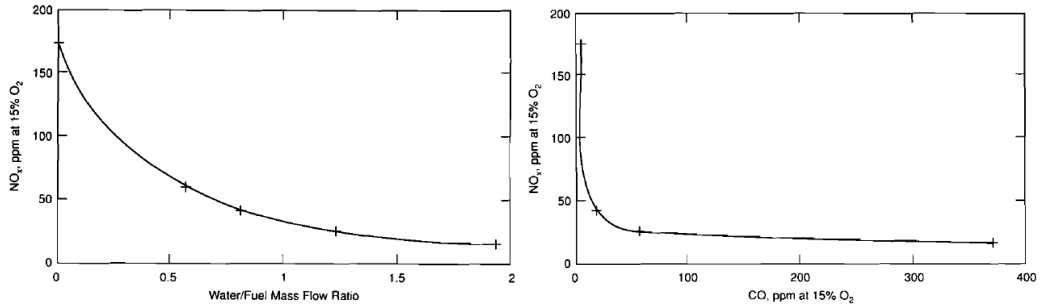

Figure 1-2 Left: Graph showing NOx as a function of water addition for a natural gas combustor with a pressure ratio of 30. Right: Graph showing the relationship between CO and NO_x formation when using water addition [3].

The second is termed Selective Catalytic Reduction (SCR) and is located at the exhaust not the combustion chamber. This technique is used where extremely low NO_x limits are required (<10ppmv). A catalyst is used in conjunction with ammonia (NH_3) converting NO_x to N_2 and H_2O. The reaction occurs within a limited temperature band of 285°C to 400°C and therefore can only be used if the gas turbine has an exhaust system where the temperature is sufficiently low. The disadvantages of this system are the handling of noxious fluids, control of the ammonia with varying operating conditions and the induced cost. Staged combustion, that of utilising a rich small pilot flame and a secondary lean combustion zone does avoid stoichiometric conditions in principle. However the limited mixing time means that the rich hot gases can not be guaranteed to mix with the air to obtain lean conditions resulting in unacceptable NO_x concentrations [3]. The third and most favoured technique is termed Dry Low NO_x as no water is involved. Dry Low NO_x makes use of the fact that NO_x is reduced when the mixture is lean. A reduction of flame temperature by utilizing

lean equivalence ratios reduces NO_x concentrations. The reduction in equivalence ratio must be such that the flame temperature is not reduced so that to cause an increase in CO and UHC concentrations. An operating range of 0.7 to 0.9 ensures the minimisation of pollutant formation corresponding to a temperature range of 1700K to 1900K. A lean flame also maintains the thermal efficiency of the gas turbine. The post combustion lean flame temperature is equal to the former stoichiometric one that is required to be diluted and cooled by the addition of dilution air. In effect using a lean premixed mixture is simply transferring the point in which the dilution air is added while achieving the same turbine entry temperature. The major problem with lean mixtures is the combustion instability throughout the operating range that has been discovered. A change from liquid fuels to natural gas has also been of benefit removing the SO_x and fuel bound NO from the gas turbine emissions.

The most important feature of pollutant formation is flame temperature. A reduction of flame temperature by utilizing lean equivalence ratios reduces NO_x concentrations. The reduction in equivalence ratio must be such that the flame temperature is not reduced so that to cause an increase in CO and UHC concentrations. An operating range of 0.7 to 0.9 ensures the minimisation of pollutant formation corresponding to a temperature range of 1700K to 1900K.

2 GAS TURBINE INSTABILITIES

Gas Turbine instabilities have been the largest single drawback of the Lean Premixed Combustion (LPC) strategy favoured to reduce emissions and pollutants. Although not a new phenomena in non premixed systems (liquid fuelled rockets) their presence in LPC systems was unexpected and directly impacts the goals of the LPC system. Instabilities lead to stability issues of blowout or flashback of the flame, hugely varying pollutant performance and structural damage through thermo mechanical fatigue. The instabilities are characterised by a fluctuating heat release rate, inlet flow and a feedback mechanism linking the two. Previous treatments have been the experimental identification of instability frequencies and the development of a mechanical solution. Typically a unit to pulsate the fuel supply out of phase with the instability or a Helmholtz resonator addition to damp the instability. In parallel to this simple 1D acoustic models are developed but are typically gas turbine specific and do not address the physics of the instability itself.

The focus of this chapter is upon LPC systems in swirl stabilised dump combustors. Firstly typically observed flow field features of stable operation will be considered for LPC swirl stabilised dump combustors. The possible causes of instabilities are briefly discussed before focusing upon experimental work and their findings.

2.1 Typical swirl stabilised dump combustor dynamics

Swirl stabilised dump combustors have become increasingly popular as a means to stabilise high velocity combustion within the chamber. Recirculation zones are created in the chamber, which recirculate radicals and hot burnt products back to interact with and ignite the fresh gas flow, thus maintaining a constant reaction rate. This depends upon the residence time of the recirculation zones, radical lifetimes, heat or radical loss to the walls and the mixing of the recirculation contents with the fresh gas flow.

The utilisation of a dump plane (sudden expansion) creates Corner Recirculation Zones (CRZ) as the flow changes from the axial to the radial direction and is subsequently drawn upstream towards the dump plane by the low pressure centre. Swirl in moderate values (S=0.6) imparts a tangential component and thusly the fluid flows in a helical motion [19]. Therefore the fluid now travels a larger distance for the same axial length of combustor. This increases the residence time of reactants, improves mixing and thusly improves the efficiency of the combustor. For stronger swirling flows the phenomena of vortex breakdown has been observed. This leads to an Internal Recirculation Zone (IRZ) which flows upstream along the chamber centre axis. The inclusion of a bluff body creating an annular type of inlet flow also promotes the formation of an IRZ as a low pressure centre will naturally be formed at the end of the bluff body. The specific arrangement of recirculation zones is highly dependent upon the combustor geometry, combusting regime (premixed or diffusion), fuel injection

method, exhaust profile and Reynolds and swirl numbers. A good overview can be found in the literature [20].

2.1.1 Vortex Breakdown

Vortex breakdown as stated is linked to the swirl number of the inlet flow. With any swirl number an axial pressure gradient is created downstream as the flow is redistributed from the axial direction. This pressure gradient is insufficient to cause a flow reversal. Above a critical swirl number a stronger correlation between axial and tangential velocity will become evident. This in turn will lead to a stronger axial pressure gradient. At this point the kinetic energy of the flow will be insufficient to overcome the gradient and flow reversal will occur [19]. Physical geometry such as a bluff body will promote the occurrence of vortex breakdown and even a sudden expansion which promotes a radial redistribution of axial velocity will increase the strength of the pressure gradient while reducing axial kinetic energy [21]. Also of importance is the presence of a flow restriction/area reduction at the exit of the combustor. This restriction will also contribute to the axial pressure gradient [22]. Once vortex breakdown has begun the shape and behaviour of this feature is controlled by the ratio of tangential and axial velocity. Various vortex breakdown structures have been observed and a total of 7 forms described [23]. These are based upon three dominant forms, the spiral, bubble (axisymmetric) and double helix type [24, 25]. Fundamental breakdown mechanisms were first investigated by using simple jet arrangements often using water and a dye solution used as a marker.

2.1.2 Bubble (Axisymmetric) Type

This breakdown type is characterised by a stagnation point on the jet centre axis followed by an expansion enveloping the recirculating fluid. The 'bubble' is axisymmetric over most of its length and although seeming quiescent, the interior is controlled by low frequency motions. This was speculated to be due to fluid exchange at the downstream part of the bubble with the surrounding flow [24, 25]. A toroidal vortex ring was found to exist towards the rear of the bubble which oscillated about the axis of the bubble with a regular frequency. The location of the bubble is susceptible to small disturbances and therefore exhibits axial variations of location. The bubble often exhibits a tail of escaping fluid due to the fluid exchange process. This is termed the recovered vortex core and has a reduced axial velocity compared to conditions upstream of the bubble. The tail at a downstream point breaks up into turbulent fluctuations and is viewed as a spiralling tail. Single or double tails are possible, although the reason for two diametrically opposite tails is unknown [26].

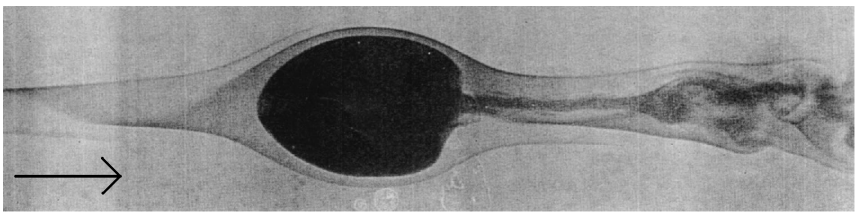

Figure 2-1 Bubble type vortex breakdown highlighted using a dye in water [24].

This breakdown mode can develop from either spiral or helical modes or directly from swelling of the original vortex core. Multiple bubble breakdowns have been observed when further increases in swirl have been created [25] creating a bubble train. Further increases in swirl resulted in the spiral tail moving upstream destroying all of the bubbles except for the first one. This bubble grew in size by drawing in fluid from downstream and moved upstream to a position it would have occupied if created at the new higher swirl value.

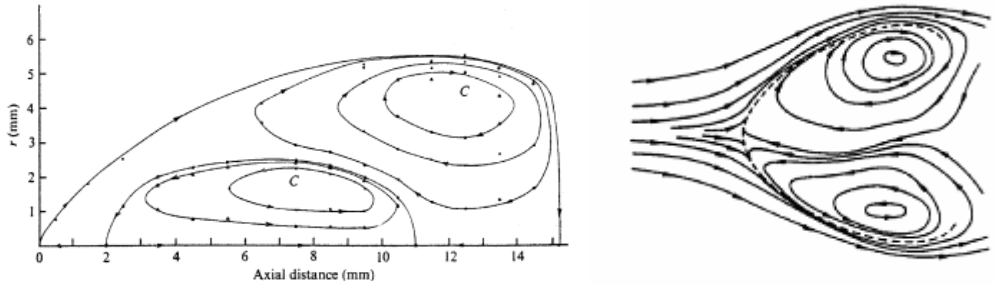

Figure 2-2 Left: Mean streamline representation from LDA data of the internal structure of the bubble showing a four celled structure [26]. Right: Instantaneous streamline representation from PTV data of the bubble showing two structures [27].

The internal structure of the bubble was first interrogated quantitivly using Laser Doppler Anemometry (LDA) [26]. A four celled counter rotating structure was revealed by the generated mean streamlines with four stagnation points. These structures were regarded as responsible for the fluid exchange process at the rear of the bubble, the downstream outer structure filling the bubble where as the inner upstream structure emptying it. This four celled arrangement is not always discerned. Particle Tracking Velocimetry (PTV) of bubble type breakdown revealed a two celled internal structure consistent with previous water and dye experiments [19, 27]. A similar structure was observed during bubble breakdown evolution from spiral breakdown. However the final structure of the breakdown revealed that the tail penetrated the bubble almost to the stagnation point with the flow moving from upstream to downstream [28]. The internal structure of the bubble therefore remains illusive to predict and is likely to be dependent on many experimental parameters.

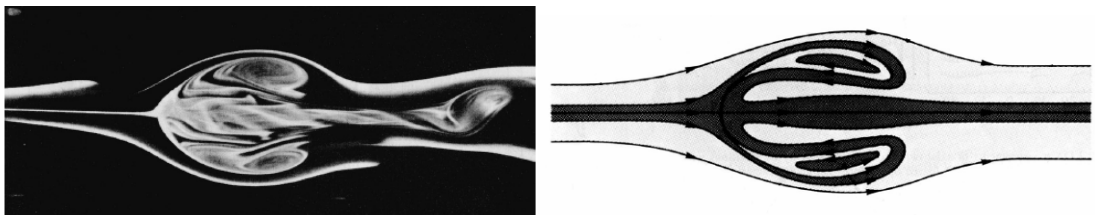

Figure 2-3 Left: Photograph of bubble internal structure. Right: Schematic representation of bubble structure showing a two celled structure and the flow of fluid from the front of the bubble through the centre and forming the tail [28].

2.1.3 Spiral/Helical Type

This breakdown mode develops after the stagnation point and is characterised by one or more spiral structures which persist for several revolutions before breaking up into large scale turbulence. The number of spiral structures is

dependent upon the induced swirl [29] so for larger values a double helical structure can be observed. The sense of the spiral structure with respect to the outer flow and direction of flow is disputed. The original work [24-26] observed that the sense of winding, rotation of the spiral and the surrounding flow were the same. Conversely the winding has been observed to be opposite to the swirling flow surrounding it, with the entire structure rotating with the outer flow [30]. This discrepancy has been suggested attributable to either the difference in swirl generation (tangential jet or guide vanes), the existence of a 'pre-breakdown' disturbance for low Reynolds number flows, or depending upon the profile of axial velocity (jet or wake). Once formed the spiral structures are able to rotate around the axis of symmetry, wrapped around the boundary of the reversed flow, becoming a Precessing Vortex Core (PVC). This core can distort in time the reverse flow region and induce a large time delay in its response. This particular aspect of vortex breakdown can excite or couple with acoustic modes of a system inducing pressure oscillations and other fluid mechanical oscillating effects which will be discussed later.

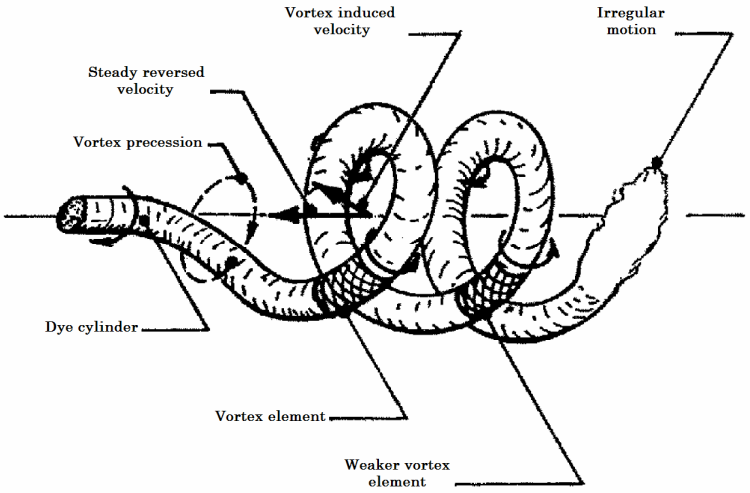

Figure 2-4 Illustration showing the spiral structure vortex breakdown type [31].

2.1.4 Vortex Breakdown Evolution

The evolution of the breakdown modes has been found to adhere to a strict hierarchy. As swirl is increased for a given Reynolds number the spiral mode of breakdown occurs first. Increases in swirl leads to a second spiral at the breakdown point, which moves upstream. Further increases result in the bubble breakdown at a further upstream position. Vortex breakdown has been studied using DNS (Direct Numerical Simulation) techniques which were sued to investigate the variables of swirl and Reynolds number independently [32]. A flow of Reynolds number of 200 was simulated at various swirl numbers starting at the critical value required for breakdown. A distinct evolution from the initial formation of a stagnation point at the critical swirl value was observed, a single spiral structure was formed, followed by a bubble structure with a spiralling tail. The final form observed was a larger, more unstable bubble structure with two helical spirals forming the tail. Similarly the simulation was repeated with a constant swirl number and the Reynolds number was varied. This test was repeated for swirl numbers of 1.3 and 1.095. For the stronger swirl case, the

bubble structure became smaller and unstable due to the development of firstly a single, and then double helical tail. Arguable the imposed swirl value was insufficient to keep the tail structure stable for increases in Reynolds number. The weaker swirl case resulted in the bubble structure completely disappearing and being replaced with a single helical structure. The DNS study agrees with what was originally observed and adds insight to the development of the tail structure downstream of the bubble breakdown.

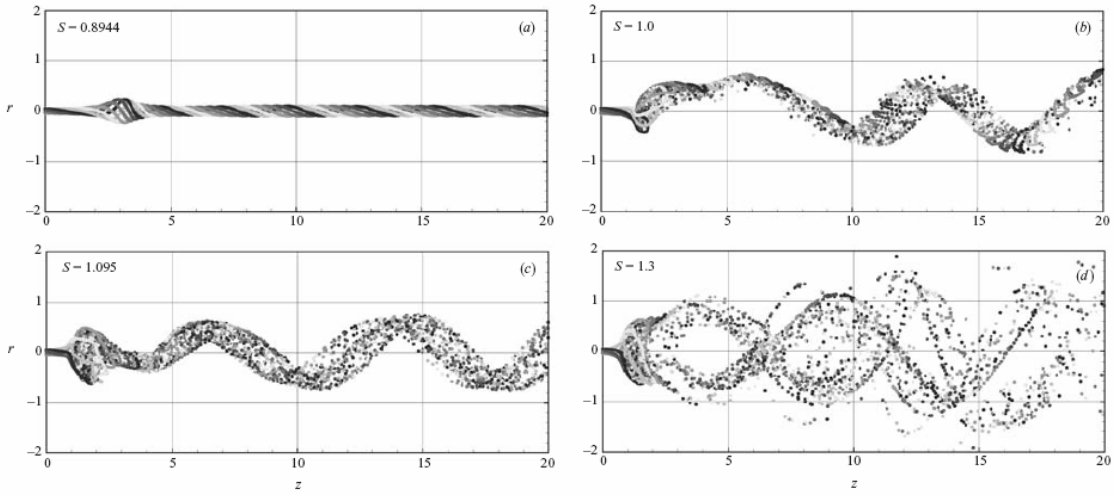

Figure 2-5 Streakline images of Reynolds number = 200 with swirl values of 0.8944, 1.0, 1.095 and 1.3. The initial breakdown occurs for the critical swirl value. Further increments lead to a helical breakdown mode, an axisymmetric bubble breakdown with a single helical tail, and finally, a bubble breakdown and two opposite helical tails [32].

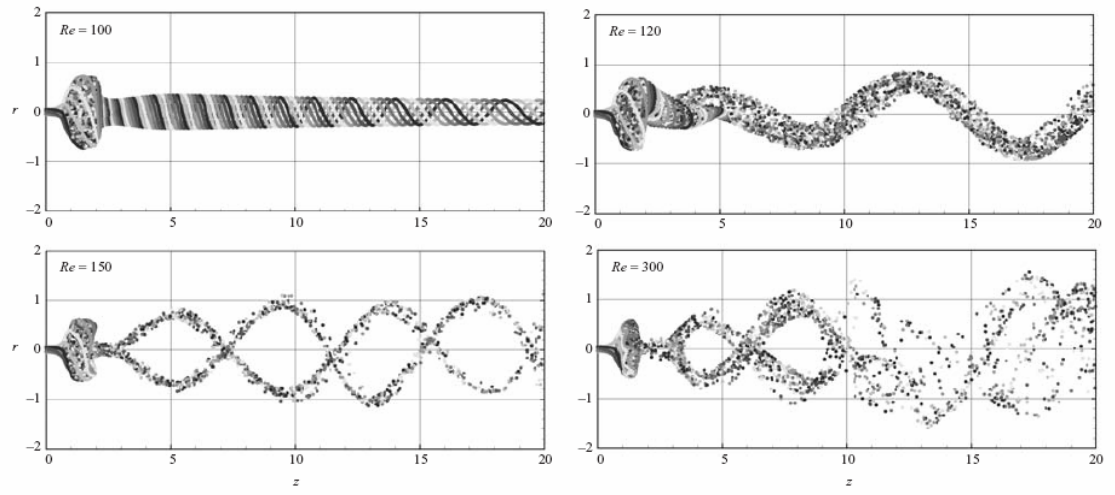

Figure 2-6 Streakline images of a flow with a swirl number of 1.3 and Reynolds numbers of 100, 120, 150 and 300. As the Reynolds number is increased the bubble breakdown becomes smaller and unstable. The tail aspect becomes helical and evolves from a single to a double helical structure [32].

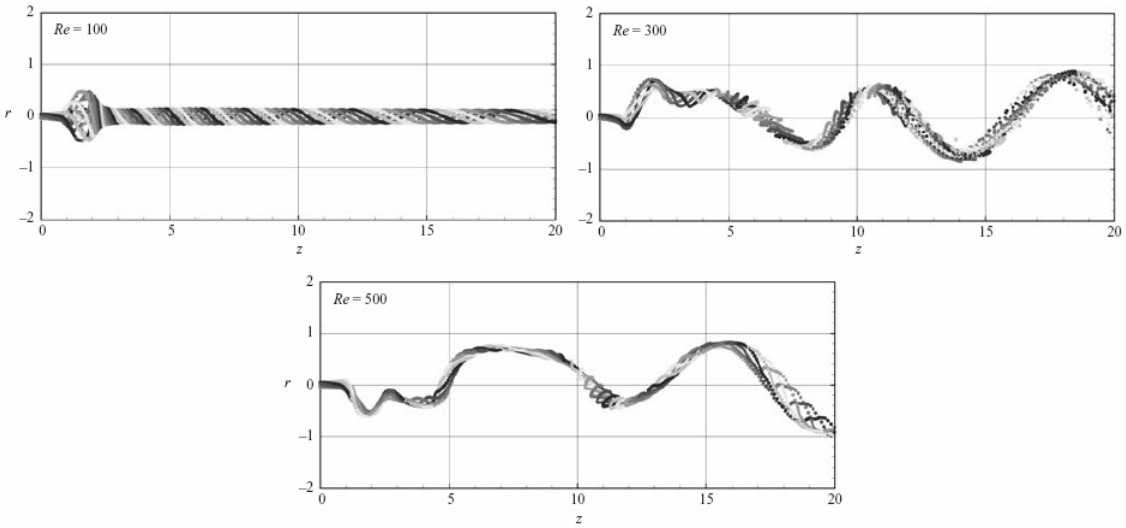

Figure 2-7 Streakline images of a flow with a swirl number of 1.095 and Reynolds numbers of 100, 300 and 500. The lowest Reynolds number flow possesses a axisymmetric bubble breakdown and a stable tail. Increments of Reynolds number result in the destruction of the bubble structure and a single spiral breakdown mode [32].

2.2 Causes of instabilities

LPC is susceptible to inherent instabilities. Previous rich diffusion operated combustors exhibited a wide spread spatial combustion regime with reactions taken place predominantly at stoichiometric locations within the chamber. This resulted in a large area where heat release occurred, naturally damping any acoustic instabilities. Moving to LPC the combustion occurs in a reaction zone which is more spatially specific. Often limited to the shear layers of the incoming flow the reaction zone is in fact a boundary separating the fresh from burnt gas (depending on turbulence levels). The heat release is now spatially specific and susceptible to intrinsic disturbances from turbulence [33, 34].

Assuming the reaction surface is initially perturbed into a convex, concave shape with respect to the fresh gas, diffusion and hydrodynamic instabilities can damp or exacerbate the disturbance. Diffusion instabilities are dependent upon the Lewis number. (ratio of thermal to mass diffusion). With Lewis numbers greater than unity reaction is intensified at the concave segment and weakened at the convex part. This will smooth the initial reaction zone distortion. Alternatively for Lewis numbers less than unity the opposite is true with increased burning at the convex segment [35, 36]. These effects cause alterations to the local flame speed. Hydrodynamic instabilities (Landau-Darrieus instabilities) are caused by the density difference across the reaction zone. Assuming the flame propagates at a constant speed equal to the laminar flame speed, and that the normal downstream velocity component at the reaction zone is larger than its upstream counterpart and the respective tangential velocity components are continuous, the streamlines diverge at convex segments and diverge at concave segments. The divergence of the streamlines results in the slowing down of the flow speed. The unchanged flame speed is therefore not locally balanced and the reaction zone moves upstream into the fresh gas. The converse argument results in the

reaction zone moving downstream [34]. Any of these mechanisms could couple with larger scale feedback mechanisms.

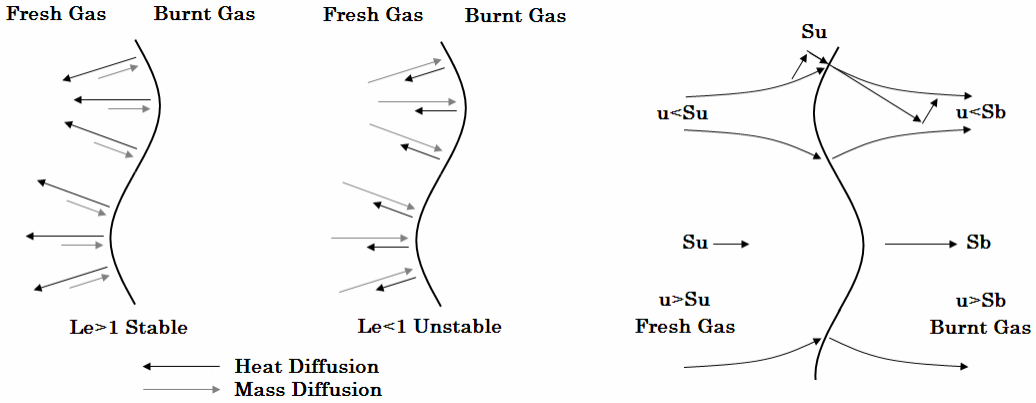

Figure 2-8 Left: Illustrations showing Diffusional thermal instabilities for two Lewis number cases. Right: Illustration showing Hydrodynamic instability

Combustion instabilities are due to the feedback mechanism linking the combustion process and acoustic characteristics of the combustion system. The specific mechanism or mechanisms is geometry and operating condition dependent. In general the fluctuations in velocity (or any thermodynamic state variable) create a fluctuation of the heat release rate. This in turn excites acoustic oscillations which generate the velocity fluctuation. This cycle is a closed feedback loop.

Several mechanisms capable of driving instabilities are depicted in Figure 2-9 for a generic geometry and limited to LPC. Independent fuel and or air oscillations can occur within the delivery system of either of these flows. This will modulate the mixture injection rate and cause a time varying equivalence ratio which together produce an oscillatory heat release rate. Equivalence ratio oscillation can occur within a premixing section and can lead to a time varying equivalence ratio of the mixture (constant total flow rate) transported into the chamber causing oscillatory heat release rate. Acoustic interaction with the reaction zone can cause the flame surface area to oscillate which in turn will result in an oscillatory heat release rate. Coherent vortex shedding from the injector or flame holder can entrain fresh gas and travel downstream. When encountering hot products the fresh gas will ignite creating a spatial and temporal variation of heat release rate. Shear layer instabilities generated at the lip of the injector can create vorticity instabilities which in turn locally cause flame surface area variations. The form of vortex breakdown utilised to achieve flame stability can become unstable causing oscillations of the IRZ which will cause local flame area oscillations and heat release oscillations.

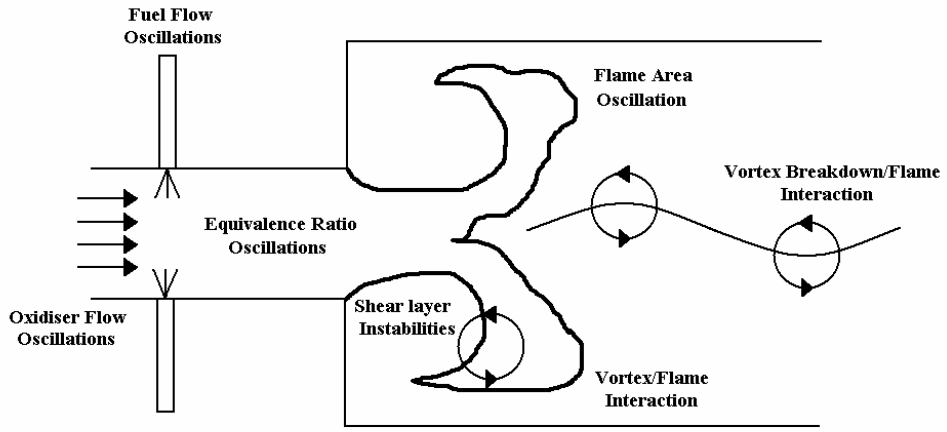

Figure 2-9 Flow and Flame processes that are able to create instabilities in a combustor.

Many works are available in the literature on the different mechanisms in various experimental devices which are operated either in non-reacting or reacting states under different combustion regimes (premixed or diffusion). A review of them here is not necessary, too large, nor entirely applicable. Therefore several recommendations are made for further information [31-33].

In order for an instability to be initiated the oscillating heat release rate must be such that a critical value is exceeded which is related to viscous damping, heat transfer and acoustic radiation [37]. Once initiated in order to determine if the combustion instability will induce sustained oscillations the satisfaction of the Rayleigh criterion must be verified. The Rayleigh criterion is applicable regardless of the mechanism of oscillation generation.

"If heat be periodically communicated to, and abstracted from, a mass of air vibration in a cylinder bounded by a piston, the effect produced will depend upon the phase of the vibration at which the transfer of heat takes place. If heat be given to the air at the moment of greatest condensation, or be taken from it at the moment of greatest rarefaction, the vibration is encouraged. On the other hand if heat be given at the moment of greatest rarefaction, or abstracted at the moment of greatest condensation the vibration is discouraged." – Lord Rayleigh 1878

The Criterion was first expressed mathematically as follows [38].

$$\int P'(t)Q'(t)dt\rangle 0 \qquad \text{Eq 2-1}$$

Where P' is the instantaneous pressure fluctuation and Q' is the instantaneous heat release rate. This expression was revised to include work done that showed to amplify a disturbance the net mechanical work done by a gas cycle must be greater than the acoustic loss through viscous dissipation [39]. Also included was the fact that temporal energy release distribution is a major factor of excitation. This non steady heat release coupled with acoustic waves convected hydrodynamically through the flow field, means the heat release is a function of time and space. The resulting analysis is more complex due to the spatial dependence on the turbulent structure of the velocity flow field [40].

$$\int_V \int_T P'(x,t)Q'(x,t)dt\,dv \geq \int_V \int_T \sum Li(x,t)dt\,dv \qquad \text{Eq 2-2}$$

The integral has been extended to include the volume of the combustion chamber. $Li(x,t)$ represents the ith damping process (viscous damping, heat release, acoustic vibration).

2.3 Experimental Investigations of LPC Instabilities

Most experimental investigations of reacting and flow fields are now performed in concert with a numerical study, most typically a LES (Large Eddy Simulation) investigation. Results of LES simulations of LPC swirl stabilised systems are presented in the next chapter and so will not be discussed here. As a result of this simultaneous effort most experimental investigations look to extract non-reacting and reacting data to validate the simulation. This will involve flow field data of a non reacting case and experimental derivation of the oscillating heat release derived from optical or Planar Laser Induced Fluorescence (PLIF) techniques. This is to be used as input data for 1d models and comparison to the LES.

2.3.1 Reacting Structures

A swirl stabilised bluff body combustion chamber has been investigated with regard to LPC of natural gas [41]. The approach adopted was to vary the inlet flow conditions and equivalence ratio to find conditions where the chamber became unstable using a 45 degree axial swirler. It was found that inlet temperatures above 650K and equivalence ratios between 0.5 and 0.7 resulted in unstable combustion, in particular at 0.6. The inlet flow velocity was 83ms^{-1} and the chamber pressure 0.47MPa. The combustion system is shown in Figure 2-10. Of note is the fused silica chamber for optical analysis and the inclusion of up to eight pressure transducers along the system.

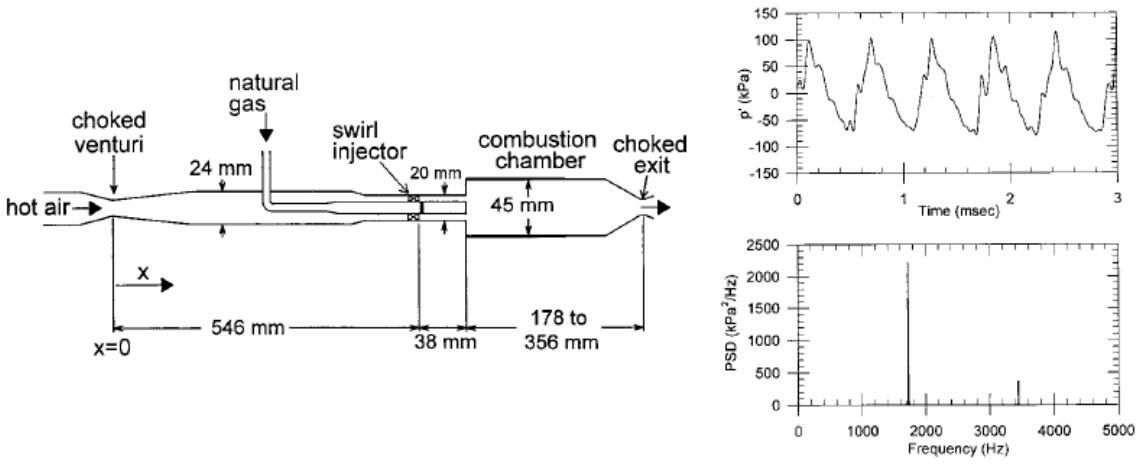

Figure 2-10 Left: Illustration of combustion chamber. Right: Top graph showing the pressure of the instability, Bottom graph power spectrum showing the two dominant modes at 1750Hz and 3500Hz [41].

Analysis of the unstable mode of operation resulted in determination of two dominant frequencies responsible for the pressure fluctuation within the

chamber, 1750Hz and 3500Hz. These were determined to be the first two longitudinal modes. The profile is displayed in Figure 2-10, the amplitude of the oscillation was approximately 0.08MPa. A numerical simulation of stable combustion revealed CRZ and a bubble vortex breakdown mechanism downstream of the bluff body. Phase locked CH* Chemiluminescence was used to reveal the mean flame structure during the instability.

The behaviour of the reacting flow field of Figure 2-11 was explained as follows. The fresh reactant mixture is entrained into the IRZ mixing with hot burnt gas. Heat release then occurs during phases 2 to 4. The dilation causes the flame to be pushed downstream and also impairs the inlet flow due to the increased pressure gradient. As a result the heat release rate begins to diminish which causes the chamber pressure to decrease. The inlet flow rate then increases (phases 6 to 8). The velocity is such that it was speculated the flame is stretched causing local extinction and the weakened flame is convected downstream (phases 9 to 11). This delays reaction of the newly injected gas until the velocity drops such that the gas is recirculated back to the CRZ (phases 12 to 1).

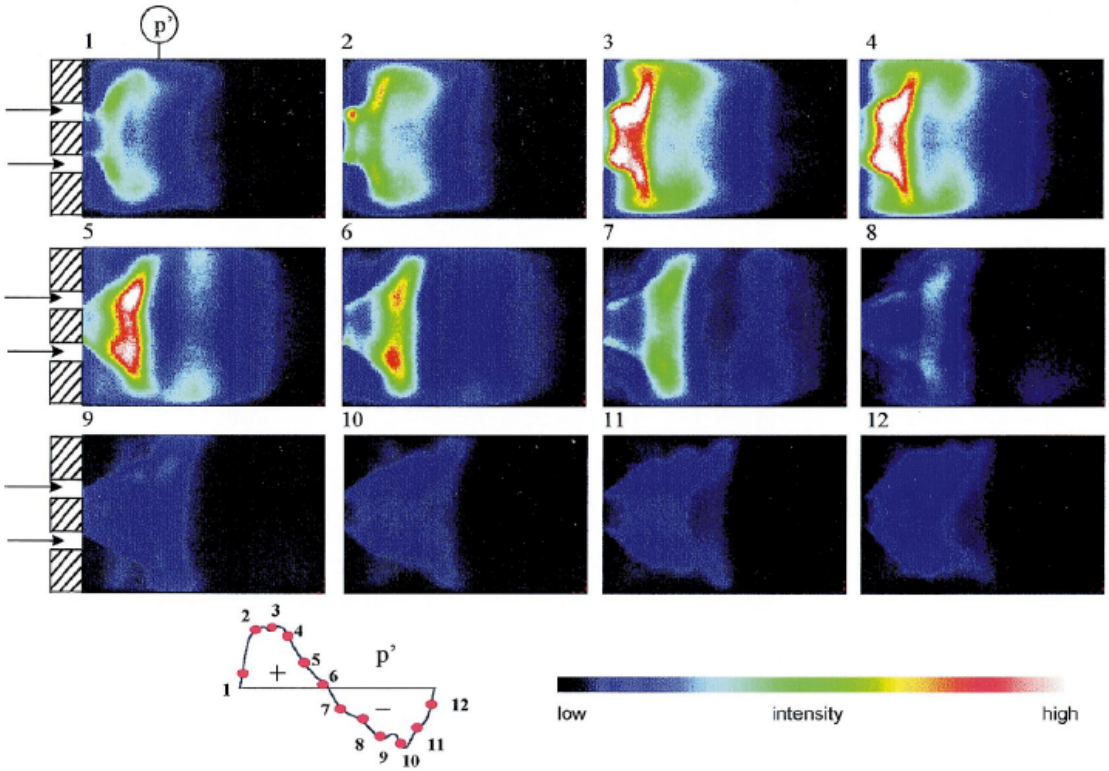

Figure 2-11 Phase resolved mean CH* Chemiluminescence images and corresponding pressure profile indicating phase location of instability at 1750Hz [41].

The local Rayleigh criterion was then evaluated by integrating the CH* images and multiplying them with the pressure fluctuation. This revealed an antinode of the Rayleigh criterion downstream of the bluff body. This was attributed to the strong vortical motions which exist between the inlet flow and IRZ, entraining fresh gas into the IRZ. The importance of inlet flow temperature was attributed to the flames' size dependence upon temperature. Higher values resulted in a more compact flame which is a more concentrated energy delivery system to the antinode than a larger flame.

The same burner at very similar conditions was investigated in greater detail with regard to the turbulent flame structure using OH* Chemiluminescence and OH PLIF in order to extract the mean reaction rate [42]. Once again natural gas was used, the inlet temperature was 600K, pressure was 0.463MPa, equivalence ratio was 0.573 and the velocity was 86.6ms^{-1}. These conditions resulted in unstable combustion with a dominant frequency of 1750Hz and a secondary frequency at 3500Hz as before. The pressure oscillation amplitude was 10%. A frequency doubled Nd:YAG at 532nm was used to excite OH radicals at 283.55nm. A laser sheet was formed and directed into the chamber. The chamber was imaged with an ICCD camera using a UV 105mm lens. An ensemble of images was collected at 12 phase positions of the oscillation. The collected OH PLIF images were converted into binary images of the progress variable Θ. From these images the local flame surface area and lengths as functions of mean progress variable were obtained. This allowed the calculation of the flame surface density term which is used in combustion modelling for the reaction rate. Simultaneously OH* Chemiluminescence was performed.

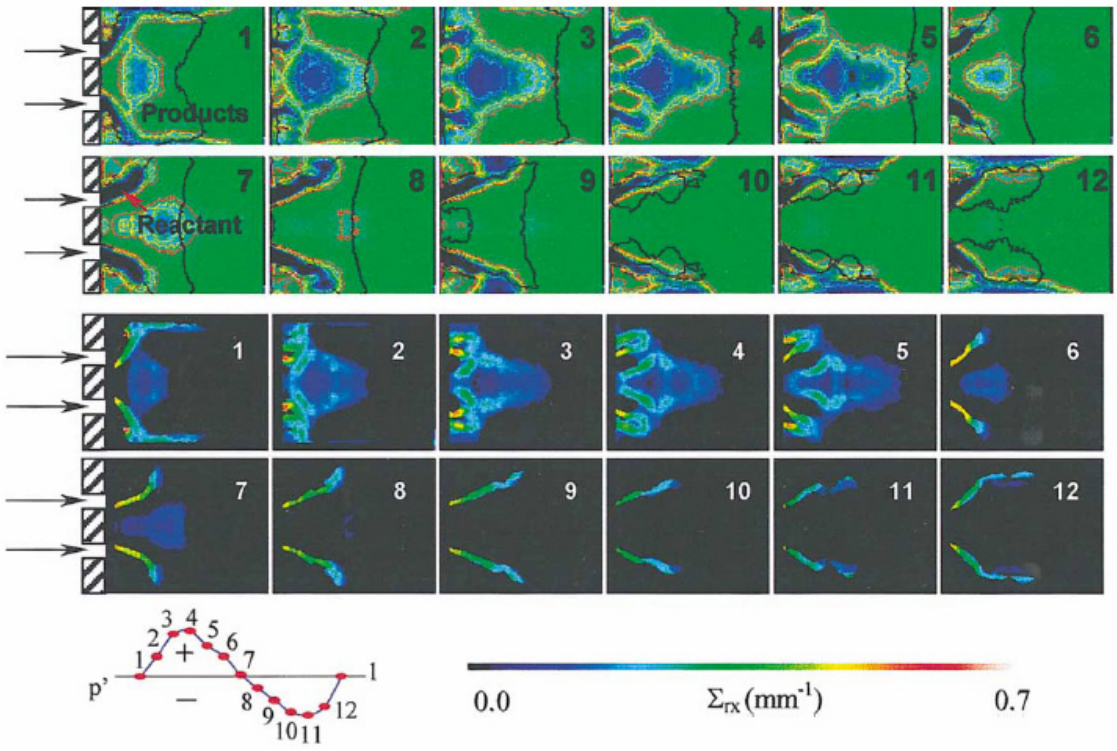

Figure 2-12 Top: Phase resolved $\overline{\Theta}$ contours obtained from OH PLIF. Dark colours represent reactants while green represents products. Superimposed as a black contour is the boundary of heat release obtained by OH* Chemiluminescence. Each image is numbered corresponding to its position in the pressure oscillation. Bottom: Local mean reaction rate per unit volume (Density corrected for the pressure oscillation). Each image is numbered corresponding to its position in the pressure oscillation [42].

The image sequence of phase resolved $\overline{\Theta}$ in Figure 2-12 clearly show a large IRZ which grows with pressure. There is substantial mixing of the burnt products and fresh reactants prior to combustion in the inlet flow structures which initially impinge and flow upstream and downstream the chamber walls. As the pressure

increases the IRZ fills with reactants, due to the mixing process between the IRZ and the inlet flow, and grows axially. This was attributed to high strain rates which are assumed to exist here preventing combustion and allowing reactant transport to the IRZ. The reaction rate images of the same figure show that reaction is occurring very close to the dump plane and significant reaction on the upstream boundary of the IRZ. As the pressure decreases and approaches its minimum there is less mixing of the inlet structure. The IRZ is seen to disappear from both sets of images as there is no transport of reactants to it. Intense regions of reaction can be seen on the inlet flow structures. The boundary of heat release can be seen to reduce drastically. At the minimum of the oscillation reactants can be seen once more impinging on the chamber wall and recirculating to the CRZ.

Once again an image of local Rayleigh index was calculated using the mean reaction images. This clearly shows that the CRZ and the IRZ immediately downstream of the bluff body are regions driving the instability. The inlet flow separating these zones is clearly damping the instability. The exact location of the shear layers is unknown due to a lack of velocity data so further interpretation regarding shear layer importance is unavailable. This work emphasises the importance of the recirculation zones involvement in the instability. No comment was made regarding the vortex breakdown mechanism, or its behaviour.

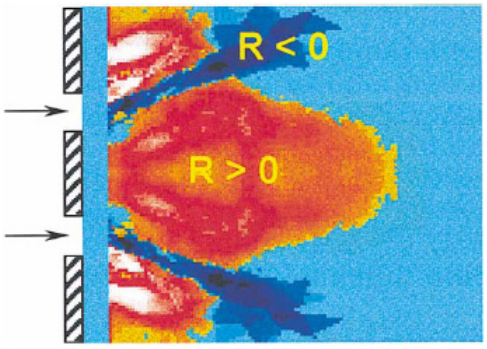

Figure 2-13 Local Rayleigh index (R) distributions. Red and white areas correspond to positive values (driving instability) and blue/dark blue areas correspond to negative values (damping instability) [42].

A similar bluff body swirl stabilised dump combustor has also been investigated with CO_2* Chemiluminescence [43]. A combination of natural gas, an inlet temperature of 673K, inlet velocity of 45ms^{-1}, swirl number of 0.45 and equivalence ratio of 0.45 operated at atmospheric pressure resulted in the combustor becoming unstable with a frequency of 235Hz. The chamber was set up without an exhaust restriction. The recorded pressure perturbation had amplitude of 0.5psi

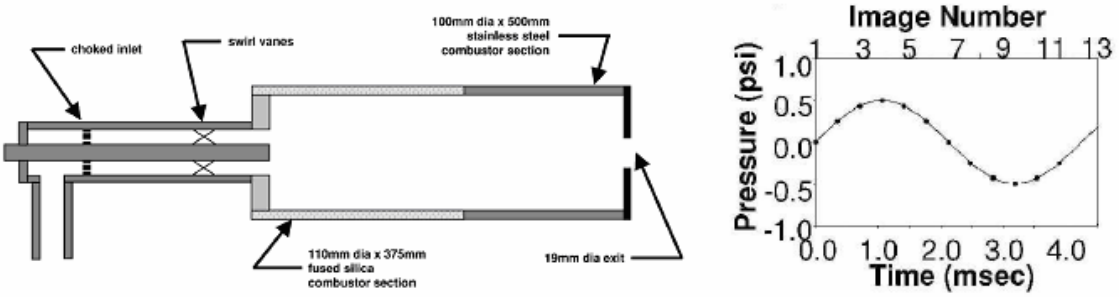

Figure 2-14 Illustration of the combustion chamber and recorded pressure perturbation under operating conditions of inlet temperature 673K, velocity 45ms-1, equivalence ratio 1 and instability frequency 235Hz [43].

The deconvoluted phase averaged CO_2* Chemiluminescence images of Figure 2-15 show that the flame is anchored to the bluff body and is present within the CRZ due to recirculation. The overall shape of the flame remains constant through the instability. The peak heat release occurs at positions 3, 4 and 5 where the flame area can be seen to be the largest indicating vortex stretching of the reaction zone. The minimum of heat release occurs at positions 9, 10 and 11 where the flame area is much smaller and local extinction is clearly evident. This could be due to the increase of inlet flow causing higher strain rates and altering the CRZ. The lack of shape change of the flame is clearly different to what has previously been described [42]. This could be due to the absence of an exhaust which will change the IRZ behaviour. The images also indicate that the chamber is close to blowout with near total extinction occurring at the low pressure images.

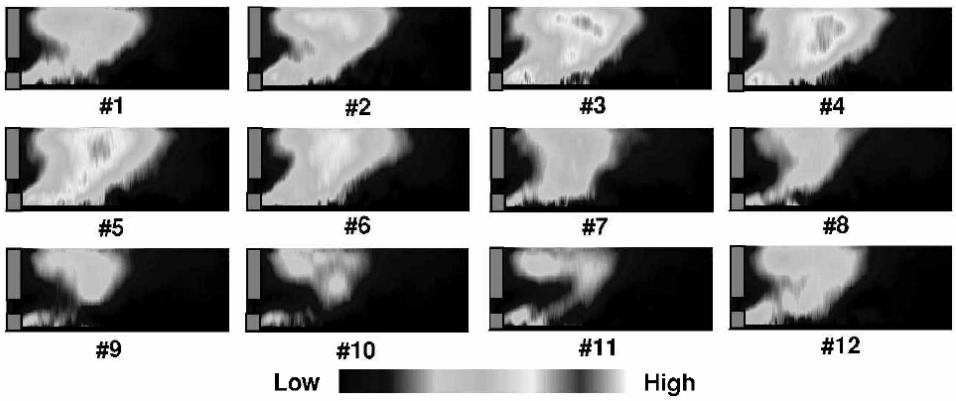

Figure 2-15 Phase resolved mean deconvoluted CO_2* Chemiluminescence images and of instability at 235Hz [43].

The same chamber was operated with different operating conditions, inlet temperature of 623K, velocity 59ms^{-1}, equivalence ratio of 0.58 yielded an instability of 350Hz. Once again this was investigated using CO_2 Chemiluminescence. The structures were more compact than previous and although stretched towards the chamber wall by the CRZ were not recirculated to the dump plane. Local extinction was observed. Once again there was no reaction within the IRZ of the chamber. The local Rayleigh criterion was calculated for this condition revealing areas of amplification (coinciding with areas of heat release) and damping.

An alternative approach is to artificially force the combustion system in order to characterise the flame response, in terms of structure and as a response function. A non swirl, bluff body stabilised combustion chamber has been acoustically forced using a loud speaker arrangement [44]. Lean premixed ethylene was used. The chamber was investigated without the exhaust, i.e. just a quartz cylinder to eliminate any acoustic effects. This has implications on any vortex breakdown mechanisms as will be discussed later. The inlet velocity was 9.9ms^{-1}, equivalence ratio of 0.55 and a Reynolds number of 19000. A range of acoustic forcing amplitudes were investigated and the transfer function of the flame was found to be non linear due to the formation of a coherent, toroidal vortex forming on the inner shear layer with a forcing amplitude of 15% or greater (of inlet velocity). The phase of the transfer function was found to be approximately constant. The conditions presented correspond to a frequency of 160Hz and a large forcing amplitude of 64%. The inlet conditions were characterised using hot wire anemometry for the non reacting flow. This was used to calibrate a two microphone pressure measurement system to obtain inlet velocity during combustion.

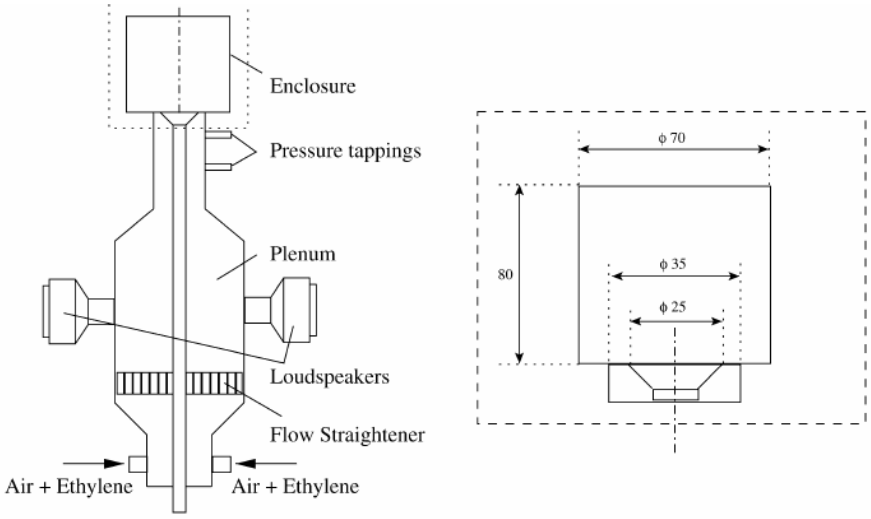

Figure 2-16 Illustration showing combustion chamber and acoustic forcing system [44].

The reacting flow field was investigated using OH* and CH* Chemiluminescence, and simultaneous OH and CH_2O PLIF. As previously described OH PLIF can be used to derive the flame surface density. The resultant image was revolved around the chamber axis and line of sight integrated to compare with the OH* Chemiluminescence data showing excellent agreement of implied heat release rate. The method of OH and CH_2O imaging to derive HCO [45] provides the most accurate reaction zone marker and a measure of heat release rate [46] (see Chapter 4.1).

The forced flame was imaged at 18 phase positions. The average Flame Surface Density (FSD) images are shown in Figure 2-17. The flame is initially anchored to the bluff body by the inner shear layer. As the pressure decreases the reaction zone begins to roll up towards the chamber centreline and the reaction zone retreats upstream from the chamber walls. The heat release reaches its minimum at phase 120°. By this point the vortex causes the reaction layer at the bluff body to wrap inwards. Meanwhile the reaction zone downstream has been

pulled firstly into the corners of the chamber and then wrapped into the forming vortex. As there is signal in the chamber corners there must be reactants being pulled into the CRZ. As the pressure increases the flame is pushed downstream with the vortex ring still intact. The recirculated reactants mix with products in the CRZ causing reaction along the outer shear layer. As the flame moves further downstream the vortex is either broken up by flame effects or is shed. Reaction along the outer shear layer is extinguished, either due to increased strain or insufficient recirculation of hot products. The peak of heat release occurs at phase 280°, as can be seen the flame area is at its largest value due to the vortex interaction.

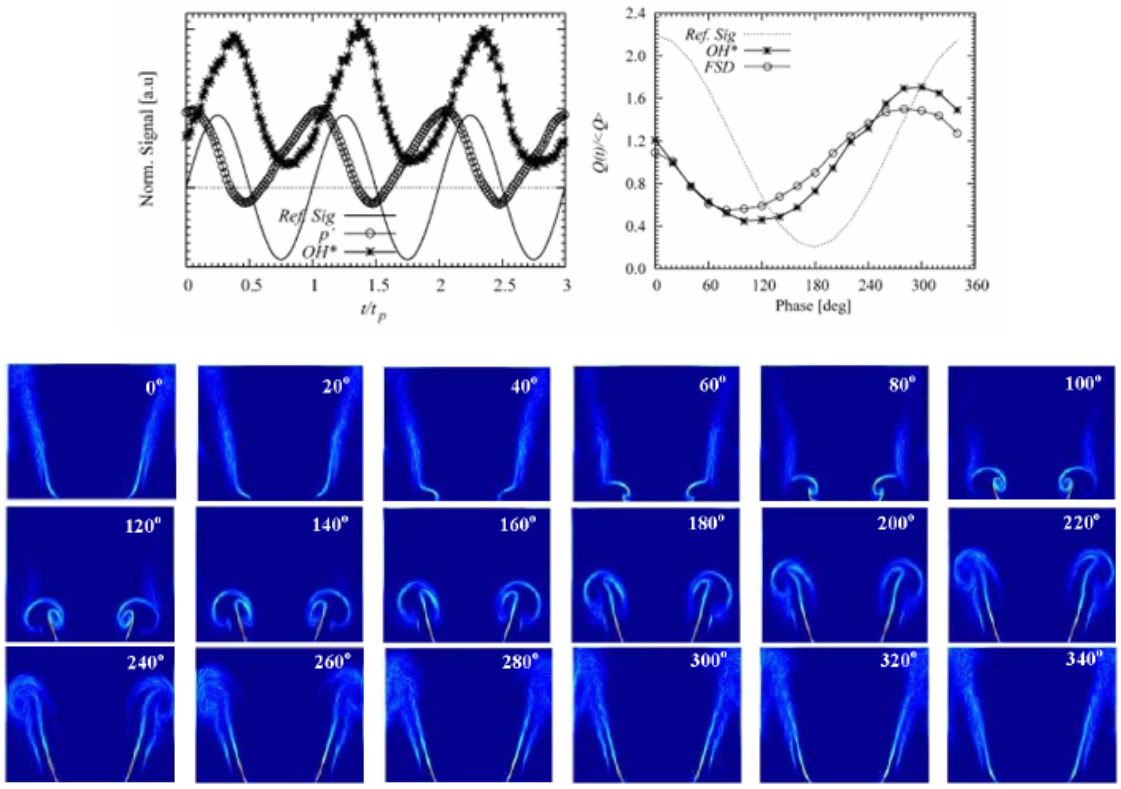

Figure 2-17 Top Left: Graph showing reference signal, pressure fluctuation and integrated OH* Chemiluminescence signal. Top Right: Graph showing the reference signal, integrated OH* Chemiluminescence signal and Flame Surface Density. Bottom: Phase resolved average FSD images of a instability at 160Hz and 64% forcing amplitude [44].

Other noticeable features was that the occurrence of vortex roll up required less amplitude of forcing for higher frequencies and that the heat release rate oscillation was attributed to increases of flame surface area rather than local strain effects as no local extinction was reported by the authors.

In a separate study the formation or coherent toroidal vortex structures was determined by using an axially swirl stabilised bluff body open burner [47]. This was pulsed using a pulsation unit. A decreasing hyperbolic relationship was found describing the onset of these coherent structures which linked the imposed perturbation frequency f_{puls} and forcing amplitude, Pu (defined as the ratio of rms inlet velocity u_{rms} and mean inlet velocity $\bar{u}$) of any flow combination (mean

axial velocity $\overline{u}_x$) and geometry (equivalent diameter d_{eq}) through the Strouhal number Str.

$$Str = f_{puls} \cdot \frac{d_{eq}}{\overline{u}_x} \quad and \quad Pu = \frac{u_{rms}}{\overline{u}} \qquad \text{Eq 2-3}$$

This shows that at low oscillation frequencies and for small inlet geometries the likelihood of large scale coherent vortex shedding is extremely low. Flame transfer functions were defined for various combinations of swirl and forcing amplitudes. These functions were correct in describing the flames response but also the onset of the toroidal vortices which were detected as the start of a negative gradient on the amplitude response graphs. OH* chemiluminescence was used to determine the heat release rate and hot wire anemometry to determine the velocity measurements. The swirling case of 0.79, with forcing amplitude of 15% and equivalence ratio 1 was presented with phase locked OH* Chemiluminescence images. This set shows a much more compact flame that is much closer to the burner than the weaker swirl images presented. Reaction is clearly occurring within the IRZ of the flow.

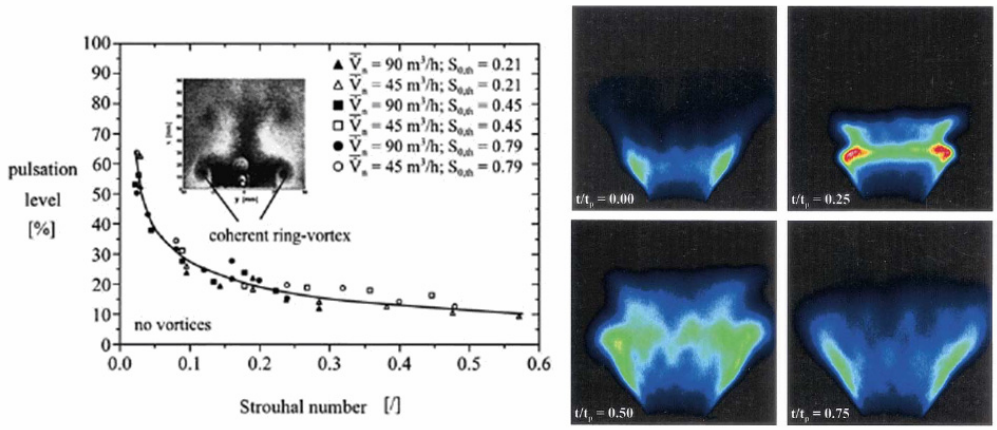

Figure 2-18 Left: Graph showing hyperbolic boundary indicating the onset of coherent vortex shedding for pulsation level against Strouhal number. Right: Phase locked time averaged OH* Chemiluminescence images of 0.79 swirl number flow, equivalence ratio is 1 and forcing amplitude is 15% at 50Hz forcing frequency [47].

2.3.2 Flow Structures

Due to the difficult nature of acquiring velocity data within enclosed chambers the information regarding flow fields is limited [48]. A liquid kerosene swirl stabilised combustor was investigated using Particle Image Velocimetry (PIV, see Chapter 4.3). Emphasis of the work was placed upon the difficulties encountered. As well as liquid droplets present the air flow was seeded using SiO_2. Numerous difficulties were encountered such as flame luminosity of the second PIV frame, greater Mie scattering from the fuel droplets than the solid seed, rapid contamination of the optical chamber walls and seeder device inconsistencies. The atmospheric condition presented revealed the symmetric inlet structure. The

central flow showed no vortex breakdown as there is no flow reversal. Flame stabilisation was attributed to the CRZ feeding hot products to the fresh gas. In order to reduce the unwanted scattering from seeding particles adhered to the laser sheet entrance and exit windows and the laser sheet the windows were offset from the main chamber using two long channels. The implications on this change of geometry upon the flow field were not quantified. It is also noteworthy that for this case the flame did not impinge upon the chamber or optical window.

2.4 Summary

In general the nature of the recirculation zones and vortex breakdown are known. What is unknown is the behaviour of these features when coupled to an unstable heat release rate and acoustic perturbations. As has been shown the mode of vortex breakdown is dependent upon swirl for a given Reynolds number. During an instability it is likely the inlet swirl value will change. This could cause a change of the vortex breakdown mode and its interaction with the flame.

Under certain conditions the mode of vortex breakdown can become unstable and begin rotating around the chamber centreline. This is the PVC. The impact of the PVC is dependent upon the mode of vortex breakdown. Typically the PVC is regarded as an additional feature of the spiral helical breakdown modes. In these cases the PVC oscillating at a particular frequency can extend large distances from the injector into the chamber causing the IRZ to change shape, size and orientation [49]. This feature is easily observed in isothermal flows by seeding the flow and has been identified in isothermal simulations and experiments [50] (see Chapter 3.2.4). However, when combustion is present, and depending on method of fuel injection, the vortex breakdown and any oscillatory behaviour is likely to change and can even be suppressed [50]. With axial fuel injection the PVC amplitude has been reduced by an order of 15 over the isothermal case. For a premixed flame a much less dramatic reduction in amplitude was found, approximately a third in PVC amplitude.

The stabilising effect of combustion was related to radial gradients of tangential momentum $(\rho \cdot vz \cdot r)$. A stability criterion has been proposed. If tangential momentum increases with chamber radius the vortex breakdown is stable. If any decreases are observed with chamber radius then the structure is unstable and will precess [50, 51]. Combustion occurring around the IRZ close to the inlet will cause increases in $(\rho \cdot vz \cdot r)$ through dilation. This means there is minimal opportunity for any negative gradients of $(\rho \cdot vz \cdot r)$ to develop. The flame will only expand away from the inlet when the inlet velocities have decayed sufficiently to allow flow and flame speeds to balance. This can push the vortex breakdown point downstream or stabilise the vortex breakdown as the flow is restricted within the combusting conical structure.

In cases where the axisymmetric bubble breakdown is observed the vortex core is wrapped around the bubble structure. Whether the vortex core survives downstream of the bubble is unclear however the recovered vortex, that is the tail structure of the bubble, can become a spiral structure and then precess.

Combustion instabilities investigated using a chamber or burner are characterised by their transfer function which measures the amplitude response

of the reaction rate and the phase delay from the inlet perturbation. Abrupt decreases in amplitude response have been shown to correspond to coherent vortex rollup generated at the inlet and can be predicted using the inlet characteristic Strouhal number and excitation level [44, 47]. As has been shown coherent vortex structures shed from the inlet are not necessarily responsible for the oscillating heat release. The reacting flow field can be highly resolved using PLIF techniques. The heat release rate can be derived from these methods or using chemiluminescence. There is sparse information regarding the flow field of any combusting flow within a chamber, stable or unstable due to technical difficulties. However the importance of the IRZ has been highlighted in swirling geometries as a feature which strongly interacts with the combustion process.

2.5 Hydrogen Addition

The addition of hydrogen to conventional hydrocarbon fuels (natural gas/methane) is an area of growing interest to reduce NO_x, CO, CO_2 and other pollutants. In addition other stabilising benefits such as improved flame propagation make hydrogen addition/content an attractive method to achieve dry LPC.

2.5.1 Effects upon Emissions

Hydrogen blended with methane has been investigated using a swirl stabilised combustion chamber [52] (see Chapter 5.1). The lean blow out limit was extended with hydrogen addition. This was measured by the chamber temperature at blowout (dependent upon Φ). The temperature was reduced form 1170°C (pure methane) to 1058°C (41.4% hydrogen). OH PLIF imaging near the lean limit revealed that a 13.8% content of hydrogen resulted in a 44% increase in OH concentration over the methane case. Further increases resulted in substantially smaller increments. The increased stability due to the presence of hydrogen is hypothesised to be the result of an increase of the radical pool, H, O and particularly OH. It was found that CO was significantly reduced with 45% hydrogen content. There was a marginal influence on NO_x production due to the low temperature of the experiment leading to the conclusion that NO_x is insensitive to hydrogen content and remains tied to the flame temperature for its production rates. Large increases of hydrogen will lead to larger flame temperatures for a given equivalence ratio and will result in increases of NO_x. The substitution of a percentage of carbon containing fuel with hydrogen will lead to reductions in CO, CO_2 and UHC, firstly due to the substitution but also due to increased oxidation of CO and UHC by the increased radical pool. In addition the inclusion of hydrogen will reduce the CO produced by high strain rates. As strain increases the amount of CO created increases by reduced radical concentration and slowing down of the oxidising reaction.

$$CO + OH \Leftrightarrow CO_2 + H \qquad \text{Eq 2-4}$$

Hydrogen addition therefore increases the radical pool and reduces the impact of strain upon this reaction. Calculations of premixed counter-flow flames confirm this. For a given strain rate ($100s^{-1}$) a 10% and 20 % hydrogen content resulted in a reduction of CO of 60% and 83% respectively [53].

2.5.2 Effects upon Strain

Hydrogen addition also improves the strain resistance capabilities of methane combustion. Figure 2-19 shows the calculated effect of hydrogen addition using a premixed counter flow configuration for three equivalence ratios. The imposed strain was determined by control of the two opposing premixed flows. The strain rate recorded was the strain rate at extinction and normalised by the extinction strain rate for pure methane. As the hydrogen content increases the extinction strain rate improves. The effectiveness of the hydrogen addition increases as the equivalence ratio is reduced. The implications of modest quantities of hydrogen addition to methane combustion are beneficial.

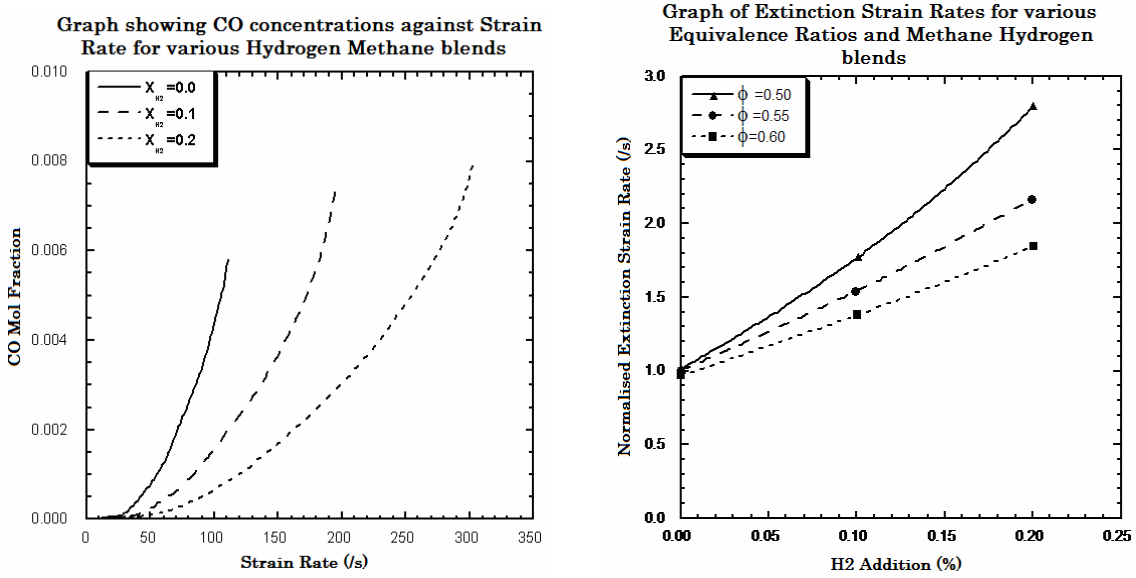

Figure 2-19 Left: CO emission levels from a premixed counter flow flame. The fuel is CH_4 with 0, 10 and 20% H_2 addition. Equivalence ratio = 0.5. X is the mole fraction of H_2 in the H_2/CH_4 fuel mixture [53]. Right: Extinction strain rate as a function of H_2 addition to a counter flow premixed CH_4/air flame [53]. The strain rate was defined as the velocity gradient normal to the flame at the position of maximum heat release.

2.5.3 Effects upon Flame Speeds

The laminar flame speed of pure methane, hydrogen or a blend is dependent upon the equivalence ratio. Figure 2-20 shows this behaviour for pure methane, hydrogen and various blends. It is clear that for a given equivalence ratio the laminar flame speed for hydrogen is much larger than that of methane. Of note is that the laminar flame speed is not increased significantly with hydrogen contents less than 50%. Above this content large increases can be seen.

A comparison between calculated laminar and measured turbulent flame speeds for various hydrogen contents blended with methane are shown in Figure 2-20. The comparison is done for two equivalence ratios, 0.5 and 0.43. The laminar flame speed increases linearly with hydrogen content and is less in the leaner case. Turbulent flame speed behaves similarly until a point where the increase

becomes highly non linear and the flame speed is far greater than the laminar value. This turning point is 30% for $\Phi = 0.43$ and 20% for $\Phi = 0.5$. Once again the leaner case has lower turbulent flame speeds. The effect of hydrogen upon the flame speed appears to begin at lower hydrogen contents for richer mixtures.

The increase found in flame speed is primarily attributed to the increase of the available radicals. The early oxidation of hydrogen creates an increased OH radical pool that accelerates the methane oxidation rate. This increases the global reaction rate and hence the flame propagation speed [52, 54]. The increased tolerance to strain will also mean the reaction zone will become more wrinkled when exposed to turbulence and the flame surface area will also increase. In addition hydrogen has a less than unity Lewis number meaning the mass diffusivity is greater than the thermal diffusivity. Differential diffusion therefore increases the hydrogen available to the reaction zone. The response of a blended mixture has been numerically investigated using DNS [55]. It was found hydrogen addition changes the response of combustion to stretch. The blended mixture tended to form more cusps (positive curvature) which translates to an increase of flame surface area and hence reaction rate.

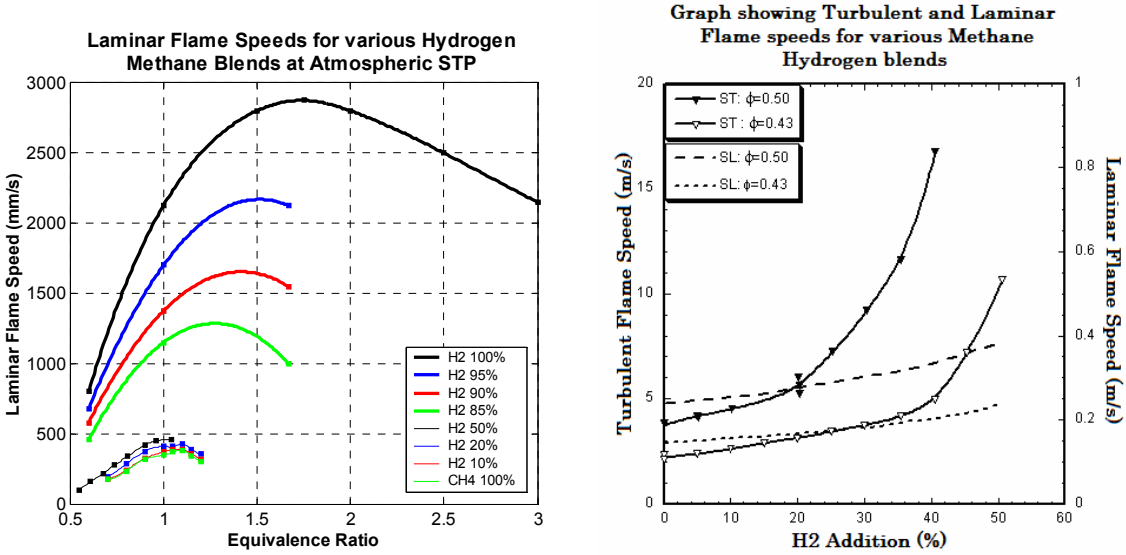

Figure 2-20 Left: Laminar flame speeds as a function of equivalence ratio for H_2-air, CH_4-air and blends of H_2-CH_4-air at STP. H2 100% to H2 85% from [56], H_2 50% from [53], and H_2 20% to CH4 100% from [57]. Right: Effect of hydrogen addition on flame speed. Data points indicate experimentally measured values. Lines indicate calculated laminar flame speeds [58]. Conditions are 5 Bar pressure and 673 K.

The implications of modest quantities of hydrogen addition to methane combustion are beneficial. Emissions and pollutant formation can be drastically reduced through improvements of oxidation. Leaner mixtures are possible due to improvements of oxidation and strain resistance. The impact upon instabilities is less clear. This will depend upon any modifications to the flame speed and the mechanism of extinction.

3 PREMIXED TURBULENT COMBUSTION

3.1 Turbulent Combustion

Turbulent combustion is encountered in most practical combustion devices such as gas turbine combustors. The need for improved fuel efficiency and reduced pollutant formation requires a more thorough understanding of this form of combustion. The difficulty of analysing the science analytically has led to the rapid development of numerical techniques. The turbulence aspect itself remains one of the most complex fields in fluid mechanics due to the difficulty in solving instantaneous balance equations.

The description of turbulence at present is done on a statistical basis and results in any quantity f being divided into a mean $\bar{f}$ and fluctuating component f'. The turbulence intensity I is defined as the ratio of the root mean square of the fluctuating components over the mean.

$$f = \bar{f} + f' \quad and \quad I = \frac{\sqrt{\overline{f'^2}}}{\bar{f}} \qquad \text{Eq 3-1}$$

However this does not fully describe the interaction of turbulence upon the flame front. Turbulence ranges in scales from the largest integral scale l_t to the smallest Kolmogorov scale η_k. How the turbulent energy is distributed through this range of scales determines the effect the particular scale size has upon the flame front. For each turbulent scale an associative Reynolds number can be defined using the kinematic viscosity v, the characteristic velocity of the motion $u'(r)$ and its size (scale) r. The Reynolds number is the ratio of inertia to viscous forces hence the larger scales are controlled by inertia and are unaffected by viscous dissipation.

$$Re(r) = \frac{u'(r)r}{v} \quad \Rightarrow \quad Re_t = Re(l_t) = \frac{u'l_t}{v} \qquad \text{Eq 3-2}$$

Assuming homogeneous and isotropic turbulence energy flows from the larger scales to the smaller ones through the Kolmogorov cascade. The flux of energy is constant and is defined as the dissipation, ε , of the kinetic energy K. The energy dissipation can be approximated as the ratio of kinetic energy and time scale. Progressing down the energy cascade the Reynolds number will approach unity where the inertia and viscous forces begin to balance. This determines the smallest of scales, the Kolmogorov scale, which is related to the viscosity and turbulent kinetic energy dissipation rate. The energy dissipation rate can be determined from measured or computationally resolved structures and then used to determine the Kolmogorov scale.

$$\varepsilon = \frac{u'^2(r)}{r/u'(r)} = \frac{u'^3(r)}{r} \quad \text{and} \quad \eta_k = \left(\frac{\nu^3}{\varepsilon}\right)^{1/4} \qquad \text{Eq 3-3}$$

The ratio of the largest to smallest structures is therefore found to be linked to the turbulent Reynolds number.

$$\frac{l_t}{\eta_k} = \frac{u'^3/\varepsilon}{\left(\nu^3/\varepsilon\right)^{1/4}} = Re_t^{3/4} \qquad \text{Eq 3-4}$$

The effect of an eddy or turbulent structure upon the flame front is exhibited by the increase of the flame front area. This is caused by the strain $k(r)$ induced by the eddy attributed to velocity gradients $u'(r)/r$. Therefore the integral and Kolmogorov scales induces respective strains where u'^2 is equal to the turbulent kinetic energy. The strain created by Kolmogorov eddies is much greater than that created by the larger eddies.

$$k(r) = \frac{u'(r)}{r} = \left(\frac{\varepsilon}{r^r}\right)^{1/3} \Rightarrow k(l_t) = \frac{\varepsilon}{u'^2} \approx \frac{\varepsilon}{K} \quad and$$
$$\text{.....} k(\eta_k) = \sqrt{\frac{\varepsilon}{\nu}} \Rightarrow \frac{k(\eta_k)}{k(l_t)} = \sqrt{\frac{l_t u'}{\nu}} = \sqrt{Re_t} \qquad \text{Eq 3-5}$$

The concept of the energy cascade allows the estimation of the change of characteristic speeds, times, Reynolds number and strain with scale r . This can be summarised on the following log-log graphs. This treatment of turbulence is based on the assumption of homogeneous isotropic turbulence which is false for practical combustion including gas turbines but is the best description available.

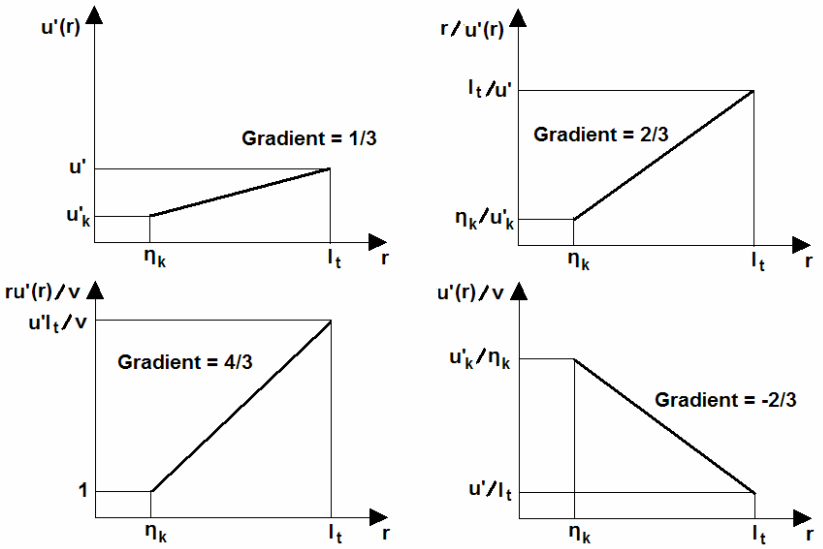

Figure 3-1 Illustration showing turbulence characteristic speeds (Top Left), times (Top Right), Reynolds number (Bottom left) and strain (Bottom Right) against scale on log-log axes [59]

For each scale of turbulence a characteristic number, $D_a(r)$ can be defined, comparing it's characteristic time, $\tau_m(r)$ to the characteristic flame time scale τ_c. For large numbers of $D_a(r)$ the chemical time scale is small compared to the turbulent time and therefore the particular turbulent scale is unable to affect the inner flame structure. For small values of $D_a(r)$ the chemical time scale is larger and or the turbulence time scale is smaller allowing the modification of the inner flame structure.

$$\tau_m(r) = \frac{r}{u'(r)} = \frac{r^{2/3}}{\varepsilon^{1/3}} \quad and \quad \tau_c = \frac{\delta}{s_L} \;\Rightarrow\; D_a(r) = \frac{\tau_m(r)}{\tau_c} \qquad \text{Eq 3-6}$$

Using the integral and Kolmogorov scales two important characteristic numbers are defined, the Damköhler D_a and Karlovitz K_a numbers. The Damköhler number is defined using the integral scale where as the Karlovitz number is defined using the Kolmogorov scale where δ is the flame thickness.

$$D_a = D_a(l_t) = \frac{\tau_t}{\tau_c} = \frac{\tau_m(l_t)}{\tau_c} = \frac{l_t/u'(l_t)}{\delta/s_L} \text{ and } K_a = \frac{1}{D_a(\eta_k)} = \frac{\tau_c}{\tau_k} = \frac{\tau_c}{\tau_m(\eta_k)} = \frac{u'(\eta_k)/\eta_k}{s_L/\delta} \qquad \text{Eq 3-7}$$

The Damköhler number can be used to distinguish two distinct descriptions of combustion depending on its value. High Damköhler numbers ($D_a > 1$) have a short chemical time compared to the turbulent time. The internal structure of the flame is unaffected by the turbulence. The reaction zone will be thin and distorted by the flow field as turbulence wrinkles and strains the flame surface. The reaction zone can be described by a laminar flame element termed a 'flamelet'. For low Damköhler numbers ($D_a < 1$) the chemical reaction is slow. All turbulent time scales are less than the chemical time scale and the reactants and products are mixed by the turbulent structures before the reaction and the situation is termed a 'perfectly stirred reactor'. Most practical situations correspond to high or medium Damköhler values.

As stated with large Damköhler numbers the flame front is thin and the inner structure is assumed unaffected by turbulence, which only wrinkles the flame surface. This is termed the 'flamelet regime' or the 'thin wrinkled flame regime'. At these conditions the smaller turbulence scales including the Kolmogorov scale, have a turbulent time larger than the chemical time. However it is also possible for the smaller scales to have a time smaller than the chemical time while still having a high Damköhler number. This transition can be described using the Karlovitz number. The Karlovitz number can be expressed alternatively.

$$K_a = \left(\frac{l_t}{\delta}\right)^{-1/2}\left(\frac{u'}{s_L}\right)^{3/2} = \left(\frac{\delta}{\eta_k}\right)^2 = \frac{\sqrt{\varepsilon/\nu}}{s_L/\delta} \qquad \text{Eq 3-8}$$

By defining the turbulent Reynolds number with the integral scale a relationship linking the Damköhler and Karlovitz number can be found.

$$Re_t = \frac{u' l_t}{\nu} = \left(\frac{u'}{s_L}\right)\left(\frac{l_t}{\delta}\right) \Rightarrow Re_t = D_a^2 K_a^2 \qquad \text{Eq 3-9}$$

The Karlovitz number is used to define the Klimov-Williams criterion. Accordingly $K_a = 1$ separates two combustion regimes both of which have high Damköhler numbers. This was initially proposed as the transition between the flamelet regime ($K_a < 1$) and the 'distributed combustion regime' or the 'thickened flame regime' ($K_a > 1$). This second regime is where the flame structure is strongly modified by the smaller scale turbulence motions. It has been shown that for a Karlovitz number greater than one the turbulent motions are able to affect the flame inner structure, but not necessarily the reaction zone [60]. The reaction zone which is the source of the heat release has a thickness δ_r lower than the thermal thickness of the flame δ, ($\delta_r \approx 0.1\delta$). Therefore the Karlovitz number can be redefined using the reaction zone thickness. The following regimes were proposed based on the observations made [60].

$$K_{ar} = \left(\frac{\delta_r}{\eta_k}\right)^2 = \left(\frac{\delta}{\delta_r}\right)^2 \left(\frac{\delta_r}{\eta_k}\right)^2 = \left(\frac{\delta}{\delta_r}\right)^2 \approx \frac{1}{100}\left(\frac{\delta}{\eta_k}\right)^2 \approx \frac{1}{100} K_a \qquad \text{Eq 3-10}$$

The flamelet or thin flame regime (Figure 3-2 (a)) corresponds to $D_a > 1$ and $K_a < 1$ where the chemical time is less than all the turbulent times and the flame thickness is less than all turbulent scales. The flame has a structure very similar to that of a laminar flame. The ratio of turbulent fluctuating velocity and laminar flame speed, u'/s_L, is used to further classify this regime. When $(u'/s_L) < 1$ the turbulent motion speed is insufficient to cause flame front turbulent interactions and results in the 'wrinkled flamelet regime'. When $(u'/s_L) > 1$ the turbulent motion velocity is greater than the flame speed increasing the wrinkling and creating isolated pockets of burnt and fresh gas. This is called the 'corrugated flamelet regime'.

The thickened wrinkled flame/thin reaction zone regime (Figure 3-2 (b)) has $D_a > 1$ and $1 < K_a \leq 100 (K_{ar} < 1)$. The turbulent motions are able to affect and thicken the flame preheat zone while the reaction zone is unaffected and still resembles a laminar reaction zone.

The thickened flame regime/well stirred reactor (Figure 3-2 (c)) has $D_a < 1$ and $K_a > 100 (K_{ar} > 1)$. Both the preheat and reaction zones are strongly affected by the turbulence and no laminar structure is evident.

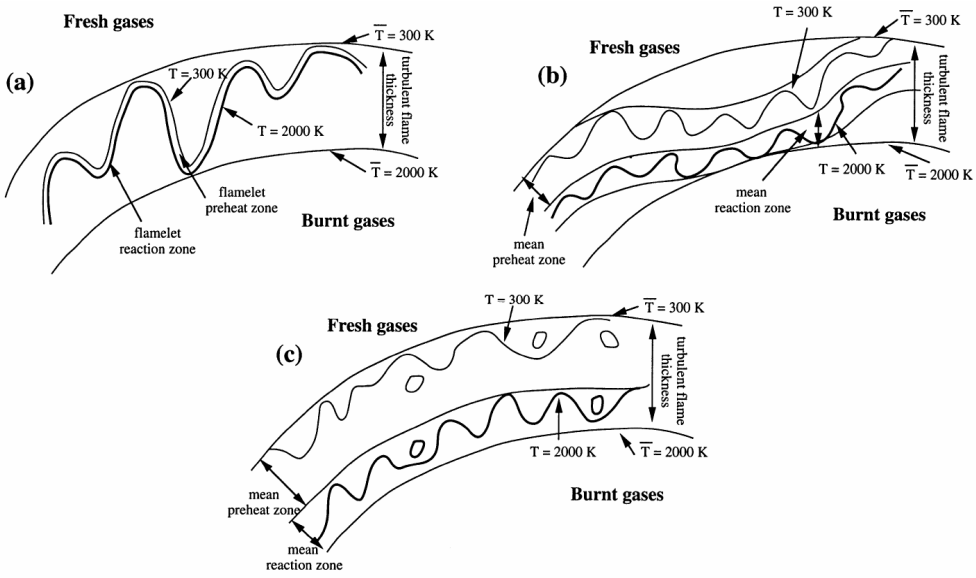

Figure 3-2 Illustration showing combustion regimes (a) flamelet (b) thickened wrinkled flame and (c) thickened flame regime [61].

The different regimes can be displayed as shown in Figure 3-3. These are segregated using the length scale ratio (l_t/δ) and the velocity ratio (u'/s_L). The Kilmov-Williams criterion ($K_a = 1$) corresponds to a flame thickness equal to the Kolmogorov scale. Below this limit the flame is thinner than all the turbulent scales. The Peters Criterion ($K_a = 100$ and $K_{ar} = 1$) separates two regimes [60, 62] Below the line the reaction zone thickness is thinner than the turbulent scales and is unaffected by turbulence. The curve named Poinsot et al indicates the limit of the flamelet regime [63]. The curve named Veynante et al is proposed to distinguish between gradient (above) and counter gradient (below) turbulent transport [64].

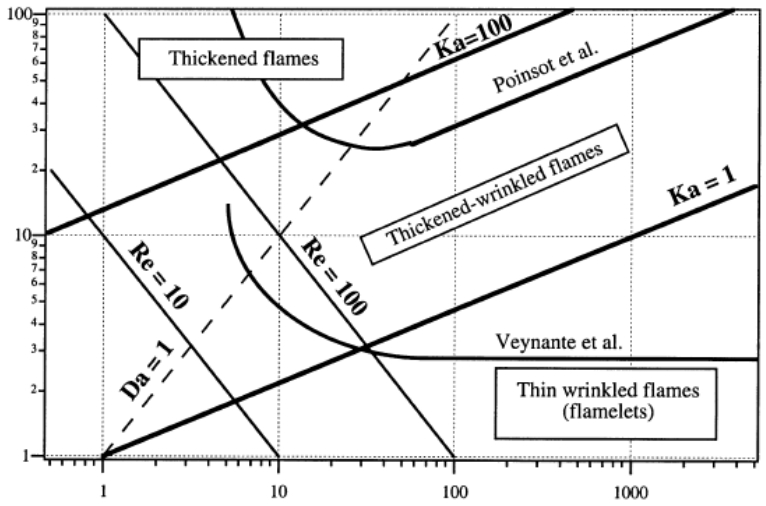

Figure 3-3 Combustion regime diagram with the length scale ratio (l_t/δ) on the x axis and the velocity ratio (u'/s_L) on the y axis [61].

Diagrams such as this can not be used to identify the combustion regime of a practical combustor. This limitation is due to the definitions being based upon only two characteristic numbers and the assumptions made regarding the turbulence. Other inconsistencies are what values to use for characteristic properties such as the flame thickness which can be thermally or diffusively defined. The lines segregating the various regimes should be viewed as indicators rather than definitive boundaries as estimates of magnitude. Never the less it is of more suitability to use this diagram as a guide to appropriately choose combustion models to further define the system within a modelling technique.

3.2 Turbulent Combustion Modelling

This chapter contains an overview of CFD methods available within combustion science. This is included as a successful appropriate simulation can allow a thorough analysis of a combustion system that experimentally could be unachievable. As this work provides validation data and utilises insights derived from CFD work it is important that the advantages and disadvantages are known.

The description of any reacting flow field begins with the balance equations for mass, momentum, species and enthalpy [65].

$$\frac{\partial \rho}{\partial t} + \frac{\partial}{\partial x_i}\left(\rho u_i\right) = 0 \qquad \text{Eq 3-11}$$

$$\frac{\partial \rho u_j}{\partial t} + \frac{\partial}{\partial x_i}\left(\rho u_i u_j\right) + \frac{\partial p}{\partial x_j} = \frac{\partial \tau_{ij}}{\partial x_i} \qquad \text{Eq 3-12}$$

$$\frac{\partial\left(\rho Y_k\right)}{\partial t} + \frac{\partial}{\partial x_i}\left(\rho u_i Y_k\right) = -\frac{\partial}{\partial x_i}\left(V_{k,i} Y_k\right) + \dot{\omega}_k \quad for\ k = 1,2,N \qquad \text{Eq 3-13}$$

$$\frac{\partial \rho h_s}{\partial t} + \frac{\partial}{\partial x_i}\left(\rho u_i h_s\right) = \dot{\omega}_T + \frac{Dp}{Dt} + \frac{\partial}{\partial x_i}\left(\lambda \frac{\partial T}{\partial x_i}\right) - \frac{\partial}{\partial x_i}\left(\rho \sum_{k=1}^{N} V_{k,i} Y_k h_{s,k}\right) + \tau_{i,j} \frac{\partial u_i}{\partial x_j} \qquad \text{Eq 3-14}$$

Computational Fluid Dynamics (CFD) has received much attention in order to obtain a satisfactory description for reacting flows. The numerical tools available are Reynolds Averaged Navier Stokes (RANS), Large Eddy Simulation (LES) and Direct Numerical Simulation (DNS).

RANS is the result of averaging and simplification of the instantaneous balance equations. This process does not result in a complete solution. A turbulence model is required to account for a complete description of the flow field. A turbulent combustion model is also required to describe species conversion and or solely heat release. Combined RANS simulations will yield average quantities over time or a number of realisations. The fundamental limitation is the inability to describe the fluctuating element to any turbulent flow giving no indication of

the combustion systems' variability. The great advantage of RANS is the comparative small computing time.

LES is the product of applying a filter to the instantaneous balance equations. This filter acts as a cut off whereby turbulent scales greater than the filter cut off are explicitly calculated where as those smaller are modelled using a sub grid model. LES will calculate instantaneous realisations of the combusting system thereby allowing the simple calculation of not only the average but the variance, standard deviation or any other statistical property of the group of realisations. Current limitations are the development of correct sub grid turbulence models and specifically in the application of LES to combustion is the inability to resolve the flame front on the grid and inclusion of complex chemistry for the reaction term.

DNS solves explicitly the instantaneous balance equations for all turbulent scales and times removing the need for a turbulence model. Instantaneous realisations are calculated allowing a dataset of realisations to be generated. Full chemistry can also be included yielding the perfect answer. The limitation to this method is the need for super computer facilities to solve even small academic flows ($5mm^3$) and the time scale for its application to a real world situation is long. Hence it will not discussed further.

The left illustration of Figure 3-4 indicates the solution of temperature using the three numerical methods outlined. The solutions are for a point in space where flame reaction zone passes through due to turbulent motions. The right hand illustration shows the turbulent energy spectrum summarising the three numerical methods' approach to turbulence.

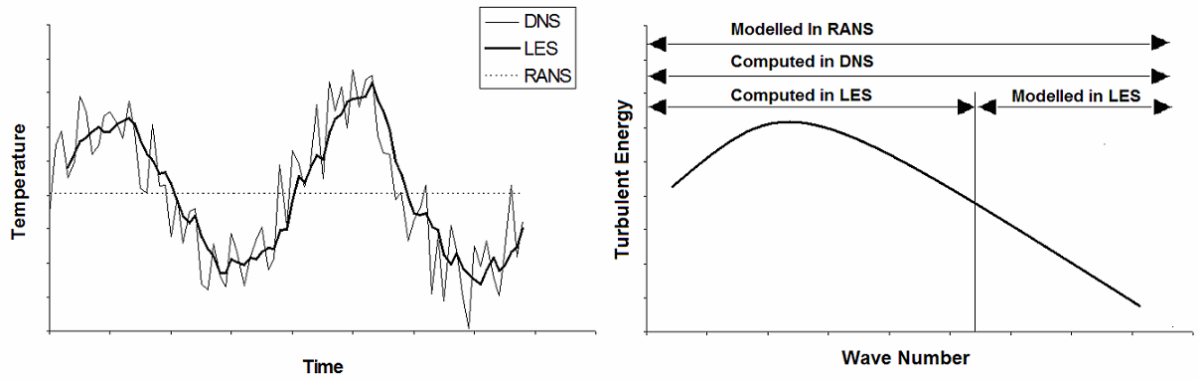

Figure 3-4 Left: Illustration of temperature against time by different computational approaches. Right: Strategy for turbulent description by different computational approaches.

3.2.1 Reynolds Averaged Navier Stokes Methods

RANS was adopted first as it was computationally impossible to calculate the instantaneous flow field. Therefore the instantaneous balance equations were averaged to yield mean flow properties. Firstly using typical Reynolds averaging where by any quantity, f is separated into a mean $\bar{f}$ and fluctuating component f', where $f = \bar{f} + f'$. Considering the balance equation for mass, Reynolds averaging results in the term $\overline{\rho' u'}$ which is the correlation between density and

velocity fluctuations and must be modelled.

$$\frac{\partial \overline{\rho}}{\partial t} + \frac{\partial}{\partial x_i}\left(\overline{\rho u_i}\right) = \frac{\partial \overline{\rho}}{\partial t} + \frac{\partial}{\partial x}\left(\overline{\rho}\,\overline{u}_i + \overline{\rho' u'}\right) \qquad \text{Eq 3-15}$$

For non constant density flows many more unclosed correlations between a quantity f and density fluctuations will occur. This is circumvented by utilising mass weighted averages (Favre). Once again any quantity, f is separated into a mean and fluctuating component.

$$\widetilde{f} = \frac{\overline{\rho f}}{\overline{\rho}} \qquad f = \widetilde{f} + f'' \;\; and \;\; \widetilde{f''} = 0 \qquad \text{Eq 3-16}$$

The Favre averaged balance equations are described below.

$$\frac{\partial \overline{\rho}}{\partial t} + \frac{\partial}{\partial x_i}\left(\overline{\rho}\widetilde{u}_i\right) = 0 \qquad \text{Eq 3-17}$$

$$\frac{\partial \overline{\rho}\widetilde{u}_j}{\partial t} + \frac{\partial}{\partial x_i}\left(\overline{\rho}\widetilde{u}_i\widetilde{u}_j\right) + \frac{\partial \overline{p}}{\partial x_j} = \frac{\partial}{\partial x_i}\left(\overline{\tau}_{i,j} - \overline{\rho}\widetilde{u_i''u_j''}\right) \qquad \text{Eq 3-18}$$

$$\frac{\partial\left(\overline{\rho}\widetilde{Y}_k\right)}{\partial t} + \frac{\partial}{\partial x_i}\left(\overline{\rho}\widetilde{u}_i\widetilde{Y}_k\right) = -\frac{\partial}{\partial x_i}\left(\overline{V_{k,i}Y_k} + \overline{\rho}\widetilde{u''Y_k''}\right) + \overline{\dot{\omega}}_k \quad for \;\; k = 1,2,N \qquad \text{Eq 3-19}$$

$$\frac{\partial \overline{\rho}\widetilde{h}_s}{\partial t} + \frac{\partial}{\partial x_i}\left(\overline{\rho}\widetilde{u}_i\widetilde{h}_s\right) = \overline{\dot{\omega}}_T + \frac{\overline{Dp}}{Dt} + \frac{\partial}{\partial x_i}\left(\overline{\lambda\frac{\partial T}{\partial x_i}} - \overline{\rho}\widetilde{u_i''h_s''}\right) - \frac{\partial}{\partial x_i}\left(\overline{\rho\sum_{k=1}^{N} V_{k,i}Y_k h_{s,k}}\right) + \overline{\tau_{i,j}\frac{\partial u_i}{\partial x_j}} \qquad \text{Eq 3-20}$$

This alternative averaging offers a solution to unknown density correlation terms however any solution must be carefully regarded as there is no simple conversion to a Reynolds averaged solution. As most experimental data will be of the Reynolds averaged form comparisons of Favre averaged to experimental is difficult. Therefore for a direct comparison conversion to a Reynolds averaged solution is desired. In order to move from one form to the other knowledge of the density fluctuation correlations, $\overline{\rho' f'}$, which are contained within the Favre averaged quantity $\overline{\rho}\widetilde{f} = \overline{\rho}\,\overline{f} + \overline{\rho' f'}$ is required.

Although density fluctuation terms have been removed there still remains terms unsolved which require addressing. Firstly the Reynolds stresses term $\overline{\rho}\widetilde{u_i''u_j''}$ from the momentum balance equation. Secondly species $\widetilde{u_i''Y_k''}$ and enthalpy $\widetilde{u_i''h''}$ turbulent fluxes from the species and enthalpy balance equations respectively. Laminar diffusive fluxes for both species $\overline{V_{k,i}Y_k}$ and enthalpy $\overline{\lambda\frac{\partial T}{\partial x_i}}$ are generally neglected in turbulent combustion. Finally the mean reaction rates for species $\overline{\dot{\omega}}_k$ must be closed.

A direct simplification is now made assuming one step chemistry based upon the fuel mass fraction Y and reduced temperature function Θ (Eq 3-21). This simplification ignores all other chemical species and assumes constant pressure, Lewis number and adiabatic conditions. By defining the fuel mass fraction Y as a scalar with values of 1 in fresh gas and 0 in burnt gas and the reduced temperature Θ (also known as the progress variable c) as a scalar with opposing values in these areas allows the assumption that the total enthalpy of the mixture is constant everywhere. Therefore it is possible to conclude that $\Theta + Y = 1$.

$$Y = \frac{Y_F}{Y_F^1} \quad and \quad \Theta = \frac{C_p(T - T_1)}{QY_F^1} = \frac{T - T_1}{T_2 - T_1} \qquad \text{Eq 3-21}$$

The instantaneous balance equations are now simplified requiring the solving of only $\bar{\rho}$, $\tilde{u}_i$ and $\tilde{\Theta}$.

$$\frac{\partial \bar{\rho}}{\partial t} + \frac{\partial}{\partial x_i}\left(\bar{\rho}\tilde{u}_i\right) = 0 \qquad \text{Eq 3-22}$$

$$\frac{\partial \bar{\rho}\tilde{u}_j}{\partial t} + \frac{\partial}{\partial x_i}\left(\bar{\rho}\tilde{u}_i\tilde{u}_j\right) + \frac{\partial \bar{p}}{\partial x_j} = \frac{\partial}{\partial x_i}\left(\bar{\tau}_{i,j} - \bar{\rho}\widetilde{u_i''u_j''}\right) \qquad \text{Eq 3-23}$$

$$\frac{\partial\left(\bar{\rho}\tilde{\Theta}\right)}{\partial t} + \frac{\partial}{\partial x_i}\left(\bar{\rho}\tilde{u}_i\tilde{\Theta}\right) = -\frac{\partial}{\partial x_i}\left(\bar{\rho}\bar{D}\frac{\partial \tilde{\Theta}}{\partial x_i} + \bar{\rho}\widetilde{u''\Theta''}\right) + \bar{\dot{\omega}}_\Theta \quad and \quad \dot{\omega}_\Theta = -\frac{\dot{\omega}_F}{Y_F^1} \qquad \text{Eq 3-24}$$

The term $\dot{\omega}_\Theta$ is the reaction rate for the reduced temperature function. An expression for enthalpy is now no longer required. Even after this simplification unknown terms still exist which require modelling. These are the Reynolds stresses $\bar{\rho}\widetilde{u_i''u_j''}$, the mean reaction rate $\bar{\dot{\omega}}_\Theta$ and the turbulent scalar transport $\bar{\rho}\widetilde{u_i''\Theta''}$.

RANS offers a solution to predicting and simulating the behaviour of combusting systems that was achievable with computing capabilities and fluid mechanic description when it was created. The drawbacks of only providing mean values and the inherent errors associated with this calculation are now no longer acceptable with the current need for cleaner and more efficient gas turbine combustion.

3.2.2 Large Eddy Simulation

The technique of large eddy simulations has become a very attractive tool for fluid flow simulation. The objective is to explicitly compute the largest structures of the flow field and model the smaller ones, the differential being the mesh size used. The application to combusting flows is recent and at the development stage where as for non-reacting flow significant development has been made.

LES is a promising tool for combustion studies. Large turbulent structures

assumed to depend on system geometry where as smaller structures have more independent features. This is important as previous models are more suited to the smaller turbulent structures. Most reacting flows exhibit large scale coherent structures. These are observed when instabilities occur from flow, heat release and acoustic coupling. As instabilities induce noise and system degradation it is hoped that LES could become a tool to predict these instabilities and numerically validate passive or active control systems. The knowledge of large scale turbulent motions can be used to help describe the effects of unresolved smaller structures. As sub grid scale models are based on similarity assumptions between the large and small structures. LES is able to give a superior description of turbulence/combustion interactions. This is because large structures are explicitly computed identifying instantaneous fresh and burnt gas zones, where the turbulence characteristics are different.

LES works by filtering various quantities, f, in spectral or physical space. The filtered and Favre mass weighted filtered quantity can be defined as;

$$\bar{f}(x)=\int f(x')F(x-x')dx \quad and \quad \overline{\rho}\widetilde{f}(x)=\int \rho f(x')F(x-x')dx' \qquad \text{Eq 3-25}$$

Where F is the LES filter. There are three common filters available. The first is a cut off filter in spectral space; this retains length scales greater than the cut off length scale. The second is a box filter in physical space which corresponds to averaging a quantity f over a box size. Thirdly a Gaussian filter in physical space can be used. The instantaneous balance equations are filtered to derive balance equations for filtered quantities $\widetilde{f}$. This quantity is resolved in the simulation where as the sub grid scale part (unresolved) f' is defined below.

$$f=\widetilde{f}+f' \qquad \text{Eq 3-26}$$

The LES filtered instantaneous balance equations are below where $\bar{f}$ and $\widetilde{f}$ are filtered quantities and not ensemble means.

$$\frac{\partial\overline{\rho}}{\partial t}+\frac{\partial}{\partial x_i}\left(\overline{\rho}\widetilde{u}_i\right)=0 \qquad \text{Eq 3-27}$$

$$\frac{\partial\overline{\rho}\widetilde{u}_i}{\partial t}+\frac{\partial}{\partial x_i}\left(\overline{\rho}\widetilde{u}_i\widetilde{u}_j\right)+\frac{\partial\overline{p}}{\partial x_j}=\frac{\partial}{\partial x_i}\left(\overline{\tau}_{ij}-\overline{\rho}\left(\widetilde{u_iu_j}-\widetilde{u}_i\widetilde{u}_j\right)\right) \qquad \text{Eq 3-28}$$

$$\frac{\partial\left(\overline{\rho}\widetilde{Y}_k\right)}{\partial t}+\frac{\partial}{\partial x_i}\left(\overline{\rho}\widetilde{u}_i\widetilde{Y}_k\right)=\frac{\partial}{\partial x_i}\left(\overline{V_{k,i}Y_k}-\overline{\rho}\left(\widetilde{u_iY_k}-\widetilde{u}_i\widetilde{Y}_k\right)\right)+\overline{\dot{\omega}}_k \quad for\ k=1,2,N \qquad \text{Eq 3-29}$$

$$\frac{\partial\overline{\rho}\widetilde{h}_s}{\partial t}+\frac{\partial}{\partial x_i}\left(\overline{\rho}\widetilde{u}_i\widetilde{h}_s\right)=\frac{\overline{Dp}}{Dt}+\frac{\partial}{\partial x_i}\left(\overline{\lambda\frac{\partial T}{\partial x_i}}-\overline{\rho}\left(\widetilde{u_ih_s}-\widetilde{u}_i\widetilde{h}_s\right)\right)+\overline{\tau_{i,j}\frac{\partial u_i}{\partial x_j}}-\frac{\partial}{\partial x_i}\left(\overline{\rho\sum_{k=1}^{N}V_{k,i}Y_kh_{s,k}}\right)+\overline{\dot{\omega}}_T \qquad \text{Eq 3-30}$$

As with the Favre mass weighted balance equations there are a number of unclosed terms which need to be addressed. These include the unresolved Reynolds stresses $\left(\widetilde{u_i u_j} - \tilde{u}_i \tilde{u}_j\right)$ and the unresolved species fluxes $\left(\widetilde{u_i Y_k} - \tilde{u}_i \tilde{Y}_k\right)$ and enthalpy fluxes $\left(\widetilde{u_i h_s} - \tilde{u}_i \tilde{h}_s\right)$. The filtered laminar diffusion fluxes for species $\overline{V_{k,i} Y_k}$ and enthalpy $\overline{\lambda \frac{\partial T}{\partial x_i}}$, and finally the filtered chemical reaction rate $\overline{\dot{\omega}_k}$. The filtered chemical reaction rate $\overline{\dot{\omega}_k}$ is simplified using the reduced temperature Θ (or fuel mass fraction) and models as described for the RANS reaction rate are adapted and used for LES.

3.2.3 LES of Premixed Turbulent Flames

The application of LES from non reacting constant density flows to combustion is not straightforward. The premixed flame thickness is approximately 0.1 to 1mm and is therefore smaller than the LES grid. This leads to computational problems as the reaction zone can not be resolved. Therefore the governing dynamics of the reaction zone are controlled and occur at the sub grid level casting serious doubt on the applicability of LES to combusting flows [66].

In order to overcome this problem different approaches have been proposed and implemented with varying results. These include an artificially thickened flame, the use of a flame front tracking technique such as the G Equation or use of a filtered version of the Θ balance equation.

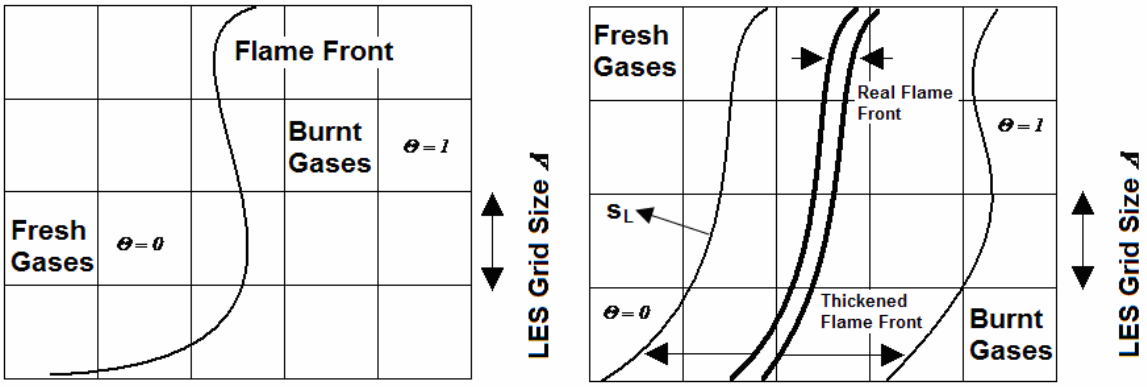

Figure 3-5 Left: Illustration showing the difficulty resolving the flame front on the LES grid. Right: Schematic of artificially thickening the flame front to allow it to be resolved on the LES grid.

The thickened flame technique [67] relates the flame speed s_L and flame thickness δ_L to thermal diffusivity D_{th} and the mean reaction rate $\overline{\dot{\omega}}$. By increasing the thermal diffusivity by a factor and decreasing the mean reaction rate constant by the same factor the flame speed is maintained while achieving a thickened flame thickness by the factor used. This can allow the resolving of the flame front on the grid provided sufficiently large factors are used, shown in Figure 3-5.

$$s_L \propto \sqrt{D_{th}\dot{\bar{\omega}}} \quad and \quad \delta_L \propto \frac{D_{th}}{s_L} = \sqrt{\frac{D_{th}}{\dot{\bar{\omega}}}} \qquad \text{Eq 3-31}$$

The thickened flame however modifies the chemical turbulence interactions. This is determined through the definition of the Damkhöler number which decreases by the factor used making the flame falsely insensitive to turbulent motions. A proposed solution to this is to use an efficiency function E [68]. This causes sub grid wrinkling effectively counteracting the insensitivity effect of the thickening factor. The function is implemented through changes to thermal diffusivity and the reaction rate.

Diffusivity:	D_{th}	$\rightarrow$	FD_{th}	$\rightarrow$	EFD_{th}
Reaction Rate:	$\dot{\bar{\omega}}$	$\rightarrow$	$\dot{\bar{\omega}}$/F	$\rightarrow$	E$\dot{\bar{\omega}}$/F
		Thickening		Wrinkling	

Therefore the sub grid turbulent flame speed and flame thickness are replaced.

$$s_T = Es_L \text{ and } \delta_T = F\delta_L \qquad \text{Eq 3-32}$$

The G Equation can be used to track the flame front. Assuming the flame front has a thickness of zero and is a propagating interface between burnt and fresh gas it is tracked using a field variable G. The resolved flame brush in the LES simulation is associated to the iso-level $G = G^*$. The resolved G field is then smoothed out over the grid. The G equation is written as [69];

$$\frac{\partial \bar{\rho}\tilde{G}}{\partial t} + \frac{\partial \bar{\rho}\tilde{u}_i\tilde{G}}{\partial x_i} = \rho_0 \bar{s}_T \left|\nabla \bar{G}\right| \qquad \text{Eq 3-33}$$

The sub grid turbulent flame speed $\bar{s}_T$ requires a model and lacking a rigid definition Eq 3-34 is used where the constants α and n must be defined. The sub grid scale turbulence $\overline{u'}$ is estimated using components of the resolved shear stresses $\tilde{S}_{ij}$. The use of a sub grid scale turbulent flame speed is expressed as a simple formulation and does not give a well defined flame. Also there is no universal model available for the quantity. The technique is illustrated in Figure 3-6.

$$\frac{\bar{s}_T}{s_L} = 1 + \alpha\left(\frac{\overline{u'}}{s_L}\right)^n \text{ and } \overline{u'} \approx \Delta\left|\tilde{S}\right| = \Delta\sqrt{\left|2\tilde{S}_{ij}\tilde{S}_{ij}\right|} \qquad \text{Eq 3-34}$$

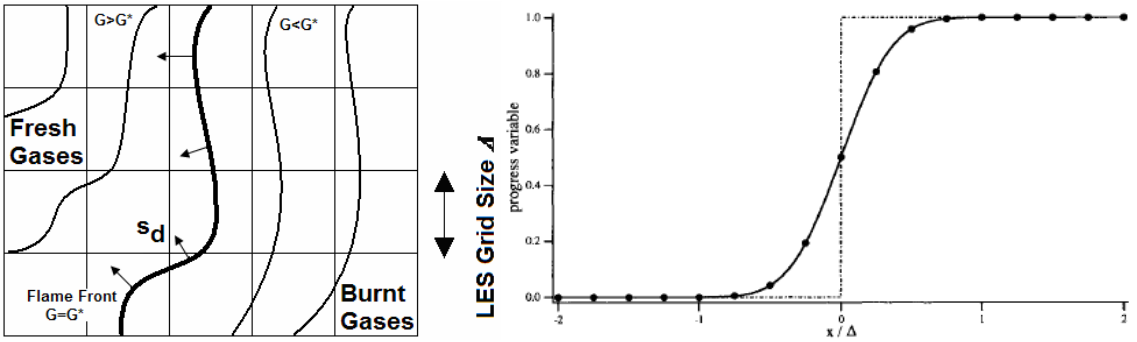

Figure 3-6 Left: Illustration showing the G-Equation employed to resolve the flame front. Right: Resolving the flame front by using a grid size greater than the LES grid, -- Unresolved flame front, — Resolved flame front using greater grid size.

A recent approach to overcome the problem of resolving the flame front is to filter the reduced temperature (progress variable) balance equation [70]. The local displacement speed s_d of the of iso surface Θ is the difference between the flow speed $\vec{u}$ and the flame front speed $\vec{w}$.

$$\frac{\partial \rho\Theta}{\partial t}+\frac{\partial \rho u_i\Theta}{\partial x_i}=\frac{\partial}{\partial x_i}\left(\rho D\frac{\partial \Theta}{\partial x_i}\right)+\dot{\omega}_\Theta=\rho s_d\left|\nabla\Theta\right| \text{ and } s_d=(\vec{w}-\vec{u})\cdot\vec{n} \qquad \text{Eq 3-35}$$

Application of the LES filter yields the following expression.

$$\frac{\partial \overline{\rho}\widetilde{\Theta}}{\partial t}+\frac{\partial \overline{\rho}\widetilde{u}_i\widetilde{\Theta}}{\partial x_i}+\frac{\partial}{\partial x_i}\left(\widetilde{\overline{\rho}\widetilde{u}_i\Theta}-\overline{\rho}\widetilde{u}_i\widetilde{\Theta}\right)=\frac{\partial}{\partial x_i}\left(\overline{\rho D\frac{\partial \Theta}{\partial x_i}}\right)+\overline{\dot{\omega}}_\Theta=\overline{\rho s_d\left|\nabla\Theta\right|} \qquad \text{Eq 3-36}$$

As the flame front is too thin to be resolved on the LES computational grid the progress variable (Θ) has been filtered and resolved using a physical space Gaussian filter. The filter uses a size greater than the LES grid size, allowing the numerical resolving of the filtered flame front, see Figure 3-6. The flame front displacement term, $\overline{\rho s_d\left|\nabla\Theta\right|}$, is then modelled. Using the sub grid scale FSD, Σ^* (flame surface density per unit volume at sub grid level) and the sub grid scale flame wrinkling factor Ξ (ratio between sub grid scale flame surface and its projection in direction of flame propagation) an expression for the flame front displacement can be derived. Both require modelling.

$$\overline{\rho s_d\left|\nabla\Theta\right|}\approx\rho_u s_L\Sigma^*=\rho_u s_L\Xi\left|\nabla\overline{\Theta}\right| \qquad \text{Eq 3-37}$$

The fresh gas density and laminar flame speed are ρ_u and s_L respectively.

3.2.4 LES of Gas Turbine Combustion and Instabilities

Application of current LES codes to laboratory and real gas turbine geometries has been undertaken demonstrating both its applicability and limitations. Most studies are of laboratory swirl stabilised dump combustors with a simplified geometry. This allows simplification of the simulation and the required mesh

generation. In parallel to most studies a real version of the combustor will exist. This will allow comparison to experimental data which is taken as the reference. The comparison is required as LES is still in its infancy and still needs to be validated with experimental data. LES must be capable of not only describing steady turbulent flows but be able to describe combustion instabilities, including their prediction, behaviour and elimination with combustor design. What follows is a review of findings from relevant LES investigations of similar simplified lean premixed dump combustors.

As a precursor to a combusting investigation a LES has been performed of a non reactive turbulent swirling flow in a dump combustor and compared to experimental data collected using Laser Doppler Velocimetry (LDV) [71]. The swirl number was set at 0.43 and the inlet flow had a Reynolds number of 20,000 and bulk inlet velocity of 2.72ms^{-1}. An illustration of the experimental and simulation geometry is shown in Figure 3-7. The LES and LDV data showed good agreement. The flow structure within the chamber exhibited a strong inner recirculation zone, a feature of vortex breakdown and possessed a PVC. This was attributed to the dump plane geometry. The turbulence was generated by two shear layers, the first at the shoulder of the dump plane and the second between the inlet flow and the inner recirculation zone. The turbulence created was highly anisotropic at the inlet and became more isotropic downstream.

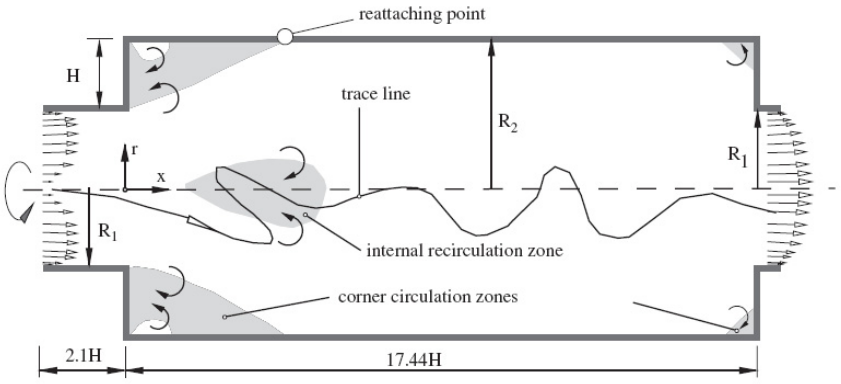

Figure 3-7 Illustration of Experimental and Simulation geometry. R1 = 25.32mm, R2 = 49.12mm, H = 23.8mm. Shaded regions show recirculation zones [71].

A second LES has been preformed of a non reactive turbulent swirling flow in a dump combustor using various swirl numbers [72]. The swirl numbers investigated were 0, 0.33 and 0.43 with corresponding Reynolds numbers 11,700 10,000 and 20,000. The inlet bulk velocities were 1.59 ms^{-1}, 1.57 ms^{-1} and 2.72 ms^{-1}. The LES was validated experimentally using LDV. Once again an IRZ was observed in the swirling cases that moved progressively upstream and became stronger as the swirl number was increased. The IRZ was found to oscillate at a single low frequency forming the PVC. The flow also displayed an off axis behaviour with the centre axis of the flow not being coincident with the chambers central axis. Corner recirculation zones were also present. Two shear layers, the first between the inlet flow and the CRZ and the second, between the inlet flow and the IRZ were present. Turbulence generation was attributed to this second shear layer where the turbulence was highly energetic and anisotropic. The dissipation of the turbulence and its return to isotropic nature was accelerated

with higher swirl along the combustor axis. The reason for this was with that swirl induces a centripetal force which drives the flow radially outwards. Stronger swirl resulted in quicker transportation to the containing wall where it is dissipated by viscous friction.

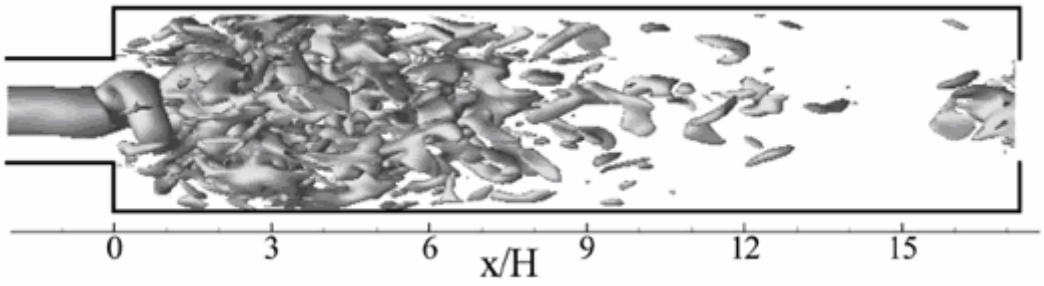

Figure 3-8 3D isosurface of instantaneous streamwise vorticity $\omega = 700\ s^{-1}$ with a swirl number 0.43. The swirling inlet flow is clearly evident entering the chamber and breaks down with the IRZ [72].

The oscillatory movement of the IRZ can be seen on the instantaneous streamlines in Figure 3-9. The IRZ can clearly be seen moving off the chamber centre line axis. This occurred when the radial component of velocity was non zero. This component was used to characterise the precessing of the IRZ and the power spectra at three locations on the central axis was determined. A single dominant frequency became more evident and persisted downstream further with stronger swirl. For the swirl number of 0.43 the frequency of the PVC was 18Hz.

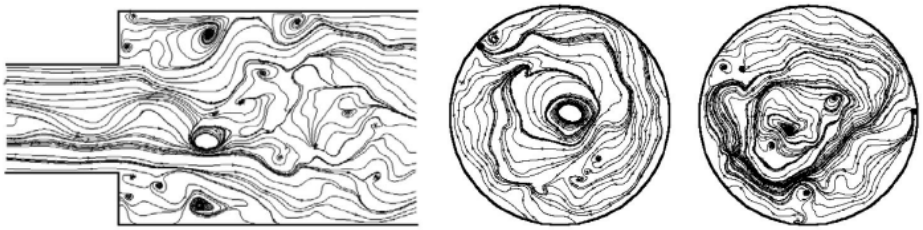

Figure 3-9 Instantaneous streamlines of LES with swirl number 0.43. Sections taken along the centreline, and across chamber at x/H =1 and x/H =5 [72].

These two non reactive LES clearly show common flow structures exhibited by swirl flows within dump combustor geometry (non annular injection) and describe the location of turbulent kinetic energy production being the shear layer between the IRZ and inlet flow. The IRZ also becomes stronger with increased swirl number changing the flow structure making the IRZ wider quicker and accelerating the dissipation of the produced turbulent energy.

A LES investigation comparing non reacting and reacting flows has been performed of a swirl stabilised non annular dump combustor using two different LES schemes [73]. The inlet diameter was 34 mm and the dump diameter was 95mm. The chamber length was unspecified. The swirl number at the inlet was 0.56 with an inlet velocity of 110 ms^{-1} with a corresponding Reynolds number of 320,000. The inlet pressure was 6 bar (g) and the inlet temperature 644K. These represent realistic operating conditions. The fuel simulated was methane fully premixed with air with an equivalence ratio of 0.56. The reacting flow

simulations were computed firstly using a flame surface density model based upon flame wrinkling to model the flame and secondly using an Arrhenius approach. This was to enable a comparison of the two combustion models which will not be pursued further. For reacting and non reacting cases a one equation eddy viscosity model was used for the sub grid modelling. The non reacting flow exhibited a toroidal vortex system, CRZs and a helicoidal system along the chamber axis forming the IRZ, Figure 3-10 (a). The flow entered the chamber at high speed and spread radially before encountering the chamber wall and travelling at relatively high speed along the wall towards the exhaust. Regions of intense vorticity and shear are found on the borders of the incoming jet and at wall regions due to local velocity gradients. Figure 3-10 (b) shows the radial spreading of vorticity (ω_Φ) to the walls and forms the toroidal vorticity system. Figure 3-10 (c) (d) and (e) show cross sectional views of vorticity (ωx) revealing the presence of an anti clockwise (blue) rotating vortex sheet outside of the clockwise swirling inlet jet (red). This feature is absorbed moving downstream to yield a single clockwise vortex ring before dissipating into clockwise structures.

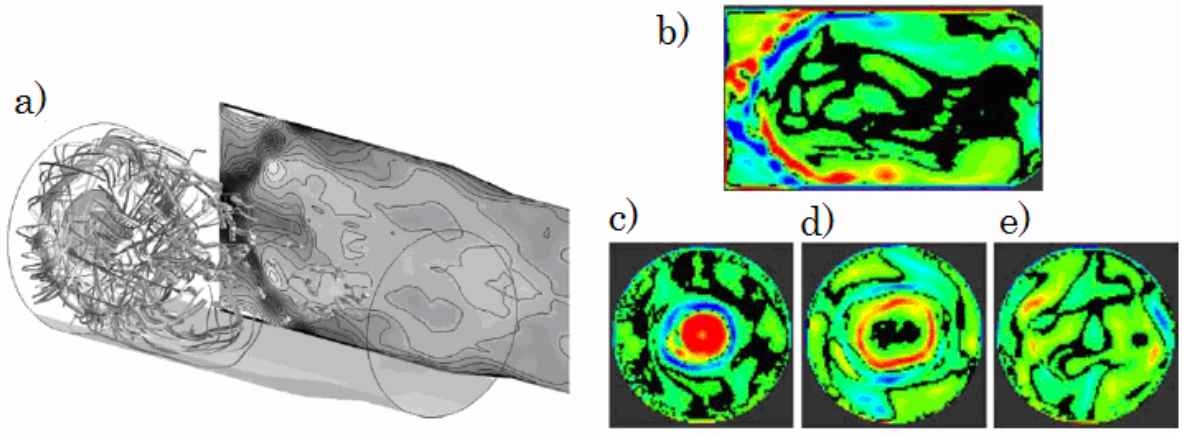

Figure 3-10 Illustration showing a) Perspective view showing stream ribbons from the jet inlet, vortex cores and axial velocity contours at the off set centre plane. b) Vorticity ($\omega\Phi$) along chamber length. c) Vorticity (ωx) at x/D = 0.18. d) Vorticity (ωx) at x/D = 0.72. e) Vorticity (ωx) at x/D = 2.33 [73].

The reacting case possesses the same global characteristics with a IRZ and a weaker CRZ. The flame is anchored to the edge of the inlet and perturbed by vorticity due to shear layer instabilities resulting in a corrugated flame surface. The flame is located between the clockwise swirling jet and the counter clockwise rotating vortex sheet. This location will mean the flame will experience stretch (strain and curvature) affecting the burning velocity and flame dynamics.

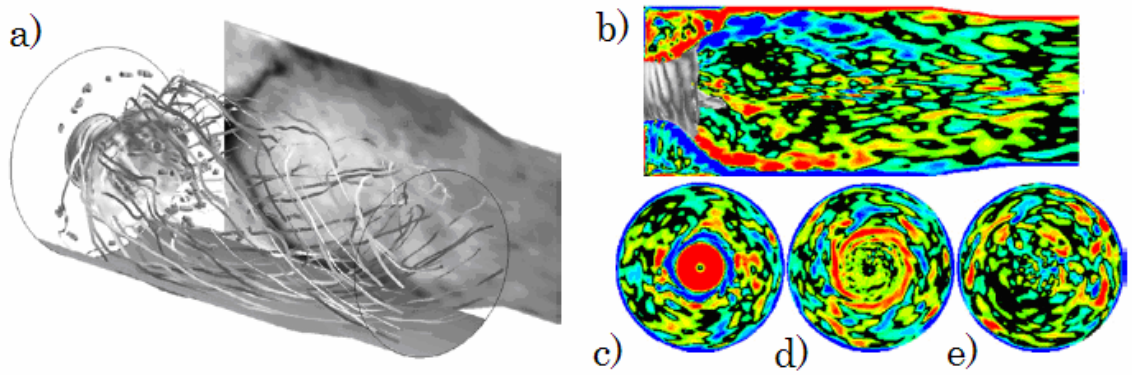

Figure 3-11 Illustration showing reacting flow a) Perspective view showing stream ribbons from the jet inlet, vortex cores, iso-surface of the flame and axial velocity contours at the off set centre plane. b) Vorticity (ω_Φ) along chamber length. c) Vorticity (ω_x) at x/D = 0.18. d) Vorticity (ω_x) at x/D = 0.72. e) Vorticity (ω_x) at x/D = 2.33 [73].

The presence of the flame leads to the creation of flame generated vorticity which is clearly shown. This produces both clockwise and anti clockwise pockets of vorticity along the length of the chamber. Once again an anti clockwise vortex sheet exists outside of the clockwise swirling inlet jet and is ultimately absorbed into a clockwise vortex sheet before dissipating.

As well as describing overall flow features and behaviour within a combustor chamber LES can also be used to investigate combustion instabilities. An LES has been performed on a swirl staged turbulent non annular dump combustor using lean premixed propane [74]. The equivalence ratio was 0.8. The combustor geometry consisted of a cylindrical inlet of 30mm diameter leading to a square cross section dump chamber, 100mm by 100mm and 500mm in length. The inlet flow velocity was 31.26ms^{-1} corresponding to a Reynolds number of 46,700. The combustion scheme utilised the thickened flame model to resolve the flame front on the LES grid and account for the acoustic effects. The sub grid scheme used was not mentioned. The results were analysed with respect to self excited combustion instabilities. The mean of the LES revealed a central IRZ and CRZs. In conjunction with using LES to compute the reacting flow field an acoustic solver was implemented based upon the Helmholtz equation which solved for all the acoustic modes of the chamber using the LES data. Additionally the total acoustic energy balance (E1) was described in terms of the Rayleigh criteria (S1) and an acoustic flux term (F1) which represents an acoustic loss term in a one dimensional analysis. Using the LES data and the mentioned acoustic tools the exhaust section of the model was changed from acoustically open to closed and back to open resulting in unsteady pressure and heat release that experienced four distinct phases termed 'growth', 'overshoot', 'limit cycle' and 'decay' which describe the creation, stabilisation and end of the dominant 380Hz instability. This is depicted in Figure 3-12.

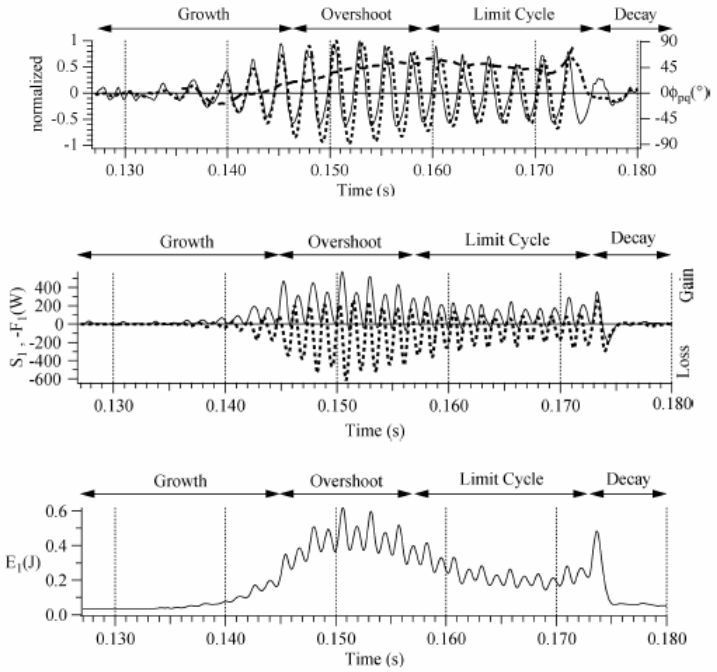

Figure 3-12 Top: Graph showing Mean normalised pressure —, heat release ⋯, and phase angle between pressure and heat release ---. Middle: Mean values of Rayleigh criterion S1 — and acoustic fluxes F1 ⋯. Bottom: Evolution of chamber acoustic energy E1 [74].

The growth phase exhibits an increase in pressure and heat release amplitudes as the phase between the two remains between 0º and 45º giving a positive S1 term. The overshoot phase is typical of combustion oscillations where an excess of acoustic energy is observed before reaching a stable oscillating nature [74]. The phase difference remains approximately at 45º and the instability becomes saturated. The limit cycle phase represents the stabilised instability where the acoustic losses have gained equilibrium with the acoustic energy production. The decay phase occurs when the exhaust acoustic boundary condition is changed to open. The phase increases sharply beyond 90º and the S1 term becomes negative damping the instability.

The interaction between the identified instability when stable and the flame was then extracted from the LES data. The longitudinal mode created a vortex ring at the outer diameter of the inlet which then detaches and is advected downstream by the mean flow. Initially the flame is stretched by the mean flow rather than local wrinkling due to the vortex ring. As the vortex ring is advected further it wrinkles the flame surface greatly increasing the reaction rate before dissipating to smaller structures.

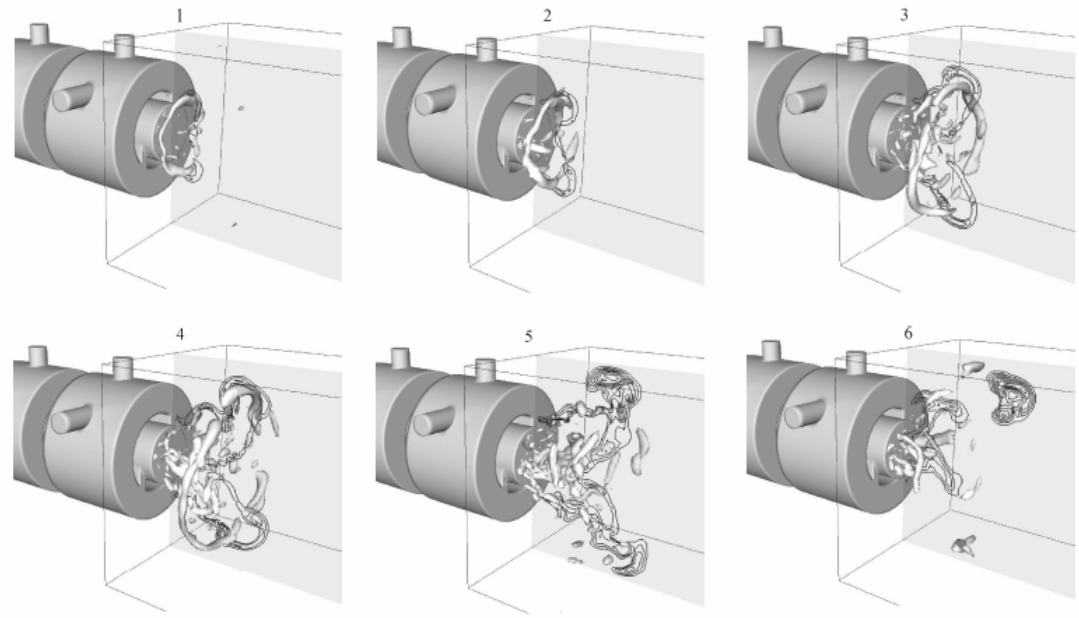

Figure 3-13 Illustration of vortex ring shedding during the limit cycle. The iso-surface represents the Q vortex criterion and the black lines represent the iso-reaction rate in the chamber central plane [74].

A Helmholtz solver was used to calculate the thermoacoustic longitudinal eigenmodes of the burner. In order to do this the Flame Transfer Function (FTF) was used relating the heat release fluctuations to velocity fluctuations through a reference point using the magnitude and phase of the FTF. These two properties were extracted from the LES data by Fourier processing the local heat release and unsteady velocity at the reference point during the steady limit cycle phase. The magnitude and phase were evaluated at all positions coinciding with the flame. The eigenmodes and growth rate determined using the Helmholtz solver showed that the fastest growing mode agreed well with the mode observed using the acoustic energy analysis of the LES data. Furthermore the eigenmodes can be reconstructed within the chamber geometry describing the evolution of the longitudinal modes. This work demonstrates how simple one dimensional acoustic models are able to approximately predict the unstable longitudinal thermoacoustic modes, however input data is required for the FTF and the effect of non longitudinal modes is neglected.

Finally a LES has been performed of a lean premixed swirl stabilised dump combustor with an annular injector investigating acoustic, flame and hydrodynamic instabilities [75]. A lean premixed methane mixture of equivalence ratio of 0.57 with a swirl number of 0.76, inlet Reynolds number of 35000 and velocity of 86.6ms^{-1} was used. The inlet temperature was 600K and chamber pressure was 4.63 bar. These conditions correspond to a previous unstable experimental arrangement [41, 42]. The experimental and simulation geometry consisted of an annulus with inner diameter of 9.53mm and outer diameter 20.3mm. The chamber diameter was 45mm and 235mm in length. The combustion scheme consisted of the level set flamelet library method [62]. Finite chemistry was used to generate the flamelet library with GRI-MECH 3.0 consisting of 325 elementary reactions and 53 species. A mean representation of the flow field revealed an IRZ in the wake of the bluff body. The corner area

exhibited two recirculation features instead of the expected one. Turbulent kinetic energy was formed at the two shear layers between the respective recirculation zones. Higher turbulent kinetic energy was created at the shear layer between the IRZ and the inlet flow.

This study allowed the systematic identification of flow features that interact and are responsible for combustion instabilities. Large vortical structures were found to be formed at the shear layers due to the swirling component. Vortices were also formed in the flame region due to dilation effects. The vortices from the shear layers were advected downstream from the annulus into the core region of the IRZ where they were dissipated. The vortex breakdown mechanism was the bubble type. CRZs were also observed. A vortex core was observed originating from the outer edge of the annulus and wrapped around the wrinkled flame structure. This structure oscillates about the chamber central axis and survived for approximately two revolutions before breaking up into smaller structures. The spiral was in the opposite direction to the swirling flow. Finally an additional bubble structure was observed to be anchored to the centre of the bluff body. A PVC was found to develop around the bubble, coinciding with the inner shear layer, when the IRZ began to precess. Both were winding in the opposite direction to the swirling flow. Although the PVC can enhance mixing and efficiency it also has the characteristic of coupling with the low frequency acoustic oscillations of the chamber. The initial vortex shedding frequency (known as the most amplified frequency) of the shear layer and the acoustic resonant and harmonic frequencies of the chamber were calculated. It was found that the initial vortex shedding frequency matched the first radial mode of the chamber and the second harmonic matched the first tangential mode of the chamber. The third harmonic agreed well with the first longitudinal mode of the inlet. The agreement of vortex shedding frequencies and acoustic modes indicate a resonance exists of the first radial and tangential chamber modes and the first longitudinal mode of the inlet.

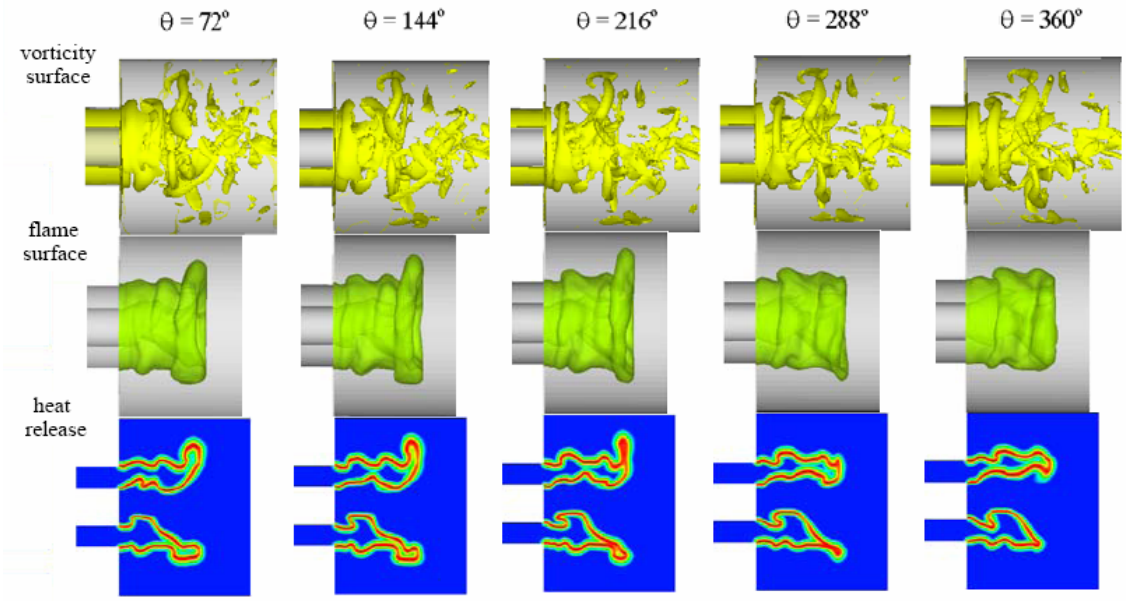

Figure 3-14 Illustrations showing temporal evolution of vorticity (75000 s^{-1}), Thermal surface (T=1700K) and normalised heat release contour over one cycle of the first tangential mode [75].

These modes lead to vortices which are formed at the outer edge of the annulus and perturb the flame front. As they are advected downstream they continue to distort the flame and can produce isolated combusting pockets. Finally the vortices move out of the flame region and dissipate into smaller structures. As the vortex changes the flame front shape it also changes the heat release rate. This is illustrated in Figure 3-14. The coupling between the heat release rate and the acoustic motions was characterised using the Rayleigh criterion indicating if the unsteady heat release is driving or damping the acoustic oscillations. As can be seen there are four asymmetrical dipole pairs located on the outer edge of the annulus and a single distributed pair attached to the bluff body. These pairs were attributed to the wave like nature of the heat release (due to local vortex perturbation of flame front). The positive (driving) dipoles are located in the burnt gas where as the negative (damping) dipoles are located in the fresh gas.

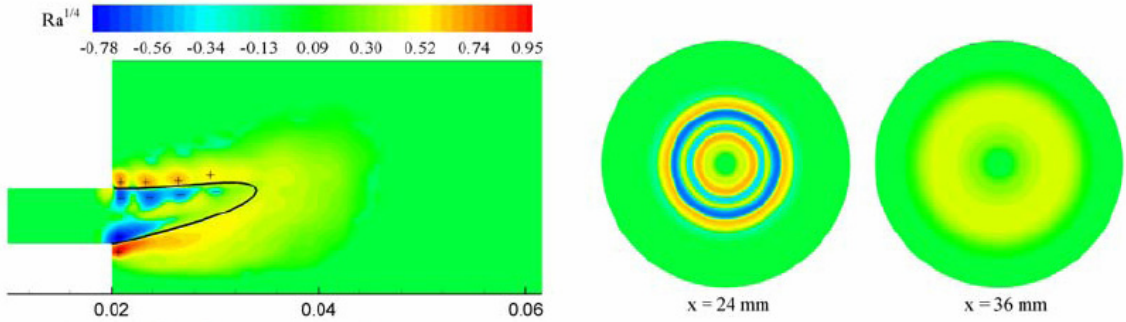

Figure 3-15 Illustration showing normalised Rayleigh parameter [75].

The proposed explanation for these dipoles was explained considering the interaction between the flame and acoustic field. As the pressure builds up the flame zone expands with the flame front moving into the burnt gas region giving a positive heat release fluctuation on the burnt side and a negative fluctuation on the fresh gas side. When the pressure has a negative fluctuation the flame zone is reduced. The flame front moves to the fresh gas region and gives a negative heat release fluctuation on the burnt gas side and a positive heat release fluctuation on the fresh gas side. In the burnt gas region the heat release fluctuation is in phase with the pressure oscillation for both positive and negative fluctuations. However on the fresh gas side the heat release oscillation is out of phase with the pressure for both fluctuations. As shown the acoustic field is correlated with the unsteady heat release. This work demonstrates the vortex shedding process is dominated by the coupling of certain acoustic modes and shear layer instabilities.

3.2.5 Summary

LES is a promising tool for turbulent combustion and combustion instability modelling. The realisation of instantaneous snapshots of the flow with small time steps allows analysis that is impossible with RANS and access to data that to determine experimentally is very difficult. However LES of combustion is far from a complete robust tool. There are three main elements of the combustion description that require modelling, the Reynolds stresses, turbulent transport of species mass fraction and the mean reaction rate. Most work has been focused on refining the mean reaction rate description. This usually involves a reaction rate

model and a model for the turbulent flame speed which need to be validated experimentally.

LES is still in its early stage of development for combusting flows and requires substantial validation regarding flow field comparisons, combustion features and other fluid mechanical characteristics with experimental data, particularly in its application to gas turbines. Part of this work is to provide experimental data to help develop LES further through comparisons. This involves the development of a novel gas turbine combustor and the collection of appropriate data to characterise the combustor.

4 COMBUSTION DIAGNOSTICS

Investigations of combusting flows regarding chemistry, structure, flow fields and interactions of these has been revolutionised with the application of laser based measurements and two dimensional detectors. Previous techniques utilising thermocouples, pressure and sampling probes resulted in altering the very quantity that was desired to measure by the physical presence of the measuring device. Optical techniques overcome this by being non intrusive allowing a true measurement to be made. The combination of laser, optics and cameras (historically film now digital) has allowed 2D and 3D non intrusive measurements to be made, greatly increasing insight into combusting flows that would have remained unknown.

The application of optical techniques begins with the source of the probing electro magnetic radiation, the laser. Simply put a laser is a device that is able to use an energy source (electrical or photonic) and convert this through an active medium of a specific material. The interaction of this energy with the active material causes an electronic population inversion at the molecular level. The relaxation of these excited molecules results in a photon of a characteristic wavelength. This wavelength may be changed by integer values using a harmonic generator (crystal) or can be used as the energy source for a second laser to obtain emission at the desired wavelength. A laser emission is typically of a single wavelength, polarised and coherent.

Laser emissions can be directed into the combusting flow and a particular interaction of the laser photons with the targeted species can be utilised to gain flow field information such as species density, temperature and flow velocity. These interaction mechanisms are briefly summarised.

Elastic scattering processes are those in which the affected molecule returns to its original state. There is no energy exchange between the molecule and incident photon and the scattered photon is of the same wavelength as the incident photon. Mie and Rayleigh scattering are both elastic scattering processes. The distinguishing feature between these two processes is the ratio of particle diameter d to incident wavelength λ. When $d/\lambda << 1$ Rayleigh scattering is present where the collected signal is dependent upon temperature and species number density. When $d/\lambda >> 1$ the scattering is Mie scattering and is independent of temperature and species number density. Raman scattering is an inelastic scattering process in that there is an energy exchange between the incident photon and the affected molecule. The internal energy of the molecule is distributed among its electronic, vibrational and rotational levels. The incident photon interacts with the vibrational energy level (which oscillate) of the molecule which causes the scattered photon to be of a longer (stokes) or shorter (anti stokes) wavelength. The collected signal can be used to provide information of temperature and species. The signal is very weak and difficult in application to practical combustion systems. Finally another type of inelastic scattering is fluorescence. The incident photon is of a tuned wavelength coinciding with a particular electronic energy level transition of a specific molecule. The molecule

is then raised to an excited state. The relaxation of the molecule is in the form of photon emission. The emission is typically of a shifted wavelength (resonance fluorescence for non shifted wavelength).

The above discussion has focused upon the interaction of laser light with molecules to determine combusting flow information. However photons are also emitted from chemically generated reaction intermediaries, combustion radicals, that can be collected to help characterise combusting flows, this process is termed chemiluminescence.

4.1 Heat Release Rate and Radical Choice

Combustion radicals are important in the continuation of the chemical reactions needed to sustain a combusting system. These molecules exist for very short periods of time as they are produced and consumed within the reactions that describe the process of hydrocarbon oxidation to carbon dioxide and water. Spatial identification of these radicals allows the location of reactions creating and consuming these radicals to be determined. Not only is the location important but the quantity of these radicals at spatial locations can offer insight into combustion behaviour. From well known radicals such as OH, CH, C, O, C_2 and HCO, predominantly OH and CH are targeted in combustion investigations either with a PLIF (Planar Laser Induced Fluorescence) or chemiluminescence strategy. This is because of the relatively higher concentration of these two radicals, importance in key reactions and well known experimental set up to achieve fluorescence.

A study into the suitability of a number of radicals was performed comparing each radical experimentally [76] and with a numerical simulation of the same set up [46]. A non swirling laminar methane flame was exposed to an unsteady vortical flow so the effect of various strain rates could be ascertained. The methane mole fraction, heat release rate, HCO, CO_2* and OH were calculated. While OH, CH and HCO PLIF and CH* chemiluminescence were performed experimentally. Comparisons of the OH and CH PLIF with the calculated heat release rate reveal that the OH images exhibit a very broad boundary which becomes distorted and eventually indistinguishable as the vortex interacts with the flame front. The CH images show a much thinner and better defined boundary similar to the calculated heat release rate. However as the vortex causes increased strain the CH signal is lost and the CH boundary is broken [76]. This is not observed on the heat release rate images. The conclusions of this comparison is that OH PLIF is not a suitable measure of heat release in regions of unsteady flame curvature and does not provide a well defined boundary under those conditions. CH PLIF provides a much better defined boundary but can not be used in high stretch regions due to CH extinction [46]. The computed HCO concentration showed excellent correlation with the calculated heat release rate and provided a well defined reaction zone under all variations of strain and curvature. A study investigating the carbon content of three different paths for the conversion of carbon to carbon dioxide revealed the importance of HCO. The first path yielded CH and CH*, the second OH, OH* and C_2 and C_2* and the third path to HCO and CO_2*. It was found that the carbon content of the first part was small and that less than 15% of the carbon is converted to CH. The

majority of carbon, 60-90% flows through HCO and although the same can be said for other intermediary species none show the excellent correlation with heat release rate that HCO does. In addition the carbon pathways are interlinked and it was found that carbon was directed from paths one and two to path three, further reducing the carbon available for other radicals. For this reason HCO is a good rate measure of the forward progress of hydrocarbon conversion to H_2O and CO_2. This was verified by performing HCO PLIF. These measurements were able to be made by using the reproducibility of the experiment. An average of 100 images was created and this was worked with. The signal to noise ratio was less than 2:1. This casts doubt on the experimental applicability of HCO diagnostics applied to turbulent flows where single images with higher signal to noise ratios are required [46].

A recent development to over come this problem has been performed [44, 45, 77]. The two parent species responsible for the creation of HCO were identified, OH and CH_2O. Both of these species were excited using PLIF and imaged simultaneously. The experimental setup allowed the product of the two images to be equal to the number densities of the two species and the temperature dependence of the two LIF signals. The temperature dependence is therefore proportional to the forward rate constant. Which implies the product of the two PLIF images is proportional to the heat release rate. This technique was successfully applied to a counter flow burner and a bluff body burner and exhibited none of the limitations outlined above providing a planar image of the reaction zone and a good estimate of the heat release rate.

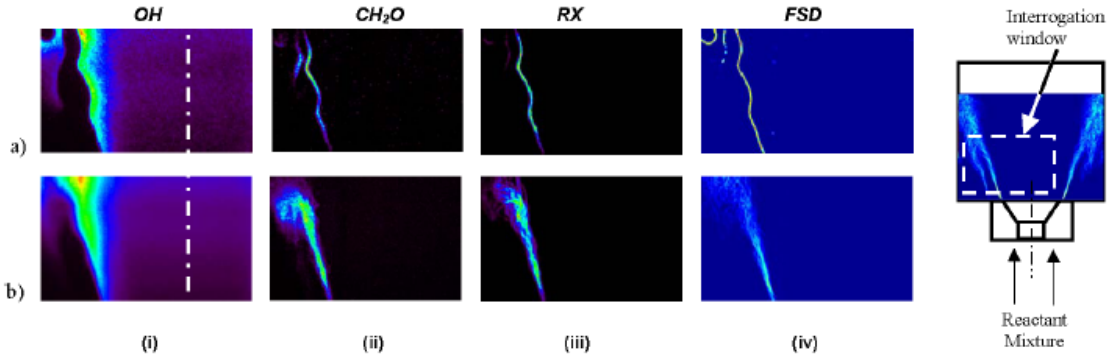

Figure 4-1 Images of a bluff body stabilised ethylene flame (a) Instantaneous simultaneous OH and CH_2O PLIF images and calculated Heat Release rate (RX) and Flame Surface Density (FSD) Images. (b) Average images of those quantities [44].

Although OH and CH as reaction zone markers exhibit deficiencies it has been shown that the chemiluminescence signal from CH* and C_2* is linearly related to the fuel mass flow rate for any equivalence ratio [78]. This was validated for flows up to a Reynolds number of 12000. The excited species are restricted to the reaction zones which can be thought of as sheet like so the total collected chemiluminescence signal can be viewed as being proportional to the reaction zone surface area [79]. In addition the dominant relaxation mechanism for excited species is through quenching which occurs faster than the species production rates. Therefore the collected signal is proportional to each species' production rate [46]. Chemiluminescence has been used to investigate the heat

release of unstable combustion in a variety of studies [41, 77, 80, 81]. Simultaneous OH* and CH* has also found use as a way of spatially measuring equivalence ratio [81-84] and sensors developed to monitor combustion instabilities in real time for active control systems [85-88].

The choice of using Chemiluminescence or a PLIF technique is dependent upon the available experimental equipment and what the collected data is to be used for. The implications to this work are that OH or CH PLIF would identify in a plane the instantaneous location of these radicals subject to the limitations outlined above. Although providing a reasonable good marker for the reaction zone, the measurement itself is not a measure of heat release rate [46]. Alternatively chemiluminescence offers a measure of heat release rate but is a line of sight measurement and therefore is not as good as a PLIF technique at characterising the structure. The new technique to effectively acquire HCO [45] offers the best solution providing heat release and a flame marker; however the method comes with increased cost and complexity of needing two PLIF systems.

4.2 Combustion Chemiluminescence

Chemiluminescence is radiation emitted from electronically excited molecules when these return to a lower energy state. The wavelength of radiation which is emitted is characteristic of the particular molecule and the particular transition the molecule undergoes. The more complex the molecule, the more complex the characteristic radiation spectrum observed. For some simple (diatomic) molecules, the spectrum exhibits one major peak and relatively few, weak secondary peaks. For complicated molecules, the radiation spectrum observed appears continuous. OH, CH and C_2 are examples of molecules exhibiting a simple spectrum with major peaks at 308 nm, 431.5 nm and 513 nm respectively, whereas CO_2 is an example of a molecule with a radiation spectrum that appears continuous.

Combustion chemiluminescence can be used in combustion studies because the concentrations of the excited species are in excess of the equilibrium concentrations expected for the same temperature without combustion. Therefore the excited molecules are produced as the result of thermal excitation and as a direct product of the combustion chemical reactions. The amount of radiation emitted by combustion at a specific wavelength is proportional to the concentration of the associated molecular species. In order to derive species concentration from its chemiluminescence signal the process of quenching must be accounted for. Also the collected chemiluminescence signal is obtained from created excited molecules of a specific species. The proportion of the total quantity of the particular specie that is excited must be known and the reaction mechanisms associated with the excited and ground states of this specie also.

With the widespread development of Chemiluminescence sensors to monitor combustion instabilities there has been a concerted drive to develop the chemical kinetics of the combustion radicals in excited states. If this can be accomplished a measured chemiluminescence signal could be used and compared with a suitable chemical model to infer in absolute units heat reaction rate and temperature. The historic proposed reactions include those of C_2 and OH [89] and later reactions involving C_2H and O or O_2 [90, 91]. These were tested experimentally and

numerically using GRI mech 3.0 for methane hydrogen blended fuels using a total of 18 reactions [92]. This work concluded the dominance of the originally proposed key reaction and recognised secondary importance of one C_2H reaction with atomic oxygen.

$$C_2 + OH \leftrightarrow CH^* + CO$$
$$C_2H + O \leftrightarrow CH^* + CO \qquad \text{Eq 4-1}$$

The authors were satisfied with the reaction library and proposed rate coefficients and proposed further testing and comparison for further validation before application to real combusting systems. Other works state the dominant CH* producing reaction was with C_2H and O. This was performed in acetylene flames and when methane was added the collected CH* signal was reduced. This was attributed to the parent molecules of CH* attacking the added methane and being consumed instead of forming CH* [93, 94]. Clearly the development of satisfactory CH* kinetics is incomplete.

For this work Chemiluminescence has been used. The radical chosen is CH* as this radical is a more definitive marker than OH for the reaction zone. The experimental apparatus used is described in Chapter 6.1.

4.3 Flow Field Measurements: Particle Imaging Velocimetry

Optical flow diagnostics are based around the interaction of light with the flow media. In an ideally homogenous media there is no significant interaction between light and fluid which would allow the collection of flow velocity data. Particle Image Velocimetry (PIV) makes visible the fluid motion with the addition of tracer elements and their subsequent displacement. The flow is illuminated normally by a pulsed laser sheet. This is typically achieved with a Nd:YAG laser with emission at 532nm. The laser radiation is formed into the desired sheet using an arrangement of optical lenses. The laser is pulsed twice with a small known time separation between pulses. A camera typically positioned perpendicularly to the laser sheet and directly in front of the target flow records the laser light which is scattered by the tracer particles according to Mie scattering theory. From the recorded images of particle position and the known time separation between laser pulses the velocity field is evaluated. The considerations of PIV are described in more detail below.

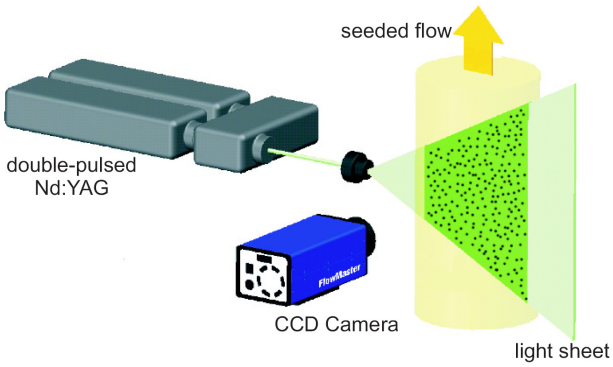

Figure 4-2 Illustration showing a typical PIV experimental set up.

The calculated velocity is inferred from the motion of seeding particles that are initially considered ideal in that they follow exactly the fluid motion, do not alter the fluid properties with their presence and have no interaction amongst themselves. The velocity of the tracer particle is measured indirectly as a displacement in a finite time interval. Ideally the tracer particles' velocity will match that of the local flow. Practically the measured displacement and inferred velocity is related to the tracers' perceived trajectory between two instances, and as such the displacement is an approximation of the fluid velocity within a finite error. The error is often negligible provided the spatial and temporal scales of the flow are large with respect to the spatial resolution and laser pulse separation time [95].

The extent to which the tracer particles ideally follow the flow can be described in terms of slip. The particles should be able to follow the streamlines of the flow without excessive slip. A simple method to evaluate this is to determine the settling velocity of the particle under gravity. Assuming the argument of Stokes' drag the settling velocity u_θ is given by [96];

$$u_\theta = \frac{g d_p^2 \left(\rho_p - \rho_f\right)}{18\mu} \qquad \text{Eq 4-2}$$

Where d_p and ρ_p are the particle diameter and density, and μ and ρ_f are the fluid viscosity and density respectively. The suitability of a tracer particle relies on the comparison between the settling velocity and the actual velocity of the flow, where the settling velocity must be much smaller than the flow velocities. In the presence of spatial or temporal gradients within the fluid the ability of the particles to follow the flow may be estimated, as the particles' inertia will cause a delay in response to any acceleration of flow [97]. The final requirement of any tracer particle is that it should be efficient at scattering the illuminating laser light [98]. The use of weak light scattering particles will require the use of powerful lasers and superior image capturing equipment making the technique more expensive.

The interaction of the laser emission and the seeding particle as already mentioned is dependent upon the ratio of particle diameter and radiation wavelength. Typical seeding particles are of the micron size. Combined with 532nm laser radiation the interaction is described by Mie scattering. The resultant scattered light is highly directional as can be seen in

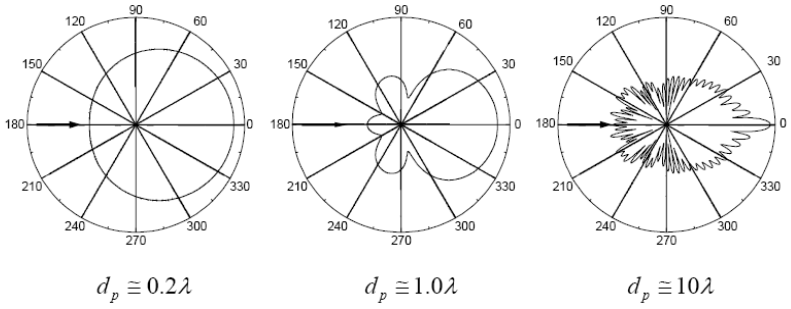

Figure 4-3 Polar plots showing elastically scattered photon intensity (log scale) for various ratios of particle and incident radiation wavelength [99].

Consideration is given to the size of the interrogation windows that the captured image is divided into. This determines the size of the smallest structures that can be resolved within the flow. It is also prudent to attempt to ensure that there are minimal velocity gradients acting within an interrogation window as the accuracy of the measurement will suffer. Once the field of view is decided and the interrogation window size known the image is calibrated to obtain a physical resolution. Using approximate knowledge of the flow velocity prior to experimentation allows the determination of the time separation between the laser pulses to be set. It is common practice to have a time separation which corresponds to a particle displacement within the image of approximately a quarter to a third of the interrogation window size.

The camera used can be operated in two modes, 'single frame double exposure' or 'double frame double exposure'. Older digital cameras were unable to capture two images in the time dictated by the laser pulse separation time. Therefore a single frame would contain the sum of the two scattering events from the two laser pulses. This single image is then processed by subdividing the image into interrogation windows and applying an auto correlation function within it to determine the particle displacement. The result of this can be seen in Figure 4-4. The auto correlation function shows a strong self correlation peak in the centre of the interrogation window with two symmetrical lesser peaks either side. The distance from the self correlation peak to either of the two lesser peaks is the same and represents the distance the particle has moved. However the function does not know the chronological order the image was created in and therefore can not determine the sign of the displacement creating a 180° directional ambiguity that can only be resolved with prior information of the flow. An additional limitation occurs when small displacements are measured. Smaller displacements will result in the displacement correlation peaks converging to the centre of the domain where the self correlation peak will be. This can lead to merging of the displacement correlation peaks and the self correlation peak making the displacement measurement invalid or obscure at best.

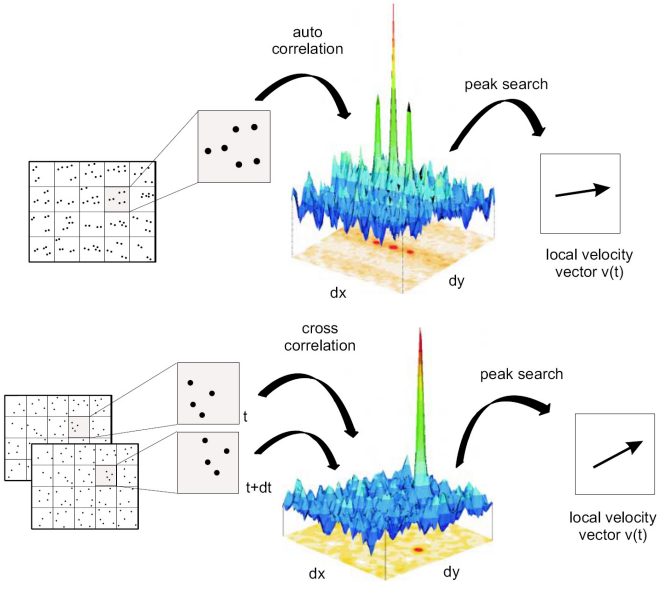

Figure 4-4 Illustration showing concept of autocorrelation and cross correlation processes to determine the velocity vector of an interrogation window.

With the advancement in scientific camera technology it is now possible to capture the two laser exposures in separate images. Therefore the chronological order is known and the directional ambiguity of auto correlation is solved. Cross correlation is employed. Again each image is divided into interrogation windows and the cross correlation of these two windows determined. This is shown in Figure 4-4. It is clear that only one displacement correlation peak is evident, removing the directional ambiguity. The absence of a self correlation peak also means that there is no interference measuring small displacements. Once the displacements for all the interrogation windows are know these are divided buy the laser pulse separation time to yield the velocity vector.

Assuming a conventional planar PIV experiment is set up where by the camera axis is perpendicular to the illuminated plane to obtain the in-plane velocity components, the measurements made are subject to perspective error [100]. This is the result of a single camera resolving the three dimensional movement of a particle in only two dimensions. The out of plane motion of a particle will not be recorded and its presence will manifest as an error of the in plane measurements. Perspective error can become a significant error for in plane measurements when the out of plane component is large and is not constant across the camera lens. All turbulent flows will exhibit some out of plane component. Common practice is to align the illumination sheet coincident with the plane with the two strongest velocity components to minimise the perspective error. However when swirling flows are used it is likely that there will be no significantly small component to set as the out of plane component and possible that all three components could be equal in magnitude, making 2D PIV inappropriate.

4.3.1 Stereoscopic Particle Imaging Velocimetry

Stereoscopic PIV makes use of two cameras to record simultaneously from two different points of view, two images of the same flow region of interest. This region is again illuminated with a laser sheet and seeded with tracer particles. Within the two images sufficient information is contained to derive the out of plane motion of the particles. There are various ways to acquire stereoscopic measurements; all are linked by the common requirement that two simultaneous images from different views must be recorded. The two views are combined using one of an assortment of algorithms to reconstruct the three dimensional flow filed. This is particularly applicable to turbulent swirling flows. Additionally the elimination of perspective error which is inherent in 2D PIV is achieved. The two main configurations to achieve stereoscopy are translational and angular displacement systems.

The Translational system places both cameras so that their planes are parallel to each other and both perpendicular to the object plane. The cameras should be symmetrically positioned as shown Figure 4-5 for convenient implementation, although this is not a must, it is a good design rule. The advantage of this technique is its simplicity. The parallel arrangement of object, lens and image plane ensures the uniform magnification of the image field so the particle image quality is constant. A satisfactory image focus is achieved without further reduction of the aperture as in conventional planar PIV (depth of field requirement unchanged). The two images from the cameras can be superposed without manipulations that a non-constant magnification would require.

Furthermore the spatial resolution of the combined field will be identical to that of the two images [101, 102].

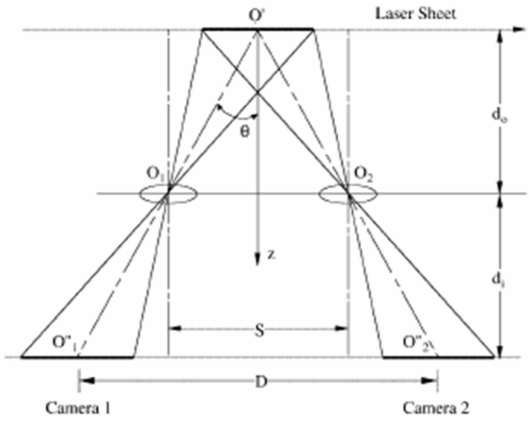

Figure 4-5 Illustration showing the Translation System (symmetric) set up [103].

Drawbacks to the Translation system include the small area that is viewed by both cameras implying that only small scale features may be studied [102]. A more important limitation is that there is an upper limit restriction on the angle of the centre of the area of interest and the lens centre, θ. This limit is imposed by the design of the lens used. If the two lenses are separated by an amount that is too large for a given distance, d_0 (between object and lens planes) the performance of the lens will degrade as it will be operating outside of its specification range.

Implementing Stereoscopic PIV via the Rotational /angular displacement method means the two camera axes are no longer parallel. Instead they are rotated such that the two axes intersect the object plane. This removes the limitations of the angle θ so that it may be much larger in value without compromising lens performance and enhancing accuracy of the out of plane component measurement. As a consequence the magnification is no longer constant over the field of view. It is also necessary to further rotate the cameras (image plane) by an angle α from the lens plane so that the object, lens and image planes are all co-linear. This satisfies the Scheimpflug condition [104] ensuring that all particles within the object field will be in focus in the image plane.

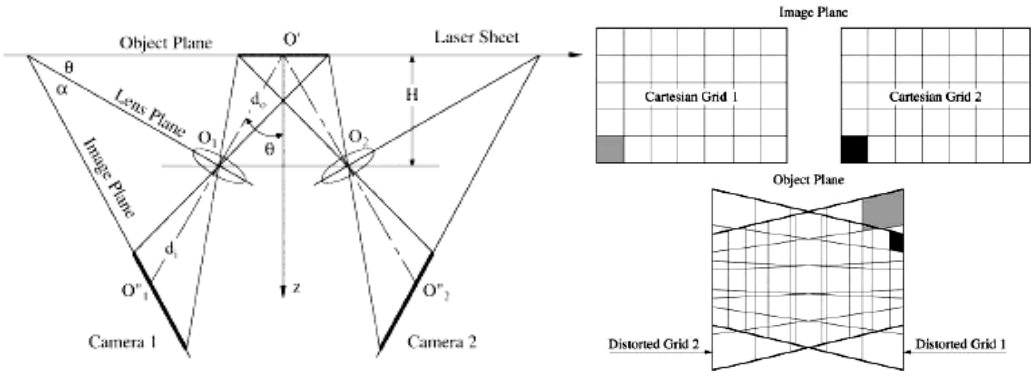

Figure 4-6 Left: Illustration showing the Angular displacement set up. Right: Illustration showing the oppositely stretched images from the Angular camera set up [103].

Meeting this requirement will ensure focus of particles but will exacerbate the non uniform magnification across the object plane. The non-uniformity increases with in plane displacement in the x direction, angle θ and Scheimpflug system magnification $\left(M_n = \tan\alpha/\tan\theta\right)$ [100]. The images collected from the two cameras in this configuration will be oppositely stretched. It is impossible to combine information from the two views in the image plane without firstly interpolating the images onto a common grid. It is possible to use the angular displacement method without satisfying the Scheimpflug condition [105]. By setting the angle between image and lens plane to zero the non uniformity of magnification is reduced. This is only viable as long as the particles remain in good focus by ensuring that the depth of field of the system is large enough to include all variances of object distance.

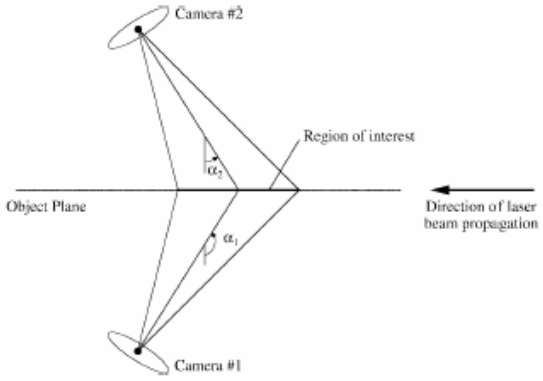

Figure 4-7 Illustration showing a novel angular displacement arrangement [106].

The typical angular displacement method depicted in Figure 4-6 has been used on several occasions [107, 108]. A novel implementation has been used where by the cameras are placed on opposite sides of the flow, Figure 4-7 .Still satisfying the Scheimpflug condition the method takes advantage of the higher scattering efficiency of forward scatter (see Figure 4-3). This will give both camera images a higher signal to noise ratio. A second benefit is that the arrangement will result in both images being stretched in the same orientation making the interpolation onto a common grid easier [106]. Thirdly the size of the common area viewed by both cameras is increased over the previous arrangement.

A comprehensive investigation for the out of plane error with respect to the in plane error has been conducted and the results depicted as a function of off axis position $\left(\tan\theta = x/d_0\right)$ shown in Figure 4-5 and Figure 4-8 [105]. For the translation system it can be clearly seen that as θ increases the error ratio decreases rapidly then converges to a steady value. This behaviour is maximised when the two lenses are a minimum distance apart (S). As this distance becomes larger the initial out of plane error is substantially less. With regard to the angular displacement the error is a weak function of off axis position with error decreasing for increasing angles of θ.

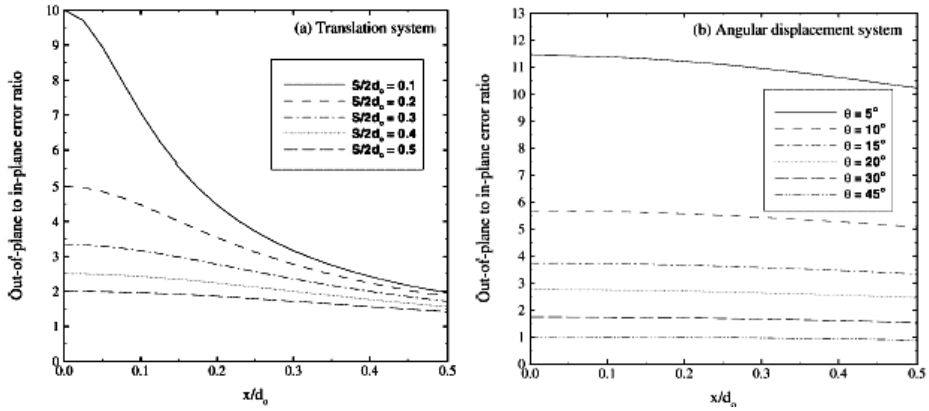

Figure 4-8 Graphs showing out of plane error ratio against off-axis position for Translational and Angular displacement systems [105].

The angular displacement arrangement yields the best error ratio, of 1, between the in and out of plane errors at an angle of 45° over the translational system. An angle greater than this will cause greater non-uniformity in magnification [105]. The above analysis performed is based purely on geometric considerations and does not include errors arising from image reconstruction and subsequent displacement calculation from this.

5 COMBUSTION CHAMBER DESIGN AND FLOW CHARACTERISATION

In order to investigate hydrogen blended fuels a 'base' combustor design was conceived by scientists at the Combustion Research Facility (CRF), Sandia, California. It is a swirling flow dump combustor and is designed to facilitate the acquisition of experimental data expressly for LES validation. The design and configuration of the individual assemblies is such that it represents the fluid dynamic, thermodynamic, thermo chemical and transport processes that occur in typical industrial gas turbine combustors. The design was optimised to allow use of laser diagnostics and non intrusive measurements.

The CRF combustor design consists of four assemblies that condition the combustible mixture prior to combustion, a fuel injector, a premixing section, a swirler section and finally a wake mixing section. These assemblies create the desired flow conditions prior to flow entry into the dump combustor chamber. The chamber is a cylindrical duct of fused silica quartz. This allows optical access to the flame and transmission of laser light for laser based imaging. Finally the combustor is finished with an exhaust section. An overview of the third generation of this combustor can be found in the literature [109].

While the CRF combustor is able to create stable flames the Cranfield combustor was designed to create unstable flames, a feature observed when operating lean combustion. This will allow investigation into combustion instabilities and the effect of hydrogen addition as a stabiliser. With this premise the overall CRF base designed was modified to include the capability of creating flow perturbations mimicking those observed in stable combustors. The Cranfield combustor retains the important dimensions of the CRF combustor so there can be an exchange of data between the two combustors.

What follows is an overview description of the Cranfield combustor design including modifications made during this work. The combustor is described from an upstream position through to the final downstream elements, the exhaust sections. A technical drawing package is included in the Appendix of this thesis for a more detailed description. A description is given of the support systems also created to operate the combustion chamber and the lean operating limits are reported.

5.1 Cranfield Combustor Overview

The Cranfield Combustor is a swirl stabilised dump combustor based upon the first generation CRF combustor. The reactant mixture is fed into the combustion chamber via an annulus of inner diameter 20mm and outer diameter of 28mm. The annulus is formed by a bluff body running the length of the mixing section until the point of entry to the chamber. Swirl stabilisation is achieved via a series of axial swirl vanes of swirl number 0.865. These key dimensions are identical to the CRF combustor to allow comparisons. The Cranfield combustor includes the addition of imposing pressure perturbations upon the mixture prior to

combustion. This capability required the inclusion of two extra sub assemblies; a siren assembly and a motor assembly to drive it. The combustor is able to induce perturbations of up to 2 KHz in frequency and any chosen pressure amplitude. What follows is a description of the key assemblies and features moving in a downstream direction. The entire system was machined and constructed from stainless steel.

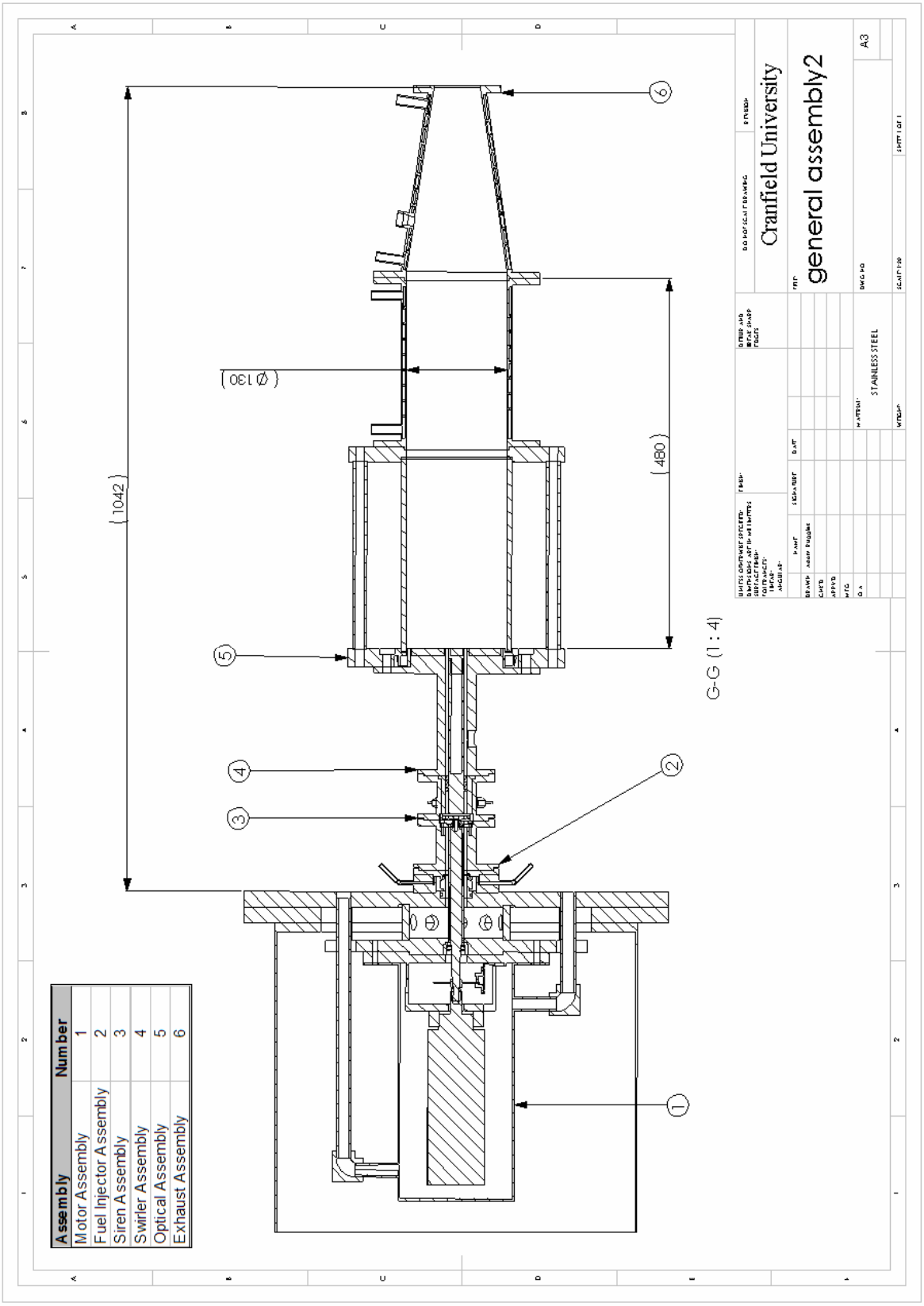

Figure 5-1 General Assembly drawing showing combustion chamber fully assembled.

5.1.1 Pre-Heat Assembly

A pre-existing assembly capable of heating air up to temperatures of 400ºC was used as a base for the combustor design. This was retained as the capability of preheating the air prior to combustion was felt to be an important capability to retain for the combustor to investigate instabilities. This assembly also acts as a pre-existing mounting point. Although not investigated in this thesis it can be utilised at a later date. The pre-heater is a cylindrical stainless steel duct 1.5m in length with an inner diameter of 464 mm and a wall thickness of 2mm. Within this are a series of electrically powered heating elements. Air from a compressor is supplied to the inlet of this duct and then subsequently flows through the combustor. This assembly was acoustically chocked using a sonic nozzle.

5.1.2 Fuel Injector Assembly

The fuel injector assembly introduces methane and hydrogen mixtures to the air via a two stage injection process. The fuel mixture is connected to the four outer injection points via a connecting ring. These four injectors distribute the fuel around the fuel gallery component. The fuel gallery itself has sixteen 1mm diameter holes evenly spaced around its circumference and is the secondary injector. This arrangement and design promotes an even fuel distribution when it is injected into the air. The fuel gallery also utilises two seals to prevent fuel leakage. The entire assembly is bolted together by eight bolts running through the outer part of the assembly.

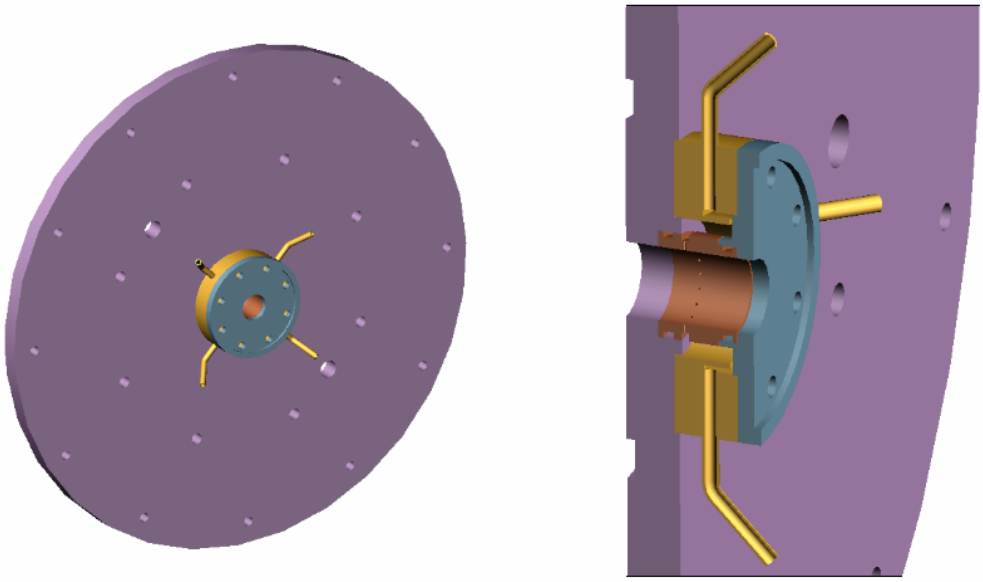

Figure 5-2 Left: Image of the Fuel injector assembly. Right: Section view showing the two stage fuel injection process.

5.1.3 Motor Assembly

The motor assembly consists of a mounting flange which is held 44mm from the base plate of the fuel injector assembly via a ring of eight cylindrical bars, through which bolts are run. With nuts at either end of the bolts the mounting flange is secured. It is located concentrically with the fuel injector assembly via a

locating ring. This ring has ten holes of 20 mm diameter evenly spaced around the circumference to allow the air to pass through to the annulus. Installed on the motor flange is a housing component to allow connection of the motor to the shaft which is used to drive the siren. An Infra Red diode and receiver were installed close to the motor. This is part of a system employed to monitor the rotational speed of the shaft. A clamp is fixed onto this housing in which the electric motor is held in position. All parts were designed such that the alignment of the motor and shaft are concentric. The motor used was a router, Ferm 850E. Finally within the motor flange is the first of two bearings (6002-2Z) for the support of the rotating shaft. The motor is then sealed within a casing and cooling air is supplied to this chamber to increase the life of the motor. The casing also shields the motor from any unwanted presences (such as seeding particles). Integration of the motor assembly and siren assembly ensure that this cooling air can not mix with the combustion air.

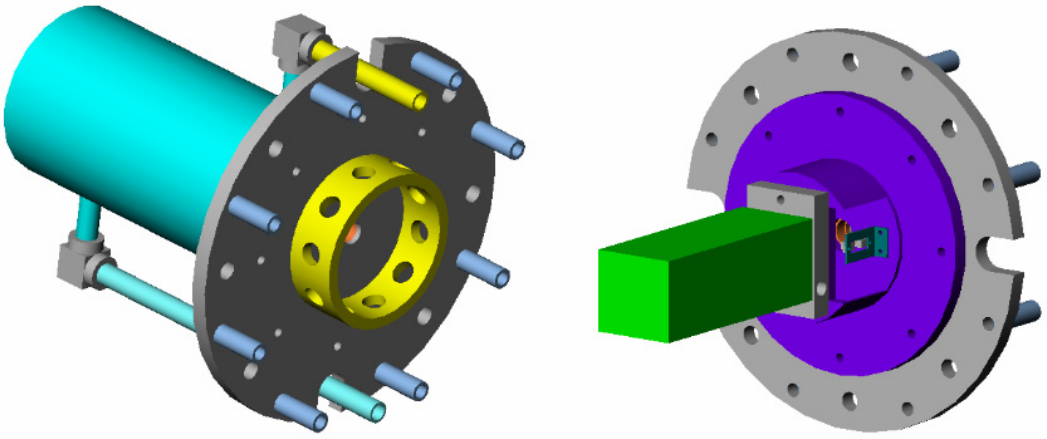

Figure 5-3 Left: Image of the Motor assembly encased and locating components. Right: Image showing the Electric motor and infra red sensor mounting bracket.

5.1.4 Siren Assembly

The siren is the feature which creates the pressure perturbation in the reactant mixture. Methods to create pressure perturbations include sirens, loudspeaker arrangements and piston arrangements. All methods pose advantages and disadvantages depending on the burner in question. A siren was chosen due to the desire to retain the air preheat capability which automatically limited available space for mechanical housing. Additionally the desired frequency range and the high inlet velocities made both piston and loudspeaker options unfeasible.

The assembly is bolted onto the fuel injector assembly and connects to the motor assembly upstream of the fuel injector. The siren is constructed using two plates, the first is stationary and fixed in position and the second is attached to the shaft. The shaft runs through the lower half of the bluff body which forms the inner part of the annulus. This part of the bluff body is located within the motor flange in the motor assembly, ensuring concentricity. The top part of this component is referred to as the stator as it also acts as part of the siren. The

second bearing (628/8-2Z) is housed within the stator and supported on its outer race. The shaft locates onto the inner race of the bearing. The outer bearing race is held in position by the bearing plate which posses the same apertures as the stator as the flow must pass through it. The bearing plate provides a clearance of 1.4mm to the shaft on the radius dimension. Finally a bearing collar is inserted between the rotor and inner race of the bearing. This arrangement fully supports the bearing and also minimises the exposure of the bearing to the flow (in particular TiO_2/ZrO_2 PIV seeding particles). The outer casing of this assembly forms the outer part of the annulus.

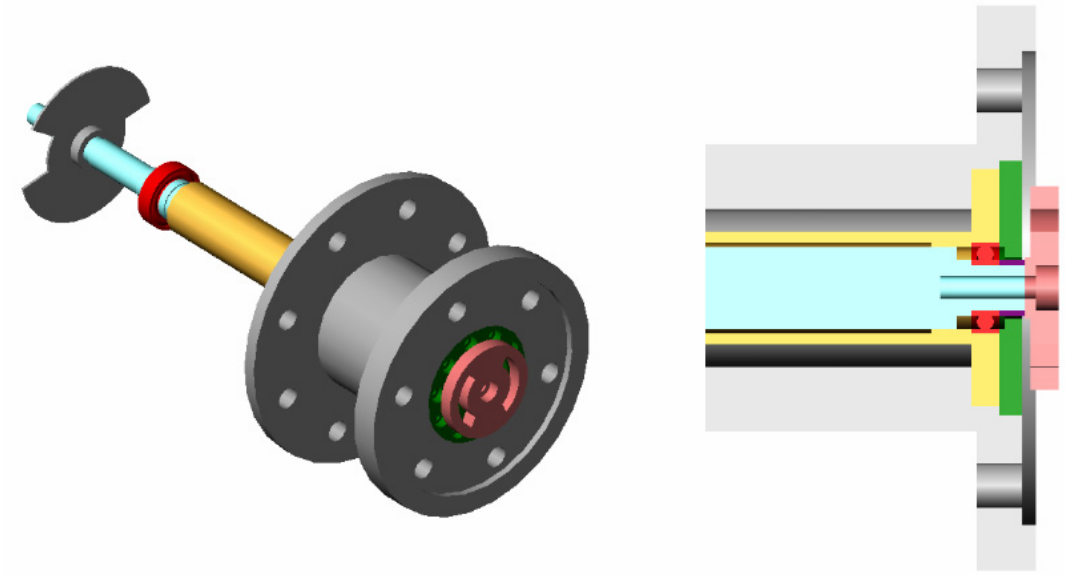

Figure 5-4 Left: Image showing the Siren assembly with shaft and sensor wheel. Right: Section view of the siren showing stator, bearing plate, bearing and rotor arrangement.

The design of the plates of the siren, the rotor and stator, involved consideration regarding the changing area of overlap of the respective apertures. In order to achieve a frequency of 2KHz a compromise was made between the overlap profile and the number of apertures. A 'two hole' and a 'four hole' arrangement was designed with a common stator (top half of the bluff body in this assembly). This resulted in the relative ease to change the configuration. As can be seen from the two aperture profile graphs in Figure 5-5, both configurations are similar in shape with differences towards the peak. The first is that the four aperture arrangement rapidly reaches its zenith while the two aperture arrangement reaches its peak linearly. The second difference is that the four aperture arrangement has its maximum aperture at an instance; the two aperture arrangement has its peak for approximately 20º of rotation. These differences are a result of the compromise of siren design. Although they are different the profiles are similar in shape. The separation distance between the rotor and bearing plate was to be one of two methods used as a measure of control over the perturbation amplitude. The second is described in the swirler assembly section.

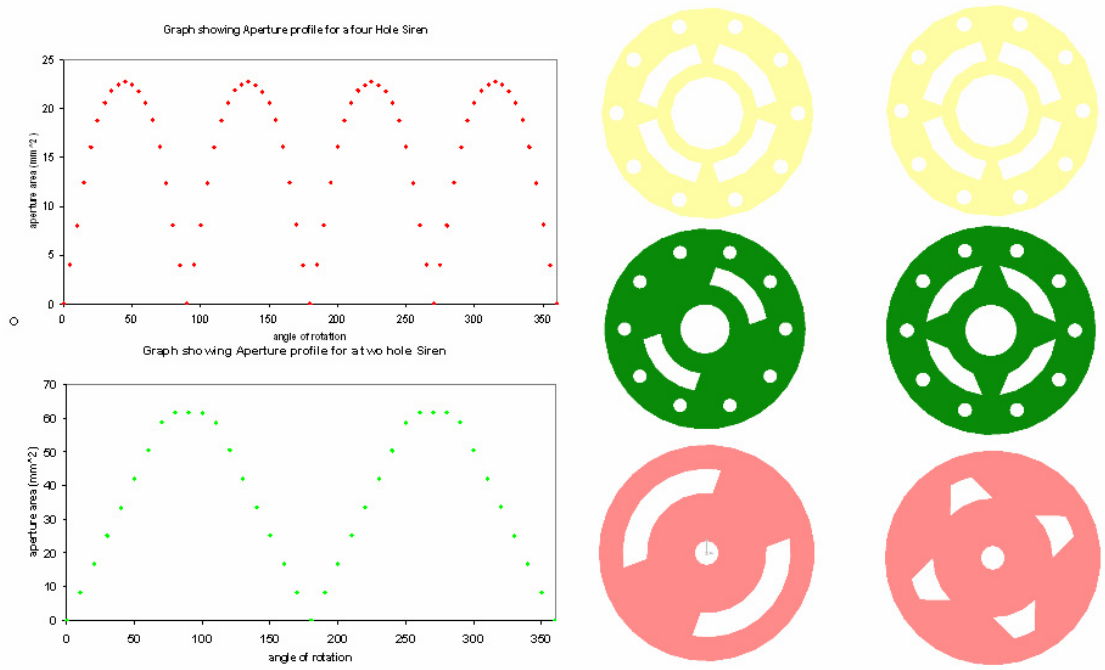

Figure 5-5 Area overlap profiles of the two and four aperture configurations. Images of the respective components for both arrangements, stator – yellow, bearing plate – green, rotor – pink.

5.1.5 Swirler Assembly

The Swirler assembly is located immediately after the siren. In order to minimise the effect of separating the bluff body into two parts, the second half is located as close as possible to the rotor part of the siren. This second bluff body also comprises the swirler. Eight axial swirl swept vanes were designed with a swirl vane angle of 45° corresponding to a swirl number of 0.865 [20][i].

$$S = \frac{2}{3}\left(\frac{1-\left(R_H/R\right)^3}{1-\left(R_H/R\right)^2}\right)\tan\alpha \qquad \text{Eq 5-1}$$

Four of the swirl vanes at alternating intervals were designed to also be structural supports to hold the bluff body concentric within the annulus. The bluff body itself has been made hollow to reduce thermal build up. The end of the bluff body is finished with a screw in cap which has a ceramic (Ceramacast 645N) layer set into it, again for thermal protection. It was originally decided to inject flow seeding particles at this assembly just before the swirl vanes begin to wrap around the bluff body. This was achieved with the use of four injection ports as shown in Figure 5-7.

---

[i] Swirl is defined as a non dimensional number and is the ratio of axial flux of angular momentum and linear momentum. $S = G_\varphi / G_x' R$. R is the hub radius. This is approximated by Eq 5-1.

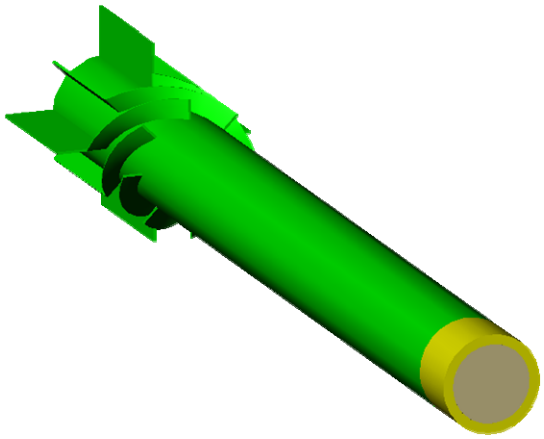

Figure 5-6 Illustration showing the bluff body, swirl vanes and ceramic tipped end.

This would inject the particles downstream of the bearings and not exposing them to the detrimental effects of the seeding particles. After initial trials it was found that there was insufficient control of the quantity of seed penetrating into the annular flow. This resulted in intermittent seeding or a hugely excessive amount of seed being transported into the chamber coating the silica duct making imaging impossible. This difficulty was attributed to the insufficient pressure of the seeding flow to penetrate into the annular flow. As a result it was decided to inject within the pre-heater section, upstream of the motor assembly, but downstream of the heating elements.

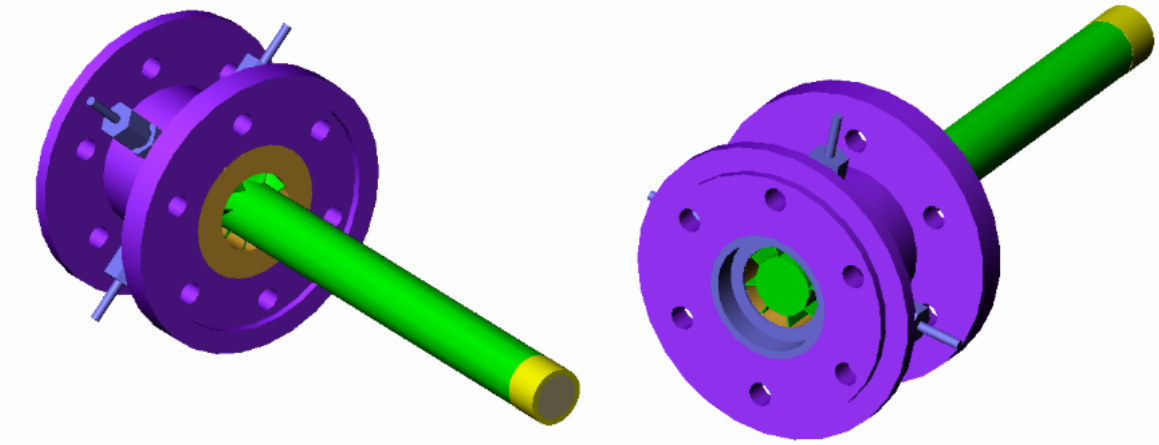

Figure 5-7 Left: Image showing the Swirler assembly with four original seeding points and ceramic tipped bluff body. Right: Image showing the insert used to provide a tight fit around the rotor part of the siren.

A variable sized insert was used at the bottom of the swirler assembly which reduced the volume of space around the rotor part of the siren. By reducing this volume the amount of volume which the mixture flow can bypass the siren is reduced. This formed the second part of control over the pressure perturbation amplitude.

5.1.6 Optical Assembly

The optical section consists of a wake mixing section, two flanges, one of which is able to supply dilution air, and a duct of optical grade fused silica which acts as the combustion chamber. The duct is 250mm long and has an inner diameter of 130mm and outer diameter of 142.7 mm. The duct is clamped between the two flanges and employs four spacers which maintain the distance between the two flanges. Studding is run through the spacers and bolted at each end. The silica duct is not held concentrically and a small clearance of 0.5 mm is allowed on the duct diameter. This allows for any thermal expansion and removes the chance of chipping, cracking and total failure. Gaskets were made for each end of the duct from 4mm thick Kaowool ceramic paper. This allowed the tightening of the spacer bolts while providing protection from chipping and vibration from the induced pressure perturbation during operation.

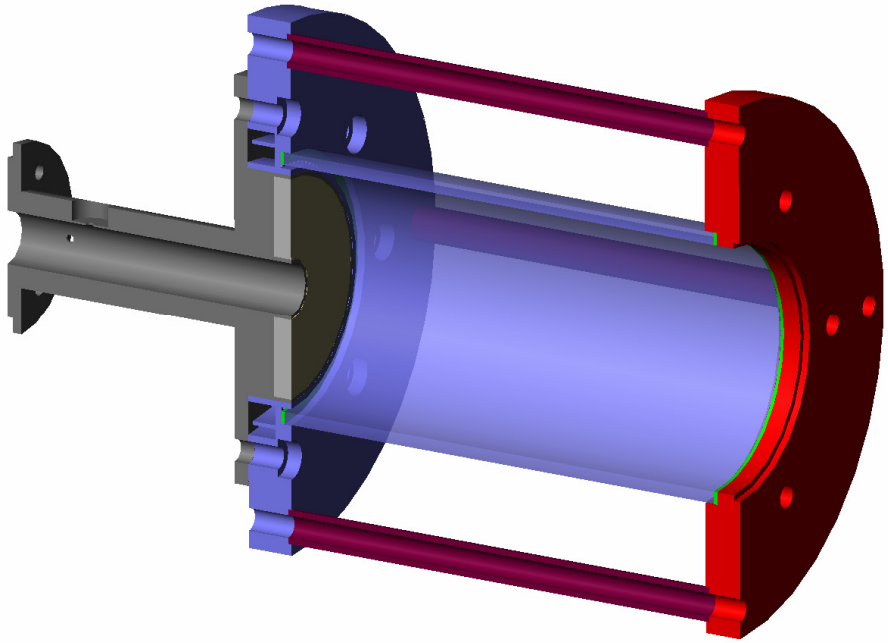

Figure 5-8 Image showing section view of the Optical assembly.

The bottom flange also has the capability to introduce additional dilution air into the chamber. This can be used to alter the flame temperature and provide a curtain of protective air for the silica duct. Eight air injection ports are arranged on the flange circumference with equal spacing. These feed an internal ring channel which forces the air to flow around the flange promoting a more uniform distribution. This channel feeds a ring of one hundred 2mm diameter holes evenly spaced. This ring is located so that the introduced air blows adjacent to the inner surface of the silica duct.

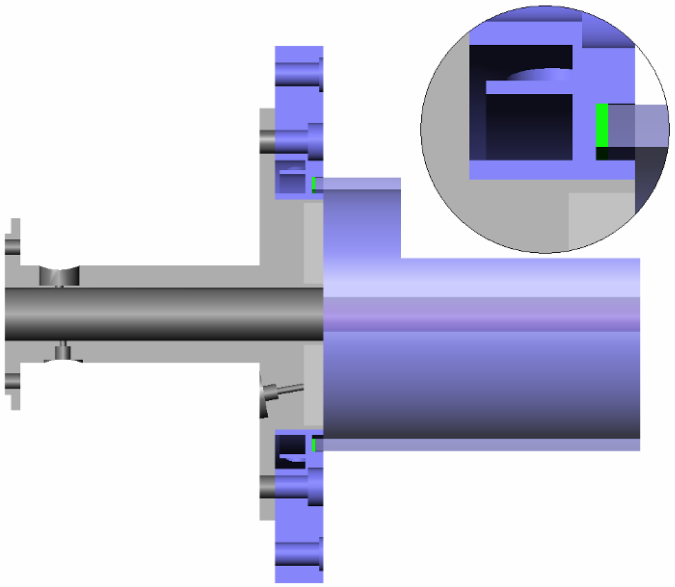

Figure 5-9 Image showing section view of the dilution air feature, pressure transducer and thermocouple mounting points and ceramic layer at the dump plane.

The wake mixing section was fitted with mounting points to allow the attachment of a pressure transducer and thermocouple to characterise the inlet conditions through the annulus. The mixing section was also modified at the dump plane with the inclusion of a ceramic layer which provided a thermal barrier for protection and attempted to make the dump plane as adiabatic as possible. The material used was Ceramacast 645N which when mixed with water is able to be cast to suit the application. It is a silica based compound with a maximum working temperature of 1650ºC and a lower thermal conductivity when compared to other products. A thermocouple was embedded into this layer. The optical assembly is bolted onto the swirler assembly such that the bluff body runs concentrically through the wake mixing section and finishes at the dump plane, thus forming the second half of the annulus.

A water cooled stainless steel replacement for the silica duct was also manufactured. This retained the same dimensions as the silica duct. This was used during initial trials and the determination of the lean operational limits in order to remove the possibility of early damage to the silica duct.

5.1.7 Exhaust Assembly

The exhaust assembly consists of two sections, a cylindrical water cooled section and the final water cooled converging nozzle. The cylindrical section is 130mm inner diameter and 220mm in length. The nozzle's first diameter is 130mm before reducing to 60mm diameter. The nozzle is 250mm in length. Each section has its own water in and out ports. The water cooling is achieved by the use of a baffle which is wrapped around the first wall of the sections. A second wall is then fixed in position around the baffles. The water is then forced to flow around the sections absorbing heat from all parts of the exhaust before leaving via out port. A mounting point for a pressure transducer has also been included in the nozzle section. The exhaust assembly is bolted onto the top of the optical assembly.

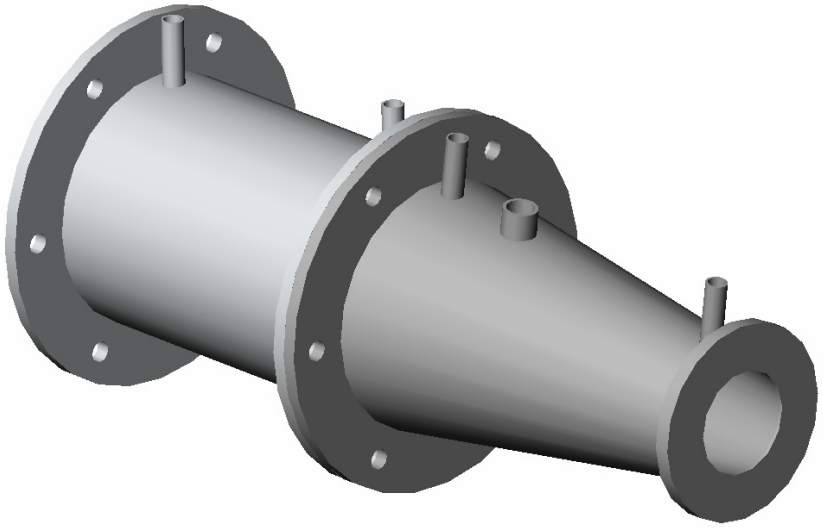

Figure 5-10 Image showing Exhaust assembly.

5.1.8 Acoustic Properties

Using ambient air conditions, speed of sound c, and roots of the Bessel functions B_{mn} the resonant and sub-harmonic frequencies of longitudinal q, radial m and tangential n modes of the chamber and mixing section can be determined for pure air [110].

$$f_{mnq} = \frac{c}{2}\left[\left(\frac{B_{mn}}{a}\right)^2 + \left(\frac{q}{L}\right)^2\right]^{1/2} \qquad \text{Eq 5-2}$$

Using Eq 5-2 and where L is the length of the cylinder and a the radius, and Table 5-1; the acoustic modes are determined.

	m = 0	**m = 1**	**m = 2**	**m = 3**
n = 0	0	1.22	2.333	3.238
n = 1	0.586	1.697	2.717	3.725
n = 2	0.972	2.135	3.173	4.192

Table 5-1 Bessel Function roots [110].

q = 0	m = 0	m = 1	m = 2	m = 3
n = 0	0	3219	6156	8543
n = 1	1546	4477	7169	9828
n = 2	2565	5633	8372	11060

q = 1	m = 0	m = 1	m = 2	m = 3
n = 0	235	3227	6160	8547
n = 1	1564	4484	7173	9831
n = 2	2575	5638	8375	11063

q = 2	m = 0	m = 1	m = 2	m = 3
n = 0	470	3253	6173	8556
n = 1	1616	4502	7184	9839
n = 2	2607	5653	8385	11070

q = 3	m = 0	m = 1	m = 2	m = 3
n = 0	705	3295	6196	8572
n = 1	1699	4533	7203	9854
n = 2	2660	5677	8401	11083

q = 4	m = 0	m = 1	m = 2	m = 3
n = 0	940	3353	6227	8595
n = 1	1809	4575	7230	9873
n = 2	2731	5711	8424	11100

q = 0	m = 0	m = 1	m = 2	m = 3
n = 0	0	21374	40873	56729
n = 1	10267	29731	47601	65261
n = 2	17029	37404	55590	73442

q = 1	m = 0	m = 1	m = 2	m = 3
n = 0	1039	21399	40887	56738
n = 1	10319	29749	47612	65269
n = 2	17061	37419	55600	73450

q = 2	m = 0	m = 1	m = 2	m = 3
n = 0	2079	21475	40926	56767
n = 1	10475	29803	47646	65294
n = 2	17156	37462	55629	73472

q = 3	m = 0	m = 1	m = 2	m = 3
n = 0	3118	21600	40992	56814
n = 1	10730	29894	47703	65335
n = 2	17312	37534	55677	73509

q = 4	m = 0	m = 1	m = 2	m = 3
n = 0	4158	21775	41084	56881
n = 1	11076	30020	47782	65393
n = 2	17529	37635	55745	73560

Table 5-2 Left: Acoustic modes of the chamber and exhaust section. Right: Acoustic modes of the mixing section.

5.1.9 Accessories

Two important additions were designed and built alongside the combustion chamber itself. These were the ignition torch and the image calibration arm. The ignition torch was the means by which the chamber was ignited. This was a stainless steel pipe connected to a propane cylinder with a gas bottle nozzle welded onto the end. Using a standard nozzle allowed the generated flame to be premixed and robustly stable. The pipe was of such shape as to allow it's insertion down the exhaust of the combustor to near the dump plane while the operator was standing away from it. The flame was resistant to blowout when the combustible mixture was introduced at light up flow rates. When the combustion chamber had successful ignition the ignition torch was removed and the combustion chamber brought up to operating conditions.

The image calibration arm was designed in order to introduce a calibration grid into the chamber when the exhaust section has been removed. This would allow a camera to focus upon the calibration plate ensuring data was collected correctly at that plane. The calibration arm also was designed to allow the calibration grid to be traversed vertically up while keeping the calibration plate flat horizontal. This was achieved by incorporating a micrometer stage into the design and allowed fine control over the vertical positioning of the grid to ensure the focal plane of the camera could be made coincident with the central horizontal plane of the chamber.

5.2 Phase Locking and Instrumentation

In order to measure the rotational speed of the motor and hence the frequency of the induced perturbation an infra red diode and receiver was used in conjunction with a rotating disc (see Figure 5-11). A thin disc was mounted on the shaft with two sections cut out to ensure balance. The disc was mounted close to the electric motor. Mounted adjacent to the disc was the infra red diode and receiver. These were positioned in front and behind the disc. The beam was able to pass when the cut out sections rotated into position. So as the disc rotated the infra red beam was blocked twice during one revolution. The infra red receiver provided an amplified TTL output which could be directly read by an oscilloscope and yielded a signal of a square wave form profile. The oscilloscope used was a Tektronics TDS1012B.

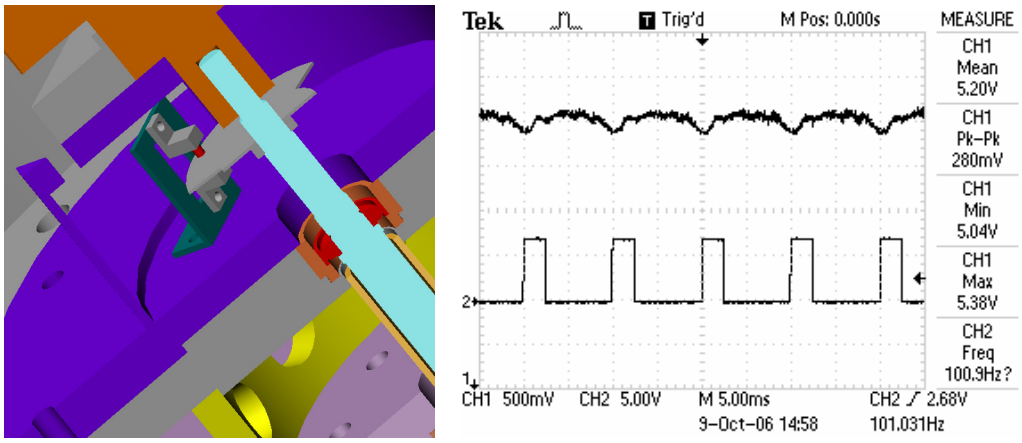

Figure 5-11 Left: Image showing infra red sensor and rotating disc used for rotational speed monitoring. Right: Example of data recorded by the oscilloscope showing synchronisation signal and pressure signal.

This output signal was used to measure the rotational speed of the shaft and hence the frequency of the oscillation. This signal was also used as a trigger signal for the phase locking of the image based diagnostics employed.

Type K thermocouples were installed in the mixing section of the optical assembly to record the inlet temperature and in the ceramic layer at the dump plane for monitoring.

To characterise the inlet flow a Kistler piezoresistive pressure transducer type 4045A2 was used calibrated to measure an absolute pressure range 0 to 2 bar. The transducer was used in conjunction with an amplifier 4618A2 to provide a real time output with a range of 0 to 10V. This was mounted within a water cooled jacket type 7511 to provide thermal protection in the event of air preheating used. The output signal was connected to the oscilloscope. The unit was supplied with a calibrated voltage output and this was verified using a Druck DPI 603 pressure calibration unit allowing the relationship between output signal voltage and pressure to be determined. The resolution of the transducer after amplification was 0.02V/2mbar.

5.3 Gas Flow and Gas Support Systems

In order to supply a gas mixture of desired inlet velocity, equivalence ratio and hydrogen content it was necessary to first calculate the stoichiometric ratio of fuel to air. This is done by assuming a simple stoichiometric combustion reaction for the fuel compositions to be considered. Below are the stoichiometric equations for pure methane, 10% hydrogen, 15% hydrogen and 20% hydrogen.

$$CH_4 + 2[O_2 + 3.76N_2] \rightarrow CO_2 + 2H_2O + 2[3.76N_2] \quad \text{Eq 5-3}$$

$$0.9CH_4 + 0.1H_2 + 1.85[O_2 + 3.76N_2] \rightarrow 0.9CO_2 + 1.9H_2O + 1.85[3.76N_2] \quad \text{Eq 5-4}$$

$$0.85CH_4 + 0.15H_2 + 1.775[O_2 + 3.76N_2] \rightarrow 0.85CO_2 + 1.85H_2O + 1.775[3.76N_2] \quad \text{Eq 5-5}$$

$$0.8CH_4 + 0.2H_2 + 1.7[O_2 + 3.76N_2] \rightarrow 0.8CO_2 + 1.8H_2O + 1.7[3.76N_2] \quad \text{Eq 5-6}$$

Using the above stoichiometric chemical equations the stoichiometric fuel air ratio (mass) can be easily determined. The equivalence ratio ϕ, is then chosen and the corresponding fuel air ratio is given. This defines the amount of each gas required.

$$\phi = \frac{(m_f / m_a)}{(m_f / m_a)_S} \quad \text{Eq 5-7}$$

The means to supply the combustion chamber with gas is summarised in Figure 5-12. The air was supplied by a RAND compressor. The mass flow rate was controlled using a pressure regulator and needle valve and monitored using a Fischer porter flow tube in conjunction with a thermocouple and pressure gauge immediately downstream of it.

The methane and hydrogen gas systems were supplied with a pack of 16 cylinders and a single cylinder respectively. This meant that the hydrogen pressure could be regulated simply using a specified regulator. The methane system required a two stage pressure regulation process due to the extremely cold ambient conditions outside of the test cell during operation and was accomplished using two remotely operated dome loaders. Both systems utilised appropriate flow tubes to control the mass flow of the respective gas (see Figure 5-12).

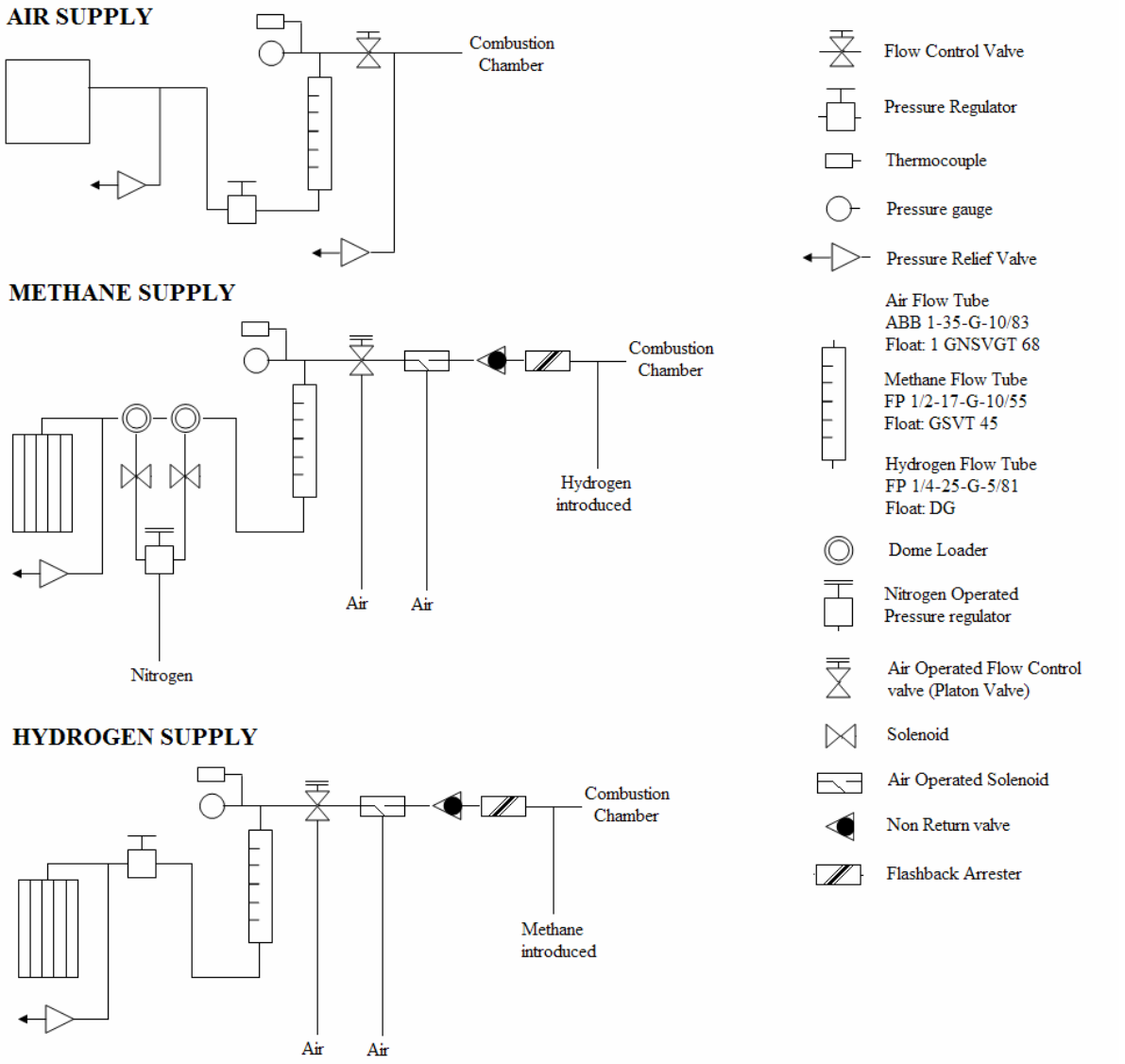

Figure 5-12 Illustration showing gas flow diagrams for the three gases employed.

5.3.1 Mass Flow System Uncertainties

The uncertainties associated with the mass flow system used are defined by firstly defining the uncertainty associated with the mass flow rate of each gas. This is then used to estimate the uncertainty in terms of equivalence ratio and inlet velocity.

The pressure gauges used were calibrated using a Budenburg hydraulic calibration device and precision made weights, and a standard test gauge. The gauges used for the flow control systems were then adjusted to match the Budenburg and therefore can be considered correct. Therefore the error associated with the pressure gauges is purely the operators' ability to distinguish the scale.

The uncertainty of the flow tubes are quantified by the manufacturer (ABB and Fischer Porter) as ±2% of the maximum flow rate of air for a given float as detailed in the appropriate datasheet at 1013 mbar and 0ºC. The maximum flow rate for the flow tube used for air was 60.54 m^3hr^{-1}, for the methane flow tube

3.14 m^3hr^{-1} and for the hydrogen flow tube 0.441 m^3hr^{-1}. In addition to this uncertainty is the operators' ability to accurately read the float with respect to the scale. This is ±0.25% of the scale.

The error associated with the thermocouples is a constant and assumed to be ±0.1ºC after keeping with best practice of using a screened twisted cable to reduce noise and ensure if any present it is on both cables so could be removed by the Digitron reader.

The equation used to quantify the mass flow rate is in Eq 5-8. The desired mass flow rates have been calculated from knowing the required mass of each gas in order to achieve the desired equivalence ratio.

$$\dot{m}_g = \rho_{air-std} \cdot \sqrt{RSG} \cdot \sqrt{\frac{P_0}{P_S}} \cdot \sqrt{\frac{T_S}{T_0}} \cdot (\%) \cdot \dot{V}_{Max} \qquad \text{Eq 5-8}$$

Where the air density at standard atmospheric conditions is multiplied by the square root of the relative specific gravity (RSG) with respect to air for the gas in question. P and T are the pressure and temperature of the gas immediately downstream of the flow tube. Subscripts 0 and S refer to flow tube downstream conditions and atmospheric standards. $(\%)$ refers to the desired position on the scale and $\dot{V}_{Max}$ is the maximum flow rate of air at the manufacturers specified conditions.

Gas	Tube	Float	Vmax(m3/hr)	Pressure (abs psi)	Temperature(K)
Air	ABB 1-35-G-10/83	GNSVGT 68	60.54	43.5	290
Methane	FP 1/2-17-G-10/55	GSVT-45	3.14	101.5	283
Hydrogen	FP 1/4-25-G-5/81	DG	0.44	43.5	285

Table 5-3 Table detailing gas flow tube information.

In order to assess the uncertainty of each mass flow Eq 5-9 was used. The constants K_i for each variable were determined.

$$\frac{\delta(\dot{m}_g)}{\dot{m}_g} = \sqrt{\left(K_P \frac{\delta(P)}{P}\right)^2 + \left(K_T \frac{\delta(T)}{T}\right)^2 + \left(K_{\%} \frac{\delta(\%)}{\%}\right)^2 + \left(K_{V_{Max}} \frac{\delta(V_{Max})}{V_{Max}}\right)^2} \qquad \text{Eq 5-9}$$

$$K_P = \frac{P}{\dot{m}_g}\frac{\partial \dot{m}_g}{\partial P} = \frac{1}{2}, K_T = \frac{T}{\dot{m}_g}\frac{\partial \dot{m}_g}{\partial T} = -\frac{1}{2}, K_{\%} = \frac{\%}{\dot{m}_g}\frac{\partial \dot{m}_g}{\partial \%} = 1, K_{V_{Max}} = \frac{V_{Max}}{\dot{m}_g}\frac{\partial \dot{m}_g}{\partial \%} = 1 \qquad \text{Eq 5-10}$$

Once calculated the uncertainties for each mass flow rate can be determined. The mass flow uncertainties were then normalised by the desired calculated mass flow rate and are plotted in Figure 5-13 for the pure methane case and Figure 5-14 for the hydrogen blends. Considering the air mass flow error the uncertainty decreases for higher flow rates and leaner equivalence ratios which require increased air mass flow. The profiles are linear indicating the majority of the error source is due to the absolute error of the flow tube. The methane mass flow uncertainties decrease with higher a velocity which is again related to the

absolute error of the flow tube. The uncertainty increases with leaner equivalence ratios as the methane mass flow rate decreases. The profile is related to the inverse square root relationship of the thermocouple error.

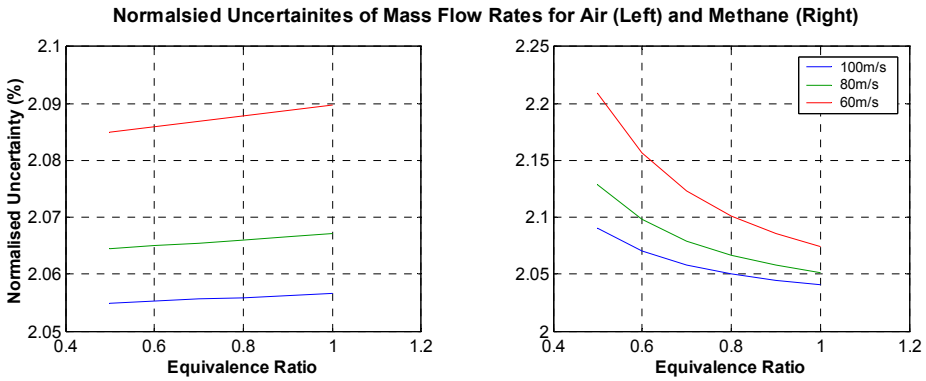

Figure 5-13 Normalised mass flow rate uncertainties for pure methane flames.

Using these uncertainties the normalised uncertainty for a desired inlet velocity was found to be within ± 2.1% for all velocities and ± 0.5% for all equivalence ratios.

The same procedure was used for the hydrogen blended conditions. The behaviour of uncertainty of hydrogen fraction reduces with increasing hydrogen content for equivalent equivalence ratio and velocity.

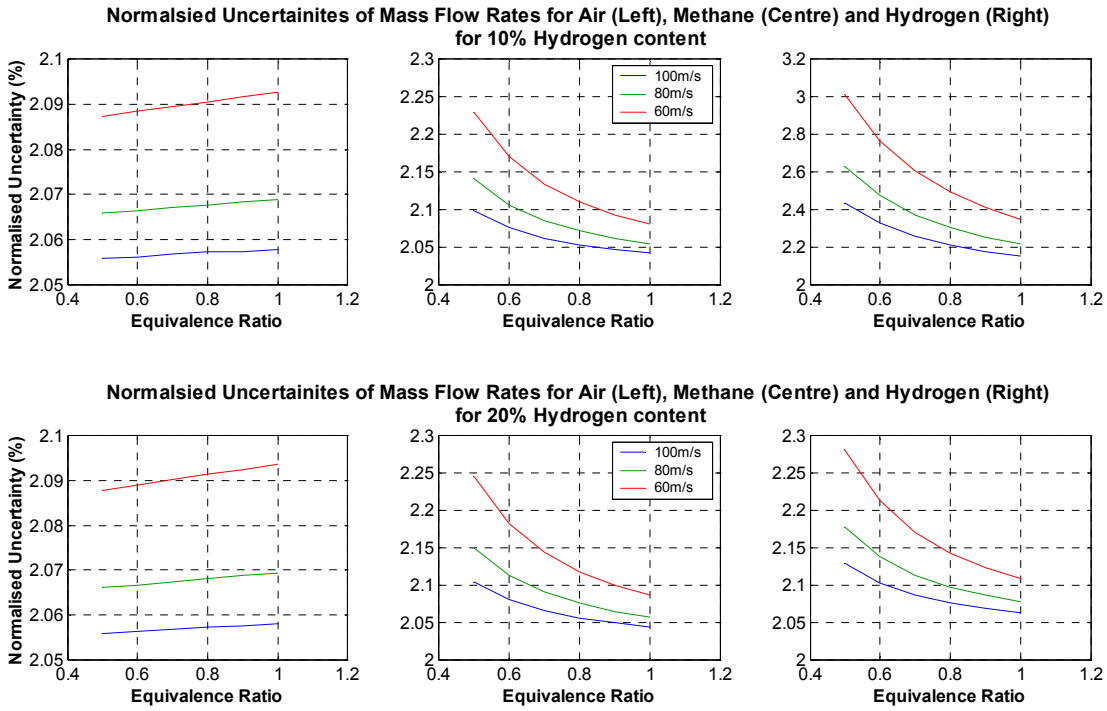

Figure 5-14 Normalised mass flow uncertainties for 10% and 20% hydrogen blended flames.

Using these uncertainties the stated uncertainties for inlet velocity and equivalence ratios remain the same. Concerning the uncertainty of hydrogen content of the fuel the associated uncertainty is ± 0.5% for a given content.

5.4 Lean Flammability Limits

The design of the gas flow system allowed independent control of the composition of the fuel, equivalence ratio of the fuel mixture, and the inlet flow velocity of the air fuel mixture. Combined with the ability to impose a desired flow perturbation frequency a series of conditions was chosen to represent realistic operating conditions and instability frequencies. The pressure perturbation amplitude was approximately 5Kpa for inlet flows of 60ms^{-1} rising to 10Kpa for 100ms^{-1}. A complete description of the pressure wave is in Chapter 5.6. The lean operating limit was determined for the above fuel compositions at various flows and perturbation frequencies. The lean limit reported is with regard to a stable limit of imposed instability. The effect of the dilution air was briefly investigated and was not used for this work. Subsequently it will not be discussed further.

Flow 1: Inlet Velocity 60 m/s				
	Frequency (Hz)			
H2 Content (%)	100	200	400	800
0	0.64	0.64	0.64	0.63
10	0.64	0.64	0.63	0.63
15	0.64	0.64	0.62	0.62
20	0.63	0.64	0.61	0.62

Table 5-4 Lean Operation Limits for various Hydrogen contents and Perturbation frequencies for Flow 1 (60 ms^{-1}).

Flow 2: Inlet Velocity 80 m/s				
	Frequency (Hz)			
H2 Content (%)	100	200	400	800
0	0.64	0.65	0.65	0.63
10	0.60	0.63	0.63	0.62
15	0.585	0.60	0.615	0.615
20	0.58	0.60	0.59	0.59

Table 5-5 Lean Operation Limits for various Hydrogen contents and Perturbation frequencies for Flow 2 (80 ms^{-1}).

Flow 3: Inlet Velocity 100 m/s				
	Frequency (Hz)			
H2 Content (%)	100	200	400	800
0	0.69	0.69	0.70	0.66
10	0.62	0.62	0.62	0.62
15	0.585	0.59	0.585	0.565
20	0.53	0.54	0.55	0.54

Table 5-6 Lean Operation Limits for various Hydrogen contents and Perturbation frequencies for Flow 3 (100 ms^{-1}).

Considering flow 1 (60 ms^{-1}) two small trends are apparent. Firstly as the hydrogen content increases the achievable equivalence ratio becomes leaner for all imposed perturbation frequencies. Secondly as the perturbation frequency is

increased the achievable equivalence ratio also becomes leaner for all hydrogen contents. The extension of the lean operating limit by hydrogen addition is intuitively correct. Extension of the lean limit due to instability frequency is less obvious and could be attributed to increased turbulent mixing or a drastic change of chamber flow dynamics.

For flows 2 and 3 the same trends are evident and the lean limit is extended due to increased hydrogen content. The lean limit of pure methane flows appears to decrease with the larger flow rates. This is due to the larger amplitude of imposed perturbation. These flows are not considered further due to technical limitations.

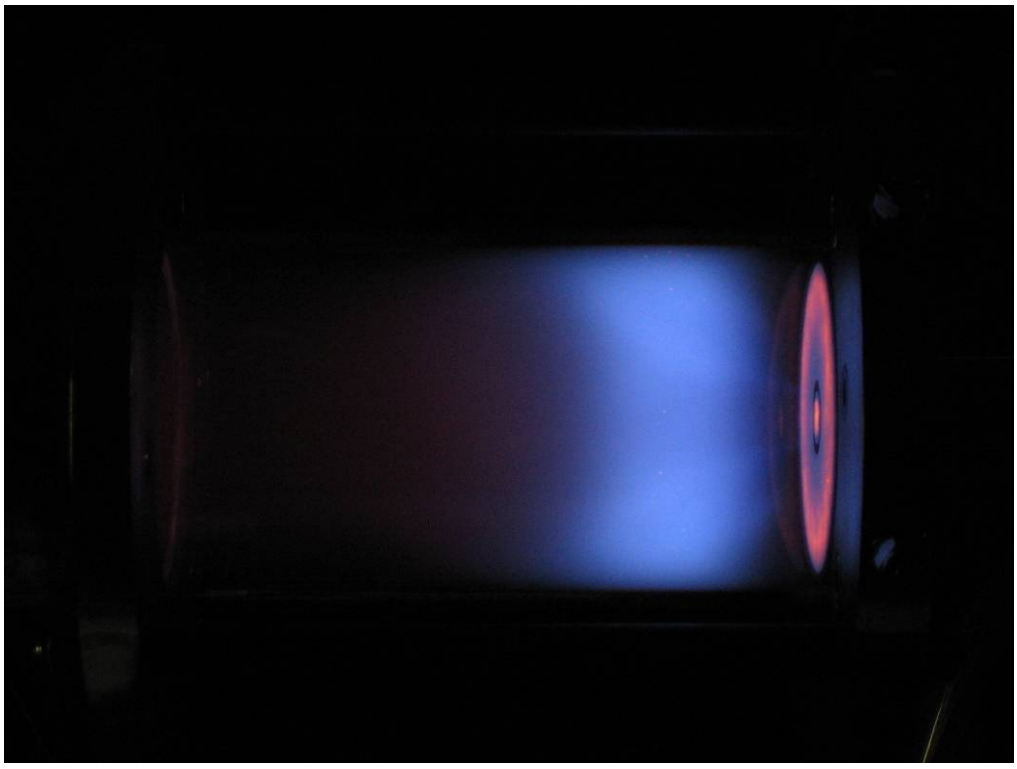

Figure 5-15 Photograph of the combustor operating at 60ms^{-1} with a fuel of pure methane, equivalence ratio 0.8 and instability frequency of 100Hz.

5.5 Chosen Operating Conditions

The operating conditions investigated in detail are summarised in Table 5-7. The means used to characterise these conditions include pressure and temperature data of the inlet annulus section prior to entry to the chamber. High speed CH* Chemiluminescence was undertaken to indicate areas of heat release and provide a qualitative indicator of heat release. Finally high speed PIV and SPIV have been used to characterise the flow field of the operating conditions and also for non reacting flows. Only a selection of these conditions is presented in this thesis.

Flame Number	Velocity (m/s)	Equivalence Ratio	H2 Content (%)	Frequency (Hz)			
1	60	0.8	0	100	200	400	800
3	60	0.7	0	100	200	400	800
4	60	0.8	10	100	200	400	800
6	60	0.7	10	100	200	400	800
10	60	0.8	20	100	200	400	800
12	60	0.7	20	100	200	400	800
13	80	0.8	0	100	200	400	800
15	80	0.7	0	100	200	400	800
16	80	0.8	10	100	200	400	800
18	80	0.7	10	100	200	400	800
22	80	0.8	20	100	200	400	800
24	80	0.7	20	100	200	400	800
25	100	0.8	0	100	200	400	800
27	100	0.7	0	100	200	400	800
31	100	0.8	10	100	200	400	800
33	100	0.7	10	100	200	400	800
34	100	0.8	20	100	200	400	800
36	100	0.7	20	100	200	400	800

Table 5-7 Table showing the experimental matrix undertaken. CH Chemiluminescence data and inlet data has been collected for all flame numbers and all frequencies. Flow field data has been collected for all flames and all frequencies highlighted in grey. Flames and frequencies highlighted in dark grey are presented in this thesis.

From this point onwards two flames are considered, Flame 1 and Flame 10 with the operating conditions in Table 5-8 experiencing instability frequencies of 100Hz, 200Hz and 400Hz. The reasons for this will be discussed in further chapters. Table 5-8 gives greater detail concerning the flow conditions of these two flames.

Equivalence Ratio	Inlet Veloicty (m/s)	H2 Content (%)	Mixture Density (Kg/m^3)	Mixture Viscosity (micro Pas)	Reynolds Number (Annulus)	Reynolds Number (Equivalent diameter)	Speed of Sound (m/s)
0.8	60	0	1.1283	18.0785	14971.7	73152.0	347.1
0.8	60	20	1.1117	18.1104	14731.7	71979.5	349.8

Table 5-8 Detailed flow conditions and properties of f1 and f10.

The mixture viscosity was determined using a mixture composition formula [111].

5.6 Characterisation of Pre-Entry Conditions

The conditions of the flow before entry into the combustion chamber are characterised by recording the temperature and pressure of the flow in the wake mixing section at positions indicated in Figure 5-9. In particular the pressure information describes the induced pressure perturbation that the combustion

chamber will experience. Flame 1 and flame 10 exposed to 100Hz, 200Hz and 400Hz are presented and analysed.

5.6.1 Temperature Measurements

As described a type K thermocouple was installed in the mixing section in close proximity but not interfering with the pressure transducer. The temperature of the flowing gas remained constant during experimentation and would see changes of one or two degrees only after prolonged operation as the stainless steel of the system became warm. The temperature for both f1 and f10 was 296K.

5.6.2 Pressure Measurements

The pressure data was recorded using the data acquisition capability of the Tektronics oscilloscope. The pressure was recorded simultaneously with the synchronisation signal from the rotational sensor within the motor sub assembly. The limited resolution of the pressure transducer (2 mbar) compared to the small amplitude pressure oscillations generated resulted in the occurrence of high frequency noise. This was eliminated by low pass filtering; damping frequencies in excess of 10KHz. Comparisons of spectra of filtered and unfiltered revealed the extreme low power of the higher frequencies (unexcited acoustic modes of inlet section) and therefore justified their removal. However even after filtering the resolution of the transducer remains the same, therefore the uncertainty is ± 1mbar.

The synchronisation signal was differentiated to yield accurate positions when the sensor wheel cut the infra red beam and marked the exact beginning of a new oscillation. These positions allowed the derivation of a mean profile and the calculation of the standard deviation at every point in phase during the mean profile. The continuous data can also be used to determine the frequencies present within the generated perturbation. The processing was performed in Matlab using a custom written macro. The results are presented in Figure 5-16, Figure 5-17 and Figure 5-18

When perturbed at 100Hz the pressure amplitudes of f1 and f10 are approximately 40 mBar(g) and are identical. Both frequency analyses show a dominant 100Hz frequency followed by small harmonics at 200Hz, 300Hz. At 200Hz the pressure profile is very different from that at 100Hz. The amplitude is approximately 50 mbar(g) for both f1 and f10. The frequency analyses show two, near equal, dominant frequencies of 200Hz and 400Hz. Smaller harmonics at 600Hz, 800Hz and 1000Hz are visible. At 400Hz the profiles are more similar to those of 100Hz. Once again f1 and f10 are identical to each other with amplitudes of near 100 mBar(g). The frequency analyses show that 400Hz is the dominant frequency with a harmonic of 800Hz.

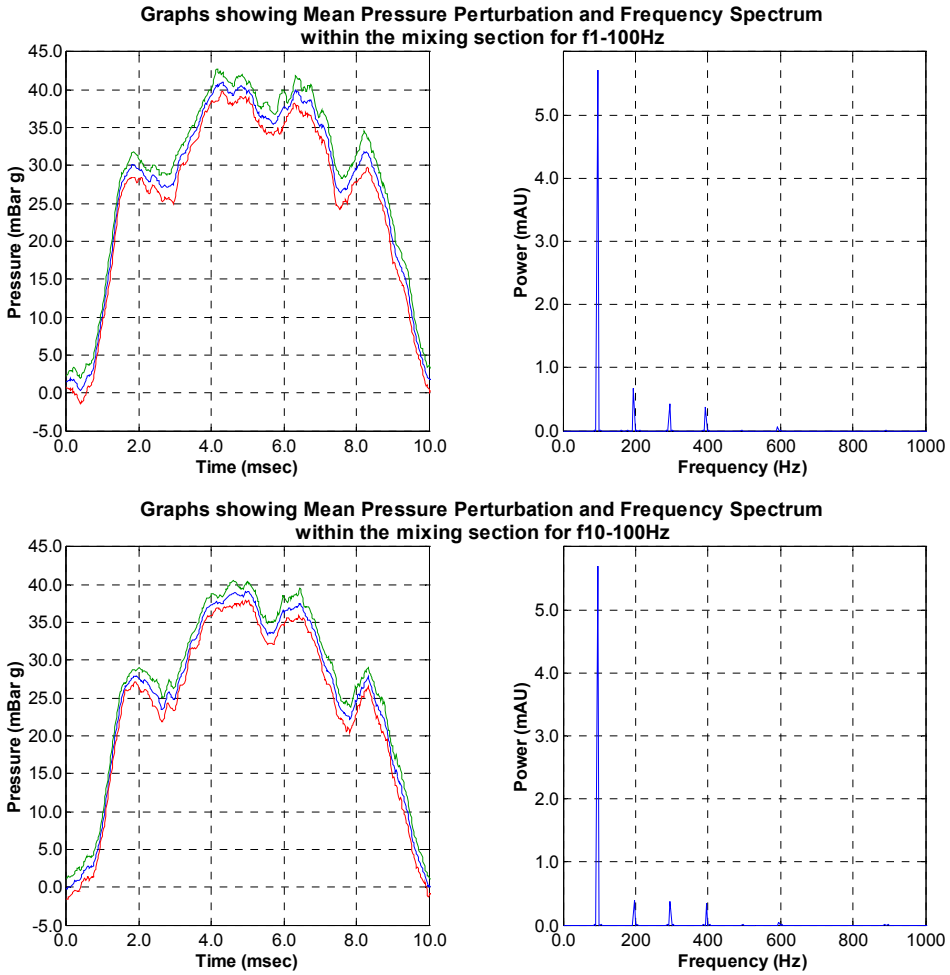

Figure 5-16 Left: Graph showing the Mean (blue), Mean +1std (green) and Mean -1std (red) pressure perturbation of f1-100Hz and f10-100Hz. Right; Graph showing Frequency Spectrum of the induced perturbation of f1-100Hz and f10-100Hz.

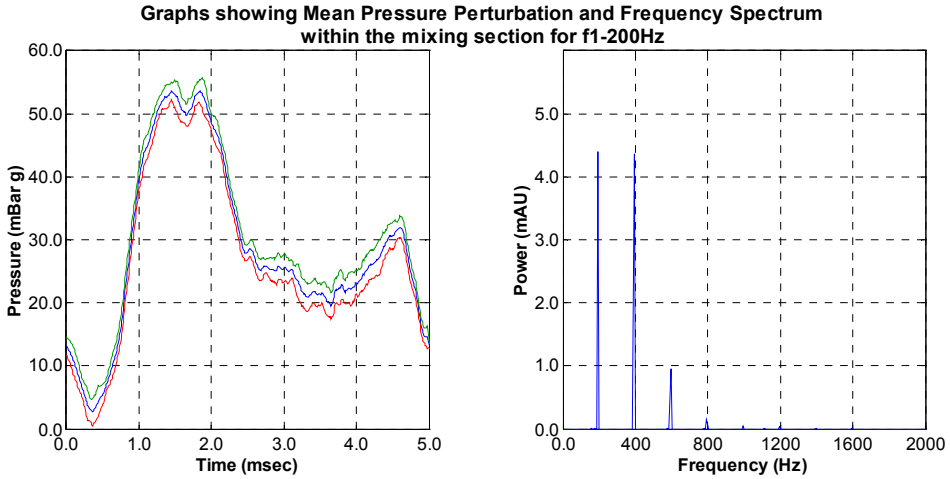

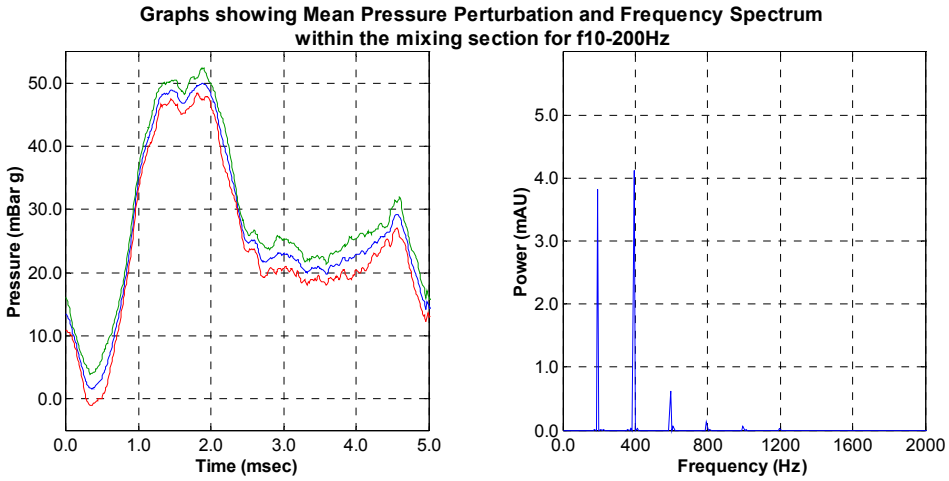

Figure 5-17 Left: Graph showing the Mean (blue), Mean +1std (green) and Mean -1std (red) pressure perturbation of f1-200Hz and f10-200Hz. Right: Graph showing Frequency Spectrum of the induced perturbation of f1-200Hz and f10-200Hz.

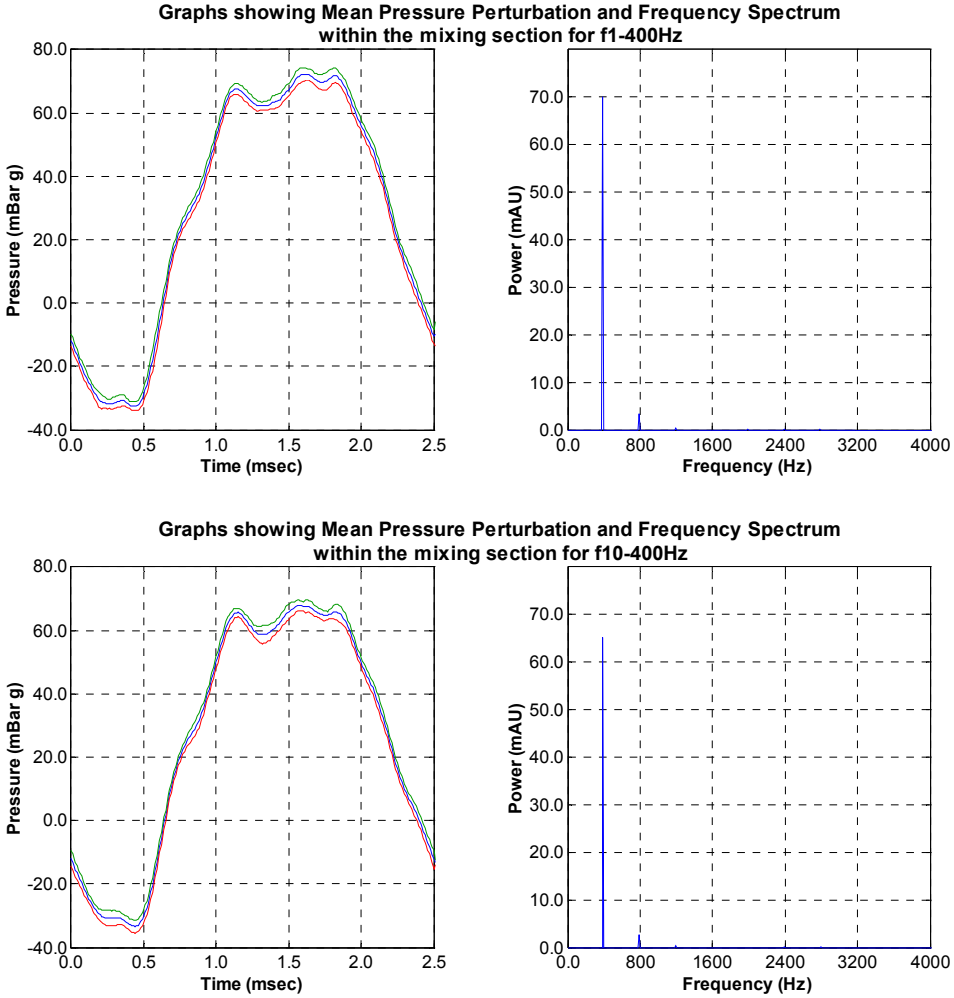

Figure 5-18 Left: Graph showing the Mean (blue), Mean +1 std (green) and Mean -1 std (red) pressure perturbation of f1-400Hz and f10-400Hz. Right: Graph showing Frequency Spectrum of the induced perturbation of f1-400Hz and f10-400Hz.

5.7 Acoustic Properties at the Chosen Operating Conditions

The acoustic properties of the chamber and inlet section will change during operation. This is due to the large temperatures and gas composition change in the chamber. The change from pure air to a flammable mixture will cause the acoustics in the inlet section to change also. Using an approximate chamber temperature of 2000K corresponding to a speed of sound of 840ms^{-1} and adiabatic index of 1.25 [110] Eq 5-2 can be used with Table 5-1 to recalculate the longitudinal, radial and tangential modes of the chamber. Regarding the inlet the speed of sound[ii] for f1 and f10 was calculated using Eq 5-11. This was then used with Eq 5-2 to determine the modes. As the speed of sound in the inlet changes so little between f1 and f10 (347.07ms^{-1} and 349.82ms^{-1}) only the values for pure methane are presented.

$$c = \sqrt{(\gamma_{Mix} R_{Mix} T)} \qquad \text{Eq 5-11}$$

q = 0	m = 0	m = 1	m = 2	m = 3
n = 0	0	7320	13998	19428
n = 1	3516	10182	16302	22350
n = 2	5832	12810	19038	25152

q = 1	m = 0	m = 1	m = 2	m = 3
n = 0	840	7368	14023	19446
n = 1	3615	10217	16324	22366
n = 2	5892	12838	19057	25166

q = 2	m = 0	m = 1	m = 2	m = 3
n = 0	1680	7510	14098	19501
n = 1	3897	10320	16388	22413
n = 2	6069	12920	19112	25208

q = 3	m = 0	m = 1	m = 2	m = 3
n = 0	2520	7742	14223	19591
n = 1	4326	10489	16496	22492
n = 2	6353	13056	19204	25278

q = 4	m = 0	m = 1	m = 2	m = 3
n = 0	3360	8054	14396	19716
n = 1	4863	10722	16645	22601
n = 2	6731	13243	19332	25375

q = 0	m = 0	m = 1	m = 2	m = 3
n = 0	0	21608	41321	57349
n = 1	10379	30056	48122	65975
n = 2	17215	37814	56198	74246

q = 1	m = 0	m = 1	m = 2	m = 3
n = 0	1157	21639	41337	57361
n = 1	10443	30078	48136	65985
n = 2	17254	37831	56210	74255

q = 2	m = 0	m = 1	m = 2	m = 3
n = 0	2314	21731	41385	57396
n = 1	10634	30145	48177	66015
n = 2	17370	37884	56246	74282

q = 3	m = 0	m = 1	m = 2	m = 3
n = 0	3471	21885	41466	57454
n = 1	10944	30256	48247	66066
n = 2	17562	37973	56305	74327

q = 4	m = 0	m = 1	m = 2	m = 3
n = 0	4628	22098	41579	57536
n = 1	11364	30410	48344	66137
n = 2	17827	38096	56388	74390

Table 5-9 Left: Acoustic modes of the chamber and exhaust section with hot burnt gas. Right: Acoustic modes of the mixing section during f1 flow.

[ii] Speed of sound calculated by determining the mixtures' gas constant R_{Mix} and adiabatic index γ. The mixtures gas constant was obtained by using the universal gas constant and the mixtures' mean molecular weight $R_{Mix} = R_U / M$. The mixtures' C_P was determined by proportioning the individual gas constants by their mass fractions in the mixture. The C_V values were obtained by $C_V = C_P - R_{Mix}$. Finally the adiabatic index can be determined $\gamma = C_P / C_V$.

6 OPTICAL APPARATUS AND PROCESSING

What follows is a description of the Optical experimental apparatus and arrangements used to characterise the induced combustion instabilities. A description of the CH* chemiluminescence set up and image processing is given. For the PIV numerous difficulties were encountered during initial trials. A brief description of this set up is given with more emphasis on the problems encountered and the chosen solutions before giving a more complete description of the revised experimental set up and processing.

6.1 CH* Chemiluminescence

6.1.1 Camera and Optics

In order to record the CH* chemiluminescence signal a High speed Phantom V7 was utilised from EPSRC. The camera is a CMOS (Complimentary Metal Oxide Semiconductor) device. The camera was operated in a purely monochrome grey scale mode in order that the amount of light be recorded, not the wavelength. The dynamic range was 256.

The camera was coupled with a Lavision intensifier in order to amplify the collected light. A Nikon 50mm lens and a filter (Newport 20BPF10-430) were used to allow the collection of light centred on 430nm (±10nm FWHM) and reject other wavelengths. An aperture of f# = 2.0 was used in order to focus light from the flame onto the chip, with the intention of deconvoluting the image during processing to recover the 2D structure of phase averaged images [112]. This therefore required long exposure times to achieve strong signal to noise ratios and an acceptable image uncertainty. Long exposure times however mean that the chemistry, flow and location of the combustion are not static as a PLIF technique would give.

Consideration was given to the exposure time compared to the time period of the combustion instability and the number of phase positions to be sampled. It was decided to sample eight phase positions for each frequency and that the exposure time at each frequency should not be more that half the time period of the sampling frequency (T_s). This arrangement offered the best compromise of minimising the exposure time and acquiring a sufficient chemiluminescence signal. The most suitable exposure times were chosen from the choices allowed by the software. The exposure times are summarized in Table 6-1.

	Combustion Instability Frequency		
	100Hz	200Hz	400Hz
Time Period T (ms)	10	5	2.5
Sampling Frequency (Hz)	800	1600	3200
Sampling Time Period Ts (ms)	1.25	0.625	0.3125
Exposure Time (ms)	0.5	0.25	0.15

Table 6-1 Sampling frequencies and exposure times for CH* Chemiluminescence imaging.

These exposure times in combination with an f# = 2.0 and the specified filter allowed an acceptable image to be obtained. The gain level of the intensifier was set to 6.5 (within linear regime) on the controller and was kept at this value for all of the experiments.

The camera, intensifier and filter were all mounted upon an optics rail using adjustable mounts to ensure correct alignment. Once in position the entire arrangement was encased within a custom designed heat shield. A water cooled jacket was wrapped around the lens to give thermal protection. Focusing was achieved using a custom designed calibration arm which allowed the insertion of a calibration grid to be held horizontally within the chamber coincident with the horizontal mid plane. The lens was then focused upon this calibration plate. A total of 1600 images were recorded for each condition, 200 images for each phase position with an image (raw) size of 512 pixels by 512 pixels. The resolution was 0.399 mm/pixel.

6.1.2 Synchronisation

The triggering to begin recording a sequence of images was accomplished using the TTL output signal from the rotational sensor mounted with the siren motor assembly (Chapter 5.2). This was connected to the camera with the camera in standby mode awaiting the trigger to begin. Phase locking was achieved by using the same output signal and using this to trigger a Texas instruments delay generator which provided a second signal with a frequency eight times that of the instability frequency (yielding 8 phase trigger pulses per combustion oscillation). This signal was fed to both camera and intensifier. The intensifier was controlled using its own control unit and the camera using a computer with its own software. This arrangement allowed true phase locking as each image received a trigger.

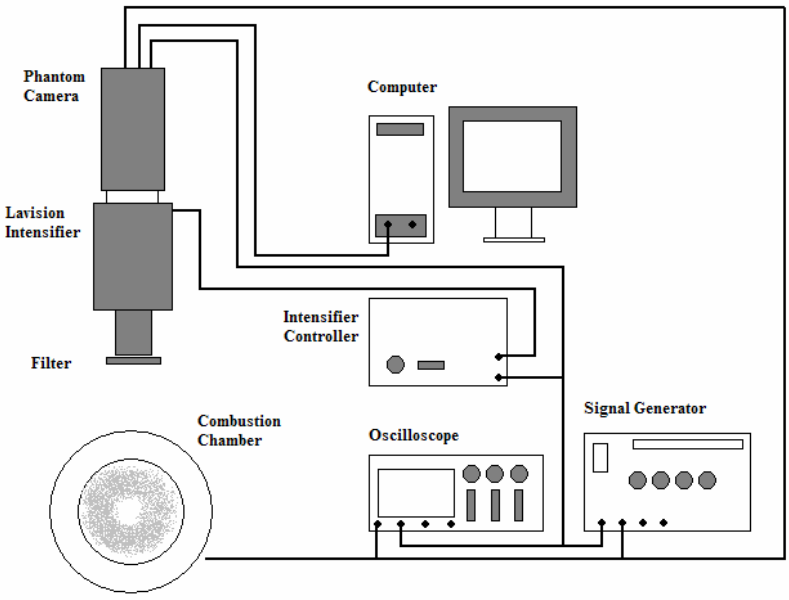

Figure 6-1 Illustration showing apparatus used for CH* Chemiluminescence imaging and triggering system.

6.1.3 Raw Image Processing

The recorded image $R_I(x,y)$ of any camera is a function of its inherent electronic bias (or platform) $E_B(x,y)$, its response to the collected light (flatfield) $F_F(x,y)$, any background light collected $B_G(x,y)$ and the collected desired light itself $I(x,y)$. This leads to a simple procedure for processing to acquire the true signal after determining the platform and camera response.

$$R_I(x,y) = F_F(x,y)[B_G(x,y) + I(x,y)] + E_B(x,y) \qquad \text{Eq 6-1}$$

Before commencing the electronic bias was determined. This was done by collecting 50 images in the absence of light and taking the mean. This was found to have a value of zero across the whole image irrespective of exposure time and will not be considered further regarding processing.

The camera response was determined by focusing the camera system upon white paper in the presence of diffused light and removing all reflective surfaces. The mean of 200 images was calculated. This image was then divided by the mean pixel value within the image and used as the response image. Each raw image was first divided by this image.

The background was determined for each instantaneous image. The coupling of the intensifier and camera resulted in the outer areas of the chip imaging the mating part of the intensifier at each corner of the image. The mean values from these areas were sequentially subtracted from the image.

The processing of the raw images commenced with each being normalised. Then the images were divided by the flat field image. Background subtraction was then performed as described above. Finally the mean at each phase was calculated. Once this is complete the maximum pixel intensity within the cycle is determined and a threshold is set to 20% of this value [42]. Each image is subsequently called again and treated the same way until being thresholded by this value after the initial background subtractions have been made. Thresholding ensures the background is fully removed. The processed instantaneous images are all saved and then used to calculate the mean and standard deviation images for each phase. Image processing was performed using Lavision Davis 7.1 software and custom written macros.

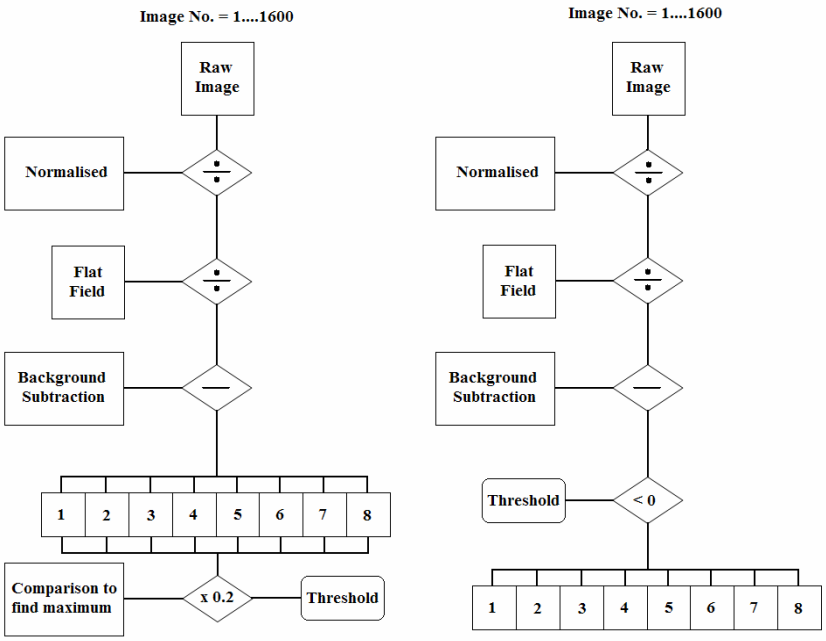

Figure 6-2 Illustration showing the image processing procedure employed.

Chemiluminescence imaging is a line of sight integration measurement technique. Therefore care must be taken when using the mean images to infer information regarding the flame structure as the image does not represent a slice through the chamber. The mean images were therefore deconvoluted to obtain an estimate of a slice through the chamber.

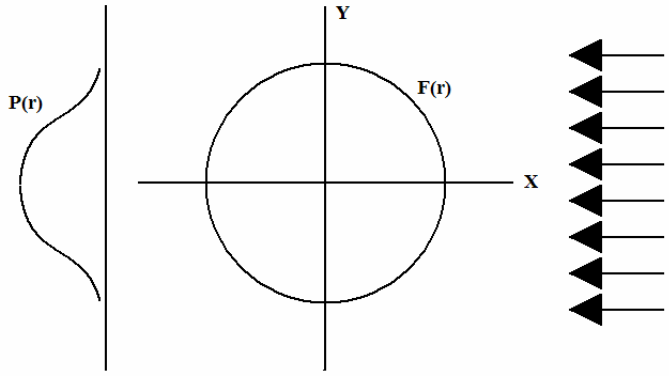

Figure 6-3 Illustration showing line of sight projection of 3D object to a 2D plane.

This was achieved using a 3 point Abel deconvolution method [113]. Assuming symmetry around the chamber centre axis and vertical line of sight integration each pixel represents the integral projection value.

$$P(r) = 2\int_0^\infty F\left[\sqrt{(r^2 + y^2)}\right]dy \quad \Rightarrow \quad F(r) = -\frac{1}{\pi}\int_r^\infty \frac{P'(r')}{\sqrt{(r'^2 - r^2)}}dr' \qquad \text{Eq 6-2}$$

Where r represents the radial distance, and y the vertical coordinate in the cylindrical cross section. $P(r)$ is the line of sight integrated field function, this corresponds to all horizontal pixel lines across the mean images. $F(r)$ is the field function and a slice through the deconvoluted 3D shape at the vertical mid point.

Eq 6-2 gives the line of sight integration projection based upon the cylindrical field function and the field function based upon the projection function. The integral to obtain the cylindrical field function is evaluated using a deconvolution operator D_{ij}. The deconvolution operator can be determined using the equations provided in [113]. Once this is done the projection data is used in combination with the appropriate deconvolution values to determine the field function.

$$F(r_i) = \frac{1}{\Delta r} \sum_{j=0}^{\infty} D_{ij} P(r_j) \qquad \text{Eq 6-3}$$

As it is assumed the field function is symmetric about the central axis the mean images where split into two and a mean constructed from the two halves. This was then used to derive the deconvoluted function which was then copied about the central axis to produce a complete image. This operation was performed using Lavision Davis 7.1 software and a custom written macro.

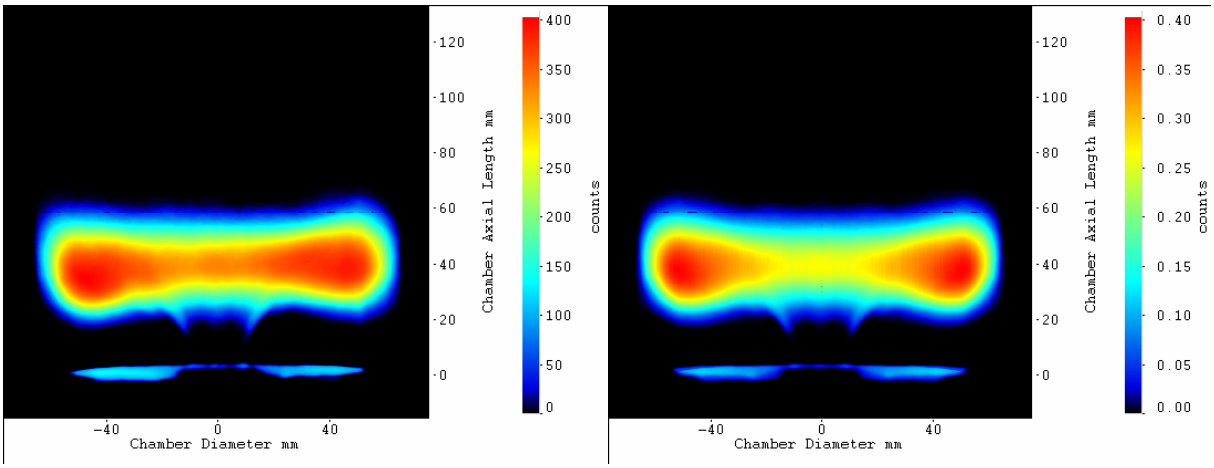

Figure 6-4 Left: Mean CH* image of f1-100Hz at phase position 3. Right: Mean CH* image of f1-100Hz at phase position 3 after the 3 point Abel deconvolution.

As can be seen in Figure 6-4 there is minimal change to the overall shape of the flame structure but a significant change in the high intensity regions. The outer regions maintain the peak intensity but the central region of high intensity in the mean image has been significantly reduced in the deconvoluted image.

6.1.4 Image Uncertainty

In order to determine the uncertainty of the recorded images the signal to noise (SNR) ratio was determined and compared with the dynamic range. This could not be performed using the collected signal as the flame is not stationary through the exposure time. Therefore an area of the raw image that captured part of the back of the intensifier was selected. This area received no reflection from the chemiluminescence signal, was uniform in signal and did not change image to image. This area shall be referred to as the interrogation area.

The raw images were used to create an average which was then used to divide all instantaneous images by. The RMS value within the area of interest therefore represents the inverse of the SNR of the particular instantaneous image at the signal level within the interrogation area. This operation was performed for each

instantaneous image for each condition. The mean SNR was then calculated. In addition the mean collected signal and RMS value for the interrogation area was determined over all the images.

The dynamic range for the ensemble was determined by interrogation of each image. The dynamic range was defined by the difference between the mean collected signal within the interrogation area and the absolute cycle maximum. Assuming the noise is dominated by photon noise, the noise is proportional to the square root of the collected signal. The ratio of the cycle maximum and mean value of the interrogation area can be square rooted and multiplied with the RMS of the interrogation area to yield an estimate of the RMS (noise) for the cycle maximum. As the assumption of photon noise being dominant is used this noise at the cycle maximum will be the largest noise for the values of the dynamic range. The ratio of this noise and the dynamic range gives the fraction of the dynamic range which is equal to the maximum noise. Hence only fractions of the dynamic range greater than this can be distinguished.

	f1			f10		
	100Hz	200Hz	400Hz	100Hz	200Hz	400Hz
Background Mean Value	52.427	25.574	15.420	56.425	27.933	17.047
Background RMS (noise)	0.725	0.502	0.391	0.717	0.506	0.394
Background SNR	72.313	50.944	39.437	78.700	55.203	43.266
Max Cycle Value	236.651	121.360	71.496	234.476	116.077	70.839
Dynamic Range	184.224	95.785	56.076	178.051	88.144	53.791
RMS at Max value (noise)	1.540	1.094	0.842	1.461	1.031	0.804
Distinguishable Fraction of Dynamic Range (%)	0.836	1.143	1.502	0.820	1.17	1.495

Table 6-2 Table detailing the distinguishable fraction of the dynamic range for the flames investigated.

Table 6-2 details the SNR at the background levels, the cycle maximum and the projected noise at the maximum. This allows the distinguishable fraction of the dynamic range to be determined. This applies to all instantaneous images. As can be seen 1% changes for the flames perturbed at 100Hz can be distinguished, 1.5 for 200Hz and 2% for 400Hz with confidence.

6.2 Particle Imaging Velocimetry

To characterise the flow field within the combustion chamber SPIV and PIV was used. The choice of seeding particles for reacting flows is dependent upon the experiment. For large scale experiments such as these a refractory oxidised material is required. Typically Titanium dioxide (TiO_2), Aluminium oxide (Al_2O_3) and Zirconia (ZrO_2) are used as solid state seeding particles. Initially TiO_2 was used as the seeding particles due to acceptable slip velocity (see Chapter 4.3) and high refractive index.

Material	Density (g/cm^3)	Particle Size (micro m)	Melting Temp (C)	Continuous Use Temp (C)	Refractive Index	Slip Velocity (micro m/s)
TiO2	4.05	3	1850	-	2.7	19.86
Al2O3	3.9	0.1	2100	1700	1.63	0.021
ZrO2	6.1	2	2650	2200	2.176	13.3
ZrO2+Y2O3 (5.4%)	5.9	0.1 to 2	2700	2200	-	0.032 to 12.86

Table 6-3 Table comparing the thermal, optical and suitability as a seeding particle of typical refractory powders.

For initial trials a single Lavision Flow Master camera was mounted above the chamber viewing the annulus and extending 80mm downstream. A Spectra physics double pulsed Nd:YAG at 532nm with a repetition rate of 8Hz was used as the illumination source. Appropriate sheet forming optics was used to create a sheet of appropriate dimensions and approximately 0.5mm thick to reduce particle drop out. The laser pulse separation time, Δt, was set by knowing the approximate inlet velocity, image resolution and desired particle displacement at the inlet velocity. This was verified by performing tests on non reacting flows.

Trials with reacting flows proved to be significantly difficult. Once the seed was introduced to the flow at an acceptable seeding density image capture was started. It was quickly discovered that after approximately 10 seconds the chamber was coated with particles that had been deposited on its inner surface. Such was the build up of particles that further imaging was impossible due to the massive scattering from these particles. With a laser repetition rate of 8Hz (with a single camera) at most 80 image pairs could be recorded and with significant doubts over images recorded towards the end of this period due to increasing background scatter collected.

The recorded images showed a non uniform distribution of background scatter. By far the worst affected part of the image was where the flame impinged upon the chamber wall. As the flow travels from the annulus into the chamber it will flow radially outwards onto the wall before recirculating up and downstream. Therefore this region of the chamber wall collected the most particles. The size of this region was extensive as the flame is pulsed and therefore travels over a large axial distance and unintentionally creates a wide band around the duct of deposited particles. These particles reduced the transmitted laser light into the chamber, created additional scattered light and obscured the ability to view through the silica into the chamber.

After it was discovered the chamber had become coated the system was shut down and allowed to cool. Once this was done the exhaust section was detached and the deposited powder was removed. However particles that were deposited where the flame is in contact with the chamber wall would not simply wipe off as at other axial positions. Closer examination revealed that these particles had become embedded into the surface of the chamber. These would not be removed with an alcohol wipe, or light abrasion with a fine very fine glass paper (see Figure 6-5). The suspected reason for this is a combination of factors. Firstly the combustion temperature is in excess of the continuous use and maximum limited use temperatures of 1223K and 1473K of fused silica [114] and as the flame in

this chamber impinges upon the wall it is highly likely the wall experiences temperatures above these. This will have an effect upon the crystalline structure and hence the optical transmission characteristics. Also it is likely that the surface becomes softer and hence impinging particles are more likely to embed themselves into the silica. In addition some of the TiO_2 will be in a glassified/softened state after moving through reaction zones and will be more likely to adhere to a surface, particularly as the flow will impinge upon the wall before proceeding to recirculate. Finally the time to acquire a sufficient number of image pairs means that particles deposited onto the silica are being exposed to high temperatures for this time, further encouraging a permanent bond.

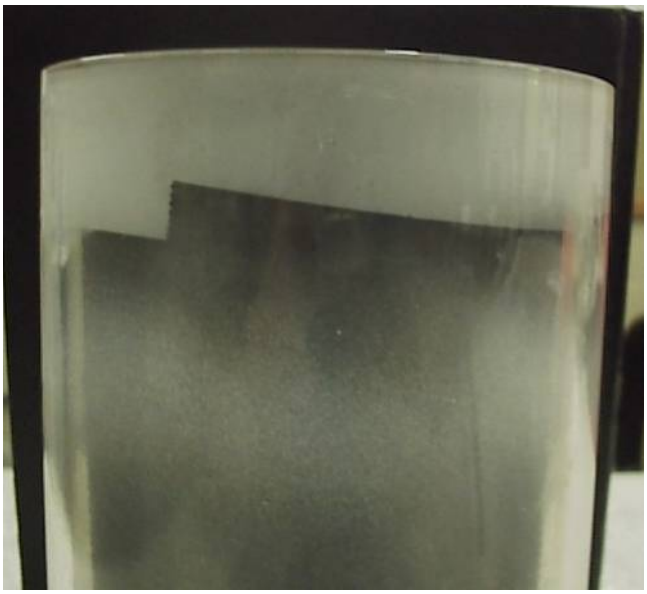

Figure 6-5 Photograph showing the band of embedded seeding particles against a black background. As is evident it is impossible to see through the duct at the band location. The top of the duct shows the effect of grit blasting.

The small time it took for the duct to become coated and the damage caused to the silica duct posed an extremely serious risk to the work. Not only in the small operating window to collect data but the financial cost of the fused silica duct. Attempts were made to find a procedure to restore the duct to its original condition. The piece was made by an extrusion process and subject to no further surface polishing. For fused silica lenses, or flat pieces the item in question typically undergoes a chemical polish with hydrofluoric acid and then a mechanical polishing procedure. The acid polish by itself is insufficient to achieve a suitable finish and subject to extreme health and safety regulations. The ability to mechanically polish the inner surface of a cylinder is further restricted by the hardness of silica and the wall thickness of the duct. A single company was found that had the capability to perform a mechanical polish using a diamond cutter. This process however could not be used as the force required would have meant destroying the duct due to its insufficient wall thickness for this process. Finally an approach was used whereby the embedded particles were removed by a fine sand blasting technique (see Figure 6-5) before being heat treated to try and obtain a suitable finish. This approach failed.

The raw images recorded using TiO_2 exhibited a drop in seeding density as the flow entered the chamber. This drop in signal is attributed to the spreading of the

inlet flow; viscosity changes post reaction zone and glassification of the particles [114]. This is where the particle becomes opaque and experiences a reduction in scattering cross section as it moves through the local high temperature of the reaction zone. This makes detection within an image difficult. For flames in a more simple geometry (such as planar) this reduction in scattered signal within an image can be used to mark the reaction zone, particularly as the particles are carried downstream[iii]. The particles in this geometry are not always carried downstream. A large portion of the flow recirculates back towards the dump plane and towards the annulus. As particles were observed within the corner and close to the inlet flow it can be surmised that some of the particles were either unglassified or cooling down sufficiently to scatter the laser light. The particles that are carried downstream have the possibility of being returned upstream through the inner recirculation zone. These particles having been away from the reaction zone have also sufficiently cooled to scatter the laser light. The premise that locations which show scattering of seeding particles coincide with fresh gas is now invalid. It is likely that particles from burnt gas could be adjacent to particles in fresh gas. Finally, the seed is injected through the annulus. Therefore the seeding density at the entry will not be constant as the inlet flow penetrates into the chamber and begins to spread. The seeding density will collapse. Using the raw Mie image an interface can be established around particles but subject to large error due to the complex flow conditions. The validity of whether the result is fresh or burnt gas and if a true reaction zone is identified is unresolved. For these reasons TiO_2 is an unsuitable seeding particle as insufficient seed survives to adequately seed the entire chamber and signal unknowns mean it can not be used as a reaction zone marker.

A different approach was therefore adopted. This was to record the required information quicker. Therefore a TSI High Speed Stereo PIV system was used. The cameras had a maximum frame rate at full resolution (1024 by 1024) of 2KHz which results in a PIV frame rate of 1KHz. Using this equipment the collection of data within the small operating window could be accomplished. In addition also reducing the number of particles embedded in the duct and reducing the time these are exposed to high temperatures. Finally a different seeding medium was used. Zirconia stabilised with 5.4% Yttria was sourced (ZrO_2 + 5.4% Y_2O_3). Being the most refractory material available the number of particles that glassify will be minimal. This will reduce the damage incurred and allow sufficient seed to be visible in the entirety of the chamber. This choice meant that the identification of the flame front from the raw Mie scattered images would be impossible based upon a drop in signal intensity. This material also possesses a reasonable refractive index. A further four fused silica tubes were purchased.

6.2.1 High Speed Stereo PIV

The SPIV system used was a High speed Stereo PIV system from TSI. The system incorporated two high speed Photron cameras (Powerview HS 2000,

[iii] Dilation also causes drop in particle density which can be used to identify the reaction zone. This would result in a few pixels with high signal intensity.

1024×1024 pixels, 2.6Gb memory), a high speed Pegasus Nd:YLF laser from New Wave capable of a repetition rate of 10KHz with a wavelength of 527nm and 25mJ per pulse, a synchroniser unit to coordinate the equipment together and finally a computer work station. The lenses used were NIKON 105mm focal length.

Initial trials with this equipment highlighted a number of serious problems. Firstly it proved extremely difficult to turn the laser unit on due to a repeating interlock failure of insufficient flow rate of the cooling system. A water cooling system was used to ensure correct operational temperature of the photodiodes. Over a short period of time it became increasingly difficult to turn the laser on. After a subsequent investigation it was found that the laser had been manufactured with brass cooling passages within the laser head which had corroded and was causing flow restriction. The laser was subsequently returned to the manufacture for repair.

The synchroniser also was faulty. The unit would not operate in a triggered mode. It was desired to send triggering signals to the SPIV system corresponding to the phase positions, to achieve phase locking, as was done for the chemiluminescence imaging outlined in Chapter 6.1.2. However the unit would not accept an input trigger so it was impossible to synchronise the SPIV system to the combustion chamber. This unit was subsequently returned to the manufacture for repair.

6.2.2 Imaging strategy, Set up and Limitations

To adequately describe the behaviour of the instability within the chamber the chamber was divided into regions. This is due to the limited size of the CMOS chips. These are termed the Corner Recirculation Zone (CRZ), the Flame Zone and the Upper Recirculation Zone (URZ). These three areas as can be seen will characterise the motion of the flame and capture the key features of the flow. These three regions were all investigated using a stereoscopic arrangement necessary for swirling flows.

Emphasis was also placed upon the annulus and this was imaged using two approaches. The first was a stereoscopic arrangement and imaged half of the annulus termed Annulus 3D. The second was a 2D arrangement imaging both sides of the annulus, Annulus 2D. Stereoscopic measurements of the whole annulus were intended however the interference from laser sheet reflections as seen on the image made this impossible. Therefore imaging one half of the annulus allowed unambiguous imaging. Performing 2D PIV of the annulus allowed some of the laser reflections to be avoided and allowed the symmetry of the entry to be ascertained.

Data concerning the boundary conditions of either the annulus or the chamber walls proved impossible to acquire. For the annulus this was because the ceramic inlay within the dump caused image interference so it was impossible to unambiguously identify the seeding particles when the ceramic was behind them on the image. For the other imaging areas the boundary condition of the walls was impossible to determine because of the high intensity scattering of the laser sheet as it passed through the silica. This would overcome the signal from the particles and saturate the camera chip. To avoid this potential damage the

cameras were positioned so scattered light from the laser sheet passing out of the chamber was not collected.

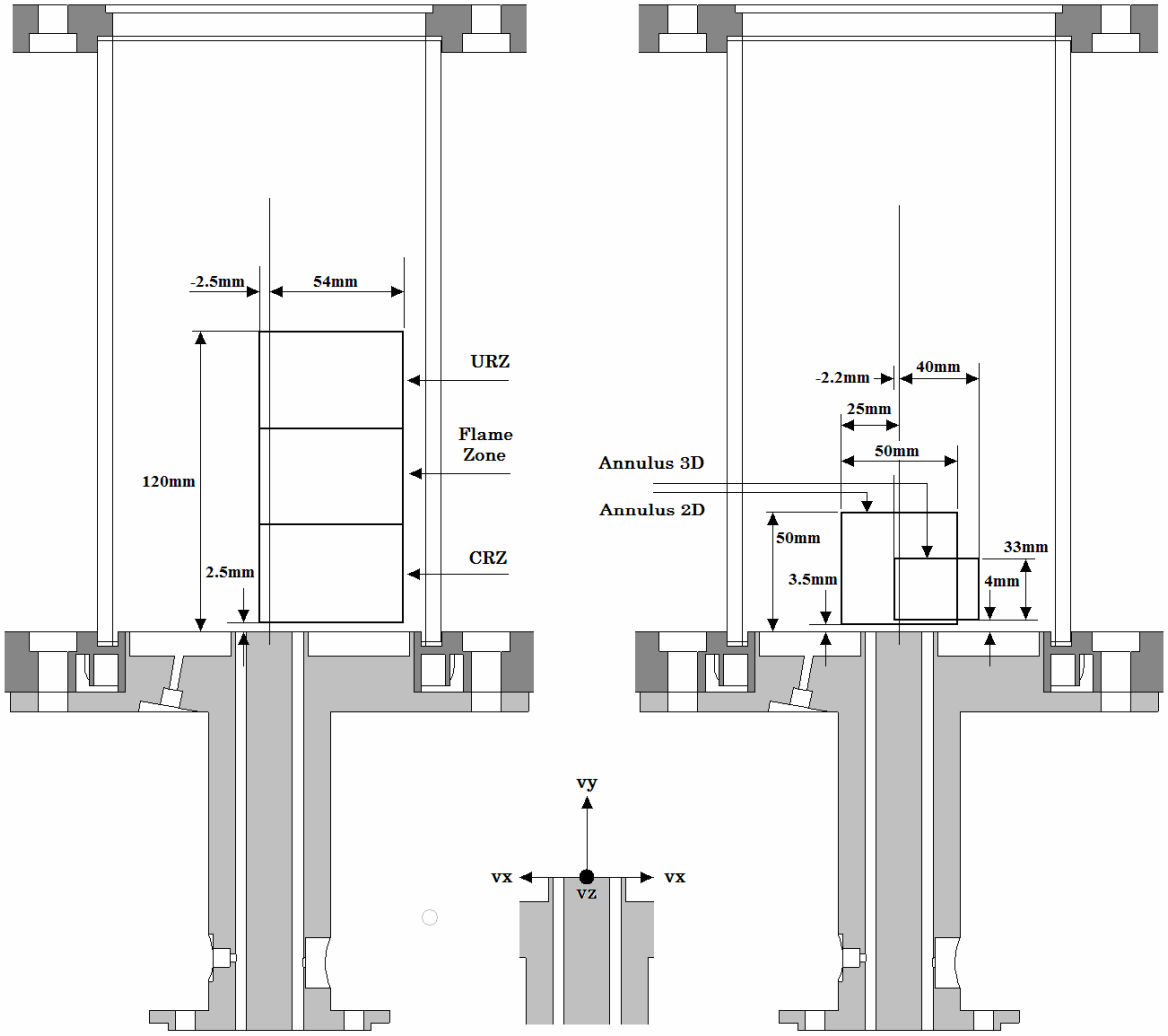

Figure 6-6 Illustrations showing the five regions investigated within the chamber. The areas and dimensions are after masking and reconstruction indicating what exactly has been measured as opposed to imaged. Left: Image showing the CRZ, Flame zone and URZ. Right: Image showing the two areas used to characterise the annulus, Annulus 3D and annulus 2D. Bottom: Reference coordinate system used.

For stereoscopic imaging the arrangement used was the angular arrangement with both cameras in forward scatter mode. This allowed a strong scattered signal to be collected for both cameras and created a larger reconstructed image. The cameras were mounted upon TSI Scheimpflug mounts to achieve good focusing across the image. The Scheimpflug mounts were themselves mounted upon custom made platforms that were attached to an optical scaffolding frame. This frame was set upon a 2D traverse which allowed both cameras to be traversed along the axial direction of the chamber without changing the cameras focusing or position on the scaffolding. Both cameras were encased within a custom made heat shield that was able to direct chilled dry air over the cameras and the lenses for thermal protection. Additional protection for the lenses was also added by using infra red filters (Comar)

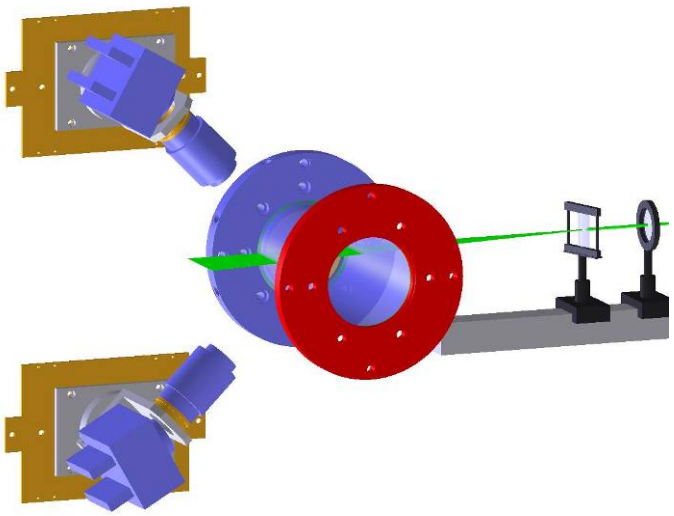

Figure 6-7 Illustration showing the Photron cameras in the forward scatter mode, The lens' are clearly visible at 45º to the laser sheet. The camera head themselves are a further 22º from this. This arrangement corresponds to the Annulus 3D set up.

The laser head was mounted and fixed upon a flat hydraulic table. The beam was directed to travel in a plane coincident to the horizontal plane of the chamber by using three dichroic mirrors (532nm) held in adjustable holders. The first mirror was positioned to direct the beam vertically upwards. The second mirror directed the beam towards the optical rail which mounted the sheet forming optics. The final mirror directed the beam towards the chamber through the sheet forming optics. Fine adjustment of these mirrors kept the laser sheet horizontal as it entered the chamber.

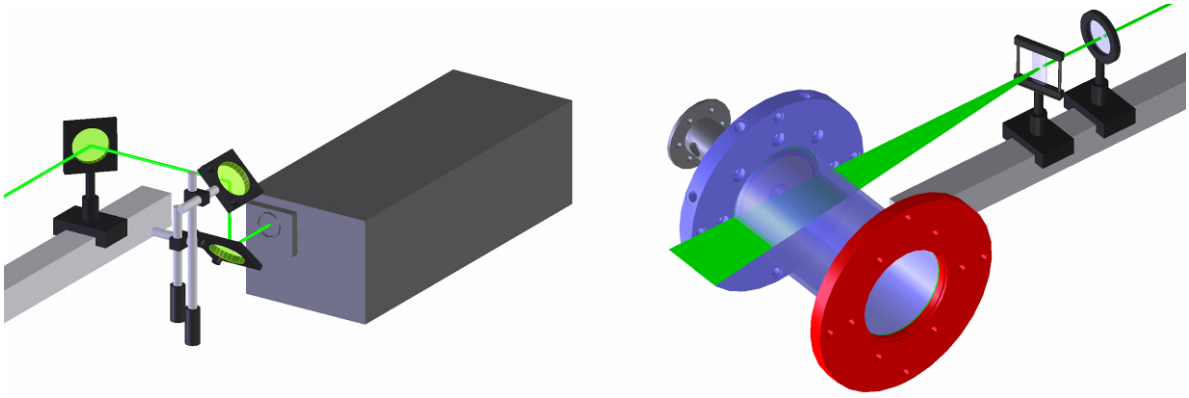

Figure 6-8 Left: Illustration showing the three dichroic mirrors used to direct the beam to the correct horizontal plane and towards the combustion chamber. Right: Illustration showing the spherical and cylindrical lens used to create an asymmetric divergent sheet entering the combustion chamber.

As the beam moved towards the chamber it passed through a spherical focusing lens and a cylindrical lens. This formed a thin diverging sheet which illuminated the seeding particles in the chamber. The cylindrical lens was a fused silica 100mm focal length lens. Two spherical lenses were employed depending upon the area being investigated. A 1000mm focal length glass lens was used for the

CRZ, Flame zone and URZ. For the annulus areas a 500mm focal length glass lens was used. In both cases the spherical lens preceded the cylindrical one.

Fine control of the last mirror ensured the laser beam incident on the cylindrical lens was just off its vertical central axis creating an asymmetric divergent sheet. By rotating the cylindrical lens the amount of divergence increased. This created a wide laser sheet. The laser head and optic path were fully encased in a sheet metal enclosure spray painted mat black to capture stray reflections. The laser sheet excited the enclosure which ended 80 mm from the chamber. The exit was a small rectangular slit with movable shutters to allow the exit area and shape to be modified. This allowed the weak intensity edges of the sheet to be cropped. This was particularly important when imaging the annulus and CRZ. A sharp laser edge was created that propagated parallel to the dump plane as close to the dump surface as possible.

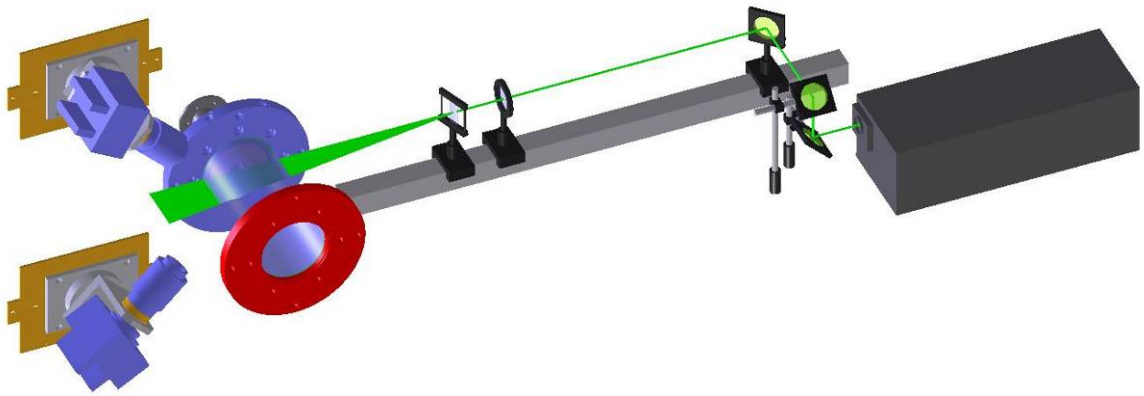

Figure 6-9 Illustration showing complete optical arrangement.

The laser sheet was safely collected in a custom made beam dump that was fixed between the cameras. This also had a shutter system to try and reduce reflected laser light back towards the chamber.

The seeding particles of ZrO_2 + 5.4%Y_2O_3 were introduced to the flow using a cyclone seeder. The unit was placed downstream of the air supply metering system. The advantages of this are that the air taken from the combustion air is dry and filtered, stopping agglomeration of the particles. The air once it has passed through the seeder and collected the particles was reintroduced to the rest of the combustion air in the preheat section (downstream of the heating elements) maintaining the same amount of air therefore maintaining the same equivalence ratio. The air used by the seeder was controlled using a needle valve.

The Photron cameras are not fast shuttered cameras and as such the TSI Insight 3G software runs the system in a 'straddled mode'. This is where the first laser pulse is fired towards the end of the first frames' exposure. The second laser pulse is fired at the beginning of the second frames' exposure. The time between the laser pulses is obviously the Δt. From the manufacture's information the time when the cameras are electronically closed was 4µs. In reality this dead time was 6µs as the response of the cameras was not immediate and the tendency for the timing system to cause drift between camera and laser required a larger inter frame time (explained in more detail below). This value is therefore the smallest time separation allowed by the system and has large implications for

what velocities can be measured for a given resolution. The resolution was determined on the raw image (not dewarped)[iv]. By taking the average resolution across the image and using the input flow rate ($60ms^{-1}$ or $80ms^{-1}$), a time can be determined which corresponds to a third of 32 × 32 pixel interrogation cell (final vector resolution). Table 6-4 shows the Δt calculated for the different imaging areas at the two flow speeds. As can be seen for $80ms^{-1}$ Δt's of 4.4 and 4.2μs are required but unobtainable with this equipment. In these cases the minimum useable Δt of 6μs was used. It is for this reason that no data concerning $100ms^{-1}$ has been collected.

The number of images recorded was limited by the size of the memory pack for each camera. This was 2.2GB. At full resolution (1024 by 1024) the maximum number of images that could be recorded was 2048 corresponding to 1024 vector maps.

Velocity (m/s)	Imaging Area	Camera Angle (degrees)	Scheimpflug Angle (degrees)	Delta T (micro s)	f#	Laser sheet Thickness (mm)	Resolution (mm/pxl)
60	CRZ, FZ, URZ	45 - 46.5	18.8 - 19.5	8.3	4	2	0.0640
	Annulus 3D	45 - 45	22 - 22.5	6.2	5.6	1.5	0.0482
	Annulus 2D	N/A	N/A	6	4	1.5	0.0547
80	CRZ, FZ, URZ	45 - 46.5	18.8 - 19.5	6.5	4	2	0.0640
	Annulus 3D	45 - 45	22 - 22.5	4.4 (6)	5.6	1.5	0.0482
	Annulus 2D	N/A	N/A	4.2 (6)	4	1.5	0.0547

Table 6-4 SPIV and PIV experimental parameters used.

6.2.3 Synchronisation

Although the synchroniser was returned and would signal the equipment to begin operation upon receiving a trigger pulse several problems were still experienced with the system, both with hardware and software. Firstly the Insight 3G software would not allow a frame rate that corresponded to the eight phase positions that was selected for the chemiluminescence experiments. Although the Photron cameras and Pegasus laser independently were able to operate at the desired frame/firing rate. Therefore the experiments were set up to obtain ten phase positions.

The hardware problems experienced were all with regard to the synchroniser. The desire was to send a trigger pulse to the synchroniser at each phase position to signal the laser and cameras. However operating in this way resulted in either the first frame or second frame being black (containing no information) and the corresponding frame containing an image of a single or double pulse. It was found with a sufficiently large time separation greater than 15μs that each frame contained a single pulse. Alternatively an attempt was made to send a single trigger to the synchroniser corresponding to the first phase position and allow the system to record the desired number of image pairs at the desired frame rate, theoretically achieving the same as recording an image pair for each pulse. This method also failed. The recorded images initially showed a single pulse per image

[iv] Although the chip size is 1024 × 1024 pixels the Scheimpflug mounts reduce this to an effective size of 900 × 900 pixels.

but after a number of images the laser shots were out of phase with the recorded images. Once again an empty first frame and a second with a single or double shot, or the reverse. Ultimately the approach taken was to trigger the synchroniser through a delay generator (DG535). The delay generator took the first trigger pulse from the combustion chamber and immediately sent a pulse to the synchroniser. The delay generator would receive a second pulse from the combustion chamber at the start of the next oscillation but would wait a specified delay time before sending a trigger pulse. Once this delay time had passed the delay generator would immediately send a pulse to the synchroniser when it received another pulse from the combustion chamber. Upon receiving a pulse from the delay generator the synchroniser would send a pulse to the system to start after an initial delay. This initial delay was such that the first recorded image pair corresponded to the first phase position. This was such for all experiments. The computer was used to set the frame rate (which corresponded to ten phase positions), the number of images (100) to record per pulse received by the synchroniser and the total number images that was to be recorded. Once these images were recorded the system waited for a second pulse. Upon receiving a second pulse another set of images was recorded. This continued until the desired number of total images was obtained. This approach although not true phase locking allowed images to be recorded at the correct phase position but avoided the observed drift described above. The number of erroneous image pairs was minimised but still occurred.

Using this method it was possible to consistently record image pairs at the correct phase positions. For the imposed frequency of 100Hz the maximum possible vector field frame rate attainable by the equipment at full resolution was 1KHz, corresponding to ten phase positions. For an imposed frequency of 200Hz the experiment was conducted with two runs. The second time using a delay on the pulse sent from the delay generator to the synchroniser unit corresponding to one phase position (0.5ms). Still maintaining a vector field frame rate of 1KHz. For the 400Hz frequency the experiment was conducted with four runs with appropriate delays for the second (0.25ms), third (0.5ms) and forth (0.75ms) experiment. Collecting the data in this fashion and filling the memory packs of the cameras allowed a total of 2048 images to be collected (corresponding to 1024 vector fields), approximately one hundred vector fields at each of the ten phase positions. With the system synchronised the acquisition of the desired images was approximately one second. This was within the discovered operational window of ten seconds before the chamber was coated with particles.

It should be noted that if the system was triggered by the operator through the computer (manually) then no errors were observed.

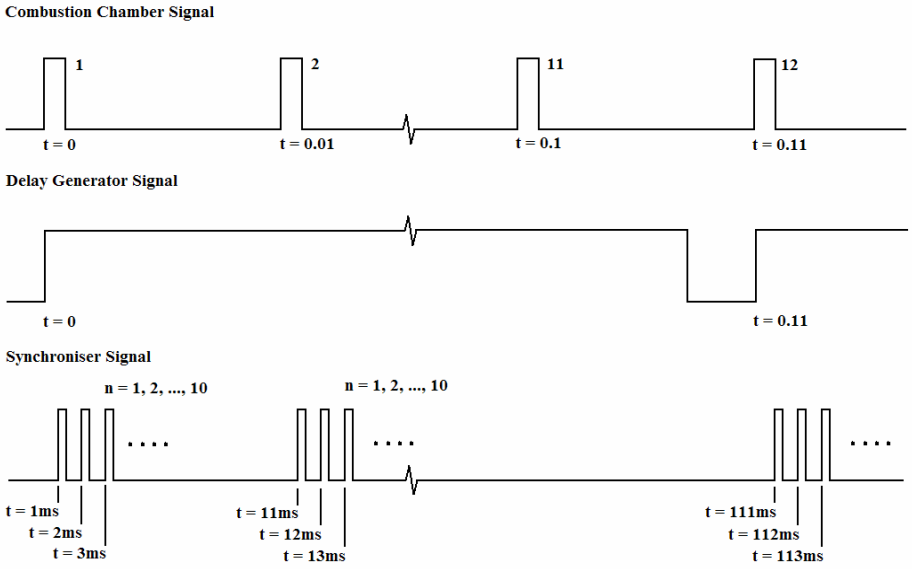

Figure 6-10 Timing Diagram for the synchronisation of flows perturbed at 100Hz. The top line shows the signal sent from the combustion chamber at the start of an oscillation. The second line shows the signal created using the DG535. This signal includes eleven pulses from the combustion chamber; however no images are recorded during the eleventh pulse to allow the system recovery time. The Third line shows the signal from the synchroniser as it sends pulses for each phase position (n).

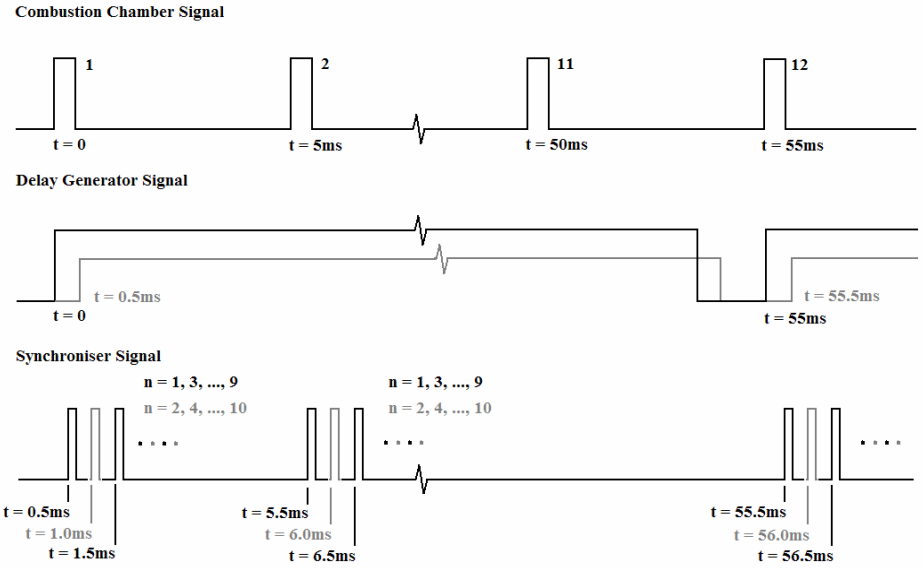

Figure 6-11 Timing diagram for the synchronisation of flows perturbed at 200Hz. The top line shows the signal sent from the combustion chamber at the start of an oscillation. The second line shows the signal created by the DG535. This signal includes eleven pulses from the combustion chamber; however no images are recorded during the eleventh pulse to allow the system recovery time. This line also shows the second run with a delay of 0.5ms corresponding to a phase position. The third line shows the signal from the synchroniser. The black line shows that odd phase positions (n) are sampled in the first run while the even phase positions (n) are sampled in the second run shown by the grey line.

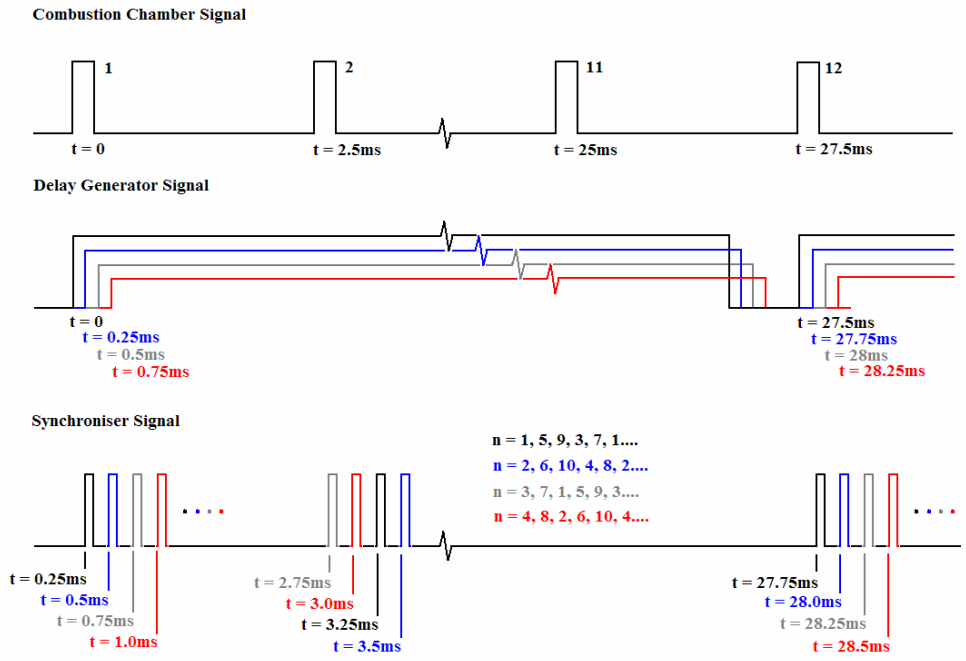

Figure 6-12 Timing diagram for the synchronisation of flows perturbed at 400Hz. The top line shows the signal sent from the combustion chamber at the start of an oscillation. The second line shows the signal created by the DG535. This line also shows the second (blue), third (grey) and forth (red) runs with a delays of 0.25ms, 0.5ms, 0.75ms corresponding the phase position time. The third line shows the signal from the synchroniser. The four runs required to sample the ten phase positions are shown. The phase positions (n) sampled by each run are different over two cycles. After this the sampling pattern repeats.

6.2.4 Operational Difficulties

The actual process of recording the required images was also problematic regarding the cyclone seeder, PIV equipment and fused silica ducts.

Control of the seeding mechanism is paramount when PIV is performed and somewhat easier in open combustion experiments as there are no windows to become coated. The cyclone seeder used here was operated using a needle valve to gradually introduce the air flow to it. It was impossible to simply supply a fixed flow rate by opening a solenoid as the sudden rush of flow produced a huge surge of seed that coated the chamber instantly making imaging through it impossible. Using the needle valve was the best solution as the flow could be introduced gradually. However once an acceptable seeding density had been achieved and the recording process was initiated there was approximately a three second delay before the PIV system finished its recording. During this interval it was common for the seeding density to change either becoming too low or too high. This meant repeating the run after the chamber was cool and could be cleaned.

A comprise regarding the seeding density was required for the upstream imaging locations. As the seed is introduced by the inlet flow through the annulus all of the seed required to seed the extremities must come from the inlet flow. Therefore the inlet flow tended to have a lot of seed and the surrounding areas

less. A compromise was struck by not over-seeding the inlet flow and not under-seeding the surroundings but resulted in non constant seeding density.

The control of the seeding density needed to be done viewing the illuminated flow within the chamber. Unfortunately the Insight 3G software was unable to provide a live image of the flow. Therefore it was almost a random process to set the correct seeding density as the quantity of seed would not be known until the images had been recorded and could be viewed. To overcome this limitation a method was devised whereby the camera's own software could be run at the same time as the Insight software. The Photron software was able to provide a live image of one or both cameras allowing the seeding density to be set in real time. Once this was done the Photron software was immediately closed and the capture command initiated in the Insight 3G software to record the images.

Once the images had been recorded to the camera memory packs they were checked to verify that the seeding density had not changed. If the images were judged to be acceptable they were downloaded from the cameras. Ordinarily the images should be downloaded through the Insight 3G software. This resulted in the loss of the image number and time history. The download time was also excessively long, approximately fifty minutes for both cameras with full memory packs. It was found that the Photron software could be re-opened and the images downloaded through this software retaining the image number, time history and take less than half the time. Therefore all images were downloaded through the Photron software in an uncompressed 8 bit bitmap (256 grey scale).

Although using ZrO_2 + 5.4% Y_2O_3 and the high speed system helped to reduce the damage done to the silica ducts damage still occurred. A new duct would transmit the laser emission effectively with minimum scattering. After time the band of particles would begin to appear where the flame impinged onto the wall and would scatter much more of the laser emission.

As PIV is an inelastic scattering process and the chamber is cylindrical laser sheet reflections were encountered. These were extremely problematic. Large stripes of high intensity appeared in the image running in parallel to the chamber central axis. The stripes were very close together and represented the two interfaces of the chamber the sheet interacts with. The exact reason for these stripes was deduced to be from a reflection from the beam dump back to the chamber in a plane coincident with the exiting laser sheet. Due to the cylindrical chamber shape it is hypothesised that the reflected light is refracted internally and reflected to the position observed on the images. Attempts were made to remove these stripes from the image by using the shutters built onto the beam dump. It was found that in most cases the stripes could be minimised but not completely eliminated. The stripes became progressively worse as the duct deteriorated. The stripes were also more apparent when an actual experiment was being performed as opposed to an empty still chamber. This is attributed to the presence of the seeding particles within the chamber.

An additional capability of the cameras is to operate at lower resolutions to allow increases in maximum frame rate. This was desired to allow measurements to be made where the increased frame rate would allow greater temporal resolution. Unfortunately selecting this option resulted in the inability to view a live image to set the seed density, even through the Photron camera software. Without this

it was impossible to set the correct seeding density and no higher temporal resolution data was acquired.

6.2.5 Raw Image Pre-processing

The processing of the collected raw images to useable vector fields followed an unorthodox route. It was decided to process the raw images using Lavision Davis 7.1 software. The reasons for this were the unavailability of the Insight license after experimentation, the closed nature of the software which does not allow access to the software functions and most importantly the inability to create a calibration file with an experimental set up of a forward scatter nature. The Lavision software alternatively is open (access to functions and macros), has the ability to create a calibration file with a forward scatter arrangement and there was no restriction regarding the license.

The pre-processing of the raw bitmap images consisted of three stages, to ensure a correct file numbering order, the removal of any erroneous images and to create files that Davis 7.1 will accept for vector processing.

For flows perturbed at 100Hz the image pairs recorded were consecutive. 2048 images were recorded. Image number 1 and image number 2 are the two frames required for vector field number 1. Image number 3 and image number 4 are the two frames required for vector field number 2 and so on. Therefore the expression relating the raw image number n_r for the first frame and the file number F_n required is shown below.

$$F_n = \frac{n_r}{2} + 0.5 \quad where \quad n_r = 1,3,5,.... \qquad \text{Eq 6-4}$$

Flows perturbed at 200Hz were recorded in two runs. The number of raw images recorded was 1024 for each run. The expression linking the raw image number of each run to the desired file number is given below.

$$Run\,1: F_n = n_r \ where \ \ n_r = 1,3,5,.... \ \ and \ \ Run\,2: F_n = n_r \ where \ \ n_r = 2,4,6,.... \qquad \text{Eq 6-5}$$

Flows perturbed at 400Hz were recorded in four runs. The number of raw images recorded in each run was 512. The phases sampled by each run are outlined in Figure 6-12. The expression linking the raw image numbers to the desired file number is:

$$\begin{aligned} Run\,1: F_n &= (2 \times n_r) - 1 \quad where \quad n_r = 1,3,5,.... \\ Run\,2: F_n &= (2 \times n_r) \qquad where \quad n_r = 1,3,5,.... \\ Run\,3: F_n &= (2 \times n_r) + 1 \quad where \quad n_r = 1,3,5,.... \\ Run\,4: F_n &= (2 \times n_r) + 2 \quad where \quad n_r = 1,3,5,.... \end{aligned} \qquad \text{Eq 6-6}$$

The file number when applied to all runs of a set will harmonise the data by creating a single folder with a maximum total of 1024 files whereby the file number will link the file to the correct phase position.

In order to remove erroneous images both images that constitute the first and second frame of both cameras were investigated. If the sum of all the pixel intensities within any of the four images was less than a threshold then it meant that that image did not contain a laser pulse. Therefore the four images could not be used.

An acceptable Lavision PIV file is a single file which contains the images from the camera (2D PIV) or cameras (SPIV). The images are stored within the file as frames. The frames are in a specific order as shown by Figure 6-13. In addition to this each Lavision file possesses frame buffer attributes. These are details which are required by the Lavision software to process the file into a vector field. By examining a file recorded using the Lavision equipment and software, and the operators manual, these attributes were identified and their usage determined. These attributes could then be created with appropriate values and applied to the raw data collected and the calculation of the vector field was possible.

A pre-processing macro was written to combine the three stages outlined. For each run the first and second raw images of each pair for both cameras was called. The appropriate file number was calculated. These images were then verified as described above. The raw files were then combined into a multi frame buffer and the appropriate frame buffer attributes were created. The multi frame buffer with the required attributes was saved with the correct file number as part of the file name. If the raw images were rejected the multi frame buffer was not created and the loop began again. This was implemented through a custom written macro and executed through the Lavision Davis 7.1 software.

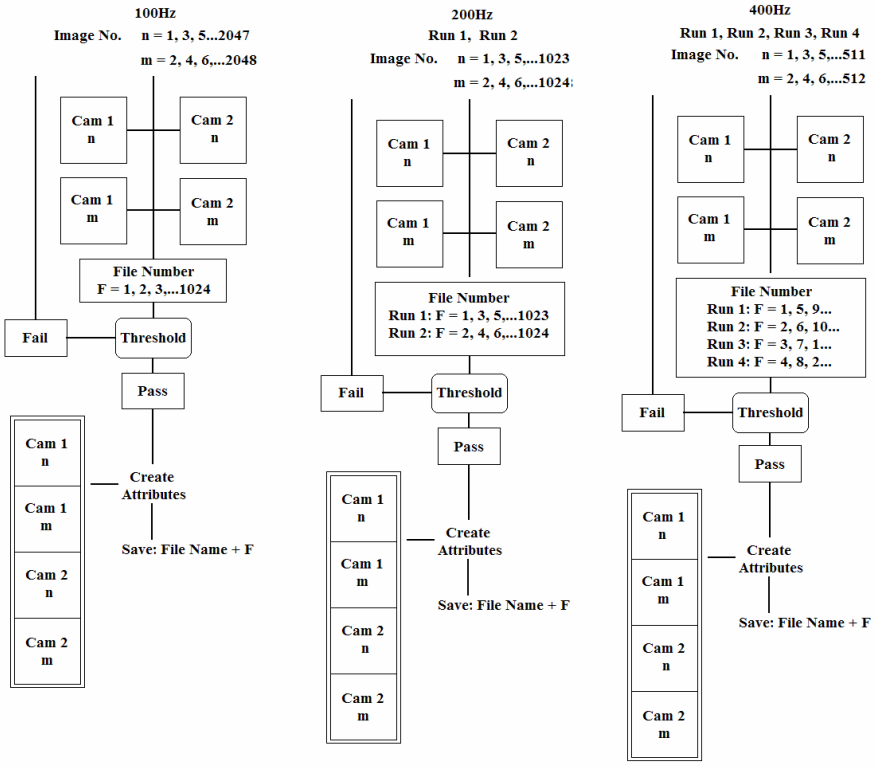

Figure 6-13 Illustration outlining the Pre-processing scheme employed to convert the raw bitmap images to single file multi frame files for 100Hz, 200Hz and 400Hz.

6.2.6 Vector Field Derivation

The derivation of vector fields from the pre-processed data is described in detail below. Each file was masked before processing and was then exposed to a multi pass procedure with a decreasing interrogation window size. With the previous pass's result being used as a reference field. Between passes stringent filters were applied to filter out spurious vectors to obtain correct vector maps. A single pass with an interrogation window size of 64 × 64 pixels was followed by two passes with interrogation sizes of 32 × 32 pixels. All passes used square window shapes and had equal weighting. The percentage overlap was 50% for all passes. The initial passes created a preliminary vector which was used to position the second interrogation window so that its displacement is in the sub pixel range. This reduces the measurement uncertainty (Chapter 6.2.10). In addition the preliminary passes are used to warp the final pass interrogation window to maximise the number of particle image pairs and include the presence of local gradients. This will be discussed in Chapter 6.2.11.

Before the vector fields were derived each file had a mask applied to it. The mask is used as an overlay over the images to remove from the calculation areas deemed to be unsuitable. For this work the edges of the images were masked, the observed laser stripes and in the cases of imaging close to the dump plane, areas of the image where the ceramic inlay could be seen.

The impact of masking was minimised by disabling the vectors at positions where the ratio of masked pixels to total pixels (per interrogation window) exceeded 30% for the first pass, and 60% for the final passes. To further minimise the impact interrogation windows which had masked pixels but not enough to warrant disabling had the correlation determined by excluding the masked pixels from the calculation (meaning masking does not contribute to the correlation result). This condition was implemented if the ratio of masked pixels to total pixels exceeded 10% and only applied to the final passes [115].

As the seeding density and background scattering were not constant the correlation function used was a normalised FFT algorithm [116].

$$C(dx,dy)=\frac{\sum_{x=0,y=0}^{x\le n,y\le n}\left(I_1(x,y)-I_{1avg}(x,y)\right)\times\left(I_2(x+dx,y+dy)-I_{2avg}(x+dx,y+dy)\right)}{RMS\left(I_1(x,y)-I_{1avg}(x,y)\right)\times RMS\left(I_2(x+dx,y+dy)-I_{2avg}(x+dx,y+dy)\right)} \quad \text{Eq 6-7}$$

Here $I_1(x,y)$ is the pixel intensity in the first interrogation window, $I_2(x,y)$ is the pixel intensity in the second interrogation window. $I_{1avg}(x,y)$ is the mean intensity in the first window, $I_{2avg}(x+dx,y+dy)$ is the mean intensity in the second. The inclusion of the window averages in the numerator means that dark areas in the window (unseeded flow) will contribute to the correlation. The RMS term of the first window is constant. The RMS term of the second interrogation window is a function of dx and dy and normalises the correlation with respect to the standard deviation of the second window. This compensates for variances in background scattering and signal intensities. The correlation was calculated via

FFT [117]. The normalised correlation removes weighting and bias errors. However pixel locking can still be experienced depending upon experimental set up.

In addition to this the initial pass was a second order function. This is performed with two shifts of the interrogation windows. The first shift is a quarter of the windows size to the right and the second the same size to the left. Two correlation results are obtained. The common area to both shifted interrogations is 50%. The two correlation planes are multiplied increasing the true correlation peak and reducing the noise.

Between passes and for post processing the vector field is subjected to a number of robust vector validation checks. These are a signal to noise check of the correlation peak and a local median filter. The correlation signal strength is defined below.

$$Q = \frac{P_1 - min}{P_2 - min} \qquad \text{Eq 6-8}$$

For each correlation plane the minimum value is subtracted from the largest and second largest peaks. The ratio between these values gives an indication of the strength of the first vector choice over the second. A value of 1.3 was used. Vectors with values less than this were removed.

A local four stage median filter was also used. Firstly the immediate surrounding vectors of a position have the median value determined (mean of the forth and fifth if even number). The RMS of the surrounding vectors is now determined, excluding the two most extreme values. This is done for all the velocity components measured. A user defined removal factor is then used to multiply the RMS values. A comparison is then made with the vector component at the particular position. If any vector component is not within the range of the median plus or minus the factor multiplied RMS the vector is invalid and removed. This is performed over the entire vector field. Once complete the filter examines the number of neighbouring vectors each position has. If the position has less than three neighbours it is removed. The third stage examines locations where a vector has been removed. By recalculating the median and RMS values, the original vector components and 2nd, 3rd and 4th choice vectors are examined. The first that satisfies the requirement of being within the range of the new median plus or minus the RMS multiplied by a re-insertion factor is inserted. This is dependent upon having a minimum of three neighbouring vectors. This process continues until no new vectors are inserted. The final stage is to remove vectors which have less than three neighbours.

6.2.7 Stereoscopic Reconstruction

The reconstruction of the 3D vector field from two 2D vector fields is performed by first dewarping the raw images and computing the two component vector fields at the correct object grid positions. This has the advantage that the vector fields are evaluated on the object grid and the evaluation has been done with the same interrogation window size for both cameras [118].

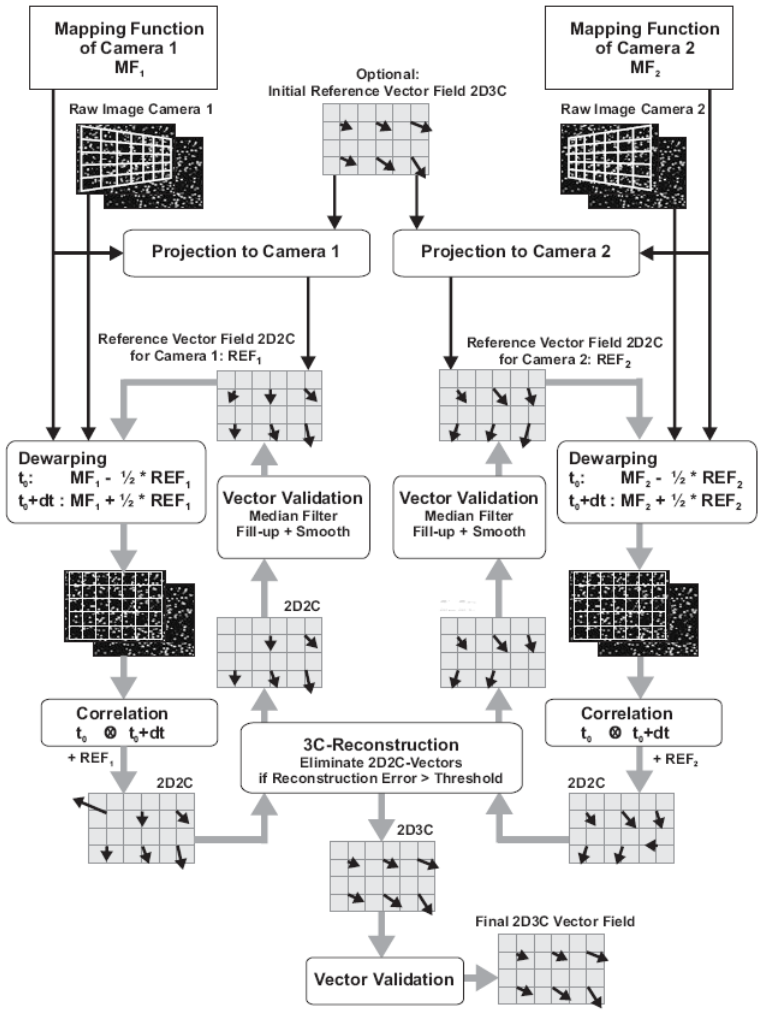

Figure 6-14 Flow diagram showing the three component vector reconstruction process [117].

The process employed by the Lavision 7.1 software in illustrated in Figure 6-14. The process is identical for both cameras. Lacking an initial reference vector field the images from the cameras are dewarped to object plane coordinates and are evaluated to obtain a two component vector (as per conditions selected). The vector fields from the two cameras are then reconstructed to a preliminary three component vector field. This is used to validate the two component vectors from each camera provided the reconstruction error is less than 1 pixel. This is effective at validating the two component vectors as two spurious vectors are highly unlikely to be correlated. The validated two component vector fields are then used as references to deform the interrogation windows for the successive pass. In reality it is computationally more efficient to deform the entire image. The reference vector is used to deform the image in the same and opposite direction to the reference vector with half the magnitude in each direction. The dewarping and deforming processes are combined. The images are then evaluated according to the settings inputted. Once again a preliminary three component vector field is created to validate the two component vector fields which are then used as reference fields. This process continues for the number of passes selected. Once the final pass is completed the resulting three component vector field is validated by calculating from this field the two component vector

fields (from both cameras). This is compared with the two component vector fields that were calculated from the final pass. Any discrepancy is termed 'reconstruction error' If the error is above a threshold value the vector in the three component field is rejected. The resultant raw three component vector field can then by assessed by a signal to noise check and a local median filter (see Chapter 6.2.6).

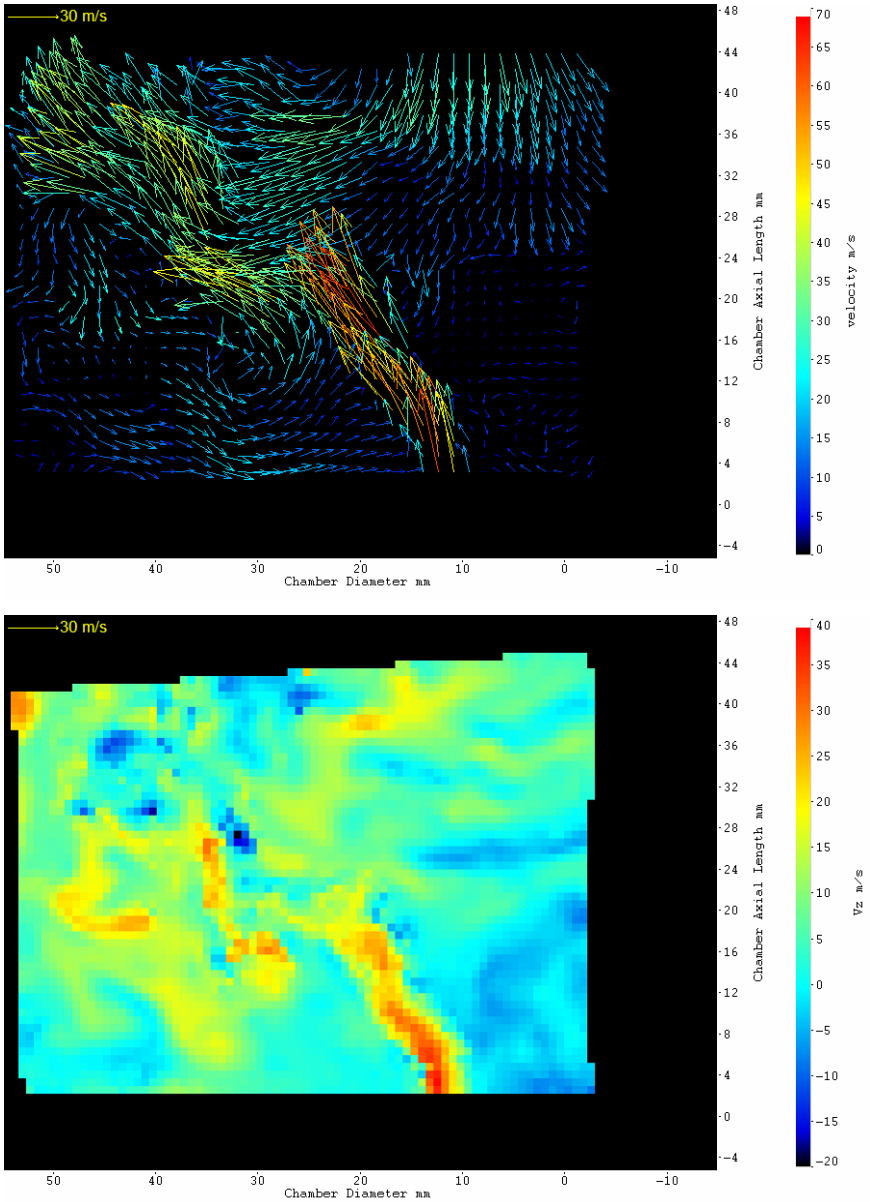

Figure 6-15 An instantaneous stereoscopic vector field of f1-100Hz recorded at the CRZ imaging area. The top image shows the in plane vector field (vx and vy). Only a quarter of the calculated vectors are shown for clarity. The colour of the vector arrow and its length represent the velocity magnitude based on all three velocity components. The bottom image shows the out of plane (vz) component as a scalar for all the calculated vector positions.

The actual reconstruction of the three component vectors is accomplished by utilising images of a calibration plate from both cameras at three out of plane positions corresponding to the centre, top and bottom of the laser sheet. These images are then used to derive a magnification matrix which is able to link the

recorded calibration images to the object volume [119]. This matrix is then used with the experimental images to derive four simultaneous equations linking the two 2D in plane image displacements to the 3D object displacement. An example of a processed three component vector field is shown in Figure 6-15.

6.2.8 Vector Field Processing

Using the instantaneous vector fields mean vector fields were calculated taking into account any absent vectors. The mean vector fields describe overall general flow field behaviour which are examined with the corresponding deconvoluted CH* images for the reacting flows. The mean vector fields and derived quantities are unconditioned vector fields. Meaning the quantity is derived from fresh and burnt gas. As identification of the reaction zone interface from the Mie scattered images was impossible this distinction could not be made for the vector fields.

From the ensemble vector fields unconditioned values of rms and turbulent intensity can be made. Turbulent intensity is typically used to partly describe the turbulence at a point within the flow field. However in the case of complex flows with recirculation zones the intensity can be artificially large due to normalisation by a small mean value which can exist in shear layers, boundary layers or recirculation zones. Therefore data is presented of the rms values of velocity at all spatial points.

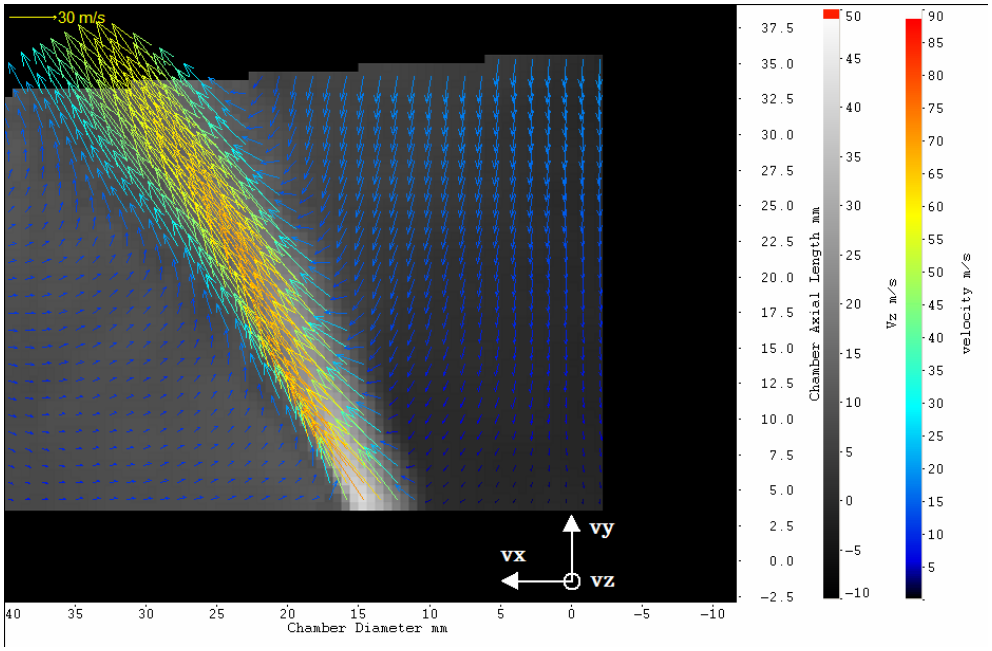

Figure 6-16 Phase 1 mean vector field of f1-100Hz at 'Annulus 3D' imaging area. The vectors show the in plane components (vx and vy). Only a quarter of the calculated vectors are shown for clarity. The colour of the vector arrow and its length represent the velocity magnitude based on all three velocity components. The third component vz is shown as a grey scale scalar background.

The axis system used for subsequent chapters is described by vx, radial velocity positive moving from right to left, vy, axial velocity positive from bottom to top, and vz, tangential velocity positively defined as being perpendicular to the plane formed by positive vx and vy (out of the page). The origin of the coordinate system is the top of the bluff body.

6.2.9 SPIV Geometrical Uncertainty Analysis

The uncertainties associated with the SPIV technique for the derivation of vectors have been assessed. The geometric error of SPIV and the inherent processing uncertainties pertaining to different experimental parameters are considered. The geometric error associated with PIV and the techniques available to reduce this have been highlighted in Chapter 4.3.1. In order to derive the geometrical error associated with the SPIV arrangement used, the model used to derive the results in chapter 4.3.1 will be considered [105]. In addition to the details provided in Table 6-4 the distances from the object plane to lens and the magnification are given in Table 6-5. The following analysis is purely for the conditions presented in this thesis.

			Image Dimensions (mm)			
Imaging Area	Magnification	Delta T	x	y	z	d0(mm)
Annulus 3D	-0.353	6.2	±20	±16.5	±0.75	250
CRZ, FZ, URZ	-0.266	8.3	±27	±20	±1	470

Table 6-5 Additional SPIV parameters and of magnification, image dimensions and object distance.

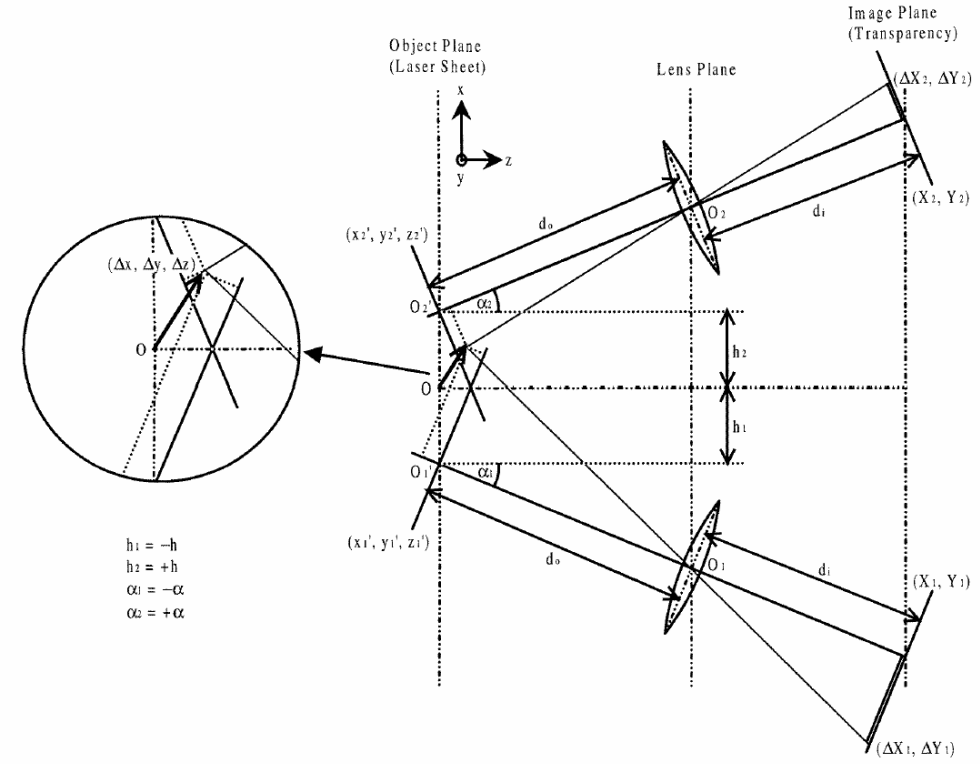

Figure 6-17 Schematic of a Stereoscopic PIV arrangement used to determine a geometrical model for the velocity measurement uncertainties [105].

A stereoscopic PIV system is schematically shown in Figure 6-17. The object plane is defined by a reference system of (x, y, z) centred on the origin O. Each camera, $j = 1, 2$, axis is rotated with respect to the z axis by θ and are viewing a common area onto their respective image planes (X_j, Y_j). The object distance from the object to lens is denoted by d_0 and image distance from lens to image by

d_i. The transfer of object plane coordinates to image plane coordinates is defined through the magnification.

$$X_j = -M_j x'_j \quad and \quad Y_j = -M_j y'_j \qquad \text{Eq 6-9}$$

The approach adopted for this work has been use to a symmetrical forward scatter arrangement. As a result the magnification, object and image distances will be regarded the same for each camera. As each camera is viewing the same position in the object plane the separation distance of camera focal points in the object pane is zero $(h = 0)$. The geometric error defined in the image plane coordinates is;

$$\delta^r(\Delta X_1) = \delta^r(\Delta Y_1) = \delta^r(\Delta X_2) = \delta^r(\Delta Y_2) \qquad \text{Eq 6-10}$$

Where represents $\delta^r(\ )$ the error of a given variable. The object plane uncertainties are Δx, Δy and Δz are expressed using the following equations.

$$\delta^r(\Delta x) = \frac{\sqrt{(b_1^2 + b_2^2)}}{|a_1 b_2 - a_2 b_1|} e_{ds} \qquad \delta^r(\Delta y) = \left(\sqrt{c_1^2 + c_2^2}\right) e_{ds} \qquad \delta^r(\Delta z) = \frac{\sqrt{(a_1^2 + a_2^2)}}{|a_1 b_2 - a_2 b_1|} e_{ds} \qquad \text{Eq 6-11}$$

These are then solved using the following;

$$a_1 = -(M\cos\theta) + (M\sin\theta / d_0)(z\sin\theta - x\cos\theta) \qquad \text{Eq 6-12}$$

$$a_2 = -(M\cos\theta) + (M\sin\theta / d_0)(z\sin\theta + x\cos\theta) \qquad \text{Eq 6-13}$$

$$b_1 = -(M\sin\theta) + (M\cos\theta / d_0)(z\sin\theta - x\cos\theta) \qquad \text{Eq 6-14}$$

$$b_2 = -(M\sin\theta) - (M\cos\theta / d_0)(z\sin\theta + x\cos\theta) \qquad \text{Eq 6-15}$$

$$c_1 = -\frac{1}{M} \qquad \text{Eq 6-16}$$

$$c_2 = -\frac{y\cos\alpha}{2M}\left(\frac{2M\sqrt{(a_1^2 + a_2^2)}}{d_0(a_2 b_1 - a_1 b_2)}\right) \qquad \text{Eq 6-17}$$

As discussed in chapter 4.3.1 using an angle $\theta = 45^\circ$ will result in the error ratio e_r of in plane to out of plane errors equalling unity. This fact has been used in the current set up. The range of values for x, y and z are shown in Table 6-5. In this case x refers to the radial direction, y the axial direction and z remains the out of plane component. The term e_{ds} is the error associated with the processing algorithms used in the Lavision software when deriving the pixel displacement for each interrogation window in the image plane and is equal to 0.1 pixels. It is

invariant for the coordinates in the image plane and for each camera due to the symmetrical setup.

$$e_{ds} = \delta^r(\Delta X_1) = \delta^r(\Delta Y_1) = \delta^r(\Delta X_2) = \delta^r(\Delta Y_2) = 0.1 pxl \qquad \text{Eq 6-18}$$

Implementing this into Eq 6-11 allows the determination of the object plane uncertainty distances. As the laser pulse separation time is known, Δt , these can be converted to velocity uncertainties for each component of the vector. Therefore each velocity vector is characterised with the uncertainties in Table 6-6.

$$e_{vx} = \frac{\delta^r(\Delta x)}{\Delta t}, \quad e_{vy} = \frac{\delta^r(\Delta y)}{\Delta t}, \quad e_{vz} = \frac{\delta^r(\Delta z)}{\Delta t} \qquad \text{Eq 6-19}$$

Object Plane Velocity Uncertainties (e_v m/s)				
Imaging Area	e_{vx}	e_{vy}	e_{vz}	Error Ratio (e_r)
Annulus 3D	0.0356	0.0030	0.0376	1.06
CRZ, FZ, URZ	0.0580	0.0030	0.0600	1.04

Table 6-6 Uncertainties for velocity components for the Imaging Areas used.

6.2.10 SPIV Experimental Parameter Uncertainty Analysis

In order to assess the vector uncertainties of the SPIV used in this investigation a comparison of the collected data with LDV data could be used. LDV is a point based measurement technique. The interrogation volume of LDV is far smaller than SPIV and hence is less susceptible to gradient uncertainties. LDV relies on a single seeding particle passing through the volume where as SPIV relies on an ensemble and is susceptible to particle drop out reducing the number of matching image pairs. LDV is also capable of determining a 3D vector. In the absence of this data results form Monte Carlo simulations can be used. Monte Carlo simulations have been performed generating artificial image pairs altering one experimental parameter at a time, such as particle density. The image pairs are then evaluated and the bias error and uncertainty for each parameter can be assessed independently [120-124].

The uncertainty of any vector derivation excluding the geometrical set up is a summation of bias and uncertainty errors. Bias errors relate to the over/underestimation of the derived vector compared to the true velocity. Uncertainty errors incorporate those arising from the correlation algorithm and seeding characteristics.

$$\varepsilon_{tot} = \varepsilon_{bias} + \varepsilon_{rms} \qquad \text{Eq 6-20}$$

For double frame single exposure images the optimum particle image diameter d_t is approximately 2.2 pixels [125]. The images collected for this work have a particle image diameter between 2 and 4 pixels throughout the images. For a 32 × 32 interrogation cell these diameters correspond to an rms uncertainty of 0.025 and 0.04 pixels. The bias error or peak locking associated with this range of

particle diameters is approximately constant and small for various displacements, -0.005 pixels [125]. This has largely been eliminated with the use of multiple passes and the specified correlation algorithm [116, 117]. Figure 6-18 shows the cumulative histograms of velocity displacements from ten consecutive instantaneous vector fields typical of this work. It is clear that pixel locking does not occur.

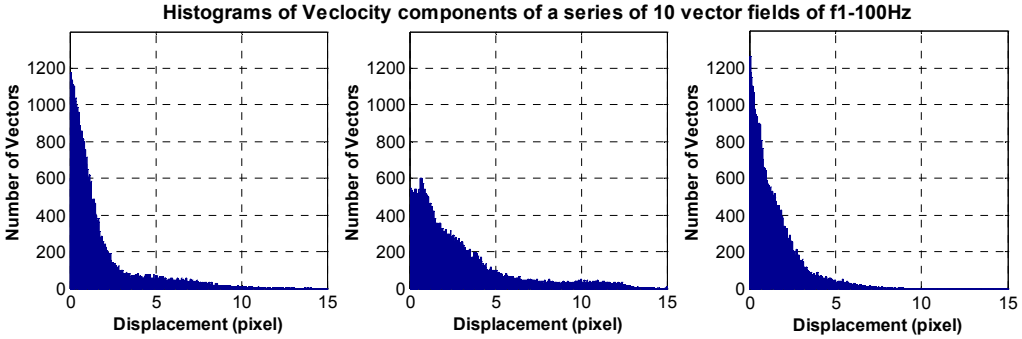

Figure 6-18 Histograms of SPIV displacement measurements from a 10 image sequence of f1-100Hz taken from imaging area 'Annulus 3D'. Bin size 0.05 pixels. Left: vx. Centre: vy. Right: vz.

The rms uncertainty associated with particle displacements is dependent upon the particle image diameter and can be quite large. The uncertainty is drastically reduced and linear below particle shifts of 0.5 pixels. This feature is taken advantage of by using multiple passes. The results from the initial passes are used to position the second interrogation window of the final pass so the displacement of the final window is in the sub-pixel range thereby minimising the uncertainty and maximising matching image pairs [125]. The uncertainty for a displacement of 0.5 pixels for particle image diameters of 2 and 4 pixels are 0.01 and 0.0375 pixels [125]. The bias error due to the cyclic nature of classical correlation algorithms has been removed by using a normalised correlation algorithm [116], see Chapter 6.2.6.

Particle image density is the number of matching image pairs occurring in both interrogation windows. This is reduced by the loss of particles due to out of plane motion (moving outside of illumination by the laser) and loss of in plane motions when the particle moves beyond the second interrogation window. This effective particle image density is important in improving the probability that a valid vector is detected. It has been shown that in order to achieve a detection probability of greater than 95% the effective particle image density, N, should be greater than 5. The effective seeding density is reduced by terms F_i and F_O which represent the loss of correlation due to the loss of particle image pairs in and out of the object plane.

$$N = N_I F_i F_O \qquad \text{Eq 6-21}$$

In order to maximise this the multi pass processing procedure uses the initial iterations to optimise the positioning of the second interrogation window thereby minimising the loss of particle image pairs due to in plane movement. In addition the warping of the interrogation window also improves the F_i term further. As

has previously been described (Chapter 6.2.6) the seeding density close to the annulus was not constant. However for all positions this minimum requirement $N \geq 5$ was achieved. Erring on the side of caution the seeding density will be assumed in this part of the uncertainty analysis to be $N = 10$. The uncertainty associated with $N = 10$ for a 32 x 32 interrogation window size is linear for pixel displacements less than 0.5. After this displacement the uncertainty is approximately constant with an rms value of 0.028 pixels. As the multi pass method with window warping was used the final pass results in these small displacements.

The dynamic range of the cameras was 8 bit corresponding to a scale of 256. The uncertainty of an 8 bit camera with particle shifts less than 0.5 pixels decreases linearly. Particle shifts greater than this have a constant uncertainty of less than 0.03 pixels rms.

The rms uncertainties considered are summarised in Table 6-7.

Parameter	Value	Uncertainty (rms pxl)
Particle Image Diameter dt (pxls)	2	0.025
	4	0.04
Particle Displacement with dt = 2 (pxls)	0.5	0.01
Particle Displacement with dt = 4 (pxls)		0.0375
Particle Image Density	10	0.028
Image dynamic Range	8 bit (256)	0.03

Table 6-7 Table summarising SPIV parameter uncertainties.

Using these the total rms uncertainty can be determined in both pixel and velocity units. These are listed in Table 6-8. These are cautious values which are applicable to all instantaneous measurements. The uncertainty analysis so far has excluded the effect of velocity gradients at the interrogation window scale.

Imaging Area	Particle Image Diameter (pxls)	Velocity Scale (m/s/pxl)	Total Uncertainty rms (pxl)	Velocity Uncertainty rms (m/s)
Annulus 3D	2	5.9987	0.049	0.2939
	4		0.068	0.4079
CRZ, FZ, URZ	2	5.6828	0.049	0.2785
	4		0.068	0.3864

Table 6-8 Table summarising total rms uncertainty for the different imaging areas.

6.2.11 SPIV Gradient Uncertainty Analysis

The impact of velocity gradients within interrogation windows is a source of concern regarding the application of PIV to flows where such gradients exist (boundary, shear, highly turbulent flows and dilation effects). Accommodation of the known gradients can be accomplished by improving the resolution of the vector field by viewing a smaller field of view. For this work due to the limitation of the attainable Δt the best resolution achievable when considering the velocity of the flow is that used for the imaging area 'Annulus 3D'. As the uncertainty due

to gradients will be location specific a treatment is provided with consideration to the turbulent analysis of Chapter 8.

Classical guidelines regarding the establishment of experimental parameters have been in the literature for some time [122]. Concerning velocity gradients the general rule is the local gradient characterised with $|a|$, must be less than the particle image diameter d_τ where M is the magnification and L is the in plane dimension of the interrogation window.

$$|a| \le d_\tau \qquad |a| = M|\Delta u|\Delta t \;\; where \;\; |\Delta u| \approx \left|\frac{\partial u}{\partial x}\right| \cdot L \qquad \text{Eq 6-22}$$

This is not always achievable. The effect of local gradients cause a decrease of the F_i and F_O terms meaning a drop of matching image pairs in the two interrogation windows. This reduces the cross correlation peak amplitude. The gradient also broadens the correlation peak as the distance between particle image pairs is now no longer constant. For small gradients the inclusion of multiple pass procedures and window warping compensate the effects producing a more ideal correlation [126]. As the gradient is increased the correlation peak amplitude further decreases and becomes broader until it is difficult to distinguishable from the noise. For constant gradients the detected correlation peak is assumed to represent a locally averaged displacement. For interrogation windows where strong sinusoidal fluctuations occur which are larger than the width of the particle image diameter, the correlation peak can exhibit twin peaks – 'peak splitting'. Neither of the peaks represents an average for the window and depends upon the algorithm for which one to be detected. Rather the peaks represent a local maximum and minimum [127]. The Lavision software used here actually records the position of four displacement peaks which are all considered in the median filter (Chapter 6.2.6). The interpretation for this work is not to regard the vectors derived from areas of high gradients as suffering form high error. Rather as either a local average, or maximum or minimum measurement (see above) of the range of flow velocities within the particular window instead of a measurement of a single value of the flow velocity. The gradients are genuine features of the flow whose contribution can not be individually resolved. Therefore the contribution is included in an ensemble way in each interrogation window.

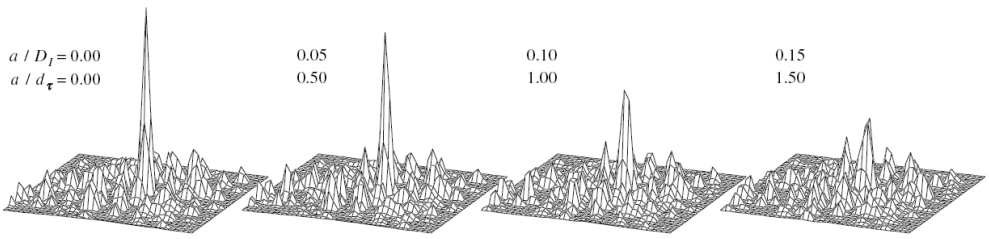

Figure 6-19 Spatial correlation for increasing acceleration a relative to the interrogation window dimension D_I and particle image diameter d_τ [127].

The gradient $|a|/d_\tau$ is plotted as a profile for f1-100Hz (whole cycle), 4mm, 15mm and 30mm downstream of the annulus in Figure 6-20. The gradient is in the

$\partial vy/\partial x$ direction (shear). Within the shear layers the gradients are much higher. These gradients decrease with downstream distance. All gradients will also increase and decrease with the imposed perturbation by varying magnitudes creating a time and spatial variation of gradients. As the gradients are determined using data whose error is determined by said gradients, care must be made when considering the largest of gradients as the error of that measured gradient is larger.

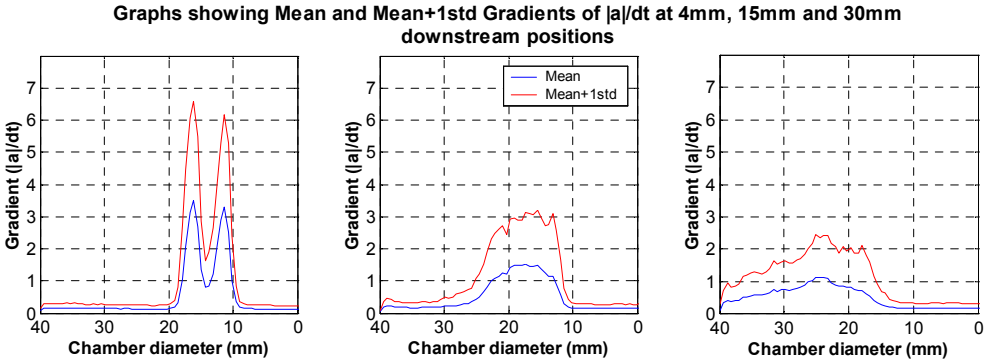

Figure 6-20 Horizontal profiles for f1-100Hz (whole cycle) of mean and mean +1 standard deviation of $|a|/d_\tau$ for $\partial vy/\partial x$ at different axial positions. Left: 4mm. Centre: 15mm. Right: 30mm. Taken from imaging area 'Annulus 3D'.

The impact upon the displacement correlation peak for both shear and strain gradients have been assessed physically [127]. Simple equations were derived that allow an assessment of a velocity bias for a given value of a. The effects of both shear and strain are depicted in Figure 6-21. Here the impact of both is compared with a displacement correlation peak which is equal to the local mean value of the flow. The case of pure shear is to increase the width of the displacement correlation peak which increases the displacement bias error of the peak centroid compared to that of a uniform flow. Positive (accelerating) strain results in the displacement correlation peak having a negative bias and a measured displacement smaller than the true local mean displacement. Negative strain creates a positive bias which means the measured displacement is larger than the true local mean value. This shows that the detected peak displacement is not equal to the locally averaged derived one.

The bias effect of pure shear upon the position of the displacement correlation peak can be simply described by Eq 6-23. Here D_I is the dimension of the interrogation window.

$$\frac{\varepsilon_b}{D_I} = -\frac{1}{F_I(s_D)}\frac{d_\tau^2}{8D_I^2} - \frac{1}{F_I(s_D)}\frac{\left(M|\Delta u|\Delta t\right)^2}{12D_I^2} \qquad \text{Eq 6-23}$$

The loss of correlation due to the in plane motion is characterised by the term $F_I(s_D)$ and is expressed simply as;

$$F_I(s_D) = 1 - \frac{|s|}{D_I} \qquad \text{Eq 6-24}$$

Here s_D is the displacement of the correlation peak. This expression does not include the effects interrogation window warping and assumes a square shaped window. This is determined by acquiring the pixel displacement of each interrogation window[128].

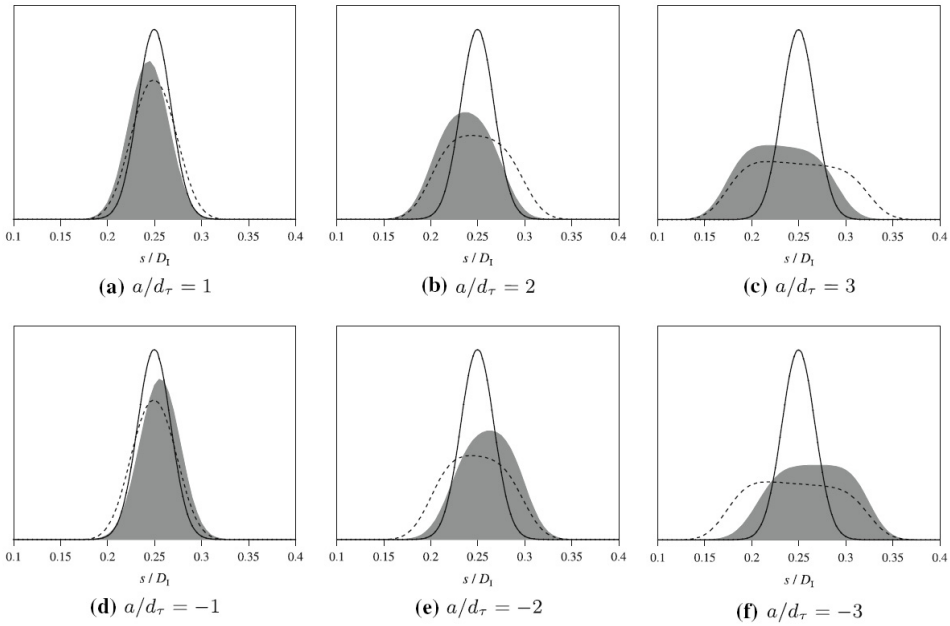

Figure 6-21 Illustration showing the effect of shear (dashed line) and strain (grey) upon the displacement correlation peak whose mean displacement (solid line) is 0.25 of the interrogation window (D_I). Both curves (solid lines) represent the displacement correlation peak of a uniform displacement that is equal to the mean displacement of the shear or strain motion. Top: For an accelerating flow ($a \geq 0$). Bottom: For a decelerating flow ($a \leq 0$) [127].

The effect of pure strain upon the displacement correlation peak is described by Eq 6-25. The term ΔX_0 is the mean displacement within the interrogation window.

$$\frac{\varepsilon_b}{D_I} = -\frac{1}{F_I(s_D)} \frac{d_D^2}{16 D_I^2} - \frac{1}{2} \frac{a/D_I}{1 + a/D_I} \left[\frac{\Delta X_0}{D_I} + \frac{1}{2} \frac{a}{D_I} \right] \qquad \text{Eq 6-25}$$

The term d_D is the width of the displacement correlation peak and is defined in Eq 6-26.

$$d_D \cong \sqrt{2 d_\tau^2 + \frac{1}{12} \left[\frac{a/D_I}{1 + a/D_I} \left(1 - \frac{\Delta X_0}{D_I} + \frac{1}{2} \frac{a}{D_I} \right) \right]^2} \qquad \text{Eq 6-26}$$

Three points along the chamber centre line corresponding to 4mm, 15mm and 30mm downstream have been sampled to characterise low gradient bias. At each point the shear gradients, $\partial vy/\partial x$ and $\partial vx/\partial vy$, have been sampled and the bias calculated. Figure 6-22 shows the bias variation against $|a|/D_I$. All profiles follow the same trend of an increasing negative bias for increasing $|a|$. As expected the bias increases with downstream distance where the velocities are greater. Also the range of bias for a given $|a|/D_I$ increases due to a larger velocity values which cause a larger loss of correlation. For all three positions the value of the bias error is small, less than -0.033ms^{-1}.

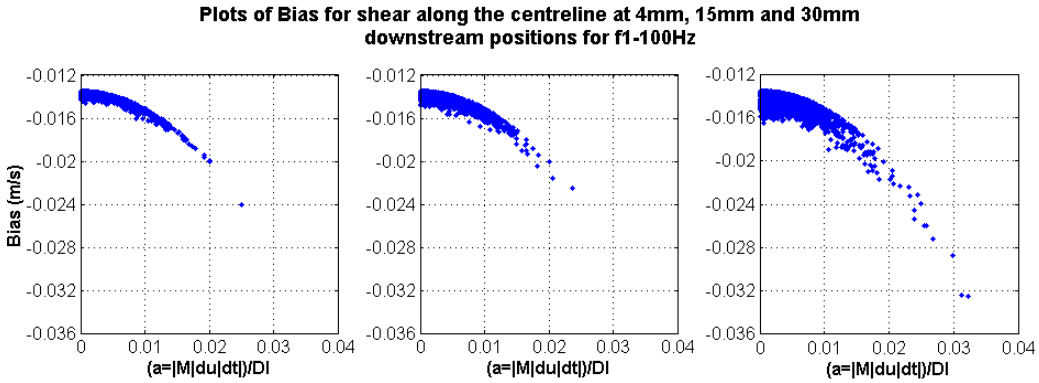

Figure 6-22 Graphs showing bias of shear ($\partial vy/\partial x$ and $\partial vx/\partial vy$) against $|a|/D_I$ along the chamber centreline different downstream positions (whole cycle) of f1-100Hz. Left: 4mm. Centre: 15mm. Right: 30mm.

The same positions were sampled with regard to strain gradients, $\partial vy/\partial y$ and $\partial vx/\partial x$. The bias is plotted as a PDF in Figure 6-23. All three PDFs show a skew to positive values which indicate a deceleration of the fluid (As it approaches the bluff body; see Chapter 7).

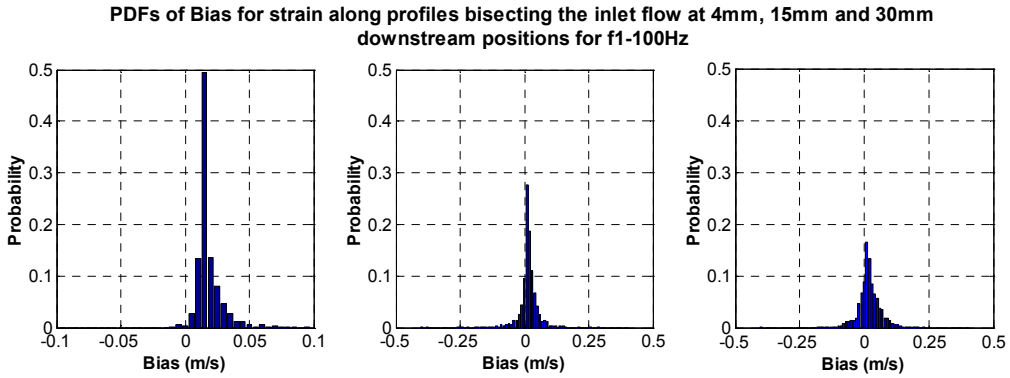

Figure 6-23 PDFs showing bias of strain ($\partial vy/\partial y$ and $\partial vx/\partial vx$) along the chamber centreline different downstream positions (whole cycle) of f1-100Hz. Left: 4mm, Bin size 0.005ms^{-1}. Centre: 15mm, Bin size 0.01ms^{-1}. Right: 30mm, Bin size 0.01ms^{-1}.

As the flow is oscillating the bias appears symmetrical about a central peak as expected. Moving downstream the values of $\pm a$ become larger as an increase of the bias is observed. For the three positions the bias range can be considered as

±0.25ms^{-1}. Bias due to strain is much larger along the chamber centreline than shear attributed bias.

A separate assessment has been undertaken for the inlet flow and adjacent shear layers. Still sampling at the same downstream positions a mask has been created for each phase position of the cycle. This is used to retain vector measurements in the desired area and discard the remaining. Once this is complete the appropriate downstream position is sampled across the image extracting data along the horizontal profile. The mask is derived by utilising the mean scalar images of vx and vy which are binarised with the positive values equal to 1. They are multiplied together to form a map of the mean inlet flow position for that phase. The map is then smoothed 5×5 and re-binarised with any positive values being set to 1, enlarging the map. This is then used to validate vectors along the bisecting profile path.

The corresponding shear induced bias is plotted in Figure 6-24. This time the bias is largest at the inlet as expected and decreases drastically with downstream distance. The largest of values of bias for each plot will occur within the shear layers and not the inner part of the inlet flow. The largest bias for each set of data are -6ms^{-1}, -4.4ms^{-1} and -3ms^{-1} which are the outliers of the. The largest bias of the main body of each set of data are -2ms^{-1}, -1.75ms^{-1} and -1.5ms^{-1}.

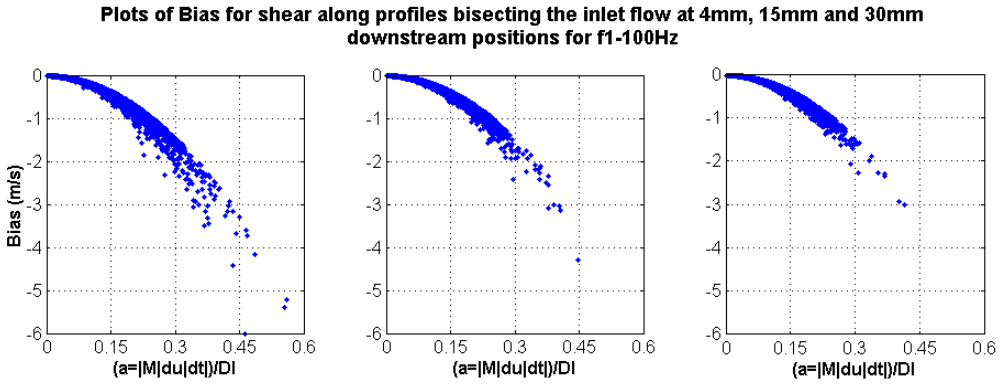

Figure 6-24 Graphs showing bias of shear ($\partial vy/\partial x$ and $\partial vx/\partial vy$) against $|a|/D_I$ along profiles bisecting the inlet flow at different downstream positions (whole cycle) of f1-100Hz. Left: 4mm. Centre: 15mm. Right: 30mm.

The strain induced bias of these profiles is plotted in Figure 6-25. All three exhibit a strong central peak which decreases in size downstream this corresponds to samples within the inlet flow structure. The tails of each distribution represent the shear layers. The width of distribution decreases with downstream distance as expected as the velocity gradients become weaker. The extremities for each profile are ±7ms^{-1}, -5ms^{-1} to 7ms^{-1}, and ±3.75ms^{-1}. For each PDF the main body of values are approximately between ±3ms^{-1}. This can be considered a typical value of bias for the shear layers. It is clear that much higher values will occur as it is possible that flow reversal at high velocity could occur in a single interrogation cell.

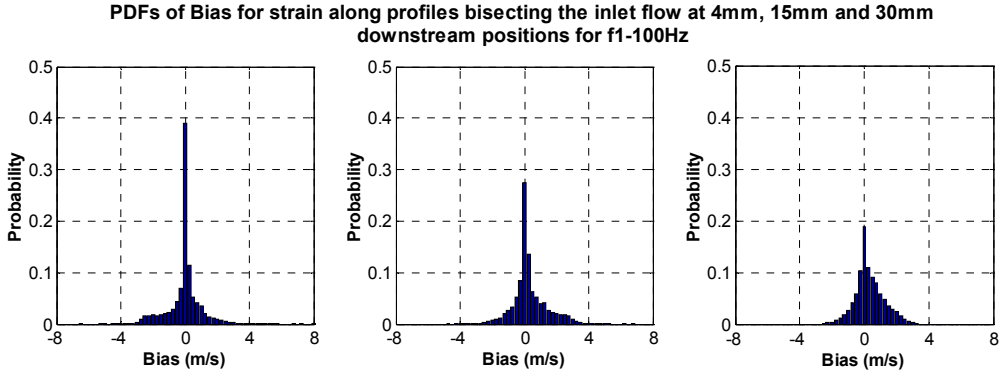

Figure 6-25 PDFs showing bias of strain ($\partial vy/\partial y$ and $\partial vx/\partial vx$) along profiles bisecting the inlet flow at different downstream positions (whole cycle) of f1-100Hz. Left: 4mm, Bin size 0.25ms^{-1}. Centre: 15mm, Bin size 0.25ms^{-1}. Right: 30mm, Bin size 0.25ms^{-1}.

An additional point is to consider the absolute mean and standard deviation of the bias collected for shear and strain. The same trends are evident in that the bias is strongest at 4mm and weakens downstream. Also the variance decreases downstream. These values indicate that the high gradients occur in a very small area, probably of the size of one or two interrogation areas. These however do not characterise those gradient intense points, these will be summarised next.

Profile Location	Gradient	mean abs (m/s)	std (m/s)
4mm	Shear	0.1071	0.2327
	Strain	0.6150	0.7956
15mm	Shear	0.1080	0.1769
	Strain	0.7139	0.7949
30mm	Shear	0.1091	0.1649
	Strain	0.7279	0.6804

Table 6-9 Statistics of bias from profiles across the inlet flow.

6.2.12 SPIV Uncertainty Summary

To summarise the analysis of Chapters 6.2.10 and 6.2.11 the overall experimental uncertainty for the SPIV performed can be considered as 0.4ms^{-1} rms. Bias from all parameter sources has been eliminated. Velocity gradients are treated as a bias which has been determined at various locations. This bias is the difference between the measured displacement with a gradient, and the displacement of a peak corresponding to a uniform flow displacement that is the average of the original displacement and the gradient. The range of uncertainties is now presented to indicate the worst case situation – not the mean statistic of the bias. It has been shown that the shear bias results in an underestimation of the average displacement. The strain bias will depend on the nature of the gradient as to whether it is an over or underestimate. Table 6-10 considers the total uncertainty along the chamber centreline (low gradient area) with the largest bias range quoted.

Experimental Paramter rms (m/s)	Shear Bias (m/s)	Strain Bias (m/s)	Total Bias (m/s)
0.4	-0.035	0.25	0.215
		-0.25	-0.285

Table 6-10 Table summarising SPIV maximum uncertainty range in low gradient areas.

A summary of the overall uncertainties of the shear layers is presented in Table 6-11. These represent worst and normal case values and quantify the uncertainty range and are not a mean statistic. The large bias values that are possible are not unrealistic when the inlet flow velocity and dimension of the annulus are considered. However it is incorrect to assume the largest bias value for every measurement at a position. The bias at a given point will have a range of values depending upon the flow field.

Experimental Paramter rms (m/s)	Profile Location	Type	Shear Bias (m/s)	Strain Bias (m/s)	Total Bias (m/s)
0.4	4mm	Extreme Shear Layer	-6.0	7.0	1.00
				-7.0	-13.00
		Norm of Shear Layer	-2.0	3.0	1.00
				-3.0	-5.00
0.4	15mm	Extreme Shear Layer	-4.4	5.0	0.60
				-5.0	-9.40
		Norm of Shear Layer	-1.8	3.0	1.25
				-3.0	-4.75
0.4	30mm	Extreme Shear Layer	-3.0	3.8	0.75
				-3.8	-6.75
		Norm of Shear Layer	-1.5	3.0	1.50
				-3.0	-4.50

Table 6-11 Table summarising SPIV uncertainty range in high gradient areas.

These estimates underline the fact that in high gradient interrogation windows a single velocity measurement is not being made. Rather in these positions a form of spatial average is calculated. This is not viewed an error. It is this spatial average which now suffers the bias ambiguity. Peak splitting is expected to occur in these regions and represents the extremes due to the gradient. The bias calculation does not take this into account and is based upon the assumption of a single displacement peak. The Lavision software as mentioned actually records four displacements and uses a median filter to select the most appropriate (Chapter 6.2.6). As the gradient is localised with less afflicted neighbouring values the median filter will select the most appropriate displacement choice which should offset the effect of bias to some degree. Therefore it is not unreasonable to assume that the actual bias of a single determined measurement is less than the calculated bias.

6.2.13 SPIV Statistical Uncertainty Analysis

Any experimental investigation involves the collection of a sample of data from which a mean, variance, standard deviation and higher moments can be derived. The question of whether these sample based statistics are representative of the true statistics is related to the size of the sample used. Indeed statistical errors are the deviation from an instantaneous sample and the true population mean. The deviation from the same sample from a sample mean is a residual. Theoretically the population mean and other statistics are unknown and will be assumed to be equal to the sample based statistics once the sample size is large enough. This can be assessed through the standard error and or the confidence intervals of the student t distribution.

The standard error (SE) is defined as;

$$SE = \frac{\sigma_S}{\sqrt{n}} \qquad \text{Eq 6-27}$$

Where σ_S is the standard deviation of the sample and n is the sample size. The standard error is the standard deviation of the sample mean from the population mean.

Student's t distribution can be used to create a series of probability distributions relating a sample of size n and $n-1$ degrees of freedom to the theoretical population distribution where $n-1$ tends to infinity.

$$t = \frac{\bar{x}_S - \bar{x}_P}{{\sigma_S}^2 / \sqrt{n}} \qquad \text{Eq 6-28}$$

The relationship linking the sample mean, $\bar{x}_S$, variance, σ_S^2 and size, n to the population mean, $\bar{x}_P$ was found and from this probability distributions of t for different degrees of freedom can be created. From a t distribution coefficients of a particular confidence can be extracted. These can be used to measure the mean probability at the same level of confidence the population mean will be between the range calculated based upon the sample mean using this technique to calculate the range. This method gives a useful indicator of the size of the statistical error for various confidence levels.

Figure 6-26 shows profiles of range estimates for the location specific mean values for all three velocity components and magnitude of f1-100Hz phase 1. The corresponding mean and rms plots are shown in Figure 7-3 and Figure 7-4. It is clear that the range increases in areas of high rms values. The confidence that the true population mean is within a range around the calculated sample mean increases for larger ranges, increasing the statistical error.

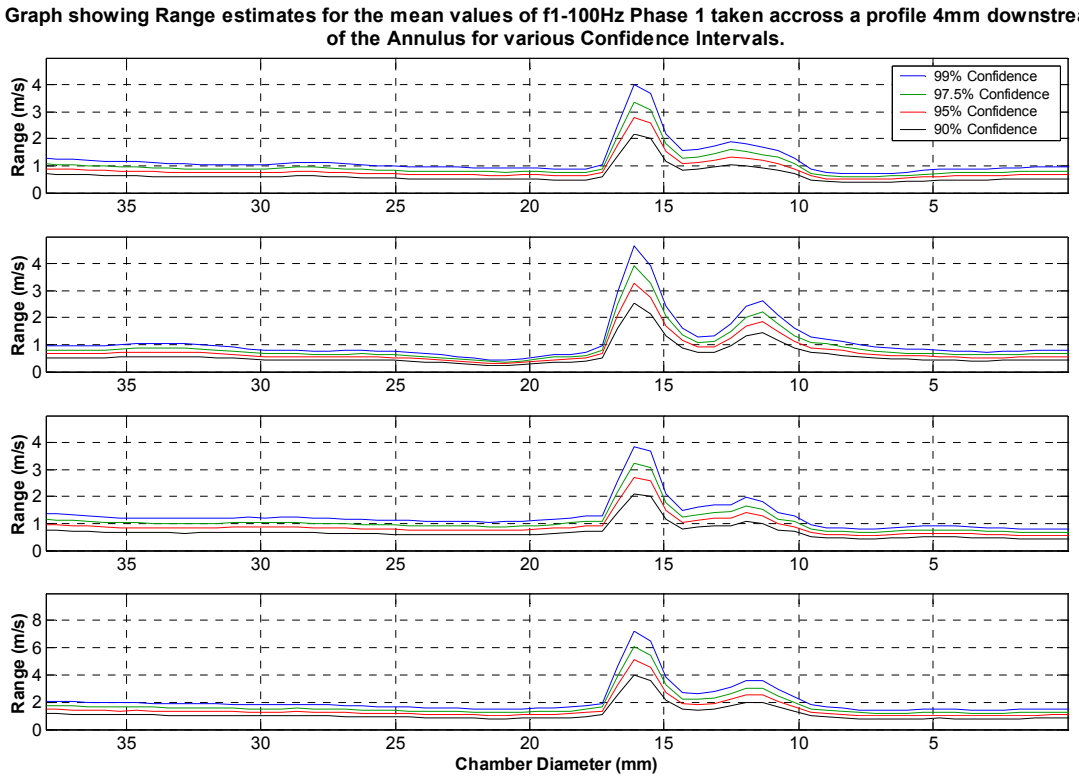

Figure 6-26 Range estimates from f1-100Hz phase 1 taken from imaging area 'Annulus 3D'. Top; vx component followed by vy, vz and |v| (bottom).

Reducing the statistical error reduces the confidence that the true mean is within the new range. The plots of Figure 6-26 show where there is a high rms value the possible range is approximately ± 4ms^{-1} to ± 2ms^{-1} moving from 99% to 90% confidence. Within the IRZ and CRZ the RMS values are less and as a result the possible ranges are much smaller, approximately ± 1.2ms^{-1} to 0.8ms^{-1} for decreasing confidence, a much smaller variation in range size. The behaviour and range sizes are approximately equal for the three velocity components.

For the data collected in this work the sample size is approximately 100 (per phase). The statistical error is location specific depending upon the location specific rms values. Locations of large velocity gradients (shear and dilation) are regarded as locations of high rms values, where as all other locations can be regarded as locations of low rms values. Considering the same profile position the calculated uncertainty range can be plotted against the rms value for all three components and various confidence intervals as in Figure 6-27. This data is constructed from all phase positions. From these plots simple equations can be derived that relate the uncertainty range for a given confidence interval to an rms value, allowing from rms data a rapid indication of the statistical error. These are simple line equations with the intercept at 0. The characteristic equations are the same for all velocity components for a given confidence. The gradients are given in Table 6-12.

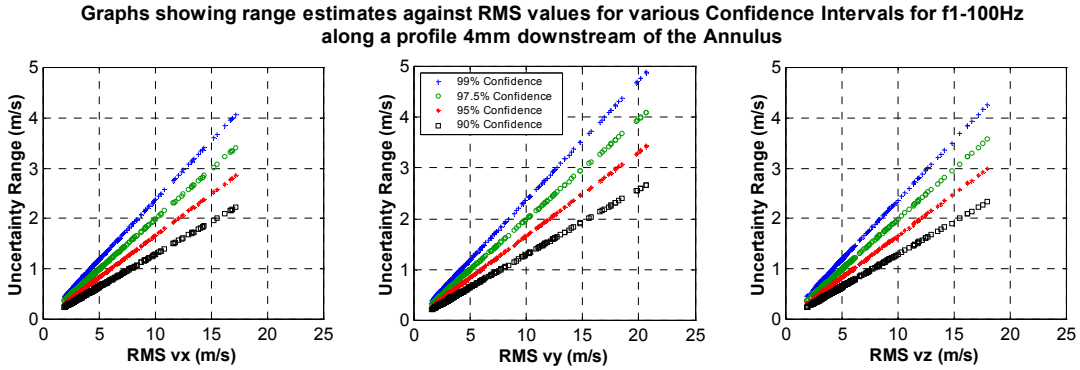

Figure 6-27 Graphs showing uncertainty range against rms values of f1-100Hz from all phase positions from imaging area 'Annulus 3D'. Left: vx. Centre: vy. Right: vz.

A typical high rms value corresponds to 20ms^{-1} and a low value to 5 ms^{-1}. Therefore the statistical error is summarised in Table 6-12 and is applicable to all mean velocities.

Confidence (%)	Gradient	RMS	
		High (20 m/s)	Low (5 m/s)
99.0	0.236	± 4.75	± 1.20
97.5	0.198	± 4.00	± 1.00
95.0	0.166	± 3.30	± 0.80
90.0	0.129	± 2.60	± 0.60

Table 6-12 Typical statistical uncertainty ranges.

The implications for the phase mean data within this thesis are that within the shear layers near the annulus where high velocity fluctuations will occur, the possible error between the sample mean and true mean could be as much as 4.75ms^{-1}. As an example it is possible for two adjacent vector positions of the same high rms values (20ms^{-1}) having the same range of ±4.75ms^{-1} about their respective sample means for a 99% confidence level. Theoretically it is possible for the difference between the two population means to be up to 9.5ms^{-1} while having the same sample mean. The reader should therefore take this into account when considering the velocity data presented.

For low rms value locations the statistical error is low. In order to achieve the same statistical error in high rms value locations the sample rms value has been taken as the population value. The range has then been calculated for various levels of confidence for increasing degrees of freedom (sample size). The coefficients of confidence were separately calculated also to include the change in degrees of freedom. Figure 6-28 shows the uncertainty range against the square root of sample size. In order to achieve the same uncertainty range for a high rms as that of the low rms the number of samples needed is approximately $50^2 = 2500$ per phase.

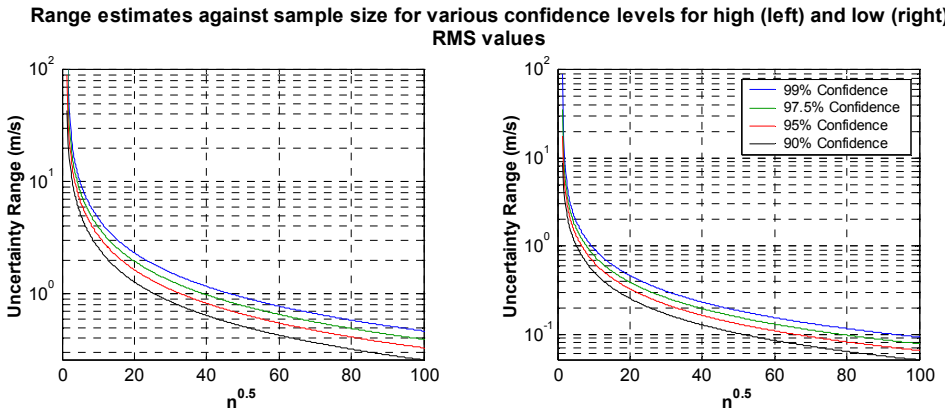

Figure 6-28 Range estimates for increasing sample size (n) of various confidence levels for different rms values. Left: High rms value ($20ms^{-1}$). Right: Low rms value ($4ms^{-1}$).

7 COMBUSTION CHAMBER DYNAMICS

The following is a detailed presentation of the reacting structures observed for f1 (pure methane) followed by a comparison with the hydrogen blended case, f10. All images presented are mean quantities unless otherwise stated. The results of the image processing allow the presentation of phase locked mean images. The Abel deconvoluted images are presented to allow comment upon a computed true 2D slice of the reacting structures. In conjunction to these are the mean 3D vector fields for the imaging areas, CRZ, Flame Zone and URZ. These are presented as streamlines with the colour representing the velocity magnitude. It should be noted that control over the streamline calculation is limited hence each imaging area has varying streamline locations and quantity. The reacting fields are described by 8 phase positions where as the flow field is described by 10 as discussed previously.

7.1 F1-100Hz

7.1.1 Entry Conditions

Using the processed vector fields of the imaging area 'Annulus 3D' horizontal profiles of the mean vector field and corresponding rms values were extracted at the position closest to the annular entry, 4mm axial distance. Information extracted from this imaging position is intended to describe the local features immediate to the inlet flow. Profiles of vx (radial), vy (axial), vz (tangential) and |v| (magnitude) for f1-100Hz are shown in Figure 7-3. From these profiles the peak value and profile integrated value (4mm length across inlet flow) at each phase for the velocity components and magnitude has been extracted and plotted against phase in Figure 7-1.

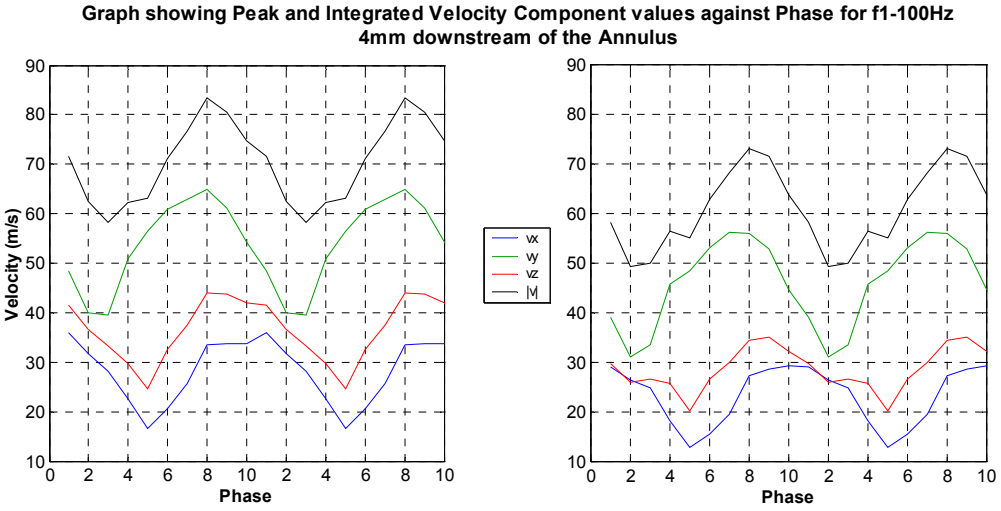

Figure 7-1 Graphs showing Peak (Left) and Integrated (Right) Velocity Component and Magnitude Values against Phase for f1-100Hz 4mm downstream of the annulus over two oscillations.

Using Figure 7-1 and the profiles taken 4mm downstream of the annulus it is apparent from the peak |v| profile that the behaviour is oscillatory. From phase 1 the value is decreasing from approximately 60ms^{-1} to a minimum of a little under 50ms^{-1} at phase 3. This then increases steadily to a maximum of 73ms^{-1} at phase 8 before starting to decrease. Analysing the peak of the velocity components it is immediately apparent that vy is the largest at all phase positions and is the dominant component influencing |v| with a similar profile. The profile also bears a good resemblance to the siren aperture profile shown in Figure 5-5. This component has its minimum at phases 2 and 3 of 32ms^{-1}. The maximum of vy occurs at phase 8 at 56ms^{-1} after a steady rise. Once reached vy then falls in the same fashion. Both vx and vz display similar trends. Both are substantially smaller in magnitude than vy with vz always greater than vx. Both components appear to be out of phase with vy having their respective minimums at phase 5 (vx = 12ms^{-1} and vz = 20ms^{-1}). The maximum of vx, 30ms^{-1}, occurs at phase 1 where as for vz, 35ms^{-1}, this is at phases 8 and 9. Both profiles have their maximums after vy and are out of phase with vy.

The profiles Figure 7-3 also yield information regarding the width and behaviour of the inlet flow during the instability. The width of the inlet flow can be defined between the points when the |v| profile becomes near horizontal and aspect (inner and outer shear layers). It is clear that during the instability the width of the inlet flow does not change at this position, remaining approximately 7mm. The radial location of the peak of |v| and all three components is very stable. The radial location is approximately 13mm from the chamber centreline with a range of 2mm.

Considering the inner part of the chamber (radial positions less than 10mm) |v| is steady during the instability at 3ms^{-1}. The behaviour of all components also does not change through the instability. Once the vx profile has dropped rapidly to 2ms^{-1} at the inner shear layer (10mm radial distance) the value decreases slowly to zero at the centreline of the chamber before becoming negative at negative radial distances. This indicates where the inner flow changes direction along the vx axis. The component vy remains constant and negative at approximately -5ms^{-1} which means the inner flow is moving upstream. Finally vz is near zero though positive for the inner flow.

The flow outside of the inlet flow (radial distances greater than 17mm) shows small changes through the instability. The value of |v| appears to remain steady at approximately 10ms^{-1}. Of the three components vx shows the most variance. From phase 4 through to 8 vx shows an increasing negative value with radial distance. This feature then returns to a horizontal aspect during the rest of the phases. The vy component remains steady in profile and increases marginally as peak vy increases, ranging from near zero at phase 3 to 2ms^{-1} at phase 8. Finally vz is also steady in its profile and shows small variation through the instability.

To summarise the inlet flow 4mm downstream of the annulus clearly does not move radially or change shape during the instability. The behaviour of |v| is dominated by the axial velocity vy. A central counter flow aspect exists along the chamber centreline with a negative axial velocity flowing opposite to the inlet flow. For positive radial locations this inner counter flow flows towards the inlet flow as proved by the positive radial component. This becomes negative when the

radial location is negative as the flow would move towards the other side of the inlet flow. A negative radial flow also exists outside of the inlet flow meaning the outer flow is moving towards the inlet flow. Considering the tangential component three distinct bodies of fluid are visible. The inlet flow has the largest tangential component as expected, followed by the flow outside of the inlet flow which has a substantially smaller value. This in turn is greater than the inner flow which has near zero values. All three bodies have positive values which imply the entire chamber is rotating around the centreline in the same direction with different speeds.

The profiles depicting the rms values of the velocity components are shown in Figure 7-4. Immediately apparent is the confirmation of two shear layers which exist on either side of the inlet flow. It is also clear the fluctuation of velocity at these layers is different through the instability. The overall profile shape of rms |v| is observed for all three rms components. From phase 1 the outer shear layer clearly shows a larger |v| rms value than the inner layer, $30ms^{-1}$ to $15ms^{-1}$. The profiles of rms vx and vz are almost identical and rms vy is marginally greater. All three show larger contributions to the outer shear layer than the inner one. At the minimum of the instability (phase 3) both peaks of rms |v| have decreased to $18ms^{-1}$ and $11ms^{-1}$ respectively. While the outer shear layer is still greater than the inner one. All three rms components follow this trend and are approximately equal in profile shape. At phase 4 when the inlet flow rate increases both shear layers show an increase in rms |v| but the difference between the outer and inner values is substantially smaller. This is again repeated for the velocity components with rms vy now greater than the other two and contributing equally to both shear layers. Both rms vx and vy tend to favour the outer shear layer. This trend continues to the peak of the oscillation at phase 8 where the outer and inner shear layers have rms |v| values of $32ms^{-1}$ and $28ms^{-1}$. As the inlet flow starts to decrease from phase 9 onwards the inner shear layer shows a drastic drop in all rms component values but primarily rms vy (rms vy is still greater than rms vx and vz). This is not observed for the outer shear layer where the rms values remain high until phase 2. The radial location of the shear layers at this axial position is invariant with the instability.

As the inlet flow at the 4mm downstream position does not exhibit width or radial position changes it is possible to perform a spectral analysis on the recorded velocities. The central position of the inlet flow was determined over the entire instability and the velocity components and magnitude were extracted from all the instantaneous vector fields at this position. The radial position was 13mm.

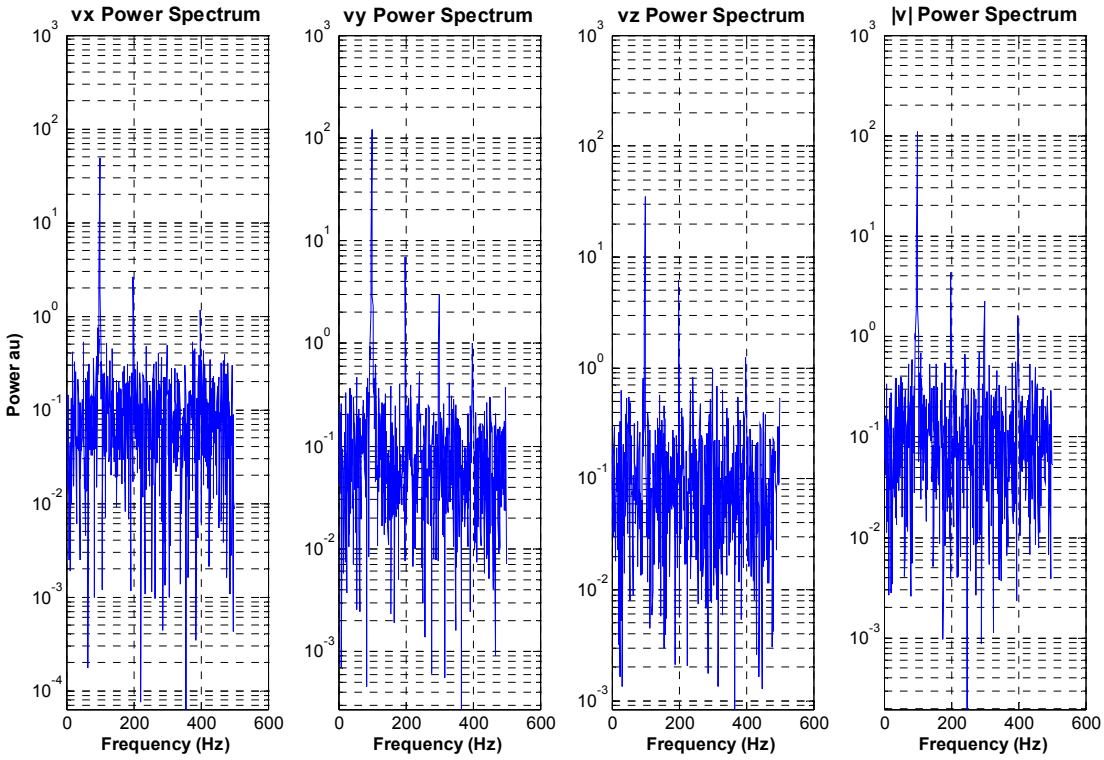

Figure 7-2 Frequency spectra taken from the f1-100Hz Instantaneous Vector fields recorded at the 'Annulus 3D' imaging area at axial position 4mm, radial position 13mm. The left corresponds to |v|, moving to the right is vx, vy and vz.

The power spectra of Figure 7-2 clearly show the dominance of the imposed frequency of 100Hz. Other frequencies are easily identifiable of 200Hz, 300Hz and 400Hz of are substantially weaker. The spectra of |v| and vy show excellent agreement once again affirming the dominance of vy on the inlet flow. The spectra for vx and vz also have a dominant 100Hz frequency but only have additional frequencies of 200Hz and 400Hz Therefore the inlet flow is being perturbed at the frequency imposed upon it. Comparing the spectrum of |v| with that derived from the pressure transducer (Figure 5-16) the inlet flow characteristics show good agreement.

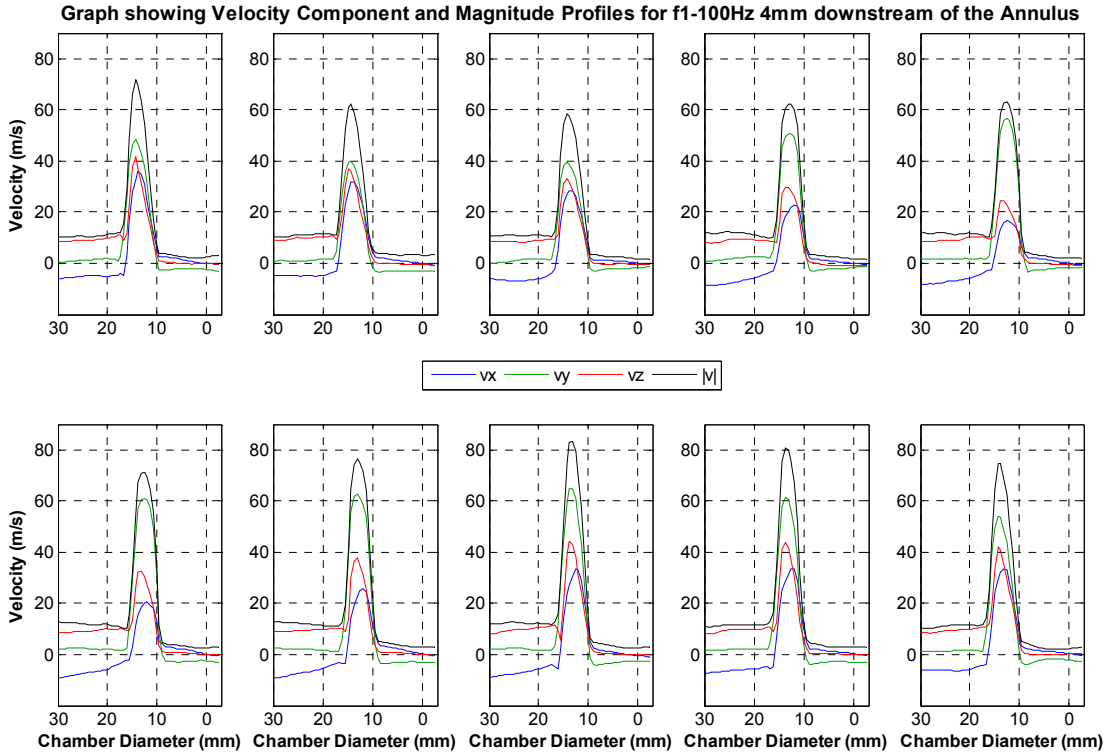

Figure 7-3 Velocity Profiles of f1-100Hz along a line 4mm downstream of the Annulus. Taken from mean vector fields from the imaging area 'Annulus 3D'. The top row consists of phases 1 to 5 from left to right. The bottom row consists of phases 6 to 10 from left to right.

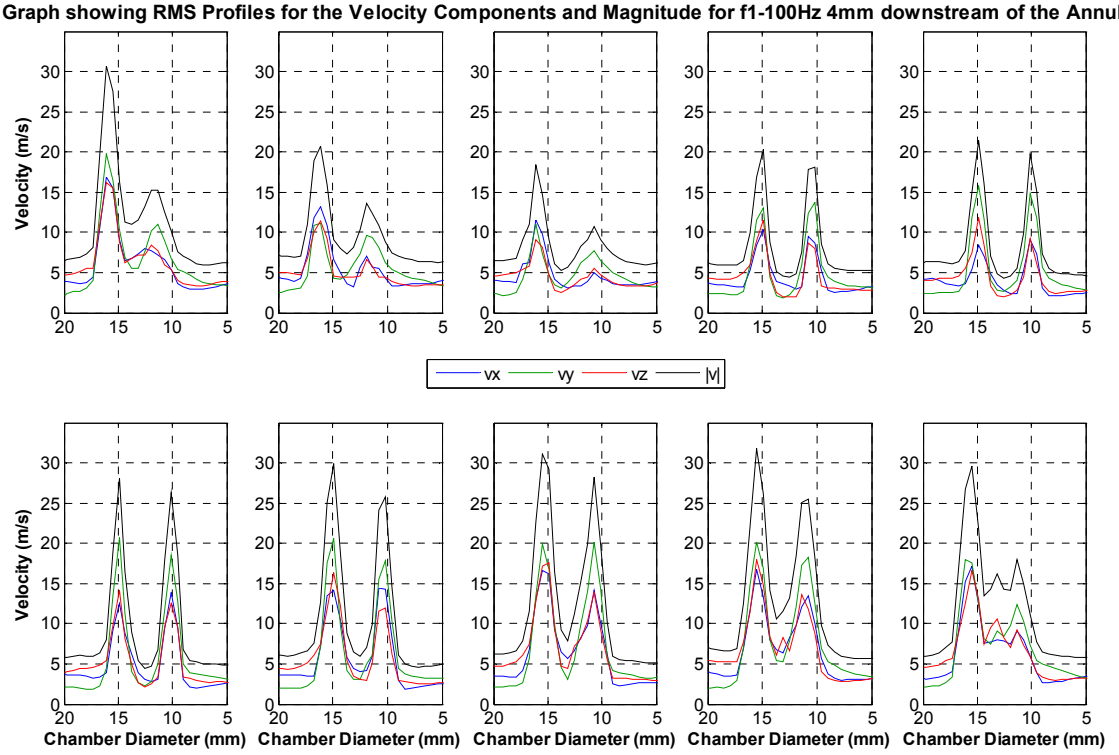

Figure 7-4 RMS Profiles of f1-100Hz along a line 4mm downstream of the Annulus. Taken from the RMS scalar field derived from the ensemble collected at the imaging area 'Annulus 3D'. The top row consists of phases 1 to 5 from left to right. The bottom row consists of phases 6 to 10 from left to right.

7.1.2 Chamber Reacting Fields and Flow Fields

The mean Abel deconvoluted flame and flow field behaviour is depicted in

Figure 7-6 and Figure 7-7. Velocity component profiles have been extracted from the vector fields at axial positions 30mm, 50mm and 70mm downstream of the annulus shown in Figure 7-8 to Figure 7-10. The motion captured by both diagnostics shows good agreement in compared behaviour. Consideration of the reacting fields is done with phases 1 through 8 and the flow fields is 1 through 10.

The total heat release behaviour can be reproduced by integrating over the image area where a pixel value is greater than zero (excluding reflection). This has been done for all instantaneous images and a corresponding mean and RMS value obtained for each phase. The time series of this data was used to create a frequency spectrum. The results are shown in Figure 7-5. The mean integrated profile shows a regular sinusoidal profile. The frequency spectrum shows the complete dominance of the induced perturbation frequency of 100Hz. Other frequencies are present above the noise of 200Hz, 300Hz and 400Hz which concurs with that detected by the inlet pressure transducer (Figure 5-16).

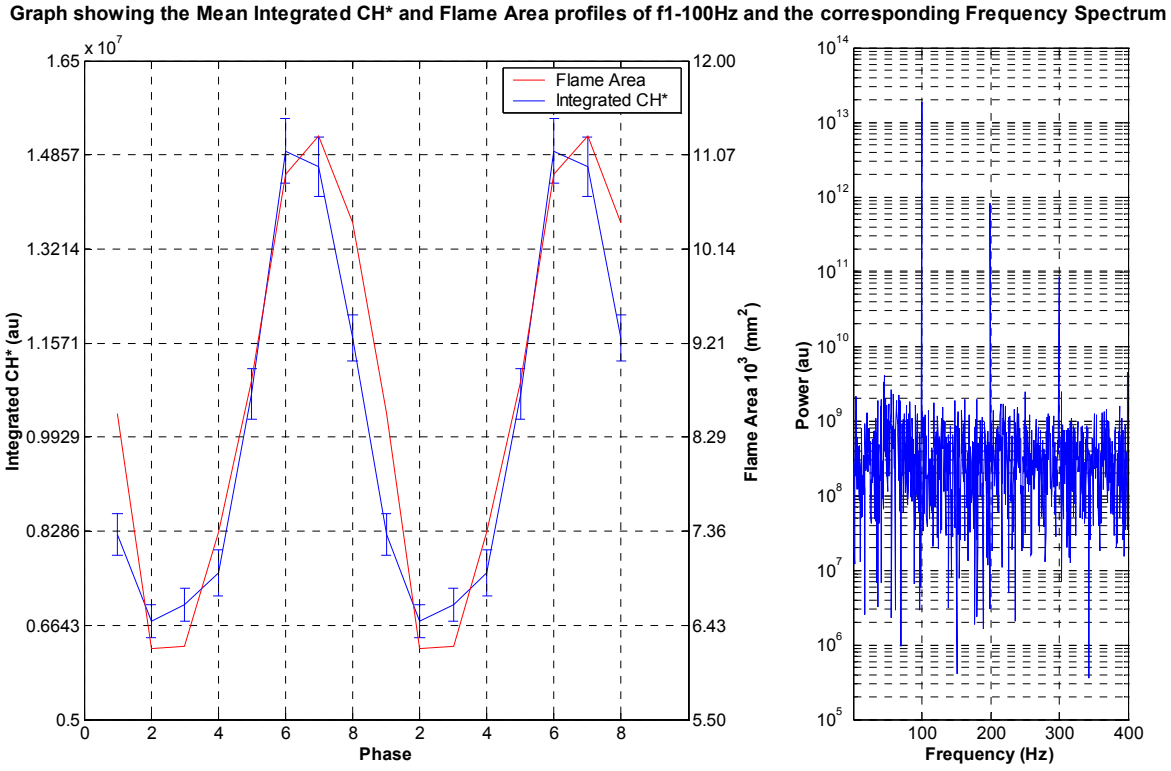

Figure 7-5 Mean Integrated CH* profile and flame area profile for f1-100Hz with corresponding Frequency Spectrum. The phase corresponds to that of the CH* images.

The behaviour of the reacting fields is oscillatory and typical of excitation of a single dominant frequency (Figure 5-16). From phase position 1 the flame is retreating towards the dump plane with small hot spots orientated in a downstream and outward (approx 60 degrees to horizontal) direction. As the flame retreats further in phase 2 the hot spots become smaller before becoming horizontal and slightly wider in phase 3. Phase 2 is the minimum of the heat

release rate but not the minimum in terms of flame position or inlet flow. This is phase 3, approximately 40mm downstream of the dump plane. The flame then begins to move downstream in phase 4 as the flow rate increases. The hot spots again remain horizontal with slight tails starting to bend towards the dump plane. The flame has moved to approximately 50mm downstream of the dump plane. The flame is pushed further downstream by phase 5 and the hot spot area has become larger as the flame starts to be stretched. The extremities of the flame still show some bending towards the dump plane. Phase 6 shows a much larger hot spot area. The lower part of the flame has burnt back towards the annulus indicating it has been able to respond to the increased flow rate while the stretching of the flame has kept the upper flame at a downstream position of approximately 90mm. The extremities have changed orientation pointing in a downstream outward direction (approx 45 degrees to horizontal). This is the peak phase position for the heat release rate. As the inlet flow rate begins to decrease phase 7 shows a decreasing hot spot area as the flame is less strained. The extremities still point outward but have become bulbous. Finally phase 8 shows a drastic reduction in hot spot area. This is due to the decreased inlet flow. The overall flame area has started to reduce.

Considering the flow field images three distinct features can be identified. These are the inlet flow, the corner recirculation zone (CRZ) and the central flow (IRZ) which flows from the exhaust towards the annulus and is the bubble vortex breakdown. The flame structure described by the deconvoluted CH* Images is controlled by the interacting behaviour of the inlet flow, the CRZ and IRZ. The flame being somewhat fixed between the two as the inlet flow moves past the inside of the CRZ and the outside of the reverse flow region. The retreating behaviour of the flame from phase 1 to 3 (CH*) has been described above. The flow field phases 1 to 4 show the bending outwards of the inlet flow as the flame retreats to the dump plane. The shape of the CRZ remains triangular as it is constrained by the chamber geometry and inlet flow. The centre is slightly deformed in a direction parallel to the inlet flow. The position of the CRZ centre shows large changes. The recirculation zone within the IRZ however is of a vertical elliptical shape which begins to exhibit a square profile at its most upstream point (Phase 4 flow field) with the inner corner being pinched and stretching down the inner shear layer by the inlet flow and central flow. This development matches the almost horizontal direction of the inlet flow at its most downstream position as the instability approaches its minimum. This recirculation zone becomes stretched vertically as the flow retreats and moves downstream. The downstream half of this recirculation zone points vertically downstream but becomes wider through phases 1 to 4.

Phases 5 to 7 of the flow field show the effect of an increasing inlet flow rate. These correspond to CH* phases 4 to 6 and the instability growth. Phase 5 of the flow field images (Phase 4 CH*) shows the effect of an increased inlet flow rate. The horizontal downstream aspect of the inlet flow remains but has been pushed further downstream. The CRZ has become stretched vertically with the centre becoming more circular and moving slightly downstream. The IRZ has also been pushed downstream. The pinched corner previously mentioned has become more defined. The downstream half of the IRZ has become wider and has begun to tilt towards the centre line of the chamber due to the increased flow rate moving

around it. Phase 6 shows that a further increase in inlet flow rate causes the inlet flow to propagate further downstream before developing a reduced horizontal aspect due to the CRZ. The CRZ is becoming stretched vertically downstream near the chamber wall although the centre remains circular. The centre itself has moved slightly further downstream. The IRZ has become horizontally compressed by the increased flow rate passing it on either side by the inlet flow and central counter flow. As a result the pinched corner is extending further down the inner shear layer and the centre has moved further downstream. The tilt observed in the previous phase has increased. Phase 7 coincides with the maximum of the instability (Phase 7 CH*) clearly shows a straight inlet jet formation which extends past the CRZ and the IRZ. The CRZ is further stretched vertically causing the centre to move further downstream and causing vertical stretching of the centre to an elliptical shape. The IRZ has become severely distorted. A definitive centre of its' recirculation zone now no longer exists. The structure appears as a stretched entity lying upon the inner shear layer between the inlet flow and central counter flow. The downstream part of the IRZ has become thinner but shows severe tilting towards the chamber centreline.

Phase 8 shows the reduction of inlet flow rate and as a consequence the jet has begun to move radially outward. The jet is till strong and maintains its previous characteristics. Therefore the CRZ remains unchanged from phase 7. The slight movement of the inlet jet has allowed the URZ to develop a large stretched centre. The overall structure is still elliptical running parallel to the inner shear layer. The downstream part of the structure exhibits less bending towards the centreline. Phase 9 shows these trends to continue as the inlet flow rate decreases further. Phase 10 corresponding to phase 8 of the CH* images again shows the IRZ widen further as the inlet flow structure moves radially outward and retreats further upstream.

The velocity profiles of Figure 7-8 (30mm) show some resemblance to those taken 4mm downstream. Consideration must be given to the fact that the shape and radial position of the inlet structure are no longer constants. The peak values (within the inlet structure) of the three components are approximately coincident regarding radial position. The component vy is a minimum at phase 3 ($19ms^{-1}$) and a maximum at phases 7 and 8 ($38ms^{-1}$). This agrees well with vy at the chamber entry (Figure 7-1). Vx also is a minimum at phase 3 ($17ms^{-1}$) but the maximum occurs at phases 9 and 10 ($27ms^{-1}$). The maximum concurs with that of vx at the inlet but the minimum does not and is 2 phase positions early. Vz is also in phase with vy which is different to that previously observed. The behaviour of vz is difficult to discern but it exhibits a small peak in phase with vy. Within the inner shear layer (when vy becomes zero) both vx and vy converge to zero at the chamber centreline. The IRZ largest vy value is at phases 7 and 8 ($-19ms^{-1}$) and proceeds to converge to a constant value through phases 1 to 4 ($-12ms^{-1}$). This damped behaviour could be due to the proximity to the bluff body and the centre of the IRZ.

Downstream the profiles taken at 50mm (Figure 7-9) exhibit the influence of a changing flow aspect, horizontal to vertical dominated, and the presence of the recirculation zone. It must also be reiterated that dilation contributions are

within this data. These factors are responsible for the behaviour of vx outside of the inner shear layer, which has a minimum at phase 3 and maximum at phase 4 and predominantly large values after. Vy and |v| exhibit more typical behaviour both having minimums at phase 4 and maximums at phase 8. Once again vz shows small variation through the phases with its general profile remaining the same. Both vx and vz converge to zero at the centreline. Within the IRZ its smallest value is at phase 4 ($-14ms^{-1}$) and largest is at phase 8 ($-30ms^{-1}$). The behaviour of the IRZ is a good indicator of the oscillatory nature of the flow at this point, as the structure does not exhibit any changes of orientation.

The same considerations must be given 70mm downstream (Figure 7-10). Here vx almost zero for much of the instability and only changes when the inlet flow increases causing the inlet structure to move inwards (phases 6 to 10). Outside of the inner shear layer |v| has its minimum at phase 5 ($15ms^{-1}$) and maximum at phase 9 ($37ms^{-1}$). Again vx and vz approach zero at the centreline. The IRZ smallest value here occurs at phase 6 ($-14ms^{-1}$), and largest at both phases 10 and 1 ($-25ms^{-1}$).

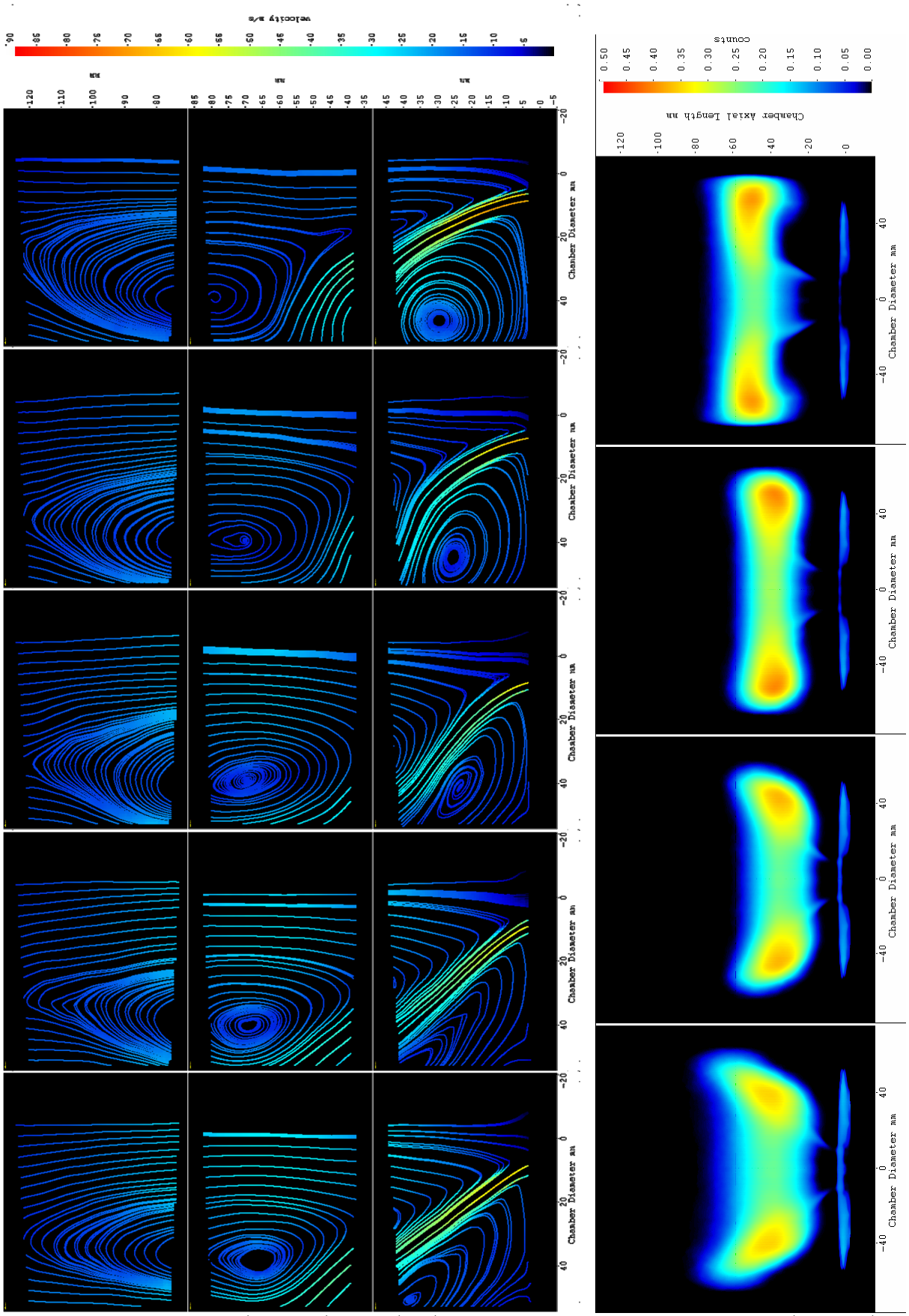

Figure 7-6. Phases 1 (bottom) to 5 (top) of the flow field and phases 1 (bottom) to 4 (top) of reacting field of f1-100Hz. The flow images were recorded in the 'CRZ', 'Flame Zone' and 'URZ' imaging areas.

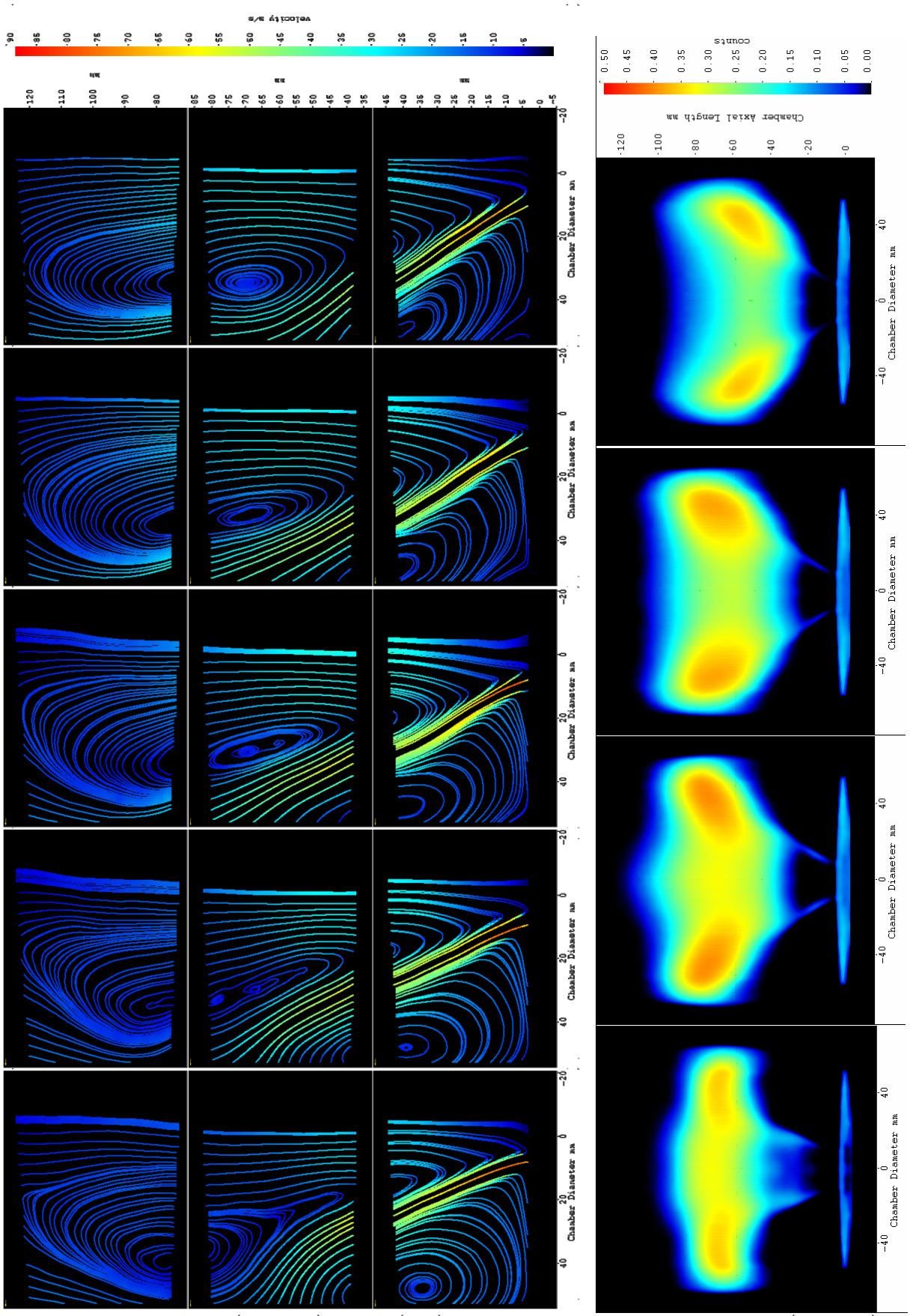

Figure 7-7 Phases 6 (bottom) to 10 (top) of the flow field and phases 5 (bottom) to 8 (top) of reacting field of f1-100Hz. The flow images were recorded in the 'CRZ', 'Flame Zone' and 'URZ' imaging areas.

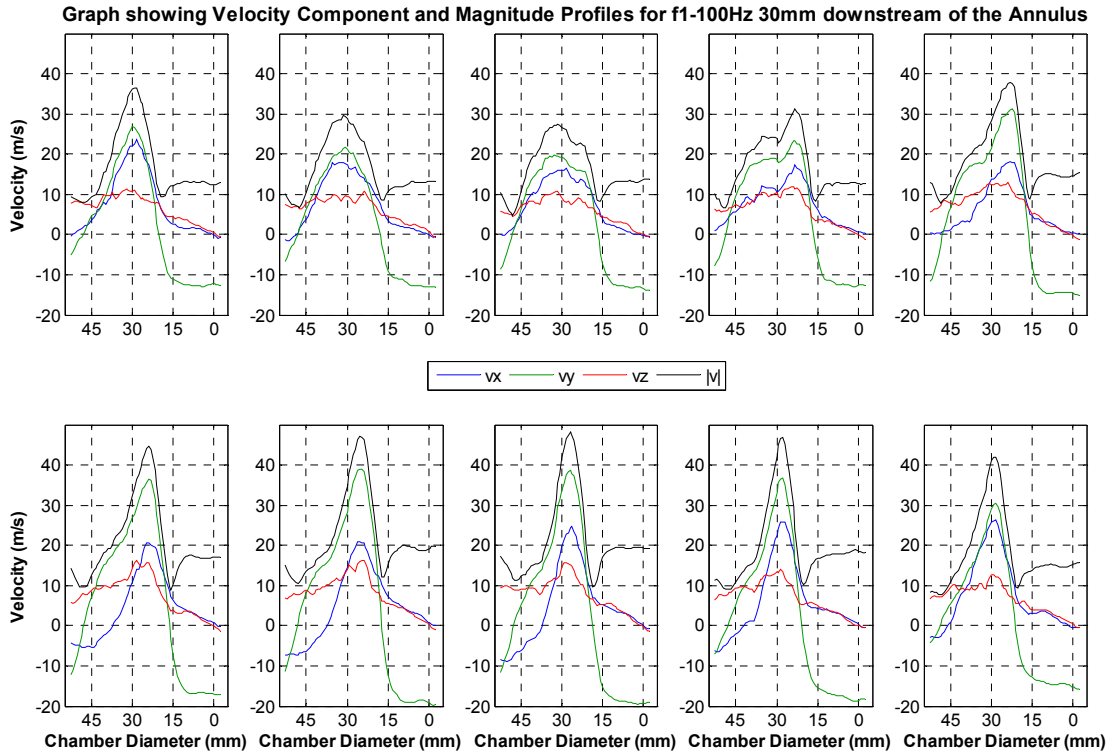

Figure 7-8 Velocity Profiles of f1-100Hz along a line 30mm downstream of the Annulus. Taken from mean vector fields from the imaging area 'CRZ'. The top row consists of phases 1 to 5 from left to right. The bottom row consists of phases 6 to 10 from left to right.

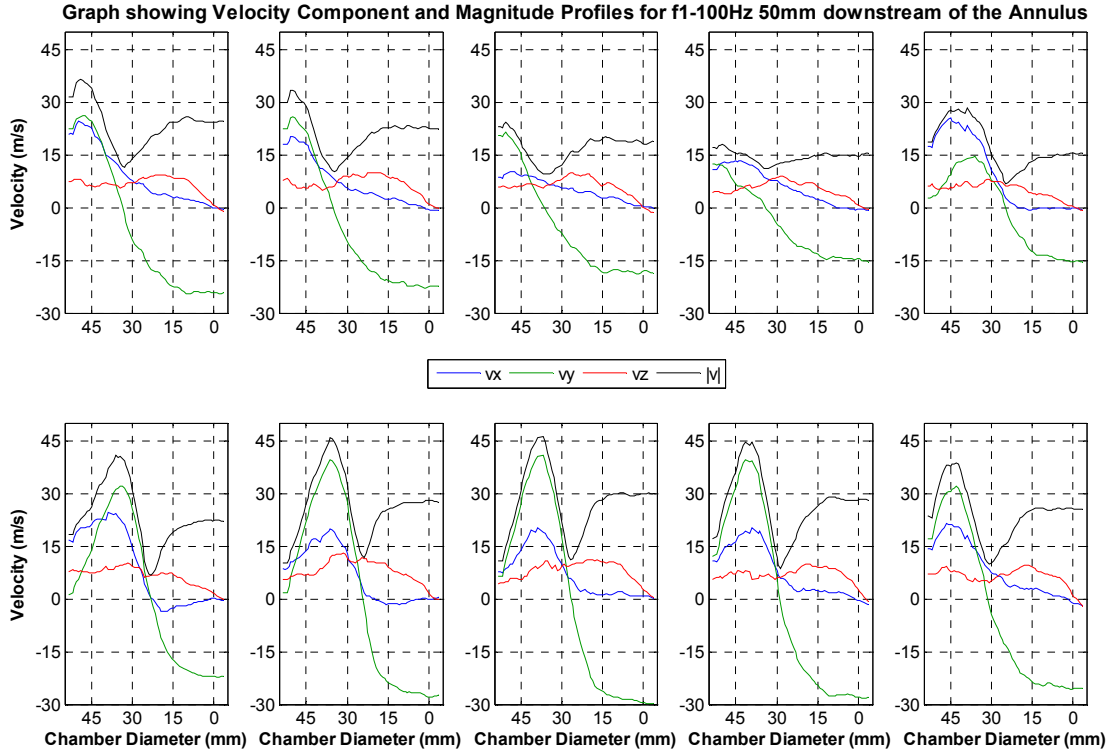

Figure 7-9 Velocity Profiles of f1-100Hz along a line 50mm downstream of the Annulus. Taken from mean vector fields from the imaging area 'Flame Zone. The top row consists of phases 1 to 5 from left to right. The bottom row consists of phases 6 to 10 from left to right.

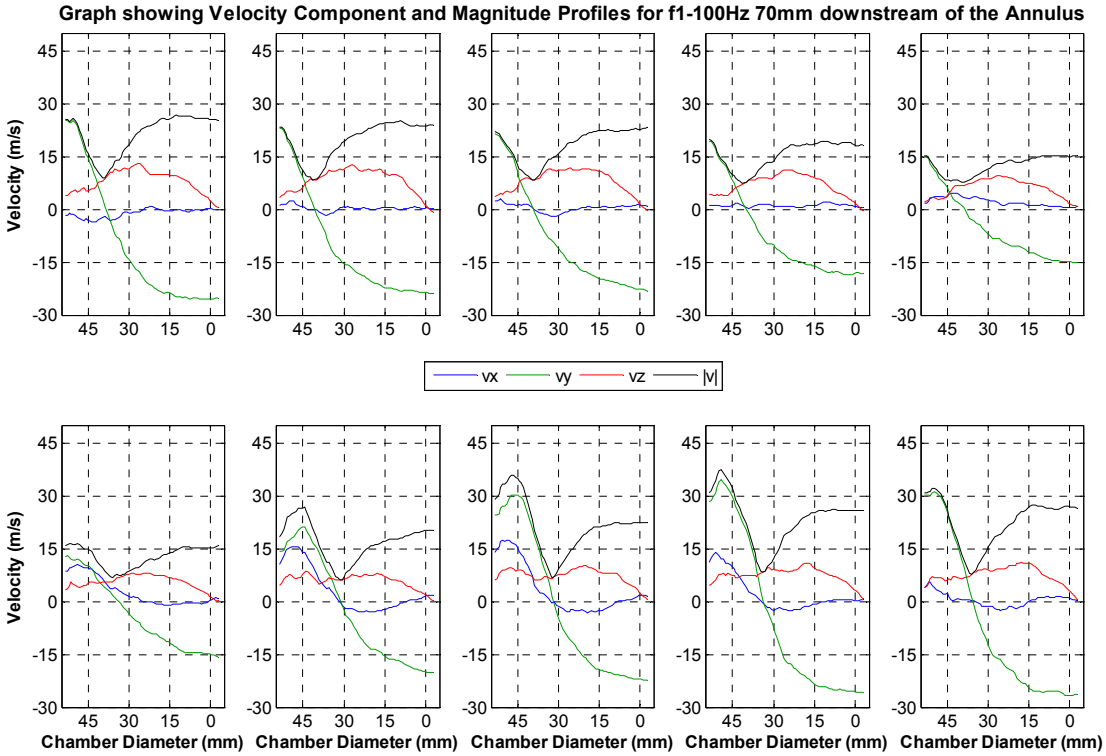

Figure 7-10 Velocity Profiles of f1-100Hz along a line 70mm downstream of the Annulus. Taken from mean vector fields from the imaging area 'Flame Zone'. The top row consists of phases 1 to 5 from left to right. The bottom row consists of phases 6 to 10 from left to right.

7.1.3 The Internal Recirculation Zone

The behaviour of the Internal Recirculation Zone is clearly oscillatory and is of the bubble/axisymmetric type of vortex breakdown. The velocity profiles of Figure 7-8 to Figure 7-10 show that as vy increases due to the inlet flow the absolute values of vy in the IRZ also increase. Figure 7-11 shows the magnitude of abs vy oscillation within the IRZ at 30mm, 50mm and 70mm. It is apparent that the magnitude of oscillation of abs vy is weakest at the 30mm position with a minimum of 12.5ms^{-1} and a maximum of 19ms^{-1}. The magnitude of abs vy variation is greatest at the 50mm position with a minimum of 15ms^{-1} and maximum of 29ms^{-1}. At the 70mm position a decrease in maximum value is evident, 26ms^{-1}. A phase delay can be seen in the respective abs vy profiles due to the reduction of inlet velocity and time required for the inlet flow to each the respective axial position.

The reason for the variation in IRZ vy velocities is attributed to transportation of reactants into the IRZ where it is mixed with and ignited by combustion products. It is speculated that the shear layer could cause local flame extinction allowing vorticity transportation to advect reactants into the IRZ. This also explains why the IRZ vy and inlet vy are in phase as more reactants will be transported due to increased flow rate and higher strain values. This has been seen in other combustors of similar type [42].

The instantaneous vector fields were sampled on the chamber centreline 30mm, 50mm and 70mm downstream from the annulus. The extracted data was then analysed to produce each components' frequency spectrum in

Figure 7-12. Vx displays weak low frequency oscillations between 0Hz and 200Hz which increase marginally in strength downstream and are generally not much stronger than the turbulent oscillations. Vy (and hence |v| as vy dominates) is clearly oscillating at a single frequency of 100Hz with a small second contribution at 200Hz. The harmonics of 300Hz and 400Hz detected in the frequency spectrum of vy at the annulus and by the pressure transducer appear to have been damped within the IRZ. The strength of the oscillation appears greatest at the 50mm position and weakest at the 30mm position. The harmonics detected are greatest in strength at the 30mm position and dampen moving downstream. The tangential component vz has easily identifiable signals at approximately 40Hz, 80Hz and 160Hz which generally become stronger downstream. These frequencies indicate that the reverse flow region is clearly oscillating with regard to its rotational speed around the centre axis. None of these frequencies coincide with any acoustic mode calculated. Lacking the SPIV temporal resolution it can not be determined if any of the acoustic modes are being excited. As strong signals are detected below 100Hz and similarly 200Hz it is feasible the original perturbation frequency (100Hz) and harmonic (200Hz) have been altered to lower frequencies.

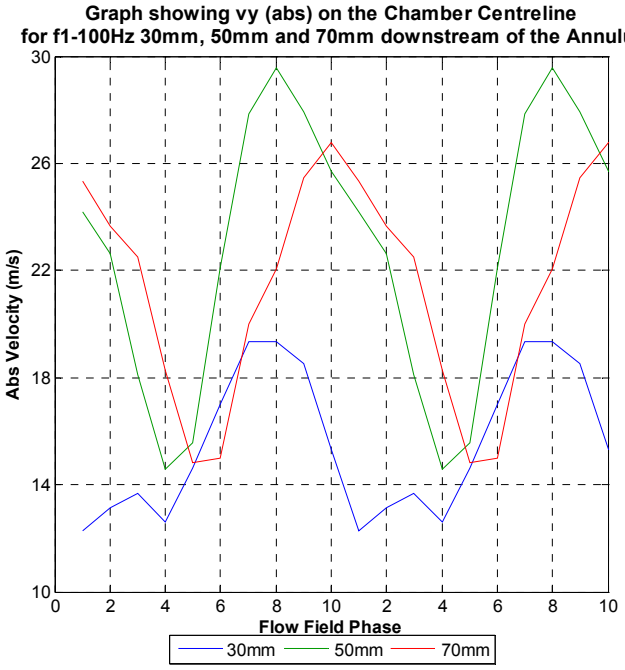

Figure 7-11 Graph showing Peak Centreline vy (abs) values against Phase for f1-100Hz within the IRZ at 30mm ,50mm and 70mm axial positions

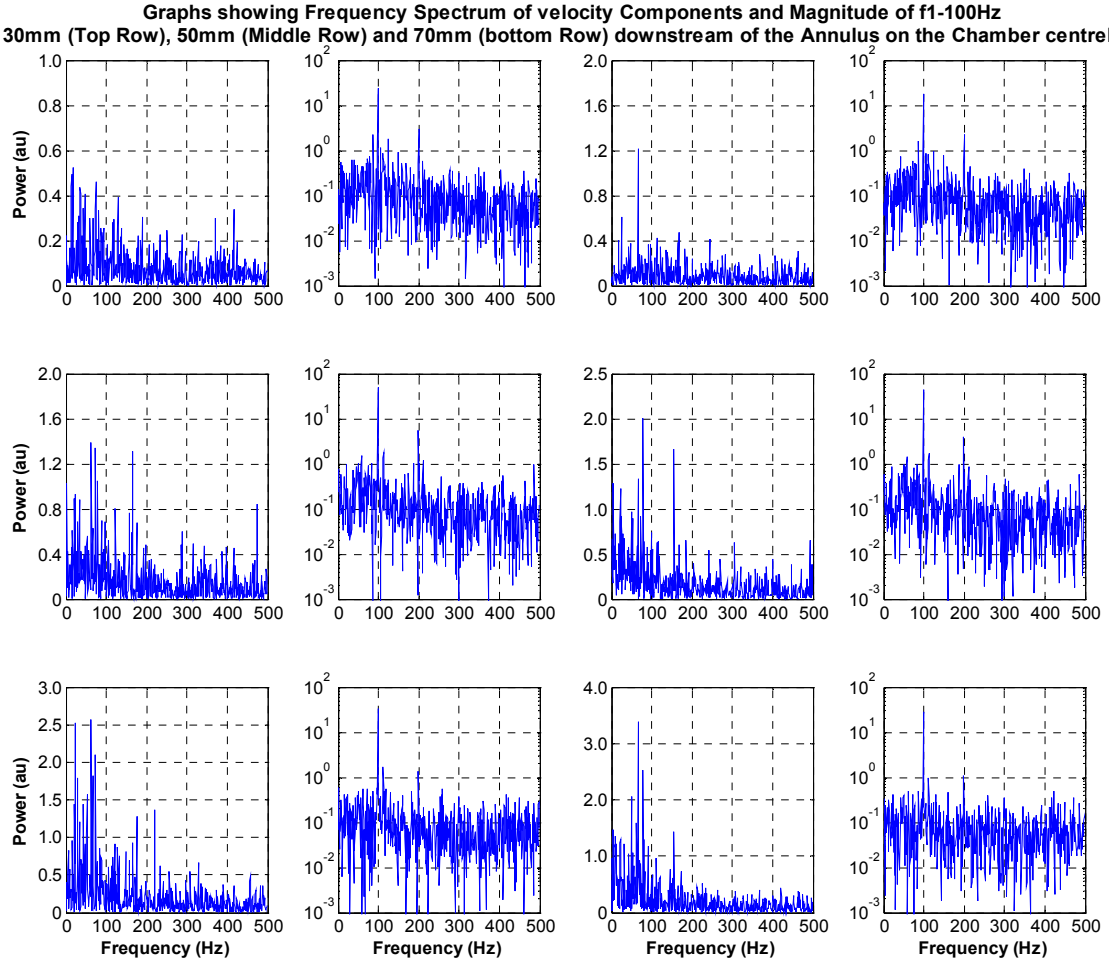

Figure 7-12 Frequency spectra of f1-100Hz extracted from 30mm, 50mm and 70mm downstream of the annulus on the chamber centreline. Vx corresponds to the left column, followed by vy, vz and |v| is the right column.

7.2 F1-200Hz

7.2.1 Entry Conditions

Velocity profiles are once again extracted from the same axial position as before to describe the entry of the flow. From these profiles the peak value and profile integrated value (4mm length across inlet flow) at each phase for the velocity components and magnitude has been extracted and plotted against phase in Figure 7-13.

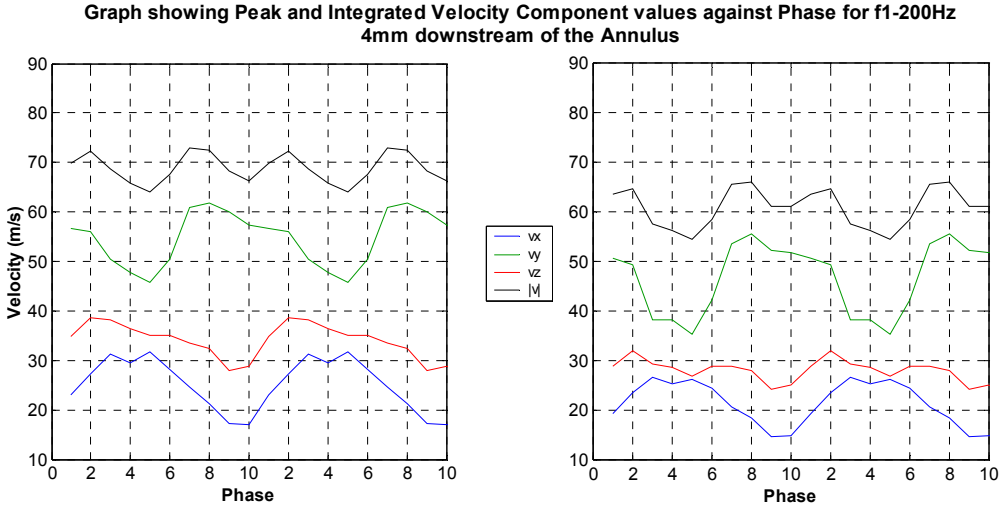

Figure 7-13 Graphs showing Peak (Left) and Integrated (Right) Velocity Component and Magnitude Values against Phase for f1-200Hz 4mm downstream of the annulus over two oscillations.

It is apparent that a large phase difference is present among vx, vy and vz. Vy is the strongest component with minimum and maximum values of 37ms^{-1} and 55ms^{-1} occurring at phases 5 and 8. Vx has two maximums either side of phase 4 of 27ms^{-1} and a minimum through phases 9 and 10 of 15ms^{-1}. Vz also has a minimum at phase 9, 14ms^{-1} and its maximum occurs at phase 2, 32ms^{-1}. None of the profiles are identical to each other and display varying skewed features. The minimum of vy is out of phase by half a cycle to that of vx and vz and the maximums under half a cycle out of phase are responsible for the profile of |v|. This profile appears to be of a frequency of 400Hz not 200Hz due to the half cycle phase lag among the velocity components.

The profiles of Figure 7-15 confirm that the width of the inlet is invariant at this position, remaining approximately 7mm. The radial position is also stable at 13mm from the centreline. Other features present are the same as those noted for f1-100Hz. The profiles within the IRZ remain largely unaffected by the instability. Both vx and vz converge to zero at the centreline where as vy is negative and shows a flat profile with a small velocity towards the bluff body. Outside of the inlet flow vx shows some variation in its negative values. This is due to change in the CRZ. Once again the entire flow is moving in the same positive tangential direction. The inlet flow has a greater tangential velocity than

the outer flow which is in turn greater than that of the IRZ, which is the smallest.

The profiles depicting the rms values of the velocity components are shown in Figure 7-16. Once again two peaks are clear identifying the shear layers. Unlike the f1-100Hz case the profiles clear oscillatory behaviour in the profiles is unclear for all components. The peak rms values in both shear layers for all components shows small amounts of change but no obvious pattern with the instability. Trends which can be discerned is that both rms vx and rms vz favour the outer shear layer with values larger than those of the inner shear layer. Conversely rms vy favours the inner shear layer with its largest values. Rms vy also contributes to the outer shear layer with values equal or greater than both rms vx and rms vz. As the inlet flow at the 4mm downstream position does not exhibit width or radial position changes a spectral analysis has been undertaken on the recorded velocities. The central position of the inlet flow was determined over the entire instability and the velocity components and magnitude were extracted from all the instantaneous vector fields at this position. The radial position was 13mm.

As the inlet flow at the 4mm downstream position does not exhibit width or radial position changes a spectral analysis has been undertaken on the recorded velocities. The central position of the inlet flow was determined over the entire instability and the velocity components and magnitude were extracted from all the instantaneous vector fields at this position. The radial position was 13mm.

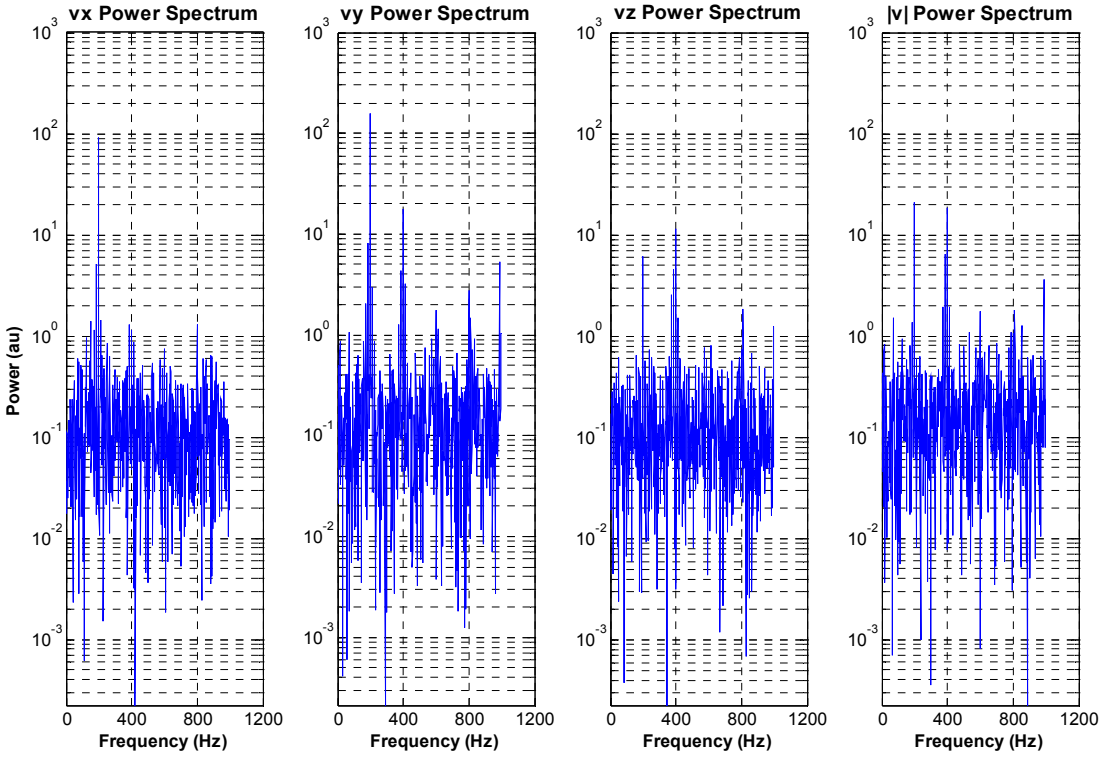

Figure 7-14 Frequency spectra taken from the f1-200Hz Instantaneous Vector fields recorded at the 'Annulus 3D' imaging area at axial position 4mm, radial position 13mm. The left corresponds to |v|, moving to the right is vx, vy and vz.

The power spectra show that vx is controlled by the imposed 200Hz frequency and possess a smaller frequencies at 400Hz and 800Hz. Vy is also dominated by 200Hz but possess not insignificant frequencies at 400Hz, 600Hz, 800Hz and 1 KHz. Interestingly vz is controlled by two frequencies but here the 400Hz frequency is stronger than the imposed one of 200Hz. The spectrum of |v| shows the two frequencies of 200Hz and 400Hz with the first slightly stronger than the latter. Less powerful frequencies are 600Hz, 800Hz and 1 KHz. This spectrum compares well with the spectrum of the inlet pressure spectrum. The reason for such a strong second frequency of 400Hz for |v| is due to the phase among the components.

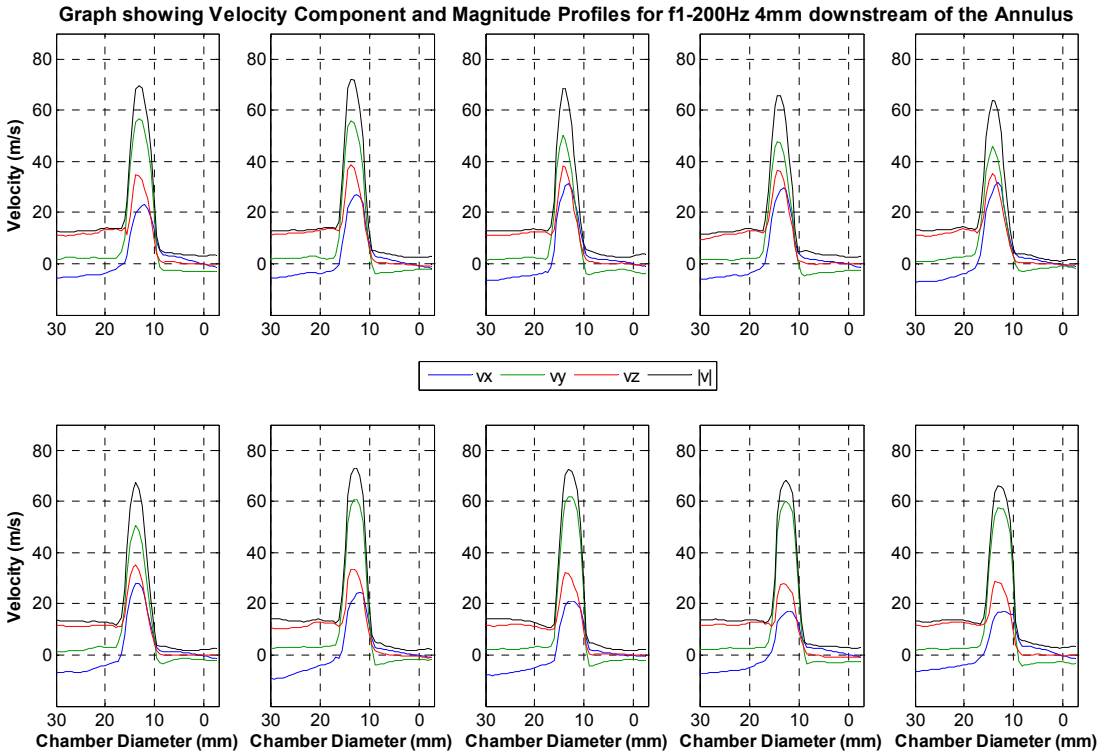

Figure 7-15 Velocity Profiles of f1-200Hz along a line 4mm downstream of the Annulus. Taken from mean vector fields from the imaging area 'Annulus 3D'. The top row consists of phases 1 to 5 from left to right. The bottom row consists of phases 6 to 10 from left to right.

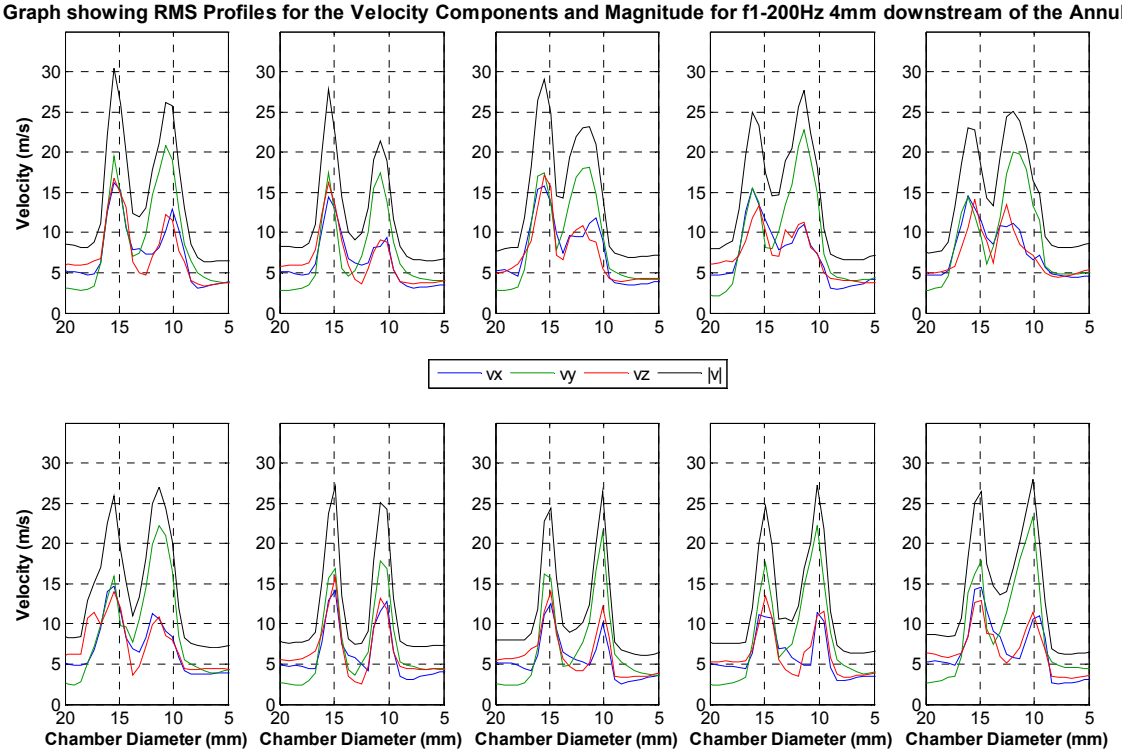

Figure 7-16 RMS Profiles of f1-200Hz along a line 4mm downstream of the Annulus. Taken from the RMS scalar field derived from the ensemble collected at the imaging area 'Annulus 3D'. The top row consists of phases 1 to 5 from left to right. The bottom row consists of phases 6 to 10 from left to right.

7.2.2 Chamber Reacting Fields and Flow Fields

The mean Abel deconvoluted flame and flow field behaviour is depicted in Figure 7-18 and Figure 7-19. Velocity component profiles have again been extracted at axial positions 30mm, 50mm and 70mm downstream of the annulus in Figure 7-20 to Figure 7-22. The motion captured by both diagnostics shows good agreement in compared behaviour. Consideration of the reacting fields is done with phases 1 through 8 and the flow fields is 1 through 10.

As the inlet flow analysis revealed a conflict over the instance of a common minimum the mean integrated CH* plot of Figure 7-17 will be used. From this figure the lowest value of mean integrated CH* occurs at phase 3 and the maximum occurs at phase 6. The profile shows two maximums and minimums consistent with that observed for the peak value |v| profile at the inlet and the pressure plot. The frequency spectrum shows strong frequencies at 400Hz, 600Hz and 800Hz. The strongest is the imposed frequency of 200Hz. These frequencies were all detected in the spectral analysis of the inlet flow. The result resembles the spectrum of |v| as this plot includes the information of the affect of all components oscillatory behaviour upon the combustor.

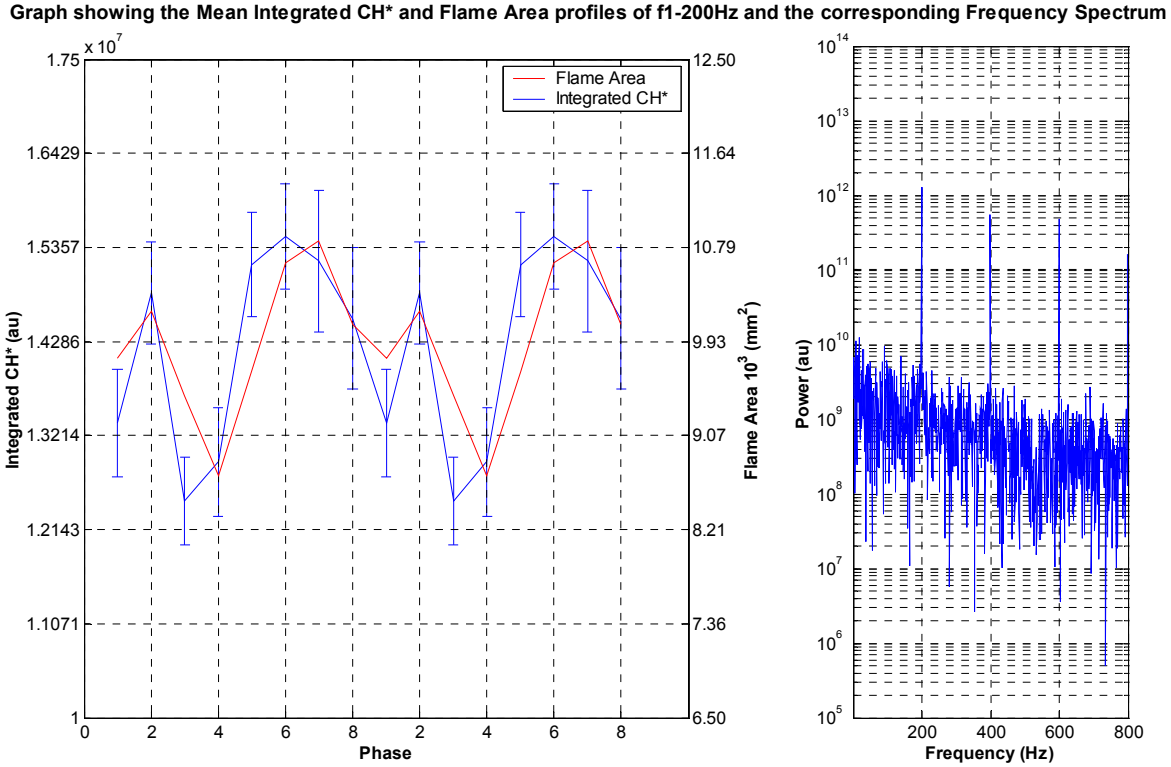

Figure 7-17 Mean Integrated CH* profile and flame area profile for f1-200Hz with corresponding Frequency Spectrum. The phase corresponds to that of the CH* images.

The reacting fields of Figure 7-18 and Figure 7-19 illustrate the impact of the phase difference among the velocity components. Phase 1 is of a 'V' type structure with extremities 60 degrees to the vertical pointing radially outward and downstream approximately 70mm from the dump plane. In phase 2 the hot spots

have increased in intensity and become physically larger moving upstream towards the annulus. This corresponds to a small decrease in inlet vy and an increase of inlet vx. The overall structure is of the same shape as phase 1. The structure retreats towards the dump plane in phase 3 and possesses less elongated and smaller hotspots at 50mm from the dump plane. Vy has continued to decrease while vx is increasing. At phase 4 a different structural shape can be seen, that of a horizontal 'B'. The structure is axially compact whereas its base has widened. The hotspots have moved radially outward and are 'C shaped. These are larger in area than the previous phase although the overall flame area has reduced. Vy of the inlet flow is now a minimum where as vx is a maximum. At phase 5 the structure has become wider with large outward downstream orientated hotspots. The structure has started to move downstream as vx is now decreasing and vy increasing. The structure has moved further downstream (70mm) in phase 6, vx is decreasing and vy has reached its maximum. The flame structure has a flat aspect to it with the hotspots near horizontal in orientation. At phase 7 the flame is still in the same position and has the same structure but the hotspots are smaller. Also noticeable is a small portion of the structure has burnt upstream towards the annulus. The inlet flow has minimums of vx and vz. Vy has begun to ebb but still remains high. Finally phase 8, is again of the same structure as previous phases but the hotspots now stretch across the chamber and is of less intensity. The extended flame area above the annulus previously noted has now disappeared and two small new structures have appeared which are new structures caused by the out of phase inlet velocity components. These will be absorbed into the main structure by phase 1. At phase 8 vx is still a minimum and vy is decreasing.

The flow fields of f1-200Hz show a marked difference to that of f1-100Hz. The IRZ, once again a axisymmetric type of vortex breakdown, exhibits a second internal recirculation zone close to the annulus through part of the oscillation, causing the inlet flow structure to bend significantly. Phase 1 shows the CRZ and IRZ with the inlet flow moving between them. However at 35mm downstream there is the beginning of a second recirculation zone on the inside of the inlet flow structure. In phase 2 this has new recirculation zone has become larger and has caused the inlet flow structure to straighten and is now orientated more axially downstream. The flow then encounters the downstream half of the IRZ and is forced radially outwards. Phase 3 is similar to phase 2 with a modest increase in size of the new recirculation zone. At Phase 4 the new recirculation zone is much wider which has completely straightened the adjacent inlet flow structure. The top half of this zone has started to stretch downstream along the inner shear layer. The bottom half of the original recirculation zone of the IRZ, which was also stretched along the inner shear layer has begun to retreat downstream. At phase 5 the new zone is wider still pushing the inlet flow structure further outward; it is still vertical in orientation here. The CRZ has become elliptical in shape as it is compressed between the chamber wall and the inlet structure. The top half of the new zone is pushing further downstream. In contrast the original recirculation zone is now shrinking in size and retreating further downstream. This motion has occurred as the inlet velocity of vy has decreased to its minimum and vx increased to its maximum.

At phase 6 vx begins to decrease and vy increases. This effect can be seen on the location where the inlet flow structure bends vertically. This location has moved downstream. The structure has also moved further outwards causing the CRZ to become stretched around the bend in the inlet flow structure. The new recirculation zone has stretched further downstream and the original zone has shrunk in size. It is clear that the new zone and the original are in the process of merging at this phase. At phase 7 the increased inlet vy velocity has pushed the inlet structure downstream. The new recirculation zone centre has moved for the first time, also downstream to a position above the reacting structure. This has caused the zone to become bigger. This in turn has meant that the original zone has been absorbed into the new recirculation zone which possesses a large downstream aspect where the former was, creating one very large recirculation zone. The inlet flow structure still has a vertical aspect to it but now adjacent to the chamber wall and the position of the bend has been pushed downstream. This has allowed the reformation of a recognisable CRZ. Phase 8 is similar to phase 7 with the small movement of the new zone slightly downstream. In phase 9 the centre of the recirculation zone has moved further downstream but the shape has changed. The bottom of the recirculation zone is starting to stretch down the inner shear layer and the centre is being stretched radially outwards. Finally phase 10, this phase is similar to phase 9. The recirculation zone is still stretching down the inner shear layer and the start of the new recirculation zone can be seen. A definitive kink can be seen in the inlet flow structure approximately 20mm from the annulus which could be due to the small additional structure observed in the reacting fields (phase 8 CH*). By phase 10 vx is a minimum and vy although past its maximum is still high in value.

The velocity profiles of 30mm, 50mm and 70mm show typical features such as the motion of the fluid past the recirculation zones. However the presence of the new recirculation, out of phase nature of the inlet flow components and changing location of combustion makes direct interpretation of these profiles exceedingly difficult. From the profiles at 30mm vx within the inlet flow structure peaks at phase 7 and is a minimum at phases 4 and 5. Vy enjoys high values from phase 8 through to 1 and low values at phases 5 and 6. The phase difference between vx and vy appears to have reduced at this point. Therefore it is more applicable to consider purely $|v|$ in this case. From the profiles at 30mm the inlet flow structure is still evident. This feature possesses maximums at phases 8, 10 and 1 of approximately $60ms^{-1}$ and minimums at phases 5 to 6 of approximately $40ms^{-1}$. This is repeated for the profiles at 50mm with a maximum over phases 9 to 1 (approx $40ms^{-1}$) and minimum over phases 5 to 7 (approx $25ms^{-1}$). This shows reasonable agreement with that observed for the inlet profile of $|v|$ which has its minimum at phase 5 and maximum at phases 7 and 8.

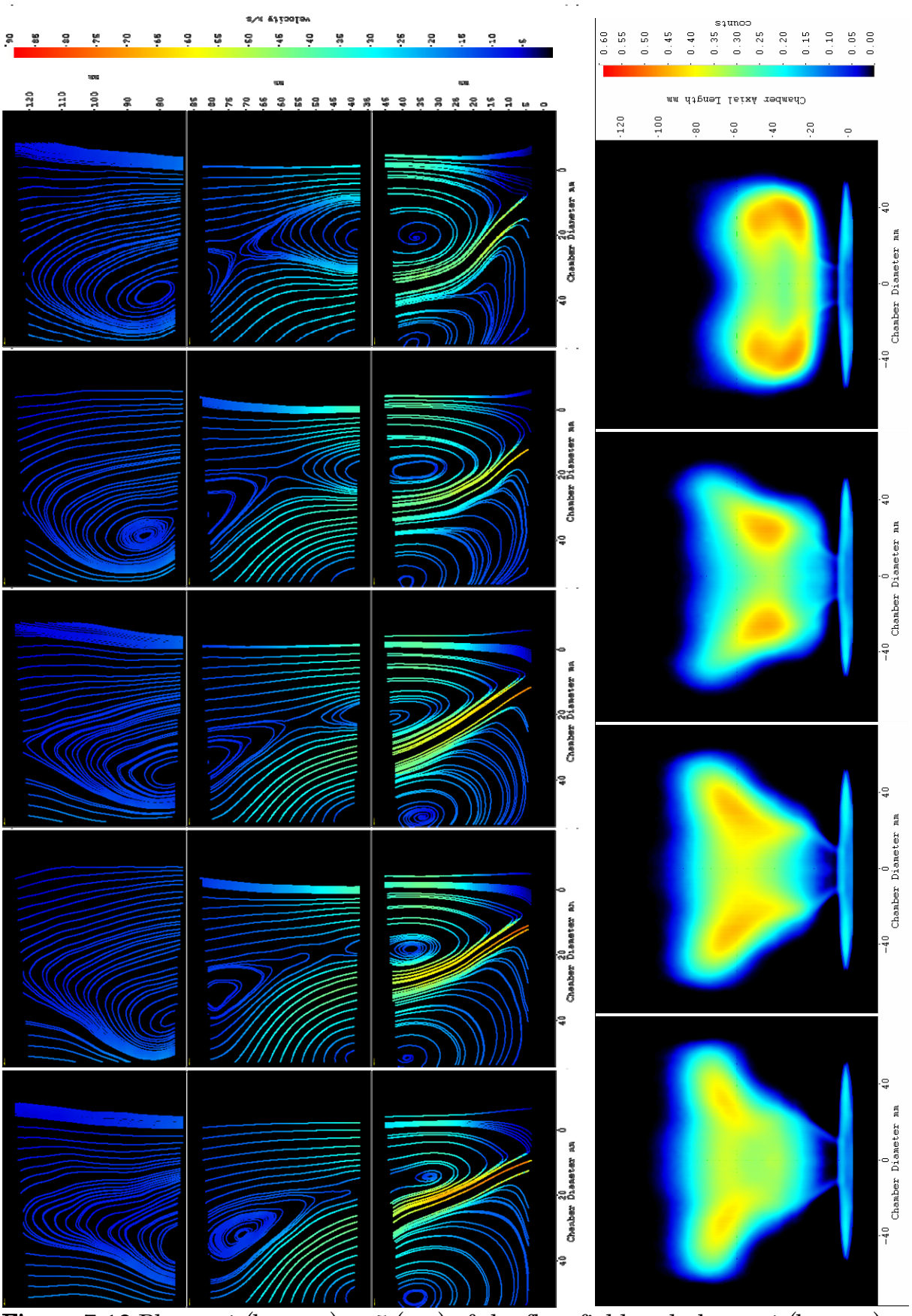

Figure 7-18 Phases 1 (bottom) to 5 (top) of the flow field and phases 1 (bottom) to 4 (top) of reacting field of f1-200Hz. The flow images were recorded in the 'CRZ', 'Flame Zone' and 'URZ' imaging areas.

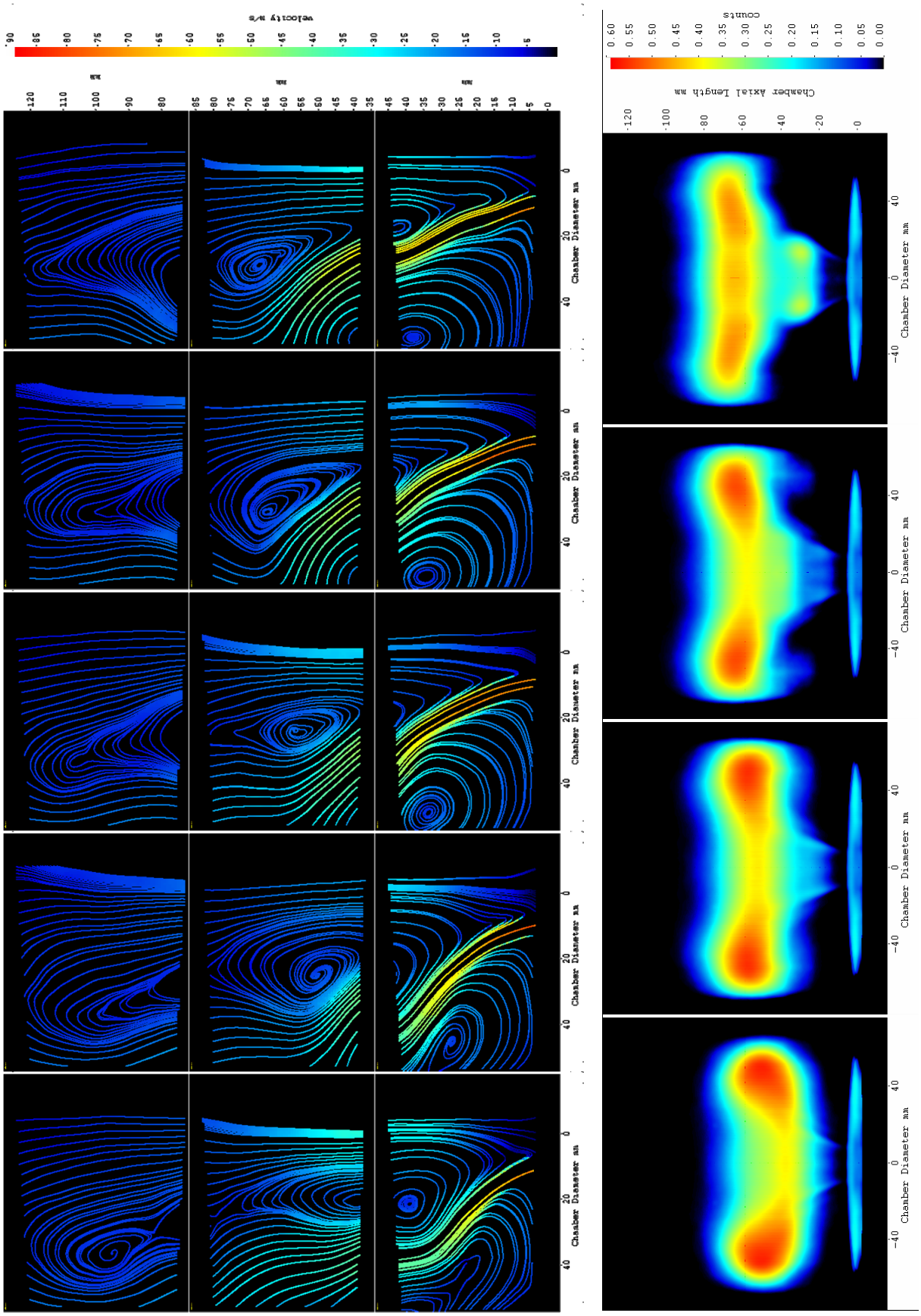

Figure 7-19 Phases 6 (bottom) to 10 (top) of the flow field and phases 5 (bottom) to 8 (top) of reacting field of f1-200Hz. The flow images were recorded in the 'CRZ', 'Flame Zone' and 'URZ' imaging areas.

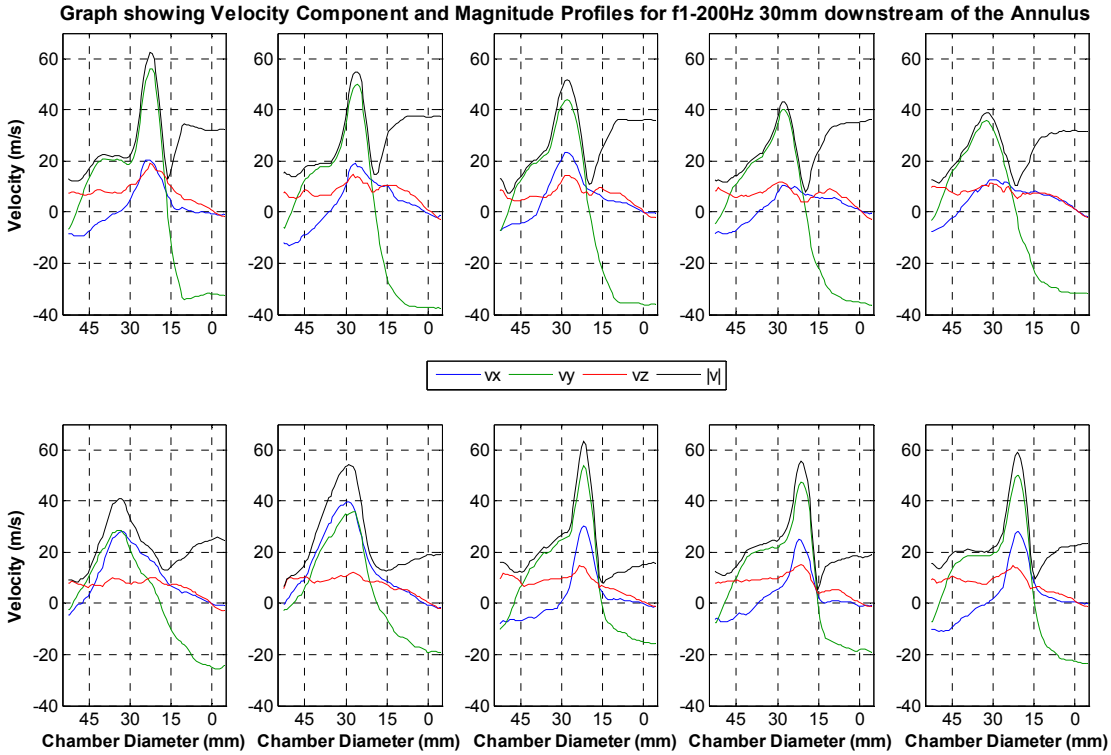

Figure 7-20 Velocity Profiles of f1-200Hz along a line 30mm downstream of the Annulus. Taken from mean vector fields from the imaging area 'CRZ'. The top row consists of phases 1 to 5 from left to right. The bottom row consists of phases 6 to 10 from left to right.

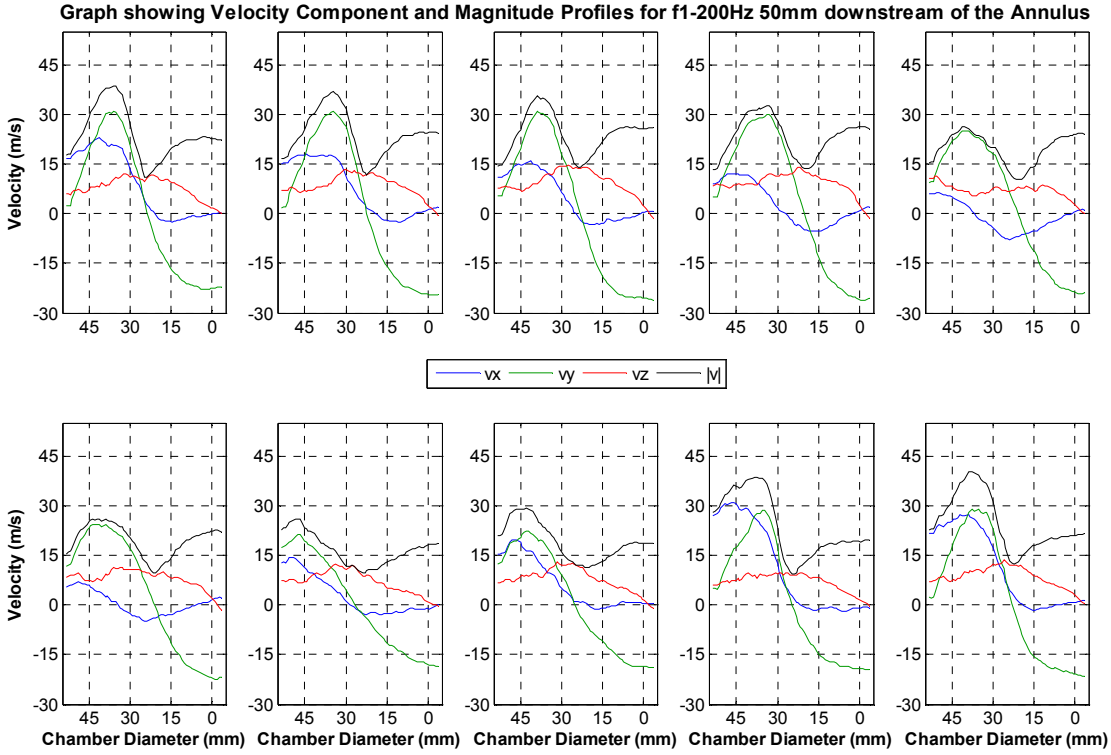

Figure 7-21 Velocity Profiles of f1-200Hz along a line 50mm downstream of the Annulus. Taken from mean vector fields from the imaging area 'Flame Zone. The top row consists of phases 1 to 5 from left to right. The bottom row consists of phases 6 to 10 from left to right.

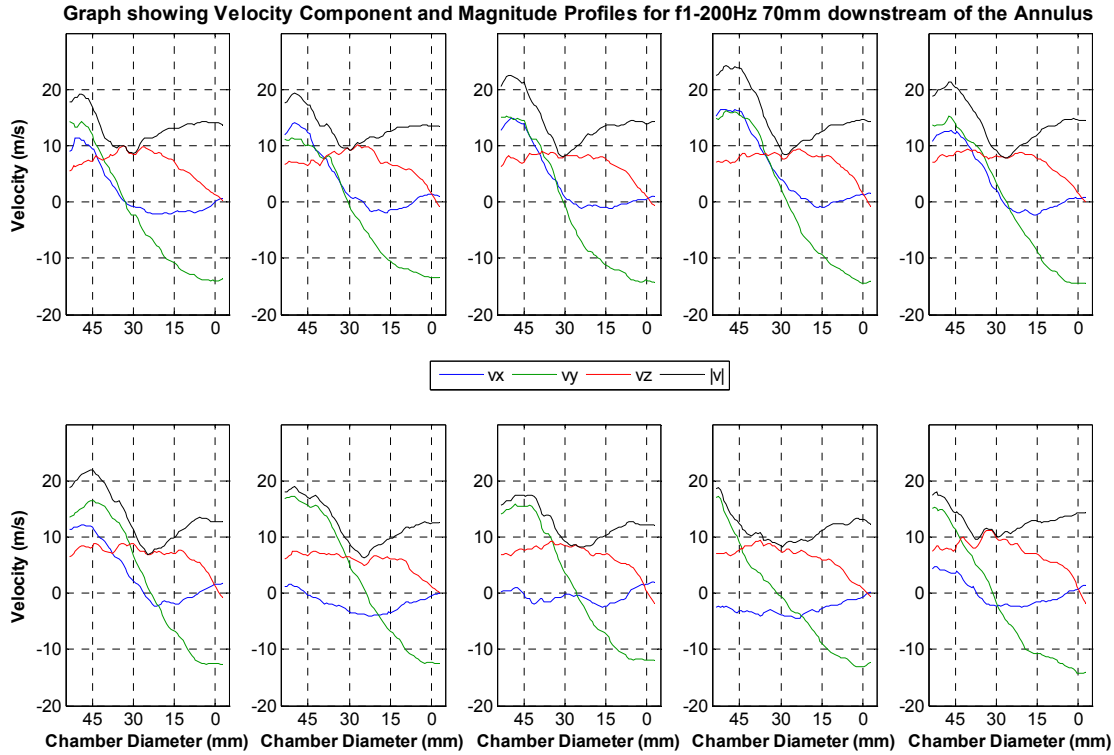

Figure 7-22 Velocity Profiles of f1-200Hz along a line 70mm downstream of the Annulus. Taken from mean vector fields from the imaging area 'Flame Zone'. The top row consists of phases 1 to 5 from left to right. The bottom row consists of phases 6 to 10 from left to right.

7.2.3 The Internal Recirculation Zone

The behaviour of the Internal Recirculation Zone in this case is more complex. Still of axisymmetric type a second recirculation cell is visible. The absolute values of vy on the chamber centreline are plotted in Figure 7-23 at three axial positions. The oscillation of abs vy is greatest at the 30mm position with a minimum of 15.2ms^{-1} and a maximum of 37.5ms^{-1}. The magnitude of oscillation decreases downstream. At 50mm the minimum and maximum are 18ms^{-1} and 26ms^{-1}. At 70mm there is no distinct waveform and a variation of 2.5ms^{-1} indicating strong damping of axial oscillations at downstream positions. The profile of 30mm is sinusoidal in shape which does not match the inlet profile of vy. At 50mm the profile exhibits a plateau feature similar to the inlet vy profile although with a more saw tooth aspect.

The instantaneous vector fields were sampled on the chamber centreline 30mm, 50mm and 70mm downstream from the annulus. The extracted data was then analysed to produce each components' frequency spectrum in Figure 7-24. The component vx has no strong signal at 200Hz; rather sub 100Hz frequencies and frequencies greater than 900Hz. Signals within these ranges become stronger with downstream distance. Vy exhibits a clear dominant peak at 200Hz at the 30mm and 50mm downstream positions. This signal becomes damped at 70mm. Although other harmonics are present, of note is that the second strongest signal is that of 800Hz detected at all three positions. Comparison of the calculated acoustic chamber modes in Table 5-9 reveals the first longitudinal mode is approximately 840Hz. It is highly likely that the longitudinal oscillation of the IRZ at 800Hz is due to this mode as there is no large 800Hz signal of vy regarding the inlet velocity or pressure data spectra (Figure 5-17 and Figure 7-14). The frequency spectra of |v| within the IRZ at all positions also show a large, and at 70mm, a dominant 800Hz frequency. The tangential component vz exhibits a similar trend to vx in that strong signals are detected below 100Hz and greater than 900Hz which become stronger with downstream distance. Also notable is the appearance of strong signals at the 50mm downstream position at approximately 320Hz, 520Hz and 750Hz which appear to be almost 200Hz apart in the frequency range which could indicate some process of frequency shifting of the harmonics associated with this perturbation frequency. A comparison of the calculated acoustic modes of Table 5-9 and Table 5-2 shows the first longitudinal mode of the inlet section is of 1157Hz for the combustible mixture and 1039Hz for pure air. Which mode, inlet or chamber, the 900Hz plus signals detected in vx and vz are attributed to is unclear. However a 1 KHz signal has been detected in the inlet velocity spectra of vy and vz of Figure 7-14 which suggest the first longitudinal mode of the inlet could be excited and responsible for the rotational oscillation of the IRZ.

The longitudinal oscillation of the IRZ is dominated by the 200Hz and 800Hz frequencies which is unlike the inlet flow or integrated CH* frequency analysis. The strength of this frequency over others becomes weaker with axial distance which explains the degradation of the profile at 50mm compared to that at 30mm in Figure 7-23.

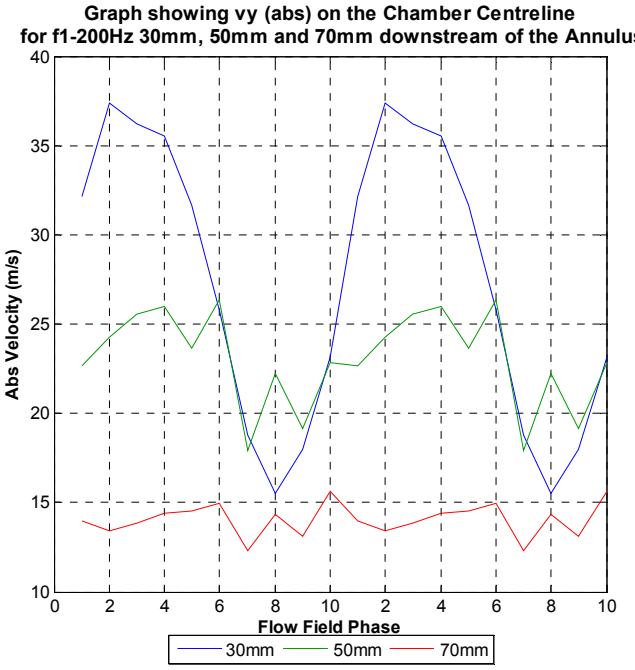

Figure 7-23 Graph showing Peak Centreline vy (abs) values against Phase for f1-200Hz within the IRZ at 30mm, 50mm and 70mm axial positions.

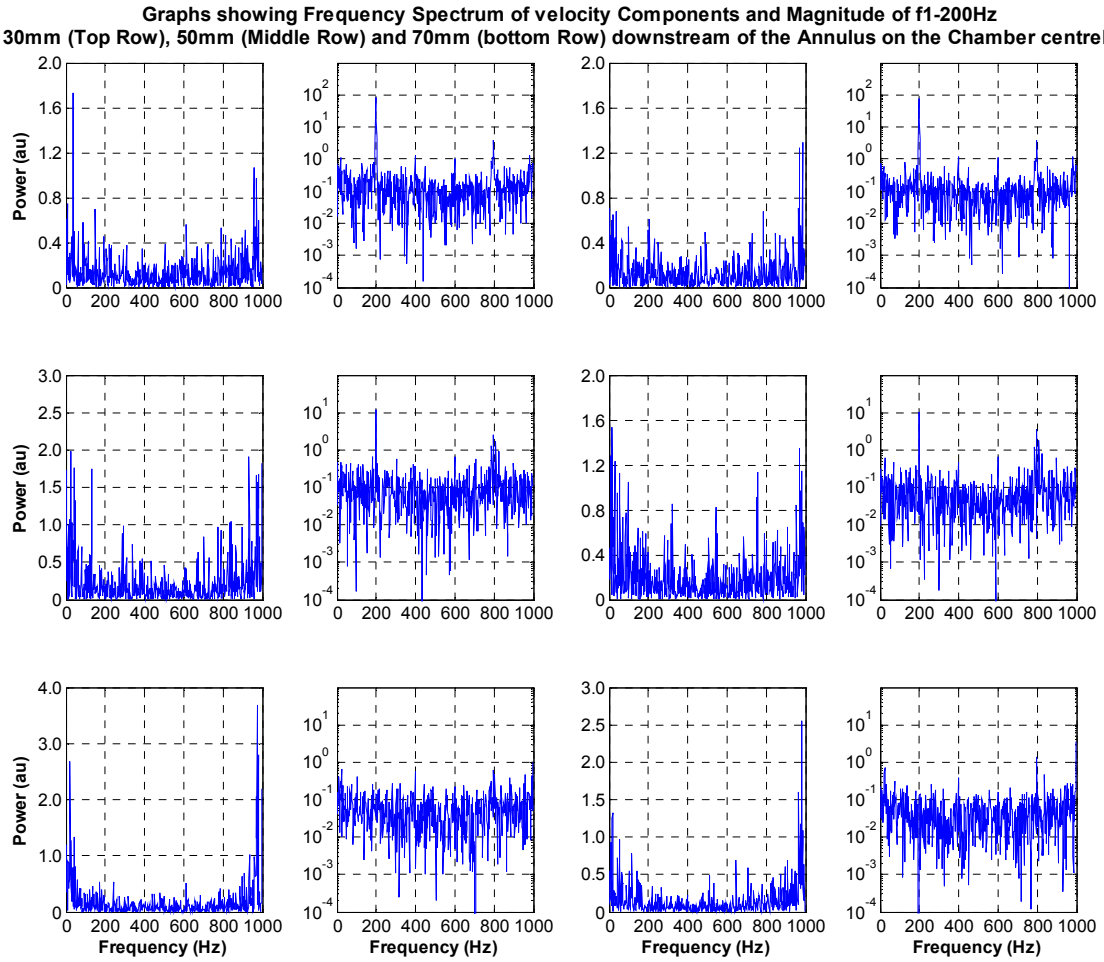

Figure 7-24 Frequency Spectra of f1-200Hz extracted from 30mm, 50mm and 70mm downstream of the annulus on the chamber centreline. Vx corresponds to the left column, followed by vy, vz and |v| is the right column.

7.3 F1-400Hz

7.3.1 Entry Conditions

Velocity profiles are once again extracted from the same axial position as before to describe the entry of the flow, Figure 7-27. From these profiles the peak value and profile integrated value (4mm length across inlet flow) at each phase for the velocity components and magnitude has been extracted and plotted against phase in Figure 7-25.

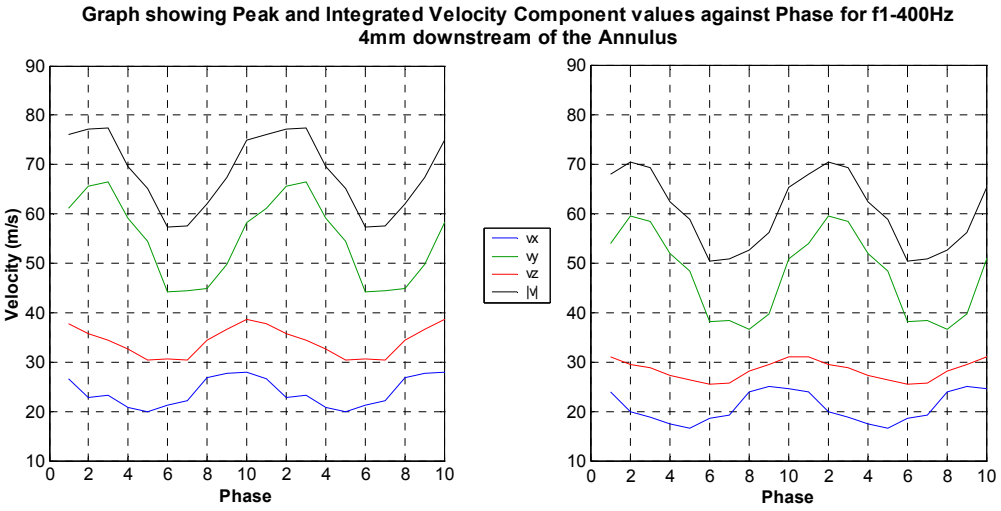

Figure 7-25 Graphs showing Peak (Left) and Integrated (Right) Velocity Component and Magnitude Values against Phase for f1-400Hz 4mm downstream of the annulus over two oscillations.

Using Figure 7-25 and the profiles taken 4mm downstream of the annulus (Figure 7-27) it is apparent from the peak component profiles are oscillatory as f1-100Hz. As expected, vy is the greatest component. The maximum of vy (60ms^{-1}) occurs at phases 2 and 3 and the minimum at phases 6 to 8 (38ms^{-1}). The profile shape of vy is similar to the siren aperture profile in Figure 5-18. As before vz is greater than vx and both have similar shaped profiles. Vz peaks at phase 10 and 1 (32ms^{-1}) and has its minimum at phase 6 of 16ms^{-1}. Vx peaks at phases 9 and 10 at 25ms^{-1} and is a minimum at phase 5 of 17ms^{-1}. It is apparent that vx is a phase position ahead of vz and approximately 4 phase positions ahead of vy. The profile of |v| shows good similarity to the corresponding mean pressure profile of Figure 5-18.

The profiles Figure 7-27 confirm that the width of the inlet is invariant at this position, remaining approximately 7mm. The radial position is also stable at 13mm from the centreline. Other features present are the same as those noted for both f1-100Hz and f1-200Hz with all three components peaking at the same radial position. The profiles within the IRZ remain largely unaffected by the instability. Both vx and vz converge to zero at the centreline where as vy is negative and shows a flat profile with a small velocity towards the bluff body. Outside of the inlet flow vx shows some variation in its negative values. This is due to change in the CRZ. Once again the entire flow is moving in the same

positive tangential direction. The inlet flow has a greater tangential velocity than the outer flow, which is in turn greater than that of the IRZ, which is the smallest.

The profiles depicting the rms values of the velocity components are shown in Figure 7-28. These show an oscillatory behaviour linked to the velocity component fluctuations. Once again all rms components show peaks at the shear layers. Vx and vz rms favour the outer shear layer where as vy rms contributes equally to both. It is for this reason that the outer layer has higher rms |v| values than the inner. Peak |v| occurs at phase 3 and is at its minimum at phases 6 and 7. Corresponding to this, rms |v| for both shear layers is a peak at phase 3 ($32ms^{-1}$ outer and $25ms^{-1}$ inner) and is a minimum for the outer layer at phase 6 ($18ms^{-1}$) and phase 8 ($10ms^{-1}$) for the inner layer. This can be explained by considering rms vy. The maximum of vy occurs at phase 3. The maximum of rms vy occurs at phase 3 for the inner shear layer and phase 2 for the outer shear layer. The minimum of vy occurs at phases 6 to 8. The minimum of rms vy occurs at phase 8 for the inner layer and phase 6 for the outer layer. This implies the turbulence fluctuates with the inlet flow as was seen for f1-100Hz. Oscillatory trends of rms vx and vz are also evident for both shear layers but their respective relationship with their velocity component is not as distinct as vy.

As the inlet flow at the 4mm downstream position does not exhibit width or radial position changes a spectral analysis has been undertaken on the recorded velocities. The central position of the inlet flow was determined over the entire instability and the velocity components and magnitude were extracted from all the instantaneous vector fields at this position. The radial position was 13mm.

The power spectra show that vx is controlled by the imposed 400Hz frequency and possess a smaller frequency of 800Hz. Vy is also dominated by 400Hz but possess not insignificant frequencies at 600Hz, 1400Hz and 1600Hz. Vz is controlled singularly by the 400Hz frequency. The spectrum of |v| is very similar to that of vy with 400Hz the greatest frequency followed by 1400Hz and 1600Hz. These harmonics show disagreement with those derived from the pressure measurements Figure 5-18.

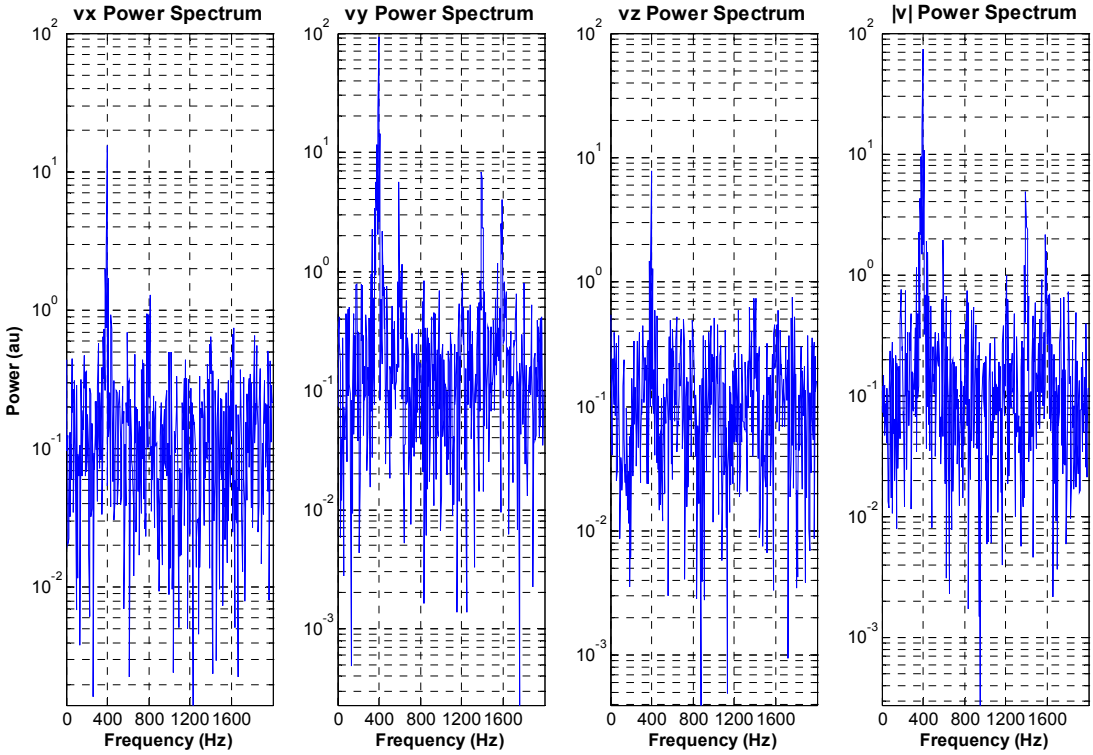

Figure 7-26 Frequency spectra taken from the f1-400Hz Instantaneous Vector fields recorded at the 'Annulus 3D' imaging area. Axial position 4mm radial position 13mm. The left corresponds to |v|, moving to the right is vx, vy and vz.

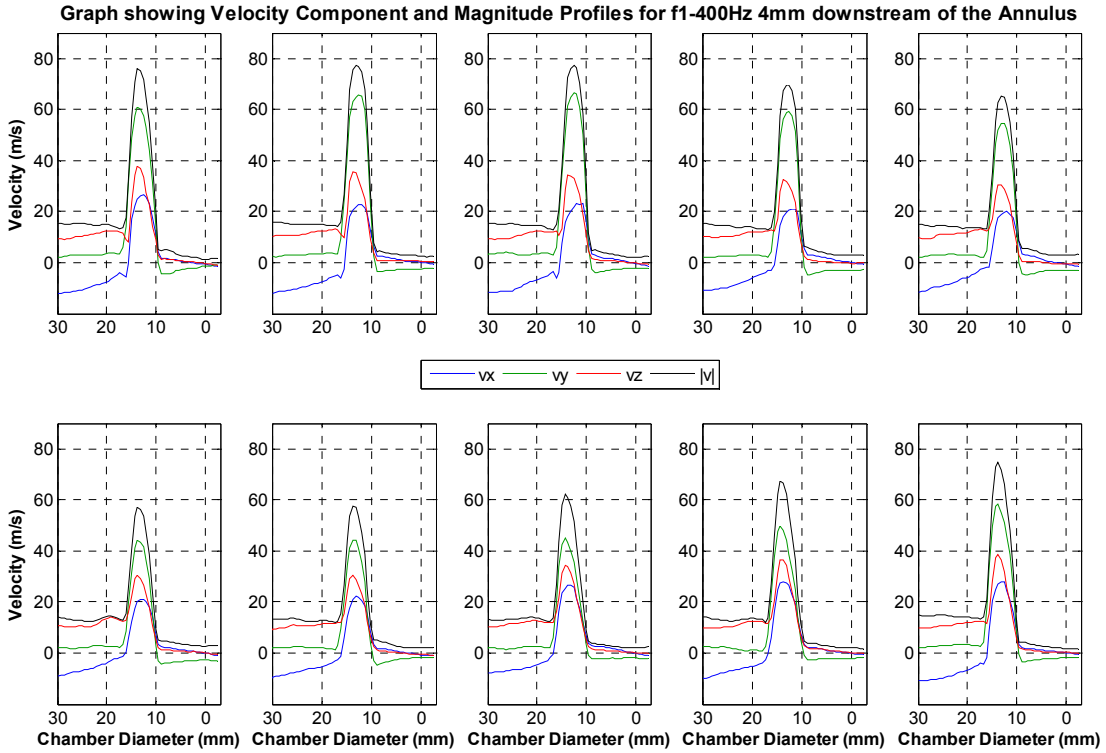

Figure 7-27 Velocity Profiles of f1-400Hz along a line 4mm downstream of the Annulus. Taken from mean vector fields from the imaging area 'Annulus 3D'. The top row consists of phases 1 to 5 from left to right. The bottom row consists of phases 6 to 10 from left to right.

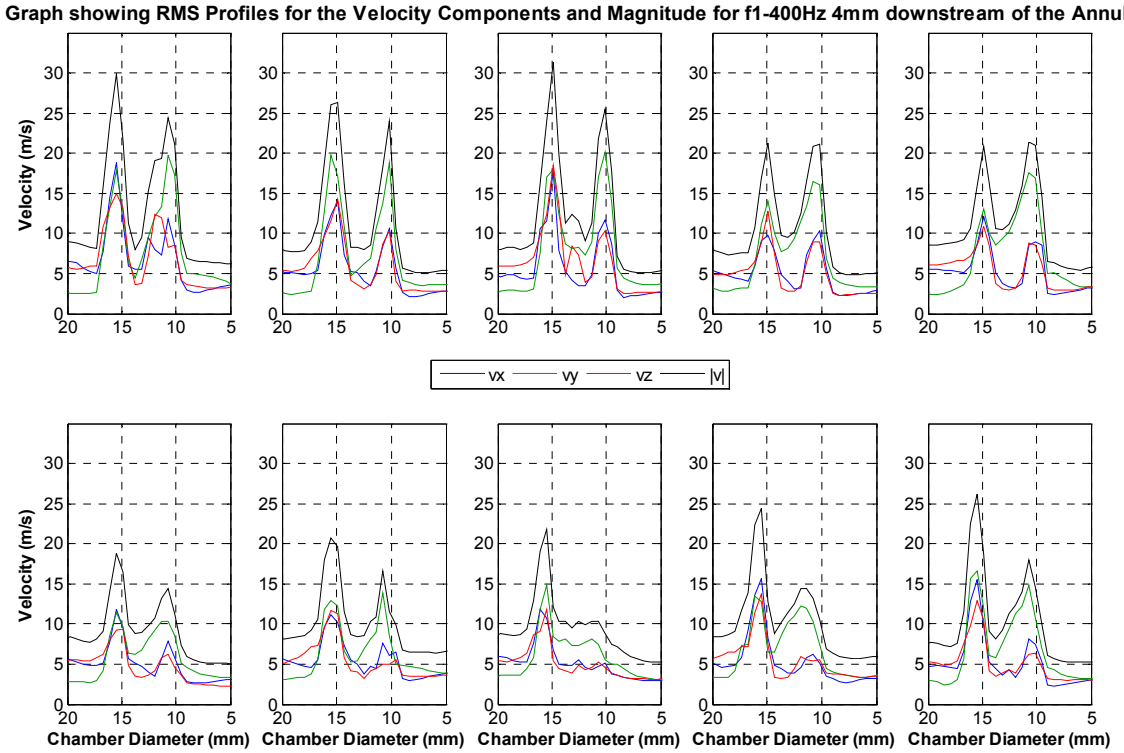

Figure 7-28 RMS Profiles of f1-400Hz along a line 4mm downstream of the Annulus. Taken from the RMS scalar field derived from the ensemble collected at the imaging area 'Annulus 3D'. The top row consists of phases 1 to 5 from left to right. The bottom row consists of phases 6 to 10 from left to right.

7.3.2 Chamber Reacting Fields and Flow Fields

The mean Abel deconvoluted flame and flow field behaviour is depicted in Figure 7-30 and Figure 7-31. Velocity component profiles have again been extracted at axial positions 30mm, 50mm and 70mm downstream of the annulus in Figure 7-32 to Figure 7-34. Consideration of the reacting fields is done with phases 1 through 8 and the flow fields is 1 through 10.

The total heat release behaviour has been discerned as before creating a mean and RMS value for each phase position. The time series of this data was used to create a frequency spectrum. The results are shown in Figure 7-29. The mean integrated profile shows a regular sinusoidal type profile. The frequency spectrum shows the complete dominance of the induced perturbation frequency of 400Hz. Other frequencies are present above the noise of 800Hz and 1600Hz, which concurs with that detected by the inlet pressure transducer (Figure 5-18).

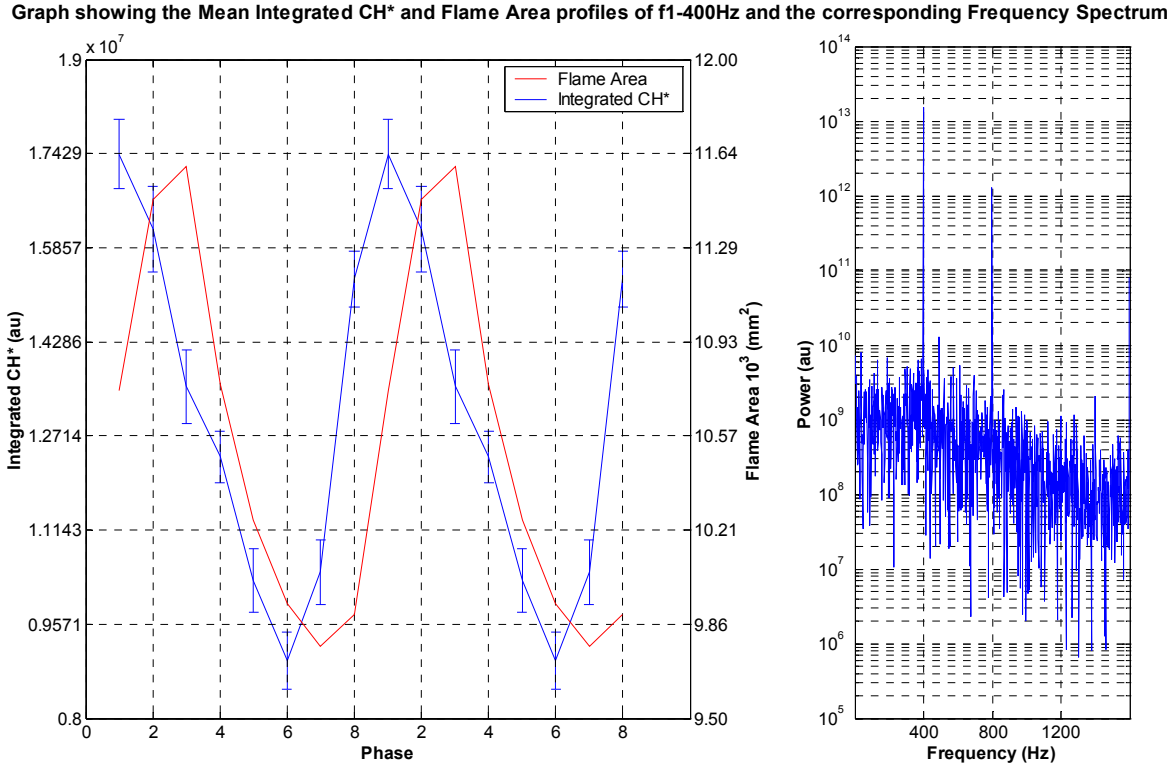

Figure 7-29 Mean Integrated CH* profile for f1-400Hz with corresponding Frequency Spectrum. The phase corresponds to that of the CH* images.

Regarding the Abel deconvoluted images phase 1 is clearly the peak of the heat release fluctuation. The structure is horizontally rectangular with hot spots at each end extended from the flame structure bottom to top. A small tail can be seen extending towards the annulus. This position coincides with the peak of inlet vy. In Phase 2 the effect of decreasing inlet vy is clear as the structure begins to retreat to the dump plane. The hot spots have become less intense and smaller. The structure has started to burn upstream along the inlet flow structure towards the annulus. Phase 3 corresponds to a decreasing vy and low vx and vz velocities. The hot spots are now indistinguishable from the overall flame structure which has lost its rectangular shape. Severe recirculation of the

flame is evident in the CRZ. The top of the flame structure is now arced inwards. The structure has moved further upstream towards the annulus along the inlet flow structure. By phase 4 vx and vz are minimums, and vy has again decreased dramatically. The flame structure has begun to retreat radially as the extremities begin to move inward. The recirculated aspects due to the CRZ are also weaker in intensity. Conversely as the flame structure becomes more compact the intensity of the flame has increased (60mm axial position). The bottom of the flame structure has started to bulge. Phase 5 is as phase 4 but the extremities have retreated radially inwards. Both vy and vz are minimums and vx has only marginally increased. Phase 6 shows further radial and axial retreat of the flame structure alongside a drop in intensity. A slight bulge is evident on the bottom of the flame structure adjacent to the inlet flow structure which corresponds to a slight increase of vx and vz. Phase 7 shows a large change of the flame structure. The radial extremities are absent and the overall shape is indicative of the large increase in inlet vy and resembles the rectangular shape previously described only smaller in aspect. The intensity has also increased over that of phase 6. Finally in phase 8 the structure has been pushed downstream and outward by the increased inlet flow. The extremities of the structure show a large increase in intensity as the reaction rate increases.

The flow field images of phase 1 show a CRZ, inlet flow structure and a IRZ as seen previously. Up to phase 3 the IRZ develops a flat horizontal aspect to its upstream portion which in turn causes the inlet flow structure to adopt a horizontal aspect. By phase 3 a small second recirculation zone can be seen developing on the inner shear layer as in f1-200Hz. This new recirculation zone does not develop into a large structure as previously seen. In phases 4 and 5 this feature moves downstream along the inner shear layer while the inlet flow structure develops a kink in it close to the annulus as the flame structure retreats. The CRZ up to this point appears not to vary and the IRZ continues to cause the inlet flow to become horizontal. In phases 6 to 8 the new recirculation zone and the original begin to merge. The IRZ starts to stretch upstream along the inner shear layer which causes the IRZ to become elongated and less horizontal in aspect. This in turns means the inlet flow begins to straighten. In phases 9 and 10 the zones have merged into a single large recirculation zone which extends down the inner shear layer which causes the inlet flow to deviate radially outwards.

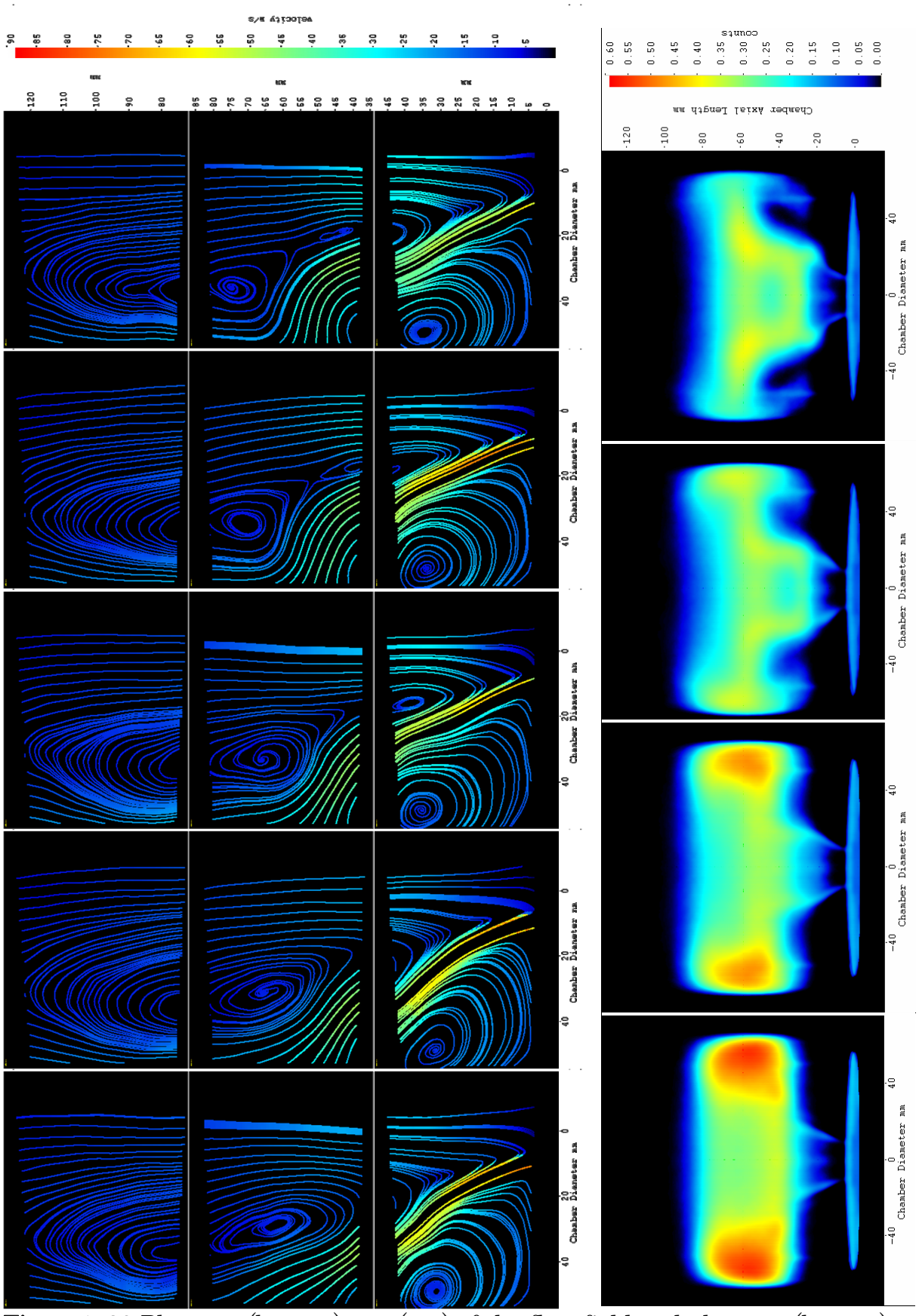

Figure 7-30 Phases 1 (bottom) to 5 (top) of the flow field and phases 1 (bottom) to 4 (top) of reacting field of f1-400Hz. The flow images were recorded in the 'CRZ', 'Flame Zone' and 'URZ' imaging areas.

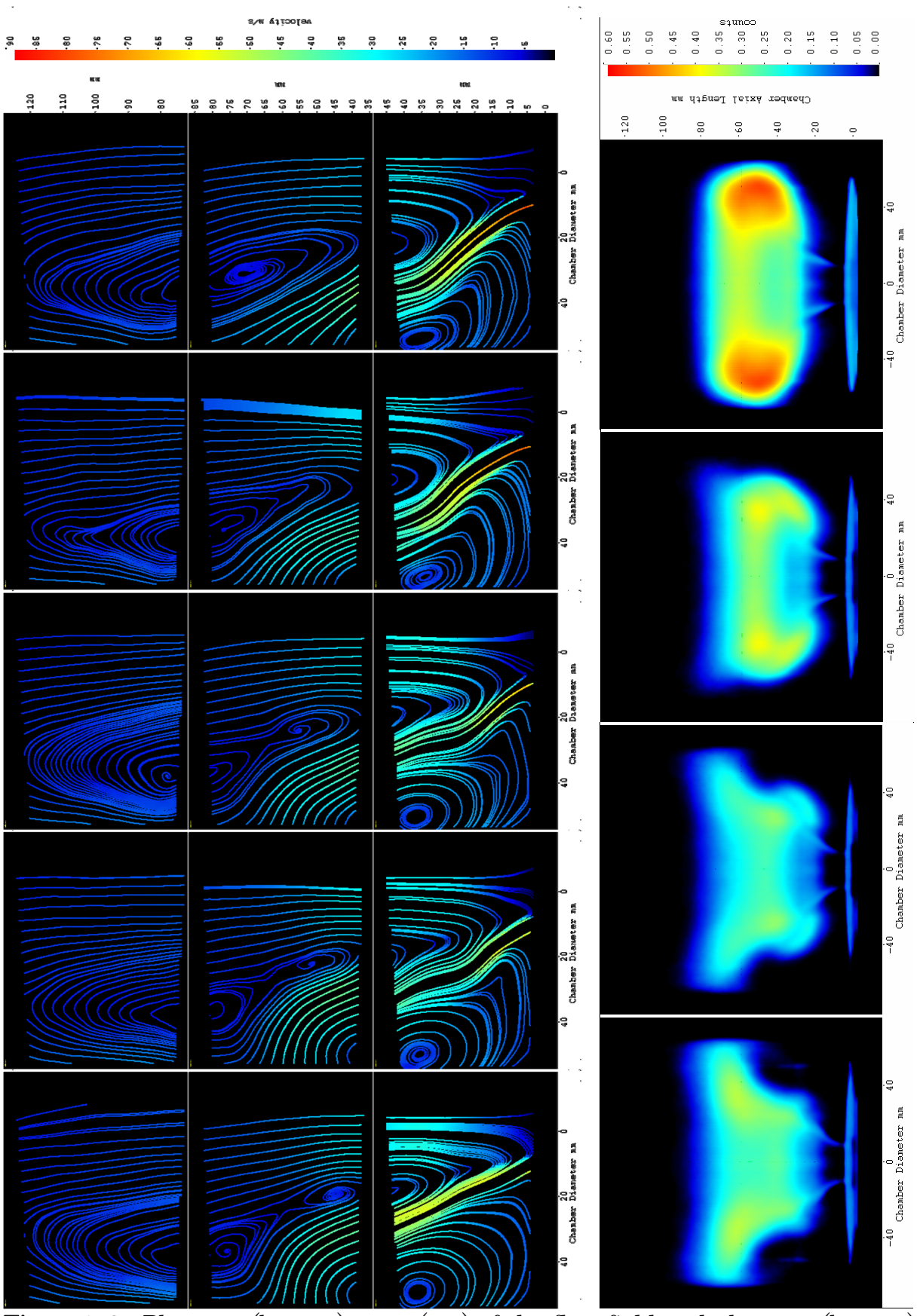

Figure 7-31 Phases 6 (bottom) to 10 (top) of the flow field and phases 5 (bottom) to 8 top) of reacting field of f1-400Hz. The flow images were recorded in the 'CRZ', 'Flame Zone' and 'URZ' imaging areas.

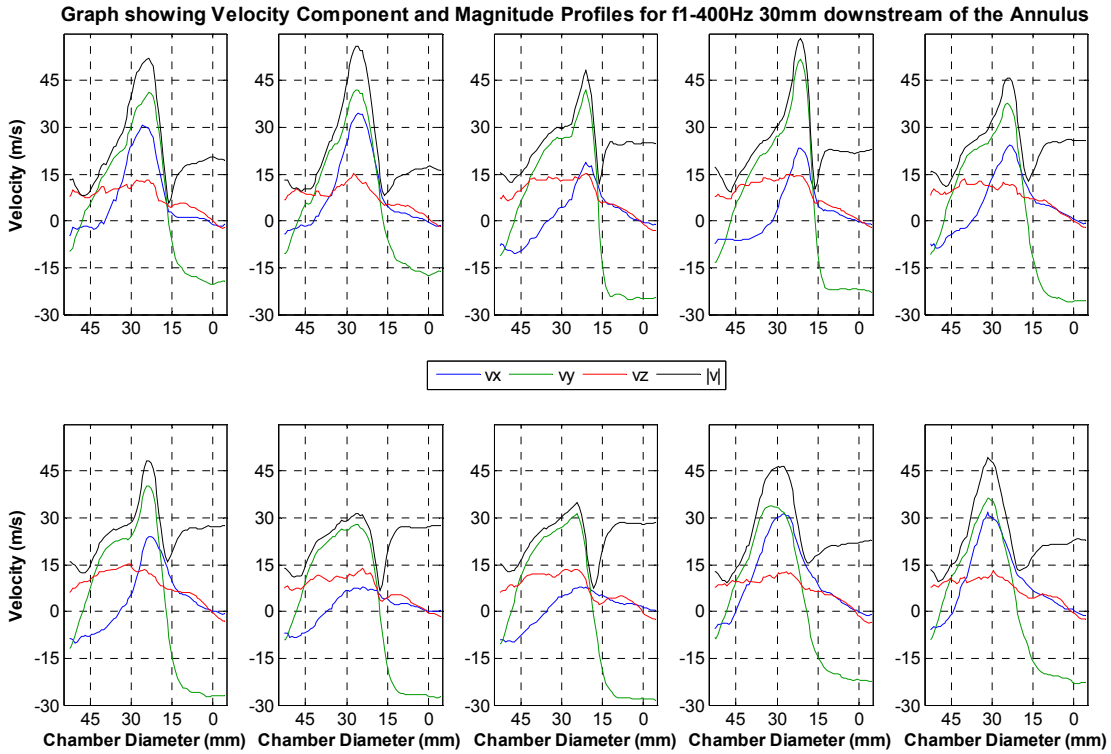

Figure 7-32 Velocity Profiles of f1-400Hz along a line 30mm downstream of the Annulus. Taken from mean vector fields from the imaging area 'CRZ'. The top row consists of phases 1 to 5 from left to right. The bottom row consists of phases 6 to 10 from left to right.

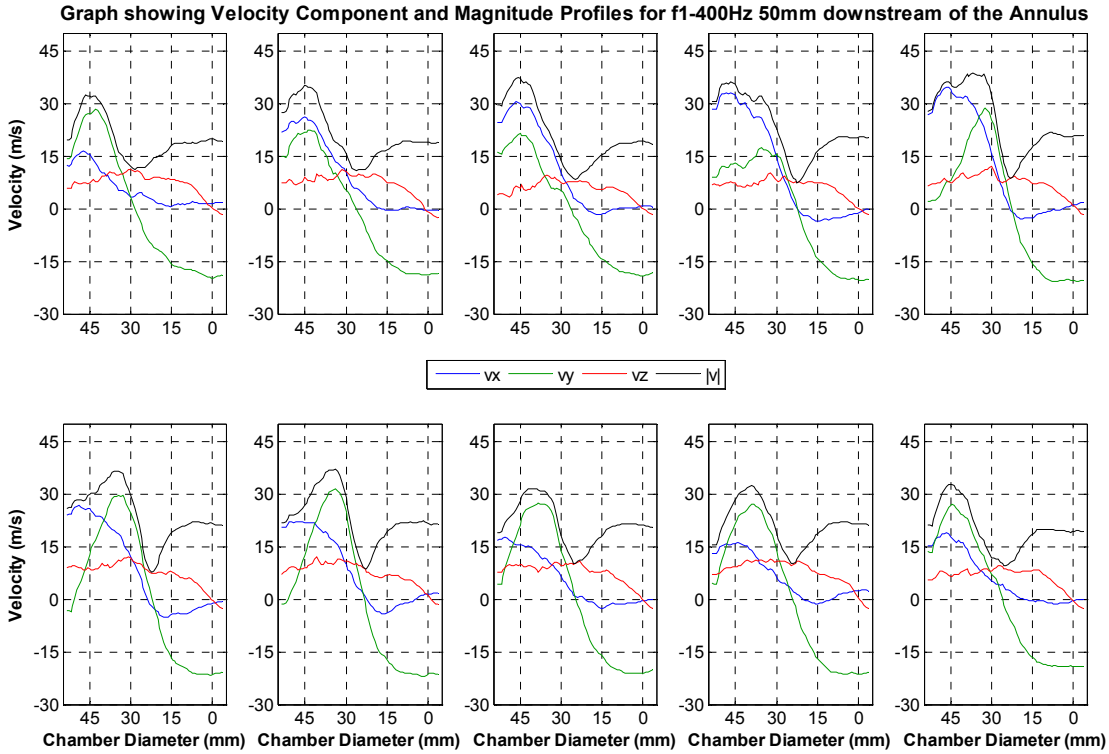

Figure 7-33 Velocity Profiles of f1-400Hz along a line 50mm downstream of the Annulus. Taken from mean vector fields from the imaging area 'Flame Zone'. The top row consists of phases 1 to 5 from left to right. The bottom row consists of phases 6 to 10 from left to right.

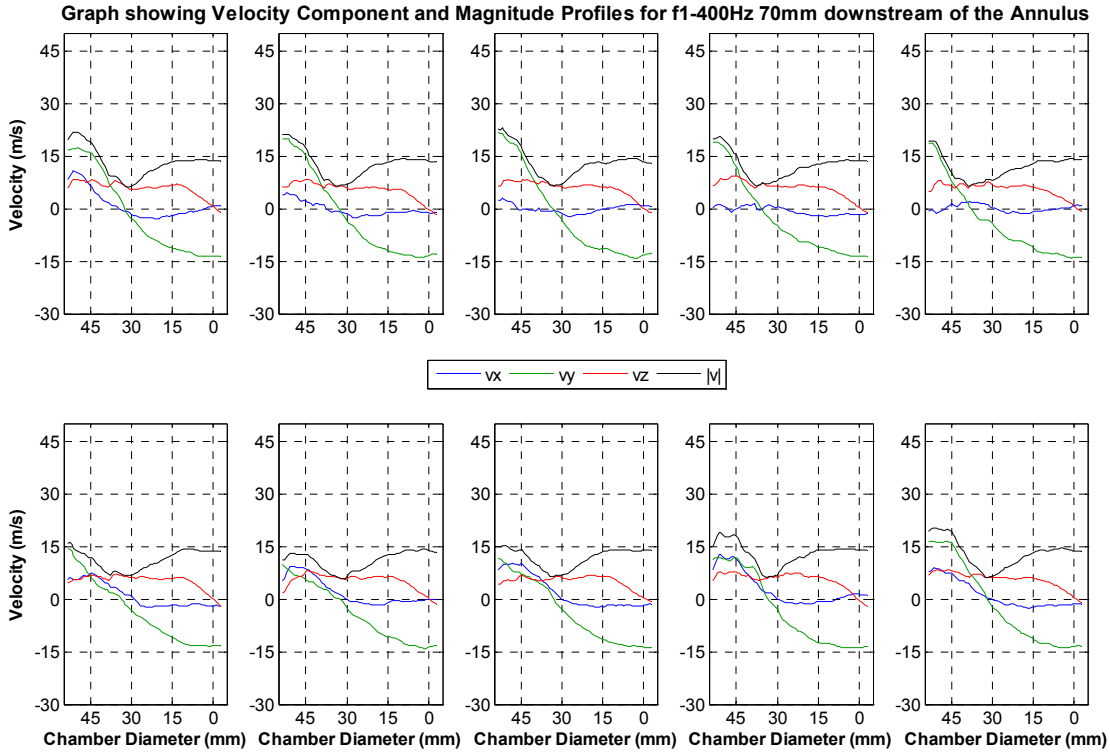

Figure 7-34 Velocity Profiles of f1-400Hz along a line 70mm downstream of the Annulus. Taken from mean vector fields from the imaging area 'Flame Zone'. The top row consists of phases 1 to 5 from left to right. The bottom row consists of phases 6 to 10 from left to right.

7.3.3 The Internal Recirculation Zone

The IRZ is of the axisymmetric type and also exhibits the formation of a second recirculation of a size considerably smaller than previously discussed. The absolute values of vy on the chamber centreline are plotted in Figure 7-35 at three axial positions. The oscillation of abs vy is greatest at the 30mm position and decreases substantially with downstream distance. As before the magnitude of abs vy oscillation is greatest at the 30mm position and decreases with axial distance until it is completely damped at 70mm.

The instantaneous vector fields were sampled on the chamber centreline 30mm, 50mm and 70mm downstream from the annulus. The extracted data was then analysed to produce each components' frequency spectrum in Figure 7-36. The vx component is consistent at all three positions. The strongest signal is centred around 1 KHz and remains approximately equal in strength at the three positions. Sub 200Hz and frequencies greater than 1.8 KHz are present and become stronger downstream. The spectra of vy at 30mm show two distinct signals at 400Hz and 1.6 KHz. At 50mm the 1.6 KHz signal is indistinct while the 400Hz has become smaller. At 70mm neither is detectable and the spectrum resembles that of vx with a collection of signals peaking around 1 KHz. The 1.6 KHz signal was detected in the inlet spectra of vy in Figure 7-26. The tangential component vz is similar to vx. At all positions there is a collection of signals centred about 1 KHz. In addition weaker collections are to be found below 200Hz and above 1.8 KHz. These features all become stronger with downstream distance indicating the amplitude of the tangential velocity of the IRZ becomes larger downstream of the combustion. Key frequencies highlighted by these spectra are 1 KHz, 1.6 KHz and 2 KHz. Firstly the 1.6 KHz signal detected in the vy spectra at the 30mm position coincides with the second longitudinal mode of the chamber of 1.68 KHz (Table 5-9). Secondly, using Table 5-2 and Table 5-9 the first and second longitudinal mode of the inlet correspond to 1.039 KHz and 2.079 KHz for pure air and 1.157 KHz and 2.314 KHz for a combustible mixture. These compare well with the detected frequencies of 1 KHz and 2 KHz.

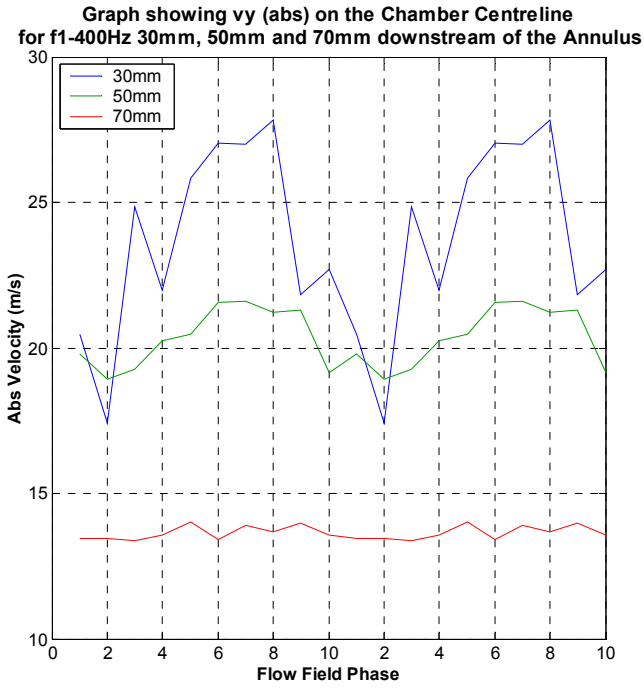

Figure 7-35 Graph showing Peak Centreline vy (abs) values against Phase for f1-400Hz within the IRZ at 30mm, 50mm and 70mm axial positions.

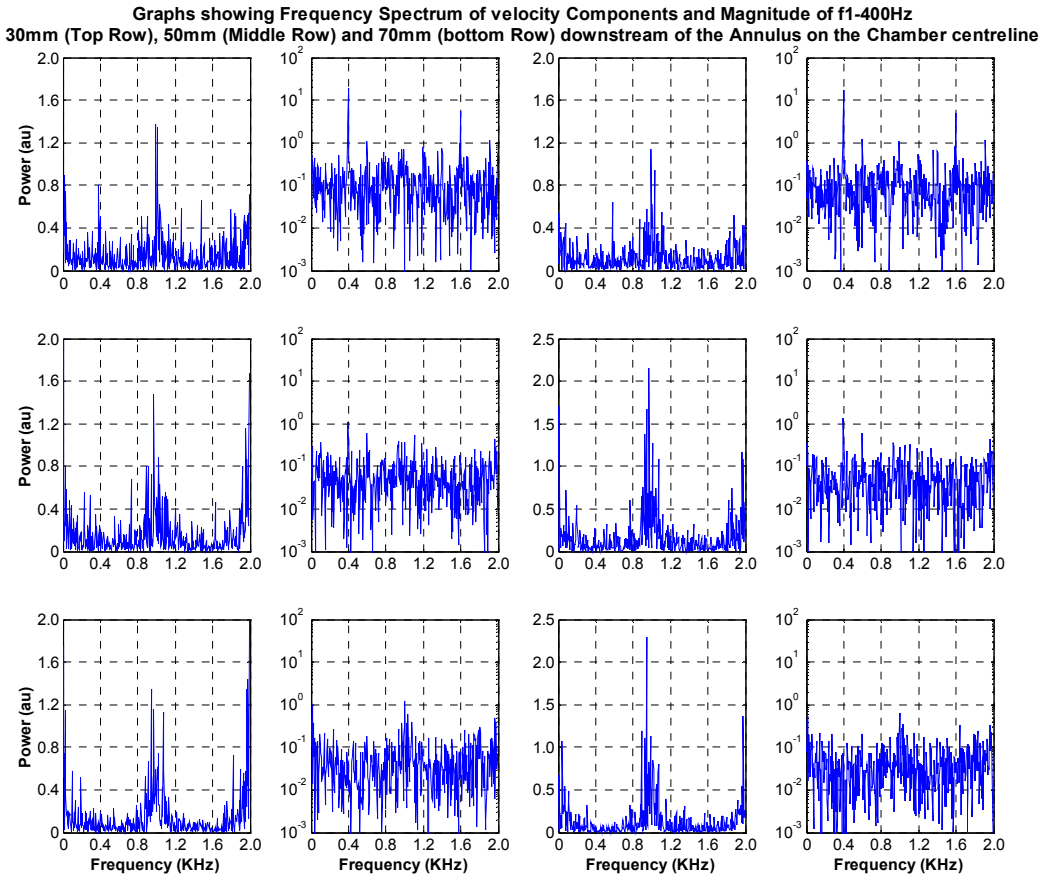

Figure 7-36 Frequency Spectra of f1-400Hz extracted from 30mm, 50mm and 70mm downstream of the annulus on the chamber centreline. Vx corresponds to the left column, followed by vy, vz and |v| is the right column.

7.4 Comparison of Methane Structures

7.4.1 Inlet Instability Profiles

The behaviour of f1 (and f10) exposed to the three different frequencies has revealed different reacting and flow structures. It is clear that the reaction of combustion to a particular frequency affects the inlet flow rate. The respective integrated velocity components have been normalised by the values in Table 7-1. These plots easily show the respective amplitude of oscillation for each component for the three frequencies. The respective behaviour of the three components for each frequency has previously been discussed. From Figure 7-37 and Table 7-1 it is clear that the amplitude of |v| oscillation is significantly reduced for f1-200Hz. This is partly attributed to the ability of the inlet flow to pass through the siren at the different perturbation frequencies. In order to control the pressure perturbation profile various features were incorporated into the design (Chapter 5.1). However due to delays in the manufacture of the burner and test cell development insufficient time was available to optimise the experimental conditions to achieve the same profile. In addition the response of the combustion is also a factor. The amplitude response of a premixed flame exposed to low frequency oscillations can be quite large. With increments of frequency the flame is unable to respond and as such the position and reaction become less variable. This will affect the pressure response of the flame which will in turn affect the inlet flow.

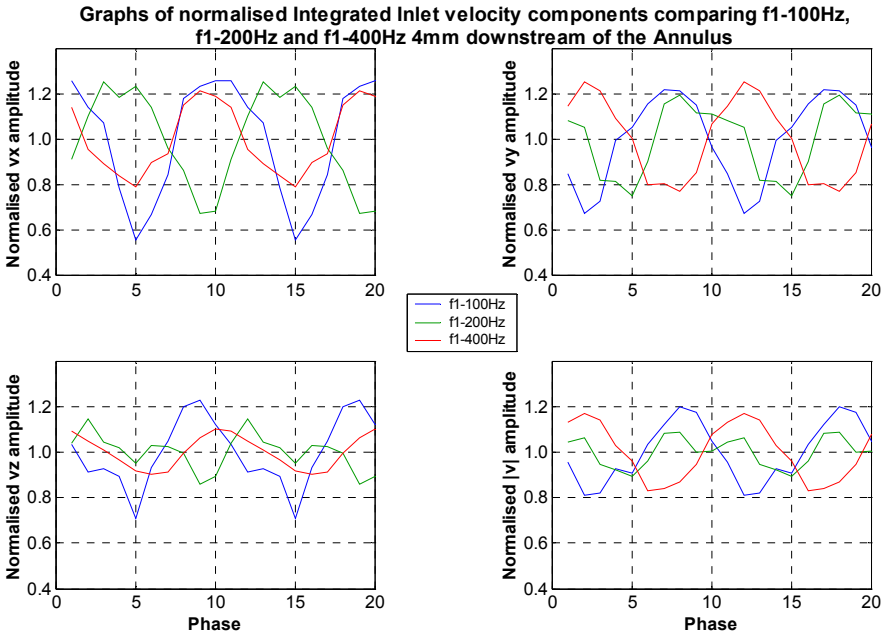

Figure 7-37 Graphs showing normalised integrated velocity components and magnitude comparing f1-100Hz, f1-200Hz and f1-400Hz of the inlet. Top Left: vx. Top Right: vy. Bottom Left: vz. Bottom Right: |v|.

F1-100Hz and f1-400Hz inlet conditions are similar regarding amplitude and profile shape of |v|. For the individual components vx and vy the profiles are similar whereas the vz profiles are quite different. The amplitudes of the respective components are greater for f1-100Hz. The amplitude of the |v| profile for f1-200Hz is approximately half that of the other frequencies. The amplitudes

of the profiles of vx and vy are less than those of f1-100Hz but greater and equal to those of f1-400Hz. The amplitude of vz is equal to that of f1-400Hz. The reduced |v| amplitude is therefore attributed to the phase delay.

The phase delays among the velocity components for f1-100Hz is vz lags vy by 1 phase and vx lags vy by 2 phases. For f1-200Hz both vx and vz lag vy by 5 phase positions. Finally for f1-400Hz vz lags vy by 9 phases and vx by 8 phases approximately. Respective phase lag has increased as the perturbation frequency has increased. These are attributed to the impact of combustion causing pressure gradients affecting the magnitude and distribution of |v| among the three components.

Flame	vx (m/s)		vy (m/s)		vz (m/s)		|v| (m/s)		Pu(%)
	Mean	rms	Mean	rms	Mean	rms	Mean	rms	
f1-100Hz	23.23	6.89	46.09	9.64	28.66	5.72	60.80	9.21	15.14
f1-200Hz	21.40	7.16	46.77	10.87	28.09	5.22	60.89	7.44	12.21
f1-400Hz	20.84	4.86	47.72	10.70	28.34	4.02	60.46	9.71	16.05

Table 7-1 Table detailing the integrated mean and rms inlet velocity components. Also the excitation defined as the rms|v| / mean|v|.

7.4.2 Combustion Instabilities

A comparison of the mean integrated CH* profiles and flame area profiles for f1 is shown in Figure 7-38. The sinusoidal nature for both heat release and flame area of f1-100Hz is clearly established. The heat release curve for f1-200Hz has a much smaller amplitude due to the twin peak nature of the |v| profile. This also results in the reaction rate being high compared to f1-100Hz (greater cycle mean). This observation is repeated when considering the flame area profiles. The behaviour of f1-200Hz can be partly attributed to the velocity component phase lag. As vy increases more reactant is supplied. As this is oxidised an increase of pressure gradient close to the annulus can be expected. Unlike the 100Hz case where the combustion can react sufficiently to the perturbation it is speculated here that the combustion process can not react sufficiently to the perturbation. This gradient then causes the development of the second recirculation cell which causes the flow to be redistributed from vy to vx and vz after a small delay. This supplies additional reactants into the chamber which oxidise around the new cell maintaining a high reaction rate for the chamber. The heat release curve for f1-400Hz is sinusoidal with an amplitude equivalent to f1-100Hz but with a higher cycle mean. This is not true when considering the flame area profile which has a much smaller amplitude, but a much greater cycle mean. At 400Hz the ability of the combustion to respond would be significantly diminished and as such the perceived movement and reaction of the combustion should approach a quasi-steady value, however when the flow field dynamics and local turbulence are considered this assertion can not be maintained. The mean reacting and flow field images are more difficult to directly interpret than either the 100Hz or 200Hz cases regarding the combustion response. For all cases investigated the mean flame area increases with perturbation frequency which is not seen in the heat release profiles. This indicates the increased stretching and turbulent transport of the flame.

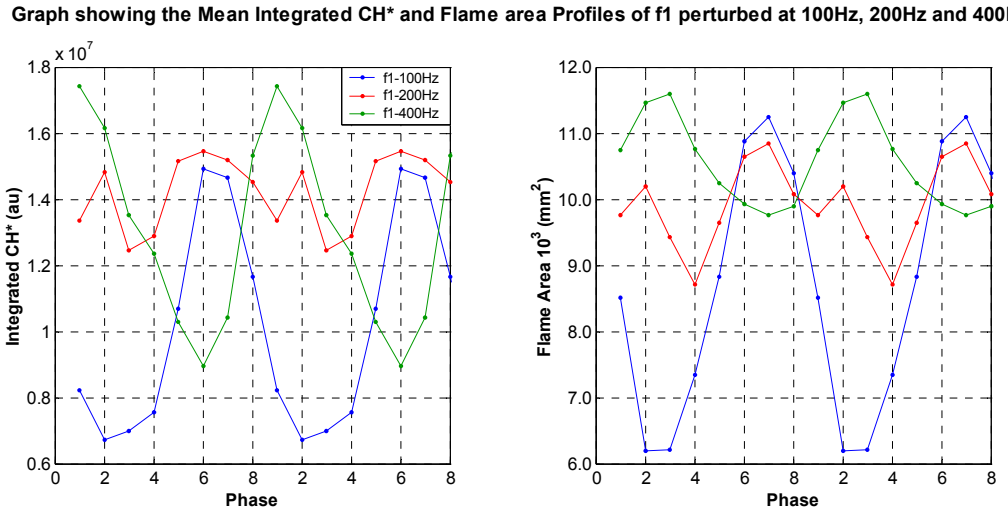

Figure 7-38 Graph comparing mean integrated CH* profiles and flame area for f1-100Hz, f1-200Hz and f1-400Hz.

The profile shapes of heat release and flame area for the respective perturbation frequencies compare well and indicate that the heat release rate behaviour is controlled by the flame area. This in turn is a function of the inlet flow rate; CRZ and IRZ which will causes flame wrinkling through the generation of shear layer turbulence. In addition the strain imposed upon the flame will influence the reaction rate through local Markstein numbers. This is exhibited by the f1-400Hz data whereby the reaction rate profile has a large amplitude but the flame area profile has a more modest amplitude. This discrepancy can be explained by consideration of local strain effects with can cause increases in reaction rate and extinction.

7.4.3 IRZ Behaviour

The difference in reacting structures can be attributed to the drastically different behaviour and structure of the IRZ in each case, which responds to the perturbation frequency and inlet conditions. Changes of vortex breakdown behaviour as described in Chapter 2.1 can be attributed to variations of inlet swirl, Reynolds number and or axial pressure gradient. Axial movement of the axisymmetric bubble have been reported with swirl variations for a given Reynolds number.

Using the mean vector fields from the imaging area 'Annulus 3D' the vectors 4mm downstream of the annulus a profile 4mm long across the inlet flow structure was sampled. The velocity components vy, vz and the magnitude |v| were extracted. The mean ratio of vz/vy over this small profile for each phase was calculated. In addition the Reynolds number was calculated for each phase by calculating the mean velocity magnitude across the profile. The length scale used was the Annulus size (4mm) and viscosity of Table 5-8. The profile of vz/vy was then divided by the profile of Reynolds number. The resulting profile indicates when the effective swirl increases regarding vortex breakdown. This has been done for the three frequencies shown in Figure 7-39 to Figure 7-41.

For f1-100Hz the resulting profile is peaking in phases 1 to 4. These phase positions correspond to the end of an oscillation and the growth of the next

oscillation. For f1-200Hz the profile is in ascendancy from phase 2 to 6. These phases correspond to the formation, growth and then start of downstream movement of the second cell of the IRZ. For f1-400Hz phases 5 to 10 are when the profile is in ascendancy. These phase positions correspond to the end of an oscillation and the start of the new oscillation. The peaks of the Reynolds normalised vz/vy ratios indicate the start of the new oscillation and correlate to large structural changes of the inlet flow and the IRZ. The profile for f1-100Hz has the largest absolute values of normalised vz/vy ratio which indicates the largest range of inlet swirl. Figure 7-11, Figure 7-23 and Figure 7-35 show the amplitude of oscillation of the IRZ for the different frequencies. These show that the IRZ for f1-100Hz has a modest amplitude at 30mm, an increase at 50mm, then a small decrease at 70mm. This indicates that the IRZ is strongly oscillating axially over a large distance. F1-200Hz has a large amplitude at 30mm which then decreases very strongly at 50mm and 70mm. The same trend is evident for f1-400Hz. This indicates the axial oscillations are weaker. The weakening of IRZ axial oscillation can therefore be partly explained by the Reynolds normalised vz/vy plots and reduced amplitude of swirl oscillations. What are unknown are the chamber pressure gradient characteristics.

The appearance of a second recirculation zone within the IRZ has not been explicitly explained. From Chapter 2.1.2 a second recirculation zone within an axisymmetric bubble has been observed previously however the reasons why were not found and finally attributed to the experimental parameters. Examination of Figure 7-13 for f1-200Hz show vx and vz have a phase lag of 5 phase positions (half a cycle) behind vy. This mean as vy is a minimum and the flame retreats upstream there is a surge of radial and tangential velocity causing the large radial movement of the flame and keeping the heat release high as can be seen. For f1-400Hz the second cell of the IRZ is not as large. The profiles of Figure 7-25 show a phase delay greater than 5 phase positions meaning that the effective swirl is reduced as vy is increasing. This means the second recirculation cell is more modest

As a point of conjecture the axial pressure gradient affects the formation of the reverse flow that characterises vortex breakdown. If the axial pressure gradient changes spatially and in value, interaction with the inlet flow could result in a very rapid radial redistribution of the inlet flow as has been seen, causing a second recirculation zone to be formed. This can not be proven as pressure transducers can not been fixed into the fused silica.

The IRZ of each condition investigated is clearly rotating around the chamber central axis in the same direction as the inlet flow. It has been shown that the reversed flow region oscillates in a longitudinal sense in accordance with the imposed perturbation frequency up to a downstream distance. The tangential velocity frequency spectra have shown that the IRZ is also rotating around the central axis in an unsteady manor. This analysis is limited to the temporal resolution in each case. The 400Hz perturbation flow reveals a large 1 KHz frequency, a reduced 2 KHz frequency and smaller sub 200Hz frequencies. The 200Hz perturbed flow exhibits only the 1 KHz frequency and sub 200Hz group and finally the 100Hz perturbed flow only the latter. Although the presence of all three frequency groups can not be confirmed experimentally as all three exhibit

the low frequency group and both the 200Hz and 400Hz perturbed flows share the 1 KHz signal it is reasonable to expect all three frequency groups to be present. The sub 200Hz frequencies detected do not correspond to any acoustic mode associated to the inlet or chamber at operating conditions. The 1 KHz and 2 KHz frequencies do correspond to the first and second longitudinal modes of the inlet, 1.039 KHz and 2.079 KHz. As the true modes of the whole combustor are a product of the resonances of the chamber and inlet it is reasonable to expect that the inlet modes will extend into the chamber and that inlet modes can be excited inside the chamber. Conversely the chamber first and second longitudinal modes are 840Hz and 1.680 KHz and it is possible for these to be shifted higher within the IRZ for the vz component. The simplified method used and assumptions made to derive the acoustic modes is also not as accurate as a 3D Helmholtz acoustic solver which must also be acknowledged.

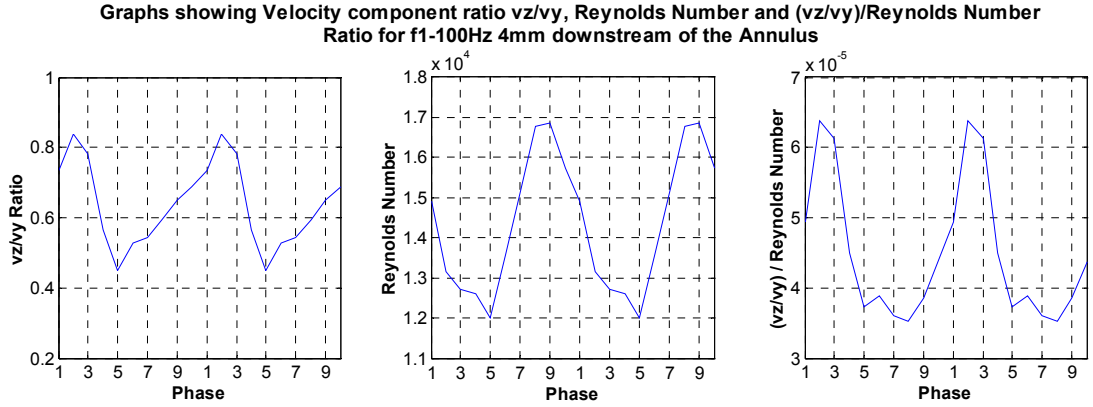

Figure 7-39 Left: Graph showing vz/vy ratio change over one oscillation. Centre: Graph showing Reynolds number change of one oscillation. Right; Graph showing Reynolds normalised vz/vy ratio. All for f1-100Hz 4mm downstream of the annulus at a 4mm profile 13mm from the Centreline.

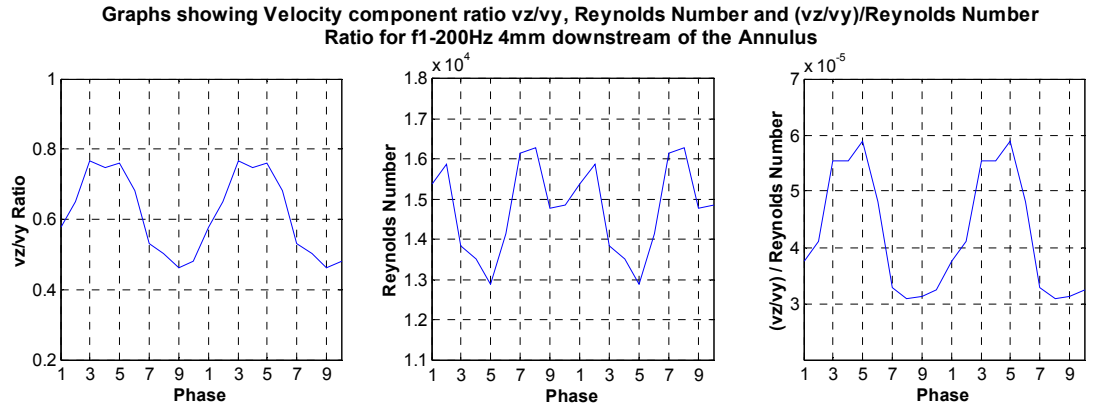

Figure 7-40 Left: Graph showing vz/vy ratio change over one oscillation. Centre: Graph showing Reynolds number change of one oscillation. Right; Graph showing Reynolds normalised vz/vy ratio. All for f1-200Hz 4mm downstream of the annulus at a 4mm profile 13mm from the Centreline.

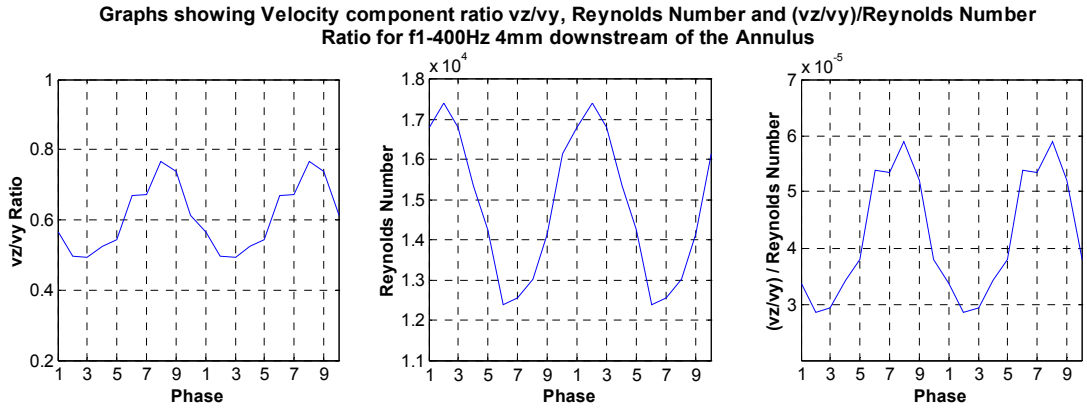

Figure 7-41 Left: Graph showing vz/vy ratio change over one oscillation. Centre: Graph showing Reynolds number change of one oscillation. Right; Graph showing Reynolds normalised vz/vy ratio. All for f1-200Hz 4mm downstream of the annulus at a 4mm profile 13mm from the Centreline.

7.5 Comparison of Hydrogen Blended Methane Structures

The 20% hydrogen blended methane flow, f10, was also exposed to the same perturbations as f1. The mean phase locked reacting field and flow field images are presented in Appendix B along with corresponding velocity profiles and the Integrated CH* and flame area graphs. Both of these diagnostics show a very similar reacting and flow field structure for f10 compared to f1. The deconvoluted CH* images do show a subtle difference to the methane cases in that the mean structures appear slightly more compact and more angular in aspect. There is also increased reaction along the inlet flow attached to the annulus. As the flow field images reveal the same features and IRZ behaviour a direct comparison is not presented.

The mean integrated CH* profiles and flame area profiles of f1 and f10 are compared for the three frequencies in Figure 7-42. For the 100Hz perturbation frequency the mean integrated CH* profile is the same in waveform with f10 only marginally smaller in value. The flame area profile is of the same waveform as that of f1, however it is consistently smaller through the oscillation. At 200Hz the integrated CH* profiles are of the same form but f10 is consistently less in value. The same is true for the flame area profiles. At 400Hz the flame area profiles show the same trend but f10 is consistently smaller in size. The integrated CH* profiles show the same oscillatory behaviour but the difference between the profiles is no longer constant. The profiles share the same minimum value at the same phase. However there is a large difference at the respective peaks.

Interpretation of f10 and a comparison with f1 is difficult. As f1 is pure methane the chemiluminescence signal is proportional to heat release rate. The signal is created by the carbon within the methane. The addition of hydrogen will increase the hydrogen related radicals (such as OH and H) but the impact of hydrogen addition upon the collected chemiluminescence signal is unknown. The inclusion of hydrogen reduces the amount of methane for the same equivalence ratio therefore the expected amount of CH* signal should decrease. Conversely, the addition of hydrogen should increase the adiabatic flame temperature and the heat release rate should therefore increase. This trend is not observed from the

collected CH* signal. The effect of an increased flame temperature upon the reaction mechanism of CH* is also unknown. Therefore direct comparison of this data is not possible. Either a chemical model that can predict the relative concentrations of CH* or an experimental diagnostic that can obtain temperature measurements should be used to adjust the position of the integrated CH* profile of f10 to f1 could be used for this correction. Additionally the use of simultaneous imaging OH* and CH* could be used to obtain a single representation indicating the flame area.

Following the discussion in Chapter 2.5 the addition of 20% hydrogen will not have an impact upon the laminar flame speed rather an effect upon the turbulent flame speed can be expected using Figure 2-20. As the flow considered here has $\phi = 0.8$ the content at which hydrogen increases the turbulent flame speed should be less than 20% after inspecting Figure 2-20. This would indicate an increase of the global reaction rate. The inclusion of 20% hydrogen does not change the overall dynamics of the instabilities investigated here as there is, as mentioned, only a subtle difference in the mean reacting structures and no detectable difference in flow structures. The subtle difference of the reacting structures could be due to the increased oxidation of carbon species and increased flame speed resulting in more compact structures. As discussed in chapter 2.5 the hydrogen content although not immediately detectable with the used diagnostics should improve the emission of CO and UHC through improved oxidation by the increased radical pool and improved extinction strain rates for the cases investigated.

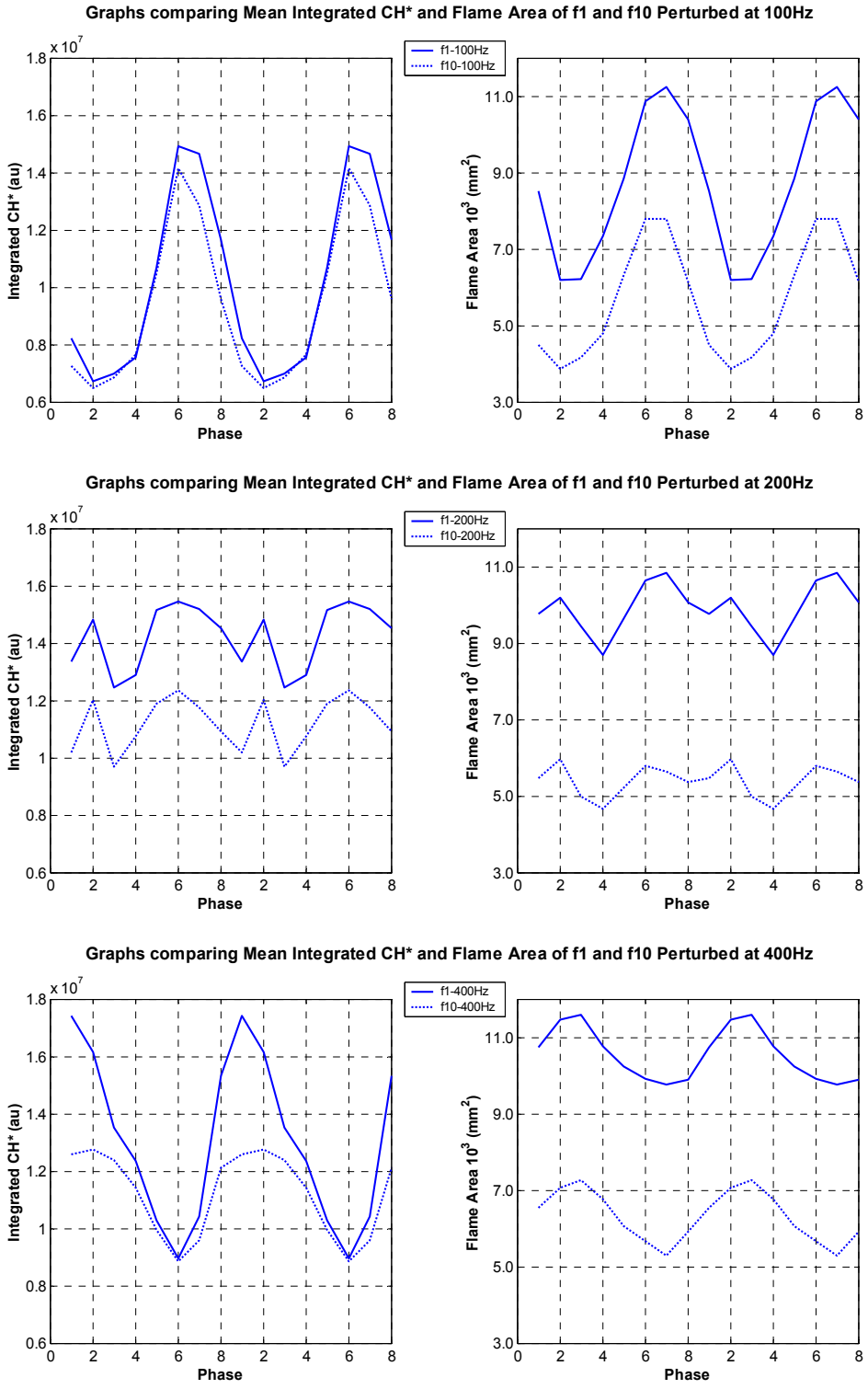

Figure 7-42 Graphs comparing mean integrated CH* profiles and flame area profiles of f1 and f10 perturbed at 100Hz, 200Hz and 400Hz.

8 SHEAR LAYER TURBULENCE

The shear layers are important as they are interfaces where hot burnt products interact and mix with fresh gas. These shear layers are created by the vortex breakdown and dump configuration creating recirculation zones which transport said gas to the shear layers for mixing. These regions are also where the transported radicals begin the oxidation reactions when in contact with the fresh gas. This is extremely important when moving downstream of the annulus. The local turbulent conditions within these shear layers will affect the combustion as covered in Chapter 3.1 through variations of strain and mixing. Defining the turbulence however is a complex task as the gas is not a homogenous mixture and the turbulence will vary spatially and temporally. The following description is presented only for f1.

8.1 Tools for Characterising Turbulence

Turbulence can be isotropic or anisotropic and homogeneous or inhomogeneous. Most practical devices will be inhomogeneous and anisotropic. The former predominantly used in fundamental investigations or simulations. Homogeneous turbulence is where the measure of fluctuation gives a result which is the same spatially. Typically the RMS can be used for component comparison. The definition of isotropic turbulence is that there is no directional preference – it is the same in all directions. This can be determined by inspection of the Reynolds stresses. The principle values of the Reynolds stress tensor are invariant with changes of the coordinate system used. The normal stresses are equal and the off diagonal components (shear stresses) are equal to zero. Conversely anisotropic turbulence can be detected by determination and comparison of the normal stresses, whether they are not equal, or that the off diagonal components are equal to zero. The Reynolds stresses themselves are the mean forces (per unit area) acting upon the mean flow by the turbulent fluctuations.

As in Chapter 3.1, turbulence can be defined as the fluctuating component of single representation with the ensemble mean subtracted, Eq 3-1. Using this definition the ensemble of fluctuating components can be characterised.

The simplest characteristic of turbulence is to calculate the RMS of the velocity components. The RMS is a single value which represents a measure of the deviation of values within an ensemble from a mean. A lot can be inferred from the RMS and comparisons among the velocity components yields good analysis. However the RMS does not indicate the range of fluctuating values, the direction and not the probability of the fluctuation to be any value within that range.

The range and probability of possible fluctuations at a point is fully characterised with a Probability Density Function (PDF). A PDF is a histogram with the probability of the fluctuating values being between values corresponding to a bin size. The integral of the PDF over all values is equal to unity. This implies that the fluctuation will be of a value within the PDF velocity range.

Typically a PDF of isotropic turbulence will be single modal centred on a velocity value of zero for all components. However it is not uncommon for bimodal or multimodal profiles to be observed in any real combusting device. This indicates a periodic and antistrophic aspect to the turbulence. As a PDF is defined at a single spatial point for each velocity component it is very cumbersome to compare different fluctuating velocity components at different spatial locations. Therefore the shear Reynolds stresses $\rho\left(\overline{u_i' u_j'}\right)$ (not Favre averaged and density omitted) can be used to determine the type of turbulence, either an image or as profiles and show the degree of anisotropy within the flow.

A frequency spectrum of the turbulent components will also yield information if any periodic fluctuation is present. This can lead to the identification of a fluid dynamic structure within the flow which could be created by an aspect of the device geometry. The identification of the integral and Kolmogorov scales (length and time) can be estimated with the use of SPIV and LDV but care must be taken when applying these to non-homogeneous anisotropic turbulence. These represent the largest and smallest scales associated to the eddies of turbulence. The energy spectrum will yield information of which size scale contains the most energy (typically within the inertial range).

This information will characterise the turbulence and therefore will allow the impact upon combustion to be determined.

8.2 Analysis Performed

For this work RMS values have been calculated and will be presented. In addition a selection of PDFs have been extracted and the Reynolds stresses calculated. This has been done for profiles and positions very close to the annulus. This decision was made to concentrate on the turbulence close to the shear layers, which is of prime importance. The analysis undertaken is unable to separate between fresh and burnt gas, and therefore can not account for effects of intermittency and dilation. Therefore any comparison of this turbulent analysis with modelled data should be done on this combined basis. The analysis is also spatially specific regarding the combustor. A typical analysis, had identification of the flame front been possible, would have been based upon the fluctuation component of vectors corresponding to the instantaneous local equilibrium position of the reaction zone.

Phase dependent RMS profiles have been plotted for f1-100Hz, f1-200Hz and f1-400Hz at 4mm, 15mm and 30mm axial positions for all three velocity components and magnitude. These allow an insight into the location of shear layers and magnitudes of fluctuations during the imposed instability. This is equivalent to performing a triple decomposition.

$$u(t) = \overline{u} + u'(t) = \overline{u} + u''(t) + u_t'''(t) \qquad \text{Eq 8-1}$$

A cycle mean vector field is first calculated $\overline{u}$, and is then subtracted from each phase mean vector field to give the large structure of the fluctuation $u''(t)$. These two are then sequentially subtracted from each instantaneous vector field to yield a fluctuating vector field independent of the imposed perturbation, $u_t'''(t)$. This

ensemble is then sampled at a rate corresponding to 10 phase positions and an RMS calculated for each component. The RMS plots presented therefore represent the RMS of the triple decomposition of which is the turbulence, broken down into respective phases.

Using these fluctuating component vector fields PDFs bisecting the annulus have been created from the ensemble set at the same axial locations as the RMS profiles. Three points on each profile have been expanded for increased clarity. It must be noted that the number of samples at a maximum will be 1024 and could be less depending upon the number of erroneous SPIV image pairs. The PDFs have been calculated taking this into account so the integral is always unity. The bin size is 2.5ms^{-1}. It was also possible to create phase specific PDFs at a single point however the number of samples would be limited to approximately 100 which is insufficient for a PDF. Skewness and kurtosis profiles of component distributions are also presented. Care must be taken as these values will be affected by any spurious data. Positive values of skewness correspond to a axisymmetric tail extending to positive values, negative values the opposite. Positive values of kurtosis indicate the distribution is more prone to outlying values (a larger fluctuation) than a normal distribution, negative values the opposite. The calculation of kurtosis has had the value 3 subtracted (that corresponding to a normal distribution).

$$Sk = \frac{E\left(x-\bar{x}\right)^3}{\sigma^3} \; and \; \; k = \frac{E\left(x-\bar{x}\right)^4}{\sigma^4} \qquad \text{Eq 8-2}$$

The shear Reynolds stresses have been calculated for the mixed components to assess the isotropy or anisotropy of the turbulence. Profiles are presented at the same axial locations.

$$VRS_{i,j} = \frac{1}{N}\sum\left[\left(u(t)-\bar{u}-u''(t)\right)_i\left(u(t)-\bar{u}-u''(t)\right)_j\right] \qquad \text{Eq 8-3}$$

Finally limited turbulent frequency spectra are presented and analysed. These are treated in a separate section to explain how this was achieved.

8.3 Statistical Uncertainty

A statistical uncertainty analysis has been conducted regarding the collected SPIV data in Chapter 6.2.13. From this the uncertainty ranges around the sample mean that the true population mean will be within for various levels of confidence were presented. Graphs showing the relationship between RMS values and uncertainty range for different levels of confidence are presented in Figure 6-27. The implications of this regarding the turbulence analysis performed is that it is unknown if the correct population mean has been subtracted from the instantaneous samples. In addition it is unknown how much the sample means deviated from the population mean for the subtraction. Therefore the instantaneous turbulent fluctuating components presented here must be regarded with the same uncertainty range and confidence levels that were presented previously Chapter 6.2.13.

In order to quantify the uncertainty associated with the Reynolds stresses presented, Figure 8-1 has been created. For each instantaneous turbulent velocity component the corresponding phase RMS velocity component was used to generate the corresponding uncertainty range using the analysis presented in Chapter 6.2.13. The Reynolds stresses were then calculated with this uncertainty range added and subtracted to each respective velocity component. Where e_i is the uncertainty range for each component.

$$VRS_{i,j} \pm e_{i,j} = \frac{1}{N}\sum\left[\left(u_i''' \pm e_i\right)\left(u_j''' \pm e_j\right)\right] \qquad \text{Eq 8-4}$$

Multiplication of the terms reveals that the range of uncertainty is defined purely as $\pm\left(e_i e_j\right)$. This is because the mean of the errors multiplied by the turbulent components is zero for both positive and negative calculations.

$$\overline{e_i v_i''' + e_j v_j'''} \; = \; \overline{-e_i v_i''' - e_j v_j'''} \; = 0 \qquad \text{Eq 8-5}$$

Figure 8-1 shows profiles of the absolute variation of off axis Reynolds stresses associated with a 99% confidence interval for those presented in Figure 8-14. The uncertainty range away from the shear layers is low, $\pm 10 m^2 s^{-2}$ to $\pm 15 m^2 s^{-2}$, where as within the shear layers values up to $\pm 63 m^2 s^{-2}$ can be experienced as shown. As the uncertainty is location specific the range within the shear layers will decrease with downstream distance. For the Reynolds stresses presented in this work scatter plots are provided alongside Reynolds stress profiles, giving an indication for the absolute uncertainty range for a given Reynolds stress.

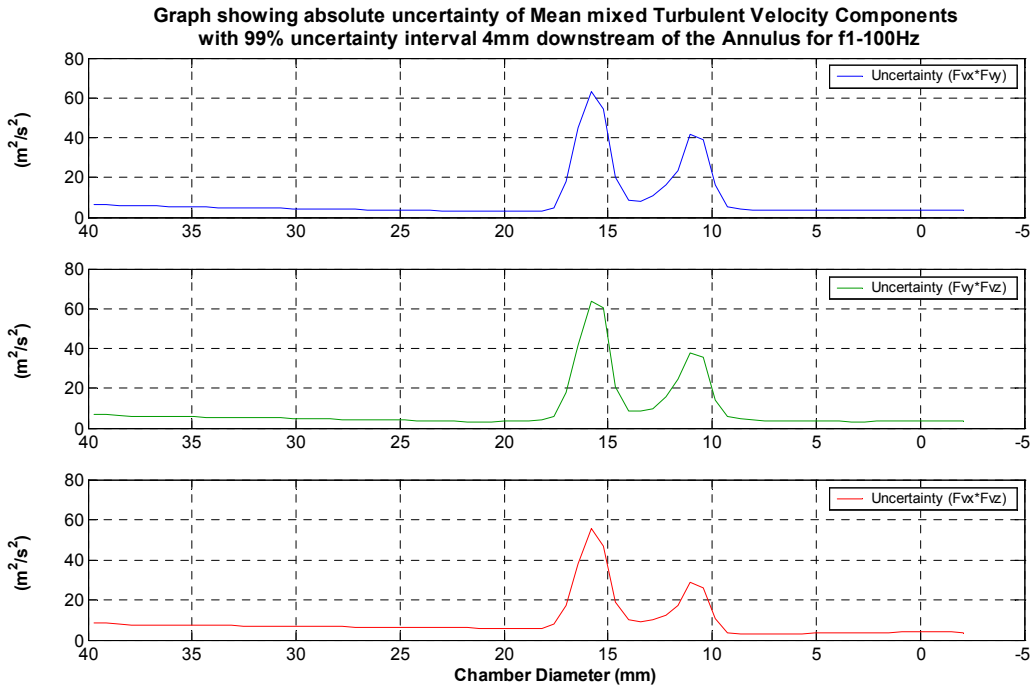

Figure 8-1 Absolute Uncertainty range for the off Diagonal (shear) Reynolds stresses for f1-100Hz along a profile taken 4mm downstream of the Annulus.

8.4 F1-100Hz

Figure 8-2, Figure 8-3 and Figure 8-4 show local RMS profiles for the velocity components and magnitude at 4mm, 5mm and 30mm downstream of the annulus. At 4mm two very thin high RMS value shear layers are present. All three components have strong spikes in these layers compared to either side of the respective shear layer. The peaks location is almost invariant through the oscillation remaining at 16mm and 1mm from the centreline. It is clear that all three components RMS values oscillate with the 100Hz perturbation. At the minimum of the oscillation (phase 3) the inner shear layer RMS components are all weaker than their outer shear layer counterparts. This trend continues through the oscillation but to a lesser extent as both shear layer RMS values grow. When the oscillation begins to ebb the inner shear layer RMS components decrease first as the outer layer RMS components remain high. Generally RMS vy is the largest component within both shear layers. RMS vx and vz are approximately equal. Outside of the outer shear layer RMS vz is largest followed by RMS vx and RMS vy. Within the inner shear layer RMS vy is the largest and RMS vx and RMS vy being equal.

At 15mm downstream all the components profile have become less smooth and are generally less in magnitude than at 4mm. Two shear layers are still evident with the magnitudes oscillating with the oscillation. The shear layers have started to move radially as well as growing wider during the oscillation reduction, then becoming thinner as the oscillation grows. This is shown by RMS $|v|$. Distinct favouritism is now displayed as RMS vy clearly is responsible for the inner shear layer and RMS vx for the outer. In opposite layers each component has a much reduced RMS value. RMS vy and RMS vx are equivalent in magnitude in their favoured shear layer. RMS vz spikes in both equally and is much smaller in magnitude

Further downstream at 30mm the layers are still evident only by considering the individual components. RMS $|v|$ is one large shear layer during the reduction half of the oscillation before showing two peaks as the oscillation grows. This is due to the widening and overlap of RMS vy and RMS vx. These two components widen and decrease in magnitude during the oscillation reduction and become thinner and larger in value as the oscillation grows. RMS vz is considerably smaller and two small peaks are barely visible at some phases. Within the IRZ the RMS components have all increased in value over the 4mm and 15mm positions. The profiles within this region remain relatively flat.

The magnitudes of the respective RMS components within the shear layers at the three axial positions clearly show they are oscillating at 100Hz. Frequency spectra at a point must be treated cautiously as it is clear even at 4mm downstream the shear layers show radial variation in location and this would result in artificial signal strength or weakness at 100Hz and possibly other frequencies. This will be treated separately Chapter 8.7.

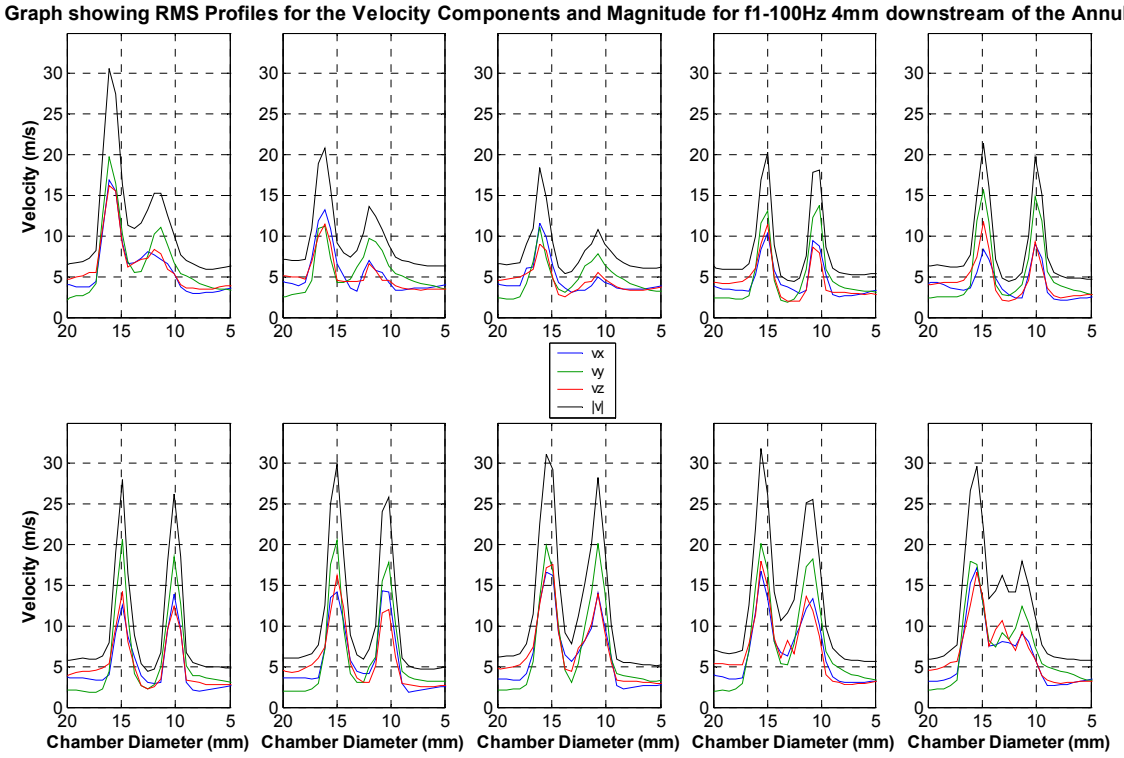

Figure 8-2 RMS Profiles of f1-100Hz along a line 4mm downstream of the Annulus. Taken from mean vector fields from the imaging area 'Annulus 3D'. The top row consists of phases 1 to 5 from left to right. The bottom row consists of phases 6 to 10 from left to right.

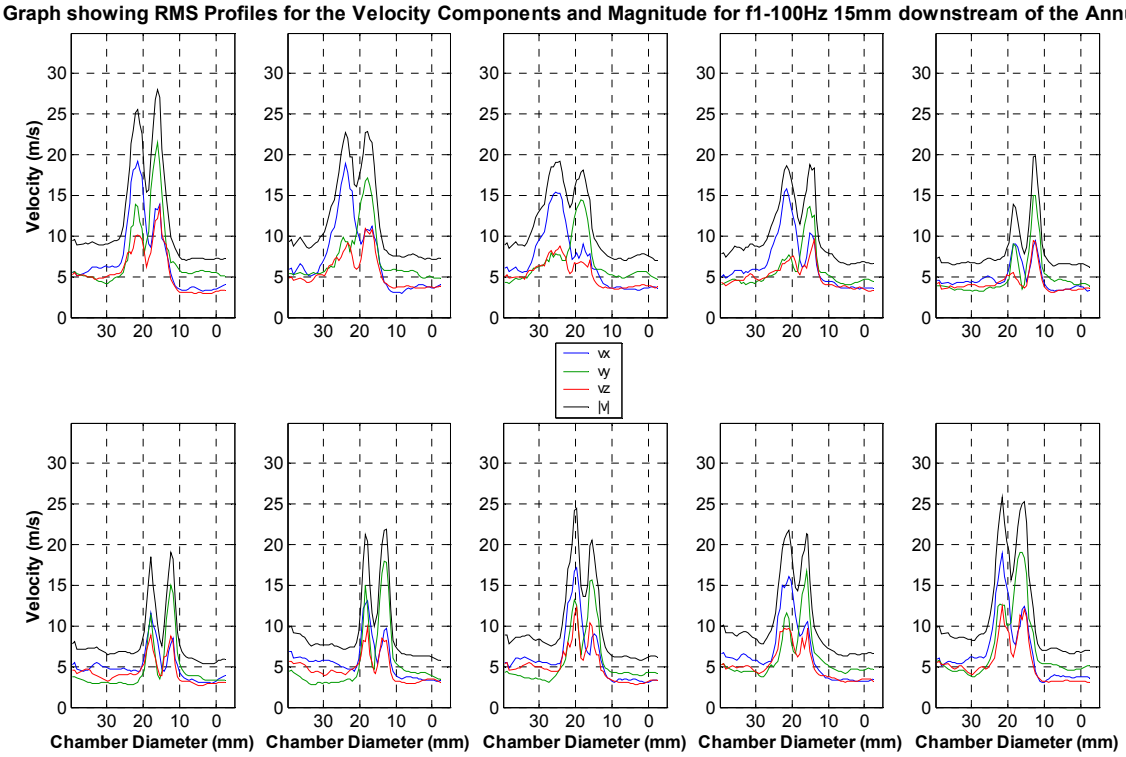

Figure 8-3 RMS Profiles of f1-100Hz along a line 15mm downstream of the Annulus. Taken from mean vector fields from the imaging area 'Annulus 3D'. The top row consists of phases 1 to 5 from left to right. The bottom row consists of phases 6 to 10 from left to right.

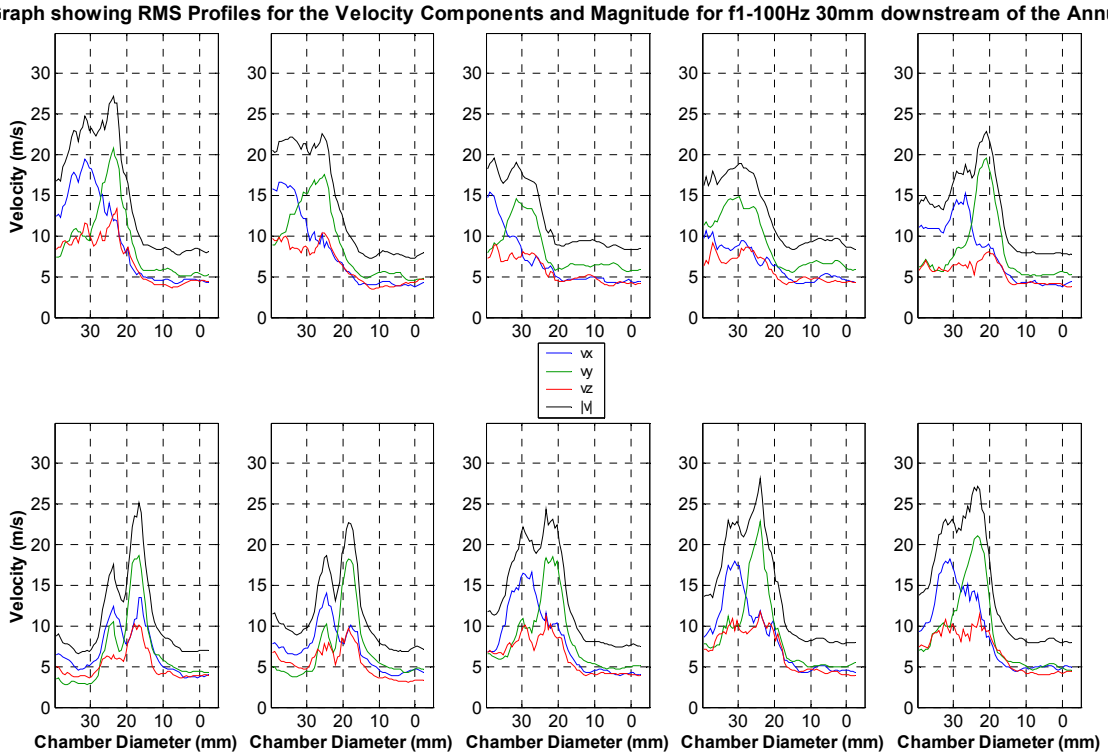

Figure 8-4 RMS Profiles of f1-100Hz along a line 30mm downstream of the Annulus. Taken from mean vector fields from the imaging area 'Annulus 3D'. The top row consists of phases 1 to 5 from left to right. The bottom row consists of phases 6 to 10 from left to right.

Following the discussion in chapter 8.2 the triple deconvoluted velocity fluctuation vector maps have been used to create PDFs of the turbulence with the imposed oscillation of 100Hz removed. Figure 8-5 at 4mm shows the PDFs across the shear layers (highlighted red). For all components the PDFs are single modal with no large shoulders or outlying values. The trend for all three components is identical. From near the centreline the PDFs are tall and thin, indicating a small range of fluctuations (approx $\pm 10 ms^{-1}$). Moving outward across the inner shear layer the PDFs become shorter and wider indicating an increase in the range of fluctuations. Once within the centre of the inlet flow the PDFs become thinner and taller as the range of fluctuations becomes smaller. Moving further outward they become shorter and wider through the outer shear layer as the fluctuation range becomes larger again. Once through the outer shear layer the PDFs once again become taller and thinner. This is the same trend as identified from the RMS profiles of Figure 8-2.

Three points along this profile are shown in Figure 8-6 with all three turbulent fluctuations superimposed. All plots are centred around zero which shows that the influence of the imposed 100Hz perturbation has been removed at these points. Firstly at 13mm which is the centre of the inlet flow structure, all three components are very similar, symmetrical and show a very narrow fluctuation range ($-15 ms^{-1}$ to $10 ms^{-1}$). All three are centred on zero with a very slight broadening at the base at $-15 ms^{-1}$ compared to the positive side. The peak probability at zero is 0.275 to 0.32 for the components. Considering the inner shear layer (11mm) vx''' and vz''' are identical with near symmetric PDFs with a larger range of approximately $-45 ms^{-1}$ to $45\ ms^{-1}$ and smaller peak probabilities

at zero of 0.18. The outlying parts of the profiles show small variations. For vy''' the PDF is broader at the base on the positive side. The overall range is the same as vx''' and vz''' but the peak probability at zero is 0.12. Finally considering the PDFs at the outer shear layer (16mm) vy''' has the lowest peak probability at 0.09 and has an asymmetric profile being wider on the negative side. For vx''' a higher centre probability is shown 0.11 and a more symmetric profile. For vz''' a centre probability of 0.13 is found with an approximate symmetric profile. All components have a wide base extending to approximately -50ms^{-1} to 50ms^{-1}. The component PDFs at this position are the widest than the other positions indicating that the outer shear layer is the most turbulent at this radial position. The PDFs of 11mm and 16mm are considerably wider (larger fluctuations) than those at 11mm and have small spikes at the tails confirming the peaks shown in RMS of Figure 8-2 and the observed oscillatory nature.

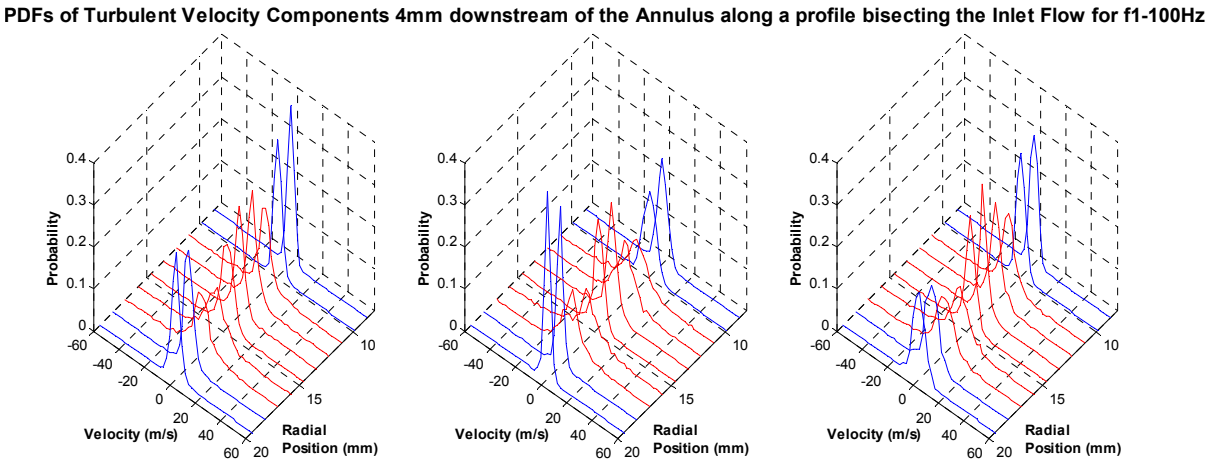

Figure 8-5 Turbulent PDFs of f1-100Hz along a line 4mm downstream of the Annulus. Left: vx'''. Centre: vy'''. Right: vz'''. Derived from the imaging area 'Annulus 3D'. PDFs highlighted in red correspond to the inlet flow structure and adjacent shear layers. Bin size 2.5ms^{-1}.

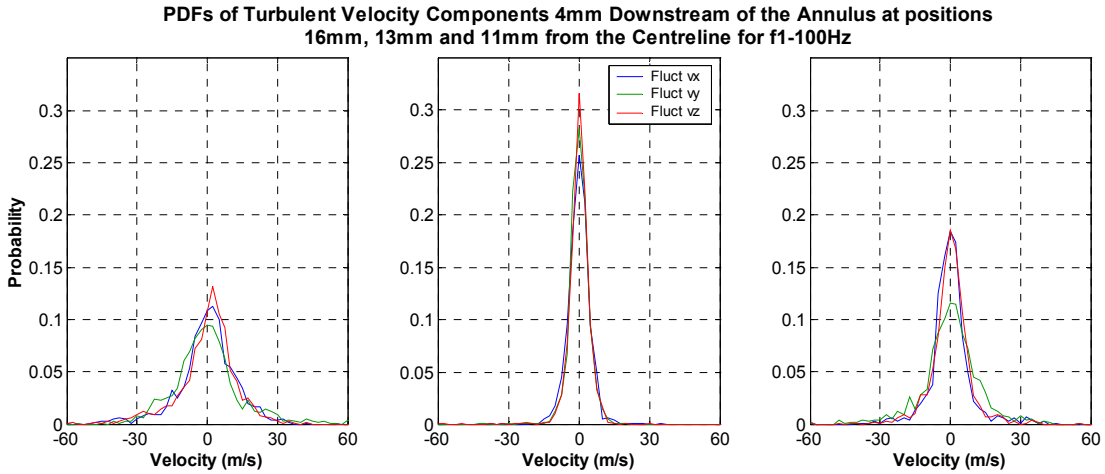

Figure 8-6 Turbulent PDFs of f1-100Hz taken from a line 4mm downstream of the Annulus, and 16mm (Left), 13mm (Centre) and 11m (Right) from the Centreline. Derived from the imaging area 'Annulus 3D'. Bin size 2.5ms^{-1}.

The skewness and kurtosis of each component distribution across the profile position are plotted in Figure 8-7. The skewness of each component does not appear to be interrelated with the majority of distributions possessing negative values (skewness to positive values). The kurtosis for each component is generally positive within the inlet flow and crossing the shear layers two peaks are evident indicating an increased propensity for large fluctuations for all components.

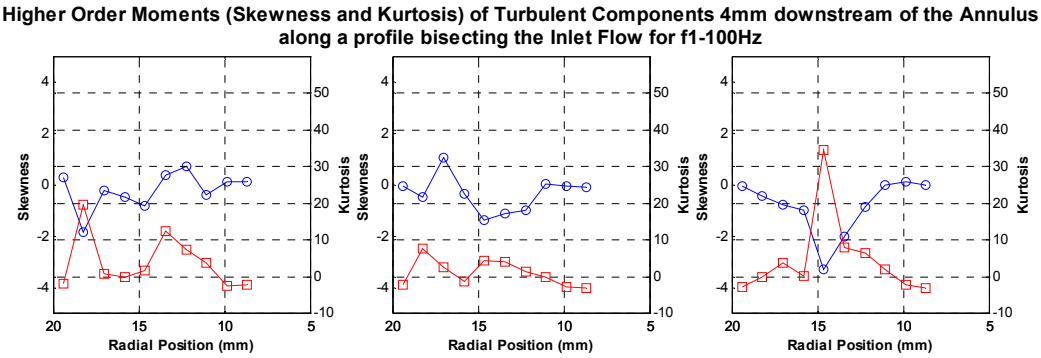

Figure 8-7 Graphs showing profiles of Skewness (blue) and Kurtosis (red) for velocity component distributions of f1-100Hz 4mm downstream of the Annulus. Left: vx'''. Centre: vy'''. Right: vz'''.

The PDFs taken at 15mm downstream are shown in Figure 8-8. The trend of the PDFs at 4mm is becoming less evident at this position. Considering vx''' The PDF close to the centreline is tall and thin. Moving outward they become shorter and wider. However instead of becoming thinner and then wider corresponding to the outer shear layer there is a slow progression of the PDFs becoming thinner and taller from the inner shear layer outward. This implies that the fluctuation range starts small and becomes larger before becoming progressively smaller. This is also evidenced for vz'''. The trend however can still be identified for vy''' although it is less dramatic. The identification of the inner shear layer from the PDFs shows the radial movement outward.

A comparison of component PDFs at 10mm, 20mm and 30mm from the centreline is shown in Figure 8-9. At 10mm, which is within the IRZ very narrow and tall profiles are seen for all components. The range is $\pm 15 ms^{-1}$ for vx''' and vy''' and $\pm 18 ms^{-1}$ for vy''' which has a small centre probability. All PDFs here are symmetrical with vy''' slightly wider than the base. At 20mm all PDFs are asymmetric about zero and have the same range, $-45 ms^{-1}$ to $32 ms^{-1}$, and show some peaks at the tails. Here vy''' and vz''' are very similar in shape with a peak probability at zero of 0.16, where as vx''' shows a small secondary peak at $15 ms^{-1}$ and a peak probability of 0.12. This position is within the shear area. Finally at 30mm the PDFs are clearly outside the shear area as they are tall and narrow. The PDFs are symmetrical until near the base where the range is $-20 ms^{-1}$ to $28 ms^{-1}$. Here vy''' and vz''' are very similar. A bulging near the bottom of vx''' is observed but its range is the same as the other components.

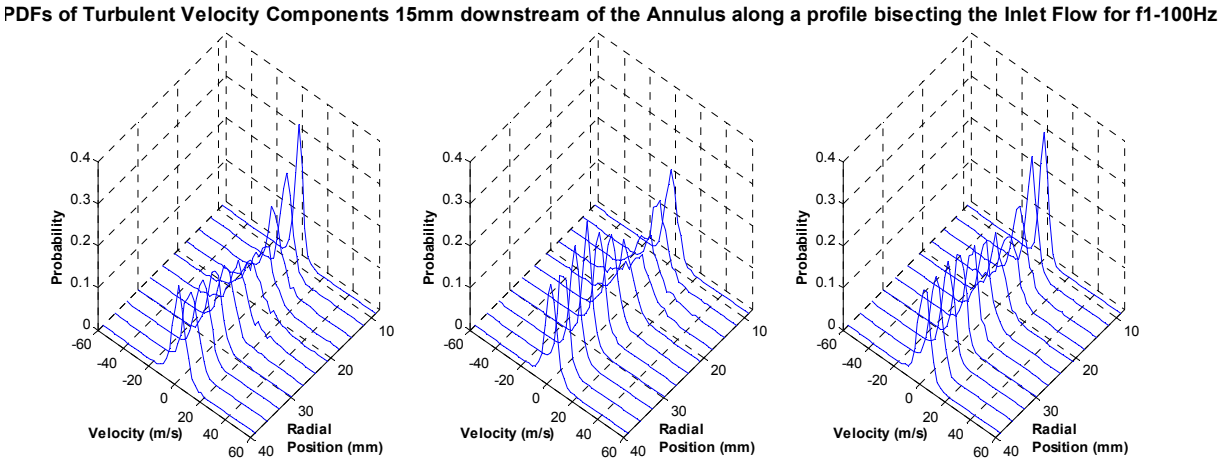

Figure 8-8 Turbulent PDFs of f1-100Hz along a line 15mm downstream of the Annulus. Left: vx'''. Centre: vy'''. Right: vz'''.Derived from the imaging area 'Annulus 3D'. Bin size 2.5ms^{-1}.

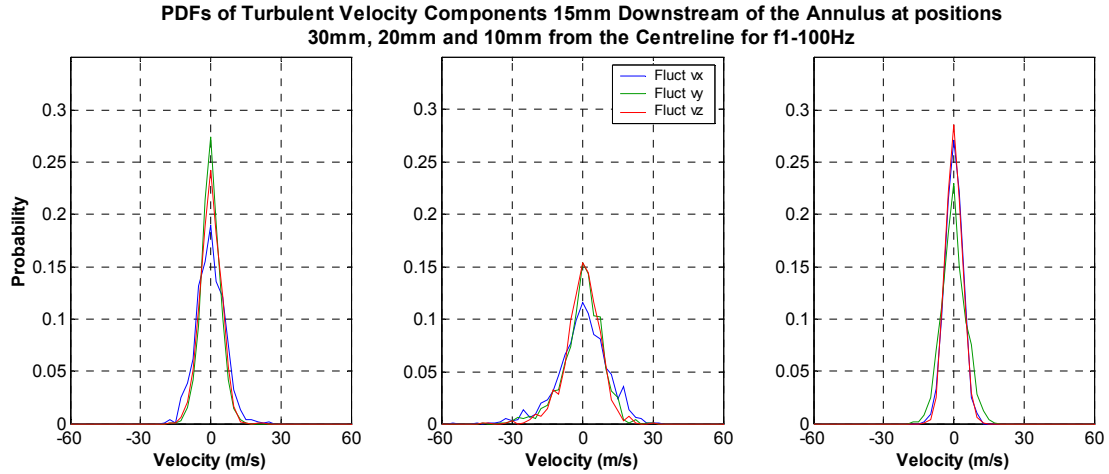

Figure 8-9 Turbulent PDFs of f1-100Hz taken from a line 15mm downstream of the Annulus, and 30mm (Left), 20mm (Centre) and 10m (Right) from the Centreline. Derived from the imaging area 'Annulus 3D'. Bin size 2.5ms^{-1}.

Figure 8-10 shows clear trends relating skewness and kurtosis. The profile shapes show good agreement with peaks and troughs occurring at the same radial locations for all turbulent components. The distributions of vx''' exhibit large positive skew traversing through the shear layers (larger positive fluctuations). This is observed also regarding the kurtosis values. The vy''' distributions of skewness are positive in the inner shear layer and negative within the outer. This is again observed of the kurtosis. The related behaviour of skewness and kurtosis of the vz''' distributions is not as distinct as the other components. However the skewness profile has the same trend as that of vx''' with positive values traversing the shear layers and negative or near zero values within the inlet flow. The inner shear layer therefore has a higher probability of experiencing fluctuations of larger positive values for all three components. Regarding the outer shear layer the kurtosis for all components is marginally negative so there is no abnormal probability of large fluctuation values. The skewness for vx''' is positive, meaning the greatest probable value will be

negative (non zero), and negative for vy''' and vz''' meaning a positive fluctuation is more probable. Within the inlet flow all components have negative skewness and marginally negative kurtosis. This means less probability of large fluctuations and an increased probability that the fluctuation will be positive.

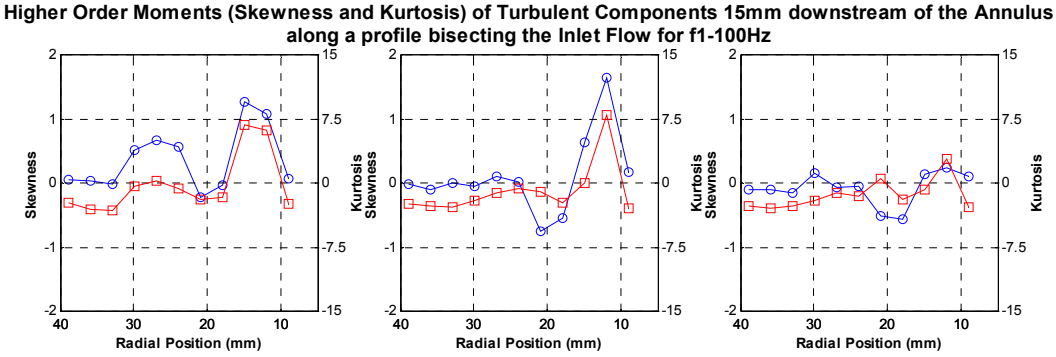

Figure 8-10 Graphs showing profiles of Skewness (blue) and Kurtosis (red) for velocity component distributions of f1-100Hz 15mm downstream of the Annulus. Left: vx'''. Centre: vy'''. Right: vz'''.

The PDFs taken at 30mm downstream are shown in Figure 8-11. Considering vx''' the PDF profiles clearly start tall and thin in the IRZ and then become shorter and wider with radial distance for all. Once again this trend is mirrored in vz'''. This indicates the range of fluctuations is becoming larger with radial distance. For vy''' the PDFs are short and broad within the central part of the sampling radial considered. There is no central PDF of taller thinner aspect indicating the central core of the inlet flow is susceptible to turbulent motions. The PDFs at this downstream location are all considerably wider (shorter) than the upstream positions which indicate the area of high fluctuations has grown from two thin shear layers to a broader area.

Three positions at 10mm, 20mm and 30mm are shown in detail in Figure 8-12. At 10mm the profiles are symmetrical and narrow with a range of is $\pm 15 ms^{-1}$ for vx''' and vz'''. The latter has a higher peak probability, 0.27 compared to 0.22. For vy''' the range is the same but the profile is wider and has two bulges either side at the base. At 20mm vx''' and vz''' have very similar symmetrical PDFs. However vy''' is broader and has a second peak on the negative side indicating an bimodal distribution. The PDFs at 30mm are broader than those at 20mm. Here vx''' has the broadest PDF and twin peaks, followed by vy''', then vz'''.

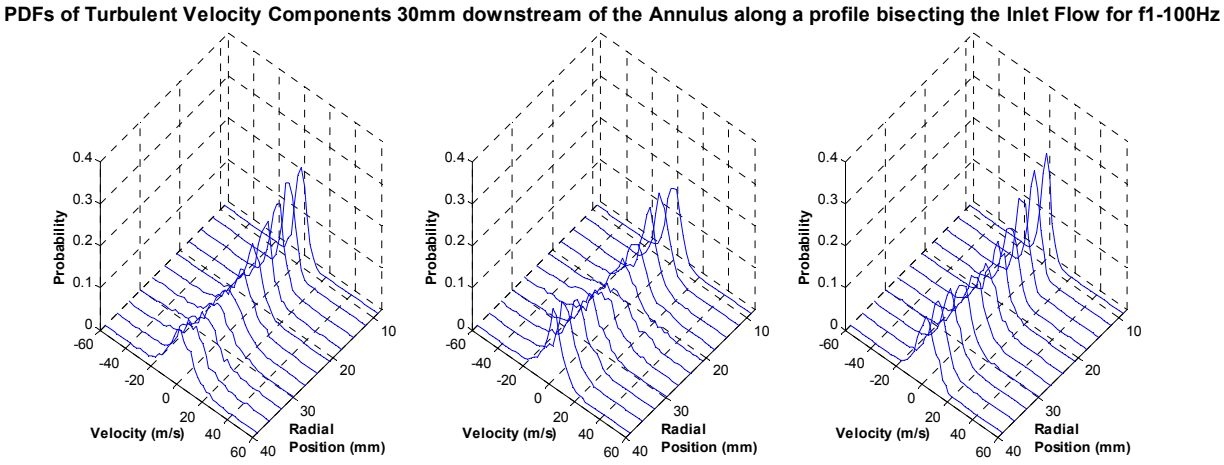

Figure 8-11 Turbulent PDFs of f1-100Hz along a line 30mm downstream of the Annulus. Left: vx'''. Centre: vy'''. Right: vz'''. Derived from the imaging area 'Annulus 3D'. Bin size 2.5ms^{-1}.

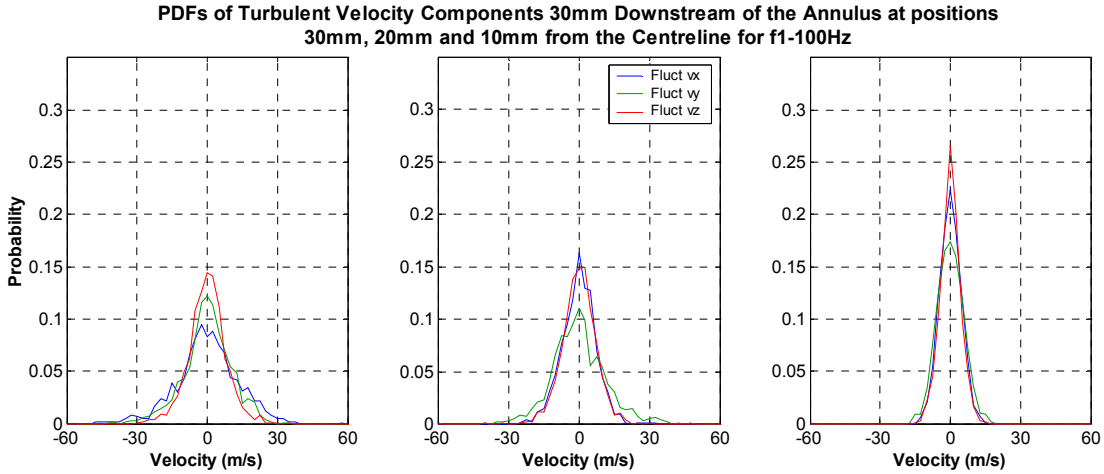

Figure 8-12 Turbulent PDFs of f1-100Hz taken from a line 30mm downstream of the Annulus, and 30mm, 20mm and 10m from the Centreline. Derived from the imaging area 'Annulus 3D'. Bin size 2.5ms^{-1}.

The behaviour of skew and kurtosis identified at 15mm downstream position are still apparent but reduced in strength at 30mm (Figure 8-13). Generally kurtosis is marginally negative. Peaks approximately positive do occur coinciding with the inner shear layer are evident for all turbulent components. This indicates the probability of large fluctuations has been greatly reduced and stabilised. The skewness profiles of vx''' and vz''' show the same trend with the former being greater in values. Both have positive values in the shear layers and negative values between them. The skewness of vy''' is positive only in the inner shear layer. This confirms that in the outer shear layer it is more probable that the fluctuations of vx''' and vz''' will be negative, in the inner shear layer it is more probable that the fluctuation of all components will be negative. Within the inlet flow it is more probable that the fluctuations of all components will be positive.

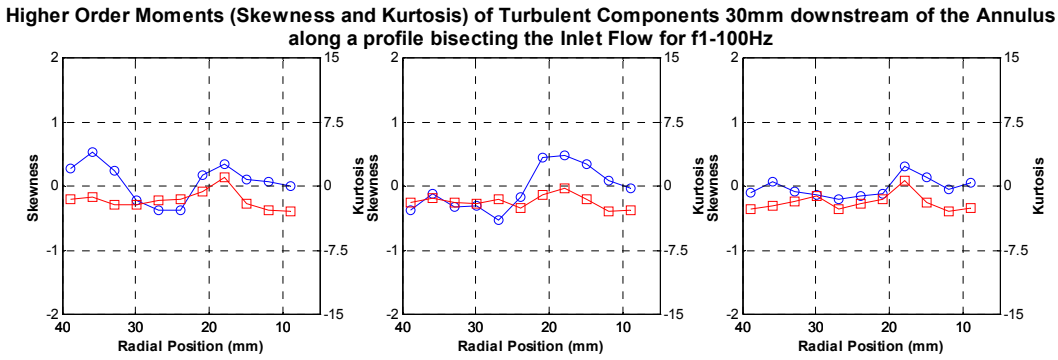

Figure 8-13 Graphs showing profiles of Skewness (blue) and Kurtosis (red) for velocity component distributions of f1-100Hz 30mm downstream of the Annulus. Left: vx'''. Centre: vy'''. Right: vz'''.

The off diagonal Reynolds stresses are shown in Figure 8-14. They show large values corresponding to the shear areas. These values decrease and spread radially moving downstream. Within the inner shear layer (IRZ) these stresses are tending towards zero indicating an approach to isentropic turbulence. Outside of the outer shear layer for 4mm and 15mm downstream positions the stresses are relatively constant. The non zero values are indicative of highly anisotropic turbulence which appears to be spreading radially and decreasing in anisotropy moving downstream. The rough aspect and multimodal features of some PDFs indicate periodic fluctuation which is likely to be partly due to the 100Hz oscillation.

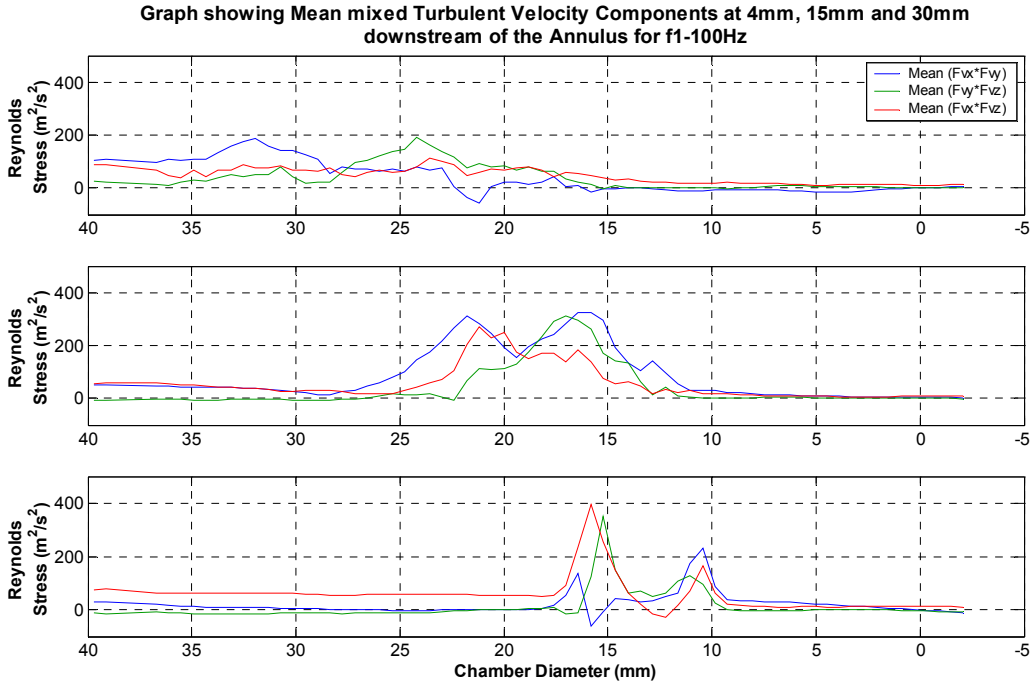

Figure 8-14 Off Diagonal (shear) Reynolds stresses for f1-100Hz along profiles taken at 4mm (Bottom), 15mm (Middle) and 30mm (Top) distances downstream of the Annulus.

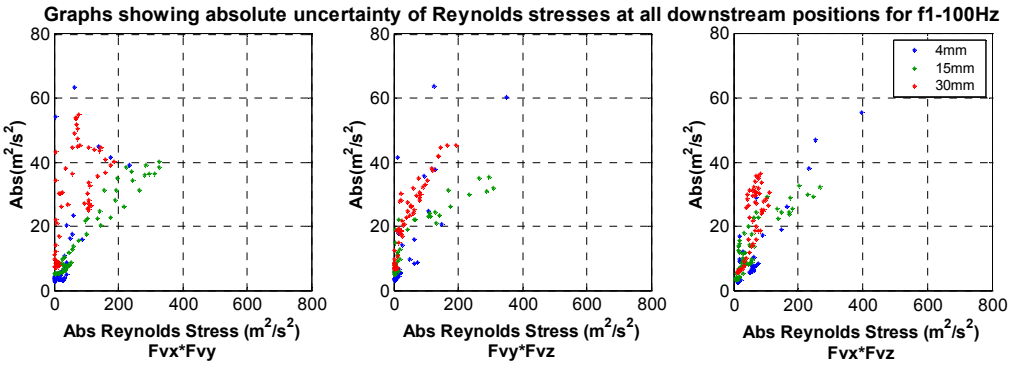

Figure 8-15 Scatter plots showing absolute uncertainty range of the calculated Reynolds stresses at all positions for f1-100Hz. Left: $\overline{vx''' \cdot vy'''}$. Centre: $\overline{vy'' \cdot vz'''}$. Right: $\overline{vx''' \cdot vz'''}$.

8.5 F1-200Hz

Figure 8-16 to Figure 8-18 show the RMS components and magnitude for 4mm, 15mm and 30mm downstream of the annulus. At 4mm as for f1-100Hz all three components show spikes within the shear layers which in some instances are wider than those of f1-100Hz. Within the outer shear layer all three RMS components are approximately equal through the phases and oscillate together. This is not the case for the inner layer where RMS vy is much larger than RMS vx which in turn is larger than RMS vz. The oscillation of RMS vy here is much larger than that of the other RMS components. The RMS peaks show a small amount of radial movement. Within the IRZ the RMS components are approximately constant spatially and show small variation through the oscillation.

At 15mm downstream the two shear layers are still evident with. The inner layer now completely dominated by RMS vy remains at high values through the phases showing small variation. The outer layer is mainly created by RMS vx with a small contribution from RMS vy. RMS vx is much smaller than RMS vy in the inner layer and shows a much larger range of values through the phases. RMS vz is much smaller than the other components and has a small contribution to each layer. There is a radial movement of the component peaks, combined with their increased width creates a wide RMS |v| profile which shows a single peak in some phases. All profiles have become coarse compared to the 4mm profiles.

At 30mm downstream of the Annulus RMS vy is very large and is solely responsible for the inner shear layer. It has a very wide base and oscillates in peak value considerably. The outer shear layer is created solely by RMS vx which is also wide near the base. It is smaller in value than RMS vy and the variation of its peak value is less. Both respective peaks show considerable radial movement and the distance between the two peaks changes also becoming very small at some instances resulting in a single RMS |v| peak through most phases. RMS vz is much smaller than the other components and now shows a single peak coinciding with RMS vy. All profiles are very coarse. Variation of the respective RMS component peak values is clear however it is not conclusively that of a single 200Hz frequency.

The magnitudes of the respective RMS components within the shear layers at the three axial positions clearly show they are oscillating. However it is unclear at this point if the oscillation frequency is that of 200Hz.

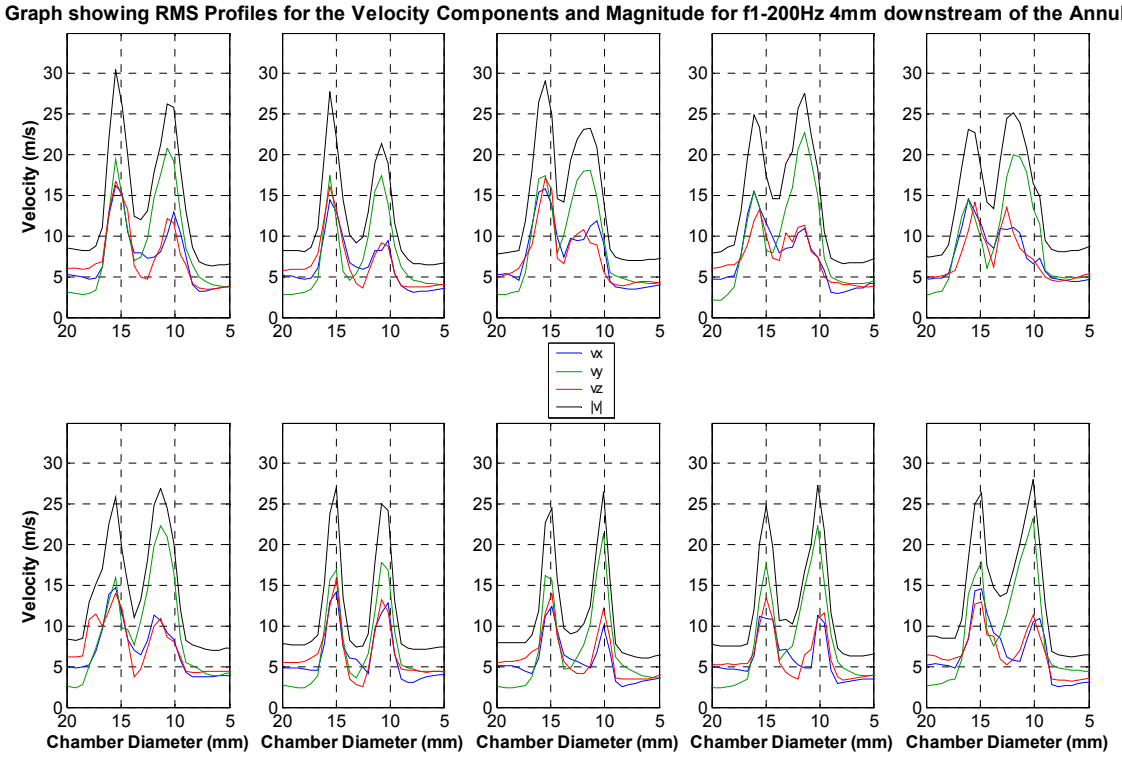

Figure 8-16 RMS Profiles of f1-200Hz along a line 4mm downstream of the Annulus. Taken from mean vector fields from the imaging area 'Annulus 3D'. The top row consists of phases 1 to 5 from left to right. The bottom row consists of phases 6 to 10 from left to right.

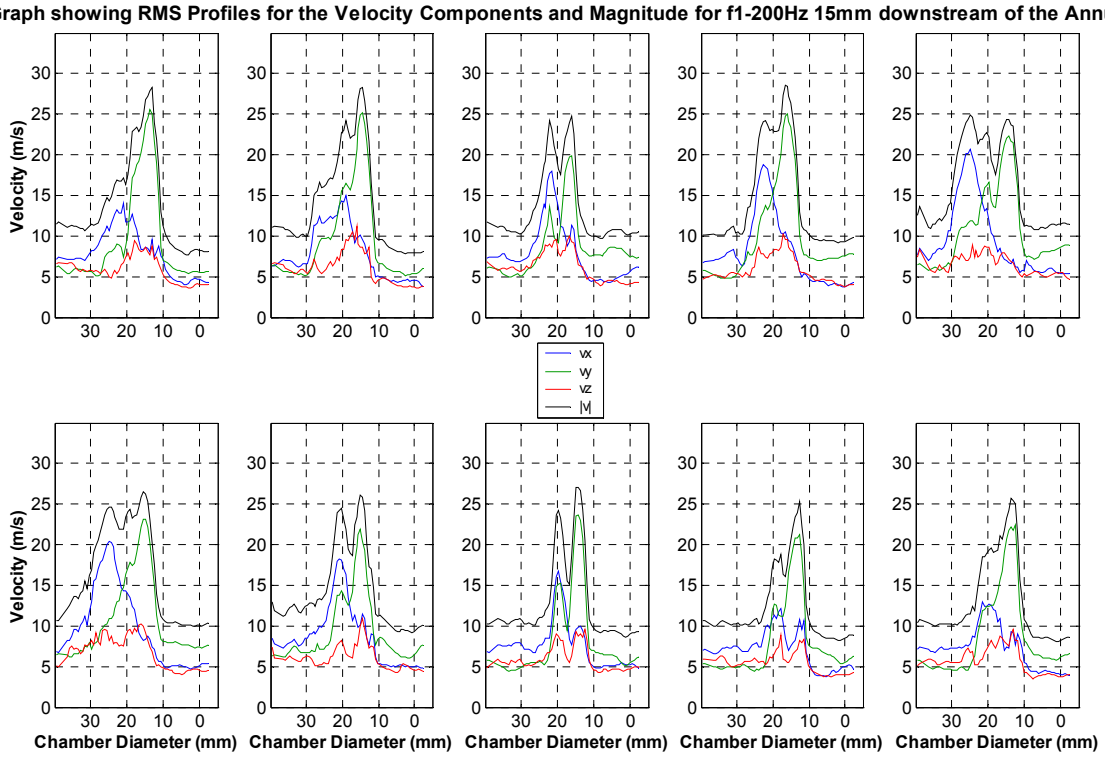

Figure 8-17 RMS Profiles of f1-200Hz along a line 15mm downstream of the Annulus. Taken from mean vector fields from the imaging area 'Annulus 3D'. The top row consists of phases 1 to 5 from left to right. The bottom row consists of phases 6 to 10 from left to right.

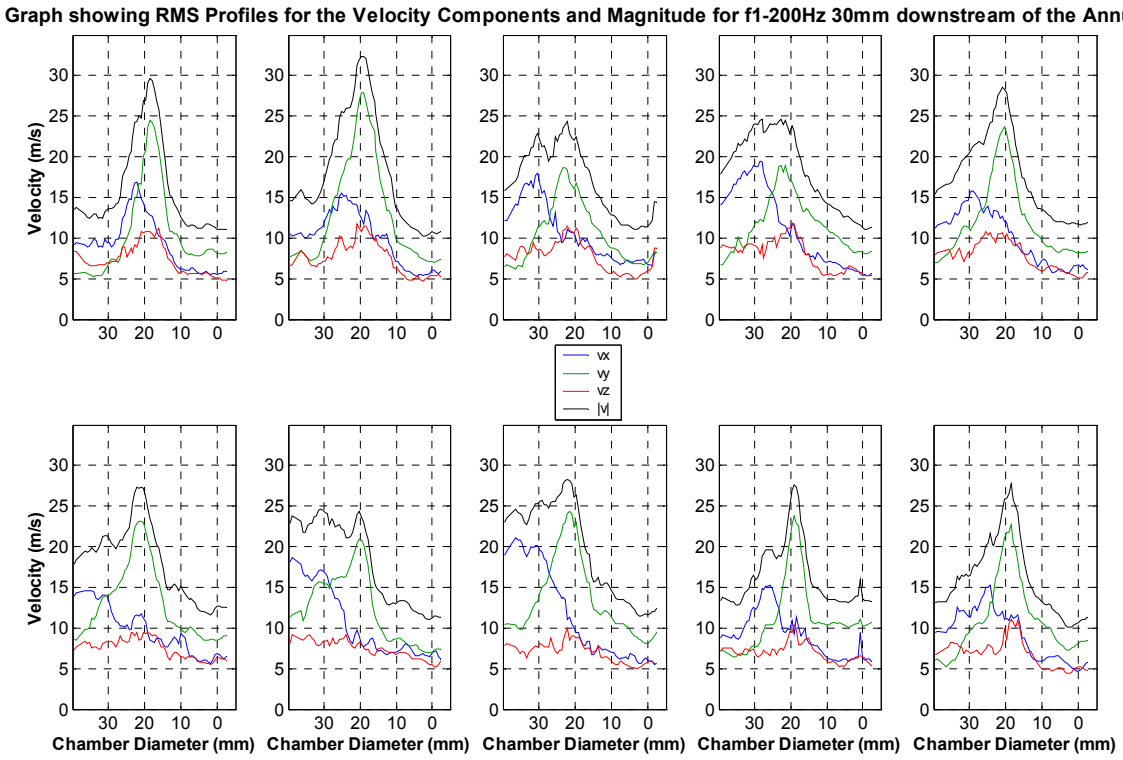

Figure 8-18 RMS Profiles of f1-200Hz along a line 30mm downstream of the Annulus. Taken from mean vector fields from the imaging area 'Annulus 3D'. The top row consists of phases 1 to 5 from left to right. The bottom row consists of phases 6 to 10 from left to right.

Figure 8-19 shows the PDFs along a profile 4mm downstream of the annulus across the shear layers (highlighted red). The trend for all three components is the same and is the same that was observed for f1-100Hz at the same position. The PDFs become wider through the shear layers. A subtle difference is that the PDFs within the shear layers have become coarser than for f1-100Hz.

Three points along this profile are shown in Figure 8-20 with all three component PDFs at radial positions, 11mm, 13mm and 16mm. In general these PDFs look similar to those of f1-100Hz at the same position and show the same trend. However there are marked differences. At 11mm (centre of inlet flow) all the PDF profiles are slightly wider with lower peak probabilities of 0.23 for vz''' to 0.16 for vx''' . The PDF of vy''' shows two distinct peaks on both positive and negative tails. The position at 11mm shows a distinct widening of vx''' and vz'''. In the case of vy''' a large change in PDF shape can be seen with three distinct peaks and a large increase in PDF width. At 16mm the PDF profiles are of the same shape but all three have very jagged profiles.

In general the range of fluctuations has become much bigger and higher probability towards larger fluctuation values than f1-100Hz. With the occurrence of several peaks and very jagged profiles it is clear that the profiles are multimodal meaning periodic structures are present.

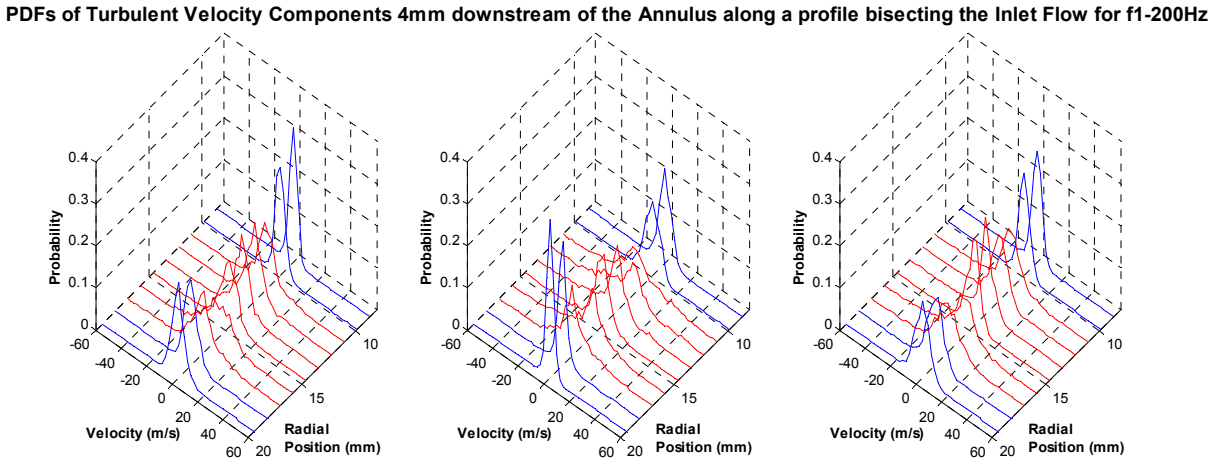

Figure 8-19 Turbulent PDFs of f1-200Hz along a line 4mm downstream of the Annulus. Left: *vx‴*. Centre: *vy‴*. Right: *vz‴*. Derived from the imaging area 'Annulus 3D'. PDFs highlighted in red correspond to the inlet flow structure and adjacent shear layers. Bin size 2.5ms^{-1}.

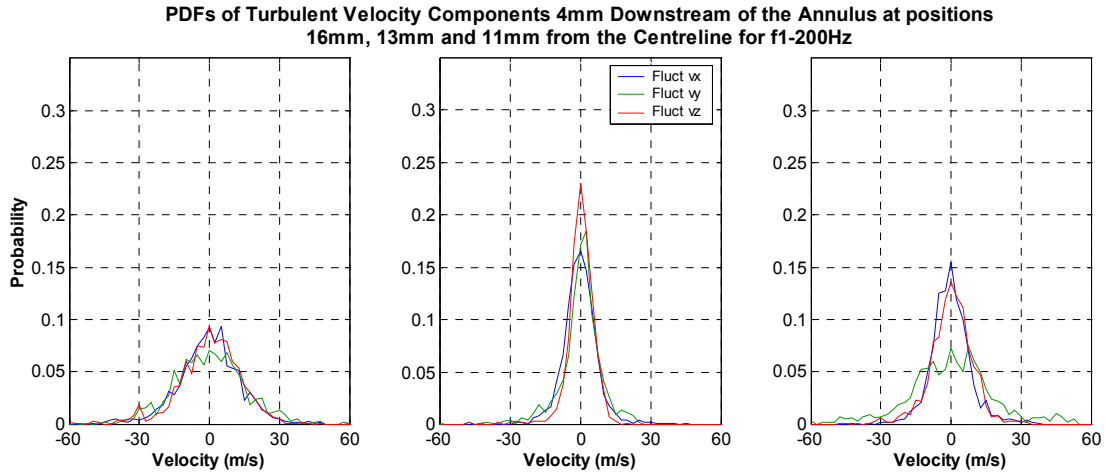

Figure 8-20 Turbulent PDFs of f1-100Hz taken from a line 4mm downstream of the Annulus, and 16mm (Left), 13mm (Centre) and 11m (Right) from the Centreline. Derived from the imaging area 'Annulus 3D'. Bin size 2.5ms^{-1}.

Profiles of skew and kurtosis for all turbulent components are shown in Figure 8-21. Both *vx‴* and *vy‴* components have positive peaks of skew and kurtosis in both shear layers. The component *vx‴* has greater peaks in the inner shear layer and *vy‴* in the outer. This means higher probability of a negative fluctuation and a larger probability of an extreme fluctuation for both components.

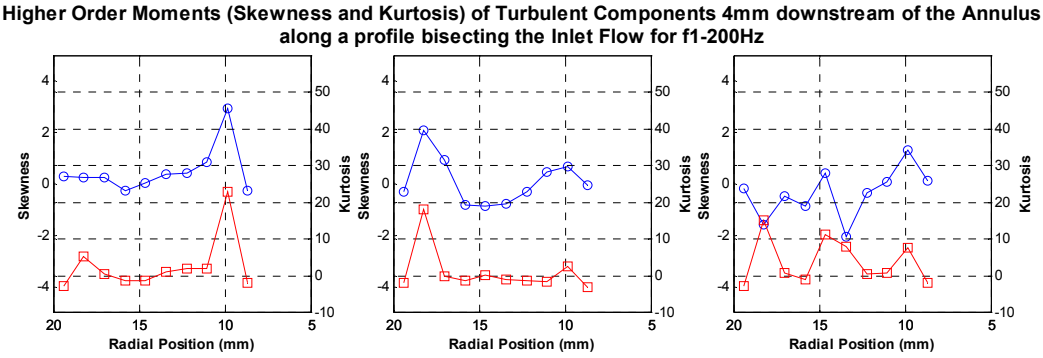

Figure 8-21 Graphs showing profiles of Skewness (blue) and Kurtosis (red) for velocity component distributions of f1-200Hz 4mm downstream of the Annulus. Left: vx'''. Centre: vy'''. Right: vz'''.

The PDFs taken at 15mm downstream are shown in Figure 8-22. Once again these follow what has been previously observed. The PDFs here are wider and coarser than those for f1-100Hz indicating a larger fluctuation range and a higher probability of the fluctuation being of a larger value.

A comparison at points 10mm, 20mm and 30mm from the centreline is given in Figure 8-23. Comparison with those for f1-100Hz shows once again a similar trend with the 20mm point having the largest fluctuation range. However all three positions here have PDFs with broader bases than those of f1-100Hz. At 10mm the PDFs of vx''' and vz''' are very similar in shape. The PDF of vy''' is asymmetrical with higher probabilities at larger fluctuation values. At 20mm all three PDFs are asymmetrical and have very coarse profiles. PDFs of vx''' and vy''' are skewed to the negative side and have larger probabilities of larger fluctuations than vz''', which displays multiple peaks at its centre. At 30mm vy''' and vz''' are identical and symmetrical. The PDF of vx''' is asymmetrical with larger probabilities for larger fluctuation values.

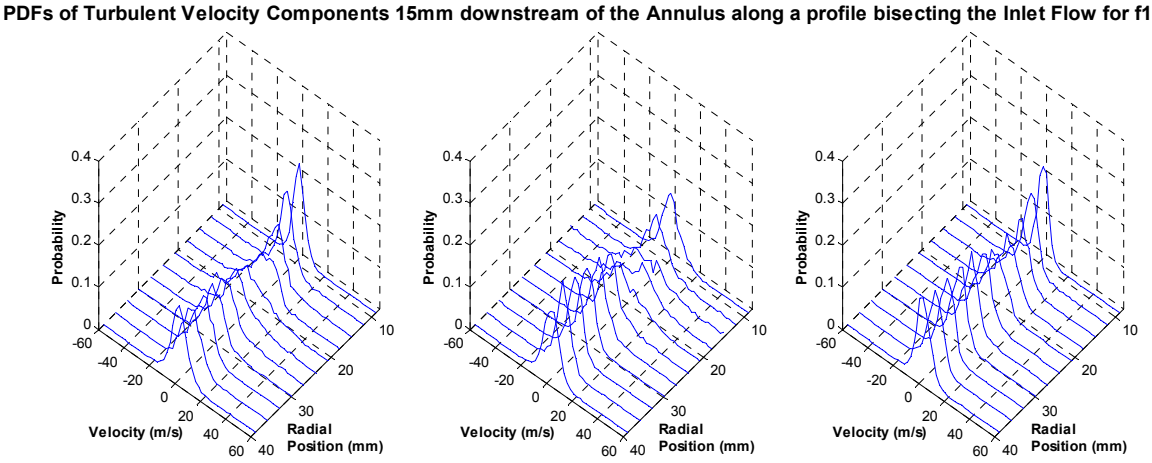

Figure 8-22 Turbulent PDFs of f1-200Hz along a line 15mm downstream of the Annulus. Left: vx'''. Centre: vy'''. Right: vz'''. Derived from the imaging area 'Annulus 3D'. Bin size 2.5ms^{-1}.

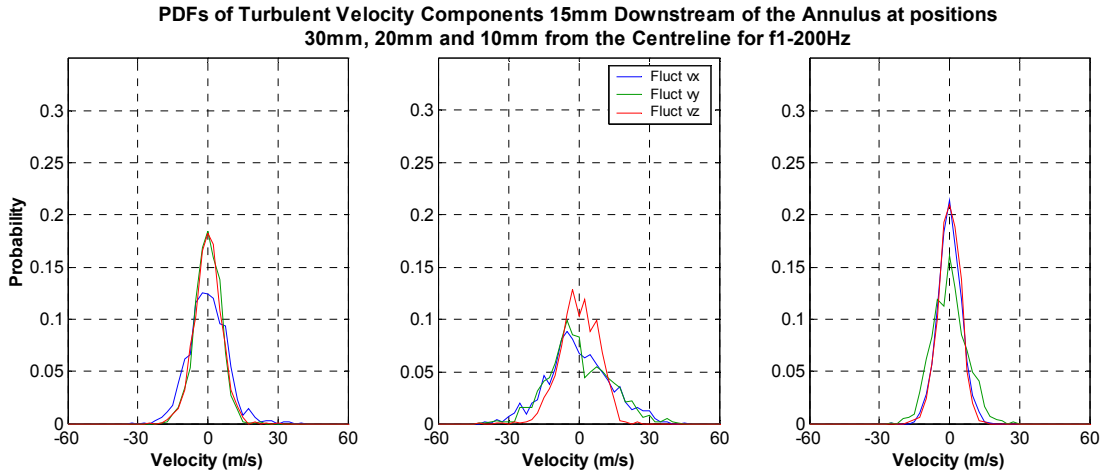

Figure 8-23 Turbulent PDFs of f1-2100Hz taken from a line 15mm downstream of the Annulus, and 16mm (Left), 13mm (Centre) and 11m (Right) from the Centreline. Derived from the imaging area 'Annulus 3D'. Bin size 2.5ms^{-1}.

The skew and kurtosis profiles at 15mm downstream position are shown in Figure 8-24 in figure x. Both vx''' and vy''' have positive skew and peaks of kurtosis (although negative for the outer shear layer) in both shear layers. Both components also have negative skew within the inlet flow. The component vz''' has a peak of skew and kurtosis in the inner shear layer and negative troughs within the inlet flow. The interpretation of this for the outer shear layer turbulence is that there is a higher probability that the fluctuation of vx''' and vy''' will be negative. Within the inner shear layer a negative fluctuation of all components is also more probable. In addition the positive kurtosis implies more extreme values. Within the inlet flow area the skewness is negative implying a positive fluctuation is more probable.

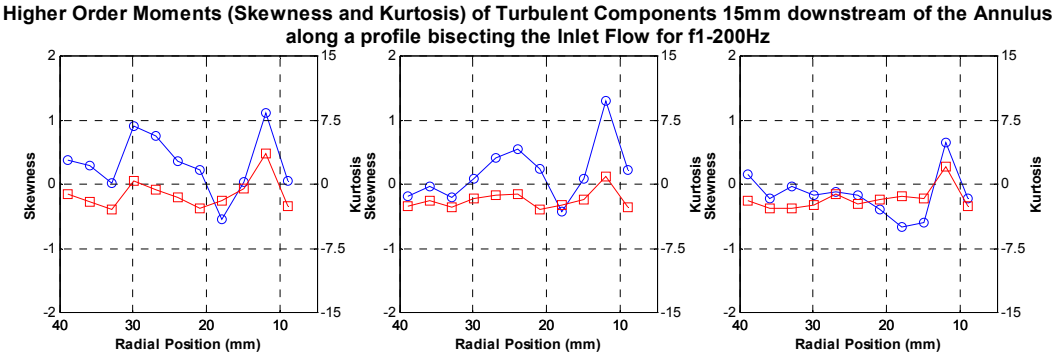

Figure 8-24 Graphs showing profiles of Skewness (blue) and Kurtosis (red) for velocity component distributions of f1-200Hz 15mm downstream of the Annulus. Left: vx'''. Centre: vy'''. Right: vz'''.

The PDFs taken at 30mm downstream are shown in Figure 8-25. These show the same pattern as f1-100Hz but are one again much coarser and wider which indicates larger fluctuations. In particular vy''' at 20mm radial position shows multiple peaks over a very large fluctuation range.

The PDFs at points 10mm, 20mm and 30mm along this radial are shown in Figure 8-26. They exhibit a coarser shape and larger fluctuations than those at

the 15mm radial and the respective f1-100Hz PDFs. Of note is the multi peak of vy''' at 20mm which shows large fluctuation values. All the PDFs are asymmetric.

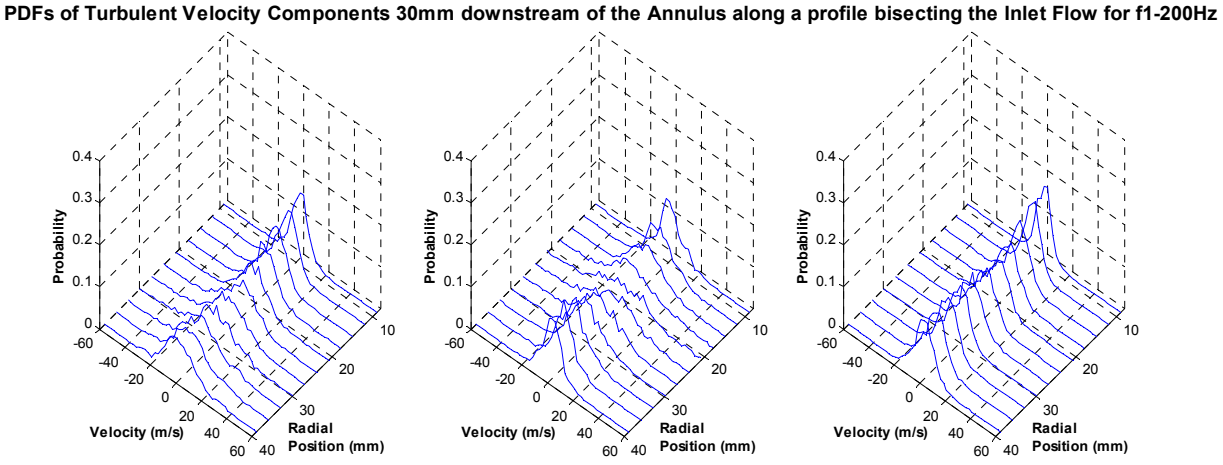

Figure 8-25 Turbulent PDFs of f1-200Hz along a line 30mm downstream of the Annulus. Left: vx'''. Centre: vy'''. Right: vz'''. Derived from the imaging area 'Annulus 3D'. Bin size 2.5ms^{-1}.

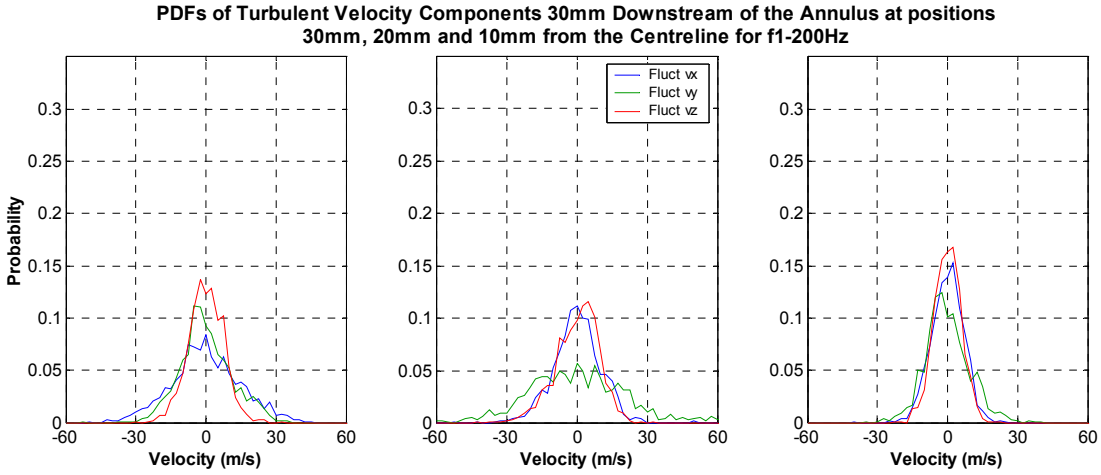

Figure 8-26 Turbulent PDFs of f1-2100Hz taken from a line 30mm downstream of the Annulus, and 16mm (Left), 13mm (Centre) and 11m (Right) from the Centreline. Derived from the imaging area 'Annulus 3D'. Bin size 2.5ms^{-1}.

The behaviour of skew and kurtosis at the 30mm downstream position is shown in Figure 8-27. The kurtosis for all components is negative and approximately invariant. The profiles of skew do not exhibit the same trend as that at 15mm. Definite peaks for each shear layer is less defined. It is clear that a trough of small negative skewness still exists for the inlet flow location.

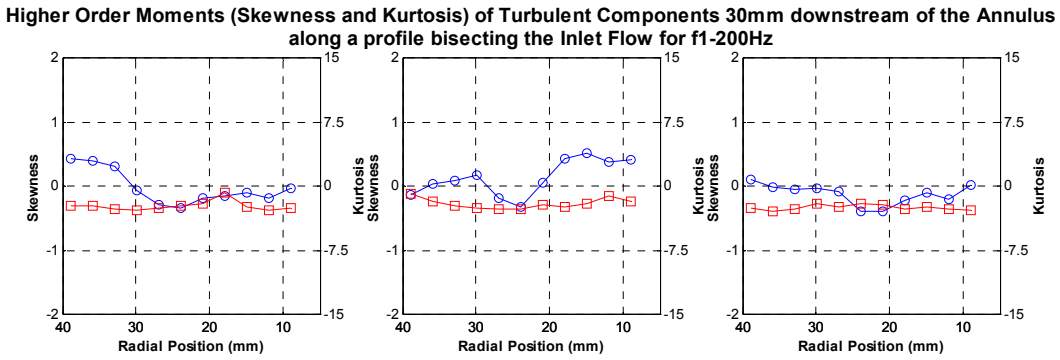

Figure 8-27 Graphs showing profiles of Skewness (blue) and Kurtosis (red) for velocity component distributions of f1-200Hz 30mm downstream of the Annulus. Left: vx'''. Centre: vy'''. Right: vz'''.

The off diagonal Reynolds stresses are shown in Figure 8-28. The same overall spatial characteristics are shown with convergence of the shear stresses towards zero within the IRZ indicating a return to isotropic conditions. This trend lessens with axial distance. The remaining positions are highly anisotropic.

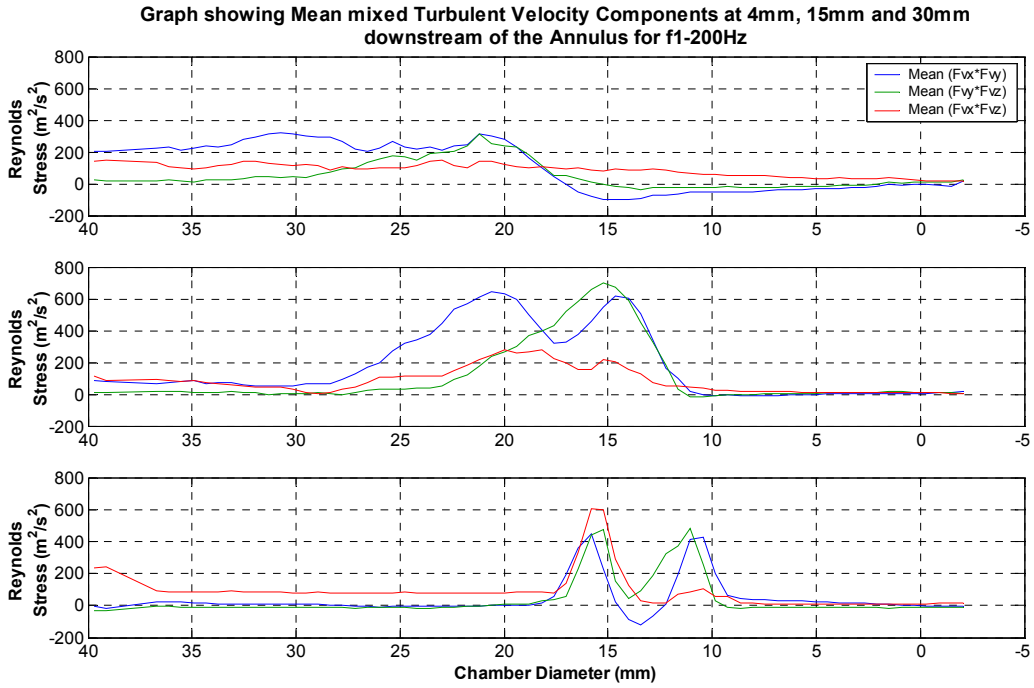

Figure 8-28 Off Diagonal (shear) Reynolds stresses for f1-200Hz along profiles taken at 4mm (Bottom), 15mm (Middle) and 30mm (Top) distances downstream of the Annulus.

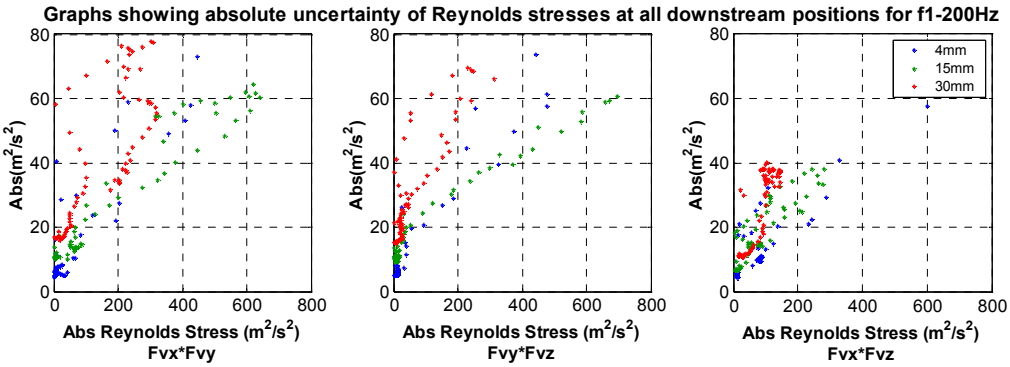

Figure 8-29 Scatter plots showing absolute uncertainty range of the calculated Reynolds stresses at all positions for f1-200Hz. Left: $\overline{vx''' \cdot vy'''}$. Centre: $\overline{vy'' \cdot vz'''}$. Right: $\overline{vx''' \cdot vz'''}$.

8.6 F1-400Hz

Figure 8-30 shows the RMS components for 4mm. The now familiar twin peaks is evident with all three components strong in each. All three components are approximately equal in the outer layer where as the inner is again dominated by RMS vy. In this case the outer shear layer is always present but the inner layer becomes very weak and the peak even disappears towards the bottom of the perturbation. The value of RMS vy in this position is still greater than RMS vx and vz. At both shear layers the RMS components are clearly oscillating through the phase positions. Between the two shear layers the RMS vy does not return to a value outside of the two layers as has been previously observed for the other conditions. RMS vx and vz do but RMS vy remains at a higher throughout most of the oscillation.

Figure 8-31 shows the RMS components at 15mm. as before two distinct shear layers are evident with RMS vy responsible for the inner and RMS vx for the outer. RMS vz is much less in value and makes small contributions to each layer. The respective component values are clearly oscillating through the perturbation and radial displacement can be seen occurring with broadening of the components profile. The same trends only greater is seen for the RMS components at 30mm (Figure 8-32). One apparent difference is the profile of RMS vx is broader than that of RMS vy indicating a wider shear layer.

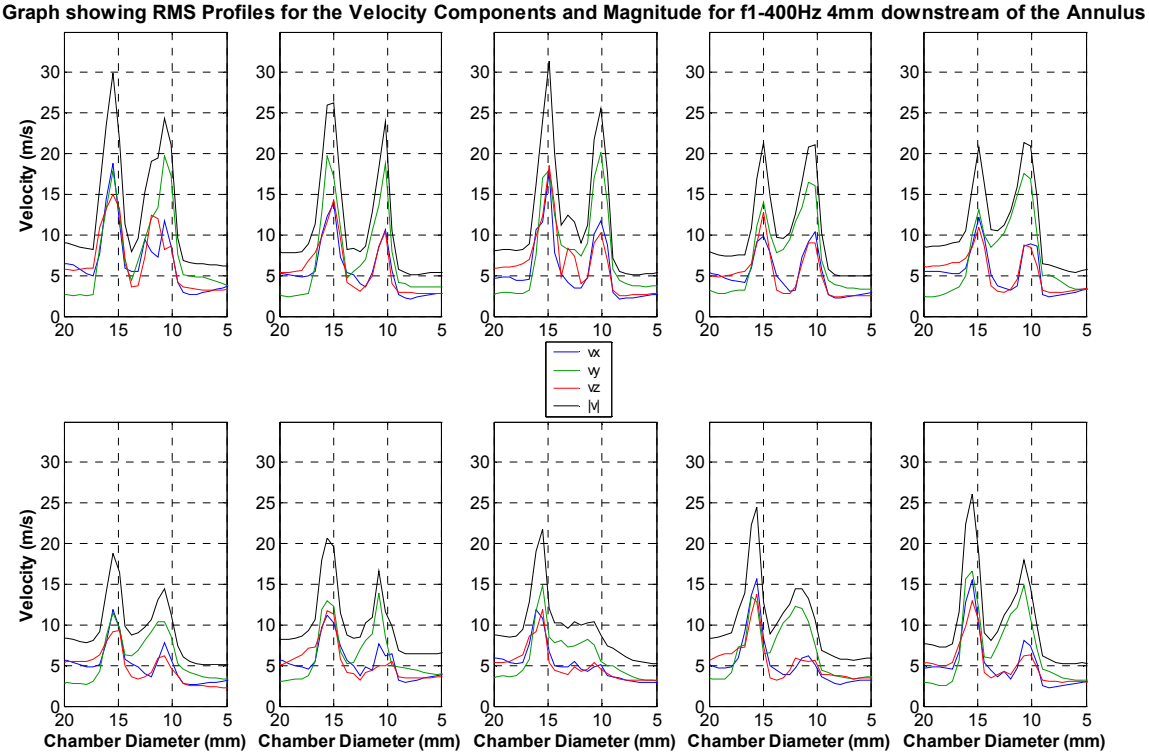

Figure 8-30 RMS Profiles of f1-400Hz along a line 4mm downstream of the Annulus. Taken from mean vector fields from the imaging area 'Annulus 3D'. The top row consists of phases 1 to 5 from left to right. The bottom row consists of phases 6 to 10 from left to right.

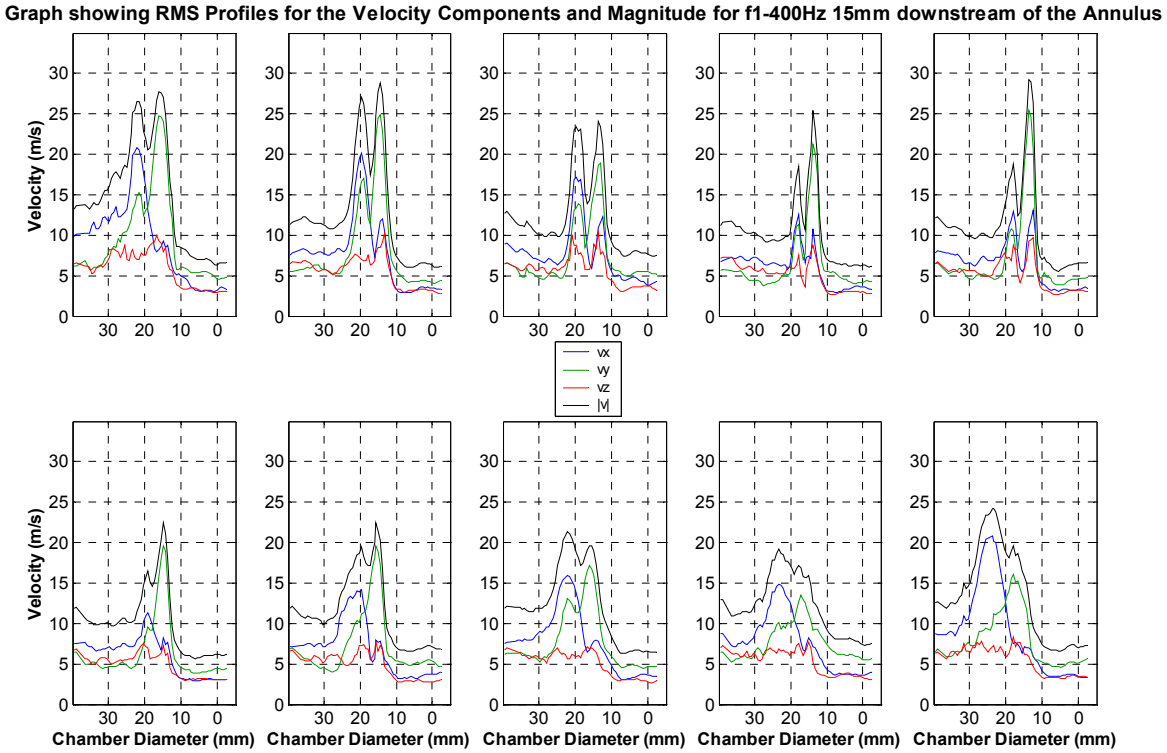

Figure 8-31 RMS Profiles of f1-400Hz along a line 15mm downstream of the Annulus. Taken from mean vector fields from the imaging area 'Annulus 3D'. The top row consists of phases 1 to 5 from left to right. The bottom row consists of phases 6 to 10 from left to right.

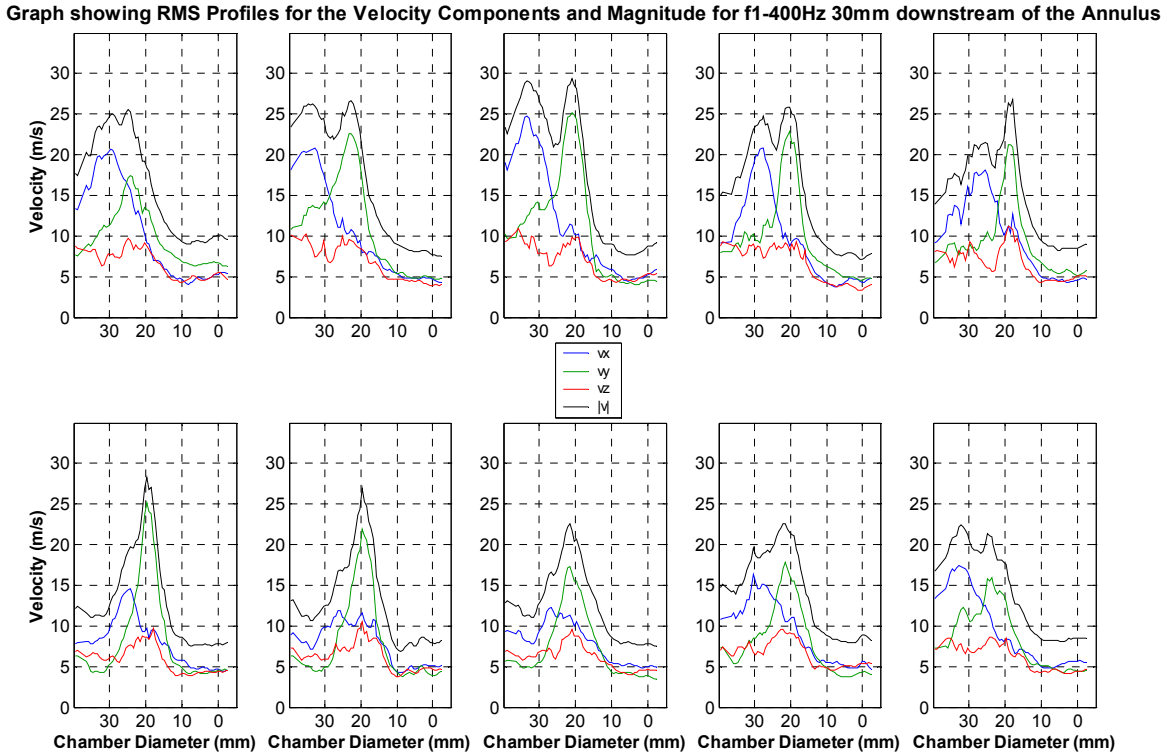

Figure 8-32 RMS Profiles of f1-400Hz along a line 30mm downstream of the Annulus. Taken from mean vector fields from the imaging area 'Annulus 3D'. The top row consists of phases 1 to 5 from left to right. The bottom row consists of phases 6 to 10 from left to right.

Figure 8-33 shows the PDFs along a profile 4mm downstream of the annulus across the shear layers (highlighted red). The trend for components *vz‴* and *vz‴* is the same and is the same that was observed for f1-100Hz at the same position. The PDFs become wider through the shear layers. For *vy‴* the PDFs are the same short wide shape through the centre of the inlet flow. This reflects the already noted feature of a relatively high RMS vy through this region.

Three points along this profile are shown in Figure 8-34 with all three component PDFs at radial positions, 11mm, 13mm and 16mm. The PDFs at 11mm are similar for *vx‴* and *vz‴*, *vy‴* however is much coarser, asymmetric with high probabilities at larger fluctuation values. As expected entering the centre of the inlet flow all PDF profiles are much smoother, thinner and more symmetrical. Once again *vx‴* and *vz‴* are very similar with *vx‴* having a slightly wider base. Two peaks can be seen for *vy‴* and the profile is wider and indicates a larger fluctuation value range. At 16mm all PDFs are very jagged, wide and asymmetric. Again *vx‴* and *vz‴* are similar.

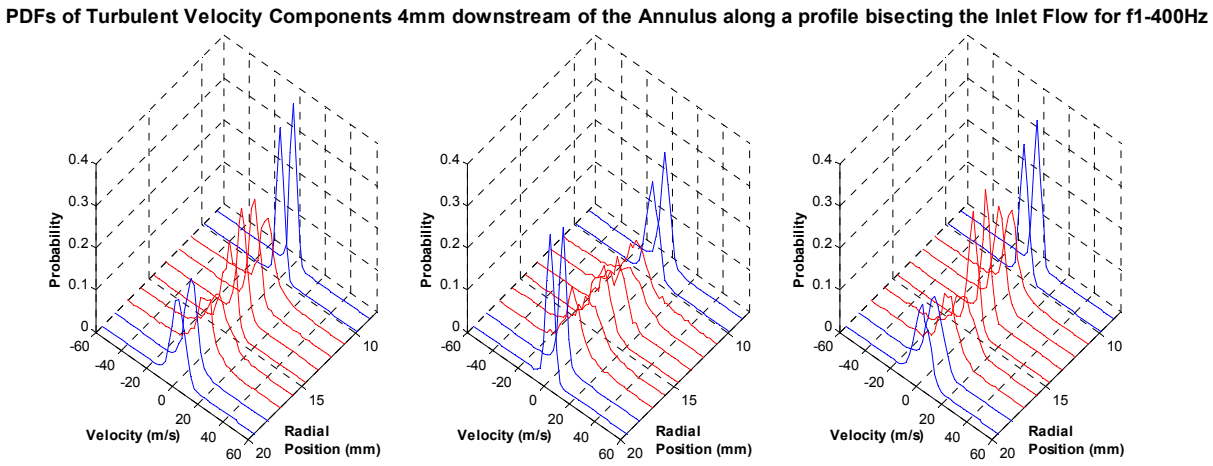

Figure 8-33 Turbulent PDFs of f1-400Hz along a line 4mm downstream of the Annulus. Left: *vx‴*. Centre: *vy‴*. Right: *vz‴*. Derived from the imaging area 'Annulus 3D'. PDFs highlighted in red correspond to the inlet flow structure and adjacent shear layers. Bin size 2.5ms^{-1}.

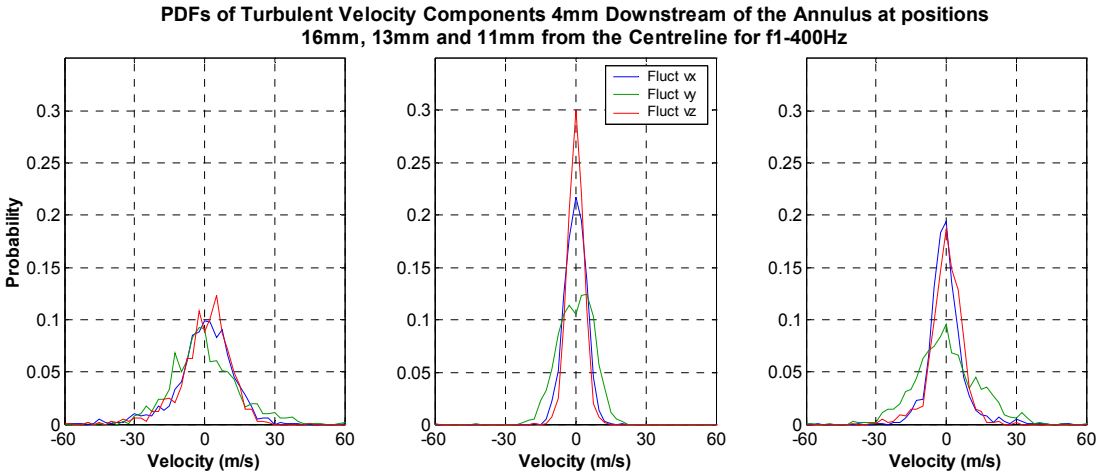

Figure 8-34 Turbulent PDFs of f1-400Hz taken from a line 4mm downstream of the Annulus, and 16mm (Left), 13mm (Centre) and 11m (Right) from the Centreline. Derived from the imaging area 'Annulus 3D'. Bin size 2.5ms^{-1}.

Profiles of skew and kurtosis for all turbulent components are shown in Figure 8-35. Both vx''' and vz''' exhibit very similar profiles of skew and kurtosis. The shear layers are not identifiable. At the same radial location both components have large negative troughs of skew and very large peaks of kurtosis. The component vy''' has large positive peak of skew and kurtosis coinciding. This is at a larger radial distance than those of vx''' and vz'''.

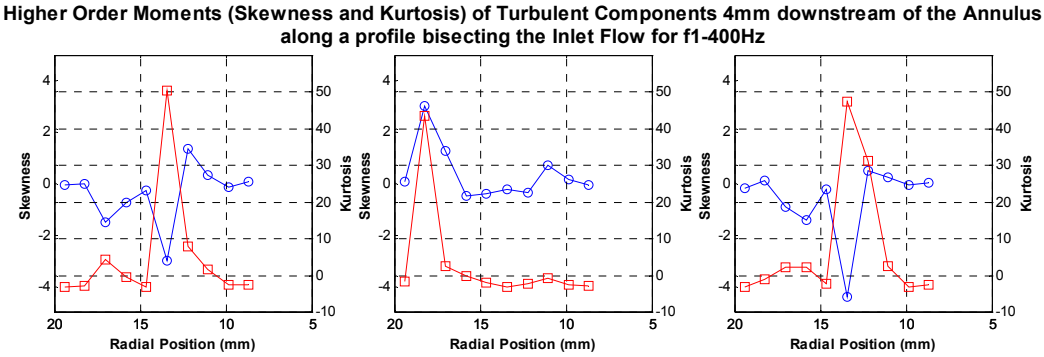

Figure 8-35 Graphs showing profiles of Skewness (blue) and Kurtosis (red) for velocity component distributions of f1-400Hz 4mm downstream of the Annulus. Left: vx'''. Centre: vy'''. Right: vz'''.

The PDFs taken at 15mm downstream are shown in Figure 8-36. These return to what has been previously observed. The PDFs here are wider and coarser than those for f1-100Hz indicating a larger fluctuation range and a higher probability of the fluctuation being of a larger value.

A comparison at points 10mm, 20mm and 30mm from the centreline is given in Figure 8-37. Comparison with those for f1-100Hz shows once again a similar trend with the 20mm point having the largest fluctuation range and the coarsest profiles. At 10mm the PDFs of vx''' and vz''' are very similar in shape. The PDF of vy''' has marginally higher probabilities at larger fluctuation values. At 20mm all three PDFs have very coarse profiles. PDFs of vx''' and vy''' are similar and have larger probabilities of larger fluctuations than vz''' which is smoother and

narrower. At 30mm *vy‴* and *vz‴* are similar and symmetrical. The PDF of *vx‴* has larger probabilities for larger fluctuation values and a very blunt top.

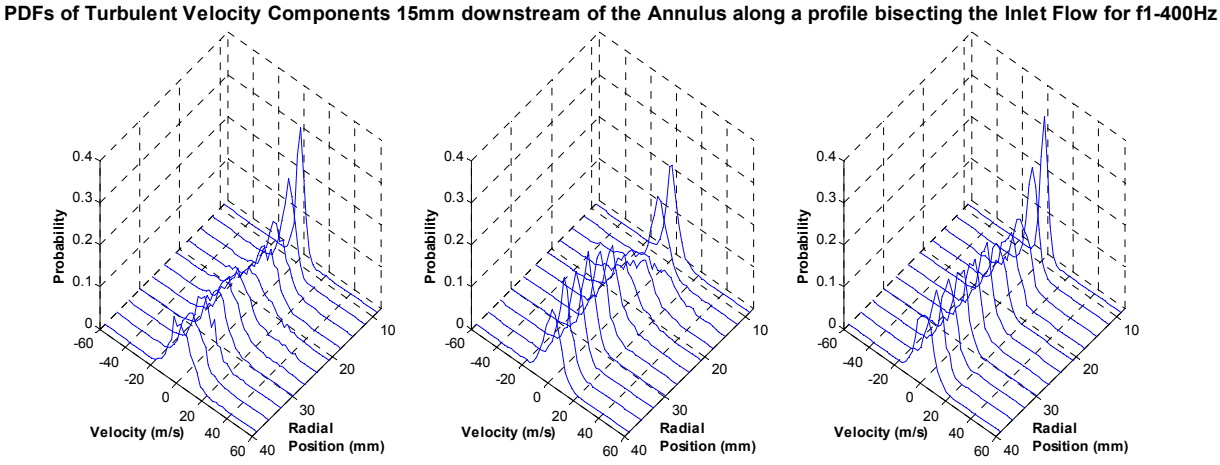

Figure 8-36 Turbulent PDFs of f1-400Hz along a line 15mm downstream of the Annulus. Left: *vx‴*. Centre: *vy‴*. Right: *vz‴*. Derived from the imaging area 'Annulus 3D'. Bin size 2.5ms^{-1}.

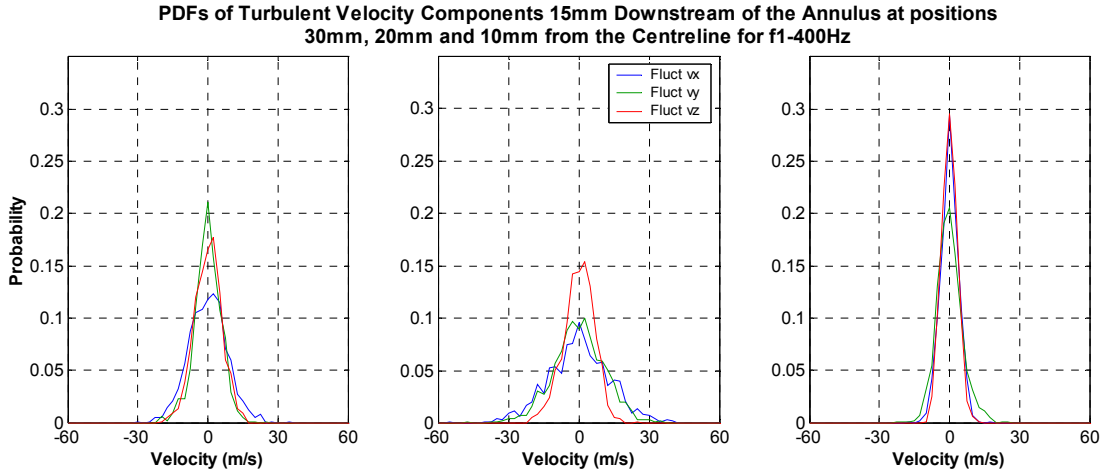

Figure 8-37 Turbulent PDFs of f1-400Hz taken from a line 15mm downstream of the Annulus, and 16mm (Left), 13mm (Centre) and 11m (Right) from the Centreline. Derived from the imaging area 'Annulus 3D'. Bin size 2.5ms^{-1}.

The profiles of skew and kurtosis at 15mm are shown in Figure 8-38. From inspection of the profiles for the individual components there is no common trend among the components and the shear layers are not identifiable form the aspect of the PDFs.

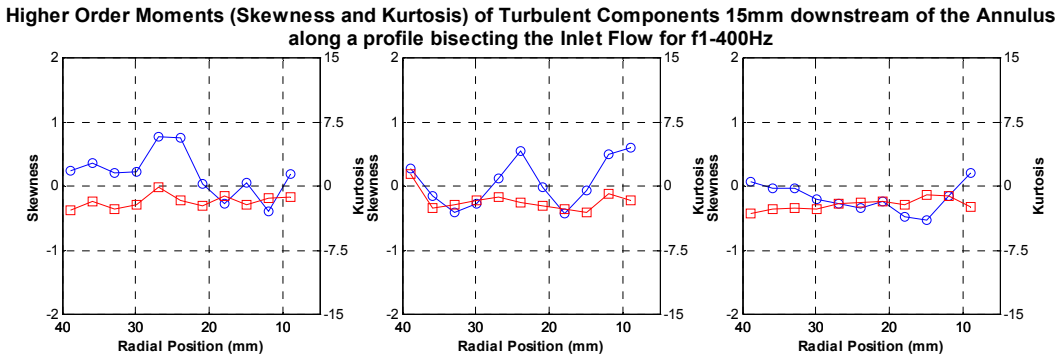

Figure 8-38 Graphs showing profiles of Skewness (blue) and Kurtosis (red) for velocity component distributions of f1-400Hz 15mm downstream of the Annulus. Left: vx'''. Centre: vy'''. Right: vz'''.

The PDFs taken at 30mm downstream are shown in Figure 8-39. These show the same pattern as f1-100Hz but are much coarser and wider which indicates larger fluctuations. In particular vy''' at 20mm and 23mm radial position shows multiple peaks over a very large fluctuation range.

The PDFs at points 10mm, 20mm and 30mm along this radial are shown in Figure 8-40. The PDFs at 30mm and 20mm exhibit a coarser shape and larger fluctuations than those at the 15mm radial and the respective f1-100Hz PDFs. All the PDFs here are asymmetric. Of note is the multi peak of vy''' at 20mm which shows large fluctuation values. At 10mm the PDFs are identical and symmetric with a very narrow base.

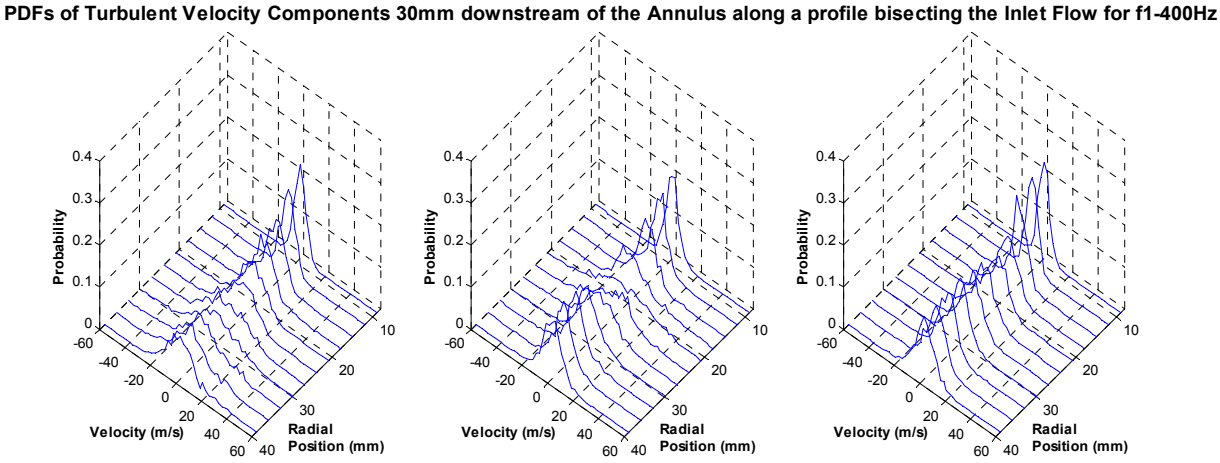

Figure 8-39 Turbulent PDFs of f1-400Hz along a line 30mm downstream of the Annulus. Left: vx'''. Centre: vy'''. Right: vz'''. Derived from the imaging area 'Annulus 3D'. Bin size 2.5ms^{-1}.

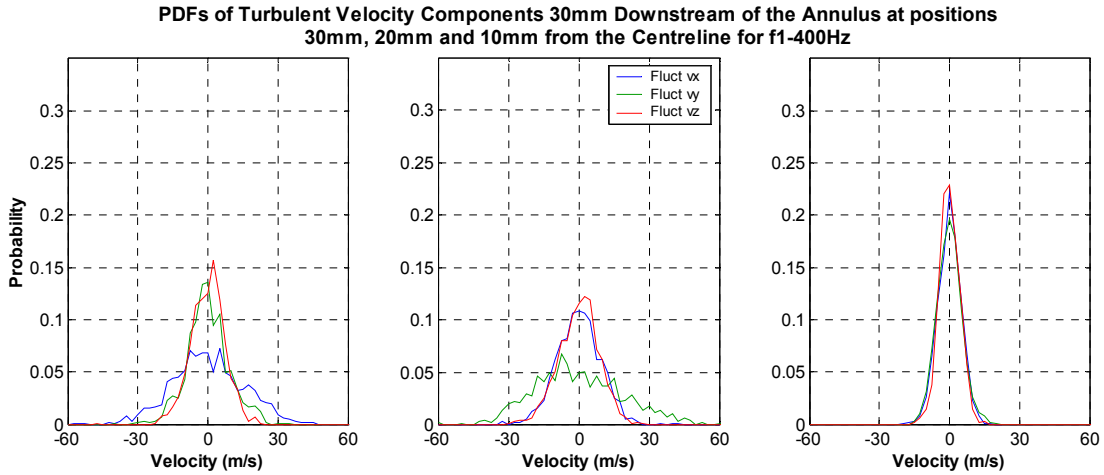

Figure 8-40 Turbulent PDFs of f1-400Hz taken from a line 30mm downstream of the Annulus, and 16mm (Left), 13mm (Centre) and 11m (Right) from the Centreline. Derived from the imaging area 'Annulus 3D'. Bin size 2.5ms^{-1}.

Does not resemble 15mm profiles. Kurtosis always negative and invariant. No similarity among components.

The profiles of skew and kurtosis at 30mm are shown in Figure 8-41. These profiles also do not show a common trend among the components. In addition the respective profiles do not resemble those of 15mm. At this position the kurtosis is negative and almost invariant.

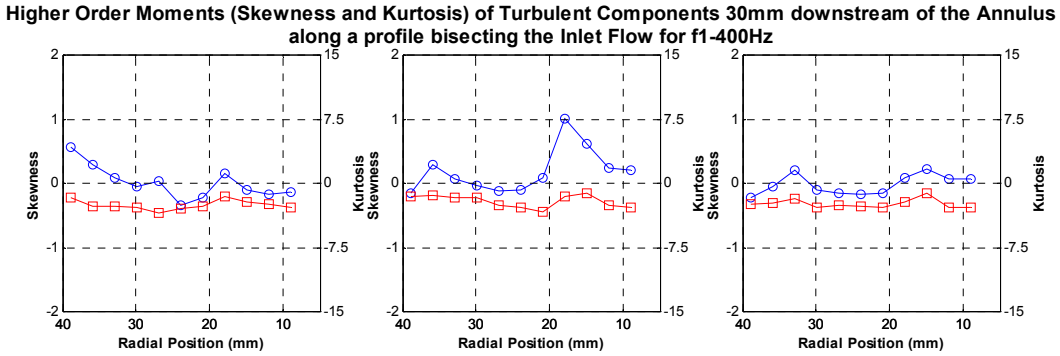

Figure 8-41 Graphs showing profiles of Skewness (blue) and Kurtosis (red) for velocity component distributions of f1-400Hz 30mm downstream of the Annulus. Left: vx'''. Centre: vy'''. Right: vz'''.

The off diagonal Reynolds stresses are shown in Figure 8-42. The same overall spatial characteristics are shown with convergence of the shear stresses towards zero within the IRZ indicating a return to isotropic conditions. This trend lessens with axial distance. The remaining positions are highly anisotropic.

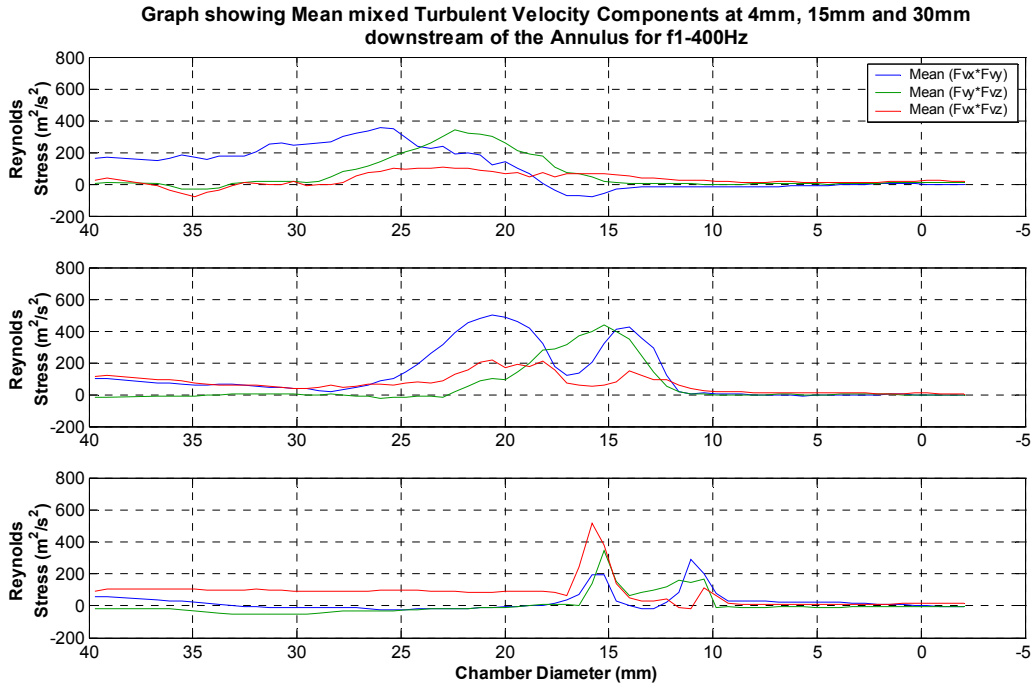

Figure 8-42 Off Diagonal (shear) Reynolds stresses for f1-400Hz along profiles taken at 4mm (Bottom), 15mm (Middle) and 30mm (Top) distances downstream of the Annulus.

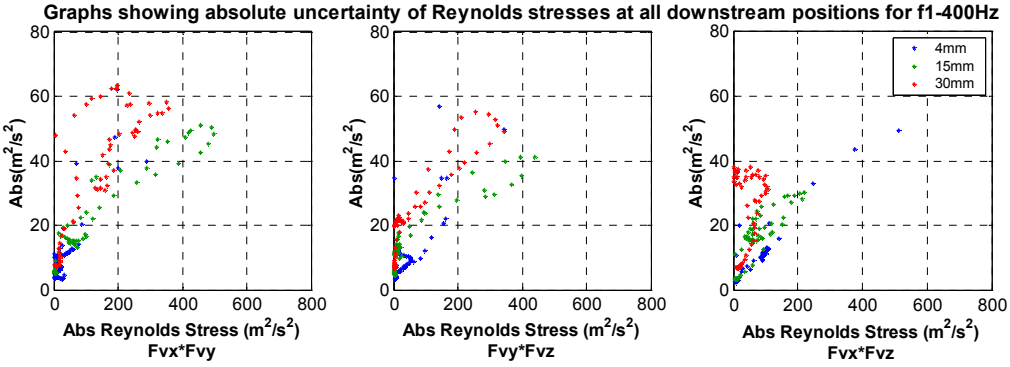

Figure 8-43 Scatter plots showing absolute uncertainty range of the calculated Reynolds stresses at all positions for f1-400Hz. Left: $\overline{vx''' \cdot vy'''}$. Centre: $\overline{vy'' \cdot vz'''}$. Right: $\overline{vx''' \cdot vz'''}$.

8.7 Turbulent Frequencies

Inspection of the phase dependent RMS plots and the PDFs for all three flows has highlighted a distinct temporal pattern in the turbulent components. This, as for f1-100Hz case is clearly at the perturbation frequency. The turbulent frequency at the shear layer is important to know as the turbulence will modify the combustion. Although the SPIV equipment has a limited temporal resolution the fact that the changes of turbulent components have been detected means that this information has been captured by the experiments. A frequency spectrum of the turbulent vector fields should reveal the dominant frequencies of the turbulence. Normally a spatial point would be sampled and analysed. This would be correct in homogeneous turbulence. However, even at 4mm there is small spatial movement of the peaks of the RMS profiles. Therefore sampling at single spatial point would then be a function of spatial deviation and alter the power of the detected frequencies. As the RMS profile gradients in the shear layers are very large this approach can not be used.

Therefore the approach adopted is to sample independent of the radial position. The two shear layers are sampled independently and the following description is for the inner layer. At 4mm downstream of the annulus the turbulent vector fields are sampled from the outer edge shear layer in the vector field to a point in between the two shear layers. The largest fluctuation of each component along this profile should correspond to the shear layer. On this assumption the maximum value is recorded. This continues for the ensemble set. The recorded data is then analysed. The same approach is used for the outer shear layer. This allows a frequency analysis of a dynamic shear layer obtaining its' true velocity fluctuation frequency. This approach was only performed at the 4mm downstream position. At 15mm downstream the inner shear layer was sampled only for vy''' and the outer only for vx''' as the layers have become dominated by the corresponding fluctuation component.

The results for f1-100Hz are shown in Figure 8-44 and Figure 8-45. Close to the annulus it is clear that all three turbulent components have a strong signal at 100Hz with no other dominant frequency at both shear layers. Moving downstream the outer shear layer shows a large signal at 100Hz for vx''' and the inner shear layer has also a large 100Hz signal for vy'''. It is clear that perturbing the flow at 100Hz results in a turbulent fluctuation frequency also of 100Hz and that initially all three components fluctuate at this frequency. Moving downstream 100Hz is still the dominant frequency however the excitation of turbulence is component and shear layer specific indicating damping of the 100Hz frequency for the remaining components in each shear layer respectively.

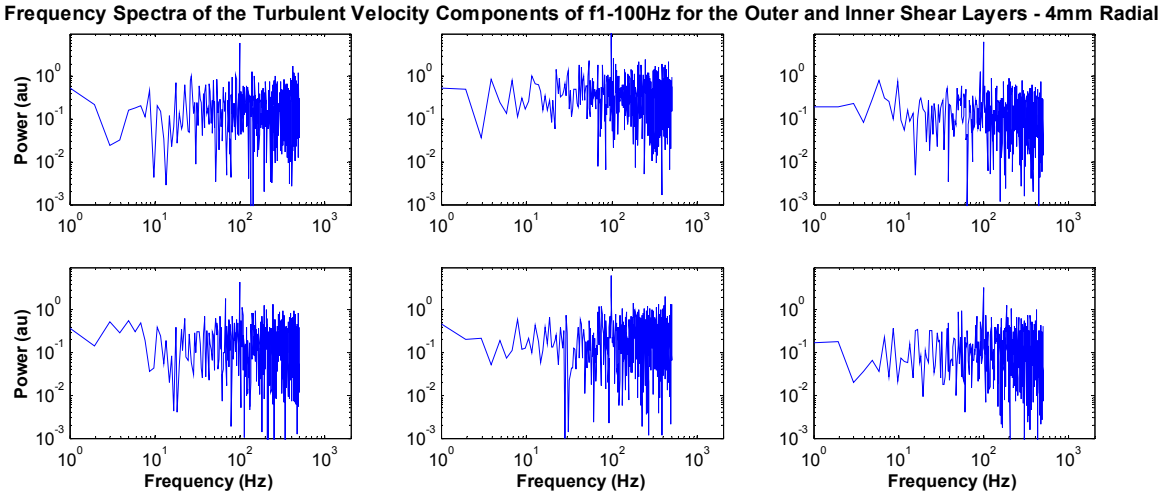

Figure 8-44 Turbulent frequency spectra for f1-100Hz 4mm downstream of the Annulus for the Outer shear layer (Top) and Inner Shear layer (Bottom). Left: vx''' Centre: vy''' Right: vz'''.

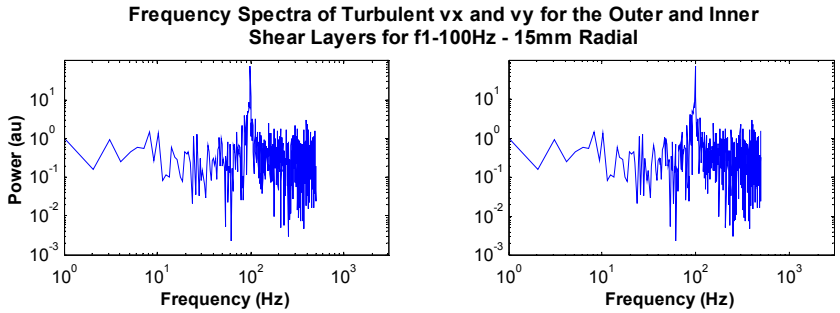

Figure 8-45 Turbulent frequency spectra for f1-100Hz 15mm downstream of the Annulus. Left: vx''' of the Outer Shear layer. Right: vy''' of the Inner shear layer.

Figure 8-46 and Figure 8-47 show the frequency spectra for f1-1200Hz. Close to the Annulus the outer shear layer has a single large frequency of 200Hz for vx''' and vz'''. This is not the case for vy''' which shows no dominant frequency. The opposite is evident for the inner shear layer where only vy''' shows any dominant frequency. The one detected is a wide peak at 200Hz. Moving downstream the outer layer has a single frequency of 200Hz for vx''' as does the inner layer for vy'''. Once more the dominant turbulent frequency matches the imposed perturbation frequency however this time not all components are excited in each shear layer. Both vx''' and vz''' are excited at 200Hz in the outer shear layer and not excited in the inner shear layer indicating a correlated behaviour. The same trend of downstream behaviour is observed with 200Hz perturbation as that of 100Hz.

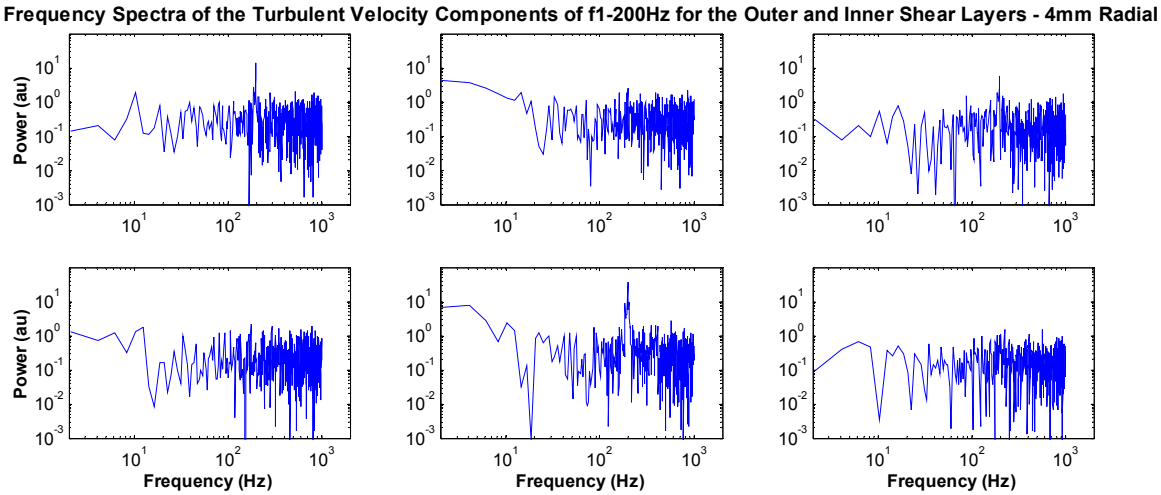

Figure 8-46 Turbulent frequency spectra for f1-200Hz 4mm downstream of the Annulus for the Outer shear layer (Top) and Inner Shear layer (Bottom). Left: *vx‴* Centre: *vy‴* Right: *vz‴* .

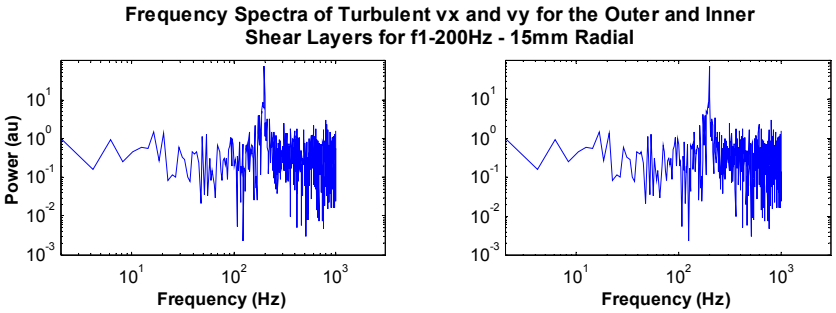

Figure 8-47 Turbulent frequency spectra for f1-200Hz 15mm downstream of the Annulus. Left: *vx‴* of the Outer Shear layer. Right: *vy‴* of the Inner shear layer.

Figure 8-48 and Figure 8-49 show the frequency spectra for f1-1400Hz. In this case the dominance of the imposed 400Hz perturbation is not complete. The outer shear layer shows a clear peak for *vz‴* and *vy‴* with the latter having strong signals of higher frequencies. The strongest frequency for *vx‴* is closer to 550Hz. 400Hz is present but is one of many strong signals. The inner layer has a weak 400Hz signal for *vx‴* and *vz‴* . For *vy‴* a large group of frequencies around 400Hz have a strong signal and two other strong higher frequencies also have a strong signal. Downstream the outer layer *vx‴* spectrum is dominated by the 400Hz signal as is the *vy‴* component of the inner layer.

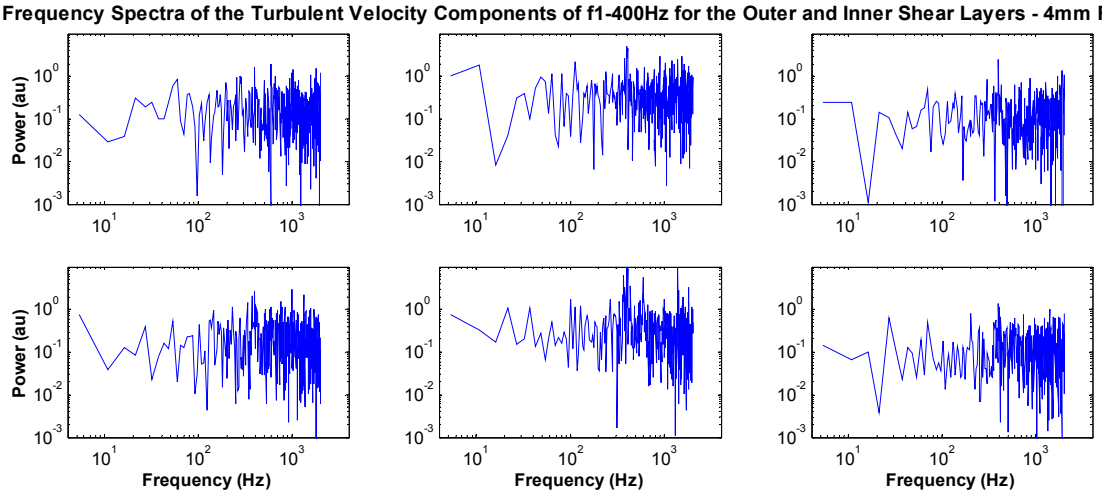

Figure 8-48 Turbulent frequency spectra for f1-400Hz 4mm downstream of the Annulus for the Outer shear layer (Top) and Inner Shear layer (Bottom). Left: vx''' Centre: vy''' Right: vz'''.

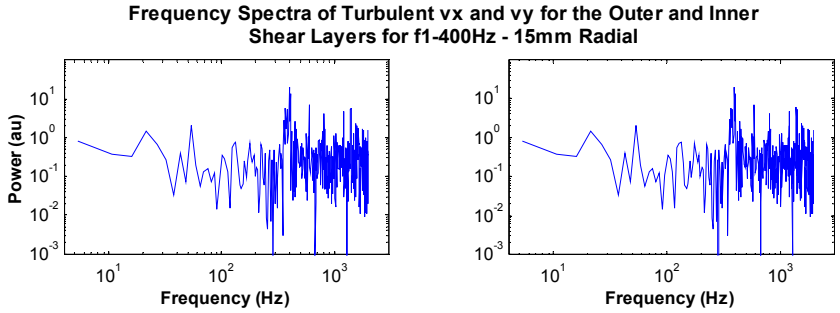

Figure 8-49 Turbulent frequency spectra for f1-400Hz 15mm downstream of the Annulus. Left: vx''' of the Outer Shear layer. Right: vy''' of the Inner shear layer.

8.8 Summary

The turbulence in the vicinity of the annulus has been characterised for f1-100Hz, f1-200Hz and f1-400Hz. Phase dependent RMS plots show the inhomogeneous state of the turbulence and identify the shear layers as regions of intense turbulent fluctuations. The PDFs presented and corresponding skew and kurtosis information allowed the range of turbulent fluctuations to be quantified. In combination it is possible to conclude that close to the annulus all three turbulent components contribute strongly to the turbulence within the shear layers. Moving downstream it is clear that the inner layer is created by vy''', the outer by vx''', and vz''' decreases rapidly. This is true for all three conditions. From the skew and kurtosis profiles it is clear that for f1-100Hz and f1-200Hz both vx''' and vz''' have positive skew in both shear layers biasing them towards a negative fluctuation. For vy''' this is only true for the inner shear layer. This trend could not be identified for f1-400Hz. The shear Reynolds stresses indicate the anisotropy of the turbulence and have shown that within the IRZ the turbulence tends to isotropy. The RMS profiles, PDFs and frequency analysis show that excitation of the turbulence within the shear layers matches the imposed perturbation frequency. This is attributed to the large scale imposed perturbation causing large scale variations of Reynolds number, in effect creating

phase specific turbulence characteristics which result in a distinct frequency of turbulence with clear structure. Excitation of all three velocity components at the imposed frequency is not always true close to the annulus. What has been consistent is that the downstream dominance of vy''' and vx''' in the inner and outer shear layers is always dominated by a frequency matching the imposed perturbation frequency. This implies that in addition to the large scale flame modification of the imposed perturbation the turbulence itself will also cause additional modification in amplifying in phase the reaction rate through flame area interaction.

9 VORTICIES AND VORTICITY STRUCTURE

The nature of combustion and vortex interaction has been shown to vary amongst the literature. A toroidal vortex rolled up at the injector can wrap the reaction zone within it. The structure is then transported downstream with the increased inlet flow rate. Alternatively shear layer instabilities can cause local alterations of the surface of the reaction zone. In this chapter the nature of vorticity and vortices is addressed.

Inspection of the mean flow field images shows no evidence of vortex shedding for f1 or f10 at any of the perturbation frequencies. Movement of the CRZ is observed but this does not constitute vortex shedding. Following the discussion in Chapter 2.3.1 and previous work performed [47] Figure 9-1 has been recreated. Using Eq 2-3 the strouhal numbers and pulsation levels for f1 and f10 for the three frequencies has been plotted[v]. It is clear that all conditions fall below the boundary required for coherent vortex shedding. As shown the pulsation level required to form these types of vortices is extremely high, consistent with previous studies [44]. The small equivalent diameter of the annulus and high axial velocity will help yield a small strouhal number. The imposed frequencies investigated are not large enough to be above the vortex formation boundary. A strouhal number of approximately 0.3 and greater would be needed (f=800Hz approximately) at the current pulsation levels.

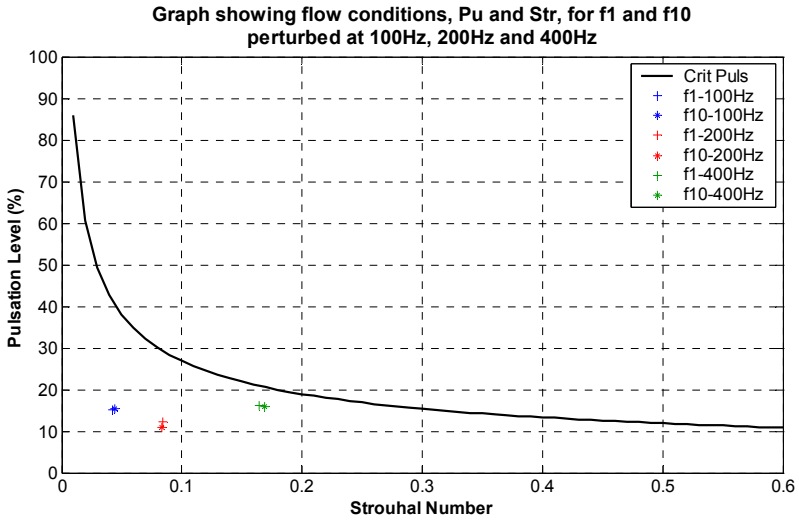

Figure 9-1 Graph showing Strouhal number and pulsation level for f1 and f10 indicating the conditions are below the coherent vortex formation boundary.

[v] The mean velocity, $\overline{u}$ and mean axial velocity $\overline{u}_x$ were determined by integrating across a profile 4mm wide at the furthest upstream position of the inlet flow using results from imaging area 'Annulus 3D'.

	Frequency (Hz)	|v| Mean (m/s)	|v| rms (m/s)	vy Mean (m/s)	Pu (%)	Str
f1	100	60.797	9.206	46.086	15.143	0.043
	200	60.894	7.435	46.768	12.210	0.084
	400	60.464	9.706	47.719	16.053	0.164
f10	100	59.348	9.205	44.585	15.510	0.044
	200	60.879	6.709	46.823	11.020	0.084
	400	59.405	9.451	46.437	15.909	0.169

Table 9-1 Table showing mean velocity magnitude and mean axial velocity integrated over the inlet flow profile. Pulsation levels and strouhal numbers for the investigated conditions also shown.

The results shown in Chapter 7 do not show vortex rollup or shedding. From Chapter 2.3.1 the majority of the presented works also do not show vortex shedding, rather large scale IRZ motion. The LES simulations in Chapter 3.2.4 also do not show large scale vortex shedding.

Inspection of the instantaneous vector fields reveals that vortices are present within the flow however. Therefore to be conclusive it is necessary to use the vector fields to determine the location of any vortices present.

9.1 Vortex Shedding

9.1.1 Vortex Identification

There is no absolute definition of a vortex, its centre or boundary. Various definitions are available in the literature where a comparison is made between strain and vorticity. The Q criterion method inspects the second invariant of the velocity gradient tensor, which subtracts the square of the strain tensor from the square of the trace of the vorticity tensor. Positive values indicating that vorticity is dominant. Other methods include the λ_2 method [129]. If the second Eigen value λ_2 of the velocity gradient tensor is negative then that point has greater vorticity than strain [130].

These were implemented and found to be unsuitable for this work. These definitions highlighted areas of high vorticity over strain as opposed to a definitive vortex structure which is what is desired in this case. A definition was found that was developed from experimentally collected vector fields and its successful application demonstrated [131]. This definition is based on two parts, the determination of a vortex centre and the subsequent determination of its boundary. A vortex centre is defined by considering a derived scalar Γ_1.

This scalar is derived considering a point P in the vector field. This point is bounded by an area S (with unit vector z normal to the vector field) consisting of N vectors at position M. For each point M within the defined area a vector is created from the point P to M and the cross product of this and the velocity vector at M calculated. This is then divided by the product of the modulus of the vector PM and modulus of the velocity vector at position M. This is equivalent to calculating the sin of the angle between position vector PM and velocity vector at M. This is calculated for all points M and divided by the number of vectors N.

This yields a scalar which indicates the rotation of the fluid around point P. If all the vectors have a direction around P of 90 degrees (perfectly circular) then the result of this calculation should be 1 or -1 depending if it the rotation is clockwise or anticlockwise. The use of a threshold can subsequently be used to determine if the scalar value represents a vortex centre.

$$\Gamma_1(P) = \frac{1}{N}\sum_S \frac{(PM \otimes U_M)\cdot z}{\|PM\|\cdot\|U_M\|} = \frac{1}{N}\sum_S \sin(\theta_M) \qquad \text{Eq 9-1}$$

A second scalar, Γ_2, is used to determine the vortex boundary. This is based upon the previous equation and utilises the same notation. In addition a local convection velocity $\overline{U}_P$ around the position P is utilised. This scalar is derived by splitting the velocity gradient tensor into its symmetric (deformation tensor) and anti-symmetric (rotation tensor) parts. Which are the rate of strain tensor and vorticity tensor.

$$\nabla U_{ij} = \frac{\partial u_i}{\partial x_j} = e_{ij} + \Omega_{ij} \qquad \text{Eq 9-2}$$

$$e_{ij} = \frac{1}{2}\left(\frac{\partial u_i}{\partial x_j} + \frac{\partial u_j}{\partial x_i}\right) \quad and \quad \Omega_{ij} = \frac{1}{2}\left(\frac{\partial u_i}{\partial x_j} - \frac{\partial u_j}{\partial x_i}\right) \qquad \text{Eq 9-3}$$

The collected vector fields allow determination of only four of the full nine parts of any tensor. The scalar Γ_2 is a comparison between local vorticity and the Eigen value of the strain tensor (local principle strain rate value). It is calculated using the following algorithm.

$$\Gamma_2(P) = \frac{1}{N}\sum_S \frac{\left[PM \otimes \left(U_M - \overline{U}_P\right)\right]\cdot z}{\|PM\|\cdot\left\|U_M - \overline{U}_P\right\|} \qquad \text{Eq 9-4}$$

Once again this scalar at a point P returns a value from 1 to -1 depending on the direction of rotation. The authors proposed absolute values of Γ_2 corresponding to instances of dominant rotation, strain or shear irrespective of magnitude. The value of Γ_2 which corresponds to purely rotation is $|\Gamma_2| \geq 2/\pi$.

9.1.2 Implementation of algorithms

In order to collect the vortex statistics every collected vector field was inspected. The vector field was called and the vx and vy components extracted as scalar fields before being enlarged by a factor of two. This required bilinear interpolation of size 2×2 but yielded a finer spatial resolution. The first scalar, Γ_1, was calculated for all points in the vector field accounting for missing vectors at the boundaries and positions where no suitable vector was calculated. Once the scalar field was derived it was treated twice for clockwise and anticlockwise vortices. Considering positive vortices the image was thresholded by a value of 0.8, all pixels with values less than this were set to zero. This image was then

scanned. When a non-zero value was encountered the neighbouring pixels were interrogated by a cross shaped cell. Pixel values of this cell were copied into a temporary image. This image was then scanned by the same interrogation cell, when a non zero value was encountered pixel values of the thresholded Γ_1 image were copied into a second temporary buffer. If these two images are identical then all valid pixel values for that vortex have been determined, the maximum of this group was then used as the centre for the particular vortex and stored in a result image. The temporary images were destroyed. The scanning of the thresholded image then continued until another non-zero value was encountered. Once complete the scalar image was then oppositely thresholded (-0.8) to allow the location of anticlockwise vortices and the scanning procedure was repeated. The locations of clockwise and anticlockwise vortices for a vector field were stored in separate images.

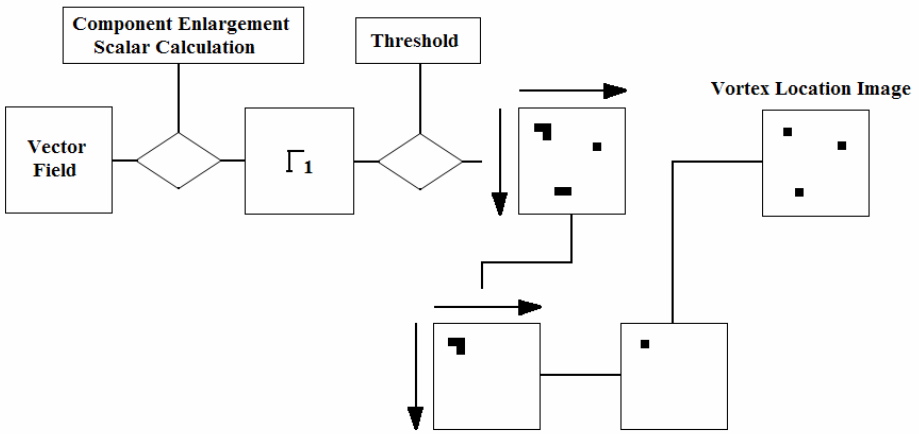

Figure 9-2 Diagram illustrating Γ_1 calculation process for an arbitrary direction of rotation.

The second scalar, Γ_2, was calculated with the enlarged velocity component scalar fields and accounted for boundaries and missing vectors. This was also treated twice for clockwise and anticlockwise vortices. Once the scalar field was calculated it was once again thresholded corresponding to $|\Gamma_2| \geq 2/\pi$. A verification was then performed ensuring that the calculated vortex centre locations had a non-zero value in the Γ_2 thresholded image. If they did not these vortex centre locations were removed (set to zero). The verified vortex location image was scanned again. When a non-zero value was encountered this pixel location was used to instigate scanning in the thresholded Γ_2 image. A cross shaped interrogation cell was used which copied the pixel values to a temporary image. This temporary image was then scanned; when a non-zero value was encountered the same cross shaped interrogation cell copied the pixel values from thresholded Γ_2 image into a second temporary image. The two temporary images were then compared, if identical the boundary of the vortex had been mapped if not the process continued until the images were identical. After this the mapped boundary was stored in a result image. The temporary images were then destroyed. Scanning of the verified vortex location image then continued and subsequently resulted in a complete result image which contained the vortex

boundaries of all valid vortices for a vector field. This process was repeated for anticlockwise vortices and the results stored in separate images.

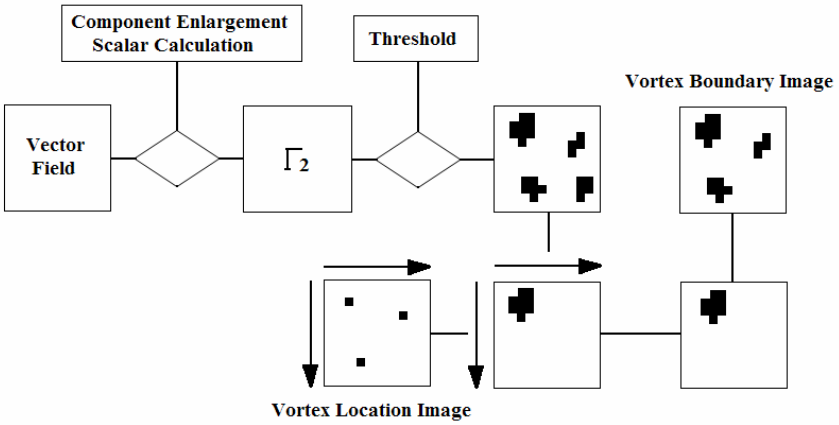

Figure 9-3 Diagram illustrating Γ_2 calculation process for an arbitrary direction of rotation

This gave a multi frame file for each vector field consisting of the two derived scalar fields, accurate locations of the vortices and their respective boundaries (both directions) with pixel locations corresponding to vector locations. This process was implemented in a custom written macro and executed through the Lavision Davis 7.1 software. Below is a vector field of f1-100Hz at phase position 2. Figure 9-5 shows four frames with the derived scalar fields of Γ_1, Γ_2 and the identified vortices from the vector field.

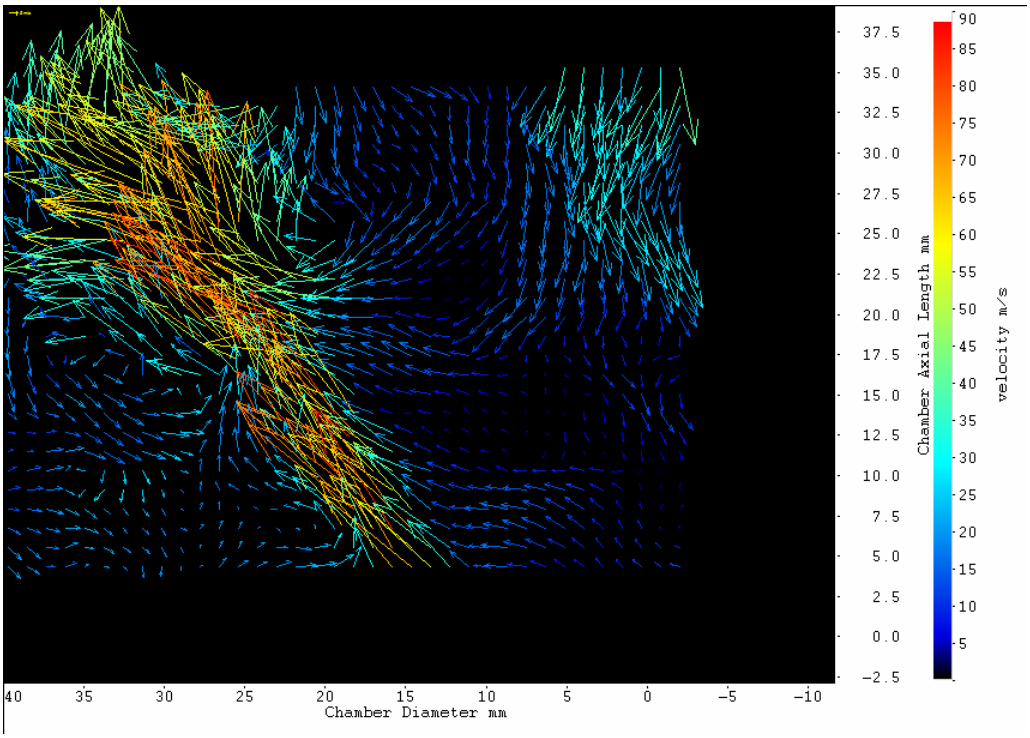

Figure 9-4 Phase 1 instantaneous vector field of f1-100Hz at the 'Annulus 3D' imaging area. The vectors show the in plane components (vx and vy). The colour of the vector arrow and its length represent the velocity magnitude based on all three velocity components. Only a quarter of the vectors are shown for clarity

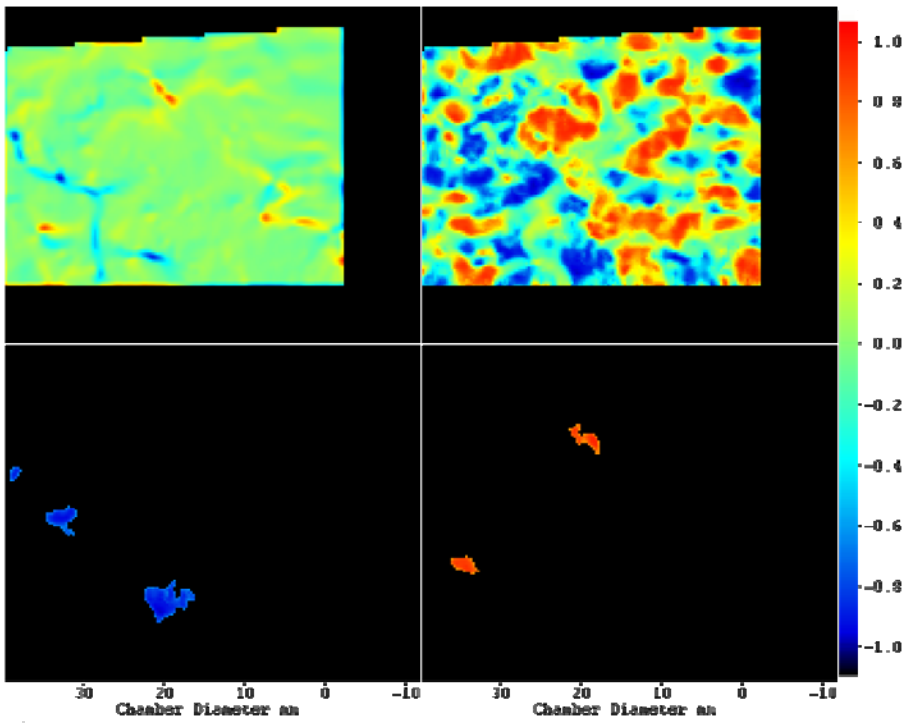

Figure 9-5 Results of the Vortex Identification algorithms. Top left frame is the scalar Γ_1, top right is the scalar Γ_2. Bottom left corresponds to identified anticlockwise vortices and bottom right to clockwise vortices.

Once each instantaneous vector field has been processed each phase can be treated to derive phase based locations of the vortices. Firstly a mean of the scalar field Γ_2 is calculated using all the instantaneous Γ_2 scalar fields. This image shows areas of the flow which are dominated by clockwise or anticlockwise vortices. The image is then thresholded to setting any positive values greater than 0.05 to 1 and any negative values less than -0.05 to -1. This creates a mask image for both directions of vortices. A summation of the vortex location images of each vector field for each phase for each direction was performed which displays the location of all vortices for the particular phase. This summation image was then multiplied with the mask image. This effectively removes vortices which occurred in a random position. The resultant vortex location image can then be used to ascertain where predominantly vortices are located.

The effect of the bilinear interpolation scheme used resulted in the doubling of image pixels for each spatial scale, doubling the resolution. This is achieved in two passes. New pixels filled in the first pass have contributions from four original pixels. New pixels filled in the second pass have contributions from two original pixels and two first pass pixels. Therefore if the first pass pixels contain contributions from 4/8 original pixels, the second pass pixels in effect contain information from 3/8 original pixels.

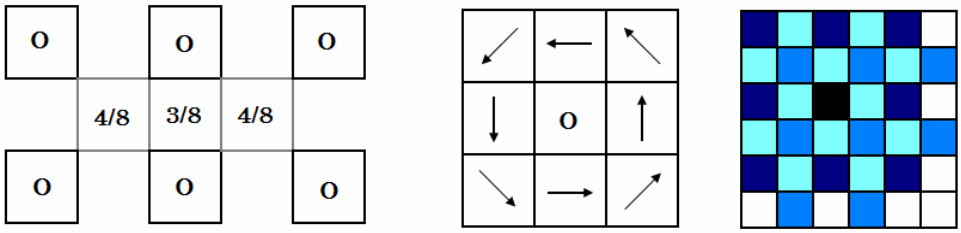

Figure 9-6 Left: Illustration showing the contribution of actual measurements to bilinear interpolated pixel positions. Right: The original vector field circulating a origin. Enlarged interpolated field showing actual measurements (Navy blue), 4/8 interpolated pixels (blue) and (3/8) interpolated pixels (sky blue). All around the origin.

Figure 9-6 shows an original vortex with vectors circulating about the centre pixel O. With this enlarged the origin, now indicated by the black pixel, does not have any original pixels in its immediate vicinity. For the ideal situation depicted this would not affect the identification of O as the centre of the vortex. In reality the highly turbulent vectors would not be distributed as this. Assuming the recorded vectors still circulated about the origin in a less ordered fashion it is possible for any of the new pixels surrounding the origin in the enlarged image to be identified as the vortex centre. Therefore the enlargement and interpolation process does allow a finer scale to asses the vortex position. However the uncertainty of this calculation is equivalent to an area of 3×3 pixels. This is 1.5 times the original scalar field resolution. The original scalar field resolution was 0.7618mm/pixel, the new resolution was 0.3809mm/pixel with an uncertainty of ±0.5714mm, 1.1428mm absolute uncertainty. This is equivalent to 1.5 times the original resolution.

9.1.3 Vortex Locations

Figure 9-14, Figure 9-16 and Figure 9-18 show the locus of identified vortices throughout the chamber for f1 perturbed at 100Hz, 200Hz and 400Hz. The results for f10 are in Appendix B. In conjunction mean vorticity images are also shown in

Figure **9-15**, Figure 9-17 and Figure 9-19. For each frequency it is clear that a distinct division exists regarding the spatial location of clockwise and anticlockwise vortices. In each case clockwise vortices are located at the inner shear layer and anti clockwise ones at the outer shear layer. This is expected due to the reverse flow of the vortex breakdown stabilisation process. Moving downstream the anticlockwise vortices are primarily found near the CRZ and are limited to the extent they are found downstream near the chamber wall. Conversely the clockwise vortices are far greater in number and spread radially outward in location with downstream distance until there are no more anticlockwise vortices present. This is due to the increased radial width of the reverse flow region. The number of clockwise vortices present in the 'Flame Zone' and 'URZ' can be attributed to some extent to flame generated vorticity. This has also been observed in LES simulations [73], see chapter 3.2.4.

Although there is a definitive pattern of vortex location and a noticeable change of this pattern for all frequencies of perturbation there is no definitive cluster of identified centres that is generated at the annulus and moving downstream. Moreover the identified vortices appear to have no relation to the imposed perturbation frequency. This confirms that there is no large scale coherent toroidal vortex formation on the shear layer of the type reported in chapter 3.2.4 [44, 74]. The same conclusion can be made for f10 whose results are presented in Appendix B.

9.2 Vorticity Structures

The vorticity structures shown in

Figure 9-15, Figure 9-17 and Figure 9-19 compare very well with the CH* images for the respective frequencies. As previously noticed a distinct boundary exists from the annulus separating positive (red) and negative vorticity (blue). Once more it is positive vorticity which survives large axial distances and dominates downstream positions. This is flame generated vorticity combing with the flow reversal of the IRZ. The distinct changes of vorticity through the induced cycles show that the vorticity structures are oscillating at the imposed perturbation frequency. F1-200Hz in particular shows the inward curling of positive vorticity structure that matches very well to what was observed in the chemiluminescence images due to the second cell within the IRZ. These structures are more easily comparable to the chemiluminescence images than the streamlines regarding common structure. In fact as the inlet flow is perturbed the mean vorticity structures can be seen to change shape due to the IRZ and CRZ behaviour. This indicates the vorticity structures are not solely a function of the inlet flow.

Mean in plane vorticity images have been created from vector fields of the imaging area 'Annulus 3D'. This was performed for each phase and profiles were extracted 4mm and 20mm downstream of the annulus. These show the two distinct clockwise and anticlockwise structures either side of the inlet flow. Considering f1-100Hz (Figure 9-7) and the profile at 4mm the anticlockwise vorticity (negative) is greater in amplitude than the clockwise vorticity as the inlet flow reduces (Phases 9 to 3). It also appears that the vorticity at the outer shear layer exhibits less variation of vorticity than the inner shear layer. Clockwise vorticity at the inner shear layer shows a much larger variation. The profiles at 20mm are shifted radially outward due to the inlet flow structure bending outward. The peaks are also considerably wider. At this position the outer shear layer vorticity is consistently less than the inner shear layer vorticity, although both are considerably less than the profiles at 4mm. This means that vorticity is a maximum at the annulus entry and decreases with axial distance until the reaction zone is encountered. It also implies that the outer shear layer vorticity decreases quicker than the inner shear layer vorticity.

Similar trends can be seen for f1-200Hz in Figure 9-8. During the reduction of inlet flow rate the outer shear layer vorticity is greater than the inner shear layers' (Phases 1 to 4) for the 4mm profiles. The outer shear layer also shows less variation during the instability where as the inner layer like f1-100Hz exhibits a drastic change of vorticity. The profiles at 20mm are less in magnitude than those of 4mm, confirming that vorticity reduces downstream. The inner shear

layer vorticity is now greater than the outer layers' at all phases. The shape of the 4mm profiles is very similar to f1-100Hz but the 20mm profiles show a deviation from those of f1-100Hz due to the modification of the inlet flow structure by the second cell of the IRZ. This is seen as an increase broadening of the peaks and more radial displacement.

The profiles of f1-400Hz (Figure 9-9) at 4mm show a much larger variation of anticlockwise vorticity than either of the other two frequencies and reduction of anticlockwise vorticity occurs with clockwise vorticity. However the anticlockwise vorticity is greater than clockwise as the inlet flow increases and decreases. It is only at the peak of inlet flow that the clockwise vorticity is greater (Phases 2 to 4). The profiles at 20mm agree with what has been observed, less in magnitude than their 4mm counterparts, broader and radially displaced. The only noticeable deviation is that anticlockwise vorticity is near zero during phases 8 and 9. This can be observed in Figure 9-9 for f1-400Hz phase 8 where along the 20mm axial distance profile of the CRZ there is a kink in the negative vorticity structure and minimal vorticity until radial distances grater than 40mm are encountered and the CRZ is reached. (The radial limit of the Annulus 3D imaging area is 40mm).

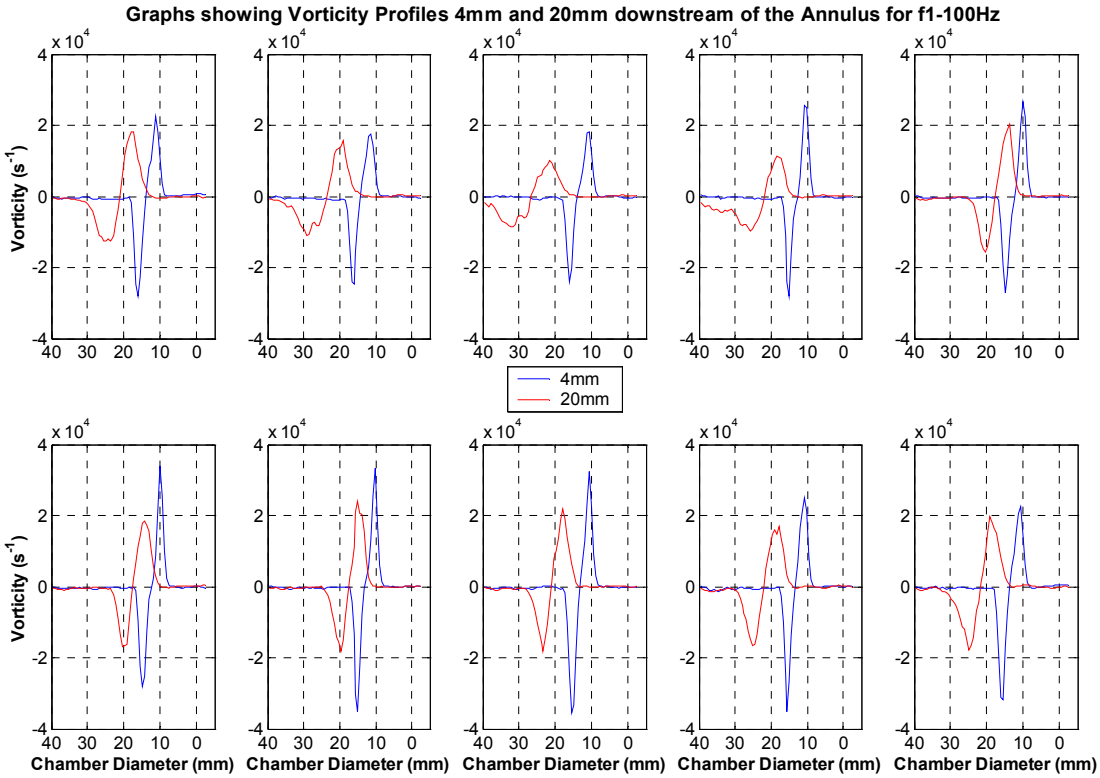

Figure 9-7 Vorticity profiles of f1-100Hz along a line 4mm downstream of the Annulus. Taken from mean vorticity fields from the imaging area 'Annulus 3D'. The top row consists of phases 1 to 5 from left to right. The bottom row consists of phases 6 to 10 from left to right.

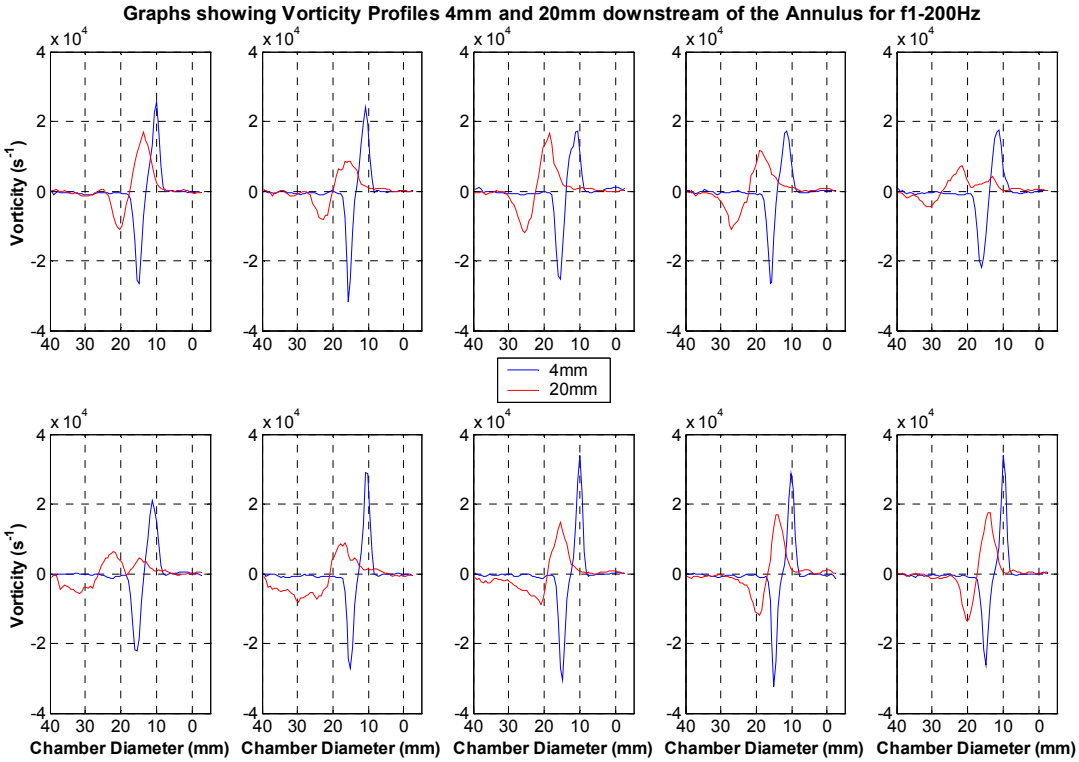

Figure 9-8 Vorticity profiles of f1-200Hz along a line 4mm downstream of the Annulus. Taken from mean vorticity fields from the imaging area 'Annulus 3D'. The top row consists of phases 1 to 5 from left to right. The bottom row consists of phases 6 to 10 from left to right.

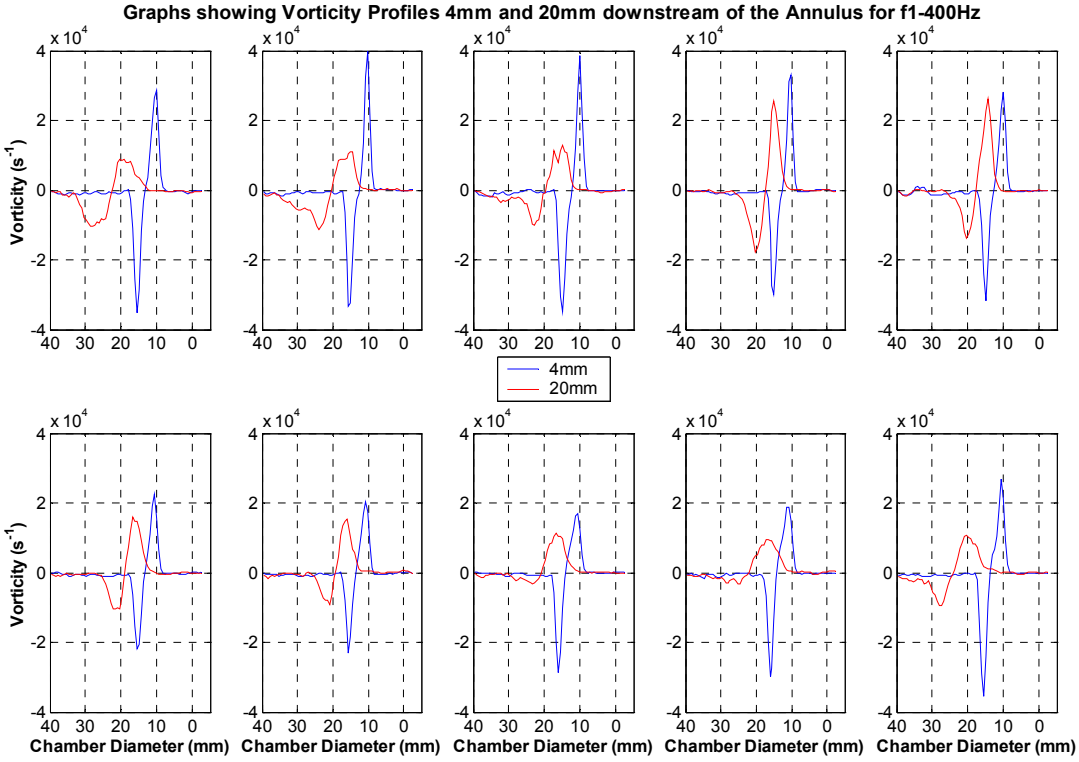

Figure 9-9 Vorticity profiles of f1-400Hz along a line 4mm downstream of the Annulus. Taken from mean vorticity fields from the imaging area 'Annulus 3D'. The top row consists of phases 1 to 5 from left to right. The bottom row consists of phases 6 to 10 from left to right.

As is demonstrated by the mean vorticity images of Figure 9-15 Figure 9-17 and Figure 9-19, and vorticity profiles of Figure 9-7, Figure 9-8 and Figure 9-9 vorticity is changing with the imposed perturbation. The instantaneous vector fields of the imaging area 'Annulus 3D' can be used to derive the instantaneous vorticity fields which can then be analysed with respect to frequency spectra as was done for the inlet velocity. Three positions have been chosen along the 4mm axial profile. These correspond to the centre of the inlet flow, centre of the inner shear layer and centre of the outer shear layer.

The results of this analysis are shown in Figure 9-10, Figure 9-11 and Figure 9-12 for f1-100Hz, f1-200Hz and f1-400Hz. Considering f1-100Hz it is clear that all three positions experience the imposed 100Hz and that this is easily the dominant frequency. This dominance is greatest at the centre of the inlet flow as shown by the centre spectrum of Figure 9-10. The inner shear layer has an equally strong 100Hz frequency and a harmonic at 200Hz of half the strength. Although these two frequencies are the strongest the other resolvable frequencies have greater strength than in the centre of the inlet flow. The outer shear layer has the strongest 100Hz signal of all three positions. Other strong frequencies are at 200Hz, 450Hz, 320Hz, 300Hz and 150Hz in descending strength. Apart from the 200Hz and 300Hz harmonics these other frequencies are not detected in the centre of the flow or the inner shear layer. The remaining frequencies in the outer shear layer have the greatest strength of the three positions. It is clear that the frequency of vorticity is dominated by 100Hz and possesses harmonics at 200Hz and 300Hz which only occur in the shear layers. These have been detected in the frequency analysis of the integrated CH chemiluminescence signal and the inlet velocity spectrums of chapter 7.1.

The frequency analysis for f1-200Hz is similar to that of f1-100Hz. The frequency detected at the centre of the inlet flow (centre plot of Figure 9-11) is purely 200Hz. The dominance of this frequency over all others is greatest at this position. The inner shear layer has the same dominant 200Hz frequency of equivalent power. As previously observed the second harmonic is present, this time at 400Hz and is approximately half the power of 200Hz. The remaining resolvable frequencies are slighter greater in power. In the outer shear layer there is no clearly dominant frequency. Peaks are found at 100Hz, 200Hz, and 400Hz of approximately the same power. The strength of these frequencies is a factor of 4 less than the 200Hz signal in the inlet flow centre and inner shear layer. As was observed for f1-100Hz, the centre of the inlet flow and inner shear layer exhibit dominant frequencies of 200Hz and the second harmonic 400Hz. However the outer shear layer is not so distinct with several weaker equal frequencies present.

For f1-400Hz the inner and outer shear layer frequency spectra are very similar. Both have an equally strong dominant frequency of 400Hz with no clear harmonic and the equal dominance over the remaining resolvable frequencies. The centre of the inlet flow also has a single dominant frequency of 400Hz but the power of this signal is less than the shear layers. Once more the dominance of this frequency over the others is greatest at this position.

The frequency analysis presented shows very good agreement with that undertaken for inlet pressure measurements (chapter 5.6.2), the inlet velocity components and magnitudes (chapters 7.1.1, 7.2.1 and 7.3.1), and the integrated CH* images (chapters 7.1.2, 7.2.2 and 7.3.2) for the respective frequencies. For both f1-100Hz and f1-200Hz at least one harmonic is detected besides the perturbation frequency. This study reveals the importance of the shear layers as these seem responsible for the harmonic frequencies previously detected. The behaviour of each shear layer appears to be similar in some cases but different for f1-200Hz. This behaviour has been characterised 4mm downstream of the annulus and not determined further downstream where it could change. Care must be taken when comparing this analysis with the frequency analyses of those above. This analysis is based purely upon in plane vorticity, that about z. The other analyses are able to take into account all aspects, either through all velocity components being measured or a scalar which automatically includes all component information. Dual plane PIV would be required to perform a full vorticity frequency analysis and compare to those already performed. It is possible the remaining weaker harmonics would be detected in vorticity about a different axis.

A feature to all modes of vortex breakdown is the vortex core. For non annular inlets the vortex breakdown mode tends to be the spiral type where the spiral is the vortex core. This survives quite large distances into the chamber. If this begins to precess then the impact upon combustion could be significant. For annular combustors the vortex breakdown is the bubble type and the vortex core is wrapped around the reverse flow IRZ coinciding with the inner shear layer. An additional vorticity structure wrapped around the outer shear layer has also been observed. From the LES studies (chapter 3.2.4) these are tightly wrapped structures which do not survive large axial distances. Again it has been shown that either can precess and affect the combustion. For the cases presented here it is impossible to identify the vortex core, or outer vorticity structure, their penetration and to ascertain if either is precessing. It is extremely likely that these features are present and do enter into the chamber from the annulus. The frequency spectra of the outer shear layer for f1-100Hz and f1-400Hz show no unexpected frequency signal. F1-200Hz is less clear with detected frequencies at 100Hz and 50Hz however these can not be attributed to a PVC. The inner shear layer spectra also show no unexpected frequency signals. The impact of the vortex core impact is assumed to be minimal when compared to the effects of the imposed perturbation.

As discussed the frequency analysis results agree with those already performed. However the results of the vortex identification analysis do not indicate a dominant frequency present or harmonic that has been associated to each respective flow. The frequency analysis of vorticity is limited due to the lack of sufficient temporal resolution offered by the high speed cameras. Previous studies have utilised linear stability analysis of turbulent shear layers to identify shear layer instabilities.

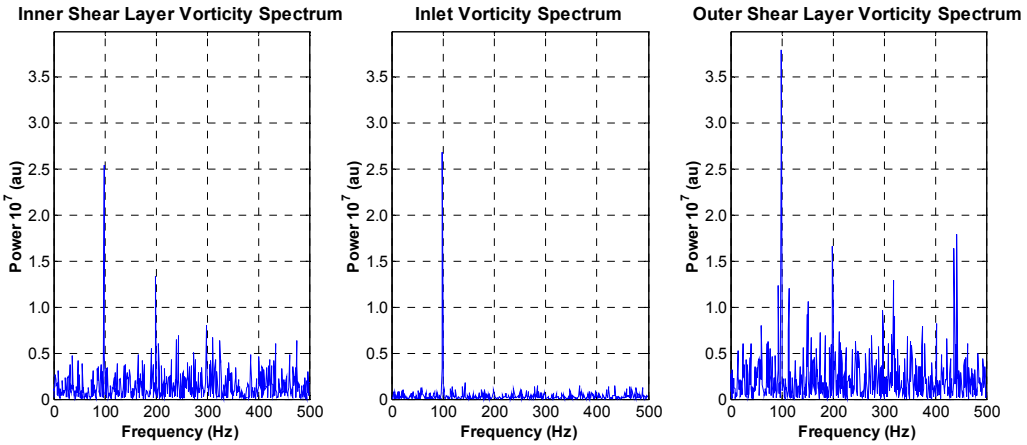

Figure 9-10 Frequency spectrums taken from the f1-100Hz Instantaneous Vorticity fields recorded at the 'Annulus 3D' imaging area. The radial position of the inner shear layer is 11mm, the inlet flow centre 13mm and outer shear layer 16mm.

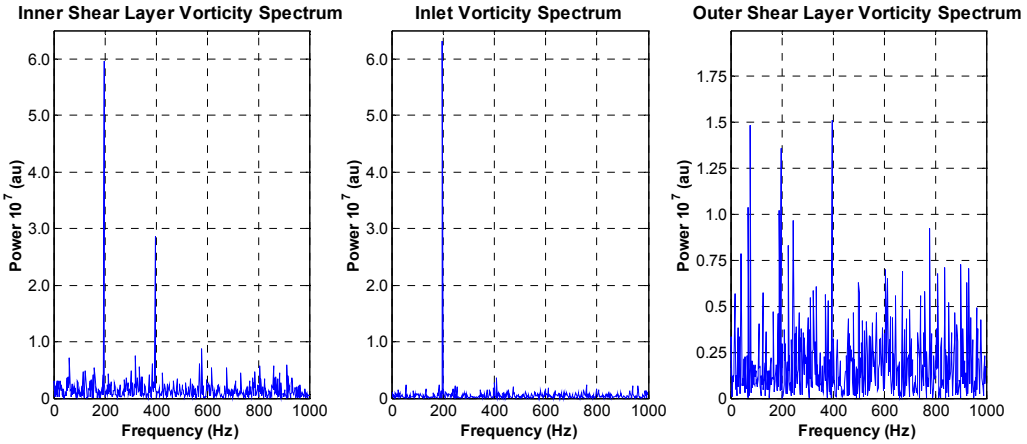

Figure 9-11 Frequency spectrums taken from the f1-200Hz Instantaneous Vorticity fields recorded at the 'Annulus 3D' imaging area. The radial position of the inner shear layer is 11mm, the inlet flow centre 13mm and outer shear layer 16mm.

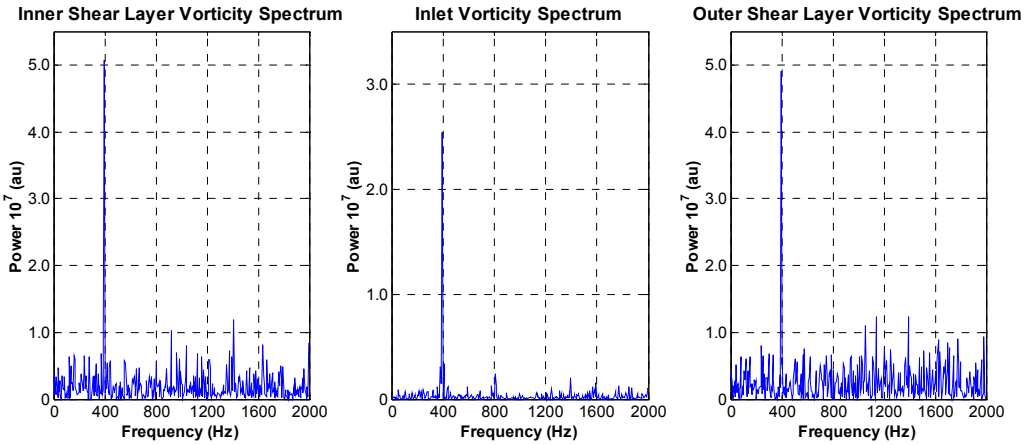

Figure 9-12 Frequency spectrums taken from the f1-400Hz Instantaneous Vorticity fields recorded at the 'Annulus 3D' imaging area. The radial position of the inner shear layer is 11mm, the inlet flow centre 13mm and outer shear layer 16mm.

9.3 Vorticity or Vortex Shedding

As has been shown the flows considered here demonstrate large scale vorticity motions which coincide with the mean streamline images and CH images of Chapter 7. The vortex identification results show that the detected vortices appear not to be related to the imposed perturbation frequencies. Of the two of more importance is vorticity shedding. Any element of fluid shed off the annulus that interacts with the reaction zone of the flame will impart local strain and curvature effects causing local extinction, surface area changes, increased reaction rates, increased flame speed and spatial deviations. In particular the LES works in chapter 3.2.4 have highlighted vorticity shedding as responsible for the variations of heat release rate. In those cases shear layer instabilities of the inlet was coupled to the oscillating heat release rate through the acoustic modes of the inlet and chamber. Distinction must be made and correct emphasis placed upon vorticity interacting with the reaction zone rather than tracking specific vortices.

Figure 9-13 shows a sequence of vorticity images taken from imaging area 'Annulus 3D'. The two oppositely rotating structures are visible on the instantaneous vorticity fields. Vorticity can be seen to vary within these two structures with small islands of very high vorticity along the shear layers. These will cause additional local combustion modulation as already described. The image sequence of Figure 9-13 shows an instantaneous structure very similar to those revealed by LES [73-75] in chapter 3.2.4 .

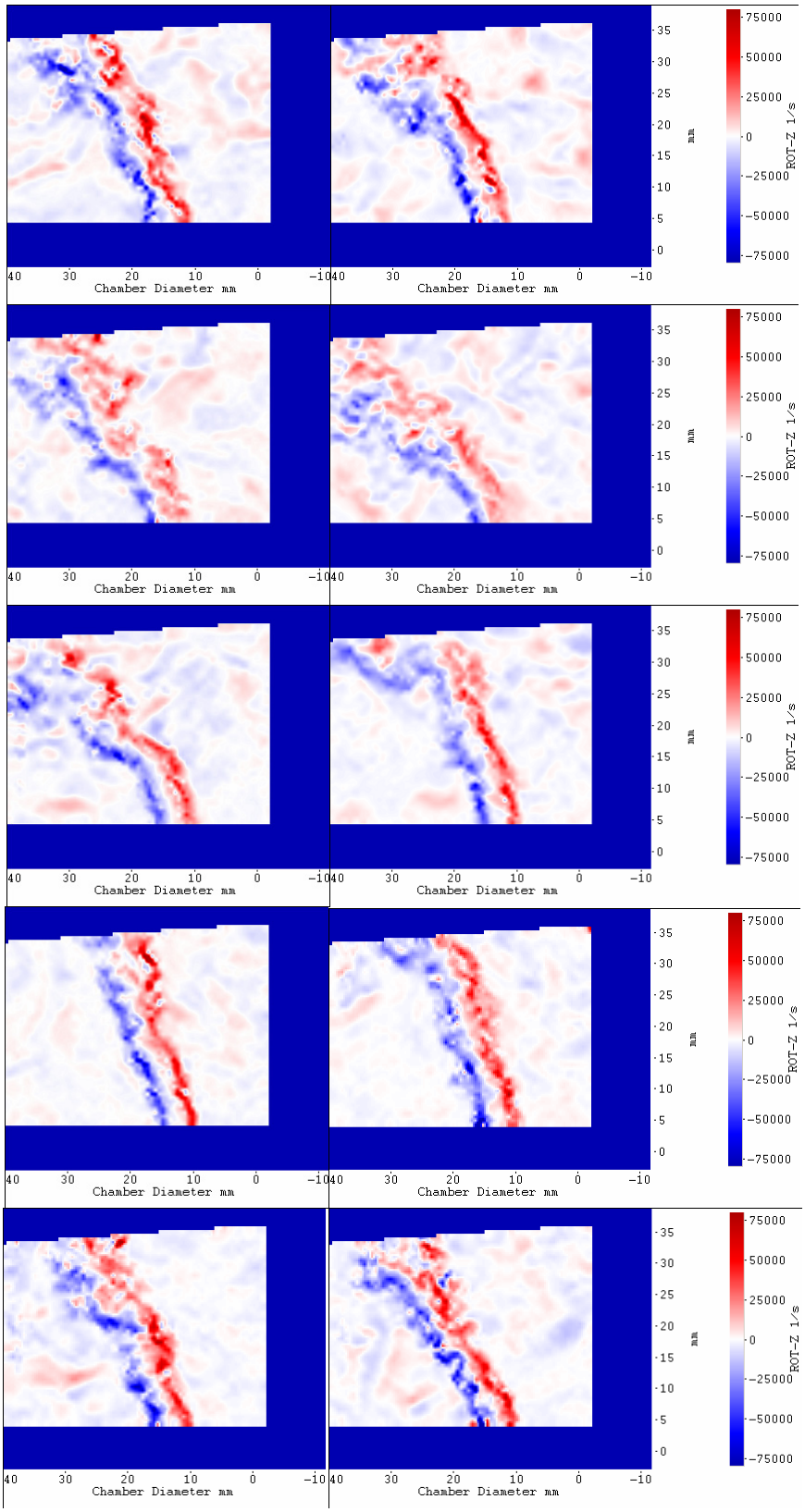

Figure 9-13 Sequence of instantaneous vorticity images for f1-100Hz at imaging area 'Annulus 3D'. The vorticity scale is artificially saturated at 80000s^{-1} and -80000s^{-1}. The top row consists of phases 1 and 2, the top middle row phases 3 and 4, the middle row phases 5 and 6, the bottom middle row phases 7 and 8 and the bottom row phases 9 and 10.

9.4 Shear Layer Instabilities

The result of analysis of jet shear layers has been applied to the shear layers of combusting systems. In particular to an LES of a premixed combustor undergoing an instability [75], Chapter 3.2.4. The most amplified frequency of the shear layer f_i was identified. Frequency spectrums of pressure were taken near the annulus and this frequency was identified along with several sub harmonics. A cut off harmonic was identified, referred to as the preferred frequency f_j which the most amplified frequency degenerated to and is a sub harmonic of f_i. These frequencies corresponded to various acoustic modes of the geometry and it was found that the combustion instability was of these frequencies.

From linear stability analysis the most amplified frequency f_i is proportional to the initial momentum thickness θ_0 and a characteristic velocity of the shear layer $\overline{U}$ in question. These are related once again through the strouhal number. It has been found that the strouhal number for turbulent jets is in the range of $St_i = 0.044 - 0.048$ [132]. The preferred frequency f_j is related again through a characteristic strouhal number $St_j = 0.25 - 0.5$, the jet diameter D and the jet velocity U_0 [133].

$$St_i = \frac{f_i \theta_0}{\overline{U}} \quad and \quad St_j = \frac{f_j D}{U_0} \qquad \text{Eq 9-5}$$

As the previous work was an LES simulation that included the annular inlet the momentum thickness upstream of the dump plane was calculated.

$$\theta_0 = \int_0^\infty \frac{U(z)}{U_0}\left[1 - \frac{U(z)}{U_0}\right]dz \qquad \text{Eq 9-6}$$

From the available experimental data the momentum thickness can not be ascertained. However using the value established in the LES work [75] ($\theta_0 = 0.1mm$) which is of a similar geometry and flow conditions an estimate of the most amplified frequency and the preferred frequency has been done. The characteristic velocity of the shear layer $\overline{U}$ was taken as the average bulk velocity in the study. For this case both $\overline{U}$ and U_0 are equivalent and were determined by integrating and averaging across a 4mm profile line at the most upstream position measured by the SPIV. This is shown in Table 9-2. The jet diameter D was defined as half the difference of annulus diameters, the annulus size 4mm.

Flame		f1		
Frequency (Hz)		100	200	400
|v| Mean (m/s)		60.797	60.894	60.464
Sti	0.044	26750.55	26793.18	26603.94
	0.048	29182.42	29228.93	29022.48
Stj	0.250	3799.79	3805.85	3778.97
	0.500	7599.59	7611.70	7557.94

Table 9-2 Most amplified frequencies f_i for strouhal number range $St_i = 0.044 - 0.048$ and preferred frequency f_j, for strouhal range $St_j = 0.25 - 0.5$ for f1 perturbed at 100Hz, 200Hz and 400Hz.

Table 9-2 shows a possible range of frequencies for shear layer instability frequencies. Although these are not accurate values due to the lack of annulus flow field data the calculated values are within the range of acoustic modes highlighted in chapter 5.7. It is highly likely that the results of the vortex identification analysis close to the annulus are a function of a shear layer frequency and possible harmonic. All the frequencies calculated in Table 9-2 are outside of the temporal resolution of the high speed SPIV system so no confirmation can be made.

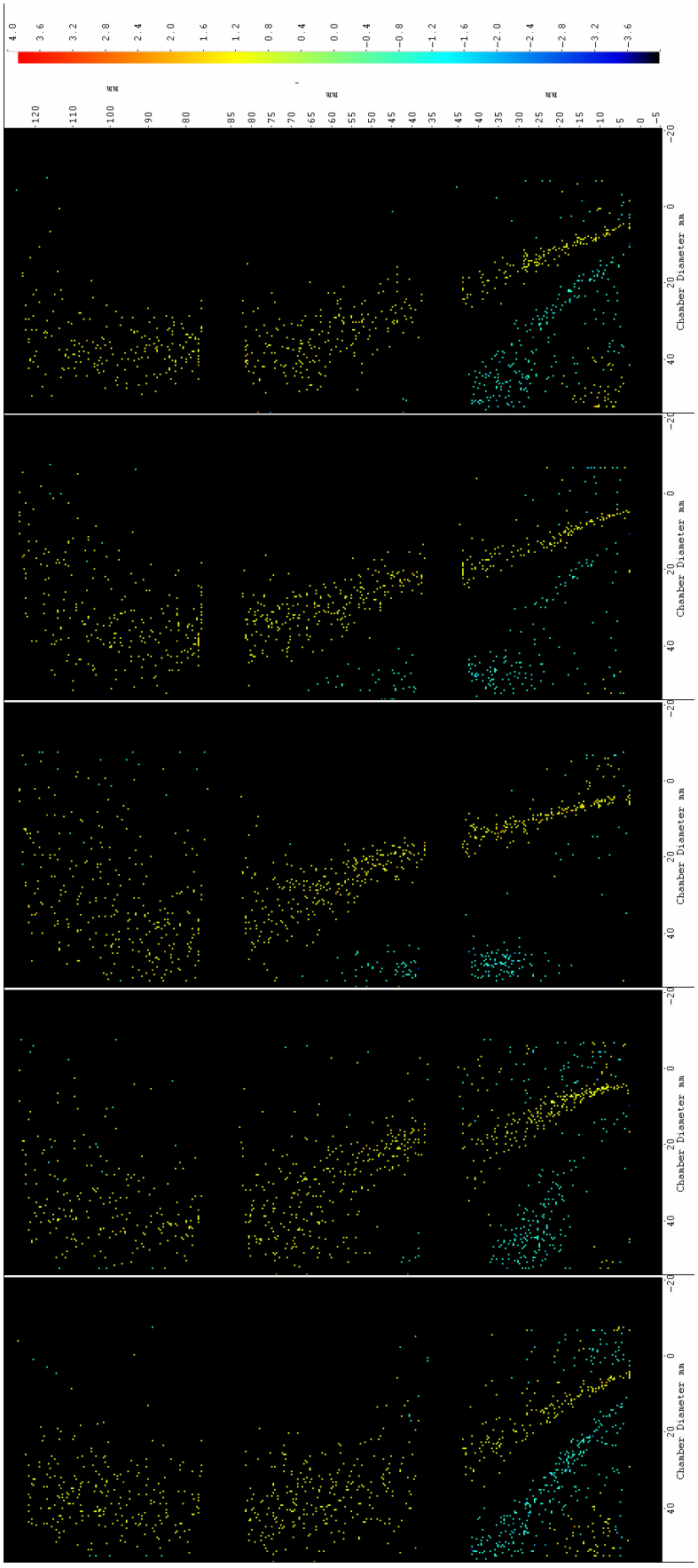

Figure 9-14 Summation images showing location of detected vortices for f1-100Hz for phases 2 (Bottom), 4, 6, 8, and 10 (Top). Positive values correspond to clockwise vortices and negative values correspond to anticlockwise vortices.

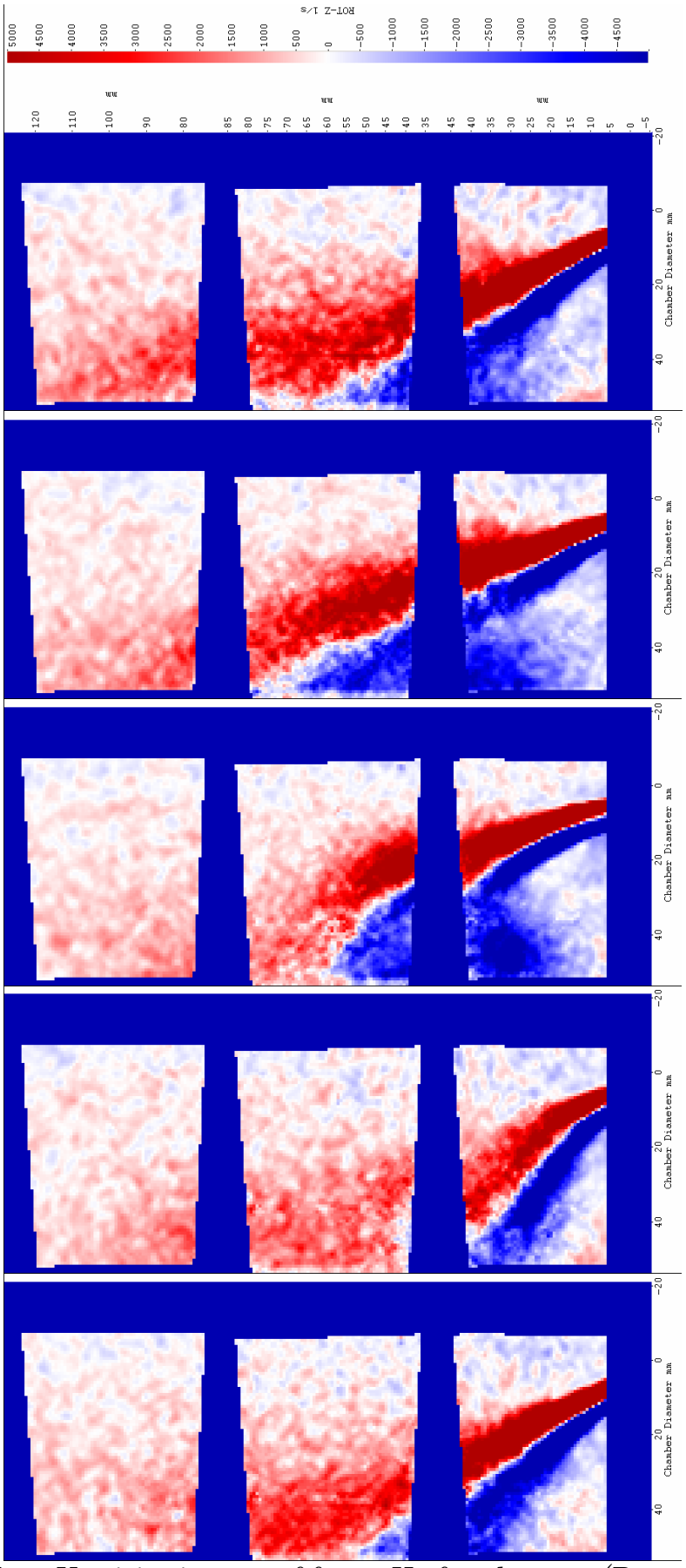

Figure 9-15 Mean Vorticity images of f1-100Hz for phases 2 (Bottom), 4, 6, 8 and 10 (Top). Clockwise (positive) and anticlockwise (negative) vorticity are artificially saturated at $5000s^{-1}$.

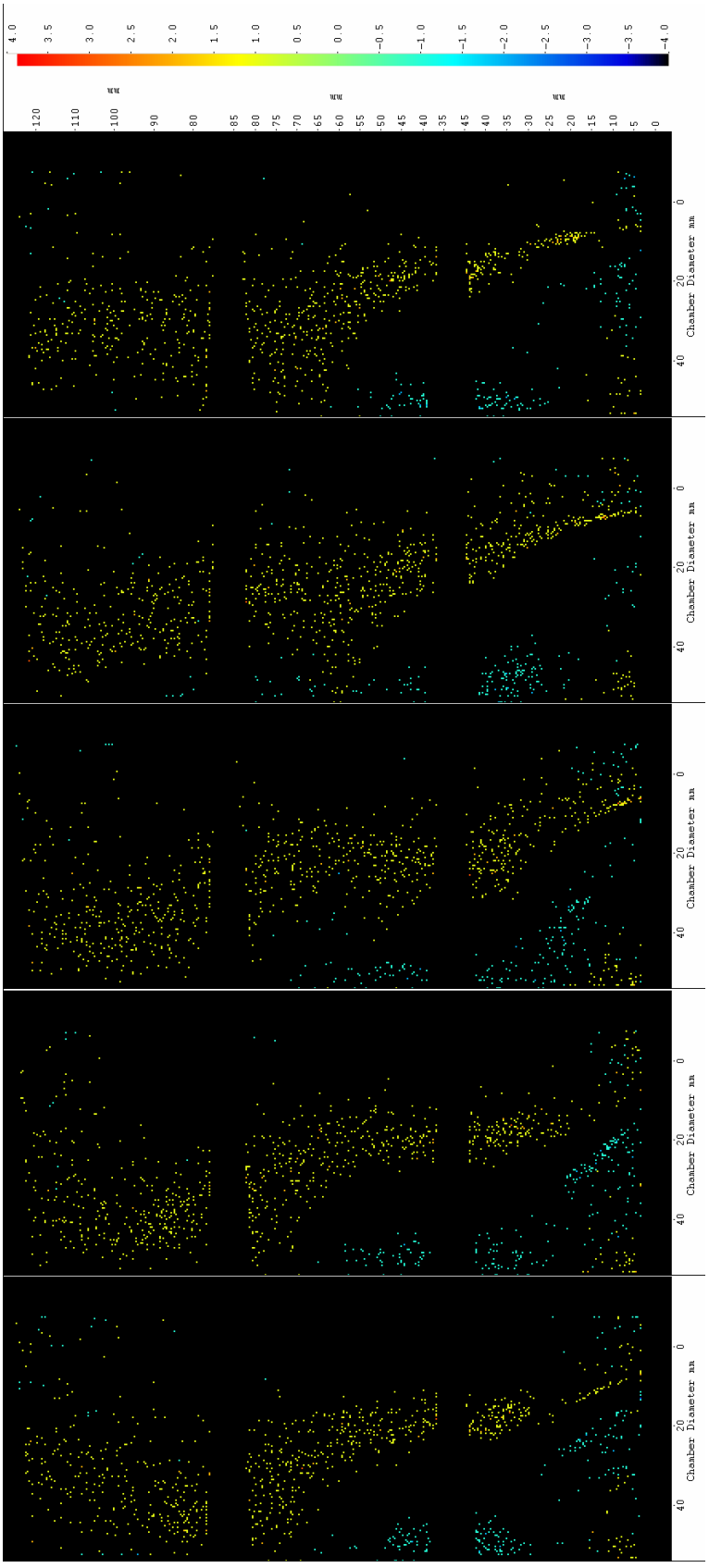

Figure 9-16 Summation images showing location of detected vortices for f1-200Hz for phases 2 (Bottom), 4, 6, 8, and 10 (Top). Positive values correspond to clockwise vortices and negative values correspond to anticlockwise vortices.

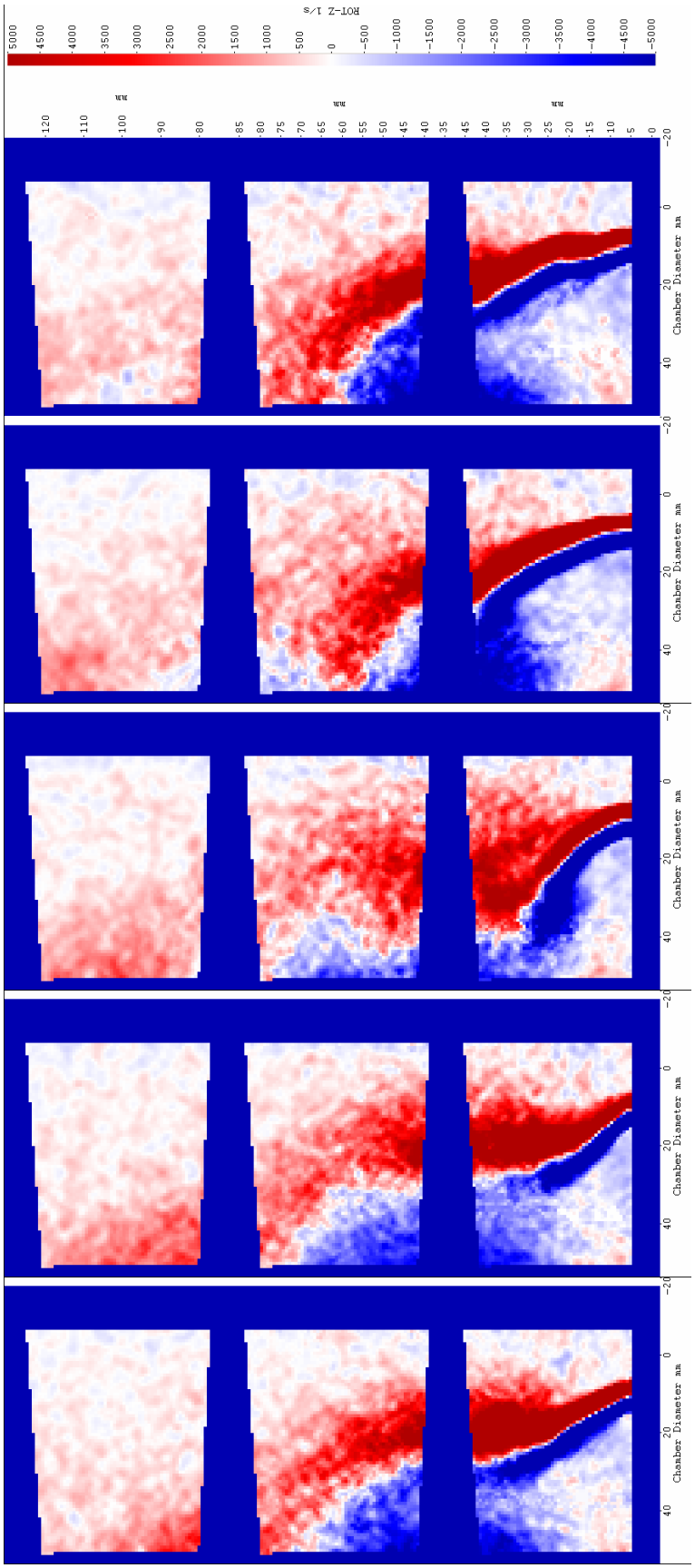

Figure 9-17 Mean Vorticity images of f1-200Hz for phases 2 (Bottom), 4, 6, 8 and 10 (Top). Clockwise (positive) and anticlockwise (negative) vorticity are artificially saturated at $5000s^{-1}$.

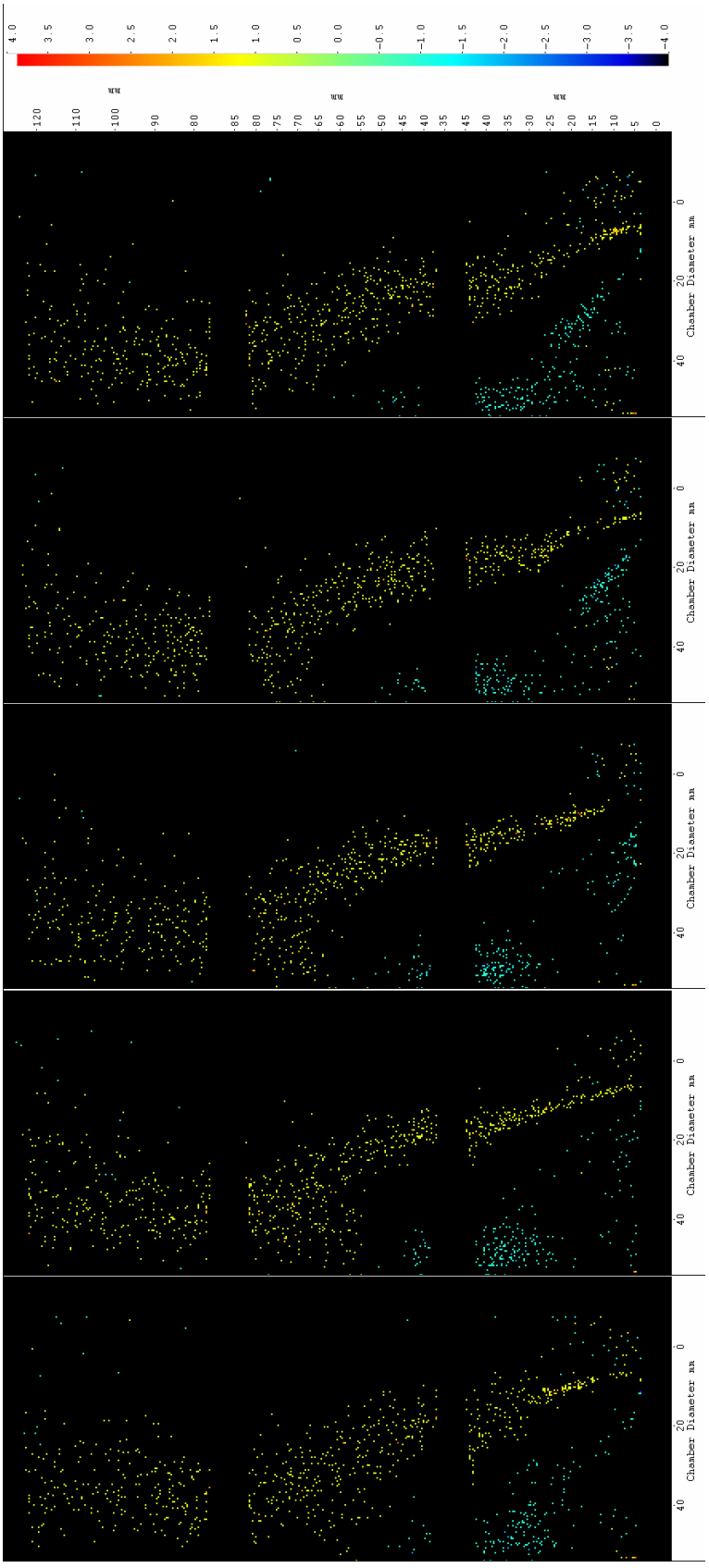

Figure 9-18 Summation images showing location of detected vortices for f1-400Hz for phases 2 (Bottom), 4, 6, 8, and 10 (Top). Positive values correspond to clockwise vortices and negative values correspond to anticlockwise vortices.

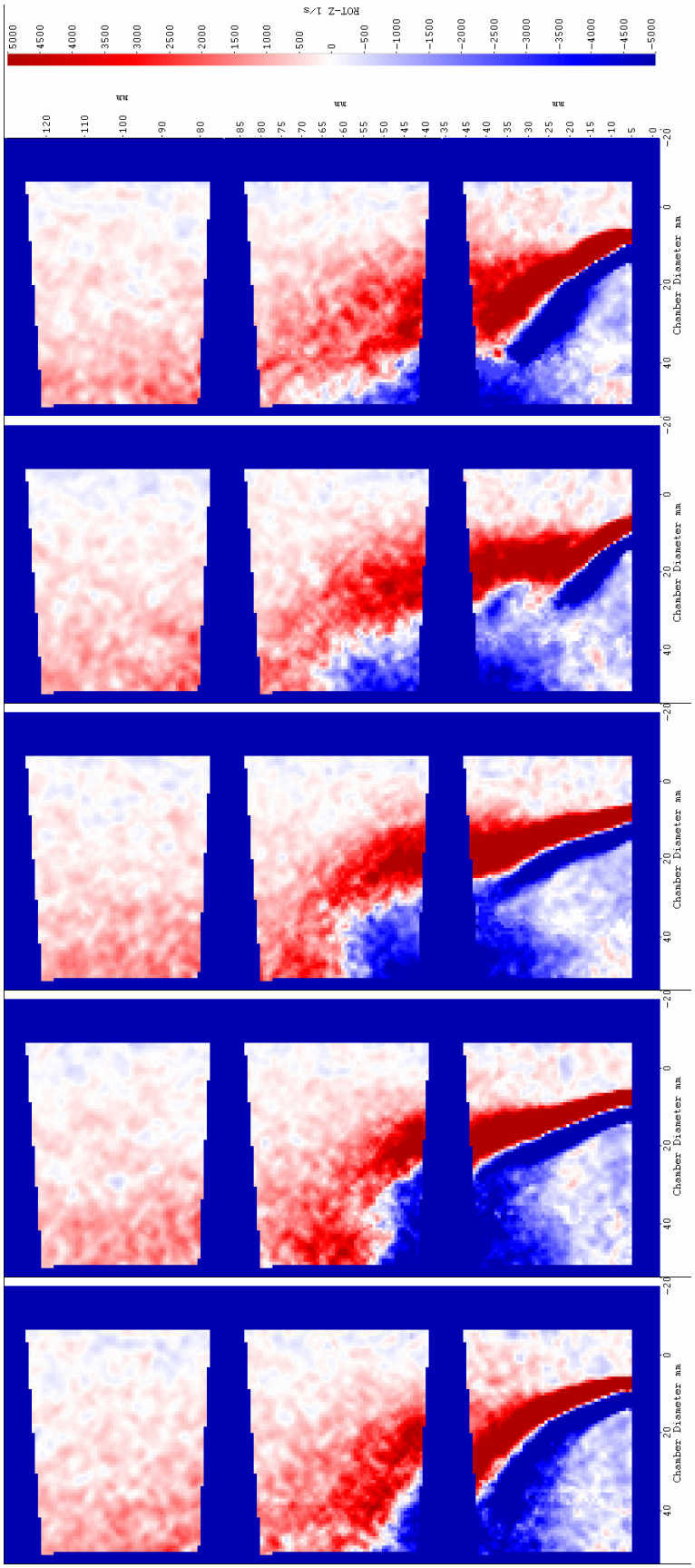

Figure 9-19 Mean Vorticity images of f1-400Hz for phases 2 (Bottom), 4, 6, 8 and 10 (Top). Clockwise (positive) and anticlockwise (negative) vorticity are artificially saturated at $5000s^{-1}$.

10 INSTABILITY COMPARISON

The combustion instabilities investigated in this thesis have revealed two oppositely rotating vortical structures attached to the inner and outer annulus circumferences. These funnel shape structures spread radially as they enter the chamber. The combustion reaction zones will be located in the centres of these two structures and experience local stretch and strain effects as already described. The imposed inlet perturbation causes these vorticity structures also to oscillate in magnitude. This vorticity shedding is the mechanism for the unstable heat release rate. In addition the recirculation zones (IRZ and CRZ) alter and deform the vorticity structures. This combination is responsible for the reacting and vorticity structures revealed. The behaviour of the vortex breakdown feature is a simple single cell axisymmetric type for f1-100Hz which shows radial and axial movement through the instability. A two cell structure is evident through part of the cycle for f1-200Hz. This is attributed to the phase delay of the inlet velocity components and changes of the spatial pressure gradients within the chamber. The same conclusion is attributed the changes of flow structure for f1-400Hz.

The nature of the vorticity structures and shedding has been shown to vary widely in the literature presented in chapter 2.3 and 3.2.4. The combusting LES of a similar chamber [73] revealed very similar counter rotating vorticity funnel shape structures attached to the inlet. Instantaneous realisations show that the reaction zone surface was wrinkled by shear layer instabilities which manifest as small variations of vorticity on the main vorticity structures. The experimental work and LES of a similar combustion chamber [41, 42, 75] revealed large scale variations of the OH chemiluminescence signal indicating large flow field structure motion, in particular, the IRZ which will affect the inlet vorticity structures. This was refined further experimentally with the use of phase locked OH PLIF which revealed the location of the reaction zones between the undefined vorticity structures. The corresponding LES simulation firstly was able to exactly define the reaction zone. (Of note is the difference of the chemiluminescence signal to the location of the reaction zone). Secondly shear layer instabilities were identified to be responsible for causing the unsteady heat release rate through surface alterations of the reaction zone. These works show very good similarity with this thesis in observations of vorticity structures and vorticity shedding present. The instability in these cases was due to shear layer instabilities where as the inlet flow was pulsed in this work causing the vorticity shedding. The vortex breakdown mechanism was the axisymmetric type but no comment was made upon any large scale flow field changes made to the vorticity structures. There was no toroidal vortex shedding from the annulus

Alternatively toroidal vortex structures have been observed forming off the inlet geometry in a LES of a non annular swirling flow [74]. The structure formed off the inlet and advected a small distance downstream where it quickly dissipated. This toroidal ring was able to cause local alterations of the reaction zone. The structure itself was quite small in cross sectional area as revealed by the Q criterion. The chamber aspect of the simulation geometry was without a

converging exhaust and just opened to atmosphere. Experimentally these types of structures have been observed, the first in a non-swirling annular chamber with no exhaust [44]. Two counter rotating toroidal structures were formed on either shear layer and proceeded to roll the reaction zone into them. As the flow increased there were advected downstream and then dissipated at the peak of the oscillation. The second was an open swirling arrangement where these structures were formed on the outer edge of the burner.

The geometry of the combustion chamber/simulation will have huge impact upon the vortex breakdown mechanism in the chamber. Annular flows (bluff body) will promote vortex breakdown and flow reversals as the bluff body provides an upstream stagnation point. The presence of a converging exhaust will also help adding to the axial pressure gradient. Of course the flow must be swirling. Without these features the vortex breakdown is likely to be weaker and not extend as far upstream. The work where toroidal structures were observed were lacking in one or more of these features. It is likely that a chamber such as in this thesis could be made to produce toroidal structures with sufficient forcing amplitude. This is a point of speculation. The results of the literature survey covered a range of geometries, equivalence ratios, forcing amplitudes and pressures.

11 CONCLUSIONS

A swirl stabilised lean premixed dump combustor based upon the CRF swirl combustor has been commissioned. The design incorporates additional features such as the ability to perturb the inlet flow at desired frequencies up to 2KHz, a preheating section capable of preheating the air up to temperatures of 400ºC, and the ability to introduce dilution air circumferentially within the chamber. The design includes a fused silica chamber to allow non intrusive optical access and a water cooled exhaust. The combustor lean limits for a variety of low rates, equivalence ratios, hydrogen contents and instability frequencies has been determined.

A database of unique reacting field and flow field descriptions has been created of a range of flows, equivalence ratios, hydrogen content and instability frequencies characterised by phase locked high speed CH* chemiluminescence and high speed PIV/SPIV – the first work to do this in this type of geometry. These can be used for simulation comparison purposes.

A pure methane flow of 60ms^{-1} and $\Phi = 0.8$ is presented in great detail exposed to a perturbation frequency of 100Hz, 200Hz and 400Hz. The mean reacting and flow field images reveal vastly different structures, both reacting and flow field. A 20% blended hydrogen methane flow of 60ms^{-1} and $\Phi = 0.8$ is also presented. The mean reacting and flow field images show no change of instability structure due to the hydrogen content. Direct comparison of inferred heat release rate is limited, however profiles created from the integrated CH* data show that the waveform of the instabilities is the same regarding flame area and phase for the respective frequencies. Direct comparison of amplitude of heat release rate can not be done at present and is unresolved.

This work has characterised the behaviour of combustion instabilities inside of a typical swirl stabilised dump combustor within the low frequency range. The cases presented represent frequencies below, equivalent to, and above a critical response frequency of the combusting system. The 100Hz and 400Hz perturbation exhibit sinusoidal behaviour of heat release and flame area. The 200Hz case exhibits smaller, twin peaked amplitude of both heat release and flame area. This has been attributed to the formation of pressure gradients causing the creation of a second cell within the IRZ axisymmetric/bubble vortex breakdown) which causes redistribution of inlet velocity to the radial and tangential components. In all cases the instability, characterised by the oscillating heat release profiles, are created by oscillations of the flame area.

An analysis of the turbulent components after a triple decomposition in close proximity to the annulus reveals highly anisotropic inhomogeneous turbulence in the shear layers. The inner shear layer is dominated by axial turbulence generated by the IRZ. The outer shear layer is dominated by radial turbulence generated by the CRZ. Tangential turbulence dissipates very quickly with downstream distance. The turbulence in these regions consists of periodic motion with frequencies corresponding to the imposed perturbation frequencies.

Excitation of both shear layers for all components was not always found and appears to rely upon the nature of the recirculation zones.

An investigation into vortex behaviour found no large scale coherent toroidal vortex shedding in any of the conditions investigated. Counter rotating vorticity structures have been found attached to the two circumferences of the annulus. Frequency spectra at the annulus corresponding to the centre of the inlet flow and the two shear layers revealed dominant frequencies matching the imposed perturbation frequency. Harmonic frequencies detected through spectral analysis of the inlet pressure data, inlet velocity components and integrated CH* data were found to occur only within the shear layers of the vorticity analysis. These two vorticity structures are affected by the inlet perturbation and the behaviour of the recirculation zones (pressure gradient dependent) causing additional structural change. These structures will impart a local hydrodynamic stretch and flame stretch upon the reaction zone which causes the oscillation of flame area and hence the oscillation of heat release rate. A vortex identification algorithm implemented revealed vortices were concentrated along the areas of high vorticity. The number of vortices was not correlated to the imposed perturbation. Indeed the results from this appear to be due to shear layer instabilities as has been observed in numerous simulations. An informal treatment to identify the shear layer instability frequencies has been performed and the identified frequencies are within the range of those derived for the chamber and annular inlet resonance modes. This implies that vortex shedding of this nature occurs and is superimposed upon the effects of the generated perturbation.

This work has contributed to the field of combustion instabilities by the experimental verification of various flame and flow structures that can occur in the low frequency range. These are all a function of flame area modification due to the interaction of flow dynamics and inlet velocity. The flame area is altered specifically by the vorticity structures which will impart stretch affects upon the reaction zone. This work has found that the shear layer turbulence contains periodic structures of frequencies matching the imposed perturbation frequencies. These additional structures will also cause in phase modulation of the vorticity structures and hence flame surface area affecting the heat release rate.

12 RECOMMENDATIONS

This work has highlighted the practical difficulties and expense incurred when investigating an enclosed combusting environment. Indeed a swirling dump combustor is one of the most difficult environments to investigate combustion within. Many diagnostics and measurements are needed to fully characterise the instability and to ascertain the underlying physics. The following is a description of potentially useful diagnostics and chamber modifications which would allow the collected work to be expanded upon and analysed in greater detail while trying to alleviate some of the limitations encountered.

As discovered the damage incurred to the fused silica chamber is a serious problem. This can not easily be remedied when using a cylindrical section. Although a circular cross section is more representative of a combustor and easier for modelling purposes it is not suitable if flow field measurements are desirable. This is because of the damage incurred and reflections of the laser sheet. A square cross section chamber with fused silica windows held within a water cooled frame would greatly reduce the expense and operational difficulties. The flat windows would still incur damage but would be able to be polished returning the window to an optical finish. Flat windows would be less expensive than an entire extruded chamber and the re-polishing is obviously less expensive than new windows.

The use of a square cross section would allow easy inclusion of pressure and temperature sensors. A single side could be replaced with a water cooled steel window with sensors embedded within it which would allow simultaneous spatial and temporal measurements during the instability and with other diagnostics. A cylindrical section of fused silica can not be drilled and tapped to include these features. For this work the dump plane was fitted with a ceramic inlay to create adiabatic conditions. If this was to be made of a water cooled steel inlay and anodised black a pressure transducer could easily be included. This would also give advantages to optical diagnostics and allow measurements to be made closer to the dump entry as reflections would be greatly reduced. A comparison between the two inlays would be advantageous.

As has been shown from the literature shear layer instabilities can be responsible for periodic variations of the reaction zone. The determination of the frequencies of these instabilities is dependent upon having flow field data within the annulus prior to the dump plane. Consideration should be given to the possibility of acquiring flow field data within the annulus. This would allow the calculation the shear layer frequencies which could be then verified with either pressure of LDV data.

The issue of clouding the chamber with seed particles (non-permanent damage) can not be avoided when using a solid seed velocity measurement system. Use of a high speed PIV system is extremely advantageous and has been shown to work. However care should be made regarding the suitability of the equipment in question. This refers to the attainable inter-frame time, delta t, and the practical use of the equipment. There are a number of seeding devices available to seed the

upstream flow (cyclone seeder – used here, fluidized bed, stirrer, etc) However the use of these with an enclosed environment is severely limited by lack of seed density control, spitting and the very small operating window before the chamber is clouded. Therefore a specific seeder needs to be designed for this application.

High speed PIV allows the collection of sufficient data samples in the small operating window. However the frame rate although far superior to conventional PIV systems still does not afford the temporal resolution required to detect the high frequencies present within flows such as these. LDV would be advantageous at a selection of positions within the flow and in particular near the annulus to determine if detectable strong frequencies coincide with shear layer frequencies.

LDV would also allow an investigation of the temporal aspect of turbulence close to the annulus. This will help describe the turbulence and allow estimates of the key turbulence scales which will affect the combustion within the shear layers.

All SPIV/PIV performed here has been done in the radial axial plane (x-y). This does allow all three velocity components to be determined in that plane. This approach does not allow the identification of the vortex core of the vortex breakdown mechanism. PIV should be performed with the laser sheet arranged in the radial tangential plane (x-z) and a camera(s) at a downstream position viewing upstream. This would allow identification of the vortex core, determination whether it is precessing and assessment of that frequency. This can be done for various axial distances to determine how far the vortex core penetrates the chamber.

The use of chemiluminescence allows information to be discerned regarding the heat release rate and the mean flow field structure once deconvoluted. This does provide useful information. However a PLIF technique is required to infer information regarding the instantaneous flame structure and reaction zone location. As already discussed OH PLIF will not yield heat release rate but is purely a reaction zone identifier. Dual PLIF techniques will allow a more accurate marker of the reaction zone radical HCO to be detected and is also a measure of heat release rate allowing analysis of both flame structure and instability amplitude and frequency. The complexity and cost of this approach is much more over chemiluminescence so consideration must be given to what is required in any study. However in work such as this a single PLIF technique must be included as a minimum. From such data scalars such as flame surface density can be derived which characterise the flame-turbulence interactions. In addition this can be used after additional processing to indicate heat release rate.

Specifically regarding multi-component fuels a means of normalising the collected signal to temperature is required when comparing with single component fuel. In this case the inclusion of hydrogen needs to be accounted for. This can either be done experimentally or by use of a chemical model which has correct CH* chemistry. This would allow direct comparison of the two cases.

Simultaneous diagnostics of a PLIF technique (single or dual) and SPIV/PIV is needed in order to be able to identify the reaction zone instantaneously with each vector field. As has been demonstrated the chamber flow field is attainable but the location of the reaction zone was undeterminable. A PLIF technique would yield the location of the reaction zone which can be used to extract reaction zone

properties from the vector field such as flame speed, strain, curvature and vorticity. This is feasible for a normal acquisition rate PIV system however there are very limited options to create a high speed PLIF system required to match a high speed PIV system when one considers also the chamber clouding issue.

The database created here can be expanded upon to determine flame transfer functions for the combustor to further characterise its dynamics. Alternatively the combustor could be modified to run 'stable' and through experimentation conditions determined where the combustor becomes unstable due to resonance. Investigations during these operational conditions will yield further insight into the combustor.

The influence of hydrogen addition upon flame structure could not be determined through analysis of the mean deconvoluted CH* images. Analysis needs to be performed upon each instantaneous image and statistics developed this way. A PLIF technique would allow this determining curvature and penetration of the reaction zone into the chamber which could indicate the effect of hydrogen upon flame speed. For example OH PLIF can be used to derive the flame surface density scalar which can be used in comparison with pure methane flows as the hydrogen impact upon the flame-turbulence interaction will be characterised.

BIBLIOGRAPHY

BEER J.M. and N.A. CHIGIER (1972). *Combustion Aerodynamics*, New York: John Wiley and Sons.

BORMAN G. and K. RAGLAND (1998). *Combustion Engineering*, Singapore: McGraw Hill.

CHUNG K LAW (2006). Combustion Physics, New York: Cambridge University Press.

COHEN H. (1996). *Gas Turbine Theory*. 4th ed: Longman Group Ltd, England.

GAYDON A. (1974). *The Spectroscopy of Flames*. 2nd ed: Chapman and Hall.

HARDING S.C. (1996). Investigation into Mixing and Combustion in an Optical, Lean, Premixed, Prevaporised Combustor. PhD. **Cranfield University**.

HARRISON R.M. (1999). *Understanding Our Environment; An Introduction to Environmental Chemistry and Pollution*, Cambridge: The Royal Society of Chemistry.

HARRISON R.M. (2001). *Pollution, Causes, Effects and Control*. 4th ed, Cambridge: The Royal Society of Chemistry.

KUO K.K. (2005). *Principles of Combustion*. 2nd ed: John Wiley and Sons.

LIM J S (1989). *Two Dimensional Signal and Image Processing*. Prentice Hall. US.

LUCCA-NEGRO O. and T. O'DOHERTY (2001). Vortex Breakdown: A Review. **Progress in Energy and Combustion Science**. Vol 27. Pg. 431-481.

LIEUWEN T.C. and V. YANG (2005). *Combustion Instabilities in gas Turbine Engines.* Vol. 210: Progress in Astronautics and Aeronautics.

LEFEBVRE A.H. (1999). *Gas Turbine Combustion*. 2nd ed: Taylor and Francis Ltd.

OATES G. (1989). *Aircraft Propulsion Systems Technology and Design*: AIAA. America.

POINSOT T. and D. VEYNANTE (2005). *Theoretical and Numerical Combustion*. 2nd ed: R T Edwards Inc.

PETERS N. (2000). *Turbulent Combustion*, Cambridge, UK: Cambridge University Press.

RUSS J C (2007). The Image Processing Handbook. 5th ed: CRC Press.

SYRED N. (2006). A review of oscillation mechanisms and the role of the precessing vortex core (PVC) in swirl combustion systems. **Progress in Energy and Combustion Science**. Vol 32. Pg. 93-161.

WILLIAMS F.A. (1985). *Combustion Theory*. 2nd ed: The Benjamin/Cummings Publishing Company.

REFERENCES

[1]. COHEN H, ROGERS, G F C and SARAVANAMUTTOO, H I H (1996). *Gas Turbine Theory*. 4th ed: Longman Group Ltd, England. Pg 26-29.

[2]. LEFEBVRE A H (1999). *Gas Turbine Combustion*. 2nd ed: Taylor and Francis Ltd. Pg 324.

[3]. CORREA S M (1991). A Review of No_x Formation under Gas Turbine Combustion Conditions. **Combustion Science and Technology**. Vol 87. Pg. 329-362.

[4]. FENNIMORE C P. (1971). Formation of Nitric Oxide in Premixed Hydrocarbon Flames. **The 13th International Symposium on Combustion**: The Combustion Institute. Pg. 373-380.

[5]. NICOL D, MALTE, P C, LAI, J, MARINOV, N N and PRATT, D T (1992). No_x Sensitivities for Gas Turbine Engines Operated on Lean-Premixed Combustion and Conventional Diffusion Flames. **ASME**. Vol 92-GT-115

[6]. MALTE P C and PRATT, D T. (1974). Measurement of Atomic Oxygen and Nitrogen Oxides in Jet Stirred Combustion. **The 15th International Symposium on Combustion**: The Combustion Institute. Pg. 1061-1070.

[7]. BOWMAN T C. (1992). Control of Combustion Generated Nitrogen Oxide Emissions. **The 24th International Symposium on Combustion**: The Combustion Institute. Pg. 859-878.

[8]. HAYHURST A N and LAWERENCE, A D (1992). Emissions of Nitrous Oxide from Combustion Sources. **Progress in Energy and Combustion Science**. Vol 18. Pg. 529-552.

[9]. OATES G (1989). *Aircraft Propulsion Systems Technology and Design*: AIAA. America.

[10]. LEFEBVRE A H (1999). *Gas Turbine Combustion*. 2nd ed: Taylor and Francis Ltd. Pg 328-330.

[11]. ANDERSON D N (1975). Effects of Equivalence Ratio and Dwell Time on Exhaust Emissions from an Experimental Premixing Prevapourising Burner. **ASME** Vol Paper 75-GT-69.

[12]. LEFEBVRE A H (1999). *Gas Turbine Combustion*. 2nd ed: Taylor and Francis Ltd. Pg 339.

[13]. BORMAN G and RAGLAND, K (1998). *Combustion Engineering*, Singapore: McGraw Hill.

[14]. COHEN H, ROGERS, G F C and SARAVANAMUTTOO, H I H (1996). *Gas Turbine Theory*: Longman Group Ltd, England. Pg 260.

[15]. HARRISON R M (1999). *Understanding Our Environment; an Introduction to Environmental Chemistry and Pollution*, Cambridge: The Royal Society of Chemistry. Pg 14.

[16]. HARRISON R M (1999). *Understanding Our Environment; an Introduction to Environmental Chemistry and Pollution*, Cambridge: The Royal Society of Chemistry. Pg 53-59.

[17]. HARRISON R M (2001). *Pollution, Causes, Effects and Control*. 4th ed, Cambridge: The Royal Society of Chemistry. Pg 194-220.

[18]. LEFEBVRE A H (1999). *Gas Turbine Combustion*: Taylor and Francis Ltd. Pg 335-337.

[19]. LUCCA-NEGRO O and O'DOHERTY, T (2001). Vortex Breakdown: A Review. **Progress in Energy and Combustion Science**. Vol 27. Pg. 431-481.

[20]. BEER J M and CHIGIER, N A (1972). *Combustion Aerodynamics*, New York: John Wiley and Sons. Pg 112.

[21]. HALLET W L H and TOEWS, D J (1987). The Effects of Inlet Conditions and Expansion Ratio on the Onst of Flow Reversal in Swirling Flow in a Sudden Expansion. **Experiments in Fluids**. Vol 5. Pg. 129-133.

[22]. HALL M G. (1967). A New Approach to Vortex Breakdown. **Proceedings of the heat transactions and fluid mechanics institute**. San Diego, La Jolla: University of California. Pg. 319-340.

[23]. LEIBOVICH S (1978). The Structure of Vortex Breakdown. **Annual review of Fluid Mechanics**. Vol 10. Pg. 221-246.

[24]. SARPKAYA T (1971). On Stationary and Travelling Vortex Breakdowns. **Journal of fluid mechanics**. Vol 45(3). Pg. 545-559.

[25]. SARPKAYA T (1971). Vortex Breakdown in Swirling Conical Flows. **AIAA Journal**. Vol 9(9). Pg. 1792-1799.

[26]. FALER J H and LEIBOVICH, S (1977). Disrupted States of Vortex Flow and Vortex Breakdown. **Physics of Fluids**. Vol 20. Pg. 1385-1400.

[27]. BRUCKER C and ALTHAUS, W (1992). Study of Vortex Breakdown by Particle Tracking Velocimetry (Ptv). Part 1: Bubble Type Vortex Breakdown. **Experiments in fluids**. Vol 13. Pg. 339-349.

[28]. ESCUDIER M (1988). Vortex Breakdown: Observations and Explanations. **Progress in Aerospace Science**. Vol 25. Pg. 189-229.

[29]. BENJAMIN T B (1962). Theory of the Vortex Breakdown Phenomenon. **Journal of Fluid Mechanics**. Vol 14. Pg. 593-629.

[30]. ESCUDIER M P and ZEHNDER, N (1982). Vortex Flow Regimes. **Journal of Fluid Mechanics**. Vol 115. Pg. 105-121.

[31]. CHANAUD R C (1965). Observations of Oscillatory Motion in Certain Swirling Flows. **Journal of Fluid Mechanics**. Vol 21(1). Pg. 111.

[32]. RUITH M R, CHEN, P, MEIBURG, E and MAXWORTHY, T (2003). Three-Dimensional Vortex Breakdown in Swirling Jets and Wakes: Direct Numerical Simulation. **Journal of Fluid Mechanics**. Vol 486. Pg. 331-378.

[33]. LIEUWEN T (2003). Modelling Premixed Combustion-Acoustic Wave Interactions: A Review. **Journal of propulsion and power**. Vol 19(5).

[34]. CHUNG K L (2006). *Combustion Physics*, New York: Cambridge University Press. Pg 456-461.

[35]. MARKSTEIN G H (1964). *Nonsteady Flame Propagation*: Pergamon. Pg.

[36]. SIVASHINSKY G I (1977). Diffusional-Thermal Theory of Cellular Flames. **Combustion Science and Technology**. Vol 15. Pg. 137-146.

[37]. PUTNAM A A (1971). *Combustion Driven Instabilities in Industry*, New York: Elsevier.

[38]. PUTNAM A A and DENNIS, W R. (1953). Organ Pipe Oscillations in a Flame Filled Tube. **The 4th International Symposium on Combustion**. Pittsburgh: The Combustion Institute. Pg. 566-574.

[39]. CHU T B (1956). Stability of Systems Containing a Heat Source – the Rayleigh Criterion. **NACA** Vol RM 56D27

[40]. ZINN T B. (1992). Pulse Combustion: Recent Applications and Research Issues. **The 24th International Symposium on Combustion**. Pittsburgh: The Combustion Institute. Pg. 1297-1305.

[41]. BRODA J C, SEO, S, SANTORO, R J, SHIRHATTIKAR, G and YANG, V. (1998). An Experimental Study of Combustion Dynamics of a Premixed Swirl Injector. **The 27th International Symposium on Combustion**: The Combustion Institute. Pg. 1849 - 1856.

[42]. LEE S Y, SEO, S, BRODA, J C, PAL, S and SANTORO, R J. (2000). An Experimental Estimation of Mean Reaction Rate and Flame Structure During Combustion Instability in a Lean Premixed Gas Turbine Combustor. **The 28th International Symposium on Combustion**: The Combustion Institute. Pg. 775 - 782.

[43]. LEE J G and SANTAVICCA, D A (2003). Experimental Diagnostics for the Study of Combustion Instabilities in Lean Premixed Combustors. **Journal of propulsion and power**. Vol 19(5). Pg. 735-750.

[44]. BALACHANDRAN R, AYOOLA, O B, KAMINSKI, C F, DOWLING, A P and MASTORAKOS, E (2005). Experimental Investigation of the Nonlinear Response of Turbulent Premixed Flames to Imposed Inlet Velocity Oscillations. **Combustion and Flame**. Vol 143. Pg. 37-55.

[45]. AYOOLA B A, BALACHANDRAN, R, FRANK, J H, MASTORAKOS, E and KAMINSKI, C K (2006). Spatially Resolved Heat Release Rate Measurements in Turbulent Premixed Flames. **Combustion and Flame**. Vol 114. Pg. 1-6.

[46]. NAJM H N, PAUL, P H, MUELLER, C J and WYCKOFF, P S (1998). On the Adequacy of Certain Experimental Observables as Measurements of Flame Burning Rate. **Combustion and Flame**. Vol 113. Pg. 312-332.

[47]. KULSHEIMER C and BUCHNER, H (2002). Combustion Dynamics of Turbulent Swirling Flames. **Combustion and flame**. Vol 131. Pg. 70-84.

[48]. WILLERT C and JARIUS, M (2002). Planar Flow Field Measurements in Atmospheric and Pressurised Combustion Chambers. **Experiments in Fluids**. Vol 33. Pg. 931-939.

[49]. SERRE E and BONTOUX, P (2002). Vortex Breakdown in a Three Dimensional Swirling Flow. **Journal of fluid mechanics**. Vol 459. Pg. 347-370.

[50]. SYRED N (2006). A Review of Oscillation Mechanisms and the Role of the Precessing Vortex Core (Pvc) in Swirl Combustion Systems. **Progress in Energy and Combustion Science**. Vol 32. Pg. 93-161.

[51]. RAYLEIGH L. (1916). On the Stability of Stratified Flow. **Proceedings of the Royal Society**. London. Pg. 148-158.

[52]. SCHEFER R W, WICKSALL, D M and AGRAWAL, A K. (2002). Combustion of Hydrogen-Enriched Methane in a Lean Premixed Swirl Stabilized Burner. **The 29th international symposium on combustion**: The combustion Institute. Pg. 843-851.

[53]. VAGELOPOULOS C M, OEFELEIN, J C and SCHEFER, R W. (2003). Effects of Hydrogen Enrichment on Lean Premixed Methane Flames. **The 14th Annual U. S. Hydrogen Conference and Hydrogen Expo USA**. Washington D.C. 4th-6th March.

[54]. JACKSON G S, SAI, R, PLAIA, J M, BOGGS, C M and KIGER, K T (2003). Influence of H2 on the Response of Lean Premixed Ch4 Flames to High Strained Flows. **Combustion and Flame**. Vol 132. Pg. 503-511.

[55]. HAWKES E R and CHEN, J H (2004). Direct Numerical Simulation of Hydrogen-Enriched Lean Premixed Methane-Air Flames. **Combustion and Flame**. Vol 138. Pg. 242-258.

[56]. LAW C K and KWON, O C (2004). Effects of Hydrocarbon Substitution on Atmospheric Hydrogen-Air Flame Propagation. **International Journal of Hydrogen Energy**. Vol 29. Pg. 867-879.

[57]. HALTER F, CHAUVEAU, C, DJEBAILI-CHAUMEIX, N and GOKALP, I. (2005). Characterisation of the Effects of Pressure and Hydroghen Concentration on Laminar Burning Velocities of Methane-Hydrogen-Air Mixtures. **The 30th International Symposium on Combustion**: The Combustion Institute. Pg. 201-208.

[58]. BOSCHEK E, GRIEBEL, P and JANSOHN., P. (2007). Fuel Variability Effects on Turbulent, Lean Premixed Flames at High Pressures. **Proceedings of GT2007 ASME Turbo Expo 2007: Power for Land, Sea and Air**. Montreal, Canada. 14th-17th May.

[59]. POINSOT T and VEYNANTE, D (2005). *Theoretical and Numerical Combustion.* 2nd ed: R T Edwards Inc. Pg 129.

[60]. PETERS N (1999). The Turbulent Burning Velocity for Large Scale and Small Scale Turbulence. **Journal of Fluid Mechanics**. Vol 384(107 - 132).

[61]. VEYNANTE D and VERVISCH, L (2002). Turbulent Combustion Modelling. **Progress in Energy and Combustion Science**. Vol 28. Pg. 193 - 266.

[62]. PETERS N (2000). *Turbulent Combustion*, Cambridge, UK: Cambridge University Press. Pg 78 - 86.

[63]. POINSOT T, VEYNANTE, D and CANDEL, S (1991). Quenching Processes and Premixed Combustion Diagrams. **Journal of Fluid Mechanics**. Vol 228. Pg. 651 - 606.

[64]. VEYNANTE D, TROUVE, A, BRAY, K N C and MANTEL, T (1997). Gradient and Counter Gradient Scalar Transport in Turbulent Premixed Flames. **Journal of Fluid Mechanics**. Vol 332. Pg. 263 - 293.

[65]. POINSOT T and VEYNANTE, D (2005). *Theoretical and Numerical Combustion*. 2nd ed: R T Edwards Inc.

[66]. POPE S B. (1990). Computations of Turbulent Combustion: Progress and Challenges. **The 23rd International Symposium on Combustion**: The Combustion Institute. Pg. 591 - 612.

[67]. BUTLER T D and O'ROURKE, P J. (1977). A Numerical Method for Two Dimensional Unsteady Reacting Flows. **The 16th International Symposium on Combustion**: The Combustion Institute. Pg. 1503 - 1515.

[68]. COLIN O, DUCROS, F, VEYNANTE, D and POINSOT, T (2000). A Thickened Flame Model for Large Eddy Simulations of Turbulent Premixed Combustion. **Physics of Fluids**. Vol 12(7). Pg. 1843 - 1863.

[69]. KERSTEIN A R, ASHURST, W T and WILLIAMS, F A (1988). Field Equation for Interface Propagation in an Unsteady Homogeneous Flow Field. **Physical Review A**. Vol 37(7). Pg. 2728 - 2731.

[70]. BOGER M, VEYNANTE, D, BOUGHANEM, H and TROVE, A. (1998). Direct Numerical Simulation Analysis of Flame Surface Density Concept for Large Eddy Simulation of Turbulent Premixed Combustion. **The 27th International Symposium on Combustion**: The Combustion Institute. Pg. 917 - 925.

[71]. WANG P and BAI, X S (2005). Large Eddy Simulations of Turbulent Swirling Flows in a Dump Combustor: A Sensitivity Study **International Journal for Numerical Methods in Fluids**. Vol 47. Pg. 99 - 120.

[72]. WANG P, BAI, X S, M, W and KLINGMANN, J (2004). Large Eddy Simulation and Experimental Studies of a Confined Turbulent Swirling Flow. **Physics of Fluids**. Vol 16(9). Pg. 3306 - 3324.

[73]. GRINSTEIN F F and FUREBY, C. (2005). Les Studies of the Flow in a Swirl Gas Combustor. **The 30th International Symposium on Combustion**: The Combustion Institute. Pg. 1791 - 1798.

[74]. MARTIN C E, BENOIT, L and SOMMERER, Y (2006). Large Eddy Simulation and Acoustic Analysis of a Swirl Staged Turbulent Combustor. **AIAAJ**. Vol 44(4). Pg. 741 - 750.

[75]. HUANG Y, SUNG, H G, HSIEH, S Y and YANG, V (2003). Large Eddy Simulation of Combustion Dynamics of Lean Premixed Swirl Stabilised Combustor. **Journal of Propulsion and Power**. Vol 19(5). Pg. 782 - 794.

[76]. NGUYEN Q-V and PAUL, P H. (1996). The Time Evolution of a Vortex Flame Interaction Observed Via Planar Imaging of Ch and Oh. . **Proceedings of the 26th international symposium on combustion**: The Combustion Institute. Pg. 357-364.

[77]. HARDALUPAS Y, PANOUTSOS, C S and TAYLOR, A M K P. (2006). Heat Release Rate Measurements in Premixed Flames Using Chemiluminescence and Reaction Rate Imaging. **The 44th AIAA Aerospace Sciences Meeting and Exhibit**. Reno, Nevada. 9th to 12th January.

[78]. HURLE I R, BPRICE, R, MSUGDEN, T and THOMAS, A (1968). Sound Emission from Open Turbulent Premixed Flames. **Proceedings of the Royal Society of London Series A**. Vol 303. Pg. 409-427.

[79]. SAMANIEGO J M, EGOLFOPOULOS and BOWMAN, C T (1995). Co_2* Chemiluminescence in Premixed Flames. **Combustion Science and Technology**. Vol 109. Pg. 183-203.

[80]. LEE J G, GONZALEZ, E and SANTAVICCA, D A. (2005). On the Applicability of Chemiluminescence to the Estimation of Unsteady Heat Release During Unstable Combustion in Lean Premixed Combustion. **The 41st AIAA/ASME/SAE/ASEE Joint Propulsion Conference & Exhibit**. Tucson, Arizona. 10th-13th July.

[81]. HARDALUPAS Y and ORAIN, M. (2005). Local Equivalence Ratio and Degree of Premixedness of Reacting Mixture in Swirl Stabilised Natural Gas Fuelled Burners. **The 43rd AIAA Aerospace Sciences Meeting and Exhibit** Reno, Nevada. 10th to 13th January.

[82]. IKEDA Y, KOJIMA, J and NAKAJIMA, T. (2002). Chemiluminescence Based Local Equivalence Ratio Measurement in Turbulent Premixed Flames. **The 40th Aerospace Sciences and Meeting Exhibit**. Reno, Nevada. 14th-17th January

[83]. VENKATA N N and SEITZMAN, J M. (2007). Chemiluminescence Measurements and Modelling in Syngas, Methane and Jet-a Fuelled Combustors. **The 45th AIAA Aerospace Sciences Meeting and Exhibit**. Reno, Nevada. 8th-11th January.

[84]. HARDALUPAS Y and ORAIN, M (2004). Local Measurements of the Time Dependent Heat Release Rate and Equivalence Ratio Using Chemiluminescent Emission from a Flame **Combustion and Flame**. Vol 139. Pg. 188 - 207.

[85]. DOCQUIER N and CANDEL, S (2002). Combustion Control and Sensors: A Review. **Progress in Energy and Combustion Science**. Vol 28. Pg. 107-150.

[86]. PASCHEREIT C O and GUTMARK, E. (2002). Passive Combustion Control Applied to Premix Burners. **The 40th AIAA Aerospace Sciences Meeting and Exhibit**. Reno, Nevada. 14th-17th January.

[87]. PASCHEREIT C O and GUTMARK, E. (2003). Passive Combustion Control for Enhanced Stability and Reduced Emissions in a Swirl-Stabilized Burner. **The 41st AIAA Aerospace Sciences Meeting and Exhibit**. Reno Nevada. 6th-9th January.

[88]. HARDALUPAS Y, PANOUTSOS, C S and TAYLOR, A M K P. (2005). Spatial Resolution of a Chemiluminescence Sensor in a Model Gas Turbine Combustor. **The 43rd AIAA Aerospace Sciences Meeting and Exhibit**. Reno, Nevada. 10th to 13th January.

[89]. GAYDON A (1974). *The Spectroscopy of Flames*. 2nd ed: Chapman and Hall. Pg 197.

[90]. GLASS G P, KISTIAKOWSKY, G B, MICHAEL, J V and NIKI, H. (1965). The Oxidation of Reactions of Acetylene and Methane. **Proceedings of the 10th International Symposium on Combustion**: The Combustion Institute. Pg. 513-522.

[91]. BRENNEN W and CARRINGTON, T (1967). Chemiluminescence of Ch in the O + C_2h_2 Reaction:Rotational Relaxation and Quenching. **The journal of Chemical Physics**. Vol 46 (1). Pg. 7-18.

[92]. MALL J M, VRIES, J, AMADIO, A R and PETERSEN, L E. (2005). Towards a Kinetics Model of Ch Chemiluminescence. **The 43rd AIAA Aerospace Sciences Meeting and Exhibit**. Reno, Nevada. 10th-13th January 2005.

[93]. DEVRIENDT K and PEETERS, J (1997). Direct Identification of the $C_2h(X^2\sigma+)+O(^3p)\rightarrow Ch(A^2\delta)+Co$ Reaction as the Source of the $Ch(A^2\delta\rightarrow X^2\pi)$ Chemiluminescence in C_2h_2/O/H Atomic Flames. **Journal of Physical Chemistry A**. Vol 101. Pg. 2546-2551.

[94]. JOKLIK R G, DAILY, J W and PITZ, W J. (1986). Measurements of Ch Radical Concentrations in an Acetylene/Oxygen Flame and Comparison to Modelling Calculations. **Proceedings of the 21st International Symposium on Combustion**: The combustion Institute. Pg. 895-904.

[95]. ADRIAN R J (1995). Limiting Resolution of Particle Image Velocimetry for Turbulent Flow. **Advances in Turbulent Research**. Vol. Pg. 1-19.

[96]. PRASAD A K (2000). Particle Image Velocimetry. **Current Science**. Vol 79(1). Pg. 51-60.

[97]. GRANT I. (1997). Particle Image Velocimetry: A Review. **Proceedings of the Institute of Mechanical Engineers**. Pg. 55-76.

[98]. MELLING A (1997). Tracer Particles and Seeding for Particle Image Velocimetry. **Measurement Science and Technology**. Vol 8. Pg. 1406-1416.

[99]. JENSON K D (2004). Flow Measurements. **Journal of the Brazillian Society of Mechanical Sciences and Engineering**. Vol 26(4). Pg. 400 - 419.

[100]. PRASAD A K (2000). Stereoscopic Particle Image Velocimetry. **Experiments in Fluids**. Vol 29. Pg. 103-116.

[101]. LECERF A, RENOU, B, ALLANO, D, BOUKHALFA, A and TRINTE, M (1999). Stereoscopic Piv: Validation and Application to an Isotropic Turbulent Flow. **Experiments in Fluids**. Vol 26. Pg. 107-115.

[102]. GAUTHIER V and RIETHMULLER, M L (1988). *Application of Pidv to Complex Flows: Measurements of the Third Velocity Component. In: Particle Image Displacement Velocimetry*. Vol. VKI-LS 1988-06, Rhode-Saint-Genese. Belgium: Von Karman Institute for Fluid Mechanics.

[103]. ARROYO P M and GREATED, C A (1991). Stereoscopic Particle Image Velocimetry. **Measurement Science and Technology**. Vol 2. Pg. 1181-1186.

[104]. ALTENHOFEN R E, *Rectification.*, in *Manual of Photogrammetry*. 1952, American Society of Photogrammetry: Washington, DO.

[105]. LAWSON N J and WU, J (1997). Three Dimensional Particle Image Velocimetry: Experimental Error Analysis of a Digital Angular Stereoscopic System. **Measurement Science and Technology**. Vol 8. Pg. 1455-1464.

[106]. WILLERT C (1997). Stereoscopic Digital Particle Image Velocimetry for Application in Wind Tunnel Flows. **Measurement Science and Technology**. Vol 8. Pg. 1465-1479.

[107]. HILL D F, SHARP, K V and ADRIAN, R J (2000). Stereoscopic Particle Image Velocimetry Measurements of the Flow around a Rushton Turbine. **Experiments in Fluids**. Vol 29. Pg. 478-485.

[108]. WESTERWEEL J and OORD, J V, *Stereoscopic Piv Measurements in a Turbulent Boundary Layer*, in *Particle Image Velocimetry; Progress Towards Industrial Applications*, J. WESTERWEEL, Editor. 1999, Kluwer: Dordrecht.

[109]. WILLIAMS T C, SCHEFER, R W, OEFELEIN, J C and SHADDIX, C R (2007). Idealized Gas Turbine Combustor for Performance Research and Validation of Large Eddy Simulations. **Review of Scientific Instruments**. Vol 78.

[110]. POINSOT T and VEYNANTE, D (2005). *Theoretical and Numerical Combustion*. 2nd ed: R T Edwards Inc. Pg 372.

[111]. WILKE C R (1950). A Viscosity Equation for Gas Mixtures. **The Journal of Chemical Physics**. Vol 18(4). Pg. 517-519.

[112]. LEE J G and A, D A S D, *Experimental Diagnostics of Combustion Instabilities*, in *Combustion Instabilities in Gas Turbine Engines*, T.C. LIEUWEN and V. YANG, Editors, Progress in Astronautics and Aeronautics. p. 210-529.

[113]. DASCH C J (1992). One Dimensional Tomography: A Comparison of Abel, Onion Peeling and Filtered Back Projection Methods. **Applied Optics**. Vol 31(8). Pg. 1146 - 1152.

[114]. HARDING S C (1996). Investigation into Mixing and Combustion in an Optical, Lean, Premixed, Prevaporised Combustor. PhD. **Cranfield University**.

[115]. RONNEBERGER O, RAFFEL, M and KOMPENHAUS, J. (1998). Advanced Evaluation Algorithms for Standard and Dual Plane Particle Image Velocimetry. **Proceedings of the 9th International symposium on Applications of Laser Techniques to Fluid Mechanics**. Lisbon.

[116]. FINCHMAN A M and SPEDDING, G R (1997). Low Cost, High Resolution Dpiv for Measurements of Turbulent Fluid Flow. **Experiments in Fluids**. Vol 23. Pg. 449 - 462.

[117]. (2005). *Davis 7.1 Software Manual for Davis 7.1*, Gottingen: LaVision GmbH.

[118]. CALLUAUD D and DAVID, L (2004). Stereoscopic Particle Image Velocimetry Measurements of the Flow around a Surface Mounted Block. **Experiments in Fluids**. Vol 36. Pg. 53 - 61.

[119]. SOLOF S M, ADRIAN, R J and LIU, Z C (1997). Distortion Compensation for Generalised Stereoscopic Particle Image Velocimetry. **Measurement Science and Technology**. Vol 8. Pg. 1441-1454.

[120]. KEANE R D and ADRIAN, R J (1990). Optimisation of Particle Image Velocimeters. Part 1: Double Pulsed Systems. **Measurement Science and Technology**. Vol 1. Pg. 1202 - 1215.

[121]. KEANE R D and ADRIAN, R J (1991). Optimisation of Particle Image Velocimeters. Part 2: Multiple Pulsed Systems. **Measurement Science and Technology**. Vol 2. Pg. 963 - 974.

[122]. KEANE R D and ADRIAN, R J (1992). Theory of Cross-Correlation Analysis of Piv Images. **Applied Scientific Research**. Vol 49. Pg. 191 - 215.

[123]. KEANE R D, ADRIAN, R J and ZHANG, Y (1995). Super-Resolution Particle Image Velocimetry. **Measurement Science and** Vol 6. Pg. 754 - 768.

[124]. WILLERT C (1996). The Fully Digital Evaluation of Photographic Piv Recordings. **Applied Scientific Research**. Vol 56. Pg. 79 - 102.

[125]. RAFFEL M, WILLERT, C, WERELEY, S and KOMPENHAUS, J (2007). *Particle Image Velocimetry: A Practical Guide*. 2nd ed, Berlin: Springer. Pg 164 - 176.

[126]. SCARANCO F (2002). Iterative Image Deformation Methods in Piv **Measurement Science and Technology**. Vol 13. Pg. R1 - R19.

[127]. WESTERWEEL J (2008). On Velocity Gradients in Piv Interrogation. **Experiments in Fluids**. Vol 44. Pg. 831 - 842.

[128]. WESTERWEEL J (1997). Fundamentals of Digital Particle Image Velocimetry. **Measurement Science and Technology**. Vol 8. Pg. 1379 - 1392.

[129]. JEONG J and HUSSAIN, F (1995). On the Identification of a Vortex. **Journal of Fluid Mechanics**. Vol 285. Pg. 69-94.

[130]. HUNT J C R, WRAY, A A and MOIN, P (1988). Eddies, Streams and Convergence Zones in Turbulent Flows.**Centre for Turbulence Research**. Stanford University, California USA.

[131]. GRAFTIEAUX L, MICHARD, M and GROSJEAN, N (2001). Combining Piv, Pod and Vortex Identification Algorithms for the Study of Unsteady Turbulent Swirling Flows. **Measurement Science and Technology**. Vol 12. Pg. 1422-1429.

[132]. HO C M and HEURRE, P (1984). Perturbed Free Shear Layer. **Annual review of Fluid Mechanics**. Vol 16. Pg. 365-424.

[133]. COATS C M (1996). Coherent Structures in Combustion. **Progress in Energy and Combustion Science**. Vol 22. Pg. 427-509.

APPENDIX A

A.1 Combustion Chamber sub Assemblies

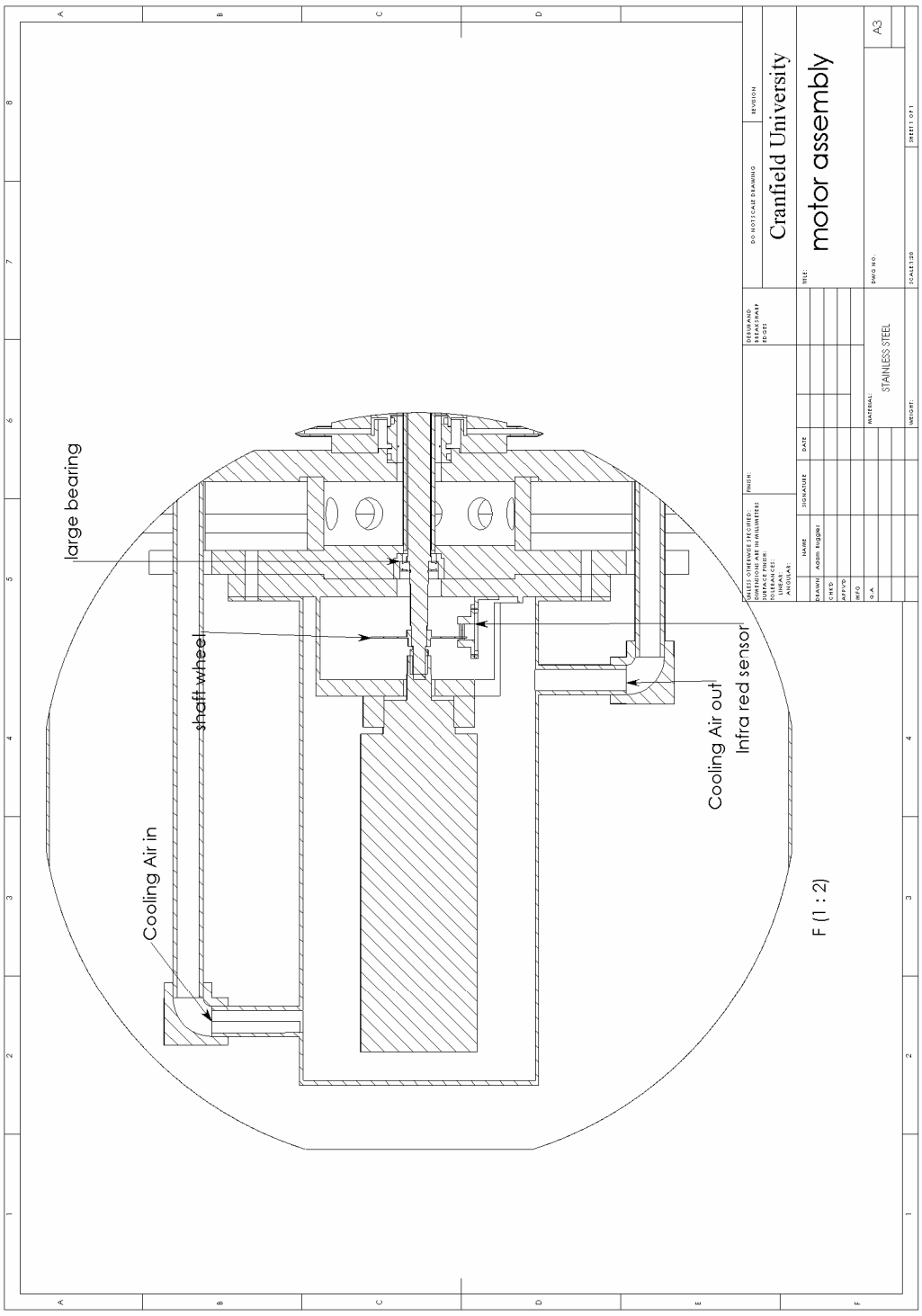

Figure A-1 Motor sub Assembly.

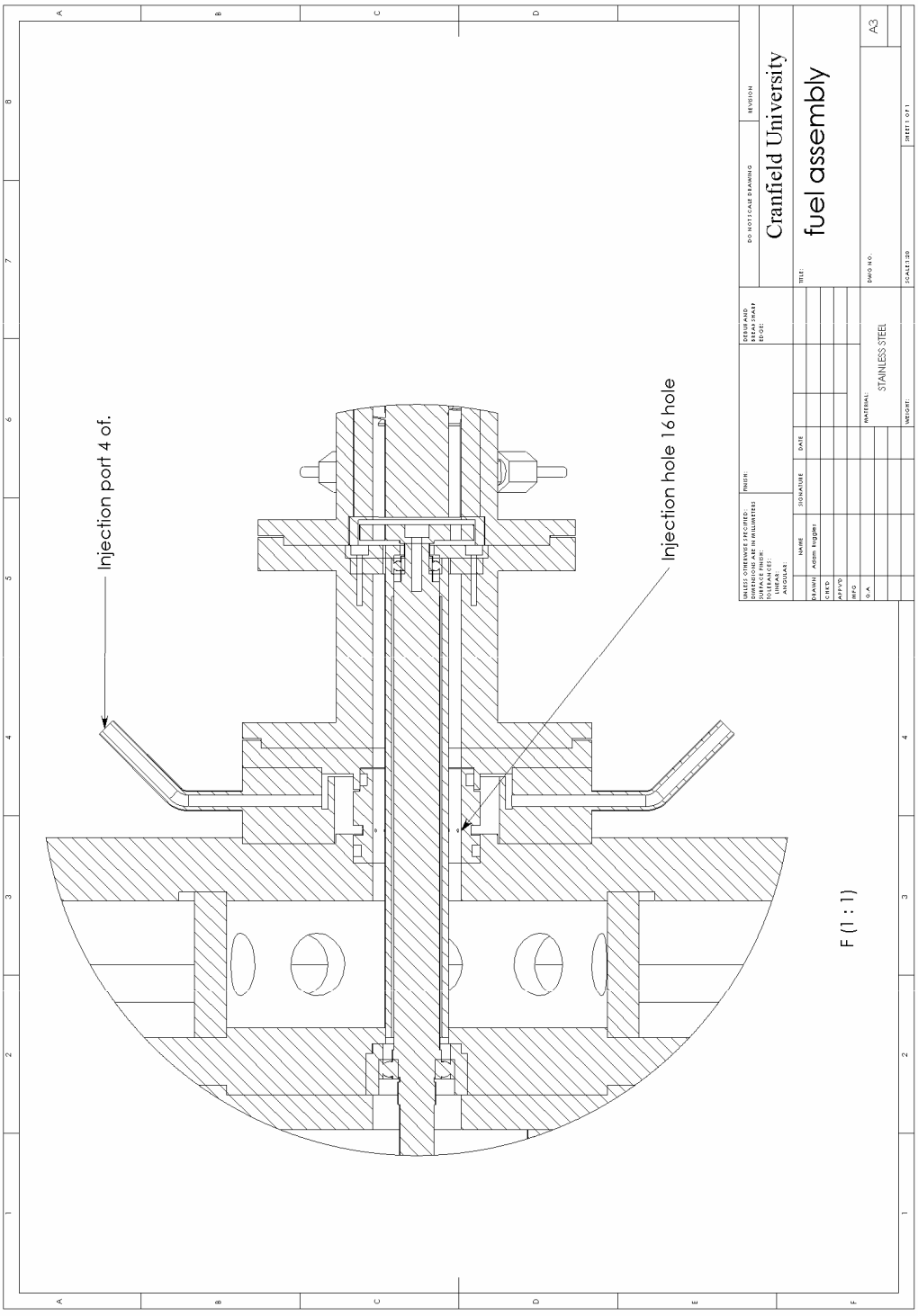

Figure A-2 Fuel injector sub Assembly.

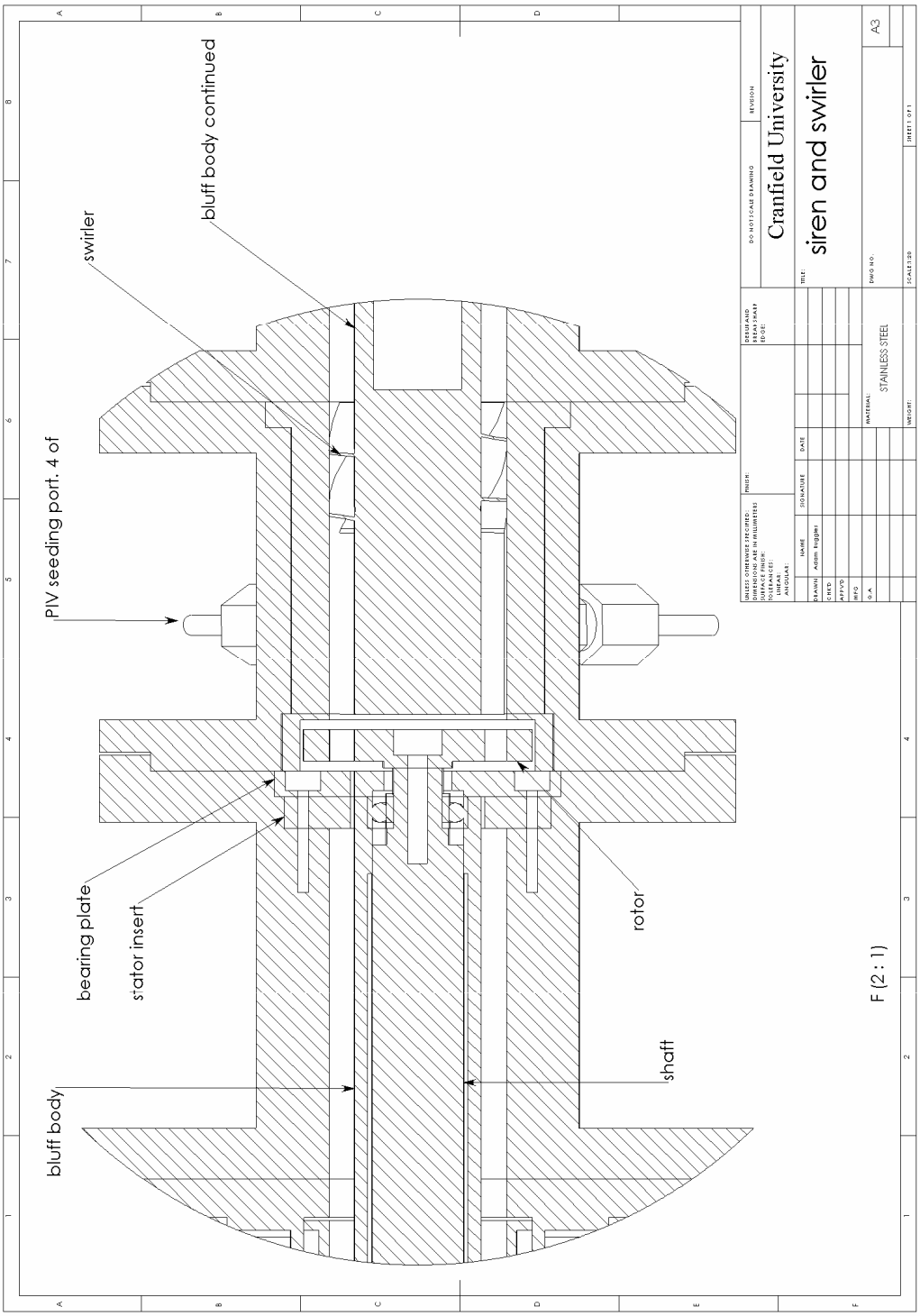

Figure A-3 Siren and swirler sub Assembly.

APPENDIX B

B.1 F10 Results – Mean CH and Flow field Images

This appendix contains the mean Abel deconvoluted CH* and flow field images for f10 perturbed at 100Hz, 200Hz and 400Hz. Included are the mean integrated CH* curves and frequency spectrums. Also included are velocity profiles taken at 30mm, 50mm and 70mm downstream of the Annulus.

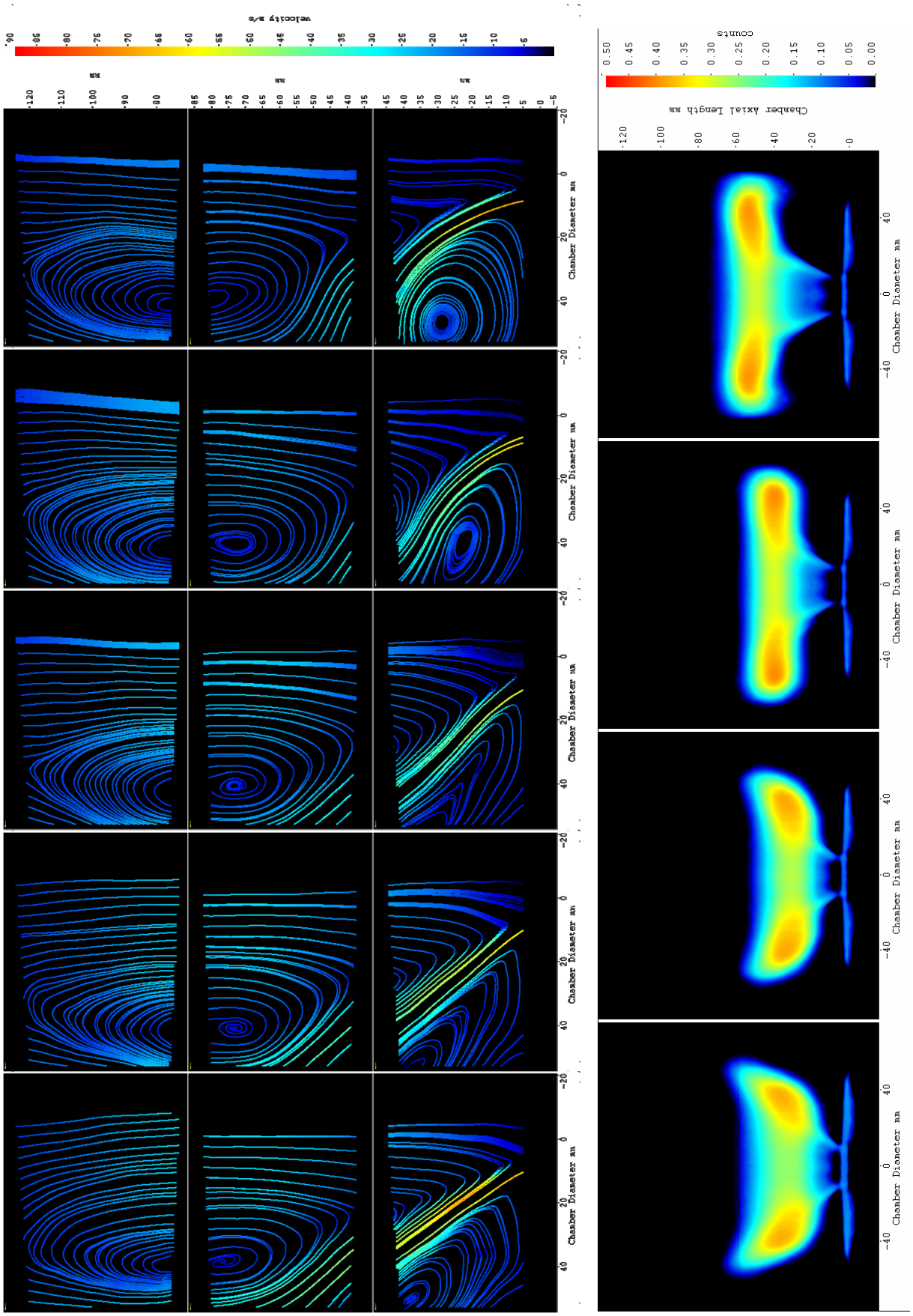

Figure B-1 Phases 1 (bottom) to 5 (top) of the flow field and phases 1 (bottom) to 4 (top) of the reacting field of f10-100Hz. The flow field images were recorded in the 'CRZ', 'Flame Zone' and 'URZ' imaging areas.

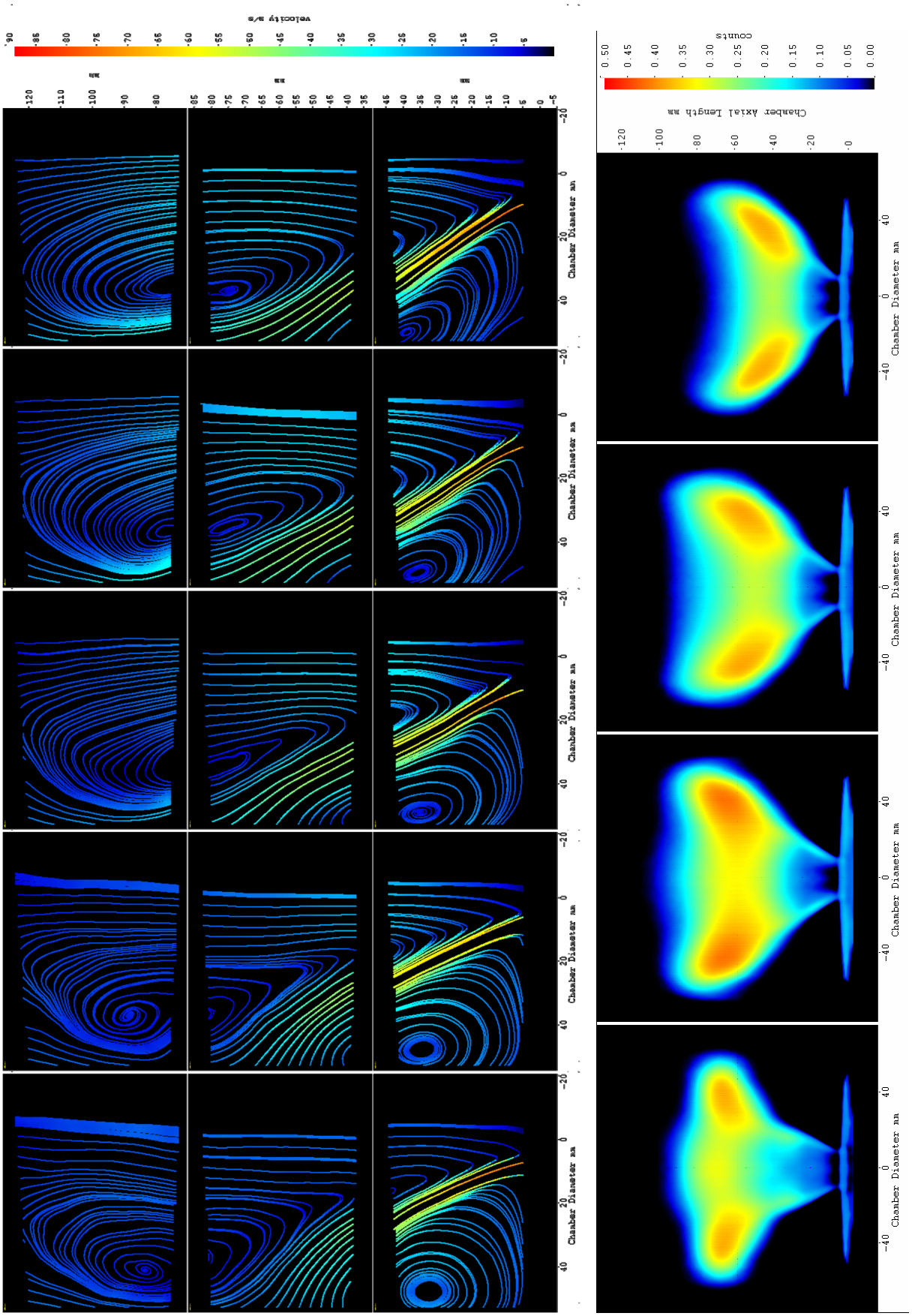

Figure B-2 Phases 6 (bottom) to 10 (top) of the flow field and phases 5 (bottom) to 8 (top) of the reacting field of f10-100Hz. The flow field images were recorded in the 'CRZ', 'Flame Zone' and 'URZ' imaging areas.

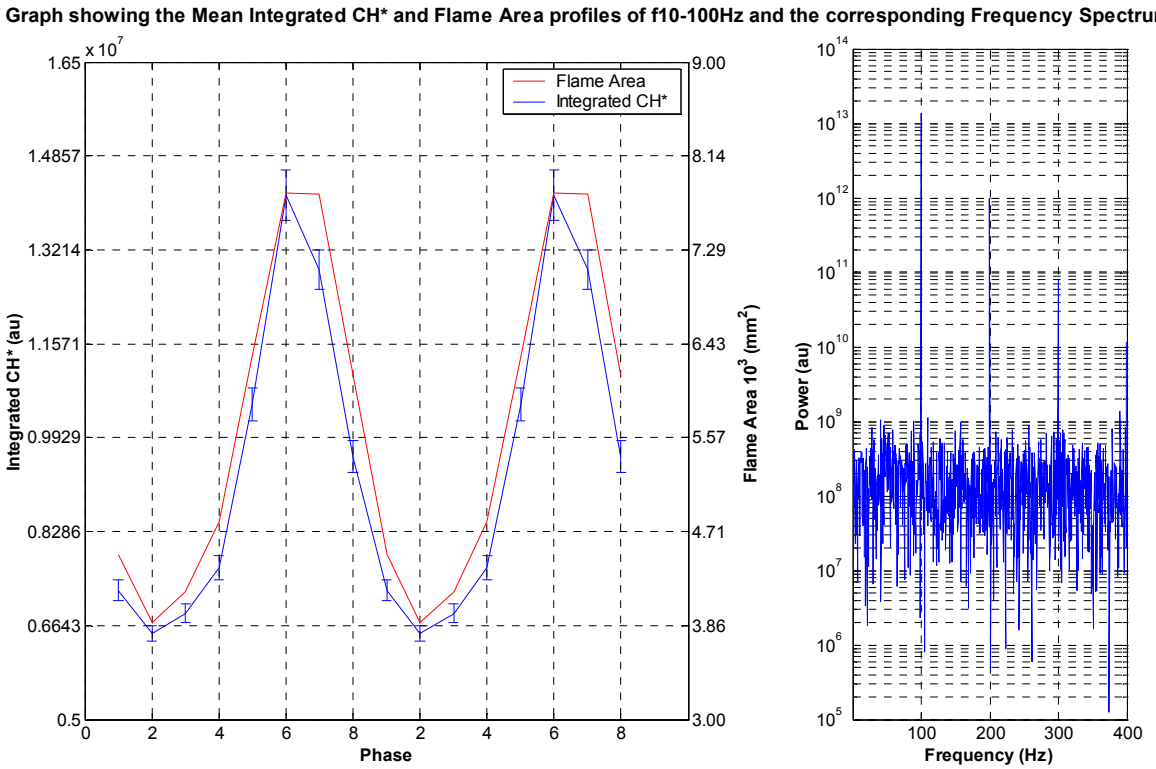

Figure B-3 Mean Integrated CH* profile and flame area profile for f10-100Hz with corresponding Frequency Spectrum. The phase corresponds to that of the CH* images.

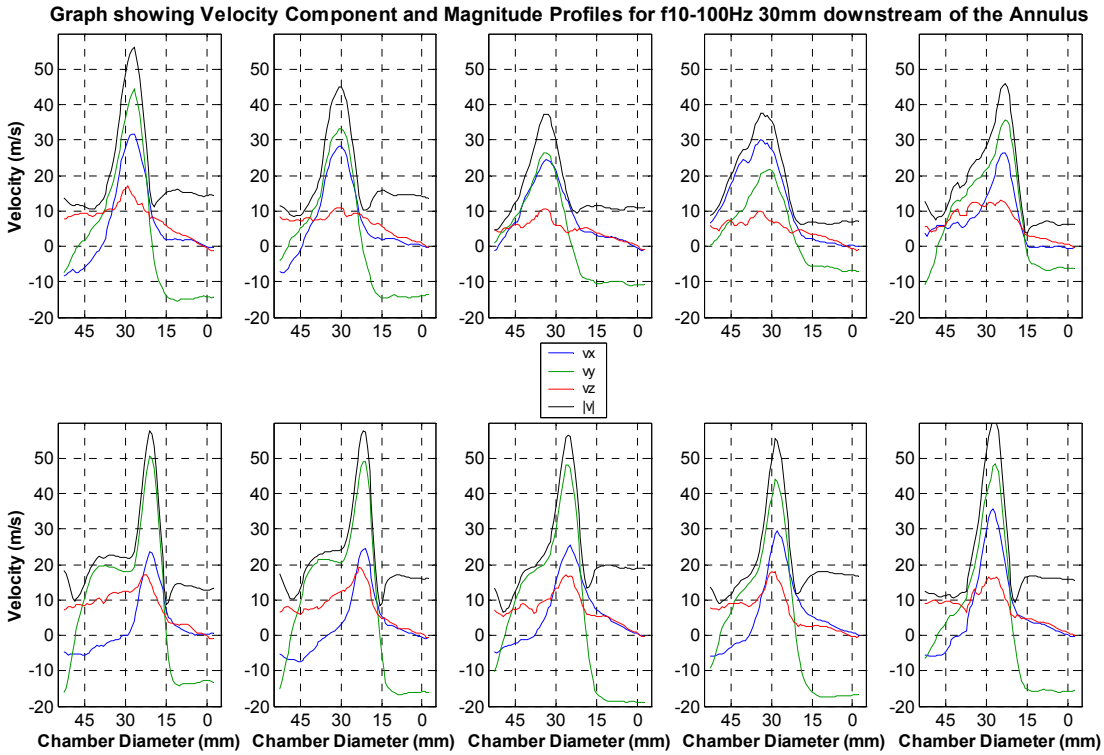

Figure B-4 Velocity Profiles of f10-100Hz along a line 30mm downstream of the Annulus. Taken from mean vector fields from the imaging area 'CRZ'. The top row consists of phases 1 to 5 from left to right. The bottom row consists of phases 6 to 10 from left to right.

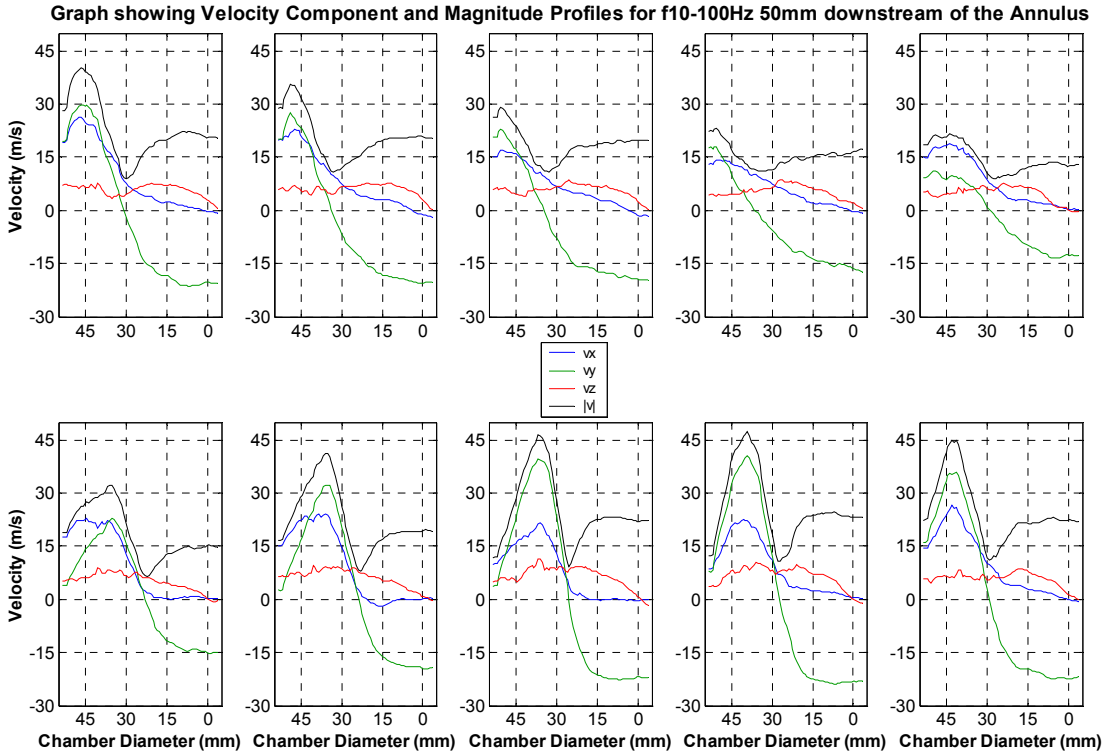

Figure B-5 Velocity Profiles of f10-100Hz along a line 50mm downstream of the Annulus. Taken from mean vector fields from the imaging area 'Flame Zone'. The top row consists of phases 1 to 5 from left to right. The bottom row consists of phases 6 to 10 from left to right.

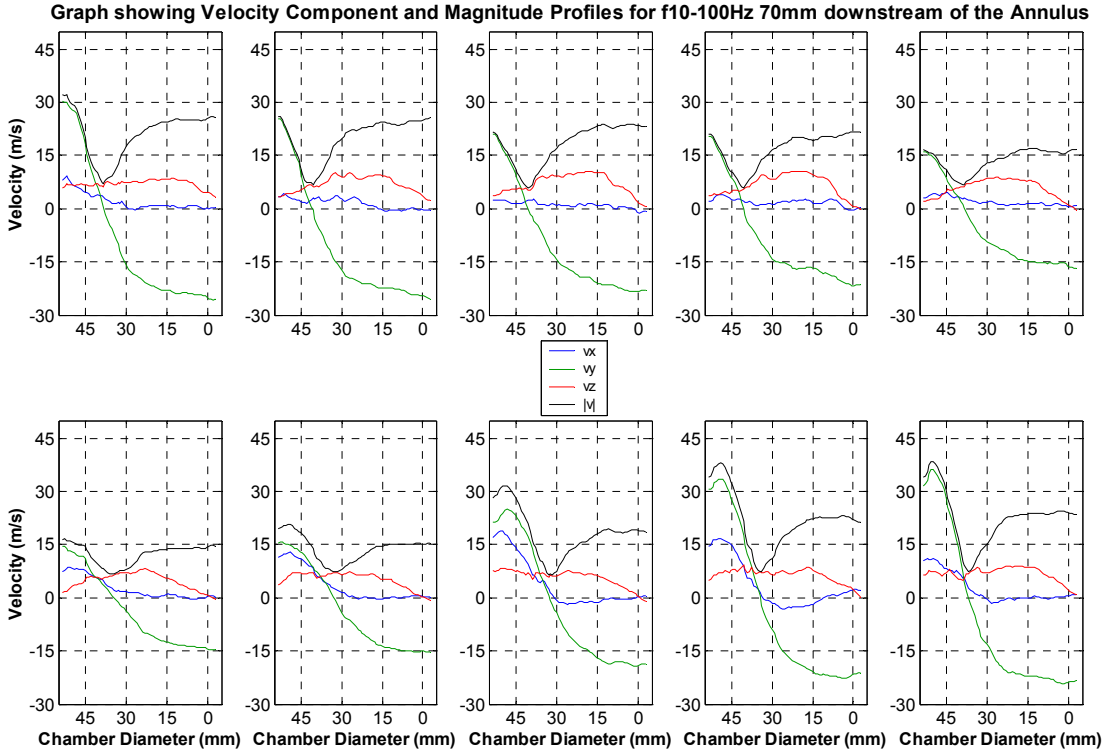

Figure B-6 Velocity Profiles of f10-100Hz along a line 70mm downstream of the Annulus. Taken from mean vector fields from the imaging area 'URZ'. The top row consists of phases 1 to 5 from left to right. The bottom row consists of phases 6 to 10 from left to right.

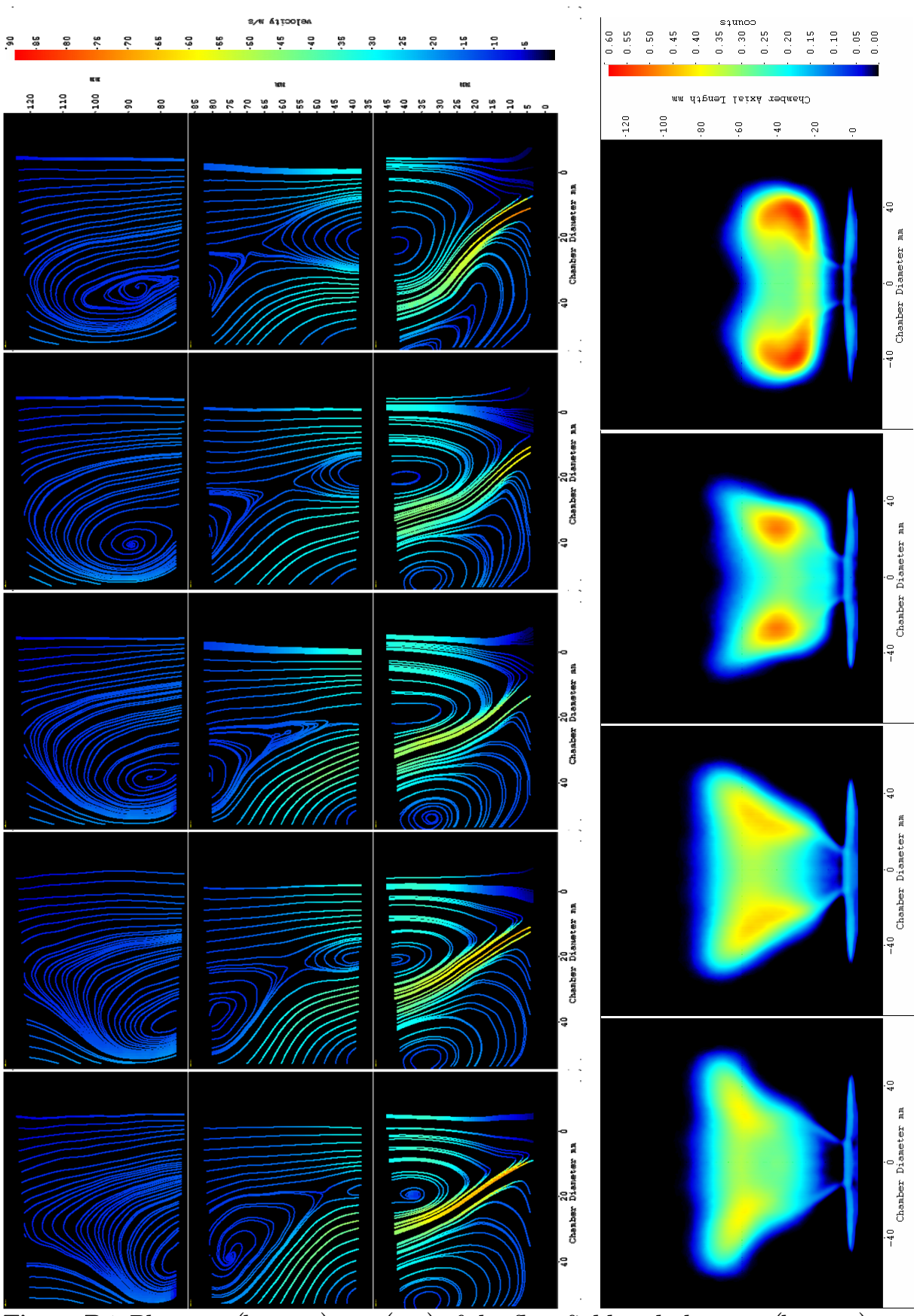

Figure B-7 Phases 1 (bottom) to 5 (top) of the flow field and phases 1 (bottom) to 4 (top) of reacting field of f10-200Hz. The flow field images were recorded in the 'CRZ', 'Flame Zone' and 'URZ' imaging areas.

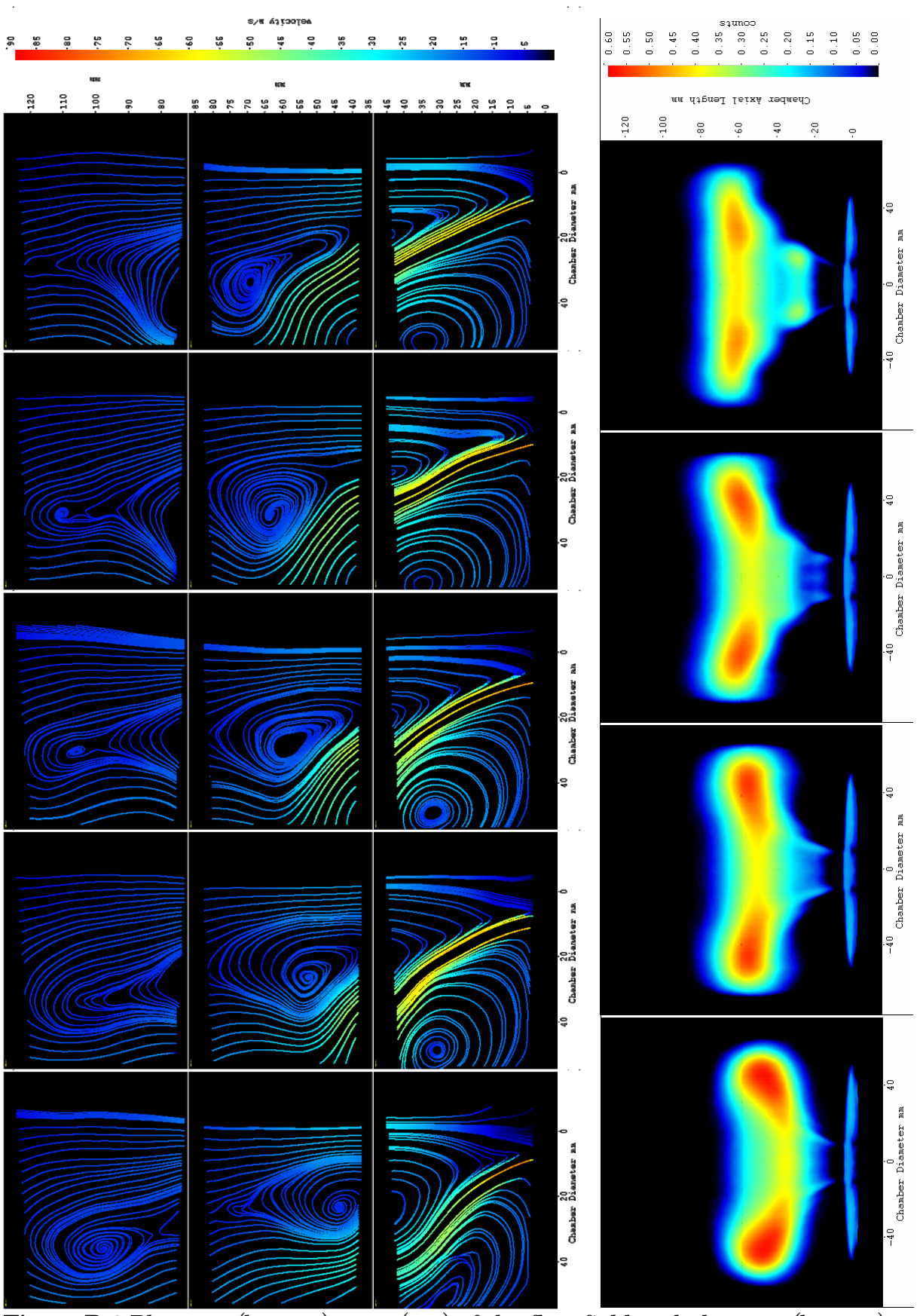

Figure B-8 Phases 6 (bottom) to 10 (top) of the flow field and phases 5 (bottom) to 8 (top) of reacting field of f10-200Hz. The flow field images were recorded in the 'CRZ', 'Flame Zone' and 'URZ' imaging areas.

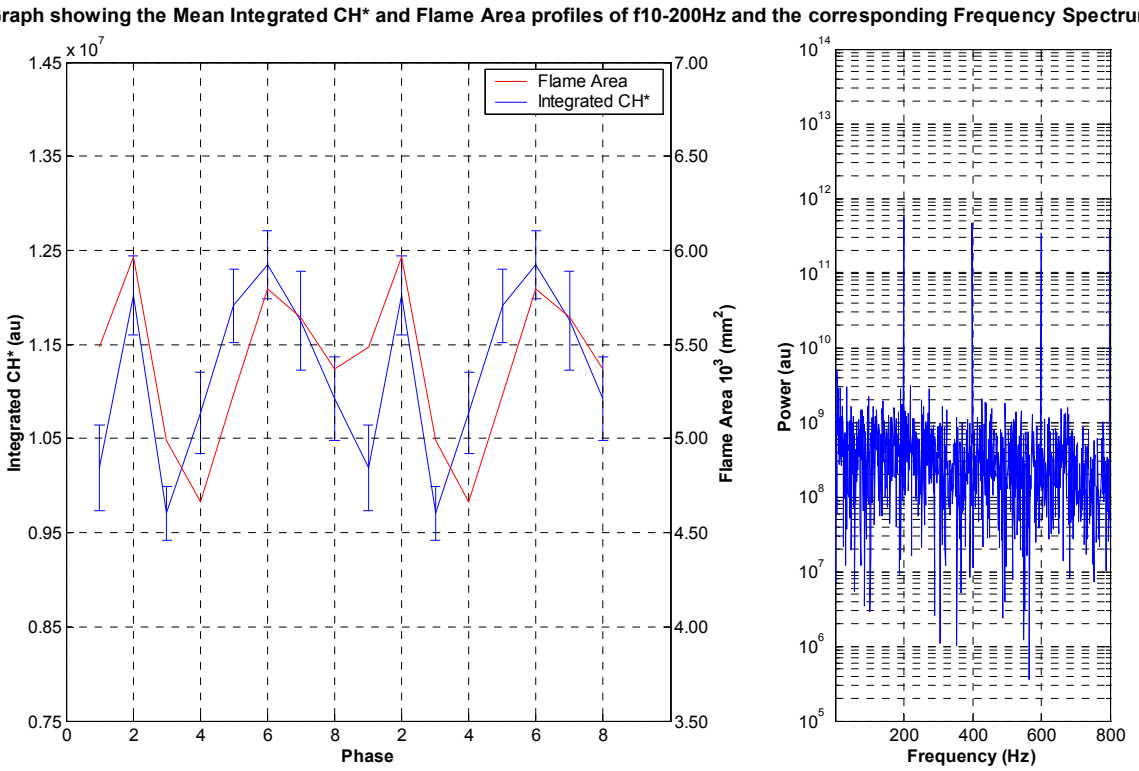

Figure B-9 Mean Integrated CH* profile and flame area profile for f10-200Hz with corresponding Frequency Spectrum. The phase corresponds to that of the CH* images.

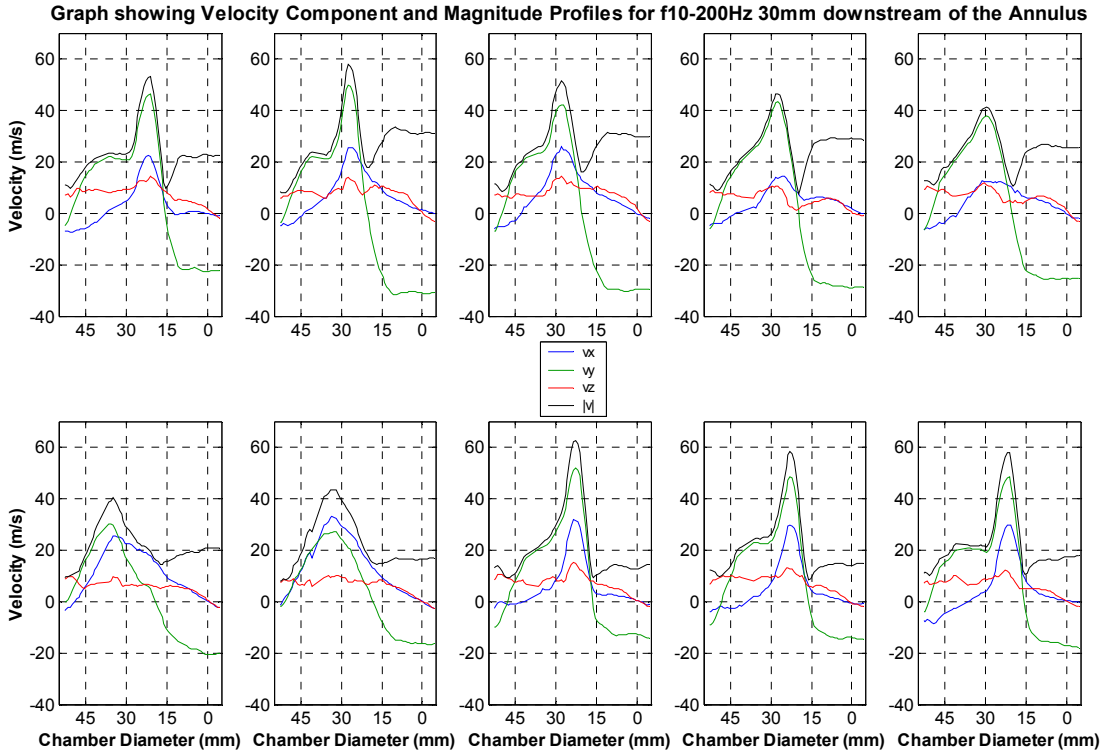

Figure B-10 Velocity Profiles of f10-200Hz along a line 30mm downstream of the Annulus. Taken from mean vector fields from the imaging area 'CRZ'. The top row consists of phases 1 to 5 from left to right. The bottom row consists of phases 6 to 10 from left to right.

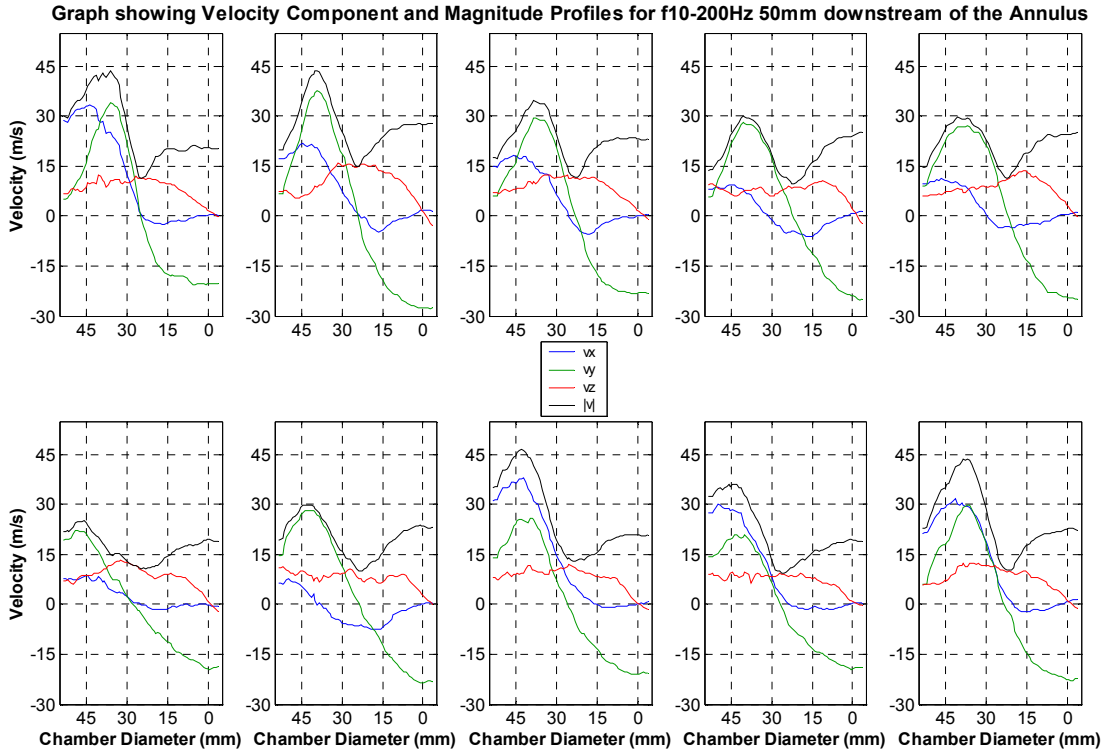

Figure B-11 Velocity Profiles of f10-200Hz along a line 50mm downstream of the Annulus. Taken from mean vector fields from the imaging area 'Flame Zone'. The top row consists of phases 1 to 5 from left to right. The bottom row consists of phases 6 to 10 from left to right.

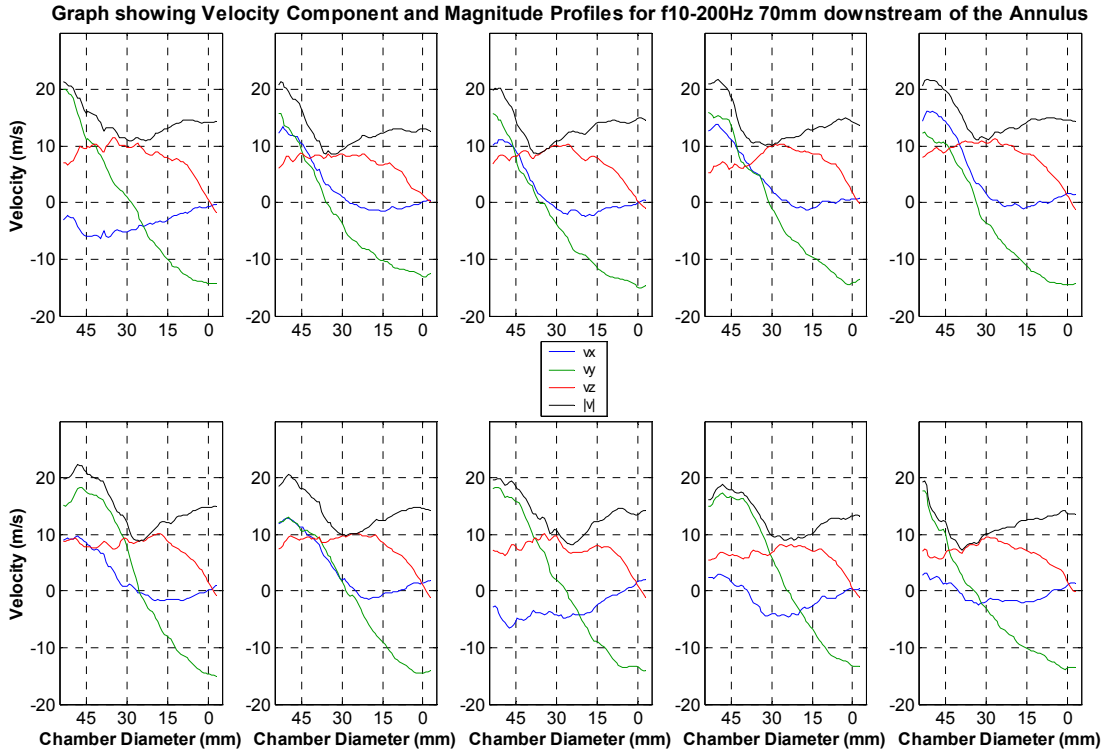

Figure B-12 Velocity Profiles of f10-200Hz along a line 70mm downstream of the Annulus. Taken from mean vector fields from the imaging area 'Flame Zone'. The top row consists of phases 1 to 5 from left to right. The bottom row consists of phases 6 to 10 from left to right.

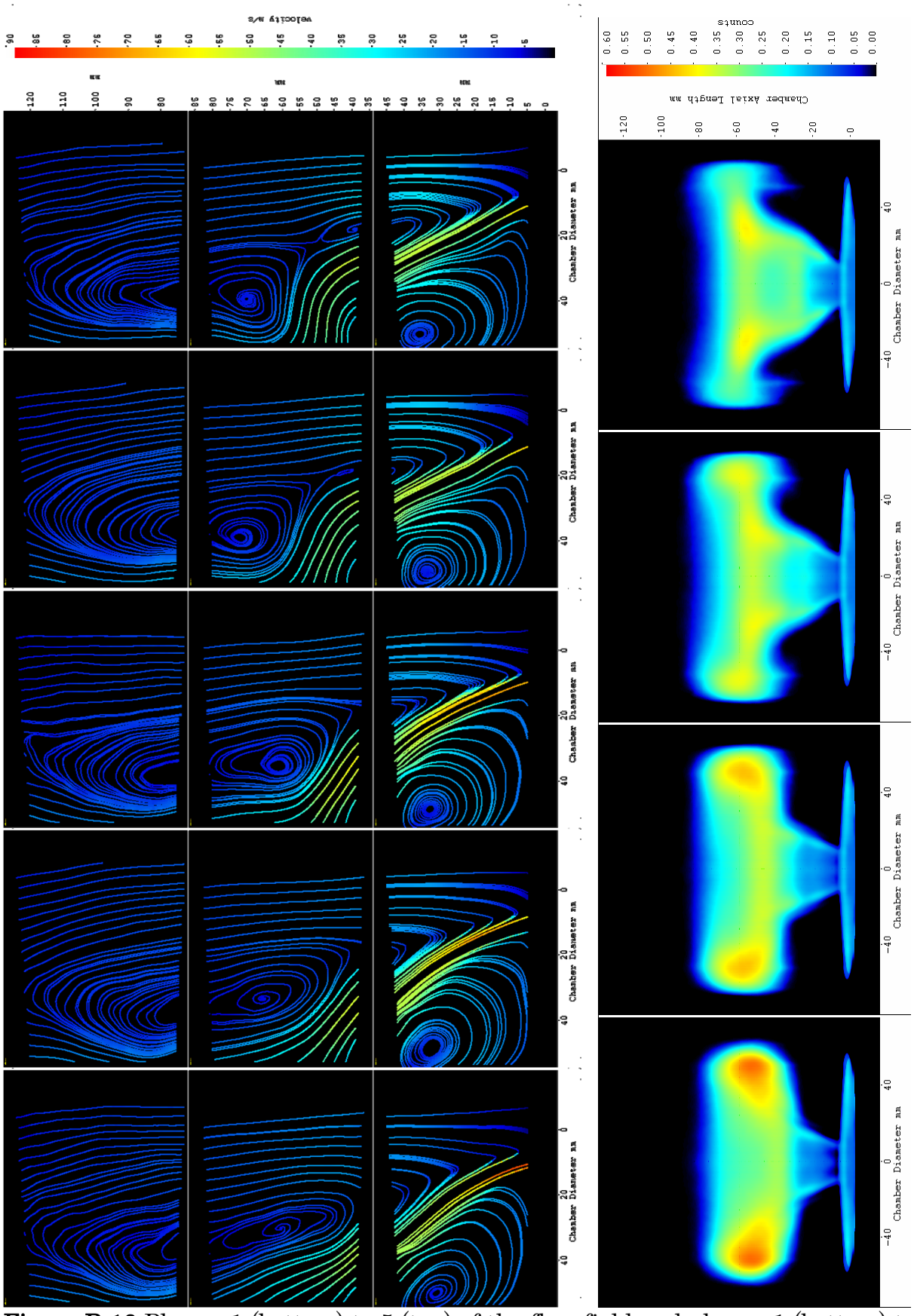

Figure B-13 Phases 1 (bottom) to 5 (top) of the flow field and phases 1 (bottom) to 4 (top) of reacting field of f10-400Hz. The flow field images were recorded in the 'CRZ', 'Flame Zone' and 'URZ' imaging areas.

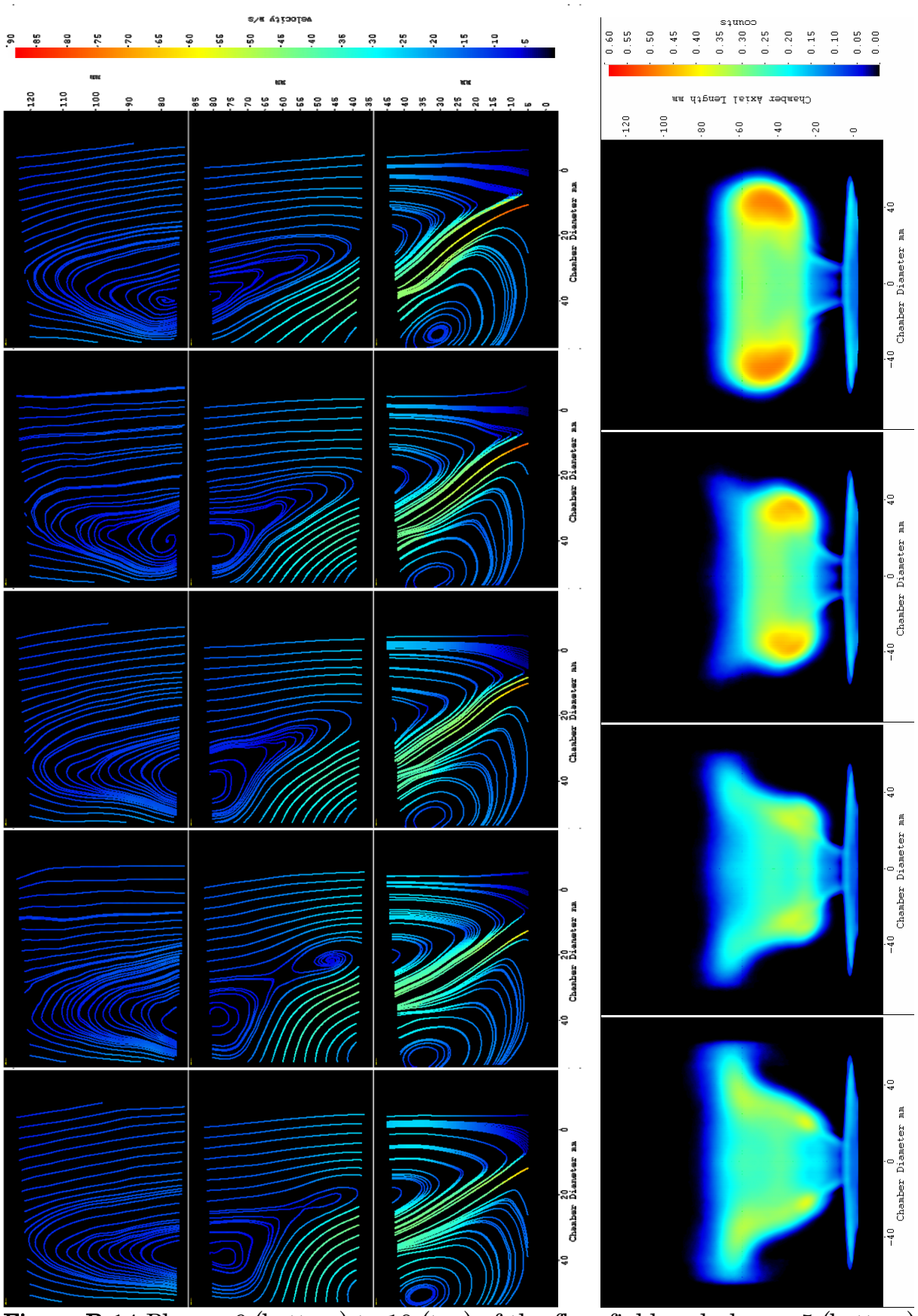

Figure B-14 Phases 6 (bottom) to 10 (top) of the flow field and phases 5 (bottom) to 8 (top) of reacting field of f10-400Hz. The flow field images were recorded in the 'CRZ', 'Flame Zone' and 'URZ' imaging areas.

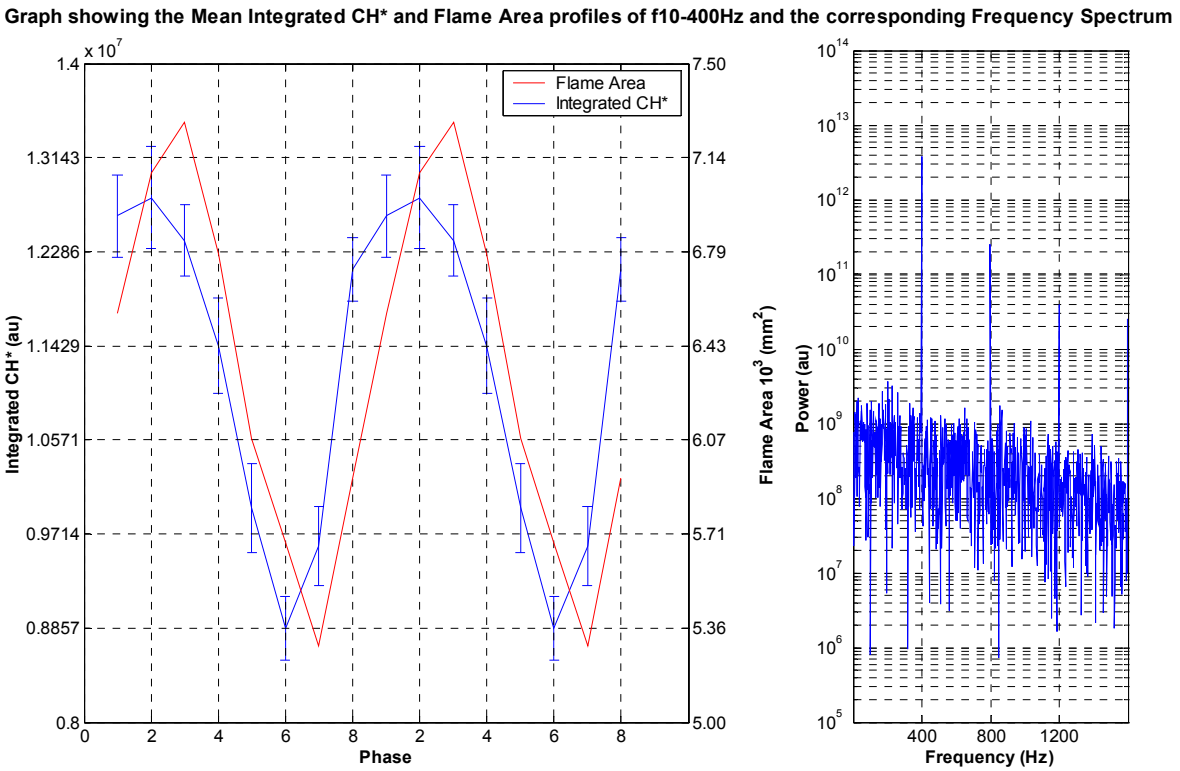

Figure B-15 Mean Integrated CH* profile and flame area profile for f10-400Hz with corresponding Frequency Spectrum. The phase corresponds to that of the CH* images.

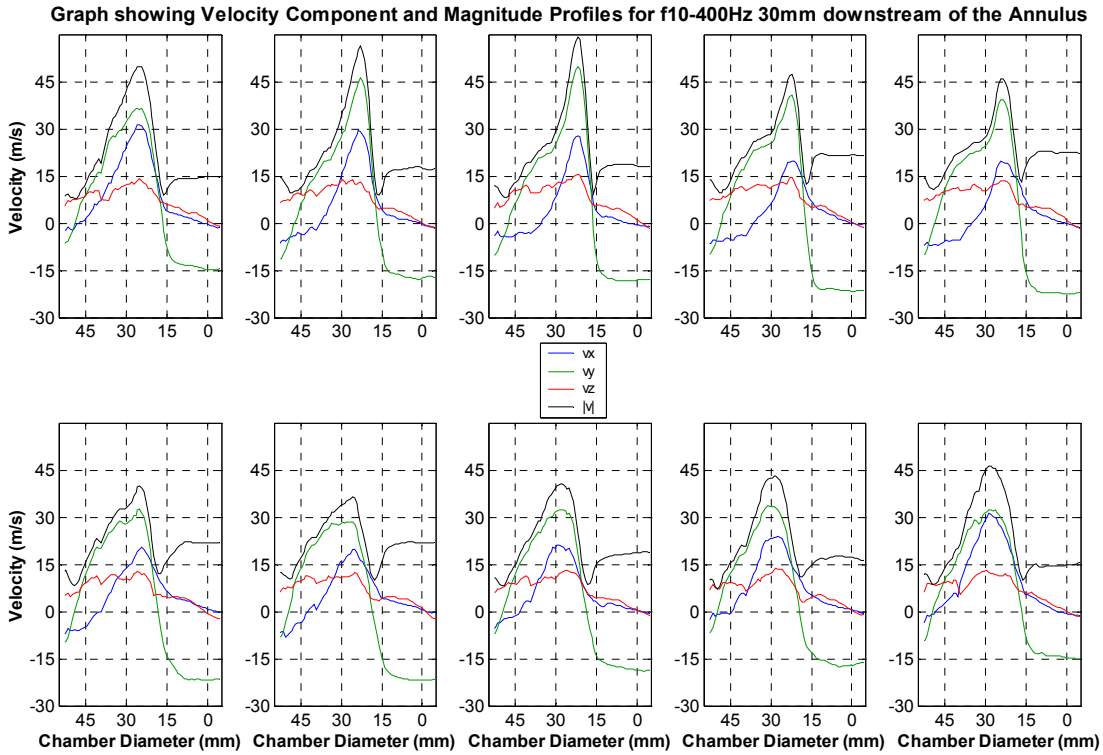

Figure B-16 Velocity Profiles of f10-400Hz along a line 30mm downstream of the Annulus. Taken from mean vector fields from the imaging area 'CRZ'. The top row consists of phases 1 to 5 from left to right. The bottom row consists of phases 6 to 10 from left to right.

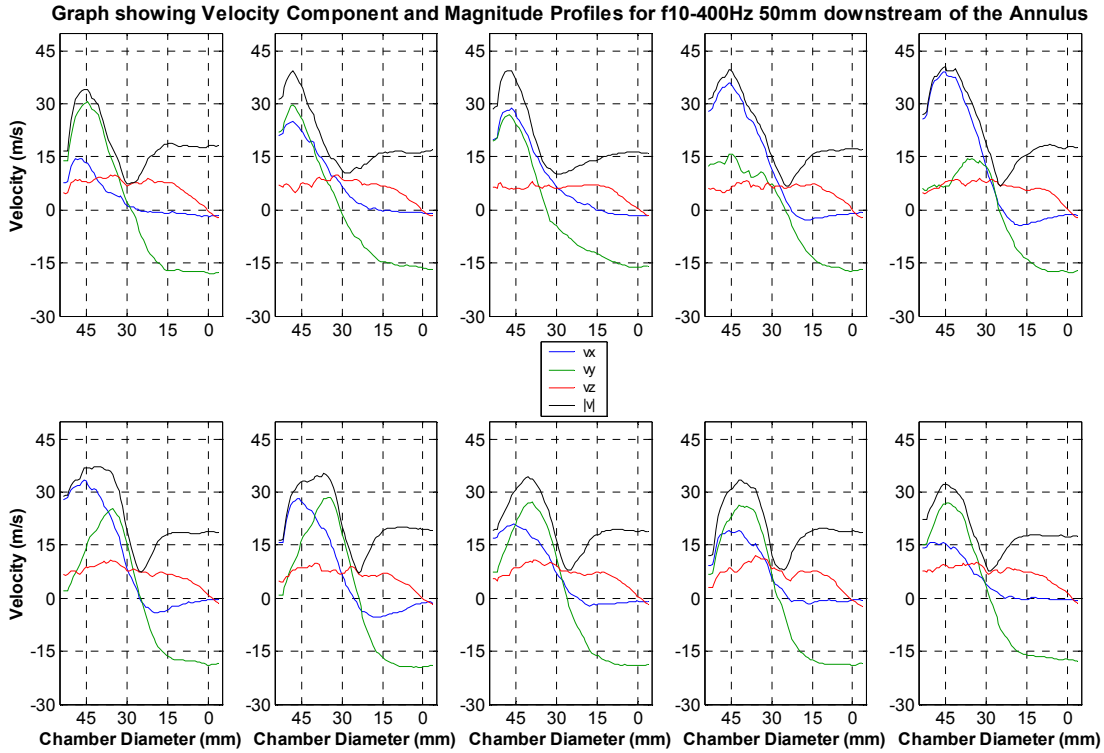

Figure B-17 Velocity Profiles of f10-400Hz along a line 50mm downstream of the Annulus. Taken from mean vector fields from the imaging area 'Flame Zone'. The top row consists of phases 1 to 5 from left to right. The bottom row consists of phases 6 to 10 from left to right.

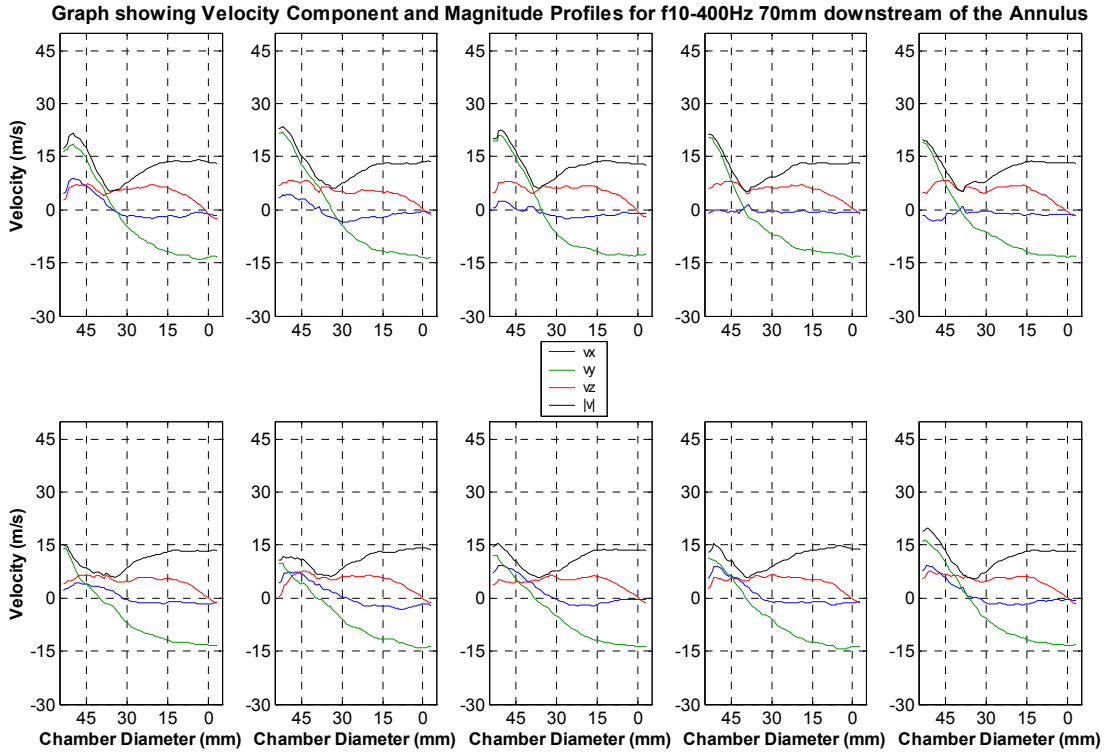

Figure B-18 Velocity Profiles of f10-400Hz along a line 70mm downstream of the Annulus. Taken from mean vector fields from the imaging area 'Flame Zone'. The top row consists of phases 1 to 5 from left to right. The bottom row consists of phases 6 to 10 from left to right.

B.2 F10 Results–Vortex Summation and Vorticity Structures

This appendix contains the summation of the vortex ID algorithm used and mean vorticity field images for f10 perturbed at 100Hz, 200Hz and 400Hz. Included are the vorticity profiles taken at 5mm and 20mm downstream of the annulus and vorticity spectra taken at the centre of the inlet flow and the inner and outer shear layers.

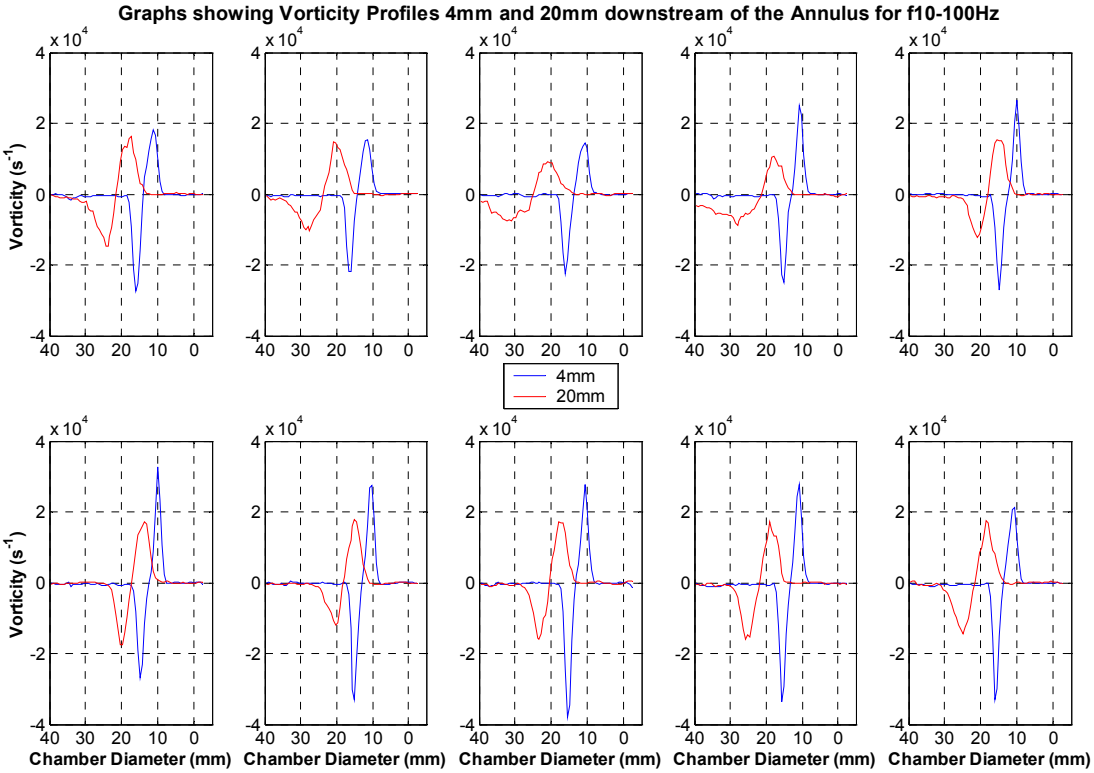

Figure B-19 Vorticity profiles of f10-100Hz along a line 4mm downstream of the Annulus. Taken from mean vorticity fields from the imaging area 'Annulus 3D'. The top row consists of phases 1 to 5 from left to right. The bottom row consists of phases 6 to 10 from left to right.

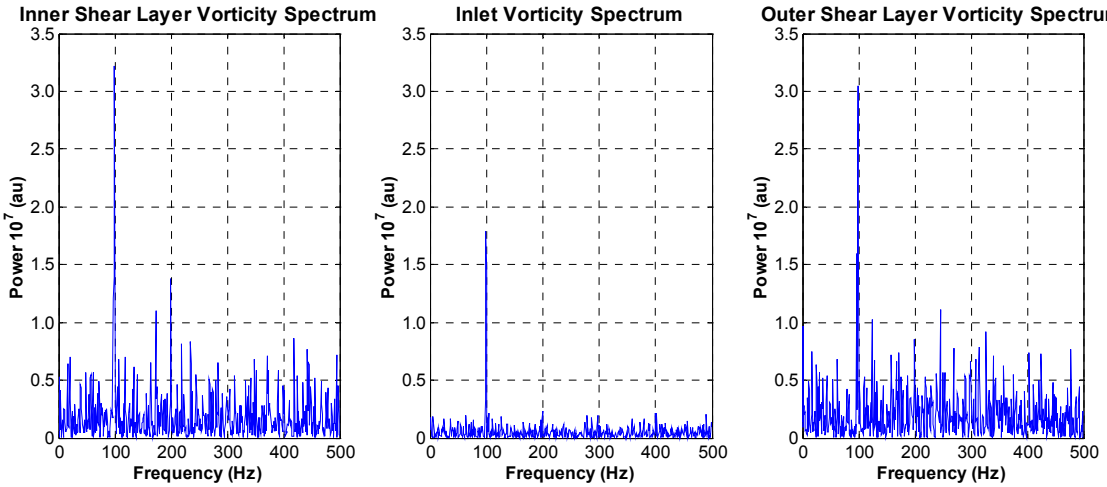

Figure B-20 Frequency spectrums taken from the f10-100Hz Instantaneous Vorticity fields recorded at the 'Annulus 3D' imaging area. The radial position of the inner shear layer is 11mm, the inlet flow centre 13mm and outer shear layer 16mm.

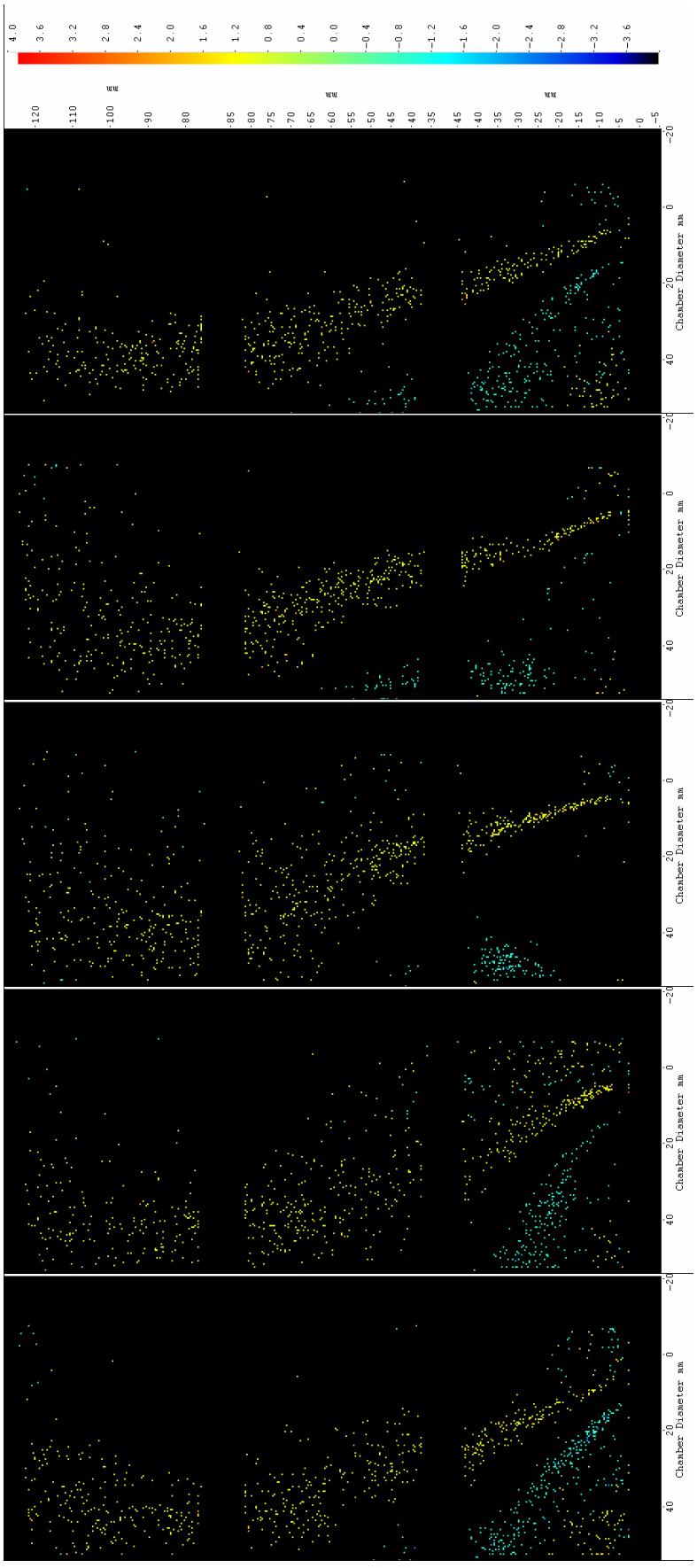

Figure B.21 Summation images showing location of detected vortices for f10-100Hz for phases 2 (Bottom), 4, 6, 8, and 10 (Top). Positive values correspond to clockwise vortices and negative values correspond to anticlockwise vortices.

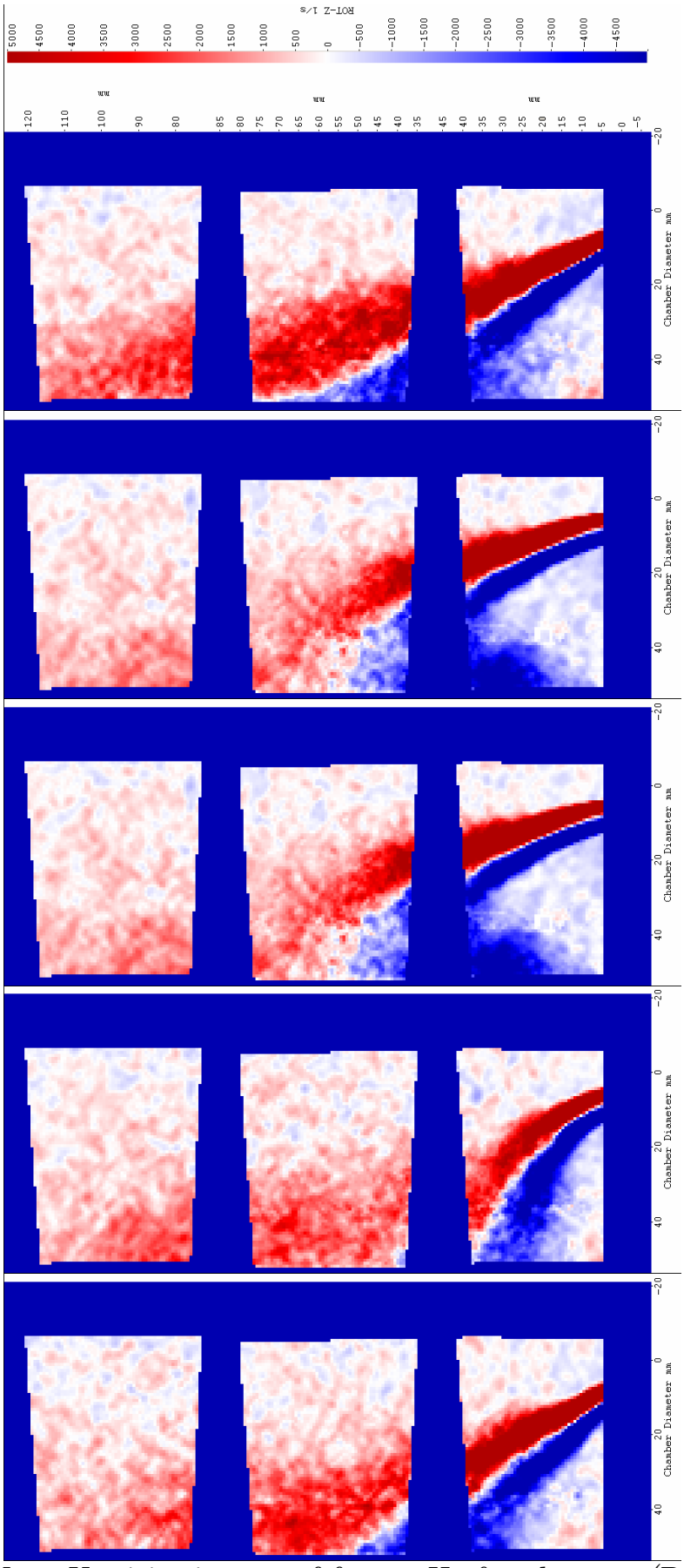

Figure B.22 Mean Vorticity images of f10-100Hz for phases 2 (Bottom), 4, 6, 8 and 10 (Top). Clockwise (positive) and anticlockwise (negative) vorticity are artificially saturated at $5000s^{-1}$.

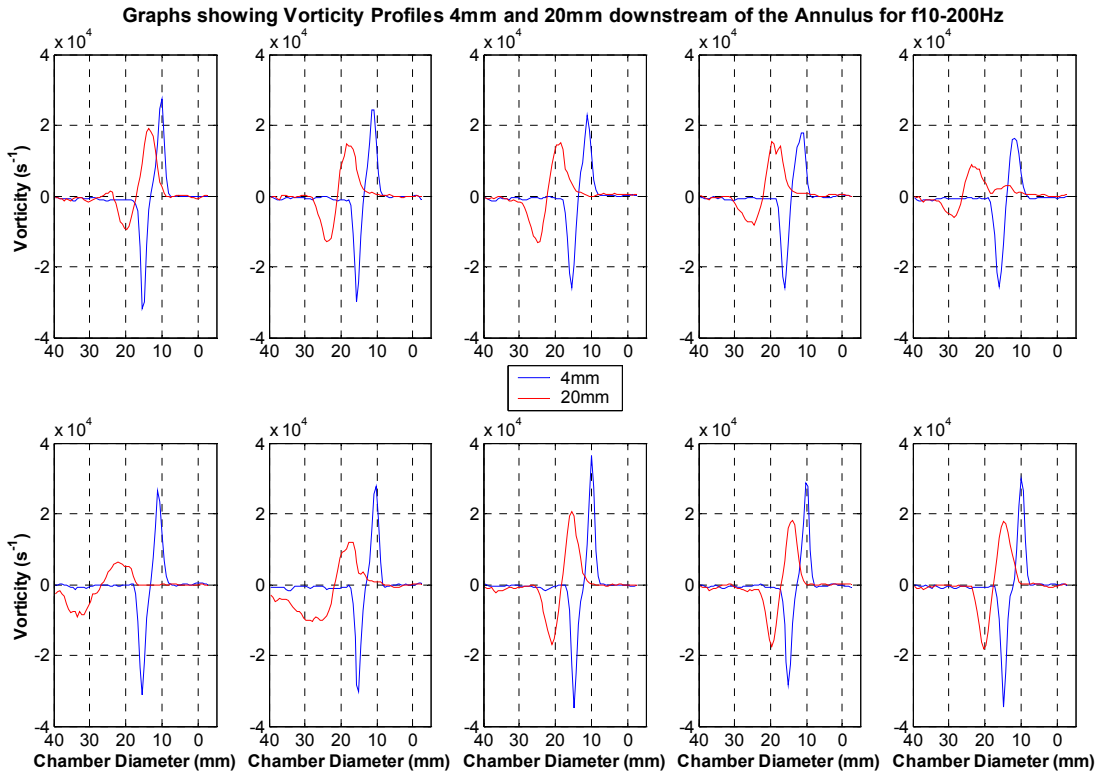

Figure B-23 Vorticity profiles of f10-200Hz along a line 4mm downstream of the Annulus. Taken from mean vorticity fields from the imaging area 'Annulus 3D'. The top row consists of phases 1 to 5 from left to right. The bottom row consists of phases 6 to 10 from left to right.

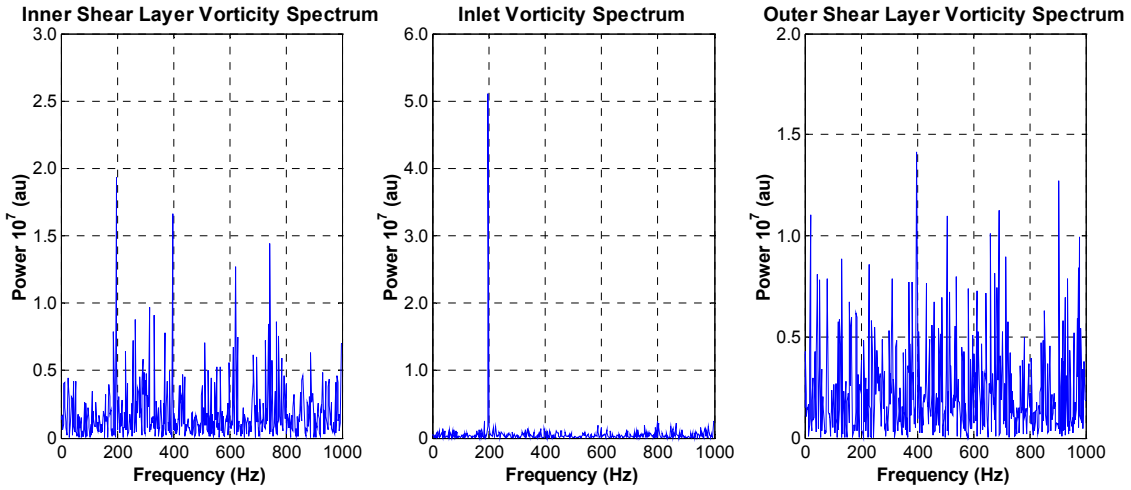

Figure B-24 Frequency spectrums taken from the f10-200Hz Instantaneous Vorticity fields recorded at the 'Annulus 3D' imaging area. The radial position of the inner shear layer is 11mm, the inlet flow centre 13mm and outer shear layer 16mm.

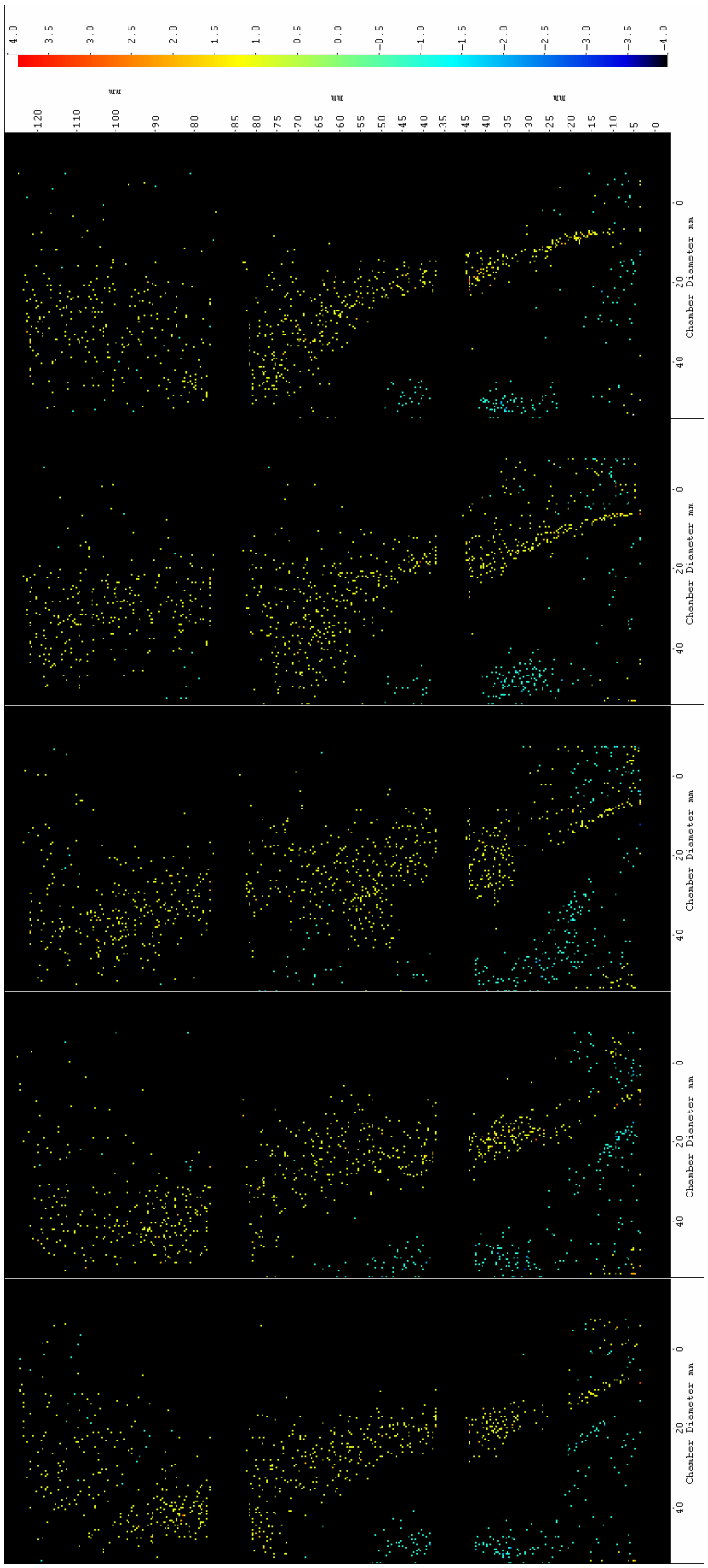

Figure B.25 Summation images showing location of detected vortices for f10-200Hz for phases 2 (Bottom), 4, 6, 8, and 10 (Top). Positive values correspond to clockwise vortices and negative values correspond to anticlockwise vortices.

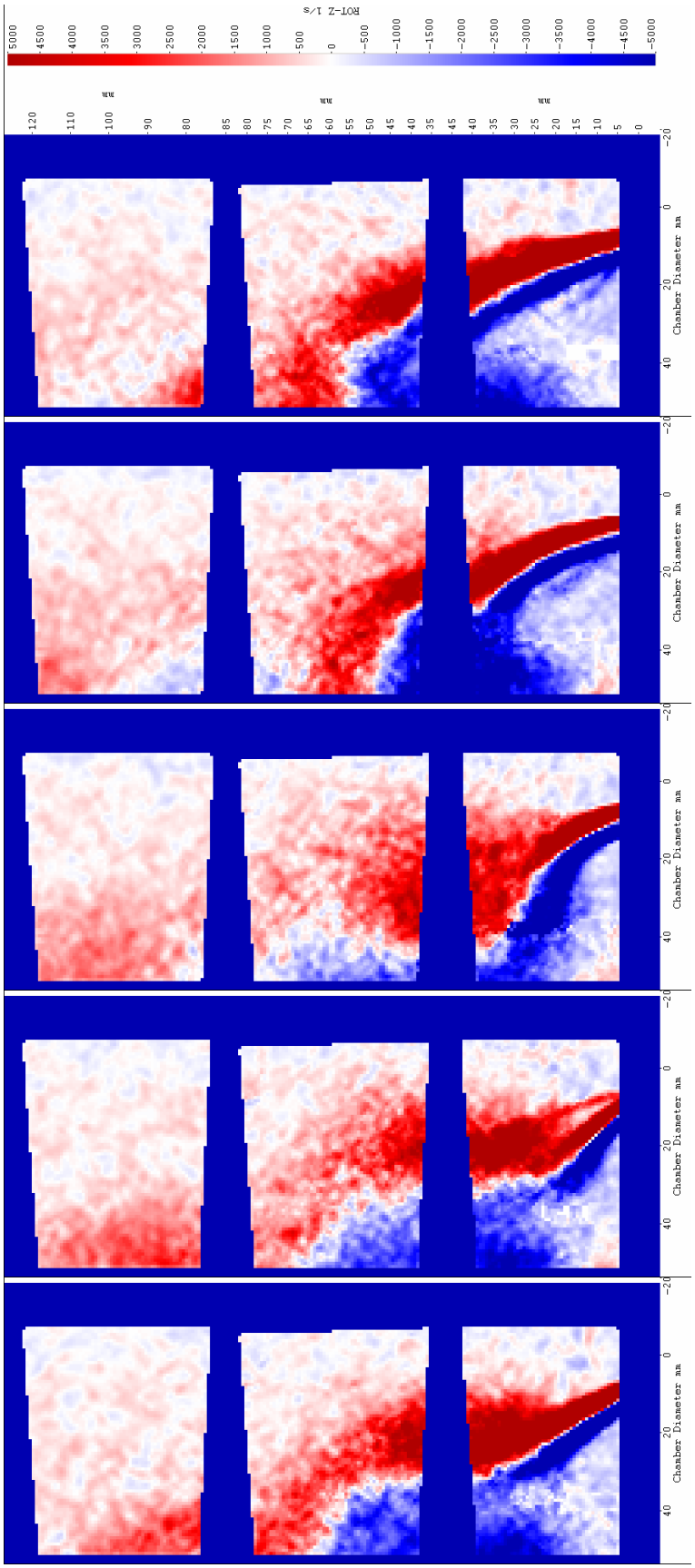

Figure B.26 Mean Vorticity images of f10-200Hz for phases 2 (Bottom), 4, 6, 8 and 10 (Top). Clockwise (positive) and anticlockwise (negative) vorticity are artificially saturated at $5000s^{-1}$.

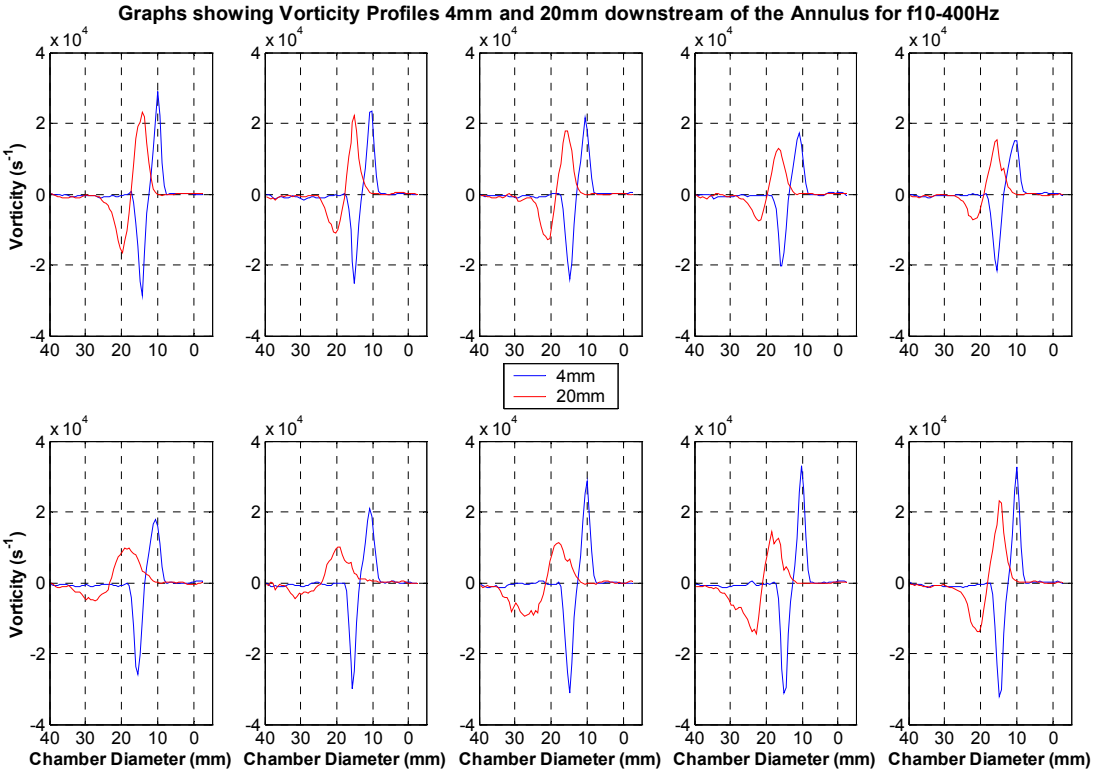

Figure B-27 Vorticity profiles of f10-400Hz along a line 4mm downstream of the Annulus. Taken from mean vorticity fields from the imaging area 'Annulus 3D'. The top row consists of phases 1 to 5 from left to right. The bottom row consists of phases 6 to 10 from left to right.

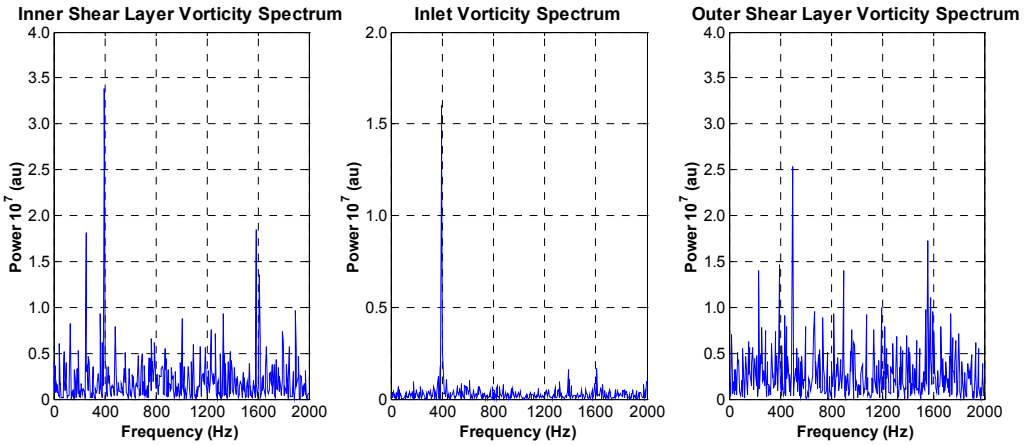

Figure B-28 Frequency spectrums taken from the f10-400Hz Instantaneous Vorticity fields recorded at the 'Annulus 3D' imaging area. The radial position of the inner shear layer is 11mm, the inlet flow centre 13mm and outer shear layer 16mm.

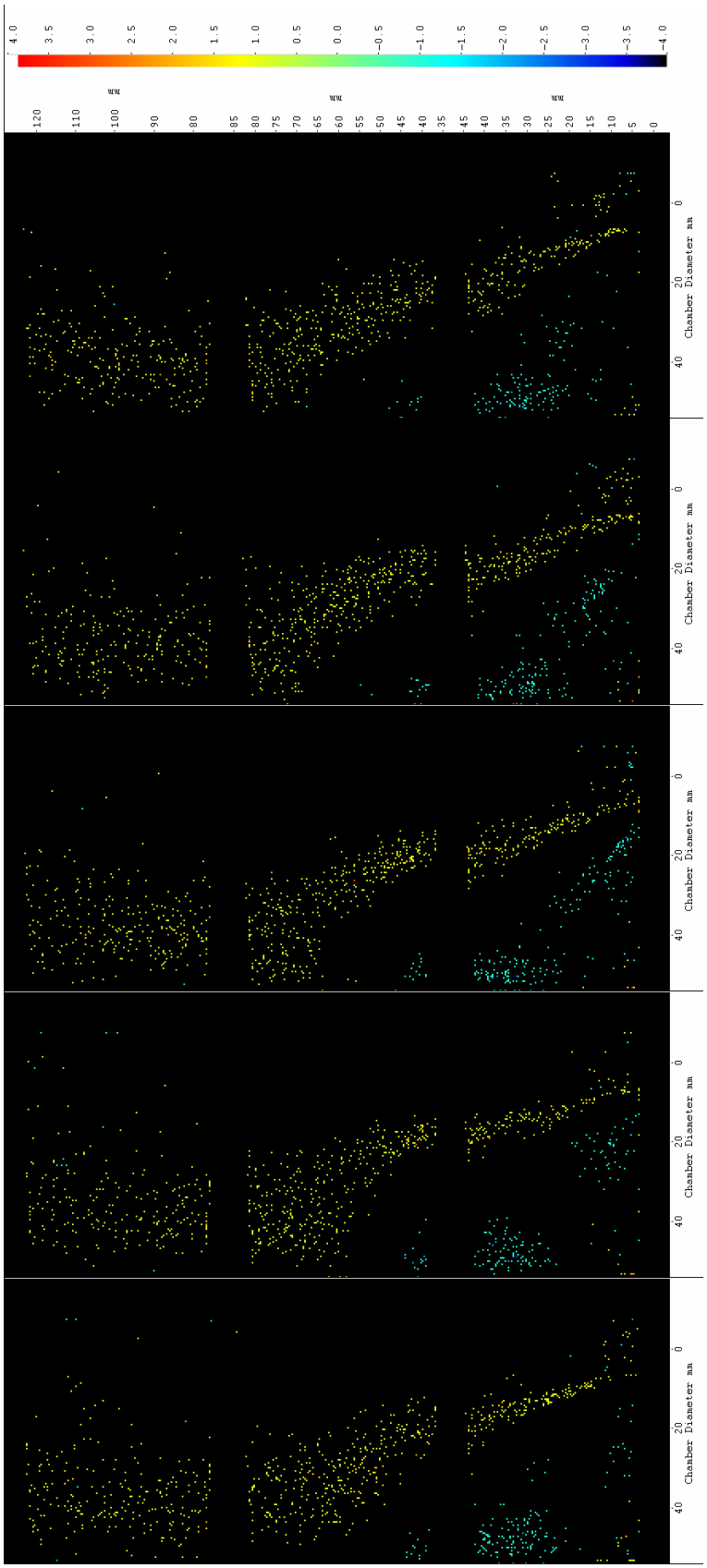

Figure B.29 Summation images showing location of detected vortices for f10-400Hz for phases 2 (Bottom), 4, 6, 8, and 10 (Top). Positive values correspond to clockwise vortices and negative values correspond to anticlockwise vortices.

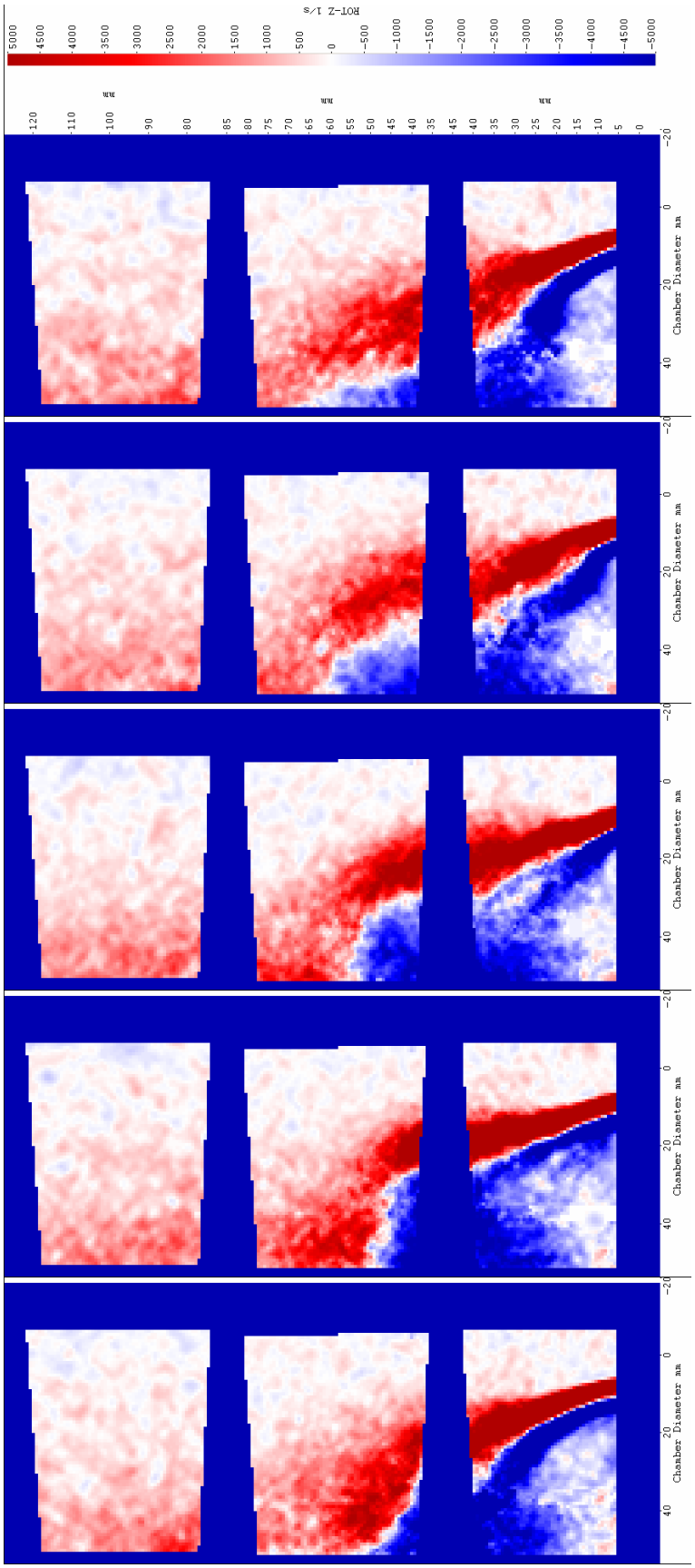

Figure B.30 Mean Vorticity images of f10-400Hz for phases 2 (Bottom), 4, 6, 8 and 10 (Top). Clockwise (positive) and anticlockwise (negative) vorticity are artificially saturated at $5000s^{-1}$.